AAAS

Science



SPECIAL ISSUE

A QUANTUM WORLD

100 years of the Schrödinger equation

4 DECEMBER 2025

Can fixing the brain's plumbing system ease dementia? p. 968

Wildlife crime standards reform in China p. 993

Antimicrobial resistance pre- and postantibiotic era p. 1015



Your bridge to successful innovation.

NEB's Customized Solutions Team is here to help, and serves as a bridge to the support and resources you need to ensure your success.

Creating the right partnership is essential when pioneering a new life science product. Every aspect of development – technical expertise, reagent optimization, manufacturing scale, turnaround time, reagent quality, and comprehensive logistical support – is vital for achieving your objectives. And in the regulated markets landscape, these challenges magnify, demanding an even more specialized approach.

Your Bridge to Successful Innovation

- Leverage NEB's 50 years of experience in enzymology and reagent manufacturing
- As an extension of your team, we prioritize a deep understanding of your objectives, work with you on an optimal solution, and help to anticipate your future needs
- Benefit from our ISO 9001- and 13485-certified processes and commitment to quality, as well as our GMP-grade* production facility, and specialized lyophilization facility for the highest quality production standards
- Access unparalleled support from our dedicated account managers, program managers, technical scientists and production teams
- We work closely with you on inventory management and global distribution through our network of NEB-owned subsidiaries, to ensure successful commercialization

NEB's Customized Solutions Team will help you access novel products, meet quality specifications, speed time to market, and streamline your supply chain, allowing you to focus more on what matters most — innovation.

Ready to start the discussion? Learn more at
www.neb.com/customizedsolutions.

NEW ENGLAND Biolabs®

** "GMP-grade" is a branding term NEB uses to describe products manufactured or finished at NEB's Rowley facility. The Rowley facility was designed to manufacture products under more rigorous infrastructure and process controls to achieve more stringent product specifications and customer requirements. Products manufactured at NEB's Rowley facility are manufactured in compliance with ISO 9001 and ISO 13485 quality management system standards. However, at this time, NEB does not manufacture or sell products known as Active Pharmaceutical Ingredients (APIs), nor does NEB manufacture its products in compliance with all of the Current Good Manufacturing Practice regulations.*

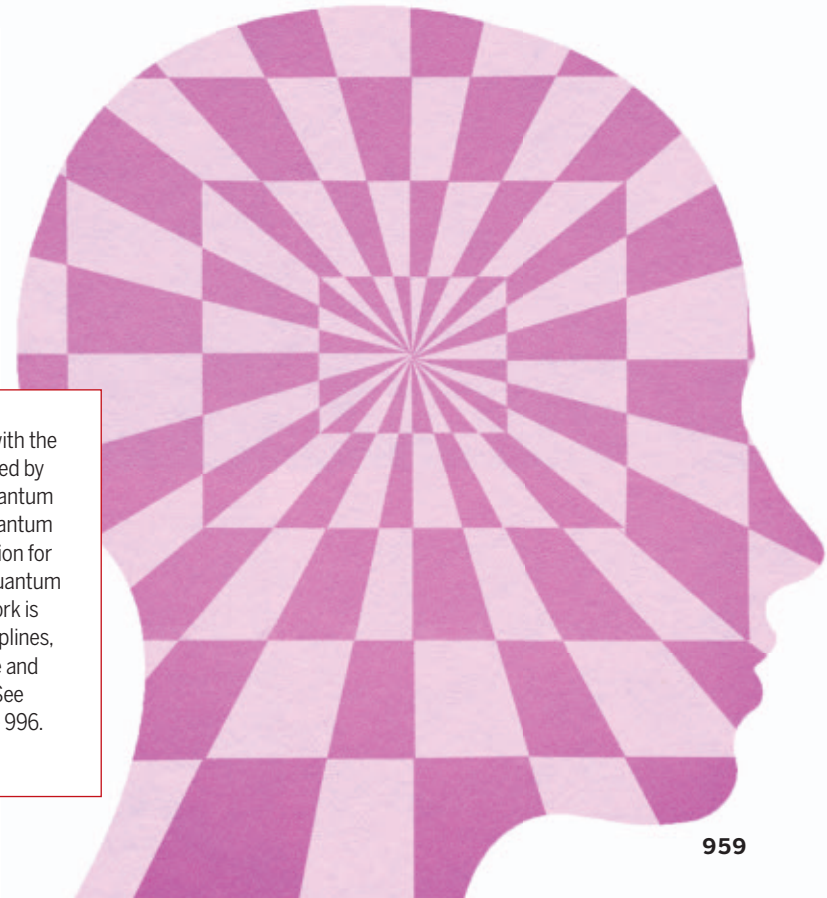
CONTENTS

4 DECEMBER 2025 | VOLUME 390 | ISSUE 6777

SPECIAL ISSUE

A QUANTUM WORLD





INTRODUCTION

996 A quantum centenary —S. Jin *et al.*

FEATURES

978 Putting the U in quantum
A century after the birth of quantum mechanics, its puzzles are pushing physicists to redefine reality—with themselves at the center
—Z. Savitsky PODCAST

PERSPECTIVES

998 One hundred years of quantum mechanics
Quantum mechanics has gone from a theory in test to becoming the foundation of new technologies —M. O. Scully and W. G. Unruh

1000 Dawn of quantum simulators
Large-scale quantum processors are beginning to uncover new physical phenomena —P. Roushan and L. Martin

1002 Cracking chemistry with quantum simulations
Dynamic characteristics of complex chemical reactions can be accurately modeled by a quantum computer
—P. Schleich and A. Aspuru-Guzik

REVIEWS

1004 Challenges and opportunities for quantum information hardware
—D. D. Awschalom *et al.*

ON THE COVER



The Schrödinger equation, together with the associated wave function often denoted by the Greek letter Ψ, is at the core of quantum mechanics. Over the past century, quantum mechanics has served as the foundation for modern physics theories, including quantum field theory. The theoretical groundwork is now being transformed into new disciplines, such as quantum information science and technology, and quantum materials. See the special section beginning on page 996. Credit: Deena So'Oteh

ILLUSTRATION: DEENA SO'OTEH

CALL FOR PAPERS

SPJ
SCIENCE PARTNER JOURNALS



Civil Engineering Sciences

OPEN ACCESS

Civil Engineering Sciences is an Open Access journal published in affiliation with the China Civil Engineering Society (CCES) and Tsinghua University (THU) and distributed by the American Association for the Advancement of Science (AAAS). The journal aims to publish cutting-edge research on scientific discoveries and technological innovations driven by major civil engineering needs, as well as breakthroughs in civil engineering technology resulting from new scientific discoveries.

The Science Partner Journals (SPJ) program was established by the American Association for the Advancement of Science (AAAS), the nonprofit publisher of the *Science* family of journals. The SPJ program features high-quality, online-only, open access publications produced in collaboration with international research institutions, foundations, funders and societies. Through these collaborations, AAAS expands its efforts to communicate science broadly and for the benefit of all people by providing top-tier international research organizations with the technology, visibility and publishing expertise that AAAS is uniquely positioned to offer as the world's largest general science membership society.

Submit your research to *Civil Engineering Sciences* today!
Learn more at: **spj.science.org/journal/cesci**

@SPJournals @SPJournals @SPJournals

ARTICLE PROCESSING FEES WAIVED THROUGH DECEMBER 2028

EDITORIAL

965 Accelerating science with AI
—D. Gil and K. A. Moler

NEWS

968 Experimental treatments target the brain's 'plumbing'
Animal studies—and controversial human surgeries—aim to boost fluid clearance to fight neurological disease —J. Smith

970 'Functional cure' for HIV comes closer to reality
Studies finger specific immune response that helps some people control the virus without drugs —J. Cohen

972 States step up to democratize AI-tailored computers
New York state is building AI-ready machines for researchers who lack access to federal or corporate supercomputers —C. Zhao

973 Abandoned antiviral shows promise against dengue
Big Pharma maker won't bring drug to maket for crippling disease —G. Vogel

975 DOE boost for AI, fusion could squeeze basic research
Reorganization could shift mission of the largest U.S. funder of physical sciences —A. Cho

976 Can a smaller U.S. National Academies remain relevant?
Loss of federal support leads to staff layoffs and fewer committees of outside experts —J. Mervis

COMMENTARY

PERSPECTIVES

983 Political persuasion by artificial intelligence
Large-scale studies of persuasive artificial intelligence reveal an extensive threat of misinformation —L.P. Argyle
RESEARCH SUMMARY p. 1016

984 Molecular basis of DNA cross-linking by bacteria
The structure of the bacterial genotoxin colibactin bound to DNA shows how it might contribute to cancer risk —O. D. Schärer
RESEARCH SUMMARY p. 1017

986 A vision of chromosome organization
Cryogenic electron tomography of condensed chromatin enables multiscale analysis of its structure —K. Zhang and V. Ramani
RESEARCH SUMMARY p. 1018

987 A tale of two forms of cohesin in DNA repair
Extrusive and cohesive cohesin cooperate to repair double-strand breaks in DNA —J. Hu
RESEARCH SUMMARIES pp. 1019 & 1020

BOOKS ET AL.

989 Centering disabled perspectives in technology
Medical testing and devices must be reimagined to combat ableism, argues a disability scholar —J. Flowers

990 Painting the phylogeny of life
An evolutionary biologist invites readers to travel back in time to meet humanity's distant ancestors —Y. Wong

LETTERS

991 SAFE Act hinders US-China collaboration
—A. J. Yang *et al.*

991 Smart irrigation needs smart policies in Iran
—A. Gohari *et al.*

992 Address domestic pressures on endangered species —C. A. Emogor

ANALYSIS

POLICY ARTICLE

993 Toward science-based conviction criteria to deter wildlife crime
Risk assessment is needed for China's new conviction standards based on monetary value —R. Hu *et al.*

RESEARCH

HIGHLIGHTS

1012 From *Science* and other journals

RESEARCH SUMMARIES

1015 Antibiotic resistance
Pre- and postantibiotic epoch: The historical spread of antimicrobial resistance —A. Cazares *et al.*

1016 Large language models
The levers of political persuasion with conversational artificial intelligence —K. Hackenburg *et al.*
PERSPECTIVE p. 983

1017 DNA damage
The specificity and structure of DNA cross-linking by the gut bacterial genotoxin colibactin —E. S. Carlson *et al.*
PERSPECTIVE p. 984

1018 Molecular biology
Multiscale structure of chromatin condensates explains phase separation and material properties —H. Zhou *et al.*
PERSPECTIVE p. 986

Molecular biology

1019 Cohesin drives chromatin scanning during the RAD51-mediated homology search —A. Marin-Gonzalez *et al.*

1020 Cohesin guides homology search during DNA repair using loops and sister chromatid linkages —F. Teloni *et al.*
PERSPECTIVE p. 987

RESEARCH ARTICLES

1021 Solar cells
Improved solvent systems for commercially viable perovskite photovoltaic modules —Y. Wang *et al.*

1029 Neutrino physics
Constraints on lepton number violation with the 2 tonne · year CUORE dataset —CUORE Collaboration

1033 Phase transitions
Hexatic phase in covalent two-dimensional silver iodide —T. A. Bui *et al.*

1038 Synthetic biology
High-fidelity human chromosome transfer and elimination —G. Petris *et al.*

1044 Actuators
Semiseparated biphasic bicontinuous dielectric elastomer for high-performance artificial muscle —X. Shi *et al.*

1050 Biocatalysis
Biocatalytic, asymmetric radical hydrogenation of unactivated alkenes —J. Vallapurackal *et al.*

1057 Materials design
A stoichiometrically conserved homologous series with infinite structural diversity —H. Zhao *et al.*

1064 Plant science
Cell wall patterning regulates plant stem cell dynamics —X. Zhu *et al.*

WORKING LIFE

1074 A writing pact —A. Shah

964 *Science* Staff
1071 New Products
1072 *Science* Careers

Science **serves as a forum for discussion of important issues related to the advancement of science by publishing material on which a consensus has been reached as well as including the presentation of minority or conflicting points of view. Accordingly, all articles published in *Science*—including editorials, news, commentary, and book reviews—are signed and reflect the individual views of the authors and not official points of view adopted by AAAS or the institutions with which the authors are affiliated.** *Science* (ISSN 0036-8075) is published weekly on Thursday, except last week in December, by the American Association for the Advancement of Science, 1200 New York Avenue, NW, Washington, DC 20005. Periodicals mail postage (publication No. 484460) paid at Washington, DC, and additional mailing offices. Copyright © 2025 by the American Association for the Advancement of Science. The title *Science* is a registered trademark of the AAAS. Domestic individual membership, including subscription (12 months): $165 ($74 allocated to subscription). Domestic institutional subscription (51 issues): $2865; Foreign postage extra: Air assist delivery: $135. First class, airmail, student, and emeritus rates on request. Canadian rates with GST available upon request, GST #125488122. Publications Mail Agreement Number 1069624. **Printed in the U.S.A. Change of address:** Allow 4 weeks, giving old and new addresses and 8-digit account number. **Postmaster:** Send change of address to AAAS, P.O. Box 96178, Washington, DC 20090–6178. **Single-copy sales:** $15 each plus shipping and handling available from backissues.science.org; bulk rate on request. **Authorization to reproduce** material for internal or personal use under circumstances not falling within the fair use provisions of the Copyright Act can be obtained through the Copyright Clearance Center (CCC), www.copyright.com. The identification code for *Science* is 0036-8075. *Science* is indexed in the *Reader's Guide to Periodical Literature* and in several specialized indexes.

Putting CAR-T therapy on the fast track



An ongoing research collaboration between Sartorius and University College London has captured major time and efficiency gains in CAR-T cell therapy production.

Since 2017, seven autologous chimeric antigen receptor (CAR) T-cell therapies—treatments that reengineer a patient's own immune cells to recognize and attack cancer—have gained FDA approval, transforming outcomes for many patients.

Yet as a treatment method, CAR-T therapy is not fully mature. Current applications remain largely restricted to a narrow range of blood cancers, including B-cell malignancies and multiple myeloma, while high costs and manufacturing complexities limit its availability even to eligible patients.

Nevertheless, CAR-T therapies are poised for significant growth as developers seek to extend the technology to solid tumors, autoimmune conditions, and other diseases. They're also looking into additional therapeutic cell types, including allogeneic T cells and natural killer cells.

Realizing these broader applications, however, depends on addressing fundamental bioprocessing bottlenecks. Encouragingly, recent results from a longstanding collaboration between Sartorius—a solutions provider for life science research and the biopharmaceutical industry—and the Cell and Gene Therapy Bioprocessing group at University College London (UCL), led by Qasim Rafiq, show considerable potential to do so.

Tricks of the trade

Many of the efficiency gains seen in other areas of bioproduction have yet to reach CAR-T cell manufacturing, highlighting clear opportunities for improvement. Still, the methods developed for large-scale bioprocessing of biologics or vaccines from cell lines do not directly translate to the autologous production of small batch, engineered T cells from individual patients.

Developers have also needed time to pinpoint which characteristics of CAR-T cell therapies drive lasting clinical benefit. "Obviously, there is an increased understanding around what clinicians are looking for in the final product, in terms of the marker profiles and phenotypes that work," says Nicola Bevan, manager of Application Development at Sartorius.

Clinical data indicate that CAR-T therapies are most effective when the infused cell product contains more long-lived, less-differentiated T cells and fewer exhausted or immunosuppressive ones. With this in mind, Sartorius and UCL collaborated to develop scalable bioprocessing strategies aimed at producing T cell products with phenotypic and functional attributes linked to improved clinical outcomes.

Accelerating growth

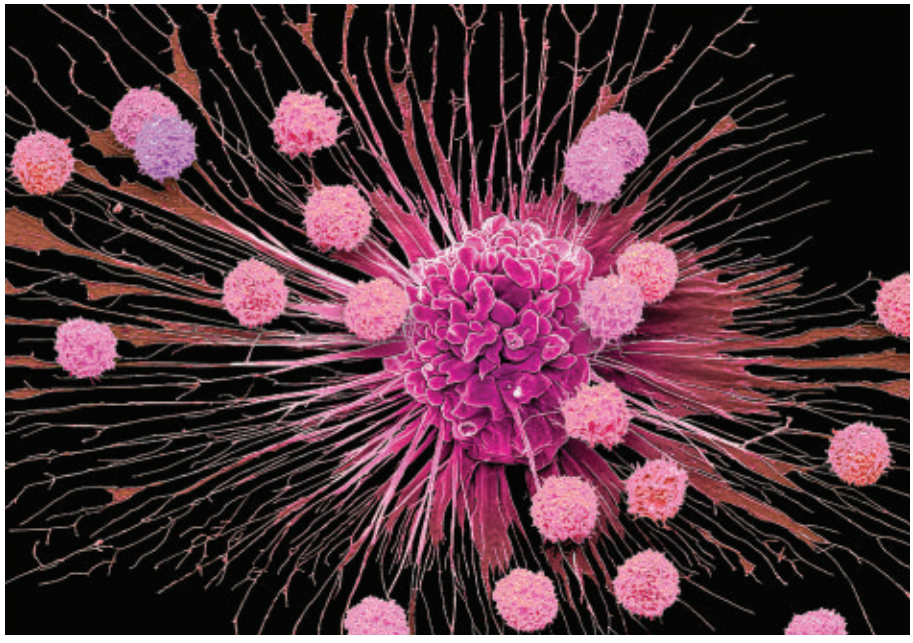
The field of cell therapy has relied on a variety of culture systems with different levels and types of agitation—from static vessels to stirred-tank and rocking-motion bioreactors—that impact T-cell expansion and phenotype. When Sartorius and UCL began their partnership, T cell therapies were just entering clinical use and little was known about their behavior in production environments. "The prevailing understanding was that T cells were fragile," says Bevan, "suggesting they could only be grown in the most gentle culture systems." However, Sartorius and UCL showed that T cells, including CAR-T cells, can be efficiently and reliably expanded in stirred-tank bioreactors without loss of quality or function.

Another major focus has been finding ways to grow patients' modified T cells more quickly, since reaching a sufficiently high cell density can be the slowest

IMAGE: PROVIDED BY SARTORIUS

step in the production process. The partners have shown that perfusion-based approaches—involving the continuous supply of fresh media to and removal of waste from a stirred-tank bioreactor—outperform conventional fed-batch methods, producing more cells in less time. By testing different perfusion rates and start times, they attained a 4.5-fold improvement in cell yield while cutting the time to reach the appropriate cell density by more than 50%. For patients with late-stage disease, speed is critical. "They don't have much time, and the focus is on generating the dose as quickly as possible," says Rafiq.

The team also developed a flexible perfusion strategy that adjusts to the growth dynamics of each individual CAR-T cell culture. This requires real-time visibility into the culture—tracking factors such as glucose consumption, lactate production, oxygen levels, and pH—and the ability to adjust the process in response to the data. "The way I like to frame it is to provide the cells with what they need when they need it," says Rafiq. The researchers learned that it was possible to reduce the perfusion rate as cell densities rise, and the culture's growth rate starts to slow. This resulted in an 11% reduction in the amount of media required without any effects on the quality of the final product. In a clinical production environment, those cost savings could be significant.



Tumor cells with immune cells.

The allogeneic opportunity

Real-time monitoring of cell cultures is increasingly recognized as an essential component for scaling CAR-T manufacturing processes. While autologous CAR-T therapies typically require smaller-scale systems—such as 250-mL stirred-tank bioreactors—to produce a personalized dose for a single patient, the need for accurate and continuous monitoring becomes more pronounced in the development of allogeneic CAR-T therapies.

Unlike autologous treatments, allogeneic therapies employ donor-derived T cells that are genetically engineered to reduce immune rejection. This enables large-scale production of standardized off-the-shelf products capable of serving multiple patients from a single manufacturing run.

Although no allogeneic CAR-T therapy has yet received regulatory approval, the promise of streamlined manufacturing continues to drive strong interest in the field. To this end, advanced analytical tools have become invaluable, offering real-time insights into key process parameters.

In the allogeneic setting, the emphasis shifts from rapid turnaround to quality and efficiency, aiming to produce multiple consistent, high-quality doses from a single batch. According to Rukmini Ladi, segment technology manager for Cell Therapy at Sartorius, the scale-up process has progressed smoothly. "We have successfully scaled our process from a 250-mL stirred-tank bioreactor to a 2-liter stirred-tank vessel while maintaining cell quality, phenotype, and expansion performance," says Ladi. "At the 2-liter scale, batch yields have reached levels that could correspond to more than 100 potential CAR-T doses, depending on clinical dose requirements and release specifications."

Real-time release?

In the autologous setting, Sartorius and UCL continue to seek new gains as well. Having established the possibility of cutting CAR-T expansion times in half, the partners now aim to reduce the entire CAR-T production cycle—from vein to vein—in half, by focusing on the other big bottleneck in the process, quality assurance.

It can take at least a week to complete the assays required to ensure that a given dose has the appropriate identity, potency, purity, and concentration. The ultimate goal is to improve production monitoring and control so that products can be released in real time, with little or no additional testing, as long as they stay within the proper quality limits. For now, that is a "utopian" ideal, says Rafiq.

In the meantime, Sartorius and UCL are looking at new functional approaches and new assays that will contribute to the development of a 'faster CAR'. By simplifying and streamlining complex production processes, they promise to bring the power and precision of CAR-T therapies to more patients.

Sponsored by

SARTORIUS

IMAGE: PROVIDED BY SARTORIUS

Science AAAS

EDITOR-IN-CHIEF Holden Thorp, hthorp@aaas.org

EXECUTIVE EDITOR Valda Vinson

EDITORS, RESEARCH Sacha Vignieri, Jake S. Yeston **EDITOR, COMMENTARY** Lisa D. Chong

DEPUTY EXECUTIVE EDITOR Lauren Kmec

DEPUTY EDITORS Stella M. Hurtley (UK), Phillip D. Szuromi **SENIOR EDITORS** Caroline Ash (UK), Michael A. Funk, Angela Hessler, Di Jiang, Priscilla N. Kelly, Marc S. Lavine (Canada), Sarah Lempriere (UK), Mattia Maroso, Yevgeniya Nusinovich, Ian S. Osborne (UK), Joana Osório (UK), L. Bryan Ray, H. Jesse Smith, Keith T. Smith (UK), Jelena Stajic, Peter Stern (UK), Yury V. Suleymanov, Valerie B. Thompson, Brad Wible **ASSOCIATE EDITORS** Jack Huang, Sumin Jin, Bianca Lopez, Sarah Ross (UK), Madeleine Seale (UK), Corinne Simonti, Ekeoma Uzogara **SENIOR LETTERS EDITOR** Jennifer Sills **NEWSLETTER EDITOR** Christie Wilcox **RESEARCH & DATA ANALYST** Jessica L. Slater **LEAD CONTENT PRODUCTION EDITORS** Chris Filiatreau, Harry Jach **SR. CONTENT PRODUCTION EDITOR** Amelia Beyna **CONTENT PRODUCTION EDITORS** Anne Abraham, Robert French, Julia Haber-Katris, Nida Masiulis, Abigail Shashikanth, Suzanne M. White **SENIOR PROGRAM ASSOCIATE** Maryrose Madrid **EDITORIAL MANAGER** Joi S. Granger **EDITORIAL ASSOCIATES** Aneera Dobbins, Lisa Johnson, Jerry Richardson, Anita Wynn **SENIOR EDITORIAL COORDINATORS** Alexander Kief, Ronmel Navas, Isabel Schnaidt, Alice Whaley (UK), Brian White **EDITORIAL COORDINATORS** Samuel Bates, Clair Goodhead (UK), Kat Kirkman, Daniel Young **ADMINISTRATIVE COORDINATOR** Karalee P. Rogers **ASI DIRECTOR, OPERATIONS** Janet Clements (UK) **ASI OFFICE MANAGER** Carly Hayward (UK) **ASI SR. OFFICE ADMINISTRATORS** Simon Brignell (UK), Jessica Waldock (UK) **COMMUNICATIONS DIRECTOR** Meagan Phelan **DEPUTY DIRECTOR** Matthew Wright **SENIOR WRITERS** Walter Beckwith, Joseph Cariz, Abigail Eisenstadt **WRITER** Mahathi Ramaswamy **SENIOR COMMUNICATIONS ASSOCIATES** Zachary Graber, Sarah Woods **COMMUNICATIONS ASSOCIATES** Kiara Brooks, Haley Riley, Mackenzie Williams

NEWS EDITOR Tim Appenzeller

NEWS MANAGING EDITOR John Travis **INTERNATIONAL EDITOR** David Malakoff **DEPUTY NEWS EDITORS** Rachel Bernstein, Martin Enserink, David Grimm, Eric Hand, Michael Price, Kelly Servick, Matt Warren (Europe) **SENIOR CORRESPONDENTS** Daniel Clery (UK), Jon Cohen, Jeffrey Mervis **ASSOCIATE EDITORS** Michael Greshko, Katie Langin **NEWS REPORTERS** Jeffrey Brainard, Adrian Cho, Phie Jacobs, Jocelyn Kaiser, Robert F. Service, Jennie Erin Smith, Erik Stokstad, Paul Voosen **CONSULTING EDITOR** Elizabeth Culotta **CONTRIBUTING CORRESPONDENTS** Vaishnavi Chandrashekhar, Dan Charles, Warren Cornwall, Andrew Curry (Berlin), Ann Gibbons, Kai Kupferschmidt (Berlin), Andrew Lawler, Mitch Leslie, Virginia Morell, Dennis Normile (Tokyo), Catherine Offord, Cathleen O'Grady, Elisabeth Pain (Careers), Charles Piller, Zack Savitsky, Richard Stone (Senior Asia Correspondent), Gretchen Vogel (Berlin), Lizzie Wade (Mexico City) **INTERNS** Celina Zhao **COPY EDITORS** Julia Cole (Senior Copy Editor), Hannah Knighton, Cyra Master (Copy Chief) **ADMINISTRATIVE SUPPORT** Meagan Weiland

CREATIVE DIRECTOR Beth Rakouskas

DESIGN MANAGING EDITOR Chrystal Smith **GRAPHICS MANAGING EDITOR** Chris Bickel **PHOTOGRAPHY MANAGING EDITOR** Emily Petersen **MULTIMEDIA MANAGING PRODUCER** Kevin McLean **DIGITAL DIRECTOR** Kara Estelle-Powers **DESIGN EDITOR** Marcy Atarod **DESIGNER** Noelle Jessup **SENIOR SCIENTIFIC ILLUSTRATOR** Noelle Burgess **SCIENTIFIC ILLUSTRATORS** Austin Fisher, Kellie Holoski, Ashley Mastin **SENIOR GRAPHICS EDITOR** Monica Hersher **GRAPHICS EDITOR** Veronica Penney **SENIOR PHOTO EDITOR** Charles Borst **PHOTO EDITOR** Elizabeth Billman **SENIOR PODCAST PRODUCER** Sarah Crespi **SENIOR VIDEO PRODUCER** Meagan Cantwell **SOCIAL MEDIA STRATEGIST** Jessica Hubbard **SOCIAL MEDIA PRODUCER** Sabrina Jenkins **WEB DESIGNER** Jennie Pajerowski

CHIEF EXECUTIVE OFFICER AND EXECUTIVE PUBLISHER

Sudip Parikh

PUBLISHER, SCIENCE FAMILY OF JOURNALS Bill Moran

DIRECTOR, BUSINESS OPERATIONS & ANALYSIS Eric Knott **MANAGER, BUSINESS OPERATIONS** Jessica Tierney **SENIOR MANAGER, BUSINESS ANALYSIS** Cory Lipman **BUSINESS ANALYSTS** Kurt Ennis, Maggie Clark, Isacco Fusi **BUSINESS OPERATIONS ADMINISTRATOR** Taylor Fisher **DIGITAL SPECIALIST** Marissa Zuckerman **ASSOCIATE DIRECTOR OF PRODUCTION AND PLATFORM** Jason Hillman **SENIOR MANAGER, PUBLISHING AND CONTENT SYSTEMS** Marcus Spiegler **CONTENT OPERATIONS MANAGER** Rebecca Doshi **PUBLISHING PLATFORM MANAGER** Jessica Loayza **PUBLISHING SYSTEMS SPECIALIST, PROJECT COORDINATOR** Jacob Hedrick **SENIOR PRODUCTION SPECIALIST** Kristin Wowk **PRODUCTION SPECIALISTS** Kelsey Cartelli, Audrey Diggs **SPECIAL PROJECTS ASSOCIATE** Shantel Agnew

MARKETING DIRECTOR Sharice Collins **ASSOCIATE DIRECTOR, MARKETING** Justin Sawyers **GLOBAL MARKETING MANAGER** Allison Pritchard **ASSOCIATE DIRECTOR, MARKETING SYSTEMS & STRATEGY** Aimee Aponte **SENIOR MARKETING MANAGER** Shawana Arnold **MARKETING MANAGER** Ashley Evans **MARKETING ASSOCIATES** Hugues Beaulieu, Ashley Hylton, Lorena Chirinos Rodriguez, Jenna Voris **MARKETING ASSISTANT** Courtney Ford **SENIOR DESIGNER** Kim Huynh

DIRECTOR AND SENIOR EDITOR, CUSTOM PUBLISHING Erika Gebel Berg **ADVERTISING PRODUCTION OPERATIONS MANAGER** Deborah Tompkins **DESIGNER, CUSTOM PUBLISHING** Jeremy Huntsinger **SENIOR TRAFFIC ASSOCIATE** Christine Hall

DIRECTOR, PRODUCT MANAGEMENT Kris Bishop **PRODUCT DEVELOPMENT MANAGER** Scott Chernoff **ASSOCIATE DIRECTOR, PUBLISHING INTELLIGENCE** Rasmus Andersen **SR. PRODUCT ASSOCIATE** Robert Koepke **PRODUCT ASSOCIATES** Caroline Breul, Anne Mason

ASSOCIATE DIRECTOR, INSTITUTIONAL LICENSING MARKETING Kess Knight **ASSOCIATE DIRECTOR, INSTITUTIONAL LICENSING SALES** Ryan Rexroth **INSTITUTIONAL LICENSING MANAGER** Nazim Mohammedi, Claudia Paulsen-Young **SENIOR MANAGER, INSTITUTIONAL LICENSING OPERATIONS** Judy Lillibridge **MANAGER, RENEWAL & RETENTION** Lana Guz **SYSTEMS & OPERATIONS ANALYST** Ben Teincuff **FULFILLMENT ANALYST** Aminta Reyes

ASSOCIATE DIRECTOR, INTERNATIONAL Roger Goncalves **ASSOCIATE DIRECTOR, US ADVERTISING** Stephanie O'Connor **US MID WEST, MID ATLANTIC AND SOUTH EAST SALES MANAGER** Chris Hoag **DIRECTOR, OUTREACH AND STRATEGIC PARTNERSHIPS, ASIA** Shoupeng Liu **SALES REP, ROW** Sarah Lelarge **SALES ADMIN ASSISTANT, ROW** Victoria Glasbey **DIRECTOR OF GLOBAL COLLABORATION AND ACADEMIC PUBLISHING RELATIONS, ASIA** Xiaoying Chu **ASSOCIATE DIRECTOR, INTERNATIONAL COLLABORATION** Grace Yao **SALES MANAGER** Danny Zhao **MARKETING MANAGER** Kilo Lan **ASCA CORPORATION, JAPAN** Rie Rambelli (Tokyo), Miyuki Tani (Osaka)

DIRECTOR, COPYRIGHT, LICENSING AND SPECIAL PROJECTS Emilie David **RIGHTS AND PERMISSIONS ASSOCIATE** Elizabeth Sandler **LICENSING ASSOCIATE** Virginia Warren **RIGHTS AND LICENSING COORDINATOR** Dana James **CONTRACT SUPPORT SPECIALIST** Michael Wheeler

EDITORIAL
science_editors@aaas.org

NEWS
science_news@aaas.org

INFORMATION FOR AUTHORS
science.org/authors/
science-information-authors

REPRINTS AND PERMISSIONS
science.org/help/
reprints-and-permissions

MULTIMEDIA CONTACTS
SciencePodcast@aaas.org
ScienceVideo@aaas.org

MEDIA CONTACTS
scipak@aaas.org

PRODUCT ADVERTISING & CUSTOM PUBLISHING
advertising.science.org
science_advertising@aaas.org

CLASSIFIED ADVERTISING
advertising.science.org/
science-careers
advertise@sciencecareers.org

JOB POSTING CUSTOMER SERVICE
employers.sciencecareers.org
support@sciencecareers.org

MEMBERSHIP AND INDIVIDUAL SUBSCRIPTIONS
science.org/subscriptions

MEMBER BENEFITS
aaas.org/membership/
benefits

INSTITUTIONAL SALES AND SITE LICENSES
science.org/librarian

AAAS BOARD OF DIRECTORS

CHAIR Joseph S. Francisco

IMMEDIATE PAST PRESIDENT
Willie E. May

PRESIDENT
Theresa A. Maldonado

PRESIDENT-ELECT
Marina Picciotto

TREASURER Carolyn N. Ainslie

COUNCIL CHAIR
Ichiro Nishimura

CHIEF EXECUTIVE OFFICER
Sudip Parikh

BOARD
Mark Dingfield
Morton Ann Gernsbacher
Kathleen Hall Jamieson
Jane Maienschein
Babak Parviz
Gabriela Popescu
Juan S. Ramírez Lugo
Susan M. Rosenberg
Vassiliki Betty Smocovitis
Roger Wakimoto

BOARD OF REVIEWING EDITORS (Statistics board members indicated with **S**)

Erin Adams, *U. of Chicago*
Takuzo Aida, *U. of Tokyo*
Leslie Aiello, *Wenner-Gren Fdn.*
Anastassia Alexandrova, *UCLA*
Mohammed AlQuraishi, *Columbia U.*
James Analytis, *UC Berkeley*
Paola Arlotta, *Harvard U.*
Madan Babu, *St. Jude*
Jennifer Balch, *U. of Colorado*
Nenad Ban, *ETH Zürich*
Carolina Barillas-Mury, *NIH, NIAID*
Christopher Barratt, *U. of Dundee*
François Barthelat, *U. of Colorado Boulder*
Franz Bauer, *Universidad de Tarapacá*
Andreas Baumler, *UC Davis*
Carlo Beenakker, *Leiden U.*
Sarah Bergbreiter, *Carnegie Mellon U.*
Kiros T. Berhane, *Columbia U.*
Aude Bernheim, *Inst. Pasteur*
Joseph J. Berry, *NREL*
Aditi Bhargav, *UCSF*
Dominique Bonnet, *Francis Crick Inst.*
Chris Bowler, *École Normale Supérieure*
Ian Boyd, *U. of St. Andrews*
Malcolm Brenner, *Baylor Coll. of Med.*
Ron Brookmeyer, *UCLA* (**S**)
Christian Büchel, *UKE Hamburg*
Johannes Buchner, *TUM*
Dennis Burton, *Scripps Res.*
Carter Tribley Butts, *UC Irvine*
György Buzsáki, *NYU School of Med.*
Annmarie Carlton, *UC Irvine*
Jane Carlton, *Johns Hopkins U.*
Pedro Carvalho, *U. of Oxford*
Simon Cauchemez, *Inst. Pasteur*
Ling-Ling Chen, *SIBCB, CAS*
Hilde Cheroutre, *La Jolla Inst.*
Wendy Cho, *UIUC*
Ib Chorkendorff, *Denmark TU*
Chunaram Choudhary, *Københavns U.*
Karlene Cimprich, *Stanford U.*
Laura Colgin, *UT Austin*
James J. Collins, *MIT*
Robert Cook-Deegan, *Arizona State U.*
Carolyn Coyne, *Duke U.*
Roberta Croce, *VU Amsterdam*
Ismaila Dabo, *Penn State U.*
Nicolas Dauphas, *U. of Chicago*
Claude Desplan, *NYU*
Sandra Díaz, *U. Nacional de Córdoba*
Samuel Díaz-Muñoz, *UC Davis*
Ulrike Diebold, *TU Wien*
Stefanie Dimmeler, *Goethe-U. Frankfurt*
Hong Ding, *Inst. of Physics, CAS*
Dennis Discher, *UPenn*
Jennifer A. Doudna, *UC Berkeley*
Ruth Drdla-Schutting, *Med. U. Vienna*
Raissa M. D'Souza, *UC Davis*
Bruce Dunn, *UCLA*
William Dunphy, *Caltech*
Scott Edwards, *Harvard U.*
Todd A. Ehlers, *U. of Glasgow*
Tobias Erb, *MPS, MPI Terrestrial Microbiology*
Beate Escher, *UFZ & U. of Tübingen*
Barry Everitt, *U. of Cambridge*
Vanessa Ezenwa, *U. of Georgia*
Toren Finkel, *U. of Pitt. Med. Ctr.*
Natascha Förster Schreiber, *MPI Extraterrestrial Phys.*
Serita Frey, *U. of New Hampshire*
Elaine Fuchs, *Rockefeller U.*
Caixia Gao, *Inst. of Genetics and Developmental Bio., CAS*
Daniel Geschwind, *UCLA*
Lindsey Gillson, *U. of Cape Town*
Alemu Gonsamo Gosa, *McMaster U.*
Simon Greenhill, *U. of Auckland*
Gillian Griffiths, *U. of Cambridge*
Nicolas Gruber, *ETH Zürich*
Hua Guo, *U. of New Mexico*
Taekjip Ha, *Johns Hopkins U.*
Daniel Haber, *Mass. General Hos..*
Hamida Hammad, *VIB IRC*
Brian Hare, *Duke U.*
Kelley Harris, *U. of Wash*
Carl-Philipp Heisenberg, *IST Austria*
Emiel Hensen, *TU Eindhoven*
Christoph Hess, *U. of Basel & U. of Cambridge*
Brian Hie, *Stanford U.*
Heather Hickman, *NIAID, NIH*
Janneke Hille Ris Lambers, *ETH Zürich*
Kai-Uwe Hinrichs, *U. of Bremen*
Pinshane Huang, *UIUC*
Christina Hulbe, *U. of Otago, New Zealand*
Gwyneth Ingram, *ENS Lyon*
Darrell Irvine, *Scripps Res.*
Erich Jarvis, *Rockefeller U.*
Peter Jonas, *IST Austria*
Sheena Josselyn, *U. of Toronto*
Matt Kaeberlein, *U. of Wash.*
Daniel Kammen, *UC Berkeley*
Kisuk Kang, *Seoul Nat. U.*
Vedika Khemani, *Stanford U.*
V. Narry Kim, *Seoul Nat. U.*
Nancy Knowlton, *Smithsonian*
Etienne Koechlin, *École Normale Supérieure*
LaShanda Korley, *U. of Delaware*
Paul Kubes, *U. of Calgary*
Deborah Kurrasch, *U of Calgary*
Laura Lackner, *Northwestern U.*
Mitchell A. Lazar, *UPenn*
Hedwig Lee, *Duke U.*
Fei Li, *Xi'an Jiaotong U.*
Jianyu Li, *McGill U.*
Ryan Lively, *Georgia Tech*
Luis Liz-Marzán, *CIC biomaGUNE*
Omar Lizardo, *UCLA*
Jonathan Losos, *WUSTL*
Ke Lu, *Inst. of Metal Res., CAS*
Christian Lüscher, *U. of Geneva*
Jean Lynch-Stieglitz, *Georgia Tech*
David Lyons, *U. of Edinburgh*
Fabienne Mackay, *QIMR Berghofer*
Vidya Madhavan, *UIUC*
Anne Magurran, *U. of St. Andrews*
Oscar Marín, *King's Coll. London*
Matthew Marinella, *Arizona State U.*
Charles Marshall, *UC Berkeley*
Christopher Marx, *U. of Idaho*
Geraldine Masson, *CNRS*
Jennifer McElwain, *Trinity College Dublin*
Scott McIntosh, *NCAR*
Rodrigo Medellín, *U. Nacional Autónoma de México*
Mayank Mehta, *UCLA*
C. Jessica Metcalf, *Princeton U.*
Tom Misteli, *NCI, NIH*
Jeffery Molkentin, *Cincinnati Children's Hospital Medical Center*
Alison Motsinger-Reif, *NIEHS, NIH* (**S**)
Rosa Moysés, *U. of São Paulo School of Medicine*
Carey Nadell, *Dartmouth College*
Thi Hoang Duong Nguyen, *MRC LMB*
Pilar Ossorio, *U. of Wisconsin*
Andrew Oswald, *U. of Warwick*
Isabella Pagano, *Istituto Nazionale di Astrofisica*
Giovanni Parmigiani, *Dana-Farber* (**S**)
Zak Page, *UT Austin*
Pierre Paoletti, *Ecole Normale Supérieure, Paris*
Sergiu Pasca, *Stanford U.*
Julie Pfeiffer, *UT Southwestern Med. Ctr.*
Philip Phillips, *UIUC*
Matthieu Piel, *Inst. Curie*
Kathrin Plath, *UCLA*
Martin Plenio, *Ulm U.*
Katherine Pollard, *UCSF*
Elvira Poloczanska, *Alfred-Wegener-Inst.*
Julia Pongratz, *Ludwig Maximilians U.*
Philippe Poulin, *CNRS*
Suzie Pun, *U. of Wash*
Lei Stanley Qi, *Stanford U.*
Simona Radutoiu, *Aarhus U.*
Maanasa Raghavan, *U. of Chicago*
Trevor Robbins, *U. of Cambridge*
Adrienne Roeder, *Cornell U.*
Joeri Rogelj, *Imperial Coll. London*
John Rubenstein, *SickKids*
Sylvie Roke, *École Polytechnique Fédérale de Lausanne*
Yvette Running Horse Collin, *Toulouse U.*
Mike Ryan, *UT Austin*
Alberto Salleo, *Stanford U.*
Miquel Salmeron, *Lawrence Berkeley Nat. Lab*
Nitin Samarth, *Penn State U.*
Erica Ollmann Saphire, *La Jolla Inst.*
Joachim Saur, *U. zu Köln*
Alexander Schier, *Harvard U.*
Susannah Scott, *UC Santa Barbara*
Anuj Shah, *U. of Chicago*
Vladimir Shalaev, *Purdue U.*
Jie Shan, *Cornell U.*
Jay Shendure, *U. of Wash.*
Steve Sherwood, *U. of New South Wales*
Ken Shirasu, *RIKEN CSRS*
Robert Siliciano, *JHU School of Med.*
Emma Slack, *ETH Zürich & U. of Oxford*
Richard Smith, *UNC* (**S**)
Ivan Soltesz, *Stanford U.*
John Speakman, *U. of Aberdeen*
Allan C. Spradling, *Carnegie Institution for Sci.*
V. S. Subrahmanian, *Northwestern U.*
Sandip Sukhtankar, *U. of Virginia*
Tavneet Suri, *MIT*
Naomi Tague, *UC Santa Barbara*
A. Alec Talin, *Sandia Natl. Labs*
Patrick Tan, *Duke-NUS Med. School*
Sarah Teichmann, *Wellcome Sanger Inst.*
Dörthe Tetzlaff, *Leibniz Institute of Freshwater Ecology and Inland Fisheries*
Amanda Thomas, *UC Davis*
Rocio Titiunik, *Princeton U.*
Shubha Tole, *Tata Inst. of Fundamental Res.*
Maria-Elena Torres Padilla, *Helmholtz Zentrum München*
Kimani Toussaint, *Brown U.*
Barbara Treutlein, *ETH Zürich*
Li-Huei Tsai, *MIT*
Jason Tylianakis, *U. of Canterbury*
Matthew Vander Heiden, *MIT*
Jo Van Ginderachter, *VIB, U. of Ghent*
Ivo Vankelecom, *KU Leuven*
Henrique Veiga-Fernandes, *Champalimaud Fdn.*
Elizabeth Villa, *UC San Diego*
Bert Vogelstein, *Johns Hopkins U.*
David Wallach, *Weizmann Inst.*
Jane-Ling Wang, *UC Davis* (**S**)
Jessica Ware, *Amer. Mus. of Natural Hist.*
David Waxman, *Fudan U.*
Alex Webb, *U. of Cambridge*
Chris Wikle, *U. of Missouri* (**S**)
Ian A. Wilson, *Scripps Res.* (**S**)
Marjorie Weber, *U. of Michigan*
Sylvia Wirth, *ISC Marc Jeannerod*
Hao Wu, *Harvard U.*
Amir Yacoby, *Harvard U.*
Benjamin Youngblood, *St. Jude*
Kenneth Zaret, *UPenn School of Med.*
Lidong Zhao, *Beihang U.*
Bing Zhu, *Inst. of Biophysics, CAS*
Xiaowei Zhuang, *Harvard U.*
Maria Zuber, *MIT*

Accelerating science with AI

Darío Gil and **Kathryn A. Moler**

By successfully integrating artificial intelligence (AI) into research workflows, researchers could substantially increase scientific productivity. Last week's announcement from the White House of the US Genesis Mission sparks a critical conversation about how to realize this potential. That discussion should center on two parallel efforts—creating the integrated infrastructure, from data and algorithms to hardware and agentic control, needed to apply AI to speed up research; and determining the policies and resources that empower scientists to fuel the feedback loop of scientific advancement and AI innovation.

Success begins with asking the right scientific questions—identifying problems that may offer transformative breakthroughs and drive advances in AI methods and human-AI teaming, thereby inspiring broader acceleration of science. For example, in fusion energy, this means using AI to contain plasma that is hotter than the Sun by predicting plasma instabilities for real-time control. In molecules and materials, it means developing predictive models of dynamics and functionality for new discoveries. And on the quantum frontier, it means accelerating algorithm development to simulate nature and solve currently intractable problems.

The value of accelerating science with AI could extend to the entire economy.

Success will also depend on the data that fuel AI models. Consider the Protein Data Bank, which provided the dataset for protein structure prediction. That success was the culmination of decades of work and investment in the experimental tools, like advanced light sources, needed to generate data, and the open-access repository required to share the information. Major instruments like the Vera C. Rubin Observatory, the Advanced Photon Source, and the Large Hadron Collider provide a strong foundation with abundant, relatively structured data. The challenge is far more difficult for the vast, messy world of heterogeneous data across the research and development (R&D) enterprise, where varying standards and incomplete metadata create barriers to discovery. Transforming isolated datasets into a unified engine for discovery calls for a concerted effort by scientists, federal agencies, and other stakeholders to prepare existing data for AI use and establish standards so that future data are born accessible and AI ready.

The next generation of scientists will need computing infrastructure that unites exascale high-performance computing, specialized AI, quantum supercomputers, secure networks, on-demand cloud computing power, and storage for massive datasets. Connections to devices, such as sensors and controllers, and specialized AI algorithms on such devices will enable real-time data acquisition and control of live experiments.

Going beyond general-purpose, language-based AI, specialized models will combine the learning capabilities of AI with the physical predictive capabilities of traditional simulations, grounded in the natural laws of physics and chemistry. Crucially, these models will augment, not replace, trusted scientific models, including checkpoints to validate or correct AI-generated results against known physical models and real-world data. Coupling hybrid models with scientific agents—AI systems that autonomously coordinate some steps of research, but under human direction—promises to compress discovery timelines, as data from each AI analysis feed a self-reinforcing cycle of improvement.

For AI to be a true partner in science, scientists must use it to produce verifiable results, with data, methodologies, code, and outputs available for public scrutiny. This requires researchers, institutions, academic journals, and funding agencies to foster open-source models, standardized tools, and ready-to-use data.

Accelerating science with AI will depend on both public and private funding. The total annual investment in US R&D is a trillion dollars, an amount that is often underappreciated. Although the federal government plays an indispensable role in catalyzing fundamental research, supporting research-based education, and enabling long-term, high-risk projects, more than 70% of this collective support comes from the private sector. Strategic public-private partnerships can amplify the value of the government's foundational role with the private sector's resources and capacity for innovation. Now is the time to pilot new forms of partnerships, such as joint investments in computing infrastructure, frameworks for data sharing, and collaborations focused on problems that develop new methods of AI-enabled discovery.

The value of accelerating science with AI could extend to the entire economy. R&D, currently at 3.5% of the US gross domestic product, is a powerful economic engine, generating returns far exceeding its cost. By empowering researchers across all disciplines and institutions to accelerate science and engineering, AI could increase the productivity and impact of research, boost innovation, fuel economic growth, and improve people's lives. That is the ultimate promise of this new era of discovery. □

Darío Gil is the undersecretary for Science, US Department of Energy, Washington, DC, USA, and director of the Genesis Mission. undersecretaryforscience@hq.doe.gov **Kathryn A. Moler** is the Marvin Chodorow Professor and a professor in the Departments of Applied Physics, Physics, and Energy Science and Engineering, Stanford University, Stanford, CA, USA. kmoler@stanford.edu

Published online 25 November 2025; 10.1126/science.aee0605

Making labs more sustainable with biobased microcentrifuge tubes



Eppendorf Safe-Lock Tubes BioBased in 0.5, 1.5, and 2.0 mL sizes.

The iconic "Eppendorf tube" has gotten a sustainability make-over, becoming 100% biobased while maintaining high quality and performance.

There's no escaping plastic in the laboratory. Lightweight and durable plastic pipette tips, conical tubes, microcentrifuge tubes, and PCR plates allow scientists to make discoveries and run routine processes every day. But these convenient consumables come at a cost to the environment, as most are made with fossil fuel–sourced materials. According to the United Nations, general plastic production with fossil fuels produced 3.4 percent of the global greenhouse gas emissions in 2019.

Concerns about laboratory plastic have reached the ears of scientists and professionals at consumables companies, who want to help customers achieve their sustainability goals. "A growing number of customers are asking us what Eppendorf is doing with respect to sustainability," says Hanae Koenig, global marketing manager at Eppendorf. "We need plastic in the lab, so it's something we have to address."

The company has examined every aspect of production. "We started years ago, changing the set-up of our buildings, using renewable energies, reducing water usage and waste—not only in our offices, but also in our production facilities," says Jan Bebermeier, global marketing manager at Eppendorf. And with the recent introduction of their biobased line of products, the company has extended this eco-friendly perspective to their tubes, tips, and plates.

From the kitchen to the lab

The plastic in the biobased line is derived from renewable, second-generation feedstocks such as waste cooking oil and inedible, leftover plant residues. These materials undergo four steps on the way to becoming a bioplastic. To transform into polypropylene, for example, the materials are pretreated to remove impurities and water, and then oxygen is removed. Next, the material is cracked, or broken down into short-chain hydrocarbons, in a process similar to the cracking of fossil fuels. Finally, one of those hydrocarbons, propene, is polymerized to produce polypropylene granules that can be molded and shaped into many different products. The biobased polycarbonate and polyethylene are produced in the same way.

Demonstrating its commitment to more sustainable consumables, Eppendorf has introduced new products to the biobased line every year since 2022, when they released Eppendorf Tubes BioBased. These screw-capped tubes range in volume from 5 mL to 50 mL, and the tubes themselves are comprised of at least 90% biobased plastic (based on mass balance approach). The caps are still made from fossil-sourced materials, but the company plans to convert them to a biobased polyethylene in the future. Several sizes of sterile epT.I.P.S. BioBased, made of 100% biobased polypropylene, debuted the following year. The pipette filter tips fit into the reusable epT.I.P.S. Box 2.0 as reload systems or as bulkware. Made from a combination of biobased polypropylene and polycarbonate, Eppendorf twin.tec Trace PCR Plates BioBased were introduced in 2024 for use in robotic systems. They are comprised of at least 86% biobased plastic on average (77% for the polycarbonate + 100% for polypropylene, based on mass balance approach).

An iconic transformation

This year, Eppendorf microcentrifuge tubes received the bio treatment with the introduction of Safe-Lock Tubes BioBased.

PHOTO: PROVIDED BY EPPENDORF

The 100% biobased plastic microcentrifuge tubes are available in 0.5 mL, 1.5 mL, and 2.0 mL volumes. The raw material and production facilities are ISCC Plus certified, ensuring that the product is made from renewable raw materials. The organization My Green Lab has given the tubes the ACT label.

Creating a biobased microcentrifuge tube presented challenges, however. "The Safe-Lock tube is not as simple of a product as most people think it is," says Andrei Schischokin, development engineer at Eppendorf. "We have very high standards for the tube, and it's difficult to find the right polymer. It's also very important that we can use it in the same injection molds we already use." As prototypes were created in the molding process, parameters like temperature were tweaked to produce a high-quality product that functions like the original fossil-sourced tubes. Fortunately, Schischokin and his team identified the right polymer and conditions for Safe-Lock Tubes BioBased within just a few months.



Eppendorf's biobased materials have the same performance as their fossil-sourced counterparts.

PHOTO: PROVIDED BY EPPENDORF

Putting the new tubes through their paces

To ensure the new microcentrifuge tubes would perform the same way as those made of fossil-sourced materials, Jana Schmidt and her team ran them through many tests. "My team's job is to be the customer inside the company," says Schmidt, who is a senior application specialist at Eppendorf.

Internally, the team tested everything from whether the lids were just as tight to whether the tubes could withstand centrifugation forces and high- and low-temperature incubations. "Basically, every standard test that any lab consumable needs to undergo, the biobased consumables also need to undergo," says Schmidt. "We're treating it as a new product even though, chemically speaking, we know it's the same." The Safe-Lock Tubes BioBased performed as well as those made from fossil fuels.

The next step was to give the tubes out to 18 scientists at external academic, government, and pharmaceutical research labs around the world for testing. The scientists used them in myriad methods and applications, including PCR prep, GC-MS, proteomics, bacterial culture, and long-term storage.

"The feedback was that the Safe-Lock Tubes BioBased worked exactly the same as the ones they had been using," says Schmidt. In fact, the scientists said they preferred the biobased version because they didn't have to sacrifice performance to be sustainable. "If we take the fear out of whether it is the same, they said they could finally start thinking about sustainability," she says.

Remaining challenges

Plastic laboratory consumables have come a long way in terms of sustainability, but there's more to be done. "The big question is still: What can we do after the product is used?" says Bebermeier. "It's contaminated, so it's not as easy as recycling plastic containers at home, but in principle, you really have to cover the complete picture."

Recycling used plastic lab consumables is made even more challenging by pressure to close the loop. However, in most cases, lab waste must be incinerated because it is contaminated with chemicals and biological materials. Burning waste emits carbon and the result is a non-recyclable material.

Manufacturing any plastic, whether conventional or biobased, emits the greenhouse gas carbon dioxide, but biobased plastics provide carbon savings compared to fossil-sourced plastics. According to a life cycle analysis by Eppendorf, each 5 mL tube has an 18% lower carbon footprint than its conventional counterpart—a modest change individually, but one that adds up across global use. Eppendorf is working on lowering carbon emissions with the biobased plastic manufacturing process, but at this point, the main sustainability benefit is in reusing waste—second-generation feedstocks—to make the materials, instead of "plasticizing" limited fossil resources.

Perhaps the largest hurdle is convincing researchers that now is the time to switch to more sustainable consumables. "Most customers really want to change, but they just don't know where to start," says Bebermeier. "We need to share the message that there are options, and it's something scientists can change today."

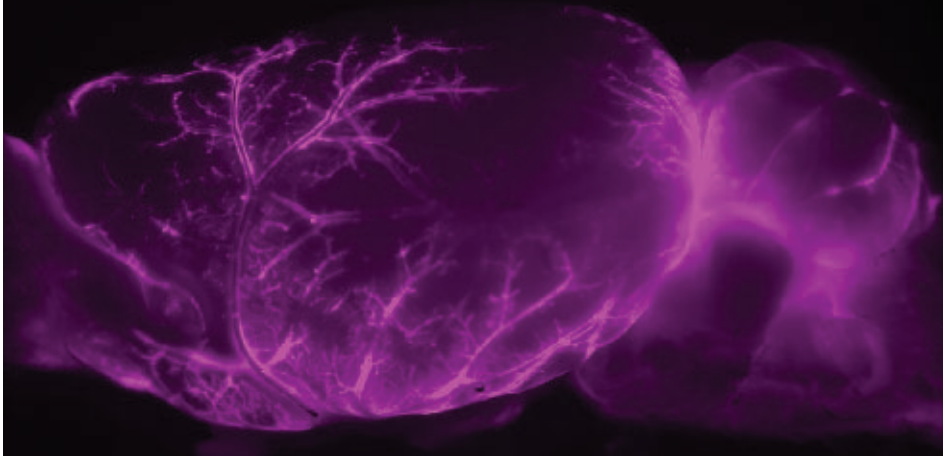
Sponsored by

eppendorf

BIOMEDICINE

Experimental treatments target the brain's 'plumbing'

Animal studies—and controversial human surgeries—aim to boost fluid clearance to fight neurological disease **JENNIE ERIN SMITH**



Bolstering glymphatic pathways, shown in the brain of a mouse, is a possible strategy for treating Alzheimer's and other diseases.

More than a decade ago, when researchers discovered a ghostly network of microscopic channels that push fluid through the brain, they began to wonder whether the brain's plumbing, as they sometimes refer to it, might be implicated in neurodegenerative diseases such as Alzheimer's. Now, they are testing a host of ways to improve it.

At the Society for Neuroscience (SfN) meeting last month in San Diego, several teams reported early promise for drugs and other measures that improve fluid flow, showing they can remove toxic proteins from animal or human brains and reverse symptoms in mouse models of neurological disease.

Plastic surgeons in China, meanwhile, have gone further, conducting experimental surgeries that they say help flush out disease-related proteins in people with Alzheimer's. The trials have generated excitement but also concern over their bold claims of success. A group of academic surgeons in the United States is planning what they say will be a more rigorous clinical trial, also in Alzheimer's patients, that could begin recruiting as early as next year.

The surgical approach "sounds unbelievable," says neuroscientist Jeffrey Iliff of the University of Washington. "But I'm not going to say I know it can't work. Remember, 13 years ago we didn't know any of this existed."

In 2012, Iliff, with pioneering Danish neuroscientist Maiken Nedergaard and colleagues, described a previously unrecognized set of fluid channels in the brain that they dubbed the glymphatic system. Three years later, other groups revealed a second, related system of fluid transport: a matrix of tiny lymphatic vessels in the meninges, or membranes covering the brain.

This early work showed the glymphatic channels form in the spaces around blood vessels, whose rhythmic contractions and dilations help push cerebrospinal fluid (CSF) through the channels. Traveling into the brain along arteries, the fluid picks up waste from deep inside brain tissue, then flows along veins to the meningeal lymphatic vessels. From there it travels to the lymph nodes of the neck, finally exiting to the bloodstream.

Brain clearance researchers have learned this system is most active during deep sleep, and that poor sleep, aging, traumatic brain injury (TBI), and cerebrovascular disease all harm it. They have begun to link impaired brain clearance to a higher risk of developing dementia, and scientists think it may be the mechanism by which poor sleep raises dementia risk. Iliff's group collaborated on a study, reported in an October preprint, that found the system flushes two proteins implicated in Alzheimer's, amyloid and tau, out of the human brain.

"We think [fluid clearance] has implications not just for Alzheimer's, Huntington's, and Parkinson's, but also stroke and headache and traumatic brain injury and probably mood disorders," Iliff says.

The research has already inspired wellness enthusiasts to tout various unproven brain-cleansing methods, ranging from neck yoga to sleeping on one's side. But researchers, too, are looking seriously at ways to improve brain clearance. One is to fortify the meningeal lymph vessels, an approach tested by neurobiologist Wenzhen Duan of Johns Hopkins University and her colleagues. They worked with mice that have the genetic mutation that causes Huntington disease, and show movement symptoms similar to those seen in people.

At the SfN meeting, Duan's group reported that injecting a protein called vascular endothelial growth factor C, which helps grow and maintain lymph vessels, flushed the toxic huntingtin protein out of the mice's brains and improved their motor coordination. The team also explored a second brain-clearing strategy targeting Aquaporin-4, a protein expressed in brain cells called astrocytes, which give glymphatic channels their structure. Using a gene therapy to increase expression of Aquaporin-4 improved clearance and reduced huntingtin levels in the brain, they found.

Tweaking vasomotion, the subtle pulsations that drive CSF through glymphatic channels, might also be beneficial, according to neuroscientist Rashad Hussain of the University of Maryland. The elevated levels of the neurotransmitter norepinephrine seen after brain injury in mice and people are known to stymie glymphatic flow. Administering a cocktail of three drugs known

IMAGE: ANTONIO LADRÓN-DE-GUEVARA AND MAIKEN NEDERGAARD

as alpha and beta blockers improved the mice's brain fluid clearance immediately after their injuries by boosting vasomotion, Hussain and his colleagues found. At the SfN meeting, Hussain reported the same drugs also normalized the animals' sleep patterns, which were disrupted after injury.

The cocktail might be used to treat both acute TBI and the lingering sleep problems it can cause, Hussain says—and ultimately might help reduce downstream consequences. "TBI is also a risk factor for Alzheimer's disease, which we know does not happen overnight—it takes years to develop, even decades," he says. "So if we can improve clearance when there is a sleep disturbance, maybe we can slow down the progression."

Mechanical interventions have also been shown to jog brain clearance. In June, a group led by vascular scientist Gou Young Koh of the Korea Advanced Institute of Science and Technology reported that stimulating the lymph nodes around the jaw with a pulsating device restored lymphatic flow from the brains of aged mice.

At the SfN meeting, Mitchell Bartlett, a brain lymphatics researcher at the University of Arizona, presented evidence from mice that such interventions might help treat Alzheimer's. Two months of twice-daily massage of the head and neck in mice engineered to develop Alzheimer's-like symptoms improved the animals' cognitive function, reduced amyloid in the brain, and lowered blood biomarkers of neurodegeneration, reported Bartlett, who also published the results in an August preprint. He hopes to launch a clinical trial of the intervention.

Neuropsychologist Sephira Ryman of the University of New Mexico presented findings published last month showing older adults and people with Parkinson's disease could increase brain vasomotion and cerebrospinal fluid flow by breathing dilute carbon dioxide, which dilates blood vessels, for short periods. The intervention also seemed to sweep proteins and peptides linked to neurodegeneration and inflammation out of the brain and into the blood. "We're really encouraged by these two findings," Ryman says, adding that the next step is to measure clinical effects.

None of these strategies is nearly as daring—or invasive—as the microsurgical procedures developed in China as a treatment for Alzheimer's. The surgery, called deep cervical lymphovenous anastomosis (dcLVA), is an adaptation of a common treatment for lymphedema, or swelling in the body caused by blocked lymphatic flow. It connects lymph nodes or lymphatic vessels in the neck to veins in the hope of boosting brain fluid clearance.

In 2020, plastic surgeon Qingping Xie of Hangzhou Qiushi Hospital was the first to perform the procedure in an Alzheimer's patient. Xie now advertises the surgeries online to people in China and overseas, urging them to "Stop progressing, Start recovering!" A meta-analysis, released in July as a preprint, reported that more than two dozen trials of dcLVA procedures, enrolling some 1300 Alzheimer's patients, are ongoing at centers across China.

The largest dcLVA study published to date came out in October: Alzheimer's researcher Jianping Ye and his colleagues at Zhengzhou University described results from 41 Chinese patients with mild to moderate Alzheimer's who underwent surgical treatment. As a surrogate measure of brain fluid clearance, the researchers measured blood and CSF levels of amyloid and tau, which showed improvement in two-thirds of patients 3 months after surgery. Ye says these changes have persisted in later follow-up tests. He and his colleagues also reported cognitive improvements. "This is the most effective therapy for [Alzheimer's], to my knowledge," Ye says.

The surgeries have faced criticisms, including from neurosurgeons in China citing a lack of solid evidence, and some experts are skeptical of the idea that glymphatic impairment is a type of brain lymphedema you can unclog. It "doesn't work literally like plumbing," Duan says, because much of the malfunction is occurring inside the astrocytes. Roslyn Bill, a brain clearance researcher at Aston University, says she, too, doubts much glymphatic function can be regained by opening the tap in the neck. "Mechanical processes may well cause all sorts of cellular pathways to be affected," she says, but no one has yet shown how.

Others are intrigued. Plastic surgeon Bohdan Pomahac of Yale

IN OTHER NEWS

SHARKS, RAYS GAIN PROTECTION Global sales of many endangered sharks and rays are expected to be banned by the Convention on International Trade in Endangered Species of Wild Fauna and Flora (CITES), which concludes its triennial conference of parties this week in Uzbekistan. The move would protect various species that have been severely depleted by the trade in their fins, meat, and oil. International trade will be banned for the critically endangered oceanic whitetip shark and whale shark, 10 species of manta and devil rays, and 16 species of sharklike rays. Other species—smoothhound sharks, the tope shark, and gulper sharks—will be added to a list that allows for international trade but requires permits. The Wildlife Conservation Society called the development "the most comprehensive advance in global shark conservation in CITES history." —Erik Stokstad

BATS HIT BY BIRD FLU In late 2022, an unprecedented outbreak of the avian influenza strain H5N1 reached South America, ravaging not only birds, but also marine mammals along the Pacific coast. Now, a preprint posted on bioRxiv last month reports the massive outbreak may have also affected vampire bat populations in coastal Peru that fed on the blood of infected marine animals. The virus—identified based on antibodies in the bats' blood—did not appear to spread between bats, but if it did, the animals could become a new reservoir, the researchers warn. And because some vampire bats also feed on livestock, they could become a bridge spreading the virus between marine and terrestrial animal populations. Another team had previously found H5N1 in flying foxes, a bat species that feeds on fruit and nectar, in Bangladesh. Those bats were likely infected by sharing a tree with house crows battered by the virus. —Martin Enserink

University remembers attending a presentation by Xie and his colleagues at surgical meeting a few years ago and finding it "bizarre." The protocols of the studies in China were "all over the map," he says, and even the published studies "were pretty poor quality and low impact." But as promising results continued to trickle in, Pomahac put together a multidisciplinary team to investigate further. Now, he is working closely with researchers at Washington University in St. Louis who are conducting dcLVA surgeries in animals.

If all goes well and federal funding comes through this month, Pomahac hopes to launch a clinical trial of an dcLVA surgery in carefully screened patients in the early stages of Alzheimer's. "No matter how unlikely it is [to work], it's worth exploring properly and studying scientifically," he says.

Bill says she would not undergo an dcLVA surgery—at least not without stronger evidence. She would, however, take a pill to keep her glymphatic system running smoothly as she ages.

In 2020, Bill reported that an antipsychotic called trifluoperazine, which prevents Aquaporin-4 from being shifted around within cells, prompted a dramatic recovery in a mouse model of CNS edema, or swelling in the brain and spinal cord, caused by injury. The mice behaved "as though they'd never been injured," she says.

Trifluoperazine "is an old, dirty drug," Bill acknowledges. "But if we could test it today, I think we would be in a position where we could save people's lives."

Iliff has also been studying an old drug—the alpha blocker prazosin, which his group found in a retrospective study to be potentially helpful in preventing dementia among veterans taking it for trauma-related nightmares. His team is testing its effects on glymphatic function and markers of Alzheimer's in rodents and nonhuman primates. (Prazosin is one of the three drugs in Hussain and colleagues' experimental cocktail.) Iliff is also working with the California biotech firm Applied Cognition on a noninvasive device to measure glymphatic clearance in real time.

"There is no direct evidence yet that lack of glymphatic efficiency leads to dementia in people," Bill points out. "But the circumstantial evidence is strong enough that it's worth a shot to drug it." □

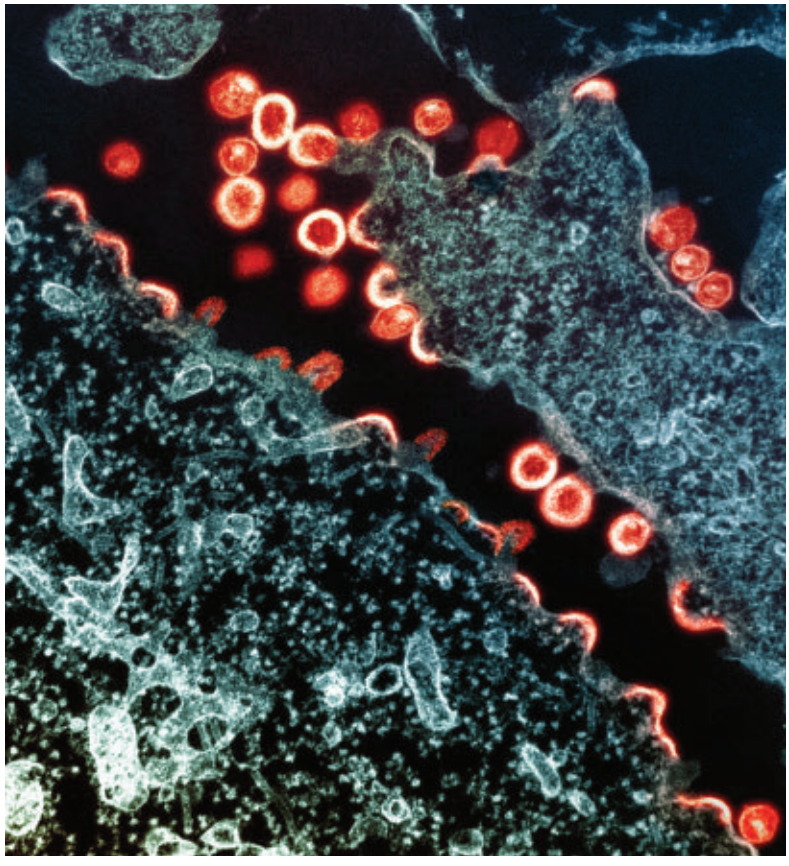


IMAGE: NATIONAL INSTITUTE OF ALLERGY AND INFECTIOUS DISEASES/NATIONAL INSTITUTES OF HEALTH

INFECTIOUS DISEASES

'Functional cure' for HIV comes closer to reality

Studies finger specific immune response that helps some people control the virus without drugs **JON COHEN**

Of the estimated 91 million people infected with HIV over the past 45 years, no one has fully defeated the virus, save for a dozen people who needed risky stem cell transplants to cure blood cancers. But a small percentage of patients in experimental trials have achieved a "functional cure," in which the immune system contains the virus and patients can stop taking antiretroviral drugs (ARVs) for many months, or even years.

Now, two independent research groups have shown that one particular class of immune cells appears to play a crucial role in these functional cures. Finding ways to nurture those cells might make it possible to free more patients from the need to take drugs for life.

Those cells "may be the magical biomarker we need for a cure," says Steve Deeks, an HIV clinician at the University of California, San Francisco (UCSF) who co-led one of the studies, which *Nature* published this week on the occasion of World AIDS Day. "It's promising for a future in which you can intervene and tilt a whole series of events back in the direction of the immune system," says Dennis Burton, an immunologist at Scripps Research who was not involved with the studies.

ARVs powerfully knock back levels of HIV in both blood and tissues, but stubborn "reservoirs" of cells that harbor dormant viral DNA persist in the body. When people stop taking drugs, the virus almost always resurges within weeks.

In a functional cure, the immune

Cells infected with HIV typically produce new viruses (orange) within weeks when people stop taking antiviral drugs. New strategies allow drug-free control for much longer.

system forestalls or even prevents the resurgence. This could help people who have difficulty taking ARVs every day—and if perfected, it might control HIV even better than medicines can. That's why Tom Perrault, a San Francisco resident who has lived with HIV for 20 years, took part in the UCSF study. Perrault says ARVs work well for him, but he worries that even very low levels of HIV in his body are causing inflammation that can lead to heart disease and damaged organs. "Taking the pills is not an automatic panacea and everything is sunshine and lollipops," Perrault says.

One of the new studies, led by immunologist David Collins of the Ragon Institute of Mass General Brigham, MIT, and Harvard, followed up on four trials that interrupted treatment after patients received not just ARVs, but also unusually potent broadly neutralizing antibodies (bNAbs) capable of disarming a wide range of HIV variants for long periods. Between 14% and 22% of participants controlled their infections for at least 2 months after the antibodies waned. Collins's team studied blood samples from seven of these people, including one who has maintained low levels of virus with no treatment for more than 7 years, and five others whose virus quickly rebounded.

The UCSF group recruited 10 patients and gave them similar bNAb infusions, but it upped the ante by adding an experimental HIV vaccine and a drug designed to reduce reservoirs. The team found that seven participants had prolonged control of the virus, including Perrault, who went without drugs for 4 months. "We just haven't seen that with interventions previously," says UCSF immunologist Rachel Rutishauser, who co-led the study.

Both teams then studied the immune response in "controllers" in great detail. One signal clearly stood out. A class of white blood cells known as memory T cells, studded with CD8 receptors, plays a critical role in targeting and destroying HIV-infected cells. Both studies found that precursors to these "killer T cells" are strongly tied to long-term control of HIV after treatment is stopped. The precursors have a stem cell–like quality, and in the controllers, they more readily made copies of themselves when the virus started to return.

"The signal is really exciting," Collins says. Stimulating the production of these "stemmy" CD8 cells, as he calls them, "might be the key to getting control in more than the small percentage of people that who are currently achieving it."

But teasing out why some people produce more of these cells is tricky. "It's totally not clear," says Michel Nussenzweig, a Rockefeller University immunologist who is a co-author of both papers. Collins suspects that when trial participants stopped ARVs, the long-acting bNAbs slowed down the return of HIV, giving the T cells a "head start." In this scenario, the stemmy CD8s have extra time to mature into large troops of killer T cells. "In a relay race, when you pass the baton, you have this running start," he says. "If you go just from standing, you might lose the race. The virus is a really fast runner."

Nussenzweig says the stemmy CD8 cells are likely one of several ways the immune system controls the virus. "Every little bit is going to count," he says. The report by the UCSF team suggests some of the control comes from the so-called vaccinal effect: When bNAbs attach to HIV, this complex stimulates immune responses that lead other T cells to keep the virus in check.

Patients' own neutralizing antibodies against HIV may play a role in the functional cure as well. These naturally occurring, "autologous" antibodies cannot by themselves control all the viral variants in an infected person, which has given them "a bad name," Nussenzweig says. But in a preprint posted on medRxiv on 6 November, his team describes how people in yet another treatment interruption study that used bNAbs were more likely to have long-term viral control if they had higher levels of autologous antibodies.

The new findings about the role of stemmy CD8 cells may only tell part of the story, says Sharon Lewin, head of the Peter Doherty Institute for Infection and Immunity, but the effort to cure HIV "urgently needs" insights like this to push it forward. "It's an extremely important observation," Lewin says. "The field can now leverage this." □

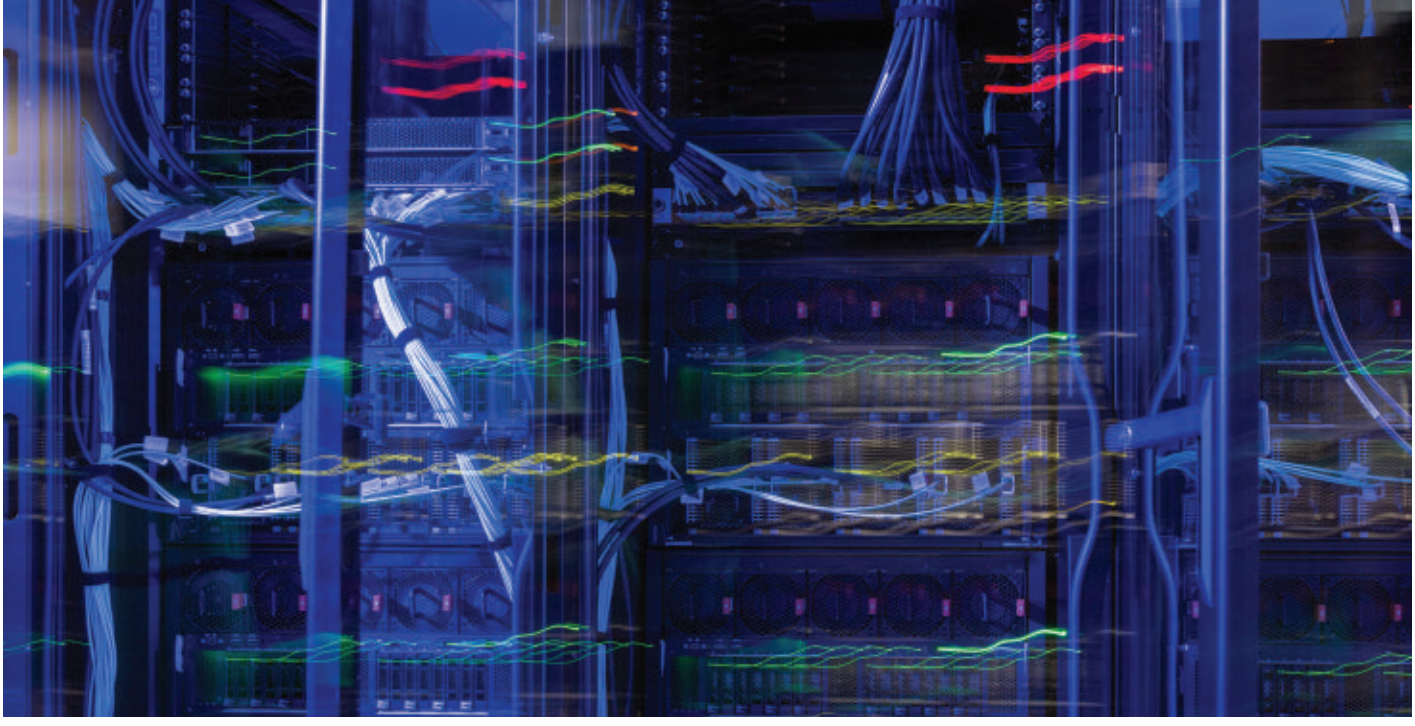
For the first time, the US FDA will acknowledge that COVID-19 vaccines have killed American children.

Food and Drug Administration (FDA) Center for Biologics Evaluation and Research (CBER) Director Vinay Prasad, in an email to agency staff last week.

THEY SAID IT

This is a really extraordinary claim that would normally merit a very detailed scientific analysis.

Infectious disease physician and former CBER Director Jesse Goodman, expressing frustration to *STAT* that Prasad made no corroborating data available.



Empire AI's first machine, Alpha, is powered by nearly 200 NVIDIA chips.

PHOTO: MEREDITH FORREST KULWICKI

ARTIFICIAL INTELLIGENCE

States step up to democratize AI-tailored computers

New York state is building AI-ready machines for researchers who lack access to federal or corporate supercomputers

CELINA ZHAO

In 2024, the Nobel Prize in Chemistry went to the Google DeepMind team behind AlphaFold, a disruptive artificial intelligence (AI) system that predicts the 3D structure of proteins based on their amino acid sequences. But proteins by nature are shapeshifters, morphing as conditions like pH or temperature change. To forecast those transformations, University at Buffalo (UB) structural biologist Thomas Grant is building a homegrown AI spinoff called SWAXSFold. And he's doing it without Google's deep pockets.

Universities are hard-pressed to afford the costly, cutting-edge AI chips that systems like SWAXSFold require, and that Silicon Valley tech giants are stockpiling in their race to build ever-larger chatbots. But New York state is now stepping in, giving researchers like Grant access to the computers they need through a $500 million, 10-year initiative called Empire AI. Launched last year, it will inaugurate its second supercomputer in the coming months—one expected to be among the most powerful AI-focused academic supercomputers in the nation.

"Before Empire AI, only a handful of massive tech companies had the computer resources to create a tool like AlphaFold," says Venu Govindaraju, senior vice president for research at UB and an Empire AI board member. "With Empire AI, a researcher in New York can now build their own."

New York isn't alone in the trend. In September, California passed a law to create CalCompute, a similar AI-focused computing initiative to be housed in the University of California (UC) system.

The goal isn't to compete with DeepMind or OpenAI, says Russell Wald, executive director of Stanford University's Institute for Human-Centered AI. Rather, the aim is to democratize access to AI computer centers so that researchers across a wide range of disciplines can create tools for the public good—without worrying about turning a profit.

Specialized chips known as graphics processing units (GPUs), able to perform trillions of calculations per second, are essential for training modern AI systems. But at tens of thousands of dollars per chip, they are prohibitively expensive for researchers. Companies have accumulated millions; academic clusters might have a few hundred at most. "It's not for lack of vision or will or even plans," says Michael Norman, a physicist at UC San Diego and former director of the San Diego Supercomputer Center. "We just don't have the money."

Some federal initiatives have tried to help. The U.S. National Science Foundation's (NSF's) CloudBank initiative subsidizes time on commercial cloud services such as Amazon Web Services or Google Cloud. And the agency's 2-year pilot of the National AI Research Resource (NAIRR), launched in 2024, has paired more than 400 researchers with Department of Energy (DOE) supercomputers and a network of computing clusters supported by NSF money.

But neither is a perfect solution. Much like renting a car, buying time on commercial clouds typically costs far more than owning the machines outright. And although federal supercomputers offer enormous power, their architectures traditionally center on chips called central processing units, optimized more for physics-heavy simulations than AI tasks such as seeking patterns in massive data sets. Although many newer systems do include GPUs, they are "several generations behind the state of the art," Norman says.

Empire AI, a consortium of nine New York universities and the Flatiron Institute of the New York City–based Simons Foundation, aims to close those gaps. The state is providing the bulk of funding, and Simons donated Empire AI's first supercomputer,

Alpha. The machine, housed at UB and powered by nearly 200 of some of NVIDIA's most advanced GPUs, is modest by AI standards.

But the second machine, Beta, will be an order of magnitude more powerful, driven by NVIDIA's latest, coveted Blackwell chips—a rare coup for the academic community. Those chips will be linked by a powerful network, allowing them to pass information far faster and with less hardware than even systems like DOE's El Capitan—the most powerful supercomputer in the world—according to Ian Fisk, an Empire AI board member and the Simons Foundation's chief technology officer. "That improvement in efficiency translates into the number of science problems you can look at," Fisk adds.

In its first year, Empire AI has already served more than 350 researchers at the member institutions. One is Columbia University statistician Tian Zheng, who is attempting to combine many scattered clues—weather records, neighborhood flood reports, and city incident logs—to predict where flash floods will strike in urban areas. Such fine-grained forecasts are beyond the reach of conventional climate models. "There are stages of research [that are] high risk and exploratory in nature," she says. Having access to Empire AI's widely available, powerful machines "vastly expands your imagination."

For New York University (NYU) neuroscientist Christine Constantinople, the biggest change has been speed. She trains virtual neural networks to mimic how brains make decisions. Runs that took 1 week on NYU's clusters now finish in 1 day on Empire AI, letting her explore different architectures, scale up model size, and iterate more freely. "It becomes transformative in terms of your ability to explore different possible models," she says.

Weill Cornell Medicine computational biomedicine researcher Ekta Khurana hopes to harness AI to diagnose an aggressive, treatment-resistant subtype of prostate cancer her team has identified. They plan to train machine-learning models on pathology images from patient biopsies—work Cornell's own clusters couldn't support. With Alpha, however, they managed to train a model on hundreds of images; with Beta, they hope to reach more than 10,000.

By 2027, Empire AI anticipates completing its third supercomputer, Gamma, which will be another 10 times more capable than Beta. A fourth machine, Delta, would come after that. "The idea is to keep a machine which is state of the art for the length of the program," Fisk says.

By then, California may have advanced its own effort. The state's new AI law, besides addressing the safety and transparency of large commercial AI models, also includes language supporting the creation of CalCompute. The governor's office is tasked with naming a group to design the program's framework by January 2027, which would still require funding through the state budget.

Federal efforts to create AI infrastructure continue. A panel of experts has recommended spending $2.6 billion over 6 years to move NAIRR beyond existing NSF-funded GPU clusters—where unmet demand often results in long queues, says Hanna Hajishirzi of the Allen Institute. Although a 56% cut in NSF's 2026 budget proposed by President Donald Trump would make it difficult for the agency to advance NAIRR past its pilot run, the administration has consistently indicated that AI is one of its few scientific priorities. Last week, for instance, Trump signed an executive order for a new Genesis Mission that directs DOE to integrate troves of federal scientific data sets into a centralized platform for AI-based research.

The directive comes on the heels of an announcement in October that DOE would join with NVIDIA and Advanced Micro Devices to build nine new AI-focused supercomputers (see story, p. 975). With the companies covering part of the cost of the systems, the deals could help DOE labs keep up with the latest hardware. But it's unclear how far that support will go. Tech firms usually "aren't in the business of philanthropy," Norman says.

The challenge ahead is finding the right balance between federal and state support. "During a year where it wasn't so easy to do research, [Empire AI] was such a bright light for our institutions to have something that didn't depend on federal funding," says Stacie Bloom, NYU's chief research officer and Empire AI board member.

But state-level initiatives alone can't ensure equitable access. "What about a researcher in Arkansas? I don't think Arkansas is going to come up with an AI computing initiative," Norman says. □

INFECTIOUS DISEASES

Abandoned antiviral shows promise against dengue

Big Pharma maker won't bring drug to market for crippling disease

GRETCHEN VOGEL

Two years ago, the pharmaceutical firm Johnson & Johnson (J&J) announced some rare good news about dengue, a crippling viral infection that threatens half of the world's population. A clinical trial had shown an antiviral compound could prevent the disease in people deliberately exposed to the virus. "The development of a dengue antiviral is critically important to global health," the company said in a press release at the time.

Last week, the full data from that trial were published in *The New England Journal of Medicine*, and encouraging data from two other trials are under review at journals. And yet the drug, called mosnodenvir, is in limbo. Last year, J&J abruptly stopped all its work on infectious diseases, including dengue. "Having watched the development for the last 10 years, I think we were all very disappointed," says Sophie Yacoub, a dengue researcher at the University of Oxford who has advised J&J but was not involved in the studies of the antiviral.

Negotiations are underway to find another company to adopt mosnodenvir and try to bring it to market, Yacoub notes. Given the positive results, she says, "It's not the end. We will see it again."

Eng Eong Ooi, who studies emerging infectious diseases at the Duke–National University of Singapore Medical School, agrees. The newly published study is "a major milestone in dengue," says Ooi, who has also consulted for J&J but was not involved in the mosnodenvir trials.

An estimated 400 million people in tropical and subtropical countries contract dengue annually. The disease causes fever, severe joint pain, rashes, and, in some cases, a potentially fatal hemorrhage that kills tens of thousands every year. There are no approved treatments.

A dengue vaccine made by Takeda, a Japanese company, has been approved in 41 countries, but the company has been unable to keep up with global demand. Sanofi has ended production of another vaccine, citing low demand, and it's unclear when a third vaccine, made by the Butantan Institute and approved in Brazil on 26 November, might become widely available. Because the vaccines contain weakened, live virus, they can't be

given to people who are immunocompromised or pregnant.

Using mosnodenvir to protect large populations during dengue epidemics—which can last for months—would likely be too expensive, but the drug could be very useful when an outbreak emerges and is spotted fast, Ooi says. "When you see a cluster of cases forming, you potentially could go in and give a prophylaxis to the people living in the area," he says, reducing their risk of getting sick and helping slow spread of the virus. Another obvious market is travelers to areas where dengue circulates.

The newly published study is a so-called human challenge trial, in which 31 volunteers agreed to be injected with a strain of dengue known to cause only mild symptoms. During the 5 days before the injection and 3 weeks after it, participants took a daily pill with either a low, medium, or high dose of mosnodenvir, or a placebo. Six of the 10 volunteers who received the high dose remained uninfected, and the other four had only low levels of virus in their blood. But only one of the six people in the medium-dose group escaped infection, and none in the low-dose and placebo groups. "It's one of the most beautiful dose-response results I've seen," says Anna Durbin, an infectious disease specialist at the Johns Hopkins University Bloomberg School of Public Health who led the study. The trial did not find any significant side effects.

Based on the results of the challenge study, J&J in 2023 launched a field trial in South America and Asia to test whether the drug could also prevent infection in close contacts of people diagnosed with dengue. That trial was halted in October 2024, when nearly 1600 people had been enrolled, because J&J had decided to focus on chronic diseases and cancer.

Data from the study, posted on ClinicalTrials.gov, show that among 265 contacts who received the high dose of the drug, none developed symptomatic dengue infections. There were three symptomatic infections in the medium-dose group and five in the placebo group. In a separate challenge trial, Durbin and colleagues have also tested a weekly dose of the drug, which would be more convenient; those data look "very good" as well, she says. Both sets of results are now under review at journals, Durbin says.

Mosnodenvir might also have potential as a treatment, but it would have to be given very early in an infection. Most patients develop serious symptoms only after the level of virus in their blood has started to fall; by then, giving an antiviral doesn't help.

A few other dengue treatments are in development. Novartis last year started a phase 2 trial of an antiviral, enrolling people with a dengue diagnosis in six endemic countries. And the Serum Institute of India is conducting a phase 3 trial of a monoclonal antibody. If it works, a single dose could provide protection for months. But antibodies are expensive to produce and have to be given via an infusion, which limits their practicality on a large scale.

Spokespeople for J&J declined to comment on mosnodenvir's future but Durbin is optimistic it will find a new home somewhere: "There is a market, and I think there will be a company that picks it up." □

IN FOCUS



Argentina's glaciers under threat

Scientists in Argentina are raising alarm about a move to modify the country's landmark glacier protection law. In 2010, Argentina became the world's first nation to legally protect glaciers, such as Perito Moreno in the Patagonian region (pictured), and periglacial areas that are frozen for all or part of the year. Now, President Javier Milei says the law unnecessarily limits mining and other economically important activities and wants to give provincial governments greater power to define protected areas. That could result in severe damage to sensitive ecosystems and key water sources, some researchers fear. Milei expects to submit the proposed changes to Argentina's Congress, which begins a new session on 10 December.
—María de los Ángeles Orfila

PHOTO: REUTERS TV/VIA REUTERS

POLICY

DOE boost for AI, fusion could squeeze basic research

Reorganization could shift mission of the largest U.S. funder of physical sciences **ADRIAN CHO**

The U.S. Department of Energy (DOE) is reorganizing its scientific efforts by establishing new offices for types of research favored by the White House. A two-paragraph press release and revised organizational chart issued on 20 November announced the launch of an Office of Fusion and an Office of Artificial Intelligence and Quantum. DOE provided no further details, but the move worries scientists. The new offices could be formed by carving pieces out of DOE's storied Office of Science, the United States's largest funder of the physical sciences and its builder of big facilities from x-ray sources to atom smashers.

Observers say the change suggests the Office of Science, which has an $8.2 billion annual budget and funds everything from biofuels research to particle physics, could shrink and effectively become DOE's office of misfit research. "We can't abandon the rest of science," warns one longtime DOE observer who requested anonymity to protect relations with the agency.

On 24 November, President Donald Trump underscored his administration's emphasis on artificial intelligence by signing an executive order to launch the Genesis Mission, a national effort "to unleash a new age of AI-accelerated innovation and discovery that can solve the most challenging problems of this century." Genesis will be led by DOE Under Secretary for Science Dario Gil. In a four-page open letter to the DOE research community, Gil, a computer scientist, calls for "an integrated science and security platform connecting the world's best supercomputers, AI systems, and next-generation quantum computers to the most exquisite scientific instruments in the nation" to create "the most complex and powerful scientific instrument ever built."

Gil's letter doesn't mention the reorganization, and at press time, DOE had not responded to emailed questions. But the new AI-quantum office is sure to play a prominent role in Genesis.

Fusion researchers have long clamored for DOE to form a separate office of fusion by extricating the $790 million fusion energy sciences program from the Office of Science. "Communities want to see their program reporting as high up in the department as possible, if not to an undersecretary, to the secretary, and if possible, to God," says James Decker, former deputy director of the Office of Science. Fusion fits the Office of Science's basic research mission poorly, Decker adds. "I always considered it an applied program."

The need for the fusion office has grown with the emergence of multiple private companies aiming to achieve fusion power in a few years, say Martin Greenwald, a physicist at the Massachusetts Institute of Technology and co-founder of Commonwealth Fusion Systems. Still, the new office will answer to Gil and not to the undersecretary for energy, "protecting it a little bit" from the pressure to produce immediate commercial results, Greenwald says.

> **"We can't abandon the rest of science."**
>
> **Longtime Department of Energy observer**

Placing both AI and quantum technologies in a single office makes sense, says Steven Girvin, a quantum engineer at Yale University, as AI has emerged as a powerful tool for developing quantum computers. The office's effectiveness will depend on coordinating myriad strains of research, he says. "It's nice to have one box on the org chart that sees the big picture of all the quantum investments," he says. "But whoever does that work has to spend all their time then making connections to all the other types of science that quantum needs."

The AI office may absorb the Office of Science's advanced scientific computing research program. In October, DOE announced a new strategy for that program, in which companies such as NVIDIA and Oracle would build and maintain cutting-edge, AI-focused supercomputers at the national labs and DOE would buy time on them. But Jack Dongarra, a computer scientist at the University of Tennessee, Knoxville, worries DOE's existing strength in high-precision simulations of phenomena ranging from climate to cosmology could be at risk. Machines designed for AI may perform worse than current ones for simulations, Dongarra says. "For AI, [the arrangement] is a good thing, but it's not good for the scientific computing and the simulations that we are traditionally doing."

The reorganization could even cost the Office of Science some of the 10 national labs it currently controls. The Princeton Plasma Physics Laboratory would likely be transferred to the new fusion office, sources say. However, practical problems may slow the changes. DOE has recently lost many employees, Decker notes, so staffing the new offices, especially the one for AI and quantum, "is going to be a real challenge."

Some observers question how dramatic the reorganization will be. Forming the new offices may be a "performative" gesture designed to show the department embraces the White House's priorities, says one former Office of Science senior manager. "But on the ground, how much is really going to change?" Still, he adds, "I think the marginalization the Office of Science is real."

Indeed, for 80 years, Democrats and especially Republicans have acknowledged the importance of the kind of basic research DOE pursues, says Robert Rosner, a physicist at the University of Chicago and former director of Argonne National Laboratory. The White House's emphasis on hot technologies such as AI may break with that tradition, Rosner says. "The compact made during World War II that the federal government has to play the leading role in maintaining science in the United States, that's coming into question," he says. "And that's really concerning." □

POLICY

Can a smaller U.S. National Academies remain relevant?

Loss of federal support leads to staff layoffs and fewer committees of outside experts

JEFFREY MERVIS

A major restructuring of how the National Academies of Sciences, Engineering, and Medicine (NASEM) does business was unavoidable after the federal government pulled its support earlier this year for more than 50 projects, says National Academy of Sciences (NAS) President Marcia McNutt (former editor-in-chief of *Science*). Her solution was to shrink the permanent staff, eliminate some of the volunteer panels that generate NASEM's government-sponsored studies, and organize the academies' work around broader topical areas rather than disciplines.

But those changes have caused consternation among the scientists serving on the panels and those working for NASEM's operating arm, the National Research Council (NRC). They worry a shrunken staff and smaller network of external experts will undermine NASEM's ability to speak with authority on the issues it is asked to address, ranging from nutrition to nuclear nonproliferation.

"My concern is how the academies will retain both the subject-matter expertise and the institutional knowledge of working with agency sponsors in the midst of the financial crisis it is facing," says William Bonvillian, vice chair of a standing committee on defense materials and manufacturing and veteran of a dozen similar committees and boards. "That's the real challenge."

McNutt, who is also NRC chair, sees a more positive side to the changes. "I'm really happy about it, because we've eliminated disciplinary silos," she says. "The new units will make it easier to address real problems, like healthy people and advancing science and technology."

The contracts canceled since President Donald Trump took office in January have largely involved activities that don't align with his priorities. "The areas that were hit hardest were in health and medicine, the environment, and the social and behavioral sciences," says Gregory Symmes, NASEM's executive officer.

Under the new structure announced in June, five largely discipline-based divisions have been folded into two overarching entities: the Center for Health, People, and Places (CHPP) and the Center for Advancing Science and Technology (CAST). Whereas each division managed as many as a dozen standing boards and committees, each of the new centers will oversee only five or six operating units.

"Some of the [existing] boards will be sunset," confirms a NASEM spokesperson, who declined a request from *Science* for a detailed listing of which bodies will remain intact and which will be folded into a larger grouping.

Having fewer administrative units has enabled NRC to eliminate redundancies and reduce its staff from 1200 to 1000, Symmes says. Some 120 program and support staff were laid off, according to the NASEM spokesperson, with the rest leaving or taking early retirement. More layoffs are possible, Symmes adds, if other, threatened federal funding cuts take effect.

The new structure is "more efficient," says Alan Leshner, who will chair the new advisory committee for CHPP, which has subsumed some or all of the previous divisions of earth and life sciences, engineering and physical sciences, health and medicine, and behavioral and social sciences. "I just hope that we don't lose the diverse representation we had on the previous boards and committees," adds Leshner, former CEO of AAAS (publisher of *Science*). Those demographics won't be clear until NASEM officials name the members of the advisory committee for CAST, which will be chaired by Julia Phillips, a retired senior administrator at Sandia National Laboratories.

In deciding which permanent staff to retain, McNutt put a premium on people with multiple areas of expertise. "We still want to cover the same waterfront [of issues], but maybe we don't need as many people to do it," she says. "And we want the remaining staff to be able to easily move around to different areas, depending on where we have funding," she adds.

But some program managers who have been let go even though their activities continue to be funded say NASEM officials never explained why they were fired. "My projects have been left intact, save for me no longer leading them," says one veteran staffer who received a layoff notice several weeks ago. "Neither my supervisor nor their supervisor knew anything about it until I told them."

A standing committee on national statistics has lost more than half of its seven-person staff despite retaining its core funding. "We're still an intact committee," says its chair, University of Maryland economist Katharine Abraham, "so what I'd really like to know is if NASEM is committed to keeping us around."

At the same time, topics favored by the Trump administration, such as



The National Academies of Sciences, Engineering, and Medicine has offered scientific advice to the U.S. government since 1863.

PHOTO: E. BILLMAN/*SCIENCE*

nuclear power, national security, and artificial intelligence, have retained government support or are expanding. For example, NRC has just created a standing committee funded by the Department of Defense to identify emerging technologies with military applications. The realignment has also left unscathed two large NRC programs with sustained and ample funding—the Gulf Research Program and the Transportation Research Board.

Private philanthropy is also helping. The new Mathematical Sciences Education Board, for example, is being funded for 3 years by the Gates Foundation. And in May the family of Philip Needleman, a former NAS and National Academy of Medicine member who died last year, gave NASEM $20 million to maintain support for a network of young scientists and expand its capacity to do rapid studies on pressing issues.

Broader threats still loom, however. "There's [also] the threatened deep cuts to indirect costs [what NRC charges the government to carry out its studies], congressional language accusing us of bias, and the budget squeeze at the agencies that typically sponsor our activities," says one veteran NRC staffer who requested anonymity because they are not authorized to speak for NASEM.

McNutt says the reorganization shouldn't affect one of NRC's most influential products—its decadal studies that lay out priorities for various disciplines. Astrophysicist Margaret Kivelson, who chairs the Space Studies Board, agrees. Her board will be folded into the newly created Aeronautics, Space, and Astronomy unit within CAST. But Kivelson, professor emeritus at the University of California, Los Angeles, says its decadal studies in astronomy and planetary science are unlikely to be affected. It's the bigger picture that worries her. "Our funding is overwhelmingly from NASA," she notes. "And there's lots to be concerned about there."

Given such uncertainties, McNutt and Symmes say the entire reorganization is likely to evolve over the next several months. "We're really looking at this as a first draft of what we want to look like, and we can change things if we need to," she says.

However, McNutt will be stepping down as NAS president in June 2026. Her successor, University of Chicago evolutionary biologist Neil Shubin, may face some hard decisions. □



PHOTO: SERGIO IZQUIERDO

IN FOCUS

Animal tracking project flies again

A space-based wildlife tracking system that could revolutionize the study of animal migrations is set to get back online with last week's launch of a SpaceX rocket. The project, called the International Cooperation for Animal Research Using Space, or ICARUS, began collecting promising preliminary data in 2019 with a prototype receiver on the International Space Station tracking tags small enough to be placed on birds such as this scarlet macaw. But in 2022, when the war in Ukraine broke out, data stopped flowing from the German-built antenna to a ground station in Russia. Now, a small spacecraft known as a CubeSat has been sent into low-Earth orbit carrying a receiver and transmitter that will collect location data from devices affixed to animals around the world. Project leaders say they plan to launch another satellite next year, and to have six up and running in 2027. —Elizabeth Pennisi



PUTTING THE U IN QUANTUM

A century after the birth of quantum mechanics, its puzzles are pushing physicists to redefine reality—with themselves at the center

ZACK SAVITSKY

Standing in a garden on the remote German island of Helgoland one day in June, two theoretical physicists quibble over who—or what—constructs reality. Carlo Rovelli, based at Aix-Marseille University, insists he is real with respect to a stone on the ground. He may cast a shadow on the stone, for instance, projecting his existence onto their relationship. Chris Fuchs of the University of Massachusetts Boston retorts that it's preposterous to imagine the stone possessing any worldview, seeing as it is a stone. Although allied in their belief that reality is subjective rather than absolute, they both leave the impromptu debate unsatisfied, disagreeing about whether they agree.

Such is the state of theoretical quantum mechanics, scientists' deepest description of the atomic world. The theory was developed 100 years ago on Helgoland, where a 23-year-old Werner Heisenberg retreated to escape a bout of hay fever—and to reimagine what an atom looks like. The leading picture at the time featured electrons hopping in discrete, or quantized, leaps of energy between fixed orbits around the nucleus. It explained the behavior of hydrogen but failed for bigger atoms. On blustery walks and cold swims in the North Sea, Heisenberg abandoned the simplistic orbital picture, instead developing a new mathematical language that would work for any atom. Later in 1925, Erwin Schrödinger conjured up a complementary lens—his eponymous wave equation—which describes the positions of electrons in probabilistic terms.

ILLUSTRATION: DEENA SO'OTEH



Within a few years, their calculations would reveal a disturbingly fuzzy picture of reality, one in which certain properties are inherently unknowable and others take on different values depending on how they're measured. "What we observe is not nature itself, but nature exposed to our method of questioning," Heisenberg wrote after winning the 1932 Nobel Prize in Physics.

This year, hundreds of physicists convened on Helgoland to commemorate the birth of quantum mechanics. It has certainly earned its keep over the past century, not only by predicting experimental outcomes with immaculate precision, but also by enabling technologies such as lasers, transistors, and atomic clocks. Yet even today, scientists struggle to interpret what the theory implies about nature. Central to the confusion is how the act of measurement pins down the indeterminate behavior of atoms. The standard framing has an unsettling anthropocentric flavor, suggesting humans play some special role in shaping the universe. Now, bolstered by a string of recent experiments, theorists such as Fuchs and Rovelli are leaning into the discomfort, emphasizing how observers do indeed create the world they inhabit. What's at stake is nothing less than reality itself.

"We don't need to fix quantum mechanics to make it compatible with what we observe; we need to recognize that there are alternative ways of looking at the world," says Alyssa Ney, a philosopher of physics at the Ludwig Maximilian University of Munich. Quantum theory compels physicists to "make room for different notions of what it means to be real."

THE MYSTERIOUS ROLE of observation in quantum mechanics is highlighted by the classic "double slit" experiment, which has been performed for decades with photons, electrons, and atoms. If you shoot a stream of individual atoms toward a blank wall through a barrier that has two slits, a squiggly interference pattern will appear on the wall. The pattern means each atom must have traveled like a wave, passing through both slits simultaneously in a "superposition" of all of its possible quantum states. However, if the experiment is repeated with a detector at each slit to track individual atoms as they pass through the barrier, the pattern on the wall will instead feature only two broad stripes, formed by individual atoms that took one path or the other. The detector somehow seems to cause the atoms to behave like particles rather than waves.

Heisenberg and his mentors, including Niels Bohr at the University of Copenhagen, took a practical view of the matter. They accepted the dual nature of atoms and that measurement "collapses" waves into particles. But this perspective, sometimes called the Copenhagen interpretation, punts on questions about how exactly the waves collapse and what constitutes a measurement.

Others, including Albert Einstein, believed the atoms must surely have some baked-in rules about how to behave, regardless of measurement. That skepticism led to experiments beginning in the 1970s called Bell tests, named after Northern Irish physicist John Bell, that probed for these so-called hidden variables. The Bell tests rely on another enigmatic phenomenon prescribed

ILLUSTRATION: DEENA SO'OTEH

by quantum mechanics: the ability to "entangle" two atoms in such a way that their quantum properties are intrinsically linked. When those properties are measured after entanglement, they're always correlated no matter how far apart the atoms are—a connection Einstein called "spooky action at a distance."

The Bell tests examine correlations between multiple quantum properties—such as the position of one atom and the velocity of another. And they demonstrate that the observed amount of correlation exceeds what's possible if both atoms merely had preconfigured positions and velocities. Assuming there's no way for atoms to send signals faster than light, the only logical conclusion is that the atoms truly are in a superposition of all possible states up until the moment of measurement—implying, as Israeli physicist Asher Peres famously put it, "Unperformed experiments have no results."



> It's a state of mind.
>
> **Chris Fuchs**
> University of Massachusetts Boston

The result is a perplexing puzzle about what is real, which can be brought into stark relief using a simple thought experiment proposed by Hungarian American physicist Eugene Wigner in 1961. Wigner stands outside a sealed lab, in which his friend Jimena measures a quantum property of her atom. To Wigner, who is oblivious to Jimena's measurement, the quantum state of the atom—and even Jimena herself—is undefined, in a superposition of possibilities. Quantum theory says Wigner should even be able to verify this superposition by treating Jimena and her lab as one entangled quantum system and performing an interference experiment. Meanwhile, inside the lab, Jimena has already measured and determined her atom's state. The two friends seem to experience different realities."We're applying the same theory in two different ways and getting contradictory results, it appears," says Nick Ormrod, a postdoctoral researcher at the Perimeter Institute who studies quantum foundations.

SINCE THEN, dozens of quantum interpretations have sprouted in an attempt to resolve this paradox, which the Copenhagen philosophy simply dodged. Some do so by invoking physical processes in the act of measurement—such as gravity or consciousness—that cause the collapse of waves into particles. Others cling to the idea that hidden variables underlie the spooky connections, opting to give up the assumption that nothing can travel faster than light. These approaches suggest Wigner is simply ignorant, and Wigner's friend experiences the real truth—either by definitively collapsing the atom's superposition or by revealing its predetermined nature. Experiments have yet to vindicate either idea. More recently, a third camp has gained support: addressing the measurement problem by rethinking reality entirely.

One who took eagerly to the challenge was Rovelli, whose insubordinate youth had primed him to challenge conventional wisdom. Studying physics in Bologna, Italy, in the 1970s, during a wave of political and cultural revolutions, Rovelli and his comrades lived on a commune and disavowed traditional societal values. "We were the explorers of a new way of living," he says. "The hope was a world without weapons, without countries, without school, without family, without fixed couples." This exercise of shedding deeply held beliefs eventually bled into his work in theoretical physics. Aided by psychedelic trips and forays into Eastern philosophy, he was willing to sacrifice orthodox intuitions about the nature of reality.

In 1996, Rovelli laid out a new interpretation of quantum theory that does away with any universal notion of existence. It draws on the "many worlds" idea, first proposed by U.S. physicist Hugh Everett in 1957 to explain the multitude of possible outcomes of a measurement. Each time a measurement is made, Everett proposed, reality splinters off into multiple branches—one in which you had cereal for breakfast and another in which you ate eggs, for example—but the branches have no ability to interact. Critics dismiss the idea as ungrounded and fantastical, pointing out the lack of an explanation of how or when this branching happens, as well as the unfathomably large number of worlds beyond our reach. But the boldness of the idea gave Rovelli the courage to get creative.

Like Everett's approach, Rovelli's relational quantum mechanics rejects the idea that one coherent story describes the universe. But rather than positing multiple branches of reality, Rovelli argues the world can only be understood from a particular point of view, which need not align precisely with any other perspective. Objects and events do not exist in and of themselves—they manifest through relationships with other physical systems. "This implies that I cannot give an absolute, universal, objective description of what is going on," Rovelli says. In the case of Wigner's friend, Rovelli argues it's a mistake to assume Jimena's reality should count for Wigner in any way.

Fuchs came to similar conclusions by dreaming big in a different direction. Growing up poor in the small town of Cuero, Texas, Fuchs was drawn to physics as an avid *Star Trek* fan but quickly became disheartened by the slim prospects of interstellar space travel. He told his best friend, "If the laws of physics won't allow us to get to the stars, the laws of physics must be wrong."

In high school in the 1980s, he attended a Texas Boys State summer camp at the University of Texas (UT) at Austin. He hated the predawn calisthenics and the right-wing politics, but for one moment, fortune smiled on his sci-fi fantasies. During his free time, he tracked down his scientific hero John Archibald Wheeler, a pioneering theorist of black holes, cosmic wormholes, and other strange children of Einstein's theory of general relativity. In Wheeler's vacant office, Fuchs found a manuscript draft with a passage that read, "There is no law

PHOTO: DAVID MORRIS, COLORIZED BY M. ATAROD/*SCIENCE*

except the law that there is no law." Fuchs saw this as his ticket to the stars: "Ca-ching," he says.

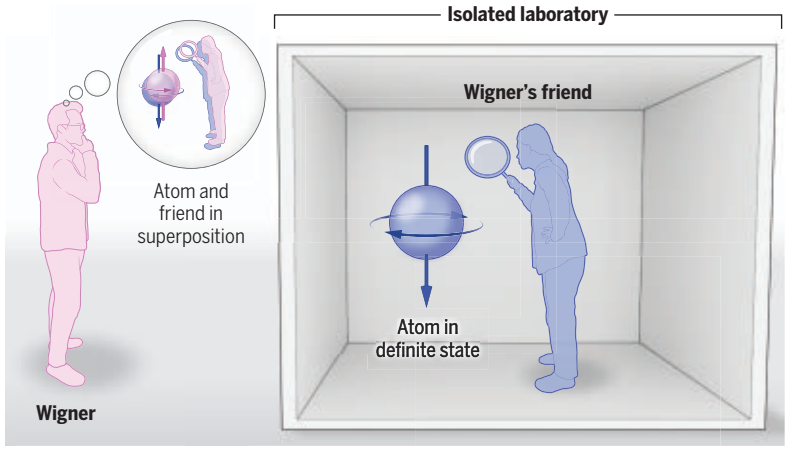
In the paper, Wheeler also argued that observers shape the universe through measurement. Fuchs would cling to that idea of agency. After studying under Wheeler at UT, Fuchs came to view quantum mechanics through the lens of those who employ it—treating the theory as a user's manual for placing smart bets on measurement outcomes.

The result was QBism—originally short for Quantum Bayesianism, a reference to a philosophy of statistics that argues probabilities are not fixed, but should be updated as new information arises. QBism extends this approach to quantum probabilities. The core premise, which Fuchs and colleagues first laid out in 2001, is that the state of a quantum object reflects the subjective degree of belief that an agent has about its properties. "It's a state of mind," Fuchs says. The outlook makes it easier to permit different observers to have conflicting descriptions of the same system, as these simply reflect perceived probabilities based on the information each one gains from measurements.

At the conference on Helgoland, Rovelli and Fuchs put their competing visions of reality head to head. For both, quantum theory describes properties of a physical system as they relate to something else. To Rovelli, that something else can be any physical object—even a stone. The stone contains information about the world around it—from the sunlight that reflects off its surface to the creatures fossilized inside it millions of years ago, he says. But Fuchs argues such information has significance only for a gambling agent who can put it to use.

Rovelli finds the distinction trivial. "QBism and relational quantum mechanics are very, very similar," he says. "In fact, for me, they are the same." But Fuchs insists the two theories have fundamentally different aspirations: QBism aims not to describe what nature is doing, but rather to offer a guidebook that coaches agents to make smart decisions when predicting measurement outcomes. "Now imagine giving the book to a rock … silly, right?" Fuchs says.

He thinks the misunderstanding stems from vague arguments on both sides that are "still at the poetic stage." But he's confident that continuing to mathematically hone their points will lead to new insights—an exercise he says is already paying off. Following the QBist prescription, Fuchs has managed to reformulate equations in quantum mechanics so they can be expressed completely in terms of probabilities. Yale University physicist Michel Devoret—recipient of this year's Nobel Prize in Physics—says the reworked equations have helped him design new experiments. "No matter the angle you choose, quantum mechanics forces you to bend your mind," Devoret says.



Wigner and his friends

In 1961, Eugene Wigner devised a thought experiment that highlights a paradox in quantum mechanics. Inside a sealed lab, Wigner's friend measures an atom, collapsing its superposition into a definite state. But the theory also implies that Wigner, not knowing the measurement outcome, should treat the atom—and his friend—as being in a superposition.

SUPPORT FOR Fuchs's and Rovelli's ideas is growing—and branching into various offshoots—amid a wave of recent work on extensions of the Wigner's friend thought experiments. Their goal is to draw out the tension between absolute events and quantum theory, no matter how it is applied. Essentially, they go as follows: Imagine a copy of Wigner and Jimena—let's call them Wagner and Jamuna. The atoms in Jimena and Jamuna's labs are entangled, so their quantum states are always correlated. From their respective labs, Jimena and Jamuna measure one quantum property of their atoms. From outside the labs, Wigner and Wagner can probe other properties of the entangled atoms by performing their own interference experiments on the entire labs.

In 2018, researchers outlined situations in which the four friends all make measurements of the systems—and cannot agree on the outcomes. Over the following years, multiple teams developed theorems to sharpen this inconsistency, suggesting the observed properties cannot take on definite values. "There are a bunch of really clever tricks designed to elevate [Bell tests] from an argument about hidden variables to an argument about the actual experiences of actual observers," Ormrod says.

In one analysis, Eric Cavalcanti, a physicist at Griffith University, used these mental games to prove that to avoid contradictions, quantum theory requires you to give up one of two things: either local agency—the idea that actions cannot influence events back in time or faster than the speed of light—or the absoluteness of observed events. Relinquishing the former would undermine all of Einstein's work on gravity, so he's more willing to sacrifice the latter. His takeaway builds off the adage from Peres: "Even performed measurements do not have absolute results," Cavalcanti says.

To Fuchs and Rovelli, these efforts only confirm what they've been arguing for years. "They're breaking a window which was already open," Rovelli says. He points out how interpretations that reject absoluteness are gaining popularity particularly among young researchers, as evidenced by a recent *Nature* poll of more than 1100 scientists about their preferred quantum interpretation. Taken together, relational and information-based frameworks (including QBism) were favored by 21% of the respondents. But significantly more Ph.D. students and early-career researchers voted for the radical theories than did advanced-career and retired scientists. Even philosophers of physics such as Ney, who had previously written off relational quantum mechanics and QBism as inconsistent and antirealist, respectively, are warming up to the ideas.

As is typical in quantum theory, not everyone agrees. Many physicists continue to defer to the Copenhagen interpretation (the most common preference in the *Nature* poll), adopting the traditional "shut up and

GRAPHIC: A. FISHER/*SCIENCE*

calculate" approach. And some hold out for alternatives that would leave objective reality intact. Ivette Fuentes, a physicist at the University of Southampton, believes the measurement problem arises because quantum mechanics is incomplete, as it leaves out gravity. "I think these gravitational effects are the culprit," Fuentes says. She dismisses interpretations that treat the quantum wave function as purely relational or informational as sweeping "the problem under the rug."

THE HALLMARK OF SUCCESS for any interpretation will be predicting new experimental results. One study in 2019 attempted to conduct a real-world extended Wigner's friend experiment in the lab using three pairs of entangled photons to represent Wigner and Wagner, Jimena and Jamuna, and their respective quantum experiments. The researchers claimed the outcomes—correlations in the photons' polarization—were observer-dependent.

Critics questioned some of the study's assumptions, including whether individual photons can count as observers. But Alessandro Fedrizzi, a physicist at Heriot-Watt University who led the experiment, stands by the conclusions. "Whenever you do something foundational, everyone pops up and … explains from their perspective why you're wrong," he says. Cavalcanti is now trying to close loopholes in the setup by using better detectors, more spaced-out photons, and "observer" photons that are coupled to increasingly macroscopic objects.

Still, a precise implementation of an extended Wigner's friend in the lab requires complete quantum control over an isolated system containing a sufficiently complex observers. To that end, Cavalcanti and colleagues have proposed experiments on large quantum computers as the ultimate realization of the thought experiment. Artificial intelligence agents running on such a computer (which has not yet been built) could act as the two observers, and the underlying qubit architecture would allow the different friends to be isolated, entangled, and operated on as needed. "Doing the experiment with more and more complex observers will make the results more and more convincing and constraining," Cavalcanti says.

The rejection of absolute events raises a crucial problem, though: If physicists can't all agree on what took place, "how can we do science?" asks V. Vilasini, a physicist at Inria, France's national research institute focusing on computer science and applied math. In a paper last year, she and a colleague proposed a framework for reckoning with Wigner's friend scenarios that are inherently perspectival. It does so by mathematically formalizing the philosophical idea of a "Heisenberg cut"—the exact rift where superposition collapses. The conclusion is that physicists can avoid paradoxes and contradictory statements by refraining from making inferences that rely on different Heisenberg cuts—such as those made by Wigner and Jimena. "You actually don't have to give up on quantum theory; you just have to use it a bit more carefully," she says.

The framework also helps explain why, in our everyday world, events seem to be absolute. Our classical perception of definite events on which we all agree is a product of us all living in the same bubble—in which outcomes are independent of the choice of Heisenberg cut. As macroscopic beings, we are incapable of tracking the intrinsic indeterminacy of quantum particles, which are routinely collapsed into definite outcomes by a constant mess of interactions that serve as measurements. "What remains is a world in which the relativity of facts is invisible," Rovelli says. "So, anything you and I agree on as fact we can call a universal fact."

Why care about the subjective nature of reality if we can't access it, then? Markus Müller, a physicist at the Institute for Quantum Optics and Quantum Information Vienna, draws a comparison to general relativity and its time dilation effects, which must be accounted for in technologies such as GPS. "It's pretty much irrelevant in everyday life," Müller says, and yet "ultimately, it turned out to be very important to understand." If non-absoluteness is indeed a general property of physical theories, we should center physics around experience, he argues. "We belong to be in the picture—that's what quantum theory tells us."

Rovelli takes the subtle lesson to heart. Recognizing the subjectivity of truth offers him a new perspective on life. "It takes away a sense of anguish because I don't access the ultimate reality," Rovelli says. "What's real is what's real relative to us." Fuchs uses a similarly mystical tone, appreciating that "the universe has this character that what you do within it matters," he says. His high school best friend recently suggested QBism is a sort of spiritual tradition. "Maybe so," Fuchs admits. "If quantum mechanics says there's room for me to change the world … somehow that makes life worth living." □



PHOTO: REBECCA MARSHALL/LAIF/REDUX, COLORIZED BY M. ATAROD/*SCIENCE*

> **What's real is what's real relative to us.**
>
> **Carlo Rovelli**
> Aix-Marseille University

COMMENTARY

PERSPECTIVES

SOCIAL SCIENCE

Political persuasion by artificial intelligence

Large-scale studies of persuasive artificial intelligence reveal an extensive threat of misinformation

Lisa P. Argyle

Democratic systems of government depend on persuasion to gain and maintain authority. In an ideal world, policymakers and voters ought to consider the evidence supporting a range of viewpoints and change their opinions and actions to align with the "unforced force of the better argument" [(*1*), p. 159]. However, this ideal process only works if people are able to consider reliable information about many positions. Technological advances have layered another concern into this arena: Will artificial intelligence (AI) technologies supercharge the spread of misinformation and the manipulation of public opinion to the detriment of democratic governance? Hackenburg *et al.* (*2*), on page 1016 of this issue, and Lin *et al.* (*3*) report a varying capacity of generative large language models (LLMs) to persuade citizens about political matters. These studies find that AI can be effectively—although not extraordinarily—persuasive, and they raise important concerns about the scope and effect of AI-generated misinformation.

...a substantial portion of the information provided by the large language models... was false.

LLMs are advanced statistical models that generate text by predicting the probability of the next word in a given sequence. When trained at incredible scale, and typically post-trained or "aligned" to improve performance or reduce unwanted behaviors, "frontier" LLMs are capable of having diverse, responsive, and natural conversations with human counterparts. A growing literature demonstrates that these models, in addition to their many other uses, are highly proficient in producing persuasive text about political topics (*4*, *5*). As people increasingly interact directly with LLMs that are built into their search engines, operating systems, and other apps, the potential for AI to influence users' political opinions—and, by extension, collective democratic outcomes—is further amplified.

Hackenburg *et al.* and Lin *et al.* conducted large-scale experiments in which survey respondents each had one short, text-based, and multiturn interaction with an LLM that was instructed to persuade the human respondent about a political issue or candidate. Hackenburg *et al.* conducted more than 77,000 surveys of UK-based respondents, testing the relative persuasiveness of 19 different LLMs and eight different persuasive strategies across ~700 political issues. Lin *et al.* tested the ability of LLMs to persuade more than 5800 people about candidates for president or prime minister during elections in the US, Canada, and Poland and 500 people about a local ballot measure in the US. Both Hackenburg *et al.* and Lin *et al.* asked respondents to rate the relevant issue or candidate on a 0 to 100 scale before and after the conversation, and both found that interactions with state-of-the-art LLMs move attitudes about a specific political issue roughly 10 points. Additionally, Lin *et al.* compared issue-based persuasion with persuasion about candidates for public office and report that the effects of LLM persuasion on attitudes toward candidates are less consistent and are several points smaller on average.

Existing research on political persuasion documents important tensions: People are reliably persuaded by information in political messages (*6*), but the average persuasive effect of a political campaign in the US is often zero (*7*, *8*), and, in some cases, attempts to persuade can backfire, leading people to be more committed to their preexisting opinions (*9*, *10*). Thus, not all political attitudes and not all political messaging can be treated interchangeably. Some political attitudes—depending on the context but often including partisanship, vote choice, out-group prejudices, or highly salient or moralized issues—are resistant to change, whereas attitudes about specific lower-salience policy matters are likely more flexible. Lin *et al.* report limitations in LLM persuasion consistent with these expectations. When LLMs tried to improve participants' opinions of a specific national candidate for executive office—for whom there is high salience and clear party cues—the LLM was only persuasive for people who initially opposed the candidate. The LLM was also less effective when discussing the personality of the candidate instead of their policy positions and was least effective in the highly polarized US context. Given those cnditions, the persuasion documented by Hackenburg *et al.* and Lin *et al.* can be interpreted as showing that AI is a very good, but likely not superhuman, persuader about the average political issue.

LLMs can produce high-quality text in response to detailed prompts almost instantaneously, which enables efficient and scalable personalized messaging. However, there are concerns that if messages from LLMs are highly personalized, they might negatively affect political reasoning by reducing the range of arguments to which someone is exposed and by appealing to idiosyncratic personal biases. This builds on previous concerns about online "echo chambers" (*11*). Both Hackenburg *et al.* and Lin *et al.* incorporated personalization into their experimental designs: A random subset of LLMs received personal information about the user, such as their existing attitudes, partisanship, or other demographic traits, and were prompted to tailor their messages specifically to those individuals. Hackenburg *et al.* found that although personalization does increase persuasiveness of a message, it is typically a very small effect of less than 1 percentage point. Lin *et al.* did not detect any persuasive gains from personalization of the message, which is consistent with other recent work (*4*, *12*).

In addition to examining message personalization, Hackenburg *et*

al. and Lin *et al.* document the central role of information provision in the persuasiveness of LLM interactions. Of the eight different persuasive strategies tested by Hackenburg *et al.*, the most effective was instructing the model to persuade by providing as much information as possible. They estimated that each fact-checkable claim was associated with ~0.3 percentage points of attitude change (individual messages could have upward of 20 claims) and concluded that information density is the primary single mechanism accounting for variation in the success of LLM persuasion across models and prompts. Testing the inverse approach, Lin *et al.* found a substantial reduction in persuasive capacity when an LLM was prompted not to use any factual claims in the persuasive interaction. The fact-based nature of LLM persuasion contrasts with evidence that information is not the dominant persuasive strategy in human interactions (*13*), which further highlights the complexity and contingency of persuasion research.

Unfortunately, a substantial portion of the information provided by the LLMs in these exchanges was false. Hackenburg *et al.* used separate, search-enabled LLMs to fact-check more than 460,000 claims made by LLMs in the persuasive exchanges. Depending on the model, between 15 and 40% of informational claims made by the LLM were likely misinformation. Lin *et al.* used a similar process and discovered that, in all three countries, LLMs are more likely to produce misinformation in support of candidates or positions on the ideological right. In both studies, the persuasiveness of informational claims did not depend on their accuracy—respondents were just as likely to be persuaded by false information as by true claims. Political decision-making on the basis of fabricated information, particularly when the generation of that information is infused with asymmetric ideological bias, is a fundamental threat to the legitimacy of democratic governance.

Persuasion is a complex, dynamic, and social phenomenon, and complete understanding of persuasive communication requires simultaneous attention to the speaker, topic, message content, medium, setting, intended outcome, message receiver, and more (*14*). The growing use of LLMs by citizens seeking information or campaign organizations and public officials seeking to spread their message introduces a "speaker" with unclear motivations, variable credibility, and potential representational biases into the democratic system. Simultaneously, this speaker is highly persuasive—and seemingly even more so because it is often unconstrained by the truth. Although Hackenburg *et al.* and Lin *et al.* provide relative optimism that manipulation through personalization provides limited marginal returns, they also demonstrate that LLMs are able to use a high density of often fabricated information to produce attitude change at scale. Researchers, policy-makers, and citizens alike need to urgently attend to the potential negative effects of AI-propagated misinformation in the political sphere and how to counteract it. □

REFERENCES AND NOTES

1. J. Habermas, *Moral Consciousness and Communicative Action* (MIT Press, 1990).
2. K. Hackenburg *et al.*, *Science* **390**, eaea3884 (2025).
3. H. Lin *et al.*, *Nature* 10.1038/s41586-025-09771-9 (2025).
4. L. P. Argyle *et al.*, *Proc. Natl. Acad. Sci. U.S.A.* **122**, e2412815122 (2025).
5. T. H. Costell, G. Pennycook, D. G. Rand, *Science* **385**, eadq1814 (2024).
6. A. Coppock, *Persuasion in Parallel: How Information Changes Minds About Politics* (Univ. Chicago Press, 2022).
7. J. L. Kalla, D. E. Broockman, *Am. Polit. Sci. Rev.* **112**, 148 (2018).
8. D. W. Nickerson, T. Rogers, *Science* **369**, 1181 (2020).
9. Y. R. Velez, P. Liu, *Am. Polit. Sci. Rev.* **119**, 1036 (2025).
10. C. A. Bail *et al.*, *Proc. Natl. Acad. Sci. U.S.A.* **115**, 9216 (2018).
11. C. R. Sunstein, *Republic.com* (Princeton Univ. Press, 2001).
12. K. Hackenburg, H. Margetts, *Proc. Natl. Acad. Sci. U.S.A.* **121**, e2403116121 (2024).
13. M. Naunov, C. Rueda-Cañòn, T. J. Ryan, *J. Polit.* 10.1086/735630 (2025).
14. J. N. Druckman, *Annu. Rev. Polit. Sci.* **25**, 65 (2022).

10.1126/science.aec9293

Department of Political Science, Purdue University, West Lafayette, IN, USA.
Email: largyle@purdue.edu

STRUCTURAL BIOLOGY

Molecular basis of DNA cross-linking by bacteria

The structure of the bacterial genotoxin colibactin bound to DNA shows how it might contribute to cancer risk

Orlando D. Schärer

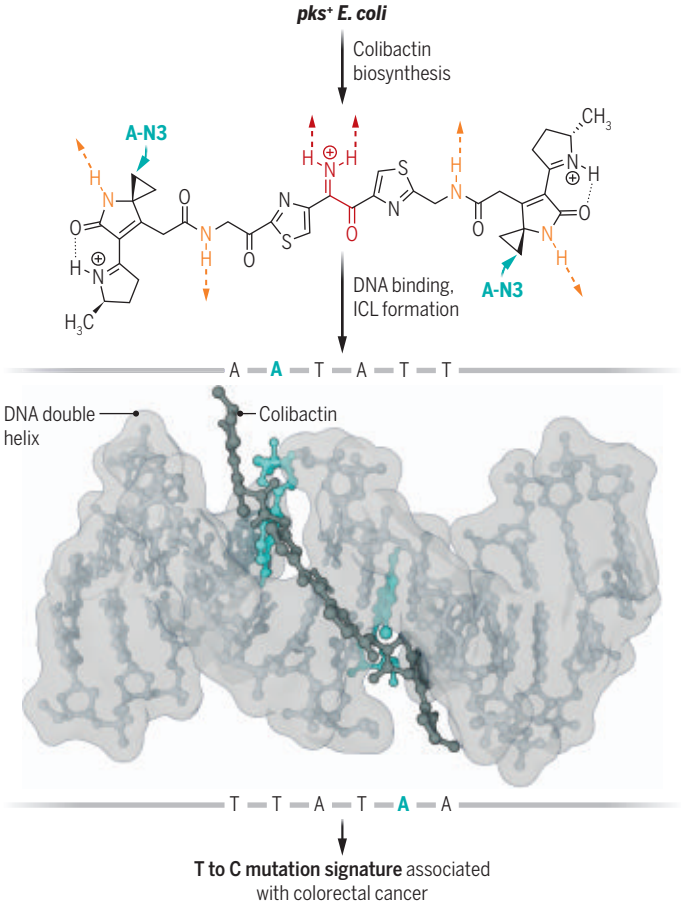
The relevance of the gut microbiome, the community of microorganisms living in the digestive tract, to human health is a topic of intense interest (*1*). However, among the numerous benevolent bacteria living in the gut, there are some species that are harmful to humans. For example, certain strains of *Escherichia coli* produce the genotoxin colibactin, which causes DNA damage and is linked with colon cancer. However, the colibactin molecule is complex and unstable, which has made it challenging to elucidate its chemical structure and the mechanism by which it damages DNA. In the culmination of years of research from multiple laboratories, on page 1017 of this issue, Carlson *et al.* (*2*) reveal the structure of the active form of colibactin bound to DNA. The findings go a long way toward explaining the mutation signatures associated with colibactin exposure and provide substantial insight into how colibactin contributes to colorectal carcinogenesis.

The cluster of genes responsible for the synthesis of colibactin is referred to as the polyketide synthase (*pks*) island. *Pks*$^+$ strains of *E. coli* can induce DNA damage (*3*) and are present with increased frequency in patients with colorectal cancer compared with healthy individuals (*4*). Furthermore, colonization of mice with these colibactin-expressing bacteria leads to increased DNA damage in the adjacent epithelium and promotes tumorigenesis, strongly suggesting a role for colibactin in colorectal cancer etiology. Exposure to colibactin-producing bacteria leads to a distinct mutation signature that is highly enriched in the genomes of colorectal cancer cells, which provides additional evidence for a direct link (*5, 6*).

These observations have triggered intense efforts toward elucidating the chemical structure of colibactin and the molecular basis by which it induces the DNA damage that ultimately causes mutations. Reaching this goal has proven to be a formidable challenge owing to the complex and unstable nature of colibactin. Nevertheless, studies to understand the biochemical mechanisms by which bacteria generate colibactin and efforts to synthesize colibactin from scratch revealed that it has a pseudosymmetrical polyamide structure and that it contains two electrophilic cyclopropane moieties (*7, 8*). Consistent with the presence of two alkylating groups, colibactin forms DNA interstrand cross-links, which are lesions that covalently link the two strands of a DNA double helix. As a block to replication and transcription, interstrand cross-links are among the most cytotoxic and mutagenic DNA lesions. Interstrand cross-link–inducing

How colibactin cross-links DNA

Colibactin is produced by *pks*⁺ *Escherichia coli* and has a pseudosymmetric structure. In the center is an α-imino ketone (red), which contains two protons that make sequence-specific contacts to adenine (A)–thymine (T) base pairs in the minor groove of DNA. The hydrogens in the four amides (orange) also contribute to sequence specificity. Colibactin forms an interstrand cross-link (ICL) between two adenines (teal) on opposing strands located four nucleotides apart; this is achieved by reacting with the nitrogen in position 3 of the adenines. These interactions are consistent with the mutation signature that is induced by colibactin and observed in colorectal cancer cells, which consists of T-to–cytosine (C) base mutations and indels in (A/T)A(A/T)(A/T)T(A/T) sequences.



GRAPHIC: A. MASTIN/*SCIENCE*

agents, such as cisplatin or cyclophosphamide, are also among the most effective cancer therapeutics (*9*).

A major challenge for the full elucidation of the interaction of colibactin with DNA has been the central α-amino ketone moiety at the pseudosymmetric axis, which is prone to oxidation and is a site of subsequent fragmentation. A stable colibactin analog with two methylene groups replacing the α-amino ketone provided a synthetic mimic that was capable of interstrand cross-link formation (*10*). Nonetheless, deciphering the mechanism of DNA cross-linking activity and mutagenicity of the natural colibactin required a strategy to overcome its limited stability. To achieve this goal, Carlson *et al.* exposed various oligonucleotides, short synthetic pieces of DNA, to *pks*⁺ *E. coli* to induce a reaction between DNA and colibactin and succeeded in capturing DNA adducts of endogenous colibactin (*2*). By systematically altering the target sequences, they determined that colibactin cross-links two adenine (A) residues on opposing strands of DNA four nucleotides apart in A- and thymine (T)–rich sequences.

In a true tour de force effort, the authors generated sufficient quantities of colibactin-adducted DNA for the determination of colibactin-DNA structures by high-resolution nuclear magnetic resonance (NMR) spectroscopy. They used an oligonucleotide that reacts well with colibactin and induced hundreds of small-scale reactions between this oligonucleotide and *pks*⁺ *E. coli*. This analysis confirmed the pseudosymmetric structure of colibactin and revealed that it has a concave shape that is highly complementary to the minor groove of the DNA double helix. It also showed that the unstable central moiety is present in oxidized form as an α-imino ketone. The authors found that the two protons of the imine make sequence-specific contacts to A-T base pairs in the minor groove, substantially contributing to colibactin's sequence preference. Additional hydrogen bonds from the amide hydrogens contribute to sequence specificity, as observed in other minor groove–binding polyamides, such as the duacarmycins (*11*). Colibactin forms an interstrand cross-link between two adenines on opposing strands located four nucleotides apart. This is achieved by reacting with the nitrogen atom at position 3 of the adenine molecules (see the figure). Notably, the colibactin analog in which the α-amino ketone had been replaced with two methylene groups exhibited a different sequence preference, demonstrating the importance of the α-amino ketone in colibactin activity. The preferred target sequence of colibactin identified by Carlson *et al.* is (A/T)A(A/T)(A/T)T(A/T), which is consistent with the sequences containing T-to–cytosine (C) base mutations and indels in the mutation signature induced by colibactin and observed in colorectal cancer.

The study of Carlson *et al.* is a milestone in the understanding of colibactin activity that will spur further investigation to ultimately reduce colorectal cancer carcinogenesis. Colibactin-inducted interstrand cross-links are removed from the genome of cells by DNA repair enzymes, and initial insights indicate that this occurs by the Fanconi anemia pathway, similar to interstrand cross-links formed by chemotherapeutic agents (*12, 13*). This repair process itself can be mutagenic, and a compelling question is therefore how cellular processing of the cross-links contributes to colibactin mutagenesis. Colorectal cancer cells frequently display alterations of DNA repair pathways, and it will be intriguing to see whether such changes exacerbate the mutagenic potential of colibactin exposure. An important question is whether the knowledge gained from the characterization of colibactin-DNA adducts can be used to find reliable markers for colibactin exposure and colorectal cancer risk. Will it be possible to use DNA adducts for this purpose or can the knowledge of adduct structure be leveraged to define more precise mutation signatures as a diagnostic? Recent reports furthermore suggest that dietary interventions to counteract inflammation (*14*) or direct inhibition of colibactin biosynthesis (*15*) may provide actionable approaches to counteract the harmful effects of *pks*⁺ *E. coli*. □

REFERENCES AND NOTES

1. J. A. Gilbert *et al.*, *Nat. Med.* **24**, 392 (2018).
2. E. S. Carlson *et al.*, *Science* **390**, eady3571 (2025).
3. J. P. Nougayrède *et al.*, *Science* **313**, 848 (2006).
4. C. M. Dejea *et al.*, *Science* **359**, 592 (2018).
5. P. J. Dziubańska-Kusibab *et al.*, *Nat. Med.* **26**, 1063 (2020).
6. C. Pleguezuelos-Manzano *et al.*, *Nature* **580**, 269 (2020).
7. M. R. Wilson *et al.*, *Science* **363**, eaar7785 (2019).
8. M. Xue *et al.*, *Science* **365**, eaax2685 (2019).
9. D. R. Semlow, J. C. Walter, *Annu. Rev. Biochem.* **90**, 107 (2021).
10. K. M. Wernke *et al.*, *J. Am. Chem. Soc.* **143**, 15824 (2021).
11. S. E. Wolkenberg, D. L. Boger, *Chem. Rev.* **102**, 2477 (2002).
12. M. Altshuller *et al.*, bioRxiv 024.01.30.576698 [Preprint] (2024); https://doi.org/10.1101/2024.01.30.576698.
13. M. Kawanishi *et al.*, *Genes Environ.* **47**, 15 (2025).
14. B. K. Thukar *et al.*, *Nat. Microbiol.* **10**, 855 (2025).
15. M. R. Volpe *et al.*, *Nat. Chem. Biol.* **19**, 159 (2023).

10.1126/science.aec9205

UPMC Hillman Cancer Center and Department of Pharmacology and Chemical Biology, University of Pittsburgh School of Medicine, Pittsburgh, PA, USA. Email: ors51@pitt.edu

STRUCTURAL BIOLOGY

A vision of chromosome organization

Cryogenic electron tomography of condensed chromatin enables multiscale analysis of its structure

Kaite Zhang[1,2] and **Vijay Ramani**[1,3]

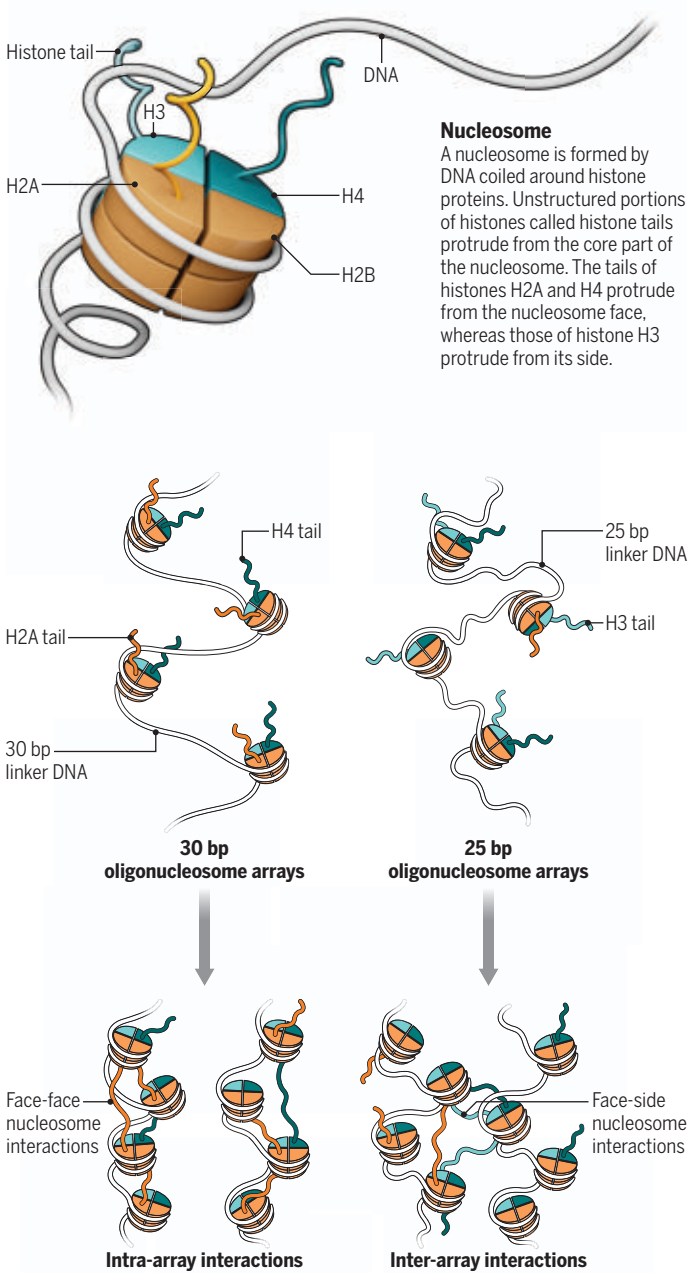
The DNA of eukaryotic organisms is packaged by histone proteins into chromatin. The structural organization of chromatin is tied to its function. Loosely packed, more transcriptionally active regions of chromatin are known as euchromatin, whereas highly condensed, less transcriptionally active regions are known as heterochromatin. Despite advances in the study of chromatin structure over the past 100 years, a biochemical understanding of how basic structural motifs beget higher-order chromatin organization remains lacking. On page 1018 of this issue, Zhou *et al.* (*1*) present an approach that enables imaging and analysis of the structure of chromatin condensates in situ, which moves the field much closer toward defining the structural chromatin motifs that underpin its nuclear functions.

Heterochromatin was first visualized in the nucleus by Emil Heitz in 1928 as dark stains that persisted throughout the cell cycle (*2*). Electron micrographs of chromatin later gave the field a view of the first level of chromatin organization, in which DNA is wrapped around histone protein complexes, forming nucleosomes ("beads") spaced by linker DNA segments ("strings") (*3*). Other electron microscopy studies revealed macromolecular complexes such as RNA polymerase I traversing this "beads-on-a-string" organization of chromatin fibers, revealing how vital cellular processes occur in the context of chromatin structure (*4*). The advent of genomics in the 21st century led to an abundance of datasets that captured aspects of chromosome structure across a wide range of eukaryotic species and cell types (*5*). Despite these advances in methods and knowledge, establishing structure-function relationships in chromosome biology has been hampered by technical limitations. Chromatin within the nucleus is difficult to image with electron microscopy in the absence of contrast agents (*6*). Routine approaches for studying chromatin structure through imaging or high-throughput DNA-sequencing, such as chromosome conformation capture methods (*7*), use harsh fixative agents that may perturb chromatin structure (*8*). In vitro chromatin reconstitution followed by cryogenic electron microscopy have been used to visualize one or two nucleosomes at a time, but studying the structure of longer chromatin fibers remains challenging. By using a combination of chromatin condensate reconstitution, cryogenic electron tomography (cryo-ET), and molecular dynamics simulations, Zhou *et al.* lay the groundwork to solving these issues. Their work also provides a high-resolution view of chromosome conformation across a range of biochemical scales: a single nucleosome, a 12-nucleosome chromatin fiber, and a network of fibers interacting in chromatin condensates.

Previous work demonstrated that reconstituted arrays of evenly spaced nucleosomes along the chromatin fiber have different propensities to form condensates in vitro (*9*, *10*). In vitro chromatin condensates approximate the natural chromatin condensates that exist in the crowded microenvironment of the nucleus (*11*). Nucleosomes that are evenly spaced by linker DNA segments measuring a multiple of 10 base pairs (bp)—"10n"—have a biochemical propensity to remain in solution at physiological salt concentrations, whereas those spaced by linker DNA measuring a multiple of 10 bp plus 5 bp (10n+5) tend to phase-separate into condensates. Zhou *et al.* explored how interactions between histone tails (unstructured portions of the histone proteins that protrude from the nucleosome core) drive chromatin condensation. In the absence of salt, histone

Chromatin interactions

Chromatin fibers have a "beads-on-a-string" conformation in which nucleosomes are "beads" on a "string" of DNA. Reconstituted chromatin fibers containing multiple nucleosomes (oligonucleosomes) spaced by linker DNA of a fixed length have different propensities to form condensates in vitro. When linker DNA is 30 base pairs (bp) long, H2A and H4 histone tails face each other, which promotes intra-array interactions. When linker DNA is 25 bp long, the arrays have a more heterogeneous conformation, including face-side interactions driven by associations between H3 histone tails from nucleosomes in different arrays. These differences in nucleosome connectivity affect the physical properties of chromatin condensates.



GRAPHIC: A. FISHER/*SCIENCE*

tails interact mainly with their own nucleosome. However, at physiological salt concentrations, the interactions of histone tails with nearby nucleosomes increase, both along the same chromatin array and between different arrays.

The authors then examined how nucleosome spacing affects the higher-order structure of chromatin (see the figure). Intuitively, steric constraints caused by DNA linker length might modulate the likelihood of histone tails interacting and therefore the interactions between chromatin fibers. In the case of 30-bp chromatin arrays, Zhou *et al*. found that the tails of histones H2A and H4 protrude from the nucleosome face, which results in an energetically favorable "face-face" nucleosome conformation that promotes stacking interactions between nucleosomes within the same chromatin fiber. Conversely, 25-bp chromatin arrays have a highly heterogeneous set of conformations involving both face-face and "face-side" interactions. Face-side interactions, which are mediated by the flexible tails of histone H3 that protrude from the nucleosome side, contribute to diverse configurations that promote interactions between different chromatin fibers. These differences in interarray interactions are sufficient to change the network connectivity and physical properties of chromatin condensates as measured with biophysical assays.

Zhou *et al*. also used the same techniques to characterize the structure of condensed chromatin from cells (native chromatin). Native condensed chromatin shared many biophysical characteristics with reconstituted 25-bp chromatin, including a heterogeneous connectivity pattern, with both face-face and face-side nucleosome interactions. These experiments are the first measurements of the biochemical underpinnings of chromatin phase separation in vitro and in the cell nucleus.

Future work should focus on defining chromatin interaction motifs in the context of chromatin function. One attractive path forward is to combine the cryo-ET and modeling methods of Zhou *et al*. with additional biochemistry and microscopy techniques. These combined approaches would enable high-resolution visualization of chromatin-associated processes on native sequences (*12*). The combinatorial role of histone tail modifications in modulating chromatin condensation should also be explored. Modifications such as acetylation are commonly found at active enhancers and have an impact on the material properties of chromatin condensates (*9*). The vision of chromatin organization provided by Zhou *et al*. is far from the morphological definition of heterochromatin from 1928. The authors' work provides a roadmap to a future in which the fundamental biophysical properties of chromatin interactions can be visualized, catalogued, and ultimately predicted directly from the genomic blueprint. □

REFERENCES AND NOTES

1. H. Zhou *et al*., *Science* **390**, eadv6588 (2025).
2. E. Heitz, *Jehrb. Wiss. Botanik* **69**, 762 (1928).
3. P. Oudet, M. Gross-Bellard, P. Chambon, *Cell* **4**, 281 (1975).
4. S. L. McKnight, O. L. Miller Jr., *Cell* **12**, 795 (1977).
5. ENCODE Project Consortium, *Nature* **489**, 57 (2012).
6. H. D. Ou *et al*., *Science* **357**, eaag0025 (2017).
7. E. Liberman-Aiden *et al*., *Science* **326**, 289 (2009).
8. K. S. Beckwith *et al*., *Nat. Commun.* **16**, 6673 (2025).
9. B. A. Gibson *et al*., *Cell* **179**, 470 (2019).
10. L. Chen *et al*., *Nat. Commun.* **16**, 6315 (2025).
11. S. F. Banani, H. O. Lee, A. A. Hyman, M. K. Rosen, *Nat. Rev. Mol. Cell Biol.* **18**, 285 (2017).
12. C. Moore *et al*., *Science* **390**, eadr0018 (2025).

10.1126/science.aed0014

[1]Institute for Data Science and Biotechnology, J. David Gladstone Institutes, San Francisco, CA, USA. [2]Tetrad Graduate Program, University of California San Francisco, San Francisco, CA, USA. [3]Department of Biochemistry and Biophysics, University of California, San Francisco, CA, USA. Email: vijay.ramani@gladstone.ucsf.edu

CELL BIOLOGY

A tale of two forms of cohesin in DNA repair

Extrusive and cohesive cohesin cooperate to repair double-strand breaks in DNA

Jiazhi Hu[1,2]

Human cells need to repair DNA damage to preserve genome integrity. Otherwise, accumulated mutations could alter gene function and lead to cell dysfunction and deleterious physiological effects. A double-strand break (DSB) in DNA is particularly dangerous because it can cause chromosomes to rearrange, resulting in the loss of genetic information or incorrect chromosome fusions. One repair process occurs during cell division when the genome is replicated, and although the mechanism is not fully understood, several key proteins have been identified. On pages 1019 and 1020 of this issue, Marin-Gonzalez *et al*. (*1*) and Teloni *et al*. (*2*), respectively, report that two forms of the cohesin protein cooperate to repair DNA in this process. The studies reveal that when the genome is replicated and homologous chromosomes are paired, cohesins facilitate the search for an intact region that is homologous to a break site, an essential step for subsequent DNA recombination and repair.

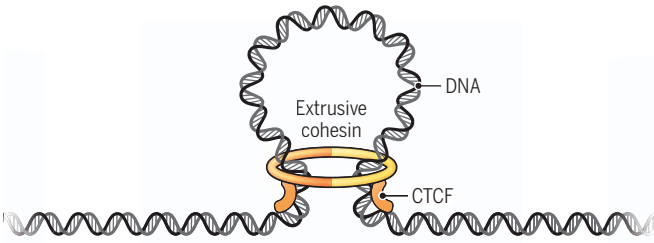
Cohesin is a ring-shaped protein complex that binds double-stranded DNA in eukaryotic cells (*3*). There are two forms of cohesin: extrusive and cohesive (see the figure). Extrusive cohesin brings distant DNA elements into close proximity, "extruding" loops of chromatin (a complex composed of DNA, RNA, and proteins) from chromosomes. This form of cohesin is involved in various cellular processes, such as the DNA recombination mechanism that generates diverse antibodies released by B cells (*4*). Cohesive cohesin is produced during the DNA replication phase of the cell-division cycle, when each chromosome is duplicated into identical copies called sister chromatids. After DNA replication, cohesive cohesin holds sister chromatids together and primes them for chromosomal compaction and segregation during mitosis, just before the cell divides (*5*–*7*).

...homologous recombination ... requires a sister chromatid's DNA to be available as a template.

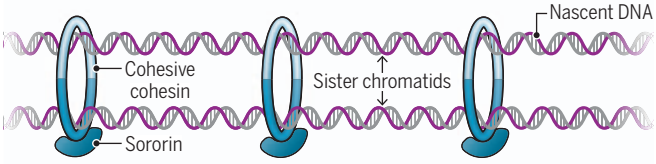
The two main pathways for sealing DSBs are high-fidelity homologous recombination and error-prone nonhomologous end joining (NHEJ). A cell-division cycle in mammalian cells comprises G_1, S, G_2, and M phases. DNA replication occurs in the S phase, and chromosomal compaction and segregation happen in the M phase. NHEJ functions throughout the entire cell cycle, whereas homologous recombination is more active in the S and G_2 phases,

A cohesin partnership

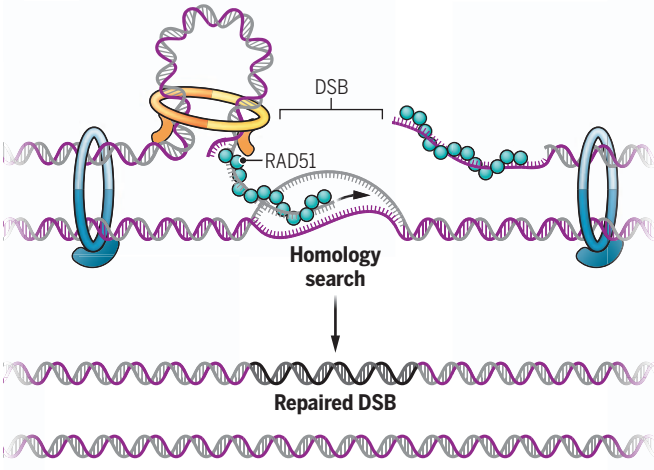
The extrusive and cohesive forms of cohesin have separate functions, but they also cooperate to repair DNA.



1 Extrusive cohesin forms DNA loops. Two CCCTC-binding factor (CTCF) proteins act as "barriers" to stall extrusion at an appropriate point, which determines the size of the loop.



2 Cohesive cohesin is stabilized by the protein sororin and establishes cohesion between sister chromatids after DNA replication.



3 Both cohesins together enable DNA repair. During homology search, single-stranded DNA fragments generated from the broken ends of a double-strand break (DSB) in DNA are coated by radiation-sensitive protein 51 (RAD51). RAD51 then "searches" the sister chromatid for an intact copy of the damaged DNA, which is used to repair the DSB.

as it requires a sister chromatid's DNA to be available as a template (*8*). By tethering sister chromatids to each other, cohesive cohesin plays an important role in homologous recombination. Extrusive cohesin is also rapidly recruited to DSB sites after DNA damage and is thought to promote the function of ataxia-telangiectasia mutated (ATM), the master kinase protein of DSB repair (*9*–*11*).

Marin-Gonzalez *et al.* and Teloni *et al.* found that the two forms of cohesin cooperate to enhance homologous recombination: Cohesive cohesin holds sister chromatids together, and extrusive cohesin directs homology search. Homology search is a key step of homologous recombination, during which a broad region of the sister chromatid is "searched" for the homologous sequence of the broken DNA. During this process, the broken ends of the DSB are extensively digested by exonuclease enzymes, producing long single-stranded DNA segments. These DNA segments are then coated by filaments of the DNA repair protein radiation-sensitive protein 51 (RAD51), and the RAD51-DNA complexes search in the paired sister chromatid for the double-stranded homologous DNA sequence that lacks the break as a template for repair (*8*). Teloni *et al.* used a reversible protein degradation system to destroy the RAD21 subunit of the cohesin complex in cultured human cells. Cohesin disruption reduced the searching scope of RAD51 and the rate of DNA repair driven by homologous recombination. Using a new method, called sister-pore-C, Teloni *et al.* also revealed that both forms of cohesin are involved in homology search. Cohesive cohesin restricts homology search to a narrow region that includes the DSB site, whereas extrusive cohesin promotes efficient movement of RAD51-coated DNA toward homologous DNA fragments in a broad region of the sister chromatid. The size of the DNA loops extruded by cohesin is usually defined by a pair of CCCTC-binding factor (CTCF) proteins that act as "barriers" to stall extrusion at an appropriate point (*12*, *13*). Marin-Gonzalez *et al.* reveal that these CTCF-bound loop "anchors" define the boundaries of homology search during homologous recombination in cultured human cells.

Extrusive cohesin initiates loop extrusion in early G_1 phase (*14*), and cohesive cohesin is generated in the S phase during DNA replication. Long-range chromatin contacts induced by loop extrusion are progressively replaced by local interactions throughout the S phase (*15*), implying that extrusive cohesin is gradually replaced by cohesive cohesin after DNA replication. Because homologous recombination is very active in the S and G_2 phases in human cells, it is plausible that extrusive cohesin remains abundant during these periods. The findings of Marin-Gonzalez *et al.* and Teloni *et al.* indicate that extrusive cohesin plays a complementary role to the cohesive form in homologous recombination. In this context, extrusive cohesin might reorganize the structure of chromatin for various purposes, including DNA repair, rather than being passive or inert after DNA replication.

Whether the two forms of cohesin can be converted into each other, and whether DNA repair proteins interact with them to coordinate their function, remains to be explored. In addition to homologous recombination, cohesin may be involved in other DSB repair pathways. Analyses of cells in G_1 would help to clarify this point, as at this phase of the cell cycle, homologous recombination is strongly repressed, NHEJ predominates, and only extrusive cohesin is present in mammalian cells. □

REFERENCES AND NOTES

1. A. Marin-Gonzalez *et al.*, *Science* **390**, eadw1928 (2025).
2. F. Teloni *et al.*, *Science* **390**, eadw0566 (2025).
3. R. Barth *et al.*, *Cell* **188**, 749 (2025).
4. Z. Ba *et al.*, *Nature* **586**, 305 (2020).
5. J. M. Peters, T. Nishiyama, *Cold Spring Harb. Perspect. Biol.* **4**, a011130 (2012).
6. H. Zhao *et al.*, *Nature* **640**, 543 (2025).
7. F. Ochs *et al.*, *Science* **383**, 1122 (2024).
8. J. Renkawitz, C. A. Lademann, S. Jentsch, *Nat. Rev. Mol. Cell Biol.* **15**, 369 (2014).
9. C. Arnould *et al.*, *Nature* **590**, 660 (2021).
10. C. Arnould *et al.*, *Nature* **623**, 183 (2023).
11. A. Piazza *et al.*, *Nat. Cell Biol.* **23**, 1176 (2021).
12. S. S. Rao *et al.*, *Cell* **159**, 1665 (2014).
13. Y. Guo *et al.*, *Cell* **162**, 900 (2015).
14. H. Zhang *et al.*, *Nature* **576**, 158 (2019).
15. T. Nagano *et al.*, *Nature* **547**, 61 (2017).

ACKNOWLEDGMENTS

The author acknowledges support by the National Natural Science Foundation of China (NSFC) (32425015), National Key R&D Program of China (2022YFC3400200), and the Ministry of Agriculture and Rural Affairs of China. The author used an artificial intelligence (AI)–assisted tool (DeepSeek 3.1) to improve the readability of an earlier version of the manuscript.

10.1126/science.aed1859

[1]State Key Laboratory of Gene Function and Modulation Research, School of Life Sciences, Peking University–Tsinghua University (PKU-THU) Center for Life Sciences, Peking University, Beijing, China. [2]Peking University Chengdu Academy for Advanced Interdisciplinary Biotechnologies, Chengdu, Sichuan, China. Email: hujz@pku.edu.cn

GRAPHIC: N. BURGESS/*SCIENCE*

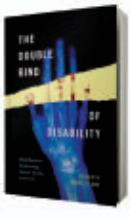


MEDICINE

Centering disabled perspectives in technology

Medical testing and devices must be reimagined to combat ableism, argues a disability scholar

Johnathan Flowers



Rebecca Monteleone
University of Minnesota Press, 2025. 216 pp.

THE DOUBLE BIND OF DISABILITY | In one sense, Rebecca Monteleone's new book, *The Double Bind of Disability*, is straightforwardly about the discursive power of medical technologies and the medical apparatus to shape our understanding of disability. As such, she argues that the cultural reliance on medicine and medical technology as the arbiter of normative embodiment increases the marginalization of embodied experience. Insofar as this is the case, disabled people are uniquely at risk for marginalization because of how disability is increasingly viewed as a problem to be solved or a disease to be cured, rather than as part of one's ongoing embodied experience. However, "in another sense, this is not a book about technology at all," writes Monteleone. "It is a book about people, about power, about knowledge." It is from this latter perspective that readers should approach *The Double Bind of Disability*.

Following a long history of scholarly work by disabled activists and scholars, Monteleone argues that while medical technology is a source of marginalization for disabled people, it is also the source of a liberatory politics and praxis that resist the individualizing pressures of the medical apparatus. It does so by redefining what is acceptable in terms of embodiment and by validating the experiential knowledge that emerges from nonnormative embodiment. Medical technology users are thus caught in a "double bind" between the oppressive structures of this type of technology and the liberatory potentials that emerge from it.

Medical technologies and medicine itself increasingly transform health and disability into the responsibility of individual persons, while simultaneously marginalizing the knowledge that emerges from the lived experiences of those with disabilities. As Monteleone's text aptly demonstrates, disabled people are often both held responsible for their conditions and considered unreliable informers about them.

The book's first chapter not only introduces Monteleone's methodological and philosophical commitments but also draws upon disability studies, philosophy, science and technology studies, and feminism to make clear the origins of our understandings of disability and why these understandings must be challenged. Chapters 2 and 3 present a compelling argument for how advances in medical technology reshape disability, while chapter 4 presents a radical vision of how users of medical technology "crip" the very apparatus responsible for their marginalization, creatively reimagining technologies to challenge able-bodied assumptions. Her focus is on three forms of medical technology: prenatal genetic testing (PGT), deep brain stimulation (DBS), and do-it-yourself artificial pancreas systems (DIYAPS).

In chapter 2, "Becoming Responsible with Prenatal Genetic Testing," Monteleone focuses on how advances in PGT have led to a perceived obligation for potential parents to seek out these tests. This obligation follows from ableist ideas of disability as either a tragic event or as a valuable addition to the diversity of a community. In both contexts, the future disabled child is decentered in favor of the implications of the disabled child for the nondisabled parents. As a result, writes Monteleone, "the introduction of these new technologies creates responsibilities that pregnant people are expected to navigate in a way that satisfies both their private and their public duties."

Monteleone's engagement with DBS in chapter 3, "Losing and Taking Control with Deep Brain Stimulation," argues that the discourse surrounding the development and use of DBS transforms disability into a physiological phenomenon to be "fixed." As DBS is framed as a means to regain the control over life that disability has stripped away, seeking DBS treatment becomes a moral obligation necessary to live ableist and neoliberal conceptions of a "good life."

It is in Monteleone's fourth chapter, "Reimagining Agency with Do-It-Yourself Artificial Pancreas Systems," where she provides the ground for the possibility of a future beyond the medical establishment. Here, she demonstrates how DIYAPS users reclaim agency over their embodiment and their disability through technology. In doing so, they develop alternatives to the individualization and medicalization of diabetes by rejecting the promise of a cure offered by the medical establishment. Instead, they reframe the risk of, and responsibility for, treatment through validation of embodied experience. This approach transforms the experience of diabetes from an individual one to a communal one through collaborative knowledge generation and circulation outside of the disciplinary structures of medicine.

Monteleone concludes by arguing for the reimagining of medical technology as a means to intervene in the very structures that marginalize and delegitimize the knowledge produced by medical technology users and disabled people. It is here that *The Double Bind of Disability* emerges as an all too necessary text in an age of rising ableist sentiment. The book provides lessons that those committed to the development of a more just world should take to heart, in this political moment and beyond. □

10.1126/science.aec0099

The reviewer is at the Department of Philosophy, California State University, Northridge, Northridge, CA, USA. Email: johnathan.flowers@csun.edu

PHOTO: JOHNER IMAGES VIA ALAMY

EVOLUTIONARY BIOLOGY

Painting the phylogeny of life

An evolutionary biologist invites readers to travel back in time to meet humanity's distant ancestors **Yan Wong**



The Tree of Life: Solving Science's Greatest Puzzle
Max Telford
Norton, 2025.
320 pp.

The tree of life is often likened to a map of the living world. Of course, a map is a human artifact: a necessary but imperfect guide to the richness of reality. As Max Telford points out in the introduction to his new book, *The Tree of Life*: "A tree on its own is like a perfectly pieced-together jigsaw puzzle with no pictures on it." The goal of this book is to paint those pictures, treating the tree of life as a portal to the past, and to "add flesh to the bare skeleton of the tree's form."

The book is crammed full of such arresting similes and metaphors. Another is Telford's description of neural crest cells as "Bedouin warriors…following invisible songlines" contrasted with the bulk of cell movements, which are more like the maneuvers of a large army. These flights of fancy make for a compelling and memorable read, even when discussing seemingly arcane details of worm anuses.

Telford is largely successful in his ambitious goal, and the reader comes away with a pleasingly impressionistic picture of life's ancestry. Moreover, he proves to be an erudite, highly informed, and frequently amusing guide to evolutionary history. His own speciality, the origin of animals, flavors the book. "The Diet of Worms," for example, is a chapter in which he describes not only collecting the enigmatic xenoturbellan worms in the field (more accurately the fjord) but also the attendant controversy about their place on the tree and what it implies for animal evolution.



The richness of life's ancestry is revealed in this vivid introduction to the phylogenetic tree.

This mix of the uncertainty of research, the excitement of new discovery, and the importance of solving "science's greatest puzzle" is what makes the book such a delight. I was rapidly infected with the enthusiasm that Telford so clearly has for his subject, and I hope this will likewise sustain the reader through the necessary but more challenging sections on phylogenetic tree reconstruction, long branch attraction, gene duplication, and so forth. This would make a fantastic informal introduction to a course on evolution—indeed, I have already recommended it to my first-year students.

For a relatively short book, much material is covered, but there is still welcome space for anecdotes, potted biographies, and etymological digressions. How did I not know, for example, that guanine—the "G" in the DNA alphabet—was named after its extraction from guano (i.e., bird droppings)? Or that the giant chromosomes in the salivary glands of *Drosophila* help make copious quantities of sticky glue to aid pupation? Or that the loss of our own tails came down to an insertion of a parasitic *Alu* element into the primate equivalent of the *Brachyury* gene? The book unearths many more fascinating nuggets of biological information, which are liberally distributed throughout.

Occasionally, Telford's metaphors are somewhat strained, such as his comparison of the scaling of life's history to the height of a human body, and I found the final section, tracing the steps toward humans, perhaps the least satisfying. This could be because the tale is necessarily condensed into 14 ancestors discussed in a mere four chapters or perhaps because of the lurking temptation of seeing purpose and inevitability in a history ending in the "summit of our climb." Nevertheless, it includes some delightful passages, such as the observation that "we humans spend our entire lives walking backwards" (I would encourage you to read the book to see why this is a convincing argument).

Our understanding of biology in general, and the tree of life in particular, has been transformed by our ability to read DNA sequences. Many technical aspects of this revolutionary change, such as the use of the molecular clock, are covered in Telford's book, but recent moves toward consideration of whole genomes—and even pangenomes—go largely unmentioned. For example, it would be possible to come away from the book thinking that a genome is almost entirely composed of genes. In fact, the 20,000 or so genes in a human genome make up only a tiny fraction of our total DNA, and there is little mention of regulatory regions, let alone the reams of viral and other "selfish DNA" that pollute our genome. Another example is the conundrum of incomplete lineage sorting. I would have loved Telford to turn his gift for explanation and analogy to this problem, which affects a surprising number of the tree's branch points and even threatens to undermine the idea of a single "species tree."

Finally, as with any fast-moving topic, some ideas are likely to be refuted by subsequent research, such as the highly doubtful suggestion of a human population crash 900,000 years ago. But as *The Tree of Life* celebrates the advancement of science through the overturning of previously proposed ideas, I am sure that the author would celebrate any such future revisions. I can heartily recommend the book to anyone interested in life on Earth, the scientific endeavor, and what it is to be human. □

10.1126/science.aec7390

The reviewer is at the Big Data Institute, University of Oxford, Oxford, UK.
Email: yan.wong@bdi.ox.ac.uk

IMAGE: ART DIRECTORS & TRIP VIA ALAMY

SAFE Act hinders US-China collaboration

The US Securing American Funding and Expertise from Adversarial Research Exploitation (SAFE) Act, introduced as Amendment 163 to the National Defense Authorization Act for Fiscal Year 2025 (*1*), would bar US scientists from federal funding if they have collaborated within the past 5 years with researchers affiliated with China, Russia, Iran, or North Korea. Prohibited activities include co-authorship on papers, joint projects, and mentoring foreign postdoctoral scholars. Such a blanket policy would fracture essential international partnerships at a moment when global challenges demand cooperative expertise.

Recent studies highlight the evolving dynamics of US-China scientific partnerships. Collaboration across disciplines increased steadily from 2000 to 2018, but this trend reversed sharply after 2019 because of US policies that began to restrict scientific relations (*2*). An analysis of millions of scientific papers found that China's role in leading US-China collaborative projects increased from 30% in 2010 to 45% in 2023. This shift reflects China's growing influence in global science (*3*). Amid geopolitical tensions, joint efforts in sustainable development research have also shown proportional declines, limiting progress on critical issues such as climate change (*4*).

Existing partnerships, however, continue to yield substantial benefits. Joint US-China efforts in artificial intelligence (AI) produce more impactful research than independent work on AI by either nation (*5*). In the automotive sector, increasing collaboration with China could revitalize US innovation by leveraging complementary strengths. For example, American expertise in advanced research and design could pair with China's manufacturing scale and cost efficiencies in electric vehicles and supply chains (*6*). Sustained US-China collaboration could accelerate innovation that benefits both nations and the world (*7*, *8*).

Safeguards already exist to protect sensitive technologies, such as the Export Administration Regulations and the International Traffic in Arms Regulations (*9*). The indiscriminate approach of the SAFE Act would isolate US researchers, accelerate shifts in global scientific leadership, and undermine the open collaboration, as warned by nearly 800 academics (*10*). Congress should reject this provision and preserve evidence-based security measures, countering unsubstantiated claims in recent congressional reports that most US-China research partnerships threaten national security (*11*).

Alex J. Yang[1,2], Richard B. Freeman[2,3], Sanhong Deng[1,4]

[1]School of Information Management, Nanjing University, Nanjing, China. [2]Center for Labor and a Just Economy, Harvard Law School, Cambridge, MA, USA. [3]Department of Economics, Harvard University, Cambridge, MA, USA. [4]International Joint Informatics Laboratory, Nanjing University, Nanjing, China. Email: alexjieyang@outlook.com

REFERENCES AND NOTES

1. J. Moolenaar, Amendment 163 to H.R. 8070 (NDAA for Fiscal Year 2025), containing the Securing American Funding and Expertise from Adversarial Research Exploitation (SAFE) Research Act of 2025, 118th Cong. (submitted 28 August 2024); https://amendments-rules.house.gov/amendments/MOOLEN_163_xml250828161843908.pdf.
2. K. Kitajima, K. Okamura, *Humanit. Soc. Sci. Commun.* **12**, 302 (2025).
3. R. Wu, C. Esposito, J. A. Evans, *Proc. Natl. Acad. Sci. U.S.A.* **122**, e2414893122 (2025).
4. R. Li *et al.*, *Humanit. Soc. Sci. Commun.* **11**, 1448 (2024).
5. B. AlShebli *et al.*, *Sci. Rep.* **14**, 28576 (2024).
6. J. P. Helveston, *Science* **390**, 446 (2025).
7. V. J. Karplus *et al.*, *Nature* **637**, 545 (2025).
8. R. N. Beachy, K. C. Seto, *Proc. Natl. Acad. Sci. U.S.A.* **120**, e2320207120 (2023).
9. US Government Accountability Office (GAO), "China: Efforts underway to address technology transfer risk at U.S. universities, but ICE could improve related data" (GAO-23-106114, GAO, 2022).
10. J. Mervis, *Science* **390**, 662 (2025).
11. J. Moolenaar, T. Walberg, "Joint Institutes, Divided Loyalties: How the Chinese Communist Party exploits U.S. university partnerships to empower China's military and repression" (2025); https://selectcommitteeontheccp.house.gov/media/reports/joint-institutes-divided-loyalties.

10.1126/science.aed7998

Smart irrigation needs smart policies in Iran

Agriculture accounts for more than 75% of Iran's water use, but water productivity—crop yield per unit of water used—is only 1.35 kg/m^3 (*1*), which can reach more than 2.0 to 2.5 kg/m^3 at the global scale (*2*). To align with its National Food Security Plan, Iran aims to reduce agricultural water consumption by 30 billion m^3 by 2032 (*3*) with smart irrigation (SI) technology that uses data and, in some cases, sensors to adjust watering, reduce waste, and enhance water productivity (*4*). SI would also use artificial intelligence (AI) to analyze data, make predictions of future environmental conditions, and better manage the supply for crops. Despite its potential, this plan is likely to fail in Iran's smallholder farming context, wasting public resources and undermining efforts to improve water and food security.

The reliability of SI in irrigation management hinges on the availability, in real time, of high-quality data on soil moisture, crop status, and local weather conditions (*5*, *6*). In Iran, these data streams are often compromised because of sparse networks of weather stations, inconsistent internet connectivity, and limited on-farm sensing infrastructure. Thus, AI may misguide irrigation scheduling, which could lead to under- or overirrigation. Evapotranspiration forecasts, critical to many irrigation algorithms, can exhibit errors of 16 to 25% for daily estimates and 11 to 16% over a 7-day span (*7*). In Iran, these errors are typically higher, ranging from 20 to 35%, depending on the region, which reflects the need for localized calibration (*8*). Moreover, the reliability of near–real-time weather predictions is especially constrained in mountainous or remote agricultural zones (*9*, *10*). Iran's complex topography, diverse microclimates, and limitations to expanding the required infrastructure compromise the applicability of SI technology.

The utility of SI also depends on access to a minimum amount of water, which is an increasingly unmet condition in many smallholder farming regions. In areas where irrigation water is already insufficient or unavailable, technologies that are unusable further widen disparities in agricultural productivity. Even in better-resourced regions, the adoption of SI may produce counterproductive outcomes through the rebound effect (*11*). As farmers improve water productivity, they may reinvest savings into expanding cultivated areas or shift to higher-value, more water-intensive crops. The resulting increase in total water use could offset efficiency gains.

Realizing the potential of SI requires implementing comprehensive water governance reforms before widespread technology deployment. This should begin with establishing basin-level governance that sets a limit on total water use, granting rights to access parts of that water, and allowing those rights to be bought and sold. The price of water should also reflect its true limited availability rather than an artificial price that can vary according to government subsidies. Without reforming water governance with smart policies, Iran likely will not achieve its ambitious water reduction target (and food security goals) through SI technology.

Alireza Gohari[1], Julie Shortridge[2], Ali Torabi Haghighi[1]

[1]Water, Energy, and Environmental Engineering Research Unit, University of Oulu, Oulu, Finland. [2]Department of Biological Systems Engineering, Virginia Polytechnic Institute and State University, Blacksburg, VA, USA. Email: alireza.gohari@oulu.fi

REFERENCES AND NOTES

1. F. Abbasi, N. Abbasi, A. Tavakoli, *Water Sustain. Dev.* **4**, 141 (2017).
2. W. G. M. Bastiaanssen, P. Steduto, *Sci. Total Environ.* **575**, 595 (2017).
3. X. Shahrivar, "Reducing agricultural water consumption by '30 billion cubic meters' on the government's agenda" (Engl. transl.), Tasnim News, 2024; https://tn.ai/3159960.



Local demand for meat is contributing to the decline of wild pangolins in African forests.

4. Tehran Times, "Over 100 smart irrigation pilot projects implemented in Iran," *Tehran Times*, 28 September 2024.
5. A. Ali, H. Tajamul, Z. Azlan, *AgriEngineering* **7**, 106 (2025).
6. L. Umutoni, V. Samadi, *Agric. Water Manage.* **294**, 108710 (2024).
7. F. Gómez, O. Lagos, P. M. Gil, J. Jara, D. Zaccaria, *Sci. Total Environ.* **957**, 177606 (2024).
8. S. Veysi, M. Nouri, A. Jabbari, *Heliyon* **10** e26531 (2024).
9. K. Hoghoughinia, B. Saghafian, S. Aminyavari, *Meteorol. Atmos. Phys.* **134**, 87 (2022).
10. M. Fathi, M. Azadi, G. Kamali, A. H. Meshkatee, *J. Earth Syst. Sci.* **128**, 133 (2019).
11. P. Hoffmann, S. Villamayor-Tomas, *Sustain. Sci.* **18**, 181 (2023).

10.1126/science.aeb8221

Address domestic pressures on endangered species

This week, the Convention on International Trade in Endangered Species of Wild Fauna and Flora (CITES) convened in Uzbekistan. A major goal was to prevent international trade in wild species from threatening their survival by listing them in one of three appendices (each with specific international trade restrictions) (*1*). Parties to the CITES and other delegates must recognize that for species exploited domestically for different purposes (or products) than for illegal export—such as for meat and skins—resolutions focused solely on international trade regulation may yield little ecological and conservation benefits, regardless of how effectively they are executed.

Commercial international trade of four African pangolin species is prohibited under CITES Appendix I, yet recent evidence suggests that the exploitation of wild pangolins in Nigeria and possibly across African forest landscapes may be driven primarily by local demand for meat, with two-thirds of pangolin scales thrown away and the rest exported as a by-product (*2*). When a local situation such as food consumption is the primary driver of species decline, successfully curbing international trade is unlikely to halt population loss. A similar local-international divergence in use occurs for pirarucu, listed in CITES Appendix II, whose meat is a crucial part of local diets and whose skins are mainly traded internationally (*3*, *4*). More broadly, among taxa for which use as a resource is a threat to their survival, four times more species are affected by local use than by international trade (*5*). This underscores the need to ensure that CITES listings of endangered species are aligned with domestic pressures on those species.

Although certain threats, such as habitat loss and climate change, fall outside the Convention's remit, those linked to exploitation should be addressed across geographic scales (local, national, and international) to avoid counterproductive outcomes. For example, unsustainable harvesting of a species can have different local and global impacts as well as short- and long-term effects. To ensure that listings achieve intended conservation goals, CITES should identify where drivers of harvest differ locally versus internationally across its ~40,900 listed species (beginning with those classed as threatened), and such assessments should be criteria for future listing decisions. Insights from these analyses could guide targeted, context-specific interventions developed in collaboration with local authorities. CITES could then better align with complementary international treaties, such as the Convention on Biological Diversity (*6*, *7*), which possess the mandate to influence national and subnational biodiversity policies and actions.

Charles A. Emogor[1,2]

[1]Department of Computer Science and Technology, University of Cambridge, Cambridge, UK.
[2]Department of Zoology, University of Cambridge, Cambridge, UK.
Email: emogorcharles@gmail.com

REFERENCES AND NOTES

1. CITES; https://cites.org/eng.
2. C. A. Emogor *et al.*, *Nat. Ecol. Evol.* **9**, 1349 (2025).
3. S. Charity, J. M. Ferreira, "Wildlife trafficking in Brazil" (TRAFFIC International, 2020).
4. D. J. Orth, "Integrating fishers in the management of *Arapaima*" in *Fish, Fishing, and Conservation* (Virginia Tech Department of Fish and Wildlife Conservation, 2023), chap. 11.
5. D. W. S. Challender *et al.*, *Nat. Ecol. Evol.* **7**, 1211 (2023).
6. D. W. S. Challender, M. 't Sas-Rolfes, S. Broad, E. J. Milner-Gulland, *Front. Ecol. Evol.* **13**, 1425267 (2025).
7. D. Roe *et al.*, *Making a Killing or Making a Living?: Wildlife Trade, Trade Controls, and Rural Livelihoods* (IIED, 2002).

10.1126/science.aed7058

PHOTO: PETE OXFORD VIA MINDEN PICTURES

POLICY ARTICLE

CONSERVATION

Toward science-based conviction criteria to deter wildlife crime

Risk assessment is needed for China's new conviction standards based on monetary value

Ruocheng Hu[1], Shuangqi Liu[2], Lingyun Xiao[3], Ziyun Zhu[1], Yuehan Dou[3], Shen Zhang[4], Xiaotong Ren[5], Fangyuan Hua[2], Zhi Lu[1]

Amid the ongoing global biodiversity crisis (*1*), a key policy mechanism for species conservation is to establish and enforce scientifically grounded rules to define whether harmful activities—such as poaching, trade, and habitat destruction—constitute criminal behavior and should be convicted (*2*). China in recent years has made multiple amendments to its conviction criteria for crime on terrestrial vertebrates, including changing the basis of the criteria from the numbers of animal individuals involved in a given offense to their monetary values (*2*). As we demonstrate with a new analysis on all of China's 522 protected bird and terrestrial mammal species, for the vast majority of species assessed, these amendments have meant that substantially greater numbers of individuals are now required for a given offense to be deemed convictable, and overwhelmingly at reduced penalty severities. The resultant risk of weakened crime deterrence has been evidenced by judicial outcomes and observations of conservation practitioners.

Anchoring on the Wildlife Protection Law instituted in 1988 (*2*), China has over the past four decades developed a framework of conviction criteria for crime on terrestrial vertebrates that comprises two main components (supplementary text and table S1). The first entails stringent protection of a list of Class I or II "State Key Protected Wild Animals" ("protected species" hereafter; Class I is of higher conservation concern than Class II; offenses on these species may be punishable by imprisonment of ≥10 years), complemented by basic protection of all other species (potential imprisonment up to 3 years; supplementary text). The second component is a set of conviction standards applicable to each protection category (table S2). Relatedly, the protection category of a species corresponds in large part to its level of conservation concern in China, and by way of conviction standards (detailed in table S2), largely determines the strength of legal deterrence to its would-be offenses and thus of its protection.

This framework was substantially amended in both components during the past 5 years, precipitated by concerns during the COVID-19 outbreak about zoonosis risks from wildlife trade and about the concerted safeguard of biodiversity and public health (*2*). First, the number of protected species increased considerably, by 78.5% (from 135 to 241 species) and 268.6% (from 347 to 1279 species) for Class I and II protection, respectively (fig. S1) (*3*), thus placing almost two-thirds of China's threatened terrestrial vertebrates—i.e., those listed as Critically Endangered, Endangered, or Vulnerable in China's Red List assessment—under stringent protection (*3*). Second, conviction standards expanded to penalize habitat destruction and the consumption of terrestrial vertebrates for food, activities not previously covered by clear regulations (*4*). These amendments occurred in 2020–2021 and have been widely regarded as a progressive step in strengthening China's legal framework for wildlife protection (*5*).

In a third amendment to China's framework of conviction criteria for crime on terrestrial vertebrates, the basis of conviction standards changed in 2022 from the numbers of animal individuals involved in a given offense to their monetary values (table S2), to be calculated on the basis of a national catalog of the per-individual values of all terrestrial vertebrates and select invertebrates in the context of wildlife offense (supplementary text and table S1). This catalog had previously been issued by the then State Forestry Administration (now named the State Forestry and Grassland Administration) in 2017 to establish standards for fines—an additional penalty form other than imprisonment—on unlawful wildlife offenses. The making of this catalog did not involve known public consultation, and it remains unclear how the per-individual values of each species were defined. As two example values provided by this catalog, one giant panda (*Ailuropoda melanoleuca*; Class I protection) is valued at CNY 500,000 (USD ~68,700, at 2025 rates), and one red panda (*Ailurus fulgens*; Class II protection) at CNY 8000 (USD ~1100).

Despite having been issued for a different purpose earlier, this catalog was directly invoked in the 2022 amendment and has since constituted a core foundation for the new monetary approach to conviction standards. Accordingly, the amended conviction standards stipulate the thresholds of total monetary values involved in a given offense—to be summed across all animal individuals involved—above which it would be deemed convictable, and at what level of penalty severity (supplementary text and table S2). Unlike the previous two amendments, the motivation for this third amendment and its switch to a monetary approach was likely less from COVID-19 than linked to a number of high-profile cases leading up to 2022, debates around which generated criticisms on China's judicial system of excessive criminalization of wildlife offenses (*6*). An additional intention of this switch may have been to simplify judicial processes in situations where multiple species were involved (*7*).

This third amendment marks a major shift in how wildlife offenses are incriminated in China and can have profound implications for the strength of crime deterrence—depending on how the new monetary conviction standards translate into thresholds of animal individuals for a given offense to be considered convictable ("convictable individual number" for short hereafter). Such implications are particularly relevant and consequential for protected species, for which crime deterrence constitutes a key conservation mechanism. Indeed, unlike the sweeping welcome received by the other two amendments, concerns have been raised about weakened crime deterrence on protected species as a result of the new monetary standards (*7–10*). Notably, two recent analyses found that for nine protected species assessed, the switch to monetary standards has substantially increased the convictable individual numbers for all species except for the giant panda, across levels of penalty severity (*7, 10*). To date, however, it remains unclear what this switch means for convictable individual numbers and crime deterrence across China's hundreds of protected terrestrial vertebrates.

Here, we report a formal assessment aimed at filling this urgent knowledge gap, focusing on all 390 bird and 132 terrestrial mammal species under Class I or II protection in China (*11*). Of all terrestrial vertebrate groups, birds and terrestrial mammals were the only groups for which conviction standards before the recent amendments—i.e., based

on the numbers of animal individuals involved in a given offense—were delineated for a reasonable number of protected species, linked to the fact that the vertebrates listed as protected preamendment were predominantly birds or terrestrial mammals. For each study species, and assuming a simplified situation where it was the only species involved in a given offense, we first converted the amended conviction standards from monetary values to the species' current convictable individual numbers (rounding up to the next integer where applicable) (*11*). We did this for each of the three levels of imprisonment severity in China's judicial system concerning crime on protected species: ≤5 years or detention ("Level 1" hereafter), 5 to 10 years ("Level 2"), and ≥10 years ["Level 3"; the level given to an offense would depend on the numbers (preamendment) or total monetary values (postamendment) of the animals it involves].

We then focused on the subset of 238 bird and 96 terrestrial mammal species already listed as protected before the recent amendments (and thus had convictable individual numbers delineated preamendment) to compare their current convictable individual numbers with the corresponding numbers preamendment. It became clear that the switch to monetary conviction standards has led to marked increases in convictable individual numbers across all 334 species assessed: for Level 1, 2, and 3 imprisonment severities, not only did these numbers increase for 55.1, 81.6, and 97.6% of species, respectively, but these increases also averaged at 2.81-, 5.94-, and 39.30-fold (see the figure) (fig. S2) (*11*). The Sino-Mongolian beaver (*Castor fiber birulai*; Class I protection), a rare and endangered subspecies of the Eurasian beaver, provides an illustrative example: Whereas an offense would have been convictable with Level 3 imprisonment severity if it captured or killed two or more individuals before the switch, with the species valued at CNY 500 (USD ~70) per individual, an offense would now have to involve at least 400 beavers—~57% of its estimated Chinese population (*12*)—to be convictable with the same severity level.

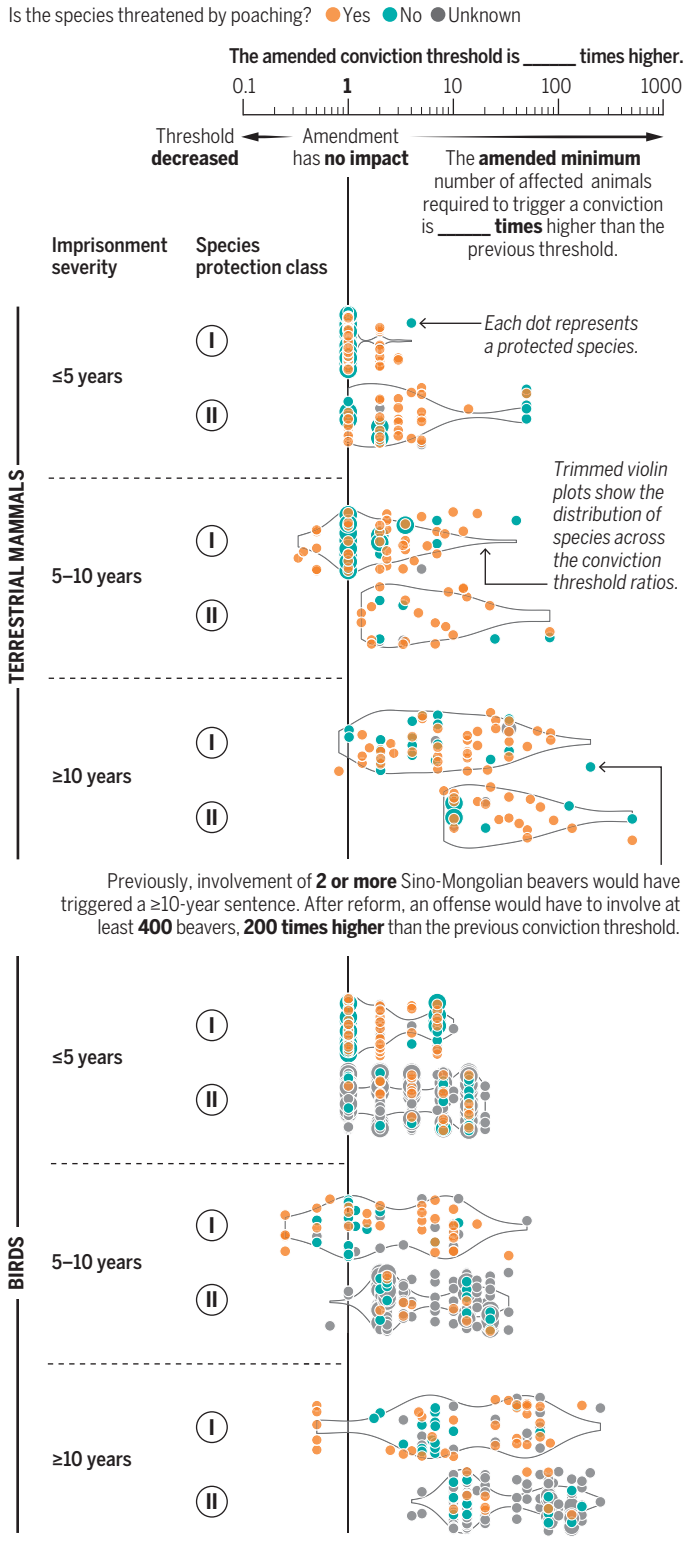
For the 188 species newly placed under Class I or II protection in the recent amendments, we were able to assess how the switch to monetary standards changed their convictable individual numbers for Level 1 imprisonment severity only. This is because before the switch, the convictable individual number for any protected species was set at one for this level (table S2), and when these 188 species were placed under protection in 2021 (i.e., 1 year before the switch to monetary standards), this one-individual conviction standard automatically applied to them. Across all these species, we found sweeping increases in their convictable individual numbers that averaged at 8.63-fold (see the figure) (*11*). However, for Level 2 and 3 imprisonment severities, preamendment convictable individual numbers were not available for the newly protected species, as these numbers were delineated for each previously protected species in a legal document released in 2000 that was never updated to include additional species (table S2).

Out of all our study species, we additionally looked at what the recent amendments meant for the subset of 159 species deemed threatened by poaching (i.e., species for which poaching was listed as a threat in China's Red List assessment) (*12, 13*)—a crime for which legal deterrence is critical. Across all such species, we found that increases in their convictable individual numbers across imprisonment severity levels were similarly widespread and substantial (see the figure) (fig. S2) (*11*). These increases indicate that while positively expanding legal protection to many previously unprotected species, the recent amendments to China's conviction criteria on wildlife crime have raised the bars and lessened the severities of conviction for offenses on most of the country's protected birds and terrestrial mammals, pointing to weakened crime deterrence concerning these species.

To provide some insights on how meaningful the amended conviction criteria are for the protection of China's terrestrial vertebrates, we next focused on a subset of 169 study species for which estimates of their population sizes in China were available from China's Red List assessment (*11–13*), to compare their current convictable individual numbers

Recent amendment elevates conviction thresholds

Ratios reflect changes in threshold numbers of animal individuals involved for a given offense to be considered convictable resulting from the amendment of conviction standards, across 522 protected bird and terrestrial mammal species. For many species, the amendment has substantially increased the conviction threshold. For some, a person could now poach the entire species population within China and still not meet the threshold for the most severe imprisonment (see fig. S3).



For the 188 species newly placed under protection, these changes could be assessed only for imprisonment severity ≤5 years. Circle size is not meaningful. Some circles are larger for visibility.

GRAPHIC: M. HERSHER/*SCIENCE*; (DATA) HTTPS://DOI.ORG/10.5281/ZENODO.17182422

with their known population sizes in China. Our rationale was that the amended criteria would be unlikely to meaningfully protect a species if its convictable individual numbers amounted to a large proportion of its Chinese population (*11*). This comparison revealed that for most of the species assessed, their convictable individual numbers—across Level 1, 2, and 3 imprisonment severities—amounted to a substantial proportion of, or even exceeded, their Chinese populations (fig. S3 and table S3). Exemplifying this overall pattern was the Chinese crested tern (*Thalasseus bernsteini*; Class I protection), a Critically Endangered species with an estimated Chinese population of ~100 individuals (*13*): Its convictable individual numbers were 7, 67, and 667 individuals for Level 1, 2, and 3 imprisonment severities, respectively.

Strikingly, for 16 species, their convictable individual numbers for Level 3 imprisonment severity exceeded their entire known populations in China, in some cases by over sixfold (fig. S3 and table S3), indicating that even if they were completely extirpated from China in a single offense, the perpetrators would still be safe from the most severe imprisonment. Aside from the Chinese crested tern, these species included the pygmy slow loris (*Nycticebus pygmaeus*; Class I protection; convictable individual number at 1.1 times its Chinese population), which faces severe poaching pressure (*12*), and the blue-crowned laughingthrush (*Garrulax courtoisi*; Class I protection; 2.7 times), a species with an extremely narrow distribution range (*13*). Additionally, for 24 species, individual offenses could jeopardize up to 1% of their Chinese populations without triggering any conviction (table S3). In sum, our findings suggest that the amended conviction criteria may fail to adequately protect many of China's protected terrestrial vertebrates.

The above indications of weakened crime deterrence and inadequate protection of China's terrestrial vertebrates—likely to result from the amendment of conviction criteria—were corroborated by empirical evidence, including judicial outcomes and observations of conservation practitioners. For judicial outcomes, we searched in two of China's leading legal databases for offenses on native terrestrial vertebrates that received nonprosecution decisions postamendment but that would have been previously convictable (*11*). Out of 94 nonprosecution cases found, we identified 42 that would have been convictable preamendment. These cases involved 19 Class II species (table S4), including three Endangered mammals deemed vulnerable to poaching (*12*): the Eurasian lynx (*Lynx lynx*), the Asiatic wildcat (*Felis silvestris ornate*), and the elk (*Cervus canadensis*).

For insights from conservation practitioners, we conducted semi-structured interviews with 10 respondents drawn from across the country who worked on combating wildlife crime, including eight law enforcement officers from six provinces and two staff members from a national-level antipoaching nongovernmental organization (*11*). In response to a set of questions about how they generally felt law enforcement on wildlife offenses had changed since 2020 (*11*), nine respondents specifically noted increased difficulty in meeting conviction thresholds for registering offenses to the local procuratorate, owing to increases in convictable individual numbers postamendment. Additionally, two respondents even noted observations of perpetrators learning to exploit these increased numbers to avoid conviction, by ensuring that the total monetary values of animals they violate do not exceed conviction standards. Overall, the above evidence suggests that in practice, the amendment of conviction criteria has resulted in a tangible weakening of the legal protection of China's terrestrial vertebrates, conceivably aggravating the threats they face, particularly for species vulnerable to wildlife crime.

Notwithstanding the caution that valuing wild species in economic terms is conceptually misaligned with species protection and can undermine societal appreciation of biodiversity (*14*), in practical terms, a critical premise for the monetary standards to work is that the valuation system reflect the true damage to species populations and ideally, to the values of the ecosystem functions and services they provide—over both the short and long terms. Unfortunately, the science underlying such valuation is far from available for most species, in most regions of the world. This is probably why the practice of monetary standards for wildlife crime is globally rare. Other than China, we are aware of only the United States using this practice, although it is always assisted by complementary standards based on the threat status of the species involved (*15*). The perverse conservation implications we uncovered of China's monetary conviction standards should serve as a note of caution to other countries in their approach to conviction standards on wildlife crime.

It is evident that a reassessment is urgently needed for China's current monetary conviction standards for wildlife crime, including whether they should be based on monetary values in the first place. Until such an assessment is concluded and rigorous standards are reestablished, we suggest that the current standards be suspended and an interim decree be issued to regulate law enforcement—supported by emergency consultation with wildlife experts. More broadly and over the longer term, we highlight the crucial importance of acquiring information on species' ecology and conservation status in setting conviction criteria, including population size, habitat status, life-history traits, vulnerability to poaching, and threats from illegal hunting and trade, etc. Specifically, expert advisory committees should be established across the central and local governments to regularly curate up-to-date scientific data on these species, and to update and publish the protected species list and Red List every 5 years, requirements laid out by China's Wildlife Protection Law but in reality rarely met. The timely upkeep of such scientific information is a critical foundation for establishing ecologically appropriate conviction criteria to deter wildlife crime. At an even broader level, policy-making and law enforcement concerning wildlife crime must enhance transparency, facilitate data accessibility, actively incorporate input from the conservation science community, and ultimately engage with the public to mainstream biodiversity. □

REFERENCES AND NOTES

1. WWF, *Living Planet Report 2024 – A System in Peril* (World Wildlife Fund, 2024).
2. L. Xiao *et al*., *Conserv. Sci. Pract.* 6, e13062 (2024).
3. J. Chen, X. Wu, H. Lin, G. Cui, *Biodivers. Sci.* 31, 22639 (2023).
4. L. Xiao, Z. Lu, X. Li, X. Zhao, B. V. Li, *Curr. Biol.* 31, R168 (2021).
5. Z. Yang, B. Qin, Y. Lin, *Environ. Prot.* 51, 37 (2023).
6. L. Jiang, *J. Soc. Sci. Hunan Norm. Univ.* **53**, 57 (2024).
7. M. Tian, G. R. Potter, J. Phelps, *Biol. Conserv.* **308**, 111238 (2025).
8. T. Jiang, M. Feng, *J. Southwest Univ. Pol. Sci. Law* **25**, 86 (2023).
9. Y. Chu, *J. Nanjing For. Univ. (Humanit. Soc. Sci. Ed.)* **24**, 108 (2024).
10. L. Deng, D. Wu, *J. East China Univ. Sci. Technol. (Soc. Sci. Ed.)* **38**, 138 (2023).
11. R. Hu *et al*., Data and methods for 'Toward science-based conviction criteria conviction criteria to deter wildlife crime,' Zenodo (2025); https://doi.org/10.5281/zenodo.17182422.
12. Z. Jiang *et al*., Eds., *China's Red List of Biodiversity: Vertebrates, Volume I, Mammals* (Science Press, 2021).
13. Y. Zhang, G. Zheng, Eds., *China's Red List of Biodiversity: Vertebrates, Volume II, Birds* (Science Press, 2021).
14. W. M. Adams, *Science* **346**, 549 (2014).
15. US Sentencing Commission, Guidelines Manual §3E1.1 (USSC, 2024).

ACKNOWLEDGMENTS

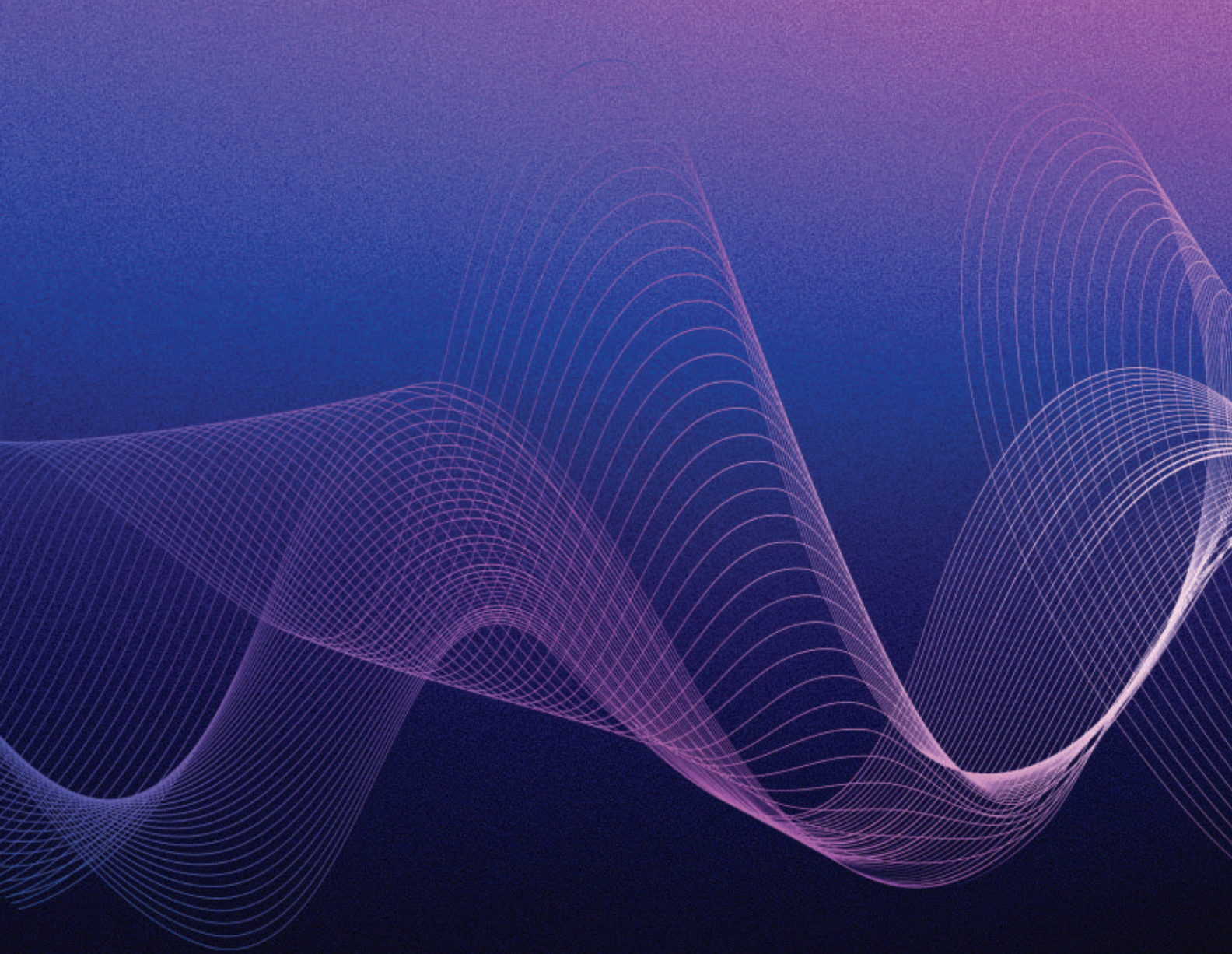
The authors thank the conservation practitioners interviewed for providing their insights. The authors thank members of the ConservationEE research group at Peking University for helpful discussions. The authors acknowledge support from the Ministry of Science and Technology of China (grant 2022YFE0209400) and the National Key Technologies R&D Program (grant 2022YFF1301500). R. Hu and S. Liu contributed equally to this work. All data and methods can be found at (*11*).

SUPPLEMENTARY MATERIALS

science.org/doi/10.1126/science.adu9077

10.1126/science.adu9077

[1]Center for Nature and Society, School of Life Sciences, Peking University, Beijing, China. [2]Institute of Ecology and Key Laboratory for Earth Surface Processes of the Ministry of Education, College of Urban and Environmental Sciences, Peking University, Beijing, China. [3]Department of Health and Environmental Sciences,Xi'an Jiaotong–Liverpool University, Suzhou, China. [4]Division of Natural and Applied Sciences, Duke Kunshan University, Kunshan, Jiangsu, China. [5]Department of Ecology and Evolutionary Biology, Princeton University, Princeton, NJ, USA. Email: fhua@pku.edu.cn; luzhi@pku.edu.cn



SPECIAL ISSUE

A QUANTUM CENTENARY

SUMIN JIN, JELENA STAJIC, and ERIC HAND

CREDITS: ALISEFOX/ISTOCK PHOTO; PANUWAT SIKHAM/ISTOCK PHOTO/ADAPTED BY M. ATAROD/*SCIENCE*



The field of physics experienced explosive growth in the early decades of the 20th century, culminating in 1925, when Werner Heisenberg and Erwin Schrödinger developed different, but equivalent, mathematical formalisms to describe the behavior of the atomic world. As the more intuitive of the two, Schrödinger's wave function and the eponymous equation became the primary theoretical tool in this new field of quantum mechanics. Although the Schrödinger equation provided the wildly successful "shut up and calculate" approach that encourages the practitioner to just trust the math, philosophical debates on quantum-mechanical concepts such as quantum measurement and entanglement persist to this day.

Quantum mechanics has enabled advances ranging from the Standard Model of particle physics to practical discoveries such as lasers, solar cells, and computer chips. But we are now on the brink of a second quantum revolution, in which the exquisite control of quantum states honed over decades of painstaking effort is harnessed in quantum computing, encryption, and simulation, all potentially far more powerful than their classical precursors. Moreover, the inability to unify quantum physics with gravity remains a gaping flaw in our understanding of the universe and may be a catalyst for another fundamental shift, almost as momentous as the birth of quantum mechanics. 10.1126/science.aee0656

PERSPECTIVES

One hundred years of quantum mechanics

Quantum mechanics has gone from a theory in test to becoming the foundation of new technologies

Marlan O. Scully[1,2,3] and **William G. Unruh**[1,4]

Radical ideas often drive scientific progress. That was the fate of Erwin Schrödinger's 1926 paper on wave mechanics, which is a centerpiece of today's quantum theory (*1*). Over the past hundred years, quantum mechanics has evolved from a theoretical basis for understanding interactions between particles and fields (*2*) to an essential element for advancing technologies (see the figure) (*3*). Philosophical problems such as Schrödinger's cat (until observed, an entity can exist in a superposition of multiple states) developed into the field of quantum informatics. Gravitational wave detection, which provides a new probe of cosmic events, is empowered by quantum optics. Concepts in quantum physics that were once purely theoretical are now observed: The Higgs boson—a fundamental field responsible for mass—has been seen; quantum materials such as graphene are produced; attosecond (10^{-18} s) laser pulses are generated; and quantum turbulence may explain the 200-year-old problem of classical turbulence.

The idea of matter exhibiting wave-like properties (in addition to existing as particles) was in Schrödinger's mind well before de Broglie's initial hypothesis of wave-particle duality. In his 1922 paper that was published before the wave mechanics paper (*1*), Schrödinger described the resonance (wave-like) character of electrons that comes from rotational symmetry in Bohr's planetary model, which posited that electrons orbit a nucleus in a fixed elliptical path. Around the same time, Werner Heisenberg and Hendrik Kramers were examining the interaction of radiation with matter, which led to another formulation of quantum mechanics in 1925. Heisenberg's matrix mechanics treats dynamic variables such as position and momentum as operators and uses them to calculate probabilities of transitioning between quantum states. Although this formalism is equivalent to Schrödinger's quantum wave mechanics, differential equations, which are the basis of wave mechanics, are more familiar to a broad range of physical scientists than is matrix mechanics. This has made Schrödinger's equation more popular. Nevertheless, Heisenberg's matrix mechanics exemplifies how the equations of classical physics can be taken over by quantum physics and become widely used in certain fields such as quantum optics.

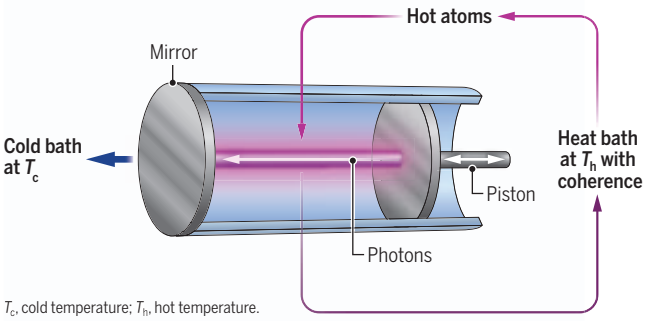
But quantum mechanics is counter-intuitive. To demonstrate its peculiarity, Schrödinger developed a thought experiment in which a cat demonstrates the concept of superposition—a key feature of a quantum system in which each possible state of the cat can have some chance of occurring. He postulated that the cat could be in a superposition of life and death simultaneously until it is observed. Although seemingly absurd, this "quantum weirdness" has become the basis for modern technologies such as quantum computing (*4*) and quantum cryptography and of improving the sensitivity of the Laser Interferometer Gravitational-Wave Observatory (LIGO).

An equally important discovery during the second quarter of the century (1925 to 1950) was quantum field theory, which combined quantum mechanics and special relativity theories to describe quantum particles and fields. This supplanted the early formulations of quantum mechanics. However, calculations of interactions between two fields (such as electrons and electromagnetic fields) frequently gave infinite values, which is nonsensical for physical quantities. Applying a "renormalized" theory to the quantum field theory eliminated infinite values by replacing bare (unphysical) quantities by dressed (physical) masses and charges.

In 1947, a hallmark experimental probe of quantum field theory was reported. The Lamb shift showed tiny changes in a hydrogen atom's energy level because of vacuum fluctuations. After World War II, this finding opened the theoretical floodgates. Theorists now had something to test their theories on. Many new frontiers were opened. For example, Julian Schwinger, Richard Feynman, and Sin-Itiro Tomonaga launched the field of quantum electrodynam-

Quantum heat engine

An optical cavity is confined between two mirrors, of which one is a piston. The piston generates useful work on expansion, which is driven by radiation pressure of photons emitted by hot atoms. This photon gas is subsequently cooled to T_c, and the cold gas is compressed. This is waste work. The ratio of waste work to useful work is the maximum efficiency for a classical Carnot heat engine. A quantum heat engine can surpass this Carnot limit by using a heat source with a small bit of coherence in the hot atoms.



T_c, cold temperature; T_h, hot temperature.

GRAPHIC: N. BURGESS/*SCIENCE*

ics (*2*), which has been crucial to developing modern quantum field theories. A prime example of the power of quantum field theory is the Standard Model (*2*), which includes fundamental particles and force carriers: quantum electrodynamics (electron and photon fields), quantum chromodynamics (quark and gluon fields), and the weak interactions (neutrinos, muons, and W and Z vector boson fields).

Since the 1950s, focus has shifted from measuring the energy levels of particles (such as atoms and nuclei), and the probability of scattering between these energy levels, to the phase of the wave function. The concept of quantum phase coherence—a stable phase relationship between quantum waves of systems in different states—emerged. For example, the phase factor of an electron's wave function can describe a constructive or destructive interaction. This notion of quantum phase coherence was also hinted at in Schrödinger's 1922 paper and has become the basis of quantum gauge theory (also called phase theory). Quantum phase coherence has been pivotal in the modern notion that varying the phase of an electron is equivalent to applying a force field (such as electromagnetism) on the electron (*1*).

Chen-Ning Yang and Robert Mills (*2*) extended this line of thinking to nuclear physics based on the fact that proton-neutron and neutron-neutron forces are equal. This symmetry led to the concept that gluons are the fundamental particles that act as the binding force between nucleons (protons and neutrons). In addition, quantum coherence served as the essence of the theory of superconductivity by John Bardeen, Leon Cooper, and John Robert Schrieffer, which has influenced the understanding of how massless fields can gain mass because of the Higgs field (a field responsible for an intrinsic mass of a particle). Phase-coherent quantum theory combines the electromagnetic and weak interactions. Much of modern quantum science involves phase coherence, such as laser and Hanbury-Brown Twiss two-photon interference experiments (*3*).

Perhaps the quintessential example of quantum coherence is the laser (light amplification by stimulated emission of radiation). Charles H. Townes laid the fundamental foundation for this important discovery despite many experts, including his supervisor, initially doubting that the laser would work (*5*). The work of Townes led to many Nobel prizes, such as nonlinear optics, quantum optics, Bose condensates, and gravitational wave detection. Laser physics also developed into modern laser technologies in femtosecond (10^{-15} s), and attosecond (10^{-18} s) time regimes, providing the tools for new discoveries and high-power lasers for potentially clean and controllable energy-producing fusion reactors.

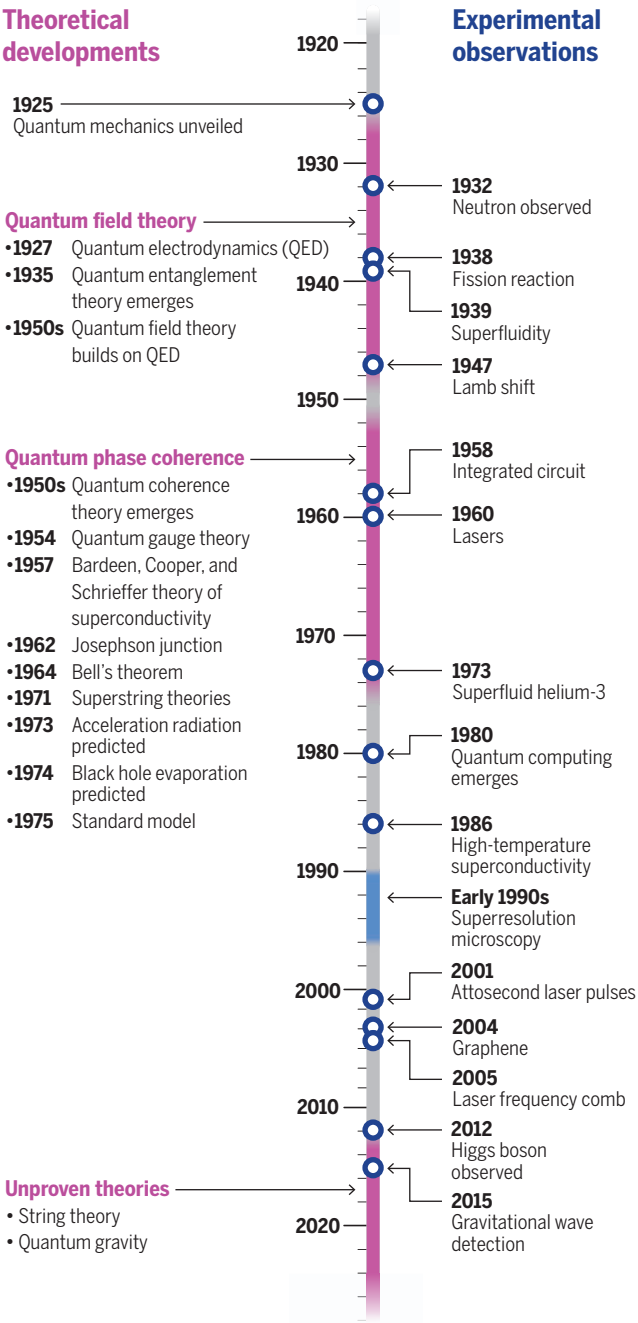
Decades after the discovery of wave mechanics, applications grounded in quantum mechanics continue to emerge. Lasers that can produce light amplification without needing more atoms in a higher energy state have been developed by using quantum coherence (*3*). Advanced techniques, such as coherent nanoscale laser spectroscopy, enables the characterization of molecules on the atomic scale. Quantum cryptography (*6*) allows the creation of secure codes that are unbreakable. Quantum computers empower calculations that are exponentially faster than on classical computers. And theoretically intriguing phenomena such as Hawking black hole radiation and Unruh acceleration radiation have deep connections to quantum entanglement that is a strong correlation between multiple quantum systems.

Quantum coherence can also enhance the sensitivity of gravitational radiation detectors through quantum entanglement in the form of "squeezed" light. This form of light uses correlations between two or more quantum systems (*3*) to reduce the vacuum fluctuations (noise) in the measured output to below the usual limits, improving measurement sensitivity. This yields marked progress from studying quantum phenomena produced by the vacuum (for example, the Lamb shift) to improving measurement by suppressing the quantum noise of the vacuum. Furthermore, quantum coherence and entanglement have led to the development of the quantum heat engine (*7*), which can operate beyond the classical Carnot limit—the maximum possible efficiency of a classical heat engine with hot and cold energy reservoirs.

Ingenious engineering applications of quantum mechanics have emerged from quantum coherence. Coherent beams of atoms enable subwavelength resolution, which surpasses the traditional optical diffraction limit (*8*, *9*). This holds promise for quantum lithography, which allows patterning high-resolution nanoscale features onto a material. Furthermore, quantum properties of light provide new tools for probing biological systems (*10*). For example, advances in coherent Raman spectroscopy have permitted mapping the surface of a single virus par-

From theories to observations

Quantum mechanics is not only a foundation of many physics theories but also of modern technologies that have led to new scientific discoveries. Nevertheless, emerging fields based on quantum mechanics such as quantum biology and quantum thermodynamics are still in the early stages of development.



GRAPHIC: N. BURGESS/*SCIENCE*

ticle with nanometer resolution (*11*). Harnessing quantum mechanics for such biological studies is a harbinger of "quantum biology."

In a fascinating turnabout, quantum mechanics has helped in solving some of the most challenging scientific problems, such as turbulent flow in fluids (*12*). In particular, the tangling of vortices in quantum superfluid helium-4 (liquid helium cooled down to nearly absolute zero) has led to deeper understanding of both quantum and classical turbulence (*13*). This interplay between classical and quantum systems is ironic in that Heisenberg studied turbulence more than a century ago with little success.

New theories based on quantum mechanics have emerged to explain fundamental physics that govern the universe, such as gravity and thermodynamics. A potentially transformative concept that developed from quantum mechanics is string theory (*14*), which replaces particles with tiny strings that oscillate because of quantum fluctuations. This could provide a different view of the infinities in quantum field theory. The problem of black hole entropy is another example of the potential of string theory. Entropy can be calculated with classical thermodynamics and statistical mechanics but also by counting the number of microstates in a system. String theory has been successfully used to calculate the entropy of a black hole by counting string states.

Nevertheless, one of the biggest unsolved mysteries is quantum gravity (*15*). Not only has gravity not yet been successfully quantized, it is also not yet clear that gravity can be quantized. Feynman made a suggestion seven decades ago (*15*) that examining the entanglement between two interferometers and a small mass coupled to their gravitational fields may solve this problem. This idea has been revived in the past decade but with some controversy.

At the beginning of the 20th century, many thought that physics was complete. However, at the beginning of the 21st century, modern physics encompasses many fundamental and applied problems that are waiting to be unraveled. □

REFERENCES AND NOTES

1. A. Duncan, M Janssen, *Constructing Quantum Mechanics* (Oxford Univ. Press 2019, 2023).
2. A. Zee, *Quantum Field Theory in a Nutshell* (Princeton Univ. Press, 2010).
3. M. O. Scully, M. S. Zubairy, in *Quantum Optics* (Cambridge, 1997): pp. 508 and 513.
4. A. Cho, *Science* **389**, 121 (2025).
5. C. Townes, *How the Laser Happened* (Oxford Univ. Press, 1999).
6. J. Yin *et al.*, *Nature* **582**, 501 (2020).
7. N. M. Myers, O. Abah, S. Deffner, *AVS Quantum Sci.* **4**, 027101 (2022).
8. M. S. Zubairy *et al.*, *Phys. Rev. Lett.* **105**, 183601 (2010).
9. L. Pan, D. R. Beck, *Phys. Rev. A* **93**, 062501 (2016).
10. A. Agarwal *et al.*, *Proc. Natl. Acad. Sci. U.S.A.* **121**, e2413938121 (2024).
11. V. Decker *et al.*, *Proc. Natl. Acad. Sci. U.S.A.* **117**, 27820 (2020).
12. M. J. Desrochers, D. J. J. Marchand, P. C. E. Stamp, *Proc. Natl. Acad. Sci. U.S.A.* **122**, e2421273122 (2025).
13. K. Sreenivasan, J. Schumacher, *Annu. Rev. Condens. Matter Phys.* **16**, 121 (2025).
14. K. Becker, M. Becker, J. Schwarz, *String Theory and M-Theory* (Cambridge Univ. Press, 2007).
15. C. DeWitt, D. Rickles, Eds., *The Role of Gravitation in Physics, Report from the 1957 Chapel Hill Conference* (Edition Open Access, 2017).

ACKNOWLEDGMENTS

M.O.S. acknowledges support from the National Science Foundation (grant PHY-2013771), Air Force OSR (award FA9550-20-1-0366), the Welch Foundation (grant A-1261), and the US Department of Energy (DE-SC-0023103, DE-AC36-08GO28308, SUB-2023-10388, and DE-SC0024882: IFE-STAR). W.G.U. acknowledges support from the Hagler Insitute and the Chancellors fund at Texas A&M University, the Natural Science and Engineering Research Council of Canada, and the University of British Columbia.

10.1126/science.ady6092

[1]Institute for Quantum Science and Engineering, Texas A&M University, College Station, TX, USA. [2]Department of Electrical and Computer Engineering, Princeton University, Princeton, NJ, USA. [3]Department of Physics and Astronomy, Baylor University, Waco, TX, USA. [4]Department of Physics and Astronomy, University of British Columbia, Vancouver, BC, Canada. Email: scully@tamu.edu; unruh@physics.ubc.ca

PERSPECTIVES

Dawn of quantum simulators

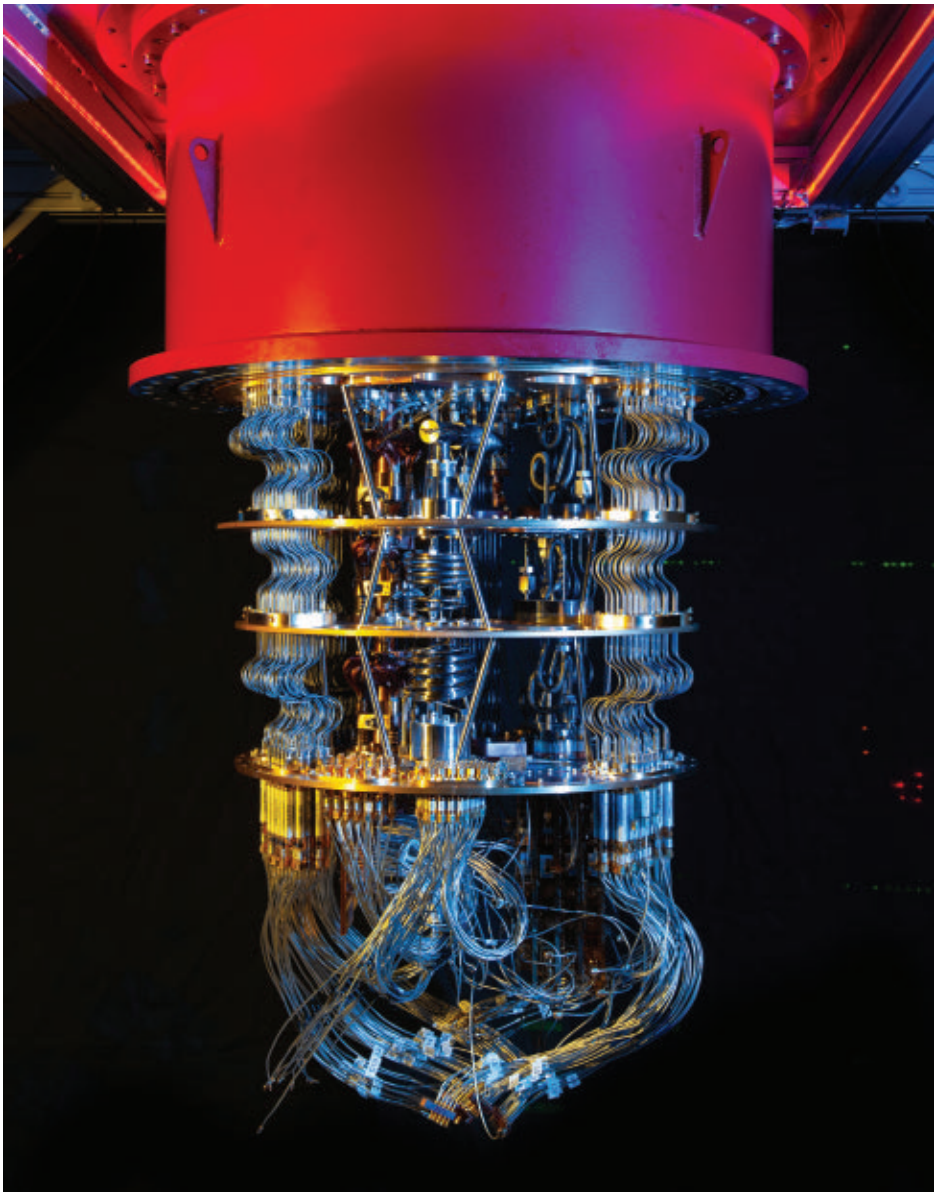
Large-scale quantum processors are beginning to uncover new physical phenomena

Pedram Roushan and **Leigh Martin**

A full-fledged quantum computer could one day solve complex scientific problems in chemistry, materials science, and physics. In the current noisy intermediate-scale quantum era (*1*), moderately sized, imperfect quantum processors are the most advanced hardware available for quantum computing. These devices involve control of individual degrees of freedom such as superconducting qubits (quantum bits) or arrays of atoms. Progress in noisy intermediate-scale quantum platforms has led to exploration of many fundamental effects in modern physics. For example, a wide range of nonequilibrium quantum phases of matter that exist in dynamic, time-evolving systems has been observed. Many-body localization in which disorder prevents a quantum system from reaching a thermal equilibrium has been demonstrated (*2*). In addition, time crystalline behavior—a phase of matter that breaks time-translation symmetry and oscillates indefinitely without energy input—has been confirmed in quantum processors (*3*). These validate quantum devices and identify key limitations for future development.

...quantum processors have begun to transition from tools of verification to engines of discovery...

Beyond demonstrations of known phenomena, quantum processors have begun to transition from tools of verification to engines of discovery, revealing physical events before theory predicts them. These include unanticipated subtleties in nonequilibrium and near-equilibrium quantum dynamics. For example, quantum many-body scars—a rare phenomenon in which a system fails to reach thermal equilibrium when initialized in certain states—was experimentally discovered in a noisy intermediate-scale quantum processor made of a one-dimensional (1D) chain of atoms (*4*). In this experiment, the atoms are first initialized in a spatially alternating pattern of low- and high-energy states, then made to interact with each other by applying a pulse of laser light. Standard thermodynamic theory predicts that the highly nonuniform distribution of energy states should relax monotonically to a thermal equilibrium. However, the atoms repeatedly entangled and disentangled, and the initial pattern of en-



The current generation of noisy intermediate-scale quantum processors has a limited number of qubits. The calculations are affected by noise, which comes from interaction of a quantum system with the environment.

PHOTO: GOOGLE QUANTUM AI

ergy states periodically disappeared and reappeared. This trend has sparked debate. Some suggest that quantum many-body scars could be linked to "proximity to integrability," which relates a phenomenon to an integrable (solvable) system or an algebraic structure such as dynamical symmetries. Nonetheless, a general understanding of when a nonintegrable quantum system can host many-body scars remains an open question.

Moreover, a quantum processor made of superconducting qubits found a bound state of microwave photons (particles of microwave radiation) that behave as a single entity and are resilient to perturbations (*5*). Stable quasiparticles in an integrable model of quantum dynamics can form a bound state, which, in theory, decays quickly when perturbed (*6*). However, the bound states decayed much more slowly than the theoretical expectation when additional interactions broke integrability of the quantum system. This finding has invited further analytical and numerical studies (*7, 8*).

In addition, an unusual propagation of quantum correlations within spin chains (1D line of particles that interact magnetically) with tunable interaction ranges was simulated in a quantum processor produced by a linear array of ions (*9, 10*). The correlations propagated at a speed that is faster-than-linear growth (the effective speed increases with time instead of being constant) for relatively short-range interactions between particles. Although faster-than-linear growth is expected for long-range interactions, there is still no consensus on whether such behavior is generically expected for long-range interactions. Although the noise and the relatively small quantum processor size limit most experiments within the capabilities of a classical computer, these studies demonstrate how a quantum computer can help discover new physical phenomena before a theory.

Noisy intermediate-scale quantum processors have also tested scientific conjectures that are difficult to solve with a classical computer. In several cases, quantum simulators have taken an active role in resolving research questions that are under debate. For example, the transport of magnetization and energy in quantum magnets often obeys simple scaling relations. These relationships are insensitive to microscopic details of the models and belong to universality classes, which categorize the behavior of many interacting physical systems within a shared scale-invariant limit. The Kardar-Parisi-Zhang universality class was proposed to describe a specific 1D quantum magnet model on the basis of theoretical evidence (*11*). The key to verifying this hypothesis is to examine the high moments of probability distribution of magnetic domain-wall relaxation at the center of a 1D spin chain, which is challenging to confirm with a classical computer. Noisy intermediate-scale quantum processors demonstrated that the third moment (skewness of a probability distribution) of transferred magnetization is governed by the Kardar-Parisi-Zhang dynamical exponent (*12*, *13*). However, initial states of a 1D spin chain that are close to equilibrium caused skewness to deviate from the predictions of the Kardar-Parisi-Zhang conjecture. In addition, the fourth moment (kurtosis that describes tails of a probability distribution) did not fall under the Kardar-Parisi-Zhang universality on the timescales of the experiment (*13*). These results suggest that the current theoretical picture is inadequate to describe the dynamics in this 1D model of magnetism.

Noisy intermediate-scale quantum processors have also computed physical parameters in correlated electron phases—a type of matter with strong electron interactions that goes beyond the standard approximations of condensed-matter theory (*14, 15*). Spin diffusion coefficients and spin conductance in the Fermi-Hubbard model of interacting electrons were experimentally measured in a quantum simulator (*14*). Furthermore, linear scaling of resistivity with temperature was observed (*15*), which is a common characteristic of correlated electron materials such as high-temperature superconductors. These findings challenge existing numerical methods and demonstrate electron transport beyond theoretical predictions.

Quantum processors could also analyze microscopic dynamics in a hypothesized superconducting phase of the Fermi-Hubbard model that cannot be simulated efficiently with classical computers, uncovering the mechanism underlying high-temperature superconductivity.

As control over a large number of qubits improves, the progress in quantum processors is slowly but steadily closing the gap between hardware capabilities and the frontiers of modern physics. However, current devices have limited reliability and tend to lose information through a phenomenon called decoherence—a process in which a quantum system loses its quantum properties by interacting with the surrounding environment. This buries the signal in noise from decoherence, challenging calculation of physical quantities and simulation of large-scale complex problems. Although the previous studies highlight physical phenomena, which were first discovered in quantum hardware, quantum processors are not yet beyond the capabilities of classical computation for most applications. Nevertheless, previous demonstrations offer a preview of how the nature of quantum research may change as hardware improves. If progress in qubit coherence and operation fidelity continues, noise of a quantum processor will reduce to the point at which noisy intermediate-scale quantum simulators unambiguously exceed the capabilities of classical computers.

The goal of achieving a full-fledged quantum computer has engaged a vast community of researchers across academic, national, and industrial labs for decades, exemplifying a large contemporary scientific effort. Traditional experiments are heavily guided by theoretical results and advanced numerical methods. Quantum processors could bring opportunities to conduct more exploratory research in which experiments are undertaken without definitive theoretical predictions for their outcomes. A reliable quantum hardware that accounts for decoherence and errors could exceed the capabilities of classical numerical methods and prove that unexpected observations are not a mere artifact. Such experiments may exceed the capabilities of the traditional numerial tools that are currently used for validating theories. Someday, quantum simulators will lead experimental research more independently. □

REFERENCES AND NOTES

1. J. Preskill, *Quantum (Vienna)* **2**, 79 (2018).
2. D. Abanin, E. Altman, I. Bloch, M. Serbyn, *Rev. Mod. Phys.* **91**, 021001 (2019).
3. V. Khemani, R. Moessner, S. Sondhi, arXiv:1910.10745 (2019).
4. H. Bernien *et al.*, *Nature* **551**, 579 (2017).
5. A. Morvan *et al.*, *Nature* **612**, 240 (2022).
6. M. Ljubotina *et al.*, *Phys. Rev. Lett.* **122**, 150605 (2019).
7. F. Surace, O. Motrunich, *PRX Quantum* **5**, 010317 (2024).
8. A. Hudomal, R. Smith, A. Hallam, Z. Papić, *PRX Quantum* **5**, 010316 (2024).
9. P. Richerme *et al.*, *Nature* **511**, 198 (2014).
10. P. Jurcevic *et al.*, *Nature* **511**, 202 (2014).
11. M. Ljubotina, M. Žnidarič, T. Prosen, *Phys. Rev. Lett.* **122**, 210602 (2019).
12. D. Wei *et al.*, *Science* **376**, 716 (2022).
13. E. Rosenberg *et al.*, *Science* **384**, 48 (2024).
14. M. A. Nichols *et al.*, *Science* **363**, 383 (2019).
15. P. T. Brown *et al.*, *Science* **363**, 379 (2019).

ACKNOWLEDGMENTS

The authors acknowledge insightful discussions with, and critical comments from, I. Bloch, G. Vidal, M. Lukin, and C. Marcus.

10.1126/science.adt1732

Google Inc., Goleta, CA, USA. Email: pedramr@google.com; leighmartin@google.com

A QUANTUM WORLD

PERSPECTIVES

Cracking chemistry with quantum simulations

Dynamic characteristics of complex chemical reactions can be accurately modeled by a quantum computer

Philipp Schleich[1,2] and **Alán Aspuru-Guzik**[1,2,3,4,5,6,7,8]

Atoms and molecules undergo changes in state as they interact with each other and the environment. The free-energy difference of a system transitioning from an initial to final state is crucial for understanding chemical reactions and other molecular processes because it informs the likelihood of a conversion to occur. Calculating the free-energy difference is often difficult because it fluctuates with temperature. Simulating properties of quantum systems (that exhibit behavior relevant at atomic and subatomic scales), such as the free-energy difference, is difficult because of the "curse of dimensionality" that arises from the number of particles involved and the many possibilities of their interaction. Quantum computers may accurately measure the free-energy differences by performing an exact simulation without introducing errors apart from those that arise from transforming continuous variables such as position and time into finite numbers. This enables precision that is not attainable with existing classical computers.

The idea of solving chemistry problems by using a quantum computer was proposed two decades ago. It was suggested that the ground state (the most stable energy state) of a molecule could be estimated using a modified version of the quantum-phase estimation algorithm (*1*). When an initial guess has reasonable overlap with the true ground state, the algorithm quantifies the ground-state energy with a small error. The algorithm determined the ground state and the first excited state of hydrogen in a minimal basis function that uses four spin orbitals (describing spatial distribution and spin state of an electron) encoded on four qubits, which are quantum bits that form the fundamental unit of information analogously to classical bits (*2*). Although early studies demonstrated the feasibility of understanding a chemical system by using a quantum computer, small-sized problems could also be solved by classical computation.

The insufficient availability of quantum hardware and techniques to correct errors in quantum computers has been a major barrier to performing more complex experiments. In the present era of quantum computing, noisy intermediate-scale quantum hardware with a limited number of qubits and corresponding algorithms are the only available platforms. Perhaps the most prevalent algorithm for noisy intermediate-scale quantum computers is the variational quantum eigensolver (*3*), in which the wave function (a mathematical function describing a quantum state) is parameterized. This hybrid quantum-classical algorithm can approximate the ground-state energy of a molecule by measuring the mathematical descriptor of the system, called a Hamiltonian, on a quantum computer, where classical optimization steps adjust the quantum computer's circuits to reach the minimum value. Experimental demonstrations validated the conceptual functionality of the variational quantum eigensolver even before techniques to mitigate hardware errors were established (*4*). Although quantum computers might eventually solve a problem that cannot be solved by a classical computer, uncontested demon-

strations for practical applications are still missing.

Nevertheless, there are several promising avenues for the use of quantum computers in chemistry. Reaction mechanisms of a quantum chemical system have been solved by using static quantities such as ground-state energies (*5*). In this approach, ground-state energies are calculated by a quantum-phase estimation algorithm, and reaction rates are estimated by using classical kinetic modeling. This method only requires around 100 logical qubits that are created by encoding information across many physical qubits. However, it takes 100 to 1000 physical qubits to produce a logical qubit. Despite the necessity of a large-scale quantum processor, approximation based on ground-state energy could theoretically deliver precise energies of large molecules that are relevant to a reaction mechanism and out of reach for exact classical methods.

A quantum computer may perform dynamical simulations of quantum chemical systems...

All systems in nature are presumably driven toward an absolute ground state of energy (or the most stable configuration) when they are isolated in vacuum and at 0 K, with minimum kinetic energy. By contrast, at a finite temperature, electronic materials and systems may reach the ground state on a longer timescale. This makes it inherently difficult to devise a simulation-based computation to determine the ground state. The amount of computational resources required to simulate a quantum system generally scales linearly with time (*6*, *7*) by a so-called quantum no–fast-forwarding theorem (*8*). This postulates that under the evolution of a system at a certain time, its simulation cannot be faster than the linear scale of the evolution time (the duration in which a quantum system changes).

Established quantum methods that estimate the ground state, such as quantum-phase estimation, do not naïvely simulate a system evolving to its zero-point energy state. Although the computational cost of quantum-phase estimation does not depend explicitly on the simulation time, there is a general limit to quantum methods for a ground-state search. As system size increases, overlaps between an initial guess of the ground-state energy and the true ground-state energy tend to decrease exponentially (*9*). Adiabatic state preparation (*1*)—in which a quantum computer follows a slow, continuous evolution toward a desired ground energy state starting from a simple, known energy state—also cannot solve this issue (*9*). Generally, finding the ground state of Hamiltonians with efficient time evolution is a challenging computational problem (*10*).

Different routes have been taken to prepare ground states and to improve the efficiency of quantum simulation for chemistry. There are heuristic approaches that can find an initial guess that is close to the true ground state. For example, open system evolution in which a system evolves through interactions with an external environment can be designed to redistribute the amplitude of its wave function toward lower-energy states and the ground state (*11*). The advantage of this approach is that success of the algorithm does not depend on (and decreases with) overlap of the initial guess of the ground state with the final predicted ground state. Although this method is heuristic and not provable, it is an example of how creative strategies could improve the search for ground states. Advanced classical heuristic approaches have also shown potential in preparing initial states with sufficient overlap with the true ground energy state (*12*).

Dynamic simulations can directly capture a phenomenon by modeling how a system evolves over time in response to interactions, instead of setting the initial state of a system with respect to static properties such as the ground-state energy. A time-evolved state can provide meaningful information for various applications, such as spectroscopy, photochemistry, and drug discovery. For example, it can measure chemical reaction rates (*13*), and a wide range of chemistry problems have been tackled efficiently by a dynamic approach (*14*). Rather than confronting a complex problem, simple initial states, which may represent atoms that constitute a specific molecule (*14*), are scattered by avoiding a rapid decrease in the overlap with the target energy state in the dynamic simulation. Alternatively, a divide-and-conquer approach that breaks up the problem into smaller subproblems mathematically can be adopted (*15*). Each simulation step stands for a chemical phenomenon of interest. Observables related to a specific application can be constructed and measured with respect to the time-evolved state. For example, in spectroscopy, these can be correlation functions across energy states of different evolution times, which can be used to determine a molecule's absorption spectrum. These demonstrate how quantum computers can model quantum chemical systems.

The ability of a quantum computer to solve problems faster than a classical computer depends on fault-tolerant algorithms. These algorithms need to be protected by error-correction techniques that allow the computing system to continue operating in the presence of errors by automatically detecting and recovering from faults. A fault-tolerant algorithm may protect the quantum information by spreading it across many physical qubits. Thus, the major bottleneck to the realization of a fault-tolerant quantum computer relies on the availability of a sufficient number of error-corrected qubits that can be maintained in quantum states for a long time.

The continuous development of hardware, error-correction methods, and algorithms is necessary for a quantum computer to outperform a classical one in practical applications. A quantum computer may perform dynamical simulations of quantum chemical systems to capture complex reaction mechanisms. □

REFERENCES AND NOTES

1. A. Aspuru-Guzik, A. D. Dutoi, P. J. Love, M. Head-Gordon, *Science* **309**, 1704 (2005).
2. B. P. Lanyon *et al.*, *Nat. Chem.* **2**, 106 (2010).
3. A. Peruzzo *et al.*, *Nat. Commun.* **5**, 4213 (2014).
4. A. Kandala *et al.*, *Nature* **549**, 242 (2017).
5. M. Reiher, N. Wiebe, K. M. Svore, D. Wecker, M. Troyer, *Proc. Natl. Acad. Sci. U.S.A.* **114**, 7555 (2017).
6. S. Lloyd, *Science* **273**, 1073 (1996).
7. D. W. Berry, G. Ahokas, R. Cleve, B. C. Sanders, *Commun. Math. Phys.* **270**, 359 (2007).
8. D. Aharonov, A. Ta-Shma, in *Proceedings of the Thirty-Fifth Annual ACM Symposium on Theory of Computing* (Association for Computing Machinery, 2003), pp. 20–29.
9. S. Lee *et al.*, *Nat. Commun.* **14**, 1952 (2023).
10. J. Kempe, A. Kitaev, O. Regev, in *FSTTCS 2004: Foundations of Software Technology and Theoretical Computer Science*, Lecture Notes in Computer Science Series , K. Lodaya, M. Mahajan, Eds. (Springer, 2004), pp. 372–383.
11. Z. Ding, C.-F. Chen, L. Lin, *Phys. Rev. Res.* **6**, 033147 (2024).
12. D. W. Berry *et al.*, *PRX Quantum* **6**, 020327 (2025).
13. I. Kassal, S. P. Jordan, P. J. Love, M. Mohseni, A. Aspuru-Guzik, *Proc. Natl. Acad. Sci. U.S.A.* **105**, 18681 (2008).
14. P. Schleich *et al.*, arXiv:2401.09268 (2024).
15. S. Simon *et al.*, arXiv:2504.03465 (2025).

ACKNOWLEDGMENTS

P.S. thanks A. Aldossary for insightful discussions. A.A.-G. acknowledges support from the Natural Science and Engineering Research Council of Canada, the Industrial Research Chairs Program, and the Canada 150 Research Chairs.

10.1126/science.ado6686

[1]Department of Computer Science, University of Toronto, Toronto, ON, Canada. [2]Vector Institute of Artificial Intelligence, Toronto, ON, Canada. [3]Department of Chemistry, University of Toronto, Toronto, ON, Canada. [4]Canadian Institute for Advanced Research, Toronto, ON, Canada. [5]Acceleration Consortium, Toronto, ON, Canada. [6]Department of Chemical Engineering and Applied Chemistry, University of Toronto, Toronto, ON, Canada. [7]Department of Materials Science and Engineering, University of Toronto, Toronto, ON, Canada. [8]NVIDIA, Toronto, ON, Canada. Email: philipps@cs.toronto.edu; aspuru@utoronto.ca

REVIEW

Challenges and opportunities for quantum information hardware

David D. Awschalom[1,2]*, Hannes Bernien[1,3,4], Ronald Hanson[5,6], William D. Oliver[7,8,9], Jelena Vučković[10,11]

Quantum technologies have made impressive progress over the past decade. In some areas, such as quantum sensing and key distribution, these technologies are moving from the laboratory to enable real-world applications. However, for areas such as quantum computing, entanglement-enhanced sensing, and a global quantum internet, we are in an equivalent of the early transistor age, and hardware breakthroughs are required in multiple arenas to reach the performance necessary for the envisioned applications. In this Review, we assess the current state of the art of quantum information hardware and identify key challenges and opportunities ahead. We draw inspiration from the history of scaling and development of classical electronics and photonics to anticipate progress in the field.

Recent progress in the fields of quantum information science and engineering includes both rapid advances in fundamental research and practical demonstrations of quantum computers, networks, and sensors. As was the case with microelectronics and photonics, the strong partnerships between academia, industry, and government have been instrumental in fueling many of the key breakthroughs that ultimately enabled scaling, adoption, and commercialization. Quantum technologies will similarly face many such challenges, some of which are familiar to classical technologies (e.g., the tyranny of wires) and others that are specific to quantum technologies (e.g., sustained, quantum-coherent control of large systems). Moreover, it is likely that advanced instrumentation for fabrication and characterization will need to be developed to reach these goals. These challenges must be met to deliver meaningful quantum advantage at scale for current and unforeseen applications.

What lessons could be learned and what expectations set for quantum information technologies from our experiences with classical (von Neumann model) computing? The cost per compute operation in MIPS/$ (millions of instructions per second per dollar) has dropped more than 14 orders of magnitude over the past 75 years (*1*), and the number of transistors on a processor chip has increased from a few thousand in the early 1970s to almost 100 billion in systems on a chip today. On the hardware side, this advancement was accomplished by radical changes in base technology, from vacuum tubes to silicon transistors (1950s), to integrated circuits (1960s to ’70s), and the move from bipolar transistors to complementary metal-oxide semiconductor (CMOS) transistors (1990s). In each case, progress was driven by innovations in materials, devices, and circuit design. A few broad principles that guided this success may be valuable for consideration in quantum technology research.

First, once the underlying physics and device concepts were established, the progress had a notably top-down–driven methodology, meaning that system-level considerations defined the specific circuit, device, and materials requirements for forthcoming innovations. The ensuing discovery-based science research thus had clear guidelines that scientists could target and map onto emerging technology. The replacement of the traditional silicon dioxide gate insulator in the transistor structure with new hafnium dioxide–based dielectrics in the early 2000s is an example, and 3D NAND Flash is another. These efforts were successful because of coordination of expertise and codesign across the technology stack. On the other hand, bottom-up approaches, although essential in the early stages of a technology for discoveries and the understanding of the fundamental principles, have proven less successful as a design strategy. For instance, materials discoveries that then sought an application for novel properties were not as successful, because of a lack of codesign perspectives.

Second, the community (industry, academia, and national facilities) spent considerable effort in developing a shared and fundamental understanding of the underlying science that was disseminated by refereed publications, which then guided future research and development. This collective body of knowledge aided the entire research community. For instance, a firm understanding of the physics of scaling and excitation transport in transistors led to Dennard’s scaling law (of which Moore’s law is a consequence) and, more recently, the move to nonplanar transistors such as FINFETs (fin field-effect transistors) and nanosheet FETs. Much of this science was considered precompetitive and avoided the inefficiencies of R&D that is prematurely siloed as confidential.

Third, materials and process science innovations underpinned almost all major progress throughout the history of classical computing. Pfann’s semiconductor purification technique (1950s) led to practical transistors, ion implantation permitted Moore’s law scaling, extreme ultraviolet (EUV) lithography enabled extreme scaling of transistors, and the advent of atomic layer deposition (ALD) made nonplanar transistors possible. Finally, patience has been a key element in many of these landmark developments and points to the importance of tempering timeline expectations in quantum technologies. For example, EUV materials and optical systems work began in earnest through a partnership between the US Department of Energy labs and industry in the mid-1990s (*2*), but it was only in 2019 that EUV, essential for building today’s high-performance transistors, was first used in manufacturing. Similarly, ALD, one of the most important thin film deposition methods used today because of its ability to conformally coat nonplanar surfaces, was developed in the 1960s and 1970s, but it was only in the 2000s that it saw use in microelectronics manufacturing.

Although it is not a given that quantum technologies will develop similarly to classical computing, important lessons can be learned. We consider the progress and opportunities in emerging hardware for quantum information processing. How do we progress from current state of the art to scalable technologies? And what are the challenges that the community may need to address and how might we address them to reach this goal?

Current state of the art

Quantum technologies today are transitioning from laboratory curiosities to technical reality. Assessing progress of these new technologies is challenging, as their future main application domains and their

[1]Pritzker School of Molecular Engineering, University of Chicago, Chicago, IL, USA. [2]Department of Physics, University of Chicago, Chicago, IL, USA. [3]Institute for Quantum Optics and Quantum Information, Austrian Academy of Sciences, Innsbruck, Austria. [4]Institute for Experimental Physics, University of Innsbruck, Innsbruck, Austria. [5]QuTech, Delft University of Technology, Delft, Netherlands. [6]Kavli Institute of Nanoscience, Delft University of Technology, Delft, Netherlands. [7]Department of Electrical Engineering and Computer Science, Massachusetts Institute of Technology, Cambridge, MA, USA. [8]Department of Physics, Massachusetts Institute of Technology, Cambridge, MA, USA. [9]Research Laboratory of Electronics, Massachusetts Institute of Technology, Cambridge, MA, USA. [10]Ginzton Laboratory, Stanford University, Stanford, CA, USA. [11]Department of Electrical Engineering, Stanford University, Stanford, CA, USA. ***Corresponding author. Email: awsch@uchicago.edu**

respective figures of merit are not yet fully known. Identifying and agreeing upon such metrics is an important challenge for the field in the coming years, benefiting researchers, developers, public and private investors, and the broader community. Lacking such established metrics today, we present in Fig. 1 the six most advanced quantum technology platforms and use the framework of "technology readiness levels" (TRLs) for quantum computing, quantum simulation, quantum networking, and quantum sensing as a proxy for technological maturity. To provide an external, aggregated view on the field, TRL values were taken directly from queries on ChatGPT and Gemini.

We would like to emphasize two important points for interpreting the TRLs. First, the original TRL mapping requires defining concepts such as prototype and operational environment, which will depend on the not yet fully known application domain. The generated output therefore mainly provides a snapshot for relative maturity between the different platforms rather than absolute progress toward the most advanced applications.

Second, achieving a higher TRL indicates that a higher level of system sophistication has been demonstrated, even if the raw performance of the platform is still consistent with an early-stage technology. For example, the Intel 4004 processor (shown in Fig. 2) was at a rather high TRL for 1971 and indeed led to commercial applications, but its performance was minimal compared with the CPUs (central processing units) and GPUs (graphical processing units) available to us today, 50 years later. In this sense, a high TRL for quantum technologies today does not indicate that the end goal is achieved, nor does it indicate that the science is done and only engineering remains. Rather, a high TRL for an emergent technology reflects a system-level demonstration in an operational environment that can (and must) be improved going forward. For instance, although today's cloud-accessible quantum computer prototypes are at relatively high TRL for the use case of research and education, they are still far away from the error-correcting machines that are required for commercial quantum utility.

Likewise, increasing TRL takes time. The first silicon ring modulators were demonstrated 20 years ago with modest TRL (*3*), and their performance and TRL have since improved substantially. Today, ring modulators are densely integrated with other photonics and electronics on circuits fabricated in commercial foundries, as shown in Fig. 3.

Similarly, quantum technologies in 2025 are advancing rapidly, and sophisticated systems demonstrations are being conducted, even in operational environments. However, as emergent early-stage technologies, their raw performance remains relatively nascent and must be considerably improved to reach their full promise. For example, implementing factoring (*4*, *5*) or quantum chemistry algorithms (*6*) at scale is estimated to require thousands to tens of thousands of fault-tolerant logical qubits (i.e., millions of physical qubits operating well beyond 99% gate fidelity) executing billions to trillions of gate operations. Realizing such mature and sustained computation with manageable overhead will require improved performance throughout the entire system—not just in the gate fidelities—and is very far beyond what is achievable with today's early-stage quantum computers (see Fig. 2 for a classical computing analogy). Similarly, whereas quantum communication allows for a few commercial applications, such as quantum key distribution, with current photonics technology, unlocking the full potential of new quantum-enabled privacy and

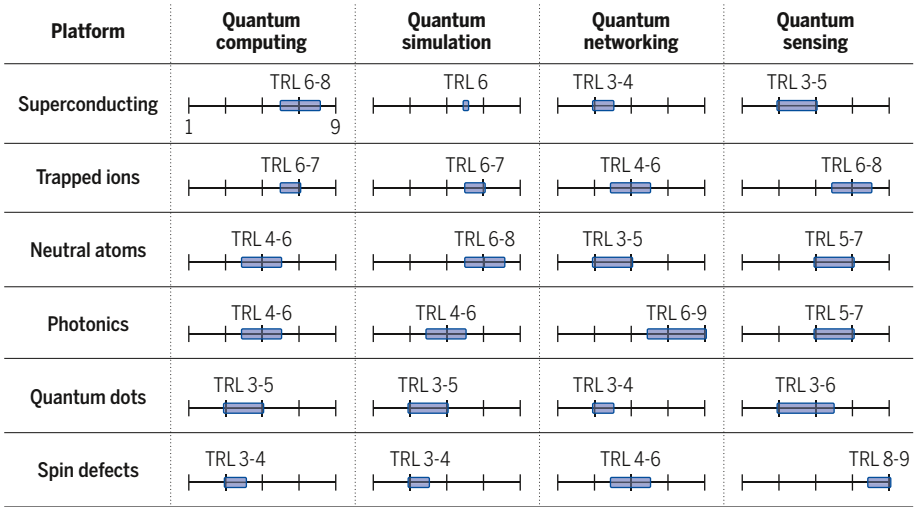


Fig. 1. Snapshot of technology readiness levels of emergent quantum platforms. Comparison of TRLs of emergent quantum platforms across key application areas as assessed by ChatGPT and Gemini (see supplementary materials). TRLs range from 1 (basic principles observed in a lab environment) to 9 (emergent platform proven in an operational environment). A TRL 7–9 platform may not yet be highly performant, but it has been transitioned out of the lab into a system-level, operational environment, even though the system itself may today be relatively immature compared with a desired future outcome. The range of TRLs output by ChatGPT and Gemini reflects, in part, the variation in subfields within each category.

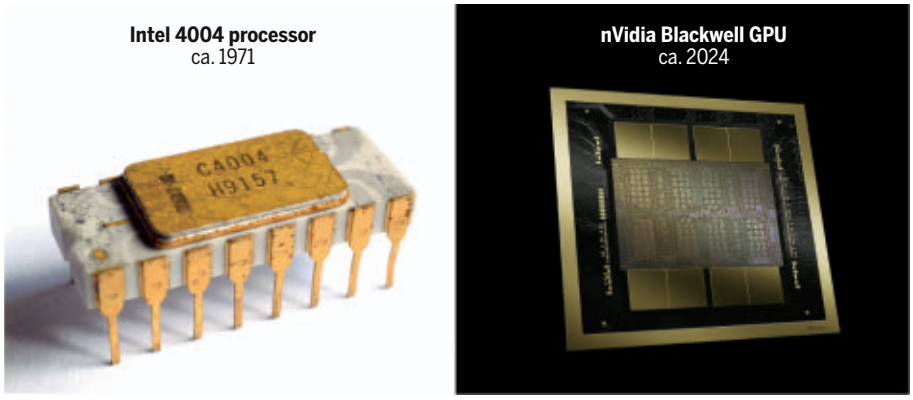


Fig. 2. Historical perspective of scaling classical electronic processors. (Left) Intel 4004, one of the first commercial integrated circuits, with 2300 transistors, 4-bit instruction set targeting integer arithmetic (not floating point), 10-μm lithography node, and 750-kHz clock capable of around 5×10^4 to 10×10^4 instructions per second. [Photo of Intel C4004 by Thomas Nguyen (https://commons.wikimedia.org/wiki/File:Intel_C4004.jpg), CC BY-SA 4.0] (Right) NVIDIA Blackwell GPU with a total of 208 billion transistors (two dies, each with 104 billion transistors), up to 32-bit instruction set targeting both integer and floating point operations, 4-nm lithography node, and a 2- to 3-GHz clock capable of 14 to 18 petaFLOPS (floating point operations per second) when executing 4-bit floating point (FP4) AI inference. [Source: NVIDIA]

CREDIT: (TOP) A. MASTIN/*SCIENCE*

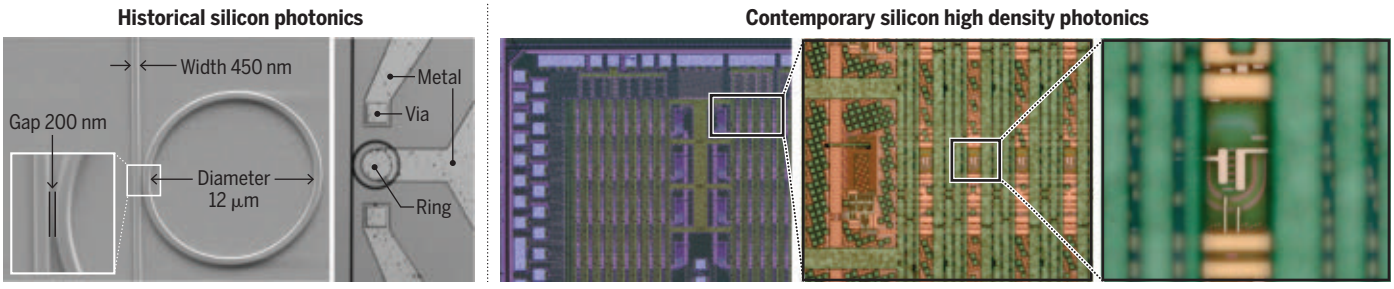


Fig. 3. Historical perspective of scaling silicon photonics. (Left) Early silicon photonics: gigahertz-speed ring resonator modulator. [Adapted with permission from Michal Lipson, Columbia University; (*3*)] (Right) State-of-the-art photonics, showing high-density integration of ring modulators (zoom ins). The circuit is a 10 Tb/s optical interconnects chip fabricated in GlobalFoundries 45CLO process. [Figure courtesy of Firooz Aflatouni, University of Pennsylvania]

communication functionalities (*7*) will require quantum networks linking qubit registers of size and performance well beyond current demonstrations (*8*). Next, we briefly summarize the current state of the art for several technology platforms.

Superconducting qubits and quantum dots

Superconducting qubits (*9*) and lithographically defined quantum dots (*10*) are both examples of "artificial atoms"—manufactured electrical structures that behave quantum mechanically at dilution refrigerator temperatures. Superconducting qubits are anharmonic electrical oscillators built from inductors, capacitors, and Josephson junctions that feature discretized states of flux, charge, or "phase." Semiconductor quantum dots use lithographically defined gates with applied voltages to trap single electrons, with the electron charge and spin states serving as the qubit. Silicon fabrication technology is utilized for the manufacture of devices for both types of qubits, albeit with careful processing windows and materials to realize coherent quantum devices.

State-of-the-art superconducting qubit processors have >100 qubits arranged in a two-dimensional (2D) array, with some processors also using a similar number of tunable couplers to turn on/off interactions between neighboring qubits. In such large arrays, the gate fidelities are in the approximately 99.95 to 99.99% range for single-qubit operations and in the approximately 99.5 to 99.9% range for two-qubit operations (*11*, *12*). Isolated devices can do about a factor of 5 to 10 better (*13*, *14*).

One advantage to superconducting qubits is their speed: Qubit operations are performed in about 10 to 40 ns (*15*), and readout can be performed with >99% fidelity in 100 to 200 ns (*16*, *17*). This speed leads to quantum error correction cycle times of around 1 μs (*15*, *18*). In a recent demonstration, increasing the error correction code distance from 3 to 5 to 7 (corresponding to surface-code logical qubits with 17, 49, and 97 physical qubits, respectively) reduced the error rates by more than a factor of two with each step, meaning: more qubits, lower error. At distances 5 and 7, the logical error rate was lower than even the best physical qubit (*12*). In the present "brute force" scaling era, where there are one to three wires per qubit, approximately 1000 to 10,000 qubits and their associated wiring can fit inside commonly available dilution refrigerators (*19*). To scale to larger numbers of qubits, such refrigerators would need to be networked together (*20*) and/or larger ones would need to be manufactured.

Spin qubits in semiconductors can be hosted in both gate-defined quantum dots, such as in Si/SiGe, Ge/SiGe, or Si-metal-oxide-semiconductor devices, and by atomically patterned dopants (optically interfaced spin qubits are discussed separately in the next subsection). Their size is set by lithographically patterned electrodes that can be fabricated by industrial processes and drive quantum gates at rates approaching gigahertz. The small size is a strong feature in terms of footprint but also leads to a wiring and cross-talk challenge in selectively addressing each qubit. In 2022, single- and two-qubit gates reaching 99% fidelities were demonstrated (*21*–*23*) and recently replicated with two-qubit devices fabricated in a 300-mm foundry environment (*24*). Electron spin qubits on dopants can also be used to facilitate coupling between nuclear spins, with >99% gate fidelities between three nuclear spin qubits reported (*25*). In Ge/SiGe quantum dots, a relatively new platform (*26*), universal control of four qubits was recently demonstrated (*27*).

A key materials challenge for Si/SiGe and Ge/SiGe qubits is achieving uniform and large valley splitting, given that the qubit states can mix with the excited valley states, causing leakage and control imperfections. Another challenge is temperature, as quantum dot spin qubits often operate at temperatures on the order of 100 mK. Although not a showstopper—superconducting qubits are operated at even lower temperatures—there is an increasingly successful push to increase this temperature in both silicon and germanium, with Clifford gate fidelities of 99.8% achieved at a temperature of 1 K (*28*).

Separate from the above, quantum dots based on III-V heterostructures are being developed toward high-efficiency photon sources (*29*, *30*). Such sources could serve as enabling technology in all four domains and set the quantum dot TRLs in Fig. 1 for networking and sensing.

Spin defects

Individual trapped atoms or ions in solids provide a combination of efficient photonic interfaces [up to about 50% photon detection efficiency at the system level (*31*)], coherence times up to seconds for electronic spins and minutes for nuclear spins (*32*, *33*), and solid-state hosts that are amenable to on-chip integration with semiconductor electrical and photonic circuits (*34*). In a quantum network setting, modules contain optically interfaced "communication" qubits such as color center electrons or ions (see next subsection) with nearby nuclear spins or different ions forming a local data qubit register. These systems combine local information processing with long-range optical photon–mediated entanglement links to achieve quantum connectivity for modular quantum computing and quantum internet applications. Additionally, these optically interfaced spins in semiconductors are also highly promising systems for sensing with nanoscale resolution (*35*).

Networks operating up to five qubits over up to three nodes have been built in the lab using diamond (*36*, *37*) as well as ytterbium-171 ions in yttrium orthovanadate crystals (*38*); silicon and silicon-carbide also hold promise (*39*, *40*). Employing quantum-frequency conversion to low-loss telecom bands and fiber stabilization architectures have enabled heralded entanglement over tens of kilometers of deployed telecom fiber (*41*) and between 10-km distant nodes (*42*). In-lab experiments have shown proof-of-principle demonstrations of quantum communication advantages (*31*), quantum network primitives (*36*, *37*, *43*), and

software-controlled entanglement distribution (*44*). In these works, single-qubit (two-qubit) logic operates with around 99% (98%) fidelity, whereas the 99.999% (99.93%) logic fidelities recently shown in an optimized two-qubit register (*45*) indicate the potential for beyond-threshold operation. Gate times on electronic spin qubits are submicrosecond, with nuclear spin qubit operation typically a factor of 1000 slower. Within a single-qubit register, mapping of a 50-spin qubit network for simulations (*46*) has been reported. Entanglement over optical channels currently reaches fidelities from 80 to 90% with rates up to tens of hertz (*37*, *43*).

The main challenges for scaling from these initial demonstrations are systematically increasing operating fidelities and efficiency as well as significantly increasing entanglement distribution rates. For the latter, massive multiplexing enabled by on-chip integration of large numbers of modules is likely required, leading to challenges that are common among all platforms (yield, power, calibration, and cost per qubit).

Atom arrays and trapped ions

Both trapped ions as well as neutral atoms have a long history in quantum technology. One of the earliest two-qubit gates was performed using trapped ions in 1995 (*47*), and quantum phase transitions were observed in 2002 in ultracold atoms (*48*). Furthermore, both systems find applications as quantum sensors and are being used as the most precise clocks (*49*). The two architectures share many commonalities: Qubit states are encoded in energy levels of the atom (typically spin levels, orbital levels, or a combination of both) and are manipulated using laser and microwave fields. The experiments take place in ultrahigh vacuum chambers, which essentially remove the ambient environment and thereby many decoherence sources. Consequently, atomic qubits offer coherence times that extend well beyond 10 s. Because atoms (ions or neutral) are all indistinguishable among the same species, these architectures are naturally homogeneous, which can be advantageous for scaling to multiple identical modules. The largest trapped-ion systems have hundreds of ions (*50*, *51*) and thousands of neutral atoms (*52*). Both architectures have recently implemented quantum algorithms with logically encoded qubits and gates (*53*, *54*).

A main difference between the two architectures is the way that the individual qubits are being trapped and the two-qubit gates are being implemented. The charge of the ion provides a convenient means to trap it using radio frequency electromagnetic fields in a quadrupole configuration. In this approach, the ions experience the same trapping potential while also experiencing a Coulomb interaction between each other. Two-qubit gates are performed by coupling the common motional modes of the ions to their internal states. Although this results in high-fidelity gates, the scaling beyond 100 qubits within the same trapping potential is challenging. One possible way forward is the quantum charge-coupled device architecture in which ions are moved along a surface trap chip between multiple separate trapping zones (*55*, *56*).

For neutral atoms, trapping potentials are provided by optical fields either in the form of counterpropagating beams that form an optical lattice or by tightly focused laser beams (optical tweezers). The first approach has been very effective in the context of quantum simulation, where atoms tunneling between different potential wells in the lattice are akin to electrons hopping in a solid-state lattice (*57*). Optical tweezers have recently also advanced quantum information processing for neutral atoms (*58*). Here, each tweezer hosts an individual qubit, and two-qubit gates are implemented by exciting to high-principal quantum number states (Rydberg states) that lead to strong interactions over typical tweezer distances of a few micrometers. An advantage of this approach is that scaling becomes a question of how many optical tweezers can be produced in the field of view of a microscope, with limits estimated to be around 100,000. Scaling beyond these limits will likely be enabled by a modular architecture, in which optical interfaces will provide the links between separate computation modules (*59*). In this direction, prototype quantum networks have been implemented both with trapped ions (*60*) and neutral atoms (*61*).

Optical photonic qubits

Current all-photonic quantum computing efforts are primarily focused on cluster-state (one-way) quantum computing (*62*, *63*) and are limited mostly by losses resulting from imperfect photonic devices (see "The challenges" section) as well as inefficient and imperfect quantum light sources based on bulk optical nonlinearities. To achieve improvements, alternative types of sources are being pursued, including high-efficiency quantum dot single-photon sources (*29*, *30*) and those based on cavity quantum electrodynamics (QED) (*64*). Cavity QED has been used to generate record-size photonic cluster states—12 photons in one dimension (*64*)—and the extension of this approach based on two atoms strongly coupled to a cavity has been used to perform fusion of two linear clusters into a 2D cluster (*65*). At present, this approach scales better in success probability than does the all-photonic approach, as it has a high efficiency of single-photon generation and detection, and uses quantum memory (atoms), which acts as an entangler between photons (*64*).

Irrespective of the quantum technology platform, photonics will play an essential role in scaling of quantum circuits. Photons are ideal for interconnecting quantum systems and for multiplexing control signals for many qubits (*66*). Photons are also necessary for trapping atoms in tweezer array quantum computers and for controlling and measuring a variety of optically interfaced qubits—atoms, ions, and artificial atoms (color centers in solids, quantum dots). However, despite major progress over the past couple of decades (see Fig. 3), state-of-the-art photonics is lossy and lacks some of the devices and functionalities needed for quantum systems, as discussed in the following section.

The challenges

The technologies in Fig. 1 have all demonstrated the fundamental DiVincenzo criteria (*67*)—the minimum requirements for a technology to be extensible in principle—with coherent operability at the level of a few qubits to hundreds of qubits. However, realizing the full promise of quantum technologies will require operability at much larger numbers of qubits. Scaling within current monolithic frameworks can support marginal increases in qubit counts, but to truly scale—as with all complex systems—architectural modularity will become necessary. The challenges to scaling are many, and we choose here to focus on four that, in broad terms, are shared by all of these platforms: materials and fabrication, wiring, power, and calibration and control. All of these challenges influence the choices encountered when defining a quantum information processing module that can be interconnected to form larger quantum systems.

Fabrication and materials

Materials science and fabrication engineering are critical to the success of all qubit platforms, whether that is manufacturing the qubits themselves or the ancillary electronics and optics needed to isolate, control, and read them out. The premium is on robust, reproducible, and scalable manufacturing. From an engineering standpoint, it is desirable to leverage existing semiconductor manufacturing while introducing as few new processes as possible. At the same time, quantum technologies are different and will require the targeted introduction of new materials systems, new fabrication flows, and new tooling to realize the advanced performance required.

All technologies in Fig. 1 leverage industry-standard fabrication tools whenever feasible to manufacture qubits and/or their control electronics. For example, superconducting qubits use aluminum, refractory metals, and refractory nitrides on silicon substrates with 3D heterogeneous integration (*68*), all of which are familiar to silicon fabrication (*69*). Surface-trapped ions (*70*) and photonic platforms (*62*, *63*) use integrated optics (e.g., Si/SiN waveguides, optical switches, phase shifters),

cryogenic CMOS control (*71*), and superconducting photodetectors (*72*). Spin defects strive for precision lateral and depth placement (*73*). The challenge lies in reproducible, robust, cost-effective fabrication with sufficiently low loss and low defect density to enable large-scale operation.

Materials science is an important, but not independent, part of the fabrication challenge. When required, new materials that offer enhanced performance, for example, electro-optic barium titanate (*62*, *74*) or strontium titanate (*75*, *76*), must be integrated into a fabrication process flow. The act of patterning, etching, and stripping resist from an otherwise pristine material certainly alters the material surface and possibly its performance. Surface and interface science is particularly important in the context of decoherence mechanisms in superconducting (*77*), semiconducting (*10*), spin defects (*78*), photonics, and trapped-ion qubits (*70*).

Photonics exemplifies the challenge: Silicon photonics fabricated in commercial foundries typically exhibits propagation loss of 0.25 to 1 dB/cm, and fiber-to-chip grating couplers available in their process design kits exhibit >3 dB of loss and are narrowband (*69*). Although lower propagation losses of decibels per meter have been reported in research-grade silicon nitride, lithium niobate, or silicon carbide photonics (*73*, *79*, *80*), these processes have not yet become widely available in a foundry environment. Moreover, state-of-the-art spatial light modulators have limited resolution and speed for scaling tweezer arrays (*81*), and solutions are needed at shorter wavelengths, with smaller pixel sizes and higher speed for trapping more atoms, reducing their separation, and controlling and moving atoms faster.

Similar challenges exist in microwave photonics, where deposited dielectrics such as silicon oxide, silicon nitride, and amorphous silicon are commonly used in foundry fabrication flows but exhibit quality factors of 10^3 to 10^5 in the microwave regime (*82*). Although this may be sufficient for most classical applications, it is generally inadequate for quantum technologies, which even today require quality factors exceeding 10^6 (*9*). The best quantum transducers and quantum frequency converters today are still very inefficient (*41*, *83*), which impedes their use of photonics in networking microwave superconducting and semiconducting quantum circuits and limits scaling of quantum networks, requiring telecom fiber communication over long distances.

All of these challenges will require materials and fabrication advances in a foundry setting. Academia is well suited for the identification of new candidate materials and fabrication concepts, as students can try a wide range of approaches, fail fast, and prototype successful options. Industry is well suited to taking these concepts, weighing the pros and cons of the often-conflicting options, and then optimizing for robust and reproducible system performance at scale.

Wiring

Once modules of qubits are assembled, the control and readout signals—the input and output of quantum computers—must be routed at scale. Most qubit modalities today require one to three channels per qubit, for the handling (trapped ions, neutral atoms), control, and readout signals, whether realized in the direct current/baseband, microwave, or optical domains. Brute-force scaling of waveguides or wires to the millions of qubits level will become impractical—both in cost and defect density—and alternative approaches must be sought.

Multiplexing signals is one approach to extensible control, where a single channel feeds multiple qubits. As an early example, two-qubit gates in an array of about 300 neutral atom qubits have been implemented by a single laser and coherently moving the atoms in and out of the beam (*53*). Challenges here include increasing the number of qubits per channel and accommodating the trade between large numbers of multiplexed qubits and the degree of control parallelization that is achievable (simultaneous versus sequential control operations). Another approach is to integrate control electronics with the qubits, whether through (cryogenic) CMOS (*21*, *71*), superconducting logic (*84*), integrated optics (*70*), or even room temperature variants where possible. The challenge—owing to noise, heating, or the trade-off between flexibility and functionality—is in maintaining high-fidelity quantum operations in the presence of these integrated, colocated control electronics and optics. An additional challenge is the development of quantum interconnects that coherently connect modules with sufficiently high fidelity to distribute entanglement throughout the quantum computer (*66*).

Calibration and control

A third challenge is the calibration of the qubits within and across modules. All qubits require some degree of calibration. Artificial atoms are manufactured qubits, each of which is nominally identical by design but practically different owing to small fabrication variations. Neutral atoms and ions have identical internal degrees of freedom, generally translating to identical single qubits, but the two-qubit operations are susceptible to variations in the trap potentials or the optical lattices that hold them (*70*). All qubits are susceptible to variations in the control and readout signals. Finally, calibrating qubits and their crosstalk with other qubits becomes a daunting task as the numbers of qubits increase (*12*). Machine learning is already being applied to assist with this challenge.

Size and power

Size and power are also challenges to extensibility. Today's development focuses largely on achieving operability, without many constraints on size or power. However, beyond-brute-force, large-scale machines will be constrained by both their size and power requirements. For example, superconducting qubits today are quite large, at ~1 mm^2 per qubit (*9*), which improves performance at the expense of real estate. Many of the technology platforms require large-scale cryogenic systems to cool the computer (qubits) and/or its peripherals (e.g., photodetectors, control electronics) (*9*, *70*). Neutral atom quantum computers rely on high-power lasers (*53*). As these technologies evolve, both the size and power will increasingly constrain the trade space and necessitate innovation to keep the cost and footprint manageable.

Outlook: What is going to give us the 1000× boost?

Modularity and architecture

Zooming out on the challenges outlined in the previous section, it is clear that although improvements can be made by optimizing elements within monolithic qubit systems, looking for 1000× improvements forces us to look at different architectures. In particular, building modularity into the systems provides a pathway that breaks the scaling into more manageable pieces. The key idea is to assemble full systems from a large set of smaller modules (Fig. 4) that are interconnected by quantum links (*85*). Such modularity will cap the wiring, size, (cooling) power, control, and calibration challenges to those of a single module. Note that modularity may be realized at different levels (e.g., within a chip by using on-chip wiring to connect small architectural modules, or between chips and modules using 3D heterogeneous integration or optical interconnects).

Besides removing scaling barriers, modularity opens the possibility of increased as well as dynamic connectivity throughout the system, enabling new functionality. One example is the use of different types of error-correction codes on quantum computers such as qLDPC (quantum low-density parity check) codes that could reduce the overall demands on the system (e.g., lower qubit number overhead). In addition, modular approaches may optimize different functionality in different parts of the system. For instance, quantum memory units might be separately optimized from quantum processing units.

Although modular architectures can thus help solve the scaling challenges outlined above and enable new opportunities, this approach comes with a major challenge: How can one efficiently interconnect these modules while maintaining the required performance?

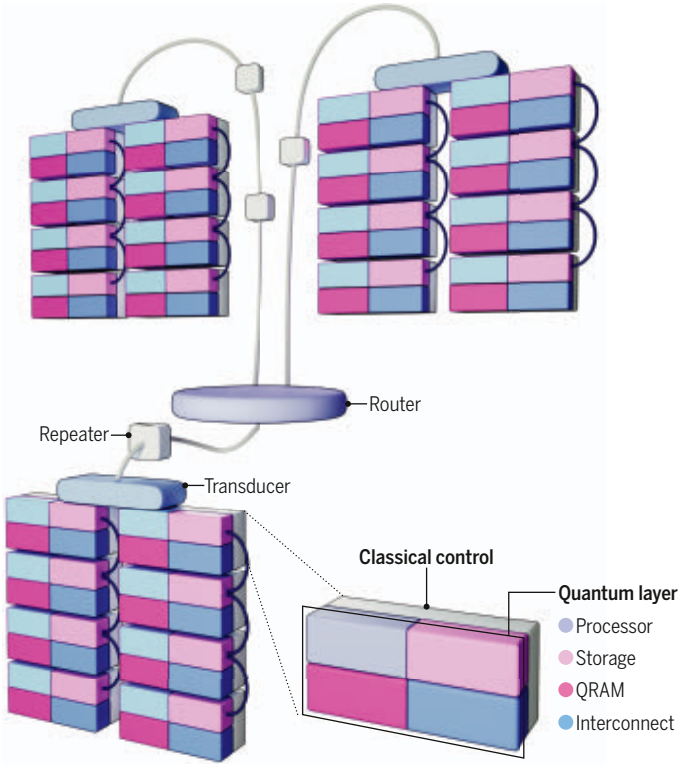


Fig. 4. Future modular architecture. Each quantum computing module (inset) consists of submodules with different functionalities as well as a classical control layer. These modules are then connected to each other through short quantum interconnects resembling a rack architecture in a data center. These racks can then be connected to others across longer distances in a quantum internet. QRAM, quantum random access memory.

The precise quantitative requirements for quantum interconnects (*66*) will differ by platform and specific application, but, qualitatively, they encompass fidelity, speed, and availability of the interconnect link. Heralding and error detection procedures allow for high-fidelity entanglement to be shared between modules but are intrinsically probabilistic. Direct transmission of qubits between chips (e.g., through transduction) is in principle deterministic, but unavoidable loss will also make these procedures probabilistic in practice. This probabilistic nature can be remedied, for instance, by adding long-lived quantum memories to make the links near-deterministic or by accounting for them in the error correction codes directly.

Heterogeneous systems

The need for modularity and integration will require heterogeneous systems at multiple levels of the architecture. For instance, the different modules for interconnecting separate computing nodes (Fig. 4) will likely consist of different modalities than the processor itself. Therefore, hybrid interfaces will need to be developed that enable quantum states to be shared between two or more different subsystems (*66*). Depending on the qubit implementation, these interfaces will need to bridge large frequency regimes, ranging from microwave to optical. The development of such interfaces will allow for the integration of different subsystems that are optimized for different quantum information tasks such as quantum memory, processing, and communication. Beyond heterogeneous quantum systems, tight integration of the classical and quantum parts of information processors will become increasingly important (Fig. 4).

Integration and interfaces

Photonics is key for scaling almost any type of quantum system, because of its essential role in quantum interconnects and multiplexing of control signals. But how can one achieve a giant boost in photonics performance needed for its inclusion into functional quantum systems? Toward this goal, innovative photonics design approaches are emerging, driven both by quantum technologies and the need for better optical interconnects for artificial intelligence (AI) hardware (*86*). New and improved photonic materials are also emerging to implement functionalities necessary for scaling quantum circuits. This includes thin-film lithium niobate for switching and microwave-to-optical transduction devices (*79*); more-powerful cryogenic electro-optic materials such as strontium titanate (*75*, *76*); wider bandgap and lower-loss materials such as silicon carbide, silicon nitride, and aluminum nitride (*72*, *80*, *87*); materials that host rare earth ions for quantum networking (*38*, *88*); and even laser systems on chip (*89*). Flat optics and metasurfaces (*90*) are candidates for scaling of tweezer arrays and atom control circuits, in combination with integrated photonics (*91*). In the microwave domain, low-loss waveguides and couplers are being 3D-integrated to distribute entanglement among chiplets within and between modules (*9*).

In all-photonic quantum computing, the efforts to employ high-efficiency single-photon sources are ongoing (*29*, *30*). In addition, cavity QED approaches to cluster state generation, which have been used to generate record-size clusters (*64*, *65*) could be translated from AMO to solid-state systems (*73*), enabling further scaling relative to atomic cavity QED platforms.

Conclusions

The past decade has witnessed extraordinary progress in the development of new hardware for quantum information processing across many platforms. This rapid acceleration has, from the start, been driven by collaborations spanning academia, industry, and national facilities. These assemblies of talent and infrastructure enable researchers to focus on material and device challenges unlike any we have experienced, from deterministic atomic-scale control of matter to the engineering of quantum entanglement. Continuing progress also hinges on advancing current technologies that will be required to deploy hybrid devices. Although quantum technologies have moved to higher TRLs, breakthroughs in performance are needed across all platforms to unlock the full power of quantum computing, entanglement-enhanced sensing, and a global quantum internet. These are extraordinary challenges that rise beyond any individual group, company, or nation. Such challenges continue to be surmounted through a combination of foundational scientific research and innovative engineering. Moreover, this is a global enterprise that is raising important ethical and legal questions ranging from privacy to the establishment of new quantum standards. Finally, the future of this field may largely depend on establishing a new legion of quantum scientists and engineers who will deliver a new form of information processing and transformative applications to society.

REFERENCES AND NOTES

1. AI Impacts, AI Timelines: Trends in the cost of computing, 10 March 2015; https://aiimpacts.org/trends-in-the-cost-of-computing/.
2. C. W. Gwyn, R. Stulen, D. Sweeney, D. Attwood, *J. Vac. Sci. Technol. B* **16**, 3142–3149 (1998).
3. Q. Xu, B. Schmidt, S. Pradhan, M. Lipson, *Nature* **435**, 325–327 (2005).
4. C. Gidney, M. Ekerå, *Quantum (Vienna)* **5**, 433 (2021).
5. C. Gidney, arXiv:2505.15917 [quant-ph] (2025).
6. A. Caesura *et al.*, *PRX Quantum* **6**, 030337 (2025).
7. S. Wehner, D. Elkouss, R. Hanson, *Science* **362**, eaam9288 (2018).
8. K. Azuma *et al.*, *Rev. Mod. Phys.* **95**, 045006 (2023).
9. M. Kjaergaard *et al.*, *Annu. Rev. Condens. Matter Phys.* **11**, 369–395 (2020).
10. G. Burkard, T. D. Ladd, A. Pan, J. M. Nichol, J. R. Petta, *Rev. Mod. Phys.* **95**, 025003 (2023).
11. Y. Kim *et al.*, *Nature* **618**, 500–505 (2023).
12. Google Quantum AI and Collaborators, *Nature* **638**, 920–926 (2025).
13. D. Rower *et al.*, *PRX Quantum* **5**, 040342 (2024).

CREDIT: A. MASTIN/*SCIENCE*

14. F. Marxer *et al.*, arXiv:2508.16437 [quant-ph] (2025).
15. Google Quantum AI, *Nature* **614**, 676–681 (2023).
16. Y. Sunada *et al.*, *Phys. Rev. Appl.* **17**, 044016 (2022).
17. F. Swiadek *et al.*, *PRX Quantum* **5**, 040326 (2024).
18. S. Krinner *et al.*, *Nature* **605**, 669–674 (2022).
19. S. Krinner *et al.*, *EPJ Quantum Technol.* **6**, 2 (2019).
20. S. Storz *et al.*, *Phys. Rev. Lett.* **135**, 030801 (2025).
21. X. Xue *et al.*, *Nature* **601**, 343–347 (2022).
22. A. R. Mills *et al.*, *Sci. Adv.* **8**, eabn5130 (2022).
23. A. Noiri *et al.*, *Nature* **601**, 338–342 (2022).
24. P. Steinacker *et al.*, *Nature* **646**, 81–87 (2025).
25. I. Thorvaldson *et al.*, *Nat. Nanotechnol.* **20**, 472–477 (2025).
26. G. Scappucci *et al.*, *Nat. Rev. Mater.* **6**, 926–943 (2021).
27. X. Zhang *et al.*, *Nat. Nanotechnol.* **20**, 209–215 (2025).
28. J. Y. Huang *et al.*, *Nature* **627**, 772–777 (2024).
29. P. Senellart, G. Solomon, A. White, *Nat. Nanotechnol.* **12**, 1026–1039 (2017).
30. M. L. Chan, A. A. Capatos, P. Lodahl, A. Søndberg Sørensen, S. Paesani, arXiv:2507.16152 [quant-ph] (2025)
31. M. K. Bhaskar *et al.*, *Nature* **580**, 60–64 (2020).
32. C. E. Bradley *et al.*, *Phys. Rev. X* **9**, 031045 (2019).
33. C. P. Anderson *et al.*, *Sci. Adv.* **8**, eabm5912 (2022).
34. L. Li *et al.*, *Nature* **630**, 70–76 (2024).
35. C. L. Degen, F. Reinhard, P. Cappellaro, *Rev. Mod. Phys.* **89**, 035002 (2017).
36. M. Pompili *et al.*, *Science* **372**, 259–264 (2021).
37. Y.-C. Wei *et al.*, *Science* **388**, 509–513 (2025).
38. A. Ruskuc *et al.*, *Nature* **639**, 54–59 (2025).
39. S. Simmons, *PRX Quantum* **5**, 010102 (2024).
40. N. T. Son *et al.*, *Appl. Phys. Lett.* **116**, 190501 (2020).
41. C. M. Knaut *et al.*, *Nature* **629**, 573–578 (2024).
42. A. J. Stolk *et al.*, *Sci. Adv.* **10**, eadp6442 (2024).
43. S. L. N. Hermans *et al.*, *Nature* **605**, 663–668 (2022).
44. C. Delle Donne *et al.*, *Nature* **639**, 321–328 (2025).
45. H. P. Bartling *et al.*, *Phys. Rev. Appl.* **23**, 034052 (2025).
46. G. L. van de Stolpe *et al.*, *Nat. Commun.* **15**, 2006 (2024).
47. C. Monroe, D. M. Meekhof, B. E. King, W. M. Itano, D. J. Wineland, *Phys. Rev. Lett.* **75**, 4714–4717 (1995).
48. M. Greiner, O. Mandel, T. Esslinger, T. W. Hänsch, I. Bloch, *Nature* **415**, 39–44 (2002).
49. A. D. Ludlow, M. M. Boyd, J. Ye, E. Peik, P. O. Schmidt, *Rev. Mod. Phys.* **87**, 637–701 (2015).
50. D. Kiesenhofer *et al.*, *PRX Quantum* **4**, 020317 (2023).
51. S.-A. Guo *et al.*, *Nature* **630**, 613–618 (2024).
52. H. J. Manetsch *et al.*, *Nature* **647**, 60–67 (2025).
53. D. Bluvstein *et al.*, *Nature* **626**, 58–65 (2024).
54. C. Ryan-Anderson *et al.*, arXiv:2404.16728 [quant-ph] (2024)
55. D. Kielpinski, C. Monroe, D. J. Wineland, *Nature* **417**, 709–711 (2002).
56. J. M. Pino *et al.*, *Nature* **592**, 209–213 (2021).
57. C. Gross, I. Bloch, *Science* **357**, 995–1001 (2017).
58. M. Morgado, S. Whitlock, *AVS Quantum Sci.* **3**, 023501 (2021).
59. J. Covey, H. Weinfurter, H. Bernien, *NPJ Quantum Inf.* **9**, 90 (2023).
60. V. Krutyanskiy *et al.*, *Phys. Rev. Lett.* **130**, 050803 (2023).
61. W. Zhang *et al.*, *Nature* **607**, 687–691 (2022).
62. PsiQuantum team, *Nature* **641**, 876–883 (2025).
63. H. Aghaee Rad *et al.*, *Nature* **638**, 912–919 (2025).
64. P. Thomas, L. Ruscio, O. Morin, G. Rempe, *Nature* **608**, 677–681 (2022).
65. P. Thomas, L. Ruscio, O. Morin, G. Rempe, *Nature* **629**, 567–572 (2024).
66. D. Awschalom *et al.*, *PRX Quantum* **2**, 017002 (2021).
67. D. P. DiVincenzo, arXiv:cond-mat/9612126 [cond-mat.mes-hall] (1996).
68. D. Rosenberg *et al.*, *NPJ Quantum Inf.* **3**, 24 (2017).
69. M. Rakowski *et al.*, 2020 Optical Fiber Communications Conference and Exhibition (OFC), paper T3H.3 (2020).
70. C. Bruzewicz, J. Chiaverini, R. McConnell, J. M. Sage, *Appl. Phys. Rev.* **6**, 021314 (2019).
71. J. Anders *et al.*, *IEEE Trans. Quantum Eng.* **4**, 5100230 (2023).
72. I. Holzman, Y. Imry, *Adv. Quantum Technol.* **2**, 1800058 (2019).
73. D. M. Lukin, M. A. Guidry, J. Vučković, *PRX Quantum* **1**, 020102 (2020).
74. S. Abel *et al.*, *Nat. Mater.* **18**, 42–47 (2019).
75. C. P. Anderson *et al.*, *Science* **390**, 394–399 (2025).
76. A. Ulrich *et al.*, *Science* **390**, 390–393 (2025).
77. I. Siddiqi, *Nat. Rev. Mater.* **6**, 875–891 (2021).
78. L. V. H. Rodgers *et al.*, *Proc. Natl. Acad. Sci. U.S.A.* **121**, e2316032121 (2024).
79. D. Assumpcao *et al.*, *Nat. Commun.* **15**, 10459 (2024).
80. C. Xiang, W. Jin, J. E. Bowers, *Photon. Res.* **10**, A82–A96 (2022).
81. R. Lin *et al.*, *Phys. Rev. Lett.* **135**, 060602 (2025).
82. W. D. Oliver, P. B. Welander, *MRS Bull.* **38**, 816–825 (2013).
83. J. Rochman, T. Xie, J. G. Bartholomew, K. C. Schwab, A. Faraon, *Nat. Commun.* **14**, 1153 (2023).
84. N. Takeuchi, T. Yamae, C. L. Ayala, H. Suzuki, N. Yoshikawa, *IEICE Trans. Electron.* **105**, 251–263 (2022).
85. C. R. Monroe, R. J. Schoelkopf, M. D. Lukin, *Sci. Am.* **314**, 50–57 (2016).
86. K. Y. Yang *et al.*, *Nat. Commun.* **13**, 7862 (2022).
87. X. Liu, A. W. Bruch, H. X. Tang, *Adv. Opt. Photonics* **15**, 236–317 (2023).
88. S. Ourari *et al.*, *Nature* **620**, 977–981 (2023).
89. J. Yang *et al.*, *Nature* **630**, 853–859 (2024).
90. A. H. Dorrah, J.-S. Park, A. Palmieri, F. Capasso, *Nat. Commun.* **16**, 3126 (2025).
91. I. Christen *et al.*, *Nat. Commun.* **16**, 82 (2025).

ACKNOWLEDGMENTS

We thank M. Eriksson, S. Guha, and B. Pingault for their assistance with this manuscript. **Funding:** D.D.A. was supported by Q-NEXT, a US Department of Energy Office of Science National Quantum Information Science Research Center, and the Air Force Office of Scientific Research. R.H. was supported by the Dutch Research Council (NWO) through the Spinoza Prize 2019 (project SPI 63-264). J.V. was supported by the Vannevar Bush Faculty Fellowship from the US Department of Defense. H.B. gratefully acknowledges funding from the US Office of Naval Research (grant N00014-23-1-2540) and the US Army Research Office (grant W911NF2410388). W.D.O. gratefully acknowledges funding from the US Army Research Office under award W911NF-23-1-0045. **Competing interests:** D.D.A. is a cofounder and shareholder of Blanqet LLC. W.D.O. was a cofounder and shareholder of Atlantic Quantum, a start-up company focused on superconducting quantum computing. Atlantic Quantum was acquired by Google in October 2025. R.H. is cofounder and shareholder of Delft Networks, a start-up company focused on quantum network products and applications. J.V. is a cofounder and a lead scientific adviser of Spins Photonics Inc, a photonic inverse design software company. H.B. is a cofounder and shareholder of CavilinQ, Inc. **License information:** Copyright © 2025 the authors, some rights reserved; exclusive licensee American Association for the Advancement of Science. No claim to original US government works. https://www.science.org/about/science-licenses-journal-article-reuse

SUPPLEMENTARY MATERIALS

science.org/doi/10.1126/science.adz8659
Supplementary Text

Submitted 8 September 2025; accepted 5 November 2025

10.1126/science.adz8659

NEWS FROM Science | AAAS

Subscribe to **News from Science** for unlimited access to authoritative, up-to-the-minute news on research and science policy.



bit.ly/NewsFromScience

TRAVEL FOR AAAS
Members and Friends

INDONESIA'S FORGOTTEN ISLANDS
September 8 – 21, 2026
AN EXPEDITION CRUISE THROUGH INDONESIA & BORNEO



20% Savings!
must book by Dec 1, 2025
Southeast Asia's captivating and rarely-seen wonders!



Culturally Stunning!

DISCOVER VIETNAM! & ANGKOR WAT
March 9 - 22, 2026

Arizona Dark Skies
April 18 - 25, 2026



Indigenous Peoples of the Southwest, Arizona in Spring & a Meteor Shower!

Wild Alaska
May 11 - 16, 2026



5% Savings!
from $ 3,876 pp twin + air

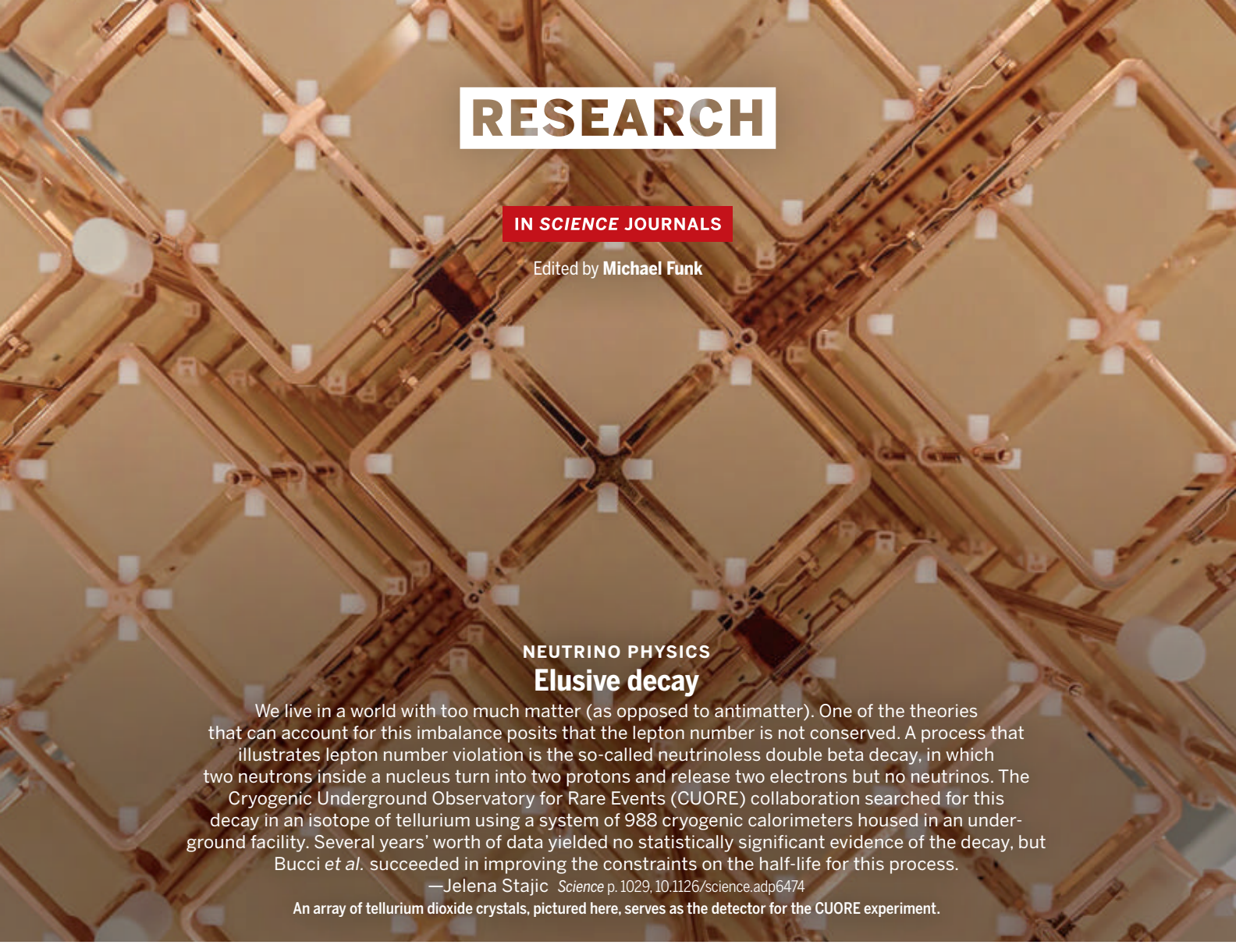
For a detailed brochure, please call (800) 252 - 4910 or (408) 252 - 4910 or Email: Info@BetchartExpeditions.com

BETCHART EXPEDITIONS INC.
17050 Montebello Rd
Cupertino, California 95014
www.BetchartExpeditions.com

RESEARCH

IN *SCIENCE* JOURNALS

Edited by **Michael Funk**



NEUTRINO PHYSICS

Elusive decay

We live in a world with too much matter (as opposed to antimatter). One of the theories that can account for this imbalance posits that the lepton number is not conserved. A process that illustrates lepton number violation is the so-called neutrinoless double beta decay, in which two neutrons inside a nucleus turn into two protons and release two electrons but no neutrinos. The Cryogenic Underground Observatory for Rare Events (CUORE) collaboration searched for this decay in an isotope of tellurium using a system of 988 cryogenic calorimeters housed in an underground facility. Several years' worth of data yielded no statistically significant evidence of the decay, but Bucci *et al.* succeeded in improving the constraints on the half-life for this process.
—Jelena Stajic *Science* p. 1029, 10.1126/science.adp6474

An array of tellurium dioxide crystals, pictured here, serves as the detector for the CUORE experiment.

PHOTO: CUORE COLLABORATION AND YURY SUVOROV

SYNTHETIC BIOLOGY

Chromosome transfer in and out of human cells

Building human genomes from scratch has the potential to transform biology and medicine but will require innovative approaches. Petris *et al*. demonstrate key steps toward this goal by developing a method to transfer a human chromosome into specialized "assembly" cells and safely manipulate it. The engineered chromosome is then used to replace the corresponding chromosome in target human cells with minimal genetic damage. By enabling accurate chromosome transplantation and replacement, this study lays the groundwork for constructing synthetic human genomes and opens new possibilities for determining chromosome function, modeling disease, and engineering cells. —Di Jiang
Science p. 1038, 10.1126/science.adv9797

SOLAR CELLS

Solvent tuning for large-area coatings

A three-component solvent that optimizes ion coordination and evaporation kinetics enables slot-die coating of void-free, high-crystalline perovskite films for solar modules. Wang *et al*. used a mixture of γ-valerolactone, 2-methyl tetrahydrofuran, and dimethylsulfoxide to replace more hazardous solvents such as *N*,*N*-dimethylformamide and added a surfactant to maintain consistent evaporation rates near the film edges. They fabricated stable, 7200-square-centimeter perovskite photovoltaic modules with a certified power conversion efficiency of 17.2%. —Phil Szuromi
Science p. 1021, 10.1126/science.adz0091

BIOCATALYSIS

Biology learns radical hydrogenation

In organic chemistry, hydrogenation of alkenes is typically catalyzed by transition metals, whereas biology uses hydride transfer, which is limited to electrophilic alkenes. Vallapurackal *et al*. hypothesized that an alternative mechanism for hydrogenation of unactivated alkenes would be possible with the right combination of functional groups and cofactors. Starting by screening for activity for a simpler intramolecular olefin-coupling probe reaction, the authors identified heme enzymes capable of generating iron-hydride species. They then expanded this activity by screening cysteine residues on the opposite face of the active site that can participate in hydrogen atom transfer, enabling radical hydrogenation. Directed evolution enhanced this activity through eight mutations throughout the enzyme, and the authors conducted scaled-up experiments and mechanistic

investigations that confirm the proposed biochemical logic for this reaction. —Michael A. Funk

Science p. 1050, 10.1126/science.aea4737

PLANT SCIENCE

Cell cycle control of cell walls

Plant cells are wrapped in a semirigid wall that reconfigures as cells expand. The chemical and material properties of pectin, a key component of cell walls, can influence cell division. Zhu *et al*. found different pectin properties in new versus mature cell walls, which are controlled by pectin-modifying enzymes such as PME5. The authors established that PME5 RNA is sequestered in the nucleus by RNA-binding proteins. The PME5 messenger RNA (mRNA) is released into the cytoplasm during cytokinesis when the nuclear envelope breaks down. By spatially controlling PME5 mRNA, modification of pectin can be precisely timed to coincide with the formation of new cell division plates. —Madeleine Seale

Science p. 1064, 10.1126/science.ady4102

PLANT BIOLOGY

Catching calcium waves in leaves

Pattern-triggered immunity in plants depends on intracellular calcium signaling downstream of receptors that are activated by microbe- or damage-associated molecular patterns (MAMPs or DAMPs). Zhang *et al*. characterized MAMP- and DAMP-induced calcium waves in *Arabidopsis thaliana* cotyledons to investigate how defense signaling spreads through leaf tissue (see the Focus by Gilroy). The waves initiated in a small number of epidermal cells and slowly propagated to nearby cells at a constant speed. By contrast, calcium waves elicited by wounding spread much faster and traveled farther but decreased in speed with distance from the wound. MAMP-induced Ca^{2+} waves were propagated by a mechanism distinct from that of wounding-induced waves. —Annalisa VanHook

Sci. Signal. (2025) 10.1126/scisignal.adw2270, 10.1126/scisignal.aeb7956

ACTUATORS

Rapid responding rubbers

Dielectric elastomers use electroactive polymers to convert electrical energy into mechanical work and vice versa. Although they are stretchable and lightweight, they require high electric fields and can be slow to respond. Shi *et al*. developed a silicone elastomer with a biphasic bicontinuous structure. Commercial silicone elastomers are cross-linked to form an interconnected dielectric phase within a soft silicone rubber. These composite materials can be actuated under low fields while still showing high energy and power density, which the authors exploited in a number of robotic devices. —Marc S. Lavine

Science p. 1044, 10.1126/science.adr3521

PHYSICS

Enantiomer selection without phase locking

Chiral molecules exist in two forms called enantiomers, which relate to each other much like our left and right hands do. The electric-dipole moment of left-handed and right-handed molecules has one component differing in sign. Zou *et al.* showed that the interference of two two-photon absorption pathways in the presence of a static electric field allows for distinguishing left-handed from right-handed molecules with electric fields only. Unlike in chiral-sensitive three-wave mixing, realized so far only with microwave pulses, no phase locking of the beams is required. This opens the door for enantiomer selection with optical fields or a combination of optical and microwave fields. —Christiane P. Koch

Sci. Adv. (2025) 10.1126/sciadv.adz4877

IN OTHER JOURNALS

Edited by **Corinne Simonti** and **Jesse Smith**

ORBITAL MECHANICS

Laser ranging for lunar navigation

Retroreflectors have been placed on the Moon since the Apollo missions and were initially designed for laser-ranging experiments from Earth. Miniature retroreflectors have been mounted on many recent lunar landers, intended for observation from lunar orbit. Cascioli *et al.* used the laser altimeter on the Lunar Reconnaissance Orbiter to observe eight retroreflectors on the Moon and incorporated the range measurements into spacecraft navigation processes. They found that determination of the spacecraft orbit improves if the retroreflector positions are precisely known. Currently, only the Apollo retroreflectors have the necessary precision, but repeated observations of the recent miniature retroreflectors hold promise for improving lunar spacecraft navigation. —Keith T. Smith *Planet. Sci. J.* (2025) 10.3847/PSJ/ae0e0b



Retroreflectors on the surface of the moon help to determine the Lunar Reconnaissance Orbiter's orbit more precisely.

POLLUTION

Cockroaches release allergens

The presence of cockroaches, particularly in lower-income urban households, is a known risk factor associated with the development of allergies or asthma among children. However, a causal relationship between cockroach presence and levels of endotoxins in homes was unclear. Kakumanu *et al.* addressed this with laboratory assays from apartments in North Carolina. They found that roach feces, especially from females, increased allergen and endotoxin levels in homes. Compared with bedrooms, kitchens had more allergens because they provided the main sources of food for roaches. Importantly, when exterminators eliminated the pests, air quality greatly improved, illustrating the need for effective pest control to protect children's health. —Ekeoma Uzogara

J. Allergy Clin. Immunol. Glob. (2026) 10.1016/j.jacig.2025.100571

COGNITION

A walk to remember

Studies in animal models of Alzheimer's disease (AD)

IMAGE: NASA/GODDARD/SVS



PHOTO: JIANMEI WANG VIA ISTOCK

FORAGING DYNAMICS

Friends for now

Lions in the Serengeti present a classic image of a large pride with many members. Examining this deeper, however, presents logistical problems. How are large prides supported when most prey don't require cooperation to capture and cooperating leads to fewer prey items shared among more individuals? Social living does offer benefits such as protection against raiding lions, suggesting a trade-off between energy and safety requirements. Fryxell *et al.* developed a behaviorally based foraging model to explore the dynamics between energy and cooperation, finding that only one to three lions are adequate for capturing most prey. Thus, large prides are only sustainable because of a fission-fusion model of sociality and cooperation where pride associations are temporary but recurring. —Sacha Vignieri

Ecol. Lett. (2025) 10.1111/ele.70211

Affiliation with large lion prides may be looser than previously thought.

have shown that physical activity might reduce disease progression. However, evidence in humans remains scarce. Yau *et al.* analyzed the relationship among pedometer-measured physical activity (steps), cognitive decline, and amyloid-β (Aβ) and tau brain accumulation in cognitively unimpaired older individuals over the course of several years. In individuals with high Aβ at baseline, a higher number of daily steps was associated with slower cognitive and functional decline and lower tau accumulation. The strongest effect was seen at moderate physical activity (5001 to 7500 steps per day) in the most sedentary group. These results suggest that physical activity interventions should be considered for testing in future AD prevention trials. —Mattia Maroso

Nat. Med. (2025) 10.1038/s41591-025-03955-6

PLANT SCIENCE

Stem cells induce regeneration from roots

Many plant genetic engineering and breeding approaches require the regeneration of plants through tissue culture. However, some economically important species are challenging or impossible to regenerate using standard hormone-based methods. Wittmer *et al.* used a targeted gene induction approach to trigger the formation of root-like stem cells in *Arabidopsis*, lettuce, tomato, and pepper plants. They found that stem cell induction was sufficient to generate new plantlets from roots and specifically required combined expression of an *AIL/PLT* family gene with a *WOX* family member. Induction of stem cell identity superseded the need for dedifferentiation of tissue, which normally occurs during somatic embryogenesis. The work provides the insight and methodology needed to expand plant regeneration methods across multiple species. —Madeleine Seale

Plant Cell (2025) 10.1093/plcell/koaf252

MACHINE LEARNING

Redesigning nonsynthesizable structures

Recent advances in data-driven machine learning approaches and quantum chemistry have revolutionized computer-aided virtual screening and the discovery of various new materials. In some cases, these methods can now even be used to make reliable predictions of synthetic feasibility using available literature data, thermodynamic stability, and other factors. Generally, materials predicted not to be synthesizable are excluded from any further analysis, representing a significant loss of potential candidates. Choi *et al.* addressed this limitation by developing a framework, powered by large language models, that redesigns nonsynthesizable candidate inorganic materials into viable structures, opening the door to discovering a much broader range of experimentally realizable compounds. —Yury Suleymanov

J. Am. Chem. Soc. (2025) 10.1021/jacs.5c07743

AROMATIC MOLECULES

Synthesizing curved cycloarenes

A π-extended quintulene synthesized on a Au(111) surface has a pentaradial cavity and a nonplanar dome-shaped geometry. Ruan *et al.* condensed five units of a precursor, 4-([1,1′-biphenyl]-2-yl)-2,6-dibromopyridine, through dehalogenative aryl-aryl coupling to form a cyclo-meta-pentapyridine core. Subsequent thermal activation yielded a pentaazaquintulene nanocone, $C_{85}N_5$, that could be inverted to a concave shape with a scanning tunneling microscope tip. The nitrogen atom could coordinate a gold atom introduced before the final annealing step. —Phil Szuromi

J. Am. Chem. Soc. (2025) 10.1021/jacs.5c11883

Edited by **Michael Funk**

ANTIBIOTIC RESISTANCE

Plasmids on the move

Autonomous mobile genetic elements such as plasmids spread antibiotic resistance and virulence genes among bacteria. We know that plasmids are dynamic, but we do not understand their recent evolution. Cazares *et al*. studied the genetic history of the Murray collection, a rare assemblage of bacterial samples from 1917 to 1954 that were collected before antibiotics were in common use, to track recent plasmid evolution. Since 1954, a few plasmids in Gram-negative bacteria acquired antibiotic resistance, and these have evolved into three families of plasmids containing multiple replicons that spread among human-associated bacteria. We have now reached a state of circulating resistance to most known antibiotic classes among human pathogenic bacteria. —Caroline Ash

Science p. 1015, 10.1126/science.adr1522

LARGE LANGUAGE MODELS

Posttraining for persuasiveness

Many fear that we are on the precipice of unprecedented manipulation by large language models (LLMs), but techniques driving their persuasiveness are poorly understood. In the initial "pretrained" phase, LLMs may exhibit flawed reasoning. Their power unlocks during vital "posttraining," when developers refine pretrained LLMs to sharpen their reasoning and align with users' needs. Posttraining also enables LLMs to maintain logical, sophisticated conversations. Hackenburg *et al*. examined which techniques made diverse, conversational LLMs most persuasive across 707 British political issues (see the Perspective by Argyle). LLMs were most persuasive after posttraining, especially when prompted to use facts and evidence (information) to argue. However, information-dense LLMs produced the most inaccurate claims, raising concerns about the spread of misinformation during rollouts of future models. —Ekeoma Uzogara

Science p. 1016, 10.1126/science.aea3884; see also p. 983, 10.1126/science.aec9293

DNA DAMAGE

How a genotoxin binds DNA

The small molecule colibactin is produced by some strains of *Escherichia coli* and has been associated with DNA damage and colorectal cancer in vitro and in humans. The chemical structure of colibactin has been the subject of intense study, but it has remained somewhat unclear due to the instability of this molecule and the difficulty in producing large quantities of authentic product. By incubating a short oligonucleotide with *E. coli*–producing colibactin, Carlson *et al*. were able to purify cross-linked DNA and investigate its structure using mass spectrometry and nuclear magnetic resonance spectroscopy (see the Perspective by Schärer). The authors observed an α-ketoiminium group bound in the DNA minor grove and other contacts that help to explain the observed AT-rich DNA specificity, a signature that has been documented in some human colorectal cancer genomes. —Michael A. Funk

Science p. 1017, 10.1126/science.ady3571; see also p. 984, 10.1126/science.aec9205

MOLECULAR BIOLOGY

Structure of chromatin condensates

How linear DNA folds into complex, three-dimensional structures within cells has long been a puzzle. Using advanced imaging and simulations, Zhou *et al*. showed that a small structural change, just five extra DNA bases between nucleosomes, the basic units of DNA packaging, can drastically change how arrays pack together (see the Perspective by Zhang and Ramani). Depending on this spacing, the droplets can behave like liquids or take on solid-like properties. These results demonstrate how subtle structural features shape the physical properties of chromatin, offering insights into genome organization on larger scales. —Di Jiang

Science p. 1018, 10.1126/science.adv6588; see also p. 986, 10.1126/science.aed0014

MOLECULAR BIOLOGY

Finding DNA's broken ends

Cells constantly face DNA damage that, if repaired incorrectly, can lead to cancer or genetic instability. Homologous recombination, one of the most accurate repair mechanisms, requires broken DNA to find a matching sequence among billions of bases. Using a powerful method to map DNA interactions inside cells, Teloni *et al*. uncovered how this search is guided by the protein complex cohesin. They found that cohesin acts in two ways: by forming loops that focus the search to DNA near the break and by clamping the broken end to its sister chromatid to scan the correct repair template. Marin-Gonzalez *et al*. found that cohesin actively reels in surrounding chromatin to help the repair protein RAD51 scan for homology. This directed, one-dimensional scanning mechanism greatly accelerates the search process. These studies reveal how cells overcome a fundamental biophysical problem in DNA repair, with implications for understanding genome instability in cancer and other diseases (see the Perspective by Hu). —Di Jiang

Science p. 1020, 10.1126/science.adw0566, p. 1019, 10.1126/science.adw1928; see also p. 987, 10.1126/science.aed1859

MATERIALS DESIGN

Modular crystal synthesis

A series of $BaSbQ_3$ crystals (where Q is sulfur or tellurium) has been synthesized, and its structural diversity is directly driven by systematically varying the S/Te ratio. Zhao *et al*. synthesized at least 10 of these "stoichiomorphs" composed of rocksalt slab fragments stacked together with polytelluride zigzag chains. Each member differed only in the size and assembly of these blocks, and the crystal phase that resulted depended on differences in anion electron affinity and sizes. —Phil Szuromi

Science p. 1057, 10.1126/science.aea8088

PHASE TRANSITIONS

Melting through an intermediate phase

The melting of a two-dimensional crystal proceeds through a hexatic phase, an orientationally ordered, liquid-like intermediate. Bui *et al*. used in situ scanning transmission microscopy and nanobeam electron diffraction to follow the structural changes of silver

iodide embedded in multilayer graphene with increasing temperature. The hexatic phase, which only forms in two-dimensional systems and has only short-range translational order, appeared in a narrow temperature window just before silver iodide melted and likely formed through a mixed-melting pathway. —Phil Szuromi

Science p. 1033, 10.1126/science.adv7915

ASTHMA

RSV and asthma link revealed

Early-life infection with respiratory syncytial virus (RSV) is considered to predispose children to allergic asthma. De Leeuw *et al.* analyzed a Danish population-wide registry, which showed that infants hospitalized for RSV bronchiolitis and born to parents with allergic asthma were at greater risk for developing asthma. The underlying mechanism was modeled in neonatal mice infected with an RSV-like virus and exposed to the house dust mite allergen. Neonatal mice born to mothers with dust mite allergy developed more severe type 2 inflammation and asthma-like symptoms, explained by maternal transfer of allergen-specific immune proteins and immune cell priming in neonates caused by the virus. Enhanced risk was mitigated when newborn mice were given RSV immunoprophylaxis. These findings provide insight into maternal factors influencing RSV-associated allergic asthma. —Christiana N. Fogg

Sci. Immunol. (2025) 10.1126/scitranslmed.adz4626

LIVER DISEASE

mRNA metabolic makeover

Metabolic dysfunction–associated fatty liver disease is characterized by metabolic stress that drives immune dysregulation in the liver. Lipid nanoparticle (LNP)–delivered messenger RNA (mRNA) strategies hold promise for targeted therapies, but LNP-induced hepatic oxidative stress can aggravate metabolic dysfunction. Yu *et al*. developed a vitamin E–functionalized LNP to deliver mRNA encoding T cell protein tyrosine phosphatase (TCPTP) to reprogram hepatic STAT signaling without stimulating oxidative stress. Across several mammalian preclinical models, TCPTP mRNA delivery with the optimized LNPs improved steatohepatitis and metabolic and immune balance and reduced progression to hepatocellular carcinoma. These findings indicate that engineered LNP strategies to counteract oxidative stress may enable more effective liver delivery of mRNA therapeutics and position TCPTP as a potential therapeutic. —Molly Ogle

Sci. Transl. Med. (2025) 10.1126/scitranslmed.adv2293

RESEARCH ARTICLE SUMMARY

ANTIBIOTIC RESISTANCE

Pre- and postantibiotic epoch: The historical spread of antimicrobial resistance

Adrian Cazares*, Wendy Figueroa, Daniel Cazares, Leandro Lima, Jake D. Turnbull, Hannah McGregor, Jo Dicks, Sarah Alexander, Zamin Iqbal*, Nicholas R. Thomson*

Full article and list of author affiliations: https://doi.org/10.1126/science.adr1522

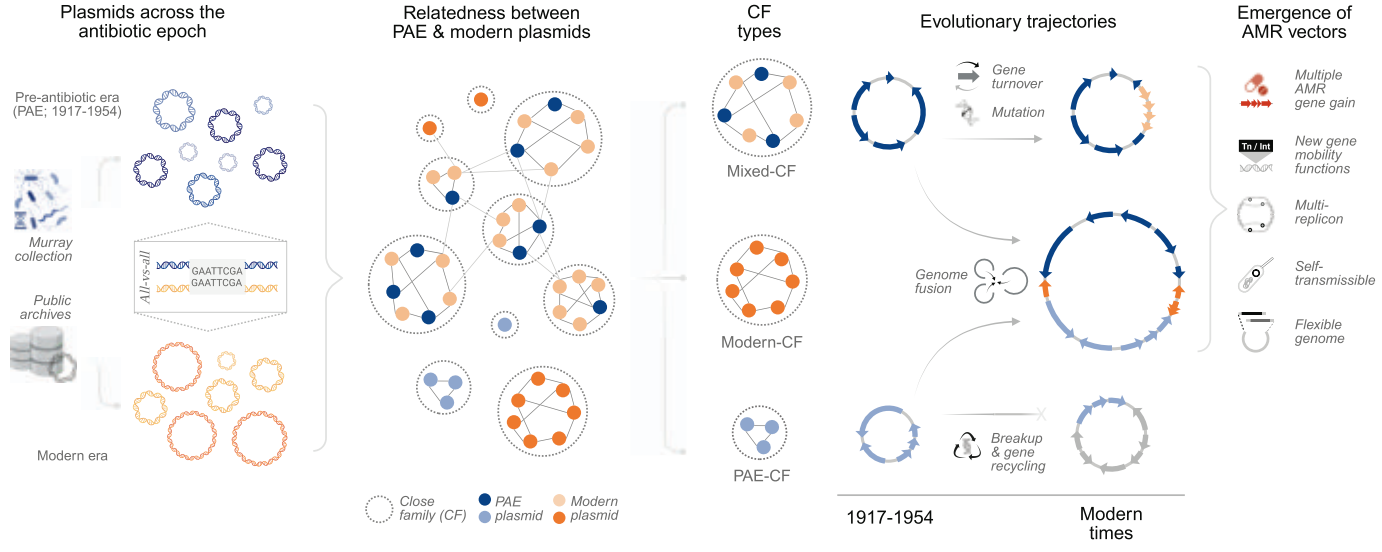
INTRODUCTION: Treatment failure linked to antimicrobial resistance (AMR) is one of the most important threats to human health. The genes that encode AMR have become highly mobile and, since the introduction and widespread use of antibiotics, have disseminated globally across a diverse set of bacteria. This has made many infections hard or impossible to treat. Extrachromosomal elements called plasmids are one of the principal mechanisms by which AMR genes have spread. Although we know that the AMR gene cassettes that plasmids carry have become more complex over time, often conferring resistance to multiple antibiotic classes, the evolution of the plasmids themselves during this antibiotic era remains poorly understood.

RATIONALE: To understand how plasmids have adapted to carry AMR genes, we sequenced plasmids from historical clinical samples taken between 1917 and 1954 (the Murray Collection) and combined this with all available sequence data from the public archive to trace their descendants among contemporary and currently circulating plasmids. Given this time span, we were able to explore the evolutionary trajectories and genetic changes that define plasmid adaptation during the antibiotic era.

RESULTS: By comparing our historical plasmids with their modern descendants by means of a genome similarity network, we defined close families of related plasmids. We found that they were divided into three categories reflecting distinct evolutionary trajectories: (i) ancestral plasmids that disappeared as intact backbones from modern public archives; (ii) those that survived to the modern day without substantial change, preserving a core genome; (iii) and those primarily formed through fusion of one or more ancestral plasmid(s), resulting in conspicuously large and complex modern plasmids. It is also clear that a relatively small group of modern plasmids carry almost all the AMR genes seen today, including those conferring resistance to first-line and last-resort antibiotics. These plasmids originated from ancestral backbones devoid of AMR genes and display characteristics linked to the ability to acquire and transmit these genes.

CONCLUSION: Our longitudinal view of plasmid evolution over the past 100 years revealed highly dynamic processes throughout their evolution to the selective pressure of antibiotic use, including gene turnover and genome fragmentation and fusion. A minority of plasmids already existing in pathogens became global multidrug-resistance vectors as humans industrialized the use of antibiotics, and their descendants now pose a high risk to human health. Their emergence involved both conservative gene acquisition into stable backbones and rapid evolution underpinned by genome recycling, fusion, and reassortment, generating complex diversity. □

*Corresponding author. Email: ac61@sanger.ac.uk (A.C.); zi245@bath.ac.uk (Z.I.); nrt@sanger.ac.uk (N.R.T.) Cite this article as A. Cazares *et al.*, *Science* 390, eadr1552 (2025). DOI: 10.1126/science.adr1522



A century of plasmid adaptation to antibiotics. We reconstructed historical plasmids from the Murray Collection of preantibiotic era (PAE) bacteria and traced their modern descendants. By comparing PAE and modern genomes, we traced the evolutionary trajectories of plasmids as antibiotics were increasingly used in medical practice. We show that modern AMR vectors emerged over the past century from a minority of plasmids already residing in PAE pathogens. [Figure created with BioRender.com]

ANTIBIOTIC RESISTANCE

Pre- and postantibiotic epoch: The historical spread of antimicrobial resistance

Adrian Cazares[1,2]*, Wendy Figueroa[1,3], Daniel Cazares[4], Leandro Lima[2], Jake D. Turnbull[5], Hannah McGregor[5], Jo Dicks[5], Sarah Alexander[5], Zamin Iqbal[2,6]*, Nicholas R. Thomson[1,7]*

Plasmids are now the primary vectors of antimicrobial resistance, but our understanding of how human industrialization of antibiotics influenced their evolution is limited by a paucity of data predating the antibiotic era (PAE). By investigating plasmids from clinically relevant bacteria sampled and isolated between 1917 and 1954 and comparing them with modern plasmids, we have captured more than 100 years of evolution. We show that although virtually all PAE plasmids were devoid of resistance genes and most never acquired them, a minority evolved to drive the global spread of resistance to first-line and last-resort antibiotics in Gram-negative bacteria. Modern plasmids have evolved through complex microevolution and fusion events into a distinct group of highly recombinogenic, multireplicon, self-transmissible plasmids that now pose the highest risk to resistance dissemination and therefore to human health.

The emergence and spread of antibiotic-resistant bacteria through the use and overuse of antibiotics is one of the most important effects human activity has imposed on our environment. In many instances, selection has favored highly transmissible multidrug-resistant (MDR) bacteria that have disseminated across the world to present an immediate threat to human health, with more than 4.95 million deaths associated with antimicrobial-resistant infections in 2019 (*1*).

In addition to carrying genes for their biosynthesis (*2*), bacteria and fungi carry other genes that confer resistance to antibiotics. Although we know a lot about antibiotic-resistant pathogens and the individual resistance genes they harbor, much less is known about the evolutionary histories of the vectors that have enabled these antibiotic-resistance genes to be widely shared among the pathogens of humans and animals (*3*). Plasmids are one of the most important vectors of antimicrobial-resistance (AMR) genes, playing pivotal roles in the emergence of MDR pathogens across all settings (*4*, *5*). It is becoming increasingly common for a single bacterial cell to harbor single or multiple different plasmids that confer resistance to many, all frontline, or even last-line treatments (*3*). Despite their importance, the origins of resistance plasmids and how the anthropogenic introduction of antibiotics influenced plasmid evolution in the first place remain largely unknown. The answers to these questions have clear implications for understanding how antibiotic usage drives plasmid-mediated resistance; to address this, we need to understand the nature and composition of plasmids spanning the antibiotic epoch.

[1]Parasites and Microbes Programme, Wellcome Sanger Institute, Hinxton, UK. [2]European Molecular Biology Laboratory European Bioinformatics Institute (EMBL-EBI), Wellcome Genome Campus, Hinxton, UK. [3]Department of Medicine, University of Cambridge, Cambridge, UK. [4]Department of Biology, University of Oxford, Oxford, UK. [5]Culture Collections, UK Health Security Agency, London, UK. [6]Milner Centre for Evolution, University of Bath, Bath, UK. [7]Department of Pathogen Molecular Biology, Faculty of Infectious and Tropical Diseases, London School of Hygiene and Tropical Medicine, London, UK. ***Corresponding author. Email: ac61@sanger.ac.uk (A.C.); zi245@bath.ac.uk (Z.I.); nrt@sanger.ac.uk (N.R.T.)**

Diversity of Murray plasmids and their relatives

We investigated the genomes ($n = 368$) of a distinctive collection of pathogenic *Enterobacteriaceae* taken from patients between 1917 and 1954 (the "Murray Collection") (*6*, *7*), a key historical period that spans the discovery and first use of therapeutic antibiotics (fig. S1A) to the current day.

We generated short-read Illumina assemblies for 765 Murray Collection plasmids (data S1 and fig. S2). Additionally, 26% of the Murray Collection was sequenced by using long-read technologies to generate 218 plasmid hybrid assemblies (data S2 and figs. S3 and S4). The hybrid assemblies were analyzed in parallel with the short-read assemblies throughout the study. These plasmids originated from six genera and nine species. We compared these sequences with 40,757 plasmid genomes retrieved from all available plasmid databases in the public archive, showing that 9186 plasmids were substantially similar [defined as 70% BLAST (Basic Local Alignment Search Tool) coverage of the Murray plasmid or being a mash distance of at most 0.05 apart, indicating high sequence similarity based on shared k-mers (oligomers of length k)] to 715 Murray Collection plasmids (fig. S1, A to C).

The 9951 Murray and related plasmids range in size from ~0.5 to 606 kb, are derived from more than 79 countries and six continents, and are linked to 25 genera and more than 72 species (fig. S5 and data S1). Notwithstanding this, most (95%) of them were identified in five genera: *Escherichia*, *Shigella*, *Klebsiella*, *Salmonella*, and *Enterobacter*, which are all deemed global priority pathogens of risk to public health by the World Health Organization (WHO) owing to their high resistance to antibiotics (*8*).

We constructed a sequence-similarity network (figs. S5 and S6A) to determine the diversity and relationships within this 9951-plasmid collection and performed a community detection analysis to define groups of evolutionarily related plasmids [supplementary materials (SM), materials and methods]. We determined relatedness (edge-weight) by a mash similarity threshold of ≥400 shared k-mers used to partition the network (fig. S1D). This resulted in the detection of 940 network communities, hereafter referred to as close families (CFs) (Fig. 1, data S3, and fig. S7). These data showed a strong population structure, both in the short-read and hybrid assemblies (fig. S8 and data S4); 22 CFs encompass 50% of the plasmids in the network. By contrast, 264 CFs are disconnected from all others and represent singletons (fig. S6A).

Composition and evolution of plasmid CFs

To understand how well plasmids collected before the widespread use of antibiotics were represented across the network, those isolated on or before 1954 (the last year sampled in the Murray Collection) were denoted "preantibiotic era" (PAE) plasmids (comprising 22 public archive sequences plus 765 Murray plasmids). All remaining plasmids were labeled modern-era plasmids or Modern (dates 1956 to 2021, 99% collected after 1990) (SM materials and methods, fig. S5, and data S1).

We defined three types of CF on the basis of the sampling dates of the constituent plasmids (Fig. 1 and figs. S6 and S8): those exclusively represented by PAE (PAE-CF; $n = 103$), or by Modern plasmids (Modern-CF; $n = 749$), and the third comprising a mixture of both PAE and Modern plasmids (Mixed-CF; $n = 88$). Our pangenome analysis of the Mixed-CFs identified a core genome in 95% of them (fig. S9 and data S5), thus indicating that plasmids can maintain a core genome for substantial periods, the longest example from this CF-type ranging from 1917 to 2020. Additionally, plasmids within the Mixed-CF category are the most common across our network (Fig. 1 and fig. S10), representing 60% of all plasmids studied here (64% of the plasmids in the hybrid assemblies network) (fig. S8) and 77% of all PAE plasmids. The remaining 23% ($n = 184$) of PAE plasmids, which comprise the PAE-CFs, have not been seen again in any publicly available plasmid database since 1954, using our search criteria.



Fig. 1. CFs of PAE plasmids and their modern relatives. (**A**) Schematic representation of CF identification and CF types (fig. S1). (**B**) Number of CFs across CF types, split by presence (+) or absence (−) of AMR genes. (**C**) Number of plasmid members across CFs and CF types. Points indicate individual CFs. [Figure created with BioRender.com]

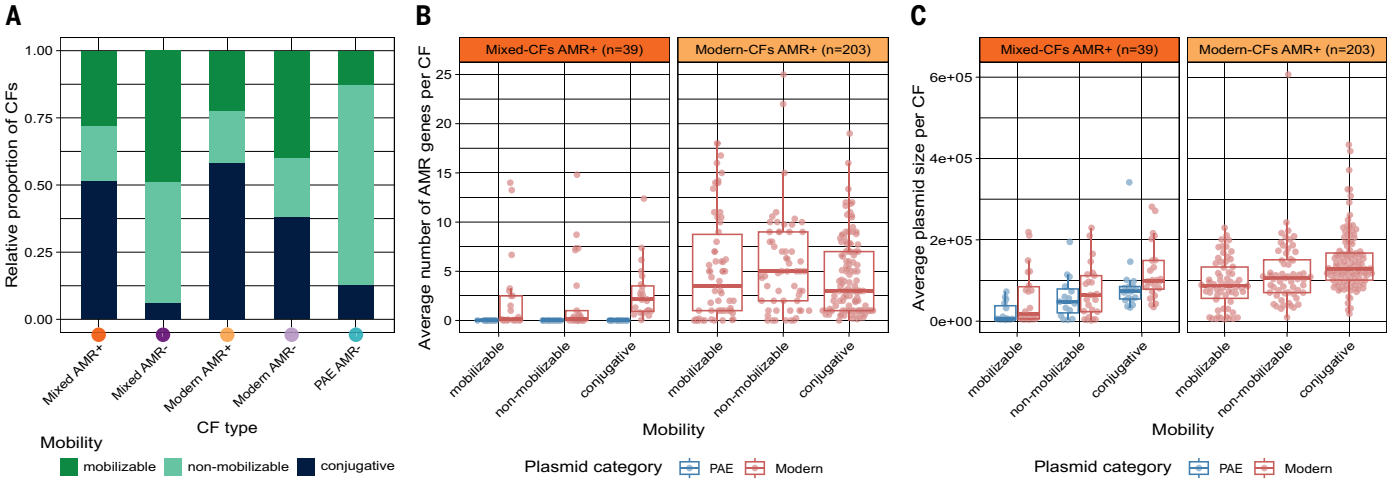


Fig. 2. Mobility, AMR gene carriage, and size distribution across plasmid CFs. (**A**) Plot showing the proportion of CFs within a given CF type classified as conjugative, mobilizable, or nonmobilizable (*x* axis). Dot colors are as in Fig. 1. The CFs mobility classification was based on the most frequent mobility category seen in the constituent plasmids (fig. S16). (**B** and **C**) Plots split by Mixed-CFs or Modern-CFs showing the average AMR gene content or average plasmid size across CFs for each mobility type, respectively. Each point in the plots indicates a CFs' average value. For Mixed-CFs, PAE and Modern plasmids are indicated in blue and red, respectively. The distribution of average plasmid size for all CFs (including those with no AMR genes) is shown in fig. S5.

Modern-CFs are dominated by large plasmids that have subsumed PAE plasmids

Our similarity network (fig. S6A) connected plasmids that were similar in sequence content and size, defining relationships through mutation and gene gain and loss. Using an alternative approach, we investigated containment relationships in which a PAE plasmid may have been subsumed by a Modern-CF plasmid (SM materials and methods). This showed that ~98% ($n = 3646$) of Modern-CF plasmids contain sequences matching at least one of 506 PAE plasmids (defined as covering at least 70% of a PAE plasmid by BLAST) (data S6), of which 93.4% were on average 12-fold larger than the PAE plasmid they contained (data S6 and fig. S11). These observations are consistent with data from hybrid assemblies (data S7 and fig. S12) and with Modern-CF plasmids being systematically larger than PAE-CF or Mixed-CF plasmids (Fig. 2C).

It was evident from these data that 58% of Modern-CF plasmids carry multiple plasmid replication genes known as *rep* (fig. S13 and data S1) [57% of those identified from the hybrid assembly data (data S2)]. These genes can be used for categorizing plasmids into incompatibility (Inc) groups (or "Inc types"), with one Inc type representing a plasmid type (*9*). Together, the evidence suggests that Modern-CF plasmids are the product of multiple fusion events.

Evidence for a plasmid-fusion birth-death process

We asked whether these data supported a plasmid evolution model of continual birth (fusion) and death (fragmentation) processes, generating diversity. Fragmentation of a plasmid can arise through repeat-mediated recombination of different plasmids, resulting in one larger and one smaller fragment (*3*). Given the cost of plasmid carriage (*10*), death through fragmentation is likely mediated by differential selection (*11*–*14*). We identified four qualitative tests of the theory. First, if birth–death was a process predating the therapeutic use of antibiotics, we should see evidence of fusion in PAE plasmids. We did see this, in that 17% of Murray plasmids were multireplicon plasmids, and 23%

(44 of 191) of CFs with historical plasmids contained PAE multireplicon plasmids. Second, we should see evidence of destabilization or fragmentation (death) of Murray plasmids. None of the PAE-CF plasmids was present in plasmid databases in their original form but survived as fragments or embedded in Modern plasmids. Third, a key test would be whether any of the diversity generated through fusion was selected for rather than merely forming transient molecules. We found that of the 17 Mixed-CFs (which had survived at least 70 years) dominated by multireplicon plasmids, 12 contained plasmids that had acquired AMR genes over this period. Moreover, ranking Mixed-CFs by the average number of AMR genes carried revealed that these 12 included the four bearing the most AMR genes. Fourth, if highly dynamic and ongoing, the birth–death process should generate many Modern-CFs, composed of one or few plasmid members, unless stabilized or expanded by selection. We found that unlike Mixed-CFs, Modern-CFs were dominated by small CF groups and singletons (one-sided t test, $t = 5.280$, $P = 4.668 \times 10^{-7}$), with those bearing AMR genes having more members (one-sided t test, $t = 4.107$, $P = 2.87 \times 10^{-5}$) (fig. S14E).

The relevance of PAE plasmids and their modern relatives to AMR dissemination

To understand the relative contribution of PAE and Modern plasmids to AMR gene dissemination, we searched for all known AMR genes. Although we found none in the PAE plasmids from Illumina assemblies, 18 genes were detected in the hybrid assemblies, including 15 genes predicted to encode efflux pump components, two linked to cationic antimicrobial peptide resistance, and a penicillin-binding protein (data S8). By contrast, we identified 21,378 instances of more than 300 different AMR genes encoded in 38% ($n = 3815$) of the Modern plasmids (data S8 and fig. S14). Many of these PAE descendants were predicted to carry genes conferring resistance to broad-spectrum and/or last-resort antibiotics, including most of the known extended-spectrum beta-lactamases (data S8) (*15*), and resistance determinants against carbapenems, tigecycline, and polymyxins. The most extreme examples carried genes conferring resistance to between eight (pSY3626C1; NZ_CP059044.1) and 13 drug classes (pHZ003; NZ_MN476094.1), with up to 40 individual AMR genes carried on a single plasmid, many showing extensive gene duplications (fig. S15).

To determine the relative contribution of different CFs to the acquisition of drug resistance, we mapped the occurrence of AMR genes across the network (Fig. 2B and fig. S14). Most CFs (75%) did not accumulate AMR genes at all (Fig. 1B). Those which did (data S3 and fig. S14) varied considerably in average number of genes borne, ranging from 0.005 to 13 (excluding CFs with a single plasmid). The proportion of resistance plasmids within a CF ranged from 0.5 to 100%. AMR genes were found in both Mixed-CFs ($n = 39$) and Modern-CFs ($n = 203$), but the majority of AMR genes (50%) were found in the latter (which only contain 22% of all plasmids in the dataset) (Fig. 1). Modern-CFs, comprising large (Fig. 2C) multireplicon (fig. S13) fusion plasmids, were more likely than Mixed-CFs to be associated with antimicrobial resistance and contained on average more AMR genes (Fig. 2B and fig. S14).

The link between plasmid size, their pangenome, mobility traits, and AMR

To investigate whether there was a link between AMR gene carriage and mobility, we divided plasmids into three mobility classes: conjugative (self-transmissible), mobilizable (needing components from helper plasmids), and nonmobilizable (data S1 and fig. S16) (*16*). Our data showed that 58 and 51% of the Modern-CFs and Mixed-CFs containing resistance plasmids, respectively, were dominated by conjugative plasmids (Fig. 2A and data S3). Conversely, Modern-CFs and Mixed-CFs with no resistance genes comprised mobilizable and nonmobilizable plasmids. Conjugative plasmids carried the most AMR genes among Mixed-CFs (Fig. 2B) and exhibited the largest average size across all CFs (Fig. 2C and fig. S5). Furthermore, 61% of them were multireplicon ($n = 5430$; 48% in Mixed-CF and 84% in Modern-CF) (fig. S13), constituting 78% of all multireplicon ($n = 4256$) plasmids identified in the network (data S1). The mobilizable and nonmobilizable types only represent 8 and 14% of multireplicon plasmids, respectively (fig. S13). These observations were replicated in our hybrid assemblies (fig. S8 and data S2 and S4).

We were also able to study the evolutionary trajectory of plasmids by comparing PAE plasmids with their conserved modern descendants within Mixed-CF groups. As before, plasmids in Mixed-CFs containing at least one resistance plasmid (AMR pos) were markedly larger than their AMR negative (AMR neg) counterparts (71.4 kb AMR pos versus 21.7 kb AMR neg; $P = 1.292 \times 10^{-9}$) and were more likely to be conjugative (Fig. 3A). They also carried more genetic elements linked to AMR dissemination (transposases and integrons) and possessed a smaller core genome (mean 12.3% versus 39.3%; $P = 1.292 \times 10^{-9}$) (Fig. 3A and fig. S9), which is indicative of greater genome flexibility and cargo capacity. We also saw a difference in virulence gene content between AMR pos and AMR neg Mixed-CF groups, albeit smaller (mean 1.6 versus 1.2; $P = 1.972 \times 10^{-10}$) (data S9). For 67% of Mixed-CFs, the PAE and Modern descendants maintained a comparable average size (±30% size difference) despite our data revealing gene acquisition in Modern plasmids (Fig. 3B). In the remaining 28 and 4% of Mixed-CFs, the Modern plasmids were on average larger (up to 3 times; $n = 25$) or smaller (4%; $n = 4$) as compared with their PAE counterpart, respectively (Fig. 3B and fig. S17). Combined, these findings indicate that a balance between gene gain, loss, and replacement has shaped the evolution of these PAE plasmids, which maintained a core genome as antibiotic use increased. These observations were also mirrored in our hybrid assembly data (figs. S8 and S18).

Beyond Murray plasmids

Last, our initial search for Murray close relatives revealed that they were markedly similar to 22% (≥70% BLAST coverage) (fig. S1C) of all publicly available plasmids. To look for all traces of Murray plasmids in any Modern plasmid, we reduced our similarity threshold to 1% plasmid coverage. In doing so, we identified Murray plasmid sequences in 38% ($n = 15{,}644$) of all reported plasmids ($n = 40{,}757$) (fig. S19 and data S11). This included the original Murray close relatives and other relatives only seen when the similarity threshold was reduced, which we denoted Murray extended relatives ($n = 6626$). By combining Murray close relatives with the extended relatives, we could now identify, in whole or part, 99% of all the PAE-CF plasmids in Modern plasmids. The remaining 25,113 plasmids in the public archive showed no similarity to any Murray plasmid sequence (data S11 and fig. S19), and we referred to these as Murray-unrelated.

To understand how Murray close, extended, and unrelated plasmids segregated across all plasmid diversity, we created a similarity network from all 40,757 sequences in our integrated database (fig. S19). Murray close relatives were largely derived from Gram-negative *Gammaproteobacteria* (98% of the sequences), mostly *Enterobacteriaceae*, and accounted for ~36% of the 58,870 AMR genes detected in our dataset. Murray-unrelated plasmids were from more diverse hosts, comprising 48 taxonomic classes with a substantial fraction from Gram-positive taxa (36%) (fig. S19).

Like the largely Gram-negative Murray relatives, the Gram-positive Murray-unrelated plasmids showed that AMR genes are concentrated in a minority of closely related plasmids that form discrete network clusters (fig. S19). The major difference identified was that the high incidence of conjugative plasmids carrying AMR genes among Gram-negative Murray relatives was not seen in Gram-positive Murray-unrelated plasmids (fig. S20). Notwithstanding this, the link between AMR gene carriage (expressed both as the number of genes carried and incidence of resistance plasmids) and the presence of multiple replicons, which is indicative of plasmid fusion, was a unifying characteristic

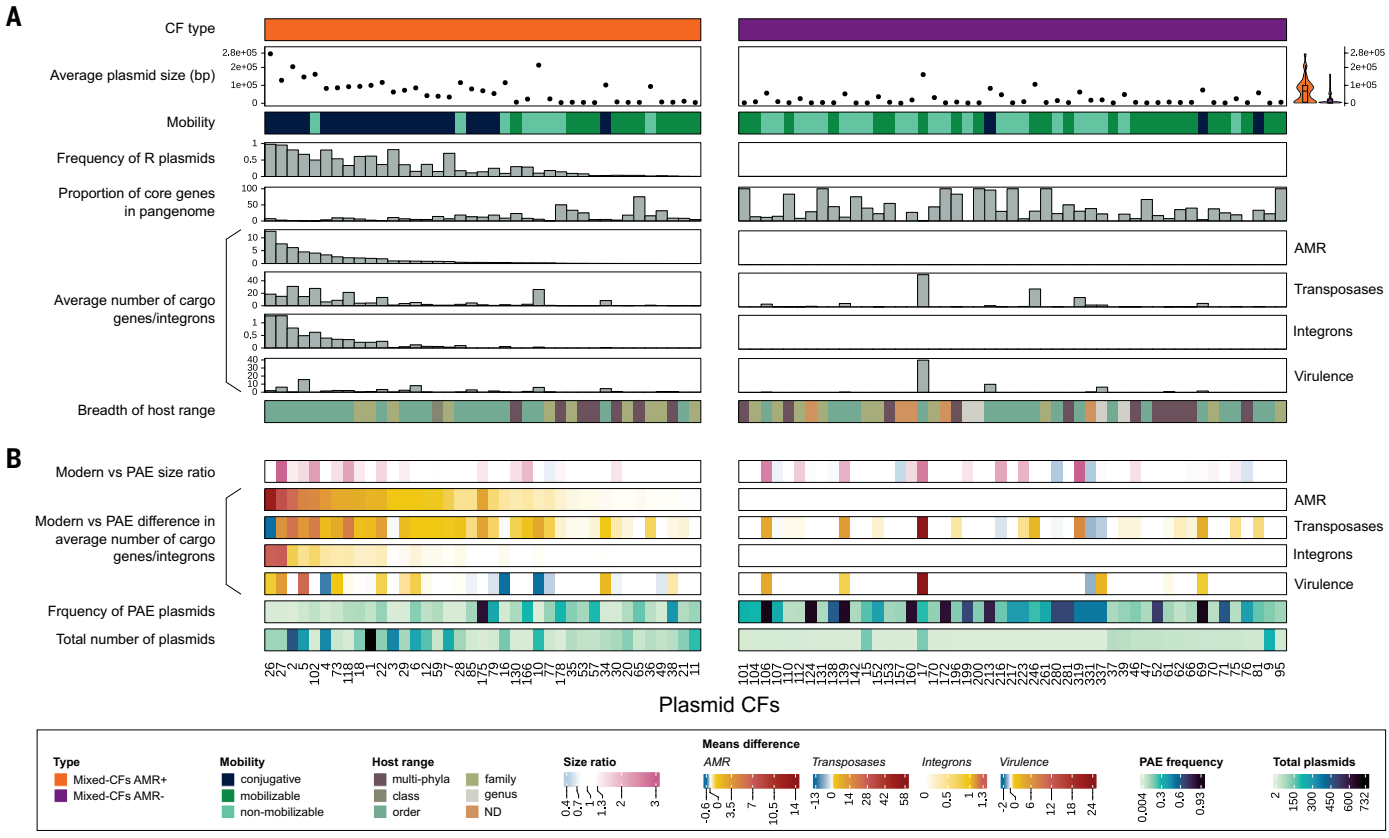


Fig. 3. Evolution of plasmids in Mixed-CFs. (**A**) Comparison of plasmid characteristics across Mixed-CFs. The 88 Mixed-CFs identified in the plasmid similarity network are indicated along the *x* axis, arranged in decreasing average number of AMR genes in the CF (left to right). The plots are split by the presence (left, orange) or absence (right, purple) of resistance plasmids in the CF. Mobility and host range were defined by the most frequent category identified in the CF. "ND" in the host range legend stands for "Nondetermined." (**B**) Differences between Modern and PAE plasmids within Mixed-CFs. The five top rows summarize differences in size and number of cargo genes expressed as the ratio of average values, using Modern plasmid values as the numerator. The significance of Modern versus PAE differences was assessed by implementing a sampling with replacement strategy, illustrated in fig. S17 (results are detailed in data S10).

between Gram-negative and Gram-positive AMR pos plasmid groups (fig. S20).

Discussion

Until now, most studies on AMR evolution, including our own, have focused on individual patients or defined communities, usually through the lens of a specific bacterial host (or hosts) (*17*–*19*). By focusing on the evolution of plasmids, our study of the Murray Collection and its modern descendants provides a longitudinal view of how these mobile genetic elements, for millennia the primary vectors of adaptive traits in bacteria, themselves adapted to the antibiotic epoch, with a fraction of them pivoting to become key multidrug resistance vectors in modern times.

By looking at the molecular fates of these historical plasmids using both short-read and hybrid assemblies, we show that all plasmids can be subdivided into three evolutionary classes of CF. PAE-CFs compose a small proportion of plasmids seen in the combined Murray and pre-1954 plasmid collection (23% of PAE plasmids). This group is absent from modern public plasmid archives in their original form and are only detectable when embedded in much larger modern plasmids or as fragments, where the gene content has been recycled into new forms. It is likely that multiple mechanisms are involved, including mobile-element-mediated recombination (*14*, *20*). Second, most (77%) PAE plasmids have continued to circulate and maintain a recognizable backbone since the PAE until the current day. These plasmids (PAE and their descendants) form the Mixed-CFs, which encompass 60% of the plasmids in our network and have been shaped by microevolutionary processes, including mutation and gene loss, gain, and replacement. Over this period, plasmids from almost half of the Mixed-CFs have gained AMR genes.

Last, Modern-CFs constitute 37% of plasmids in the network and have mainly formed through the absorption of one or more PAE plasmid backbones and other genetic elements through continual processes of fusion and fragmentation. The result is a group of conspicuously large, highly diverse plasmids, characterized by multiple replicons and associated with high levels of AMR gene carriage. Most of these plasmids represent short-lived molecular plasmid "instances" or snapshots, likely owing to structural instability, and are untypable based on a standard Inc typing scheme because they carry multiple different plasmid *rep* genes (*21*).

Looking across Gram-negative and Gram-positive taxa, we found a strong association between AMR gene carriage and the possession of conjugative machinery for Gram-negative taxa, which does not hold for Gram-positive hosts, for which plasmids with conjugative machinery are known to be comparatively rare (*16*, *22*, *23*). However, the possession of multiple replicons, which is indicative of plasmid fusion, is a common characteristic between AMR plasmids from both Gram-negative and Gram-positive bacteria. Plasmid mosaics are relatively common, comprising ~19% of plasmids across all major phyla (*24*–*26*), and clinically, multireplicon fusion plasmids are increasingly being linked to

virulence and multidrug resistance (*27*–*33*). What was not previously clear was the relative importance of the differing evolutionary trajectories (microevolution and fusion) underlying the emergence of multidrug-resistant plasmids across bacteria, nor that Modern-CF fusion plasmids, which compose 22% of the plasmids in our network, carry 50% of all the AMR genes we detected across the whole dataset. On average, plasmids from this group carry more AMR genes than do Mixed-CF plasmids, underscoring that not all plasmids are equal with regards to AMR gene spread.

Although the Murray Collection is a distinctive resource with considerable provenance (its origins and maintenance over 70 years, including historical correspondence, are detailed in appendices S1 and S2), its history and composition has several important gaps, and therefore, this study has limitations. Although we were able to draw similarities between resistance plasmids from Gram-negative and Gram-positive hosts (the latter using only publicly available genome data), the Murray Collection lacks reference Gram-positive bacteria, restricting our ability to fully investigate the origins and evolution of AMR vectors in several relevant human pathogens. Similarly, the Murray Collection does not include bacteria taken directly from environmental samples. Although the study of historical bacteria from a broader set of sources would be valuable to extend the insights revealed here, we acknowledge the impact this relatively small group of plasmids has had on all areas of clinical medicine today (*6*).

Together, the trajectories revealed in our study provided both conservative and high-risk strategies for responding to the widespread use of antibiotics over short evolutionary time scales. Under this model, Mixed-CF plasmids not only act as a storehouse—preserving the integrity and circulating genetic diversity of plasmids and serving as the molecular substrate needed to rapidly respond to changing selective pressures through gene acquisition—they also generate highly complex Modern-CF plasmids through fusion and reassortment. Both groups have been fundamental in adapting to antibiotics, and in our collection, we have identified them in clinical and environmental samples [for example, farm and wastewater treatment works (*34*)], indicating a broad ecological impact of antibiotic selection on plasmid evolution. Still, the survival of multiple non-AMR multireplicon CFs serves as a reminder that there are other strong selective pressures on plasmids, providing constraints that bear further study.

Materials and methods summary

We assembled whole genomes for 368 strains of the Murray Collection using Illumina-generated short reads (*7*). Additionally, we sequenced 95 Murray strains using long-read Oxford Nanopore Technologies (ONT) and generated hybrid whole-genome assemblies by combining Illumina and ONT reads. All genomes were generated with unicycler v0.4.7 (*35*). Linear contigs were processed for circularization with circlator v1.5.5 (*36*). Hybrid assemblies were polished with polypolish v0.5.0 (*37*), and metrics for all assemblies were calculated by use of quast v4.5 (*38*). We identified and reconstructed plasmids from the Murray Collection by means of a combination of chromosomal contigs depletion with plasmidverify, contigs sequence comparison against a collection of 40,757 plasmids from public archives with minimap2 v2.17-r941 (*39*), and plasmid identification by use of mob_recon from the mob_suite package v3.0.1 (*40*).

The 765 plasmids reconstructed from Murray Illumina genome assemblies, the 218 identified in Murray hybrid genome assemblies, and the 40,757 from our collection of public sequences were annotated with prokka v1.14.6 (*41*). Plasmid mobility classification was carried out with mob_typer v3.0.1 (*40*). Replicon and mobility typing were performed with mob_typer v3.0.1 (*40*) and abricate v1.0.1 (*42*) by use of the plasmidfinder database (*9*). AMR genes were identified with abricate v1.0.1 by use of the Comprehensive Antibiotic Resistance Database (CARD) (*43*), National Center for Biotechnology Information (NCBI) (Bioproject PRJNA313047), ARG-ANNOT (Antibiotic Resistance Gene-Annotation) (*44*), and Resfinder (*45*) databases. Virulence genes were detected with abricate v1.0.1 by use of the Virulence Factor Database (VFDB) (*46*) and Ecoli_VF (*47*) databases. Integrons were detected by use of Integron finder v2.0.1 (*48*). Genes encoding transposases were identified from prokka annotations.

We identified close relatives of Murray plasmids by use of mash v2.3 (*49*) (distance < 0.05) and BLAST v2.10.1+ (*50*) (coverage ≥ 70%) comparisons at the nucleotide level against our dataset of public plasmid sequences. Murray plasmids' extended relatives were detected with BLAST (coverage < 70%). The diversity and similarity relationships between Murray plasmids and their close relatives, or between the 40,757 plasmids collected from public archives, were determined by means of *k*-mers comparison by use of mash v2.3 (*49*), followed by network clustering in Cytoscape v3.8.1 (*51*). Disconnected components of the mash similarity network were detected with the "Connected components cluster (CC)" algorithm from clusterMaker v2.0 (*52*). Plasmid CFs were identified by partitioning the network into communities with the Markov Clustering Algorithm (MCL) (*53*) from clusterMaker v2.0. Alongside the MCL communities detected, singletons and outliers in the similarity network were considered distinct CFs. The Murray plasmids and close relatives isolated during the same period (up until 1954; $n = 22$) were categorized as PAE plasmids; the rest were classified as modern. CFs were classified according to their PAE and modern plasmids composition, resulting in PAE-CFs (only PAE), Mixed-CFs (PAE and modern), and Modern-CFs (only modern). Containment of Murray plasmids within Modern-CF plasmids was identified with BLAST (coverage ≥ 70%). The results were summarized at the level of CF and visualized in a containment network by use of Cytoscape v3.8.1. For CFs with at least two members, the pangenome was determined by use of Panaroo v1.2.9 (*54*). Plasmids' pairwise comparisons at the nucleotide level were carried out with Easyfig v2.2.2 (*55*) and at the protein level with clinker v0.0.28 (*56*).

The plots and statistical analyses presented in this study were generated in RStudio v2023.06.0 by use of R v4.3.1. Networks were generated with Cytoscape v3.8.1. Figure 1 and figs. S1, S10, and S21 were created with BioRender.com. When required, manual figure editing was carried out with Inkscape v1.2.2. To account for differences in plasmid number across CFs, we used mean values per CF when plotting the distribution of features such as plasmid size; number of replicons; core genes; integrons; and genes encoding AMR determinants, transposases, or virulence factors. To account for sampling bias, we implemented a sampling with replacement strategy, followed by pairwise comparison of distributions with the nonparametric Kolmogorov–Smirnov (K-S) test when assessing the statistical significance of differences between PAE and modern plasmids of the same Mixed-CF or between CFs. Differences in the size of CFs (the number of plasmids in the CF) between CF types were assessed by using a Welch two-sample *t* test.

REFERENCES AND NOTES

1. C. J. L. Murray *et al.*, Global burden of bacterial antimicrobial resistance in 2019: A systematic analysis. *Lancet* **399**, 629–655 (2022). doi: 10.1016/S0140-6736(21)02724-0; pmid: 35065702
2. K. C. Nicolaou, S. Rigol, A brief history of antibiotics and select advances in their synthesis. *J. Antibiot.* **71**, 153–184 (2018). doi: 10.1038/ja.2017.62; pmid: 28676714
3. S. R. Partridge, S. M. Kwong, N. Firth, S. O. Jensen, Mobile genetic elements associated with antimicrobial resistance. *Clin. Microbiol. Rev.* **31**, e00088-17 (2018). doi: 10.1128/CMR.00088-17; pmid: 30068738
4. S. Castañeda-Barba, E. M. Top, T. Stalder, Plasmids, a molecular cornerstone of antimicrobial resistance in the One Health era. *Nat. Rev. Microbiol.* **22**, 18–32 (2024). doi: 10.1038/s41579-023-00926-x; pmid: 37430173
5. J. Davies, D. Davies, Origins and evolution of antibiotic resistance. *Microbiol. Mol. Biol. Rev.* **74**, 417–433 (2010). doi: 10.1128/MMBR.00016-10; pmid: 20805405
6. N. Datta, V. M. Hughes, Plasmids of the same Inc groups in Enterobacteria before and after the medical use of antibiotics. *Nature* **306**, 616–617 (1983). doi: 10.1038/306616a0; pmid: 6316165
7. K. S. Baker *et al.*, The Murray collection of pre-antibiotic era *Enterobacteriacae*: A unique research resource. *Genome Med.* **7**, 97 (2015). doi: 10.1186/s13073-015-0222-7; pmid: 26411565
8. World Health Organization, *WHO Bacterial Priority Pathogens List, 2024: Bacterial Pathogens of Public Health Importance, to Guide Research, Development, and Strategies*

to Prevent and Control Antimicrobial Resistance (World Health Organization, 2024); https://play.google.com/store/books/details?id=UjAJEQAAQBAJ.
9. A. Carattoli *et al.*, In silico detection and typing of plasmids using PlasmidFinder and plasmid multilocus sequence typing. *Antimicrob. Agents Chemother.* **58**, 3895–3903 (2014). doi: 10.1128/AAC.02412-14; pmid: 24777092
10. A. San Millan, R. C. MacLean, Fitness costs of plasmids: A limit to plasmid transmission. *Microbiol. Spectr.* **5**, 5.5.02 (2017). doi: 10.1128/microbiolspec.MTBP-0016-2017; pmid: 28944751
11. C. Stevenson, J. P. J. Hall, M. A. Brockhurst, E. Harrison, Plasmid stability is enhanced by higher-frequency pulses of positive selection. *Proceedings of the Royal Society B: Biological Sciences* 10.1098/rspb.2017.2497 (2018). doi: 10.1098/rspb.2017.2497
12. T. Wein, Y. Wang, N. F. Hülter, K. Hammerschmidt, T. Dagan, Antibiotics Interfere with the Evolution of Plasmid Stability. *Curr. Biol.* **30**, 3841–3847.e4 (2020). doi: 10.1016/j.cub.2020.07.019; pmid: 32795438
13. S. Ballester, P. Lopez, M. Espinosa, J. C. Alonso, S. A. Lacks, Plasmid structural instability associated with pC194 replication functions. *J. Bacteriol.* **171**, 2271–2277 (1989). doi: 10.1128/jb.171.5.2271-2277.1989; pmid: 2708307
14. Z. Liu *et al.*, Structural diversity, fitness cost, and stability of a BlaNDM-1-bearing cointegrate plasmid in *Klebsiella pneumoniae* and *Escherichia coli*. *Microorganisms* **9**, 2435 (2021). doi: 10.3390/microorganisms9122435; pmid: 34946035
15. M. Castanheira, P. J. Simner, P. A. Bradford, Extended-spectrum β-lactamases: An update on their characteristics, epidemiology and detection. *JAC Antimicrob. Resist.* **3**, dlab092 (2021). doi: 10.1093/jacamr/dlab092; pmid: 34286272
16. C. Smillie, M. P. Garcillán-Barcia, M. V. Francia, E. P. C. Rocha, F. de la Cruz, Mobility of plasmids. *Microbiol. Mol. Biol. Rev.* **74**, 434–452 (2010). doi: 10.1128/MMBR.00020-10; pmid: 20805406
17. R. C. MacLean, A. San Millan, The evolution of antibiotic resistance. *Science* **365**, 1082–1083 (2019). doi: 10.1126/science.aax3879; pmid: 31515374
18. J. M. Lewis *et al.*, Genomic analysis of extended-spectrum beta-lactamase (ESBL) *Escherichia coli* producing colonising adults in Blantyre, Malawi reveals previously undescribed diversity. *Microb. Genom.* **9**, mgen001035 (2023). doi: 10.1099/mgen.0.001035; pmid: 37314322
19. F. Lassalle *et al.*, Genomic epidemiology reveals multidrug resistant plasmid spread between *Vibrio cholerae* lineages in Yemen. *Nat. Microbiol.* **8**, 1787–1798 (2023). doi: 10.1038/s41564-023-01472-1; pmid: 37770747
20. S. R. Partridge, Analysis of antibiotic resistance regions in Gram-negative bacteria. *FEMS Microbiol. Rev.* **35**, 820–855 (2011). doi: 10.1111/j.1574-6976.2011.00277.x; pmid: 21564142
21. M. P. Garcillán-Barcia, S. Redondo-Salvo, F. de la Cruz, Plasmid classifications. *Plasmid* **126**, 102684 (2023). doi: 10.1016/j.plasmid.2023.102684; pmid: 37116631
22. K. Hardy, *Bacterial Plasmids* (Springer, 1986); https://books.google.com/books/about/Bacterial_Plasmids.html?hl=&id=e_ZxZaahQt8C.
23. J. P. Ramsay, N. Firth, Diverse mobilization strategies facilitate transfer of non-conjugative mobile genetic elements. *Curr. Opin. Microbiol.* **38**, 1–9 (2017). doi: 10.1016/j.mib.2017.03.003; pmid: 28391142
24. P.-E. Douarre, L. Mallet, N. Radomski, A. Felten, M.-Y. Mistou, Analysis of COMPASS, a new comprehensive plasmid database revealed prevalence of multireplicon and extensive diversity of IncF plasmids. *Front. Microbiol.* **11**, 483 (2020). doi: 10.3389/fmicb.2020.00483; pmid: 32265894
25. M. W. Pesesky, R. Tilley, D. A. C. Beck, Mosaic plasmids are abundant and unevenly distributed across prokaryotic taxa. *Plasmid* **102**, 10–18 (2019). doi: 10.1016/j.plasmid.2019.02.003; pmid: 30797764
26. V. F. Lanza, A. P. Tedim, J. L. Martínez, F. Baquero, T. M. Coque, The plasmidome of firmicutes: Impact on the emergence and the spread of resistance to antimicrobials. *Microbiol. Spectr.* **3**, 0039–2014 (2015). doi: 10.1128/microbiolspec.PLAS-0039-2014; pmid: 26104702
27. K. L. Hopkins *et al.*, Replicon typing of plasmids carrying CTX-M or CMY beta-lactamases circulating among Salmonella and Escherichia coli isolates. *Antimicrob. Agents Chemother.* **50**, 3203–3206 (2006). doi: 10.1128/AAC.00149-06; pmid: 16940132
28. T. J. Johnson *et al.*, Plasmid replicon typing of commensal and pathogenic *Escherichia coli* isolates. *Appl. Environ. Microbiol.* **73**, 1976–1983 (2007). doi: 10.1128/AEM.02171-06; pmid: 17277222
29. M. M. Cameranesi, J. Morán-Barrio, A. S. Limansky, G. D. Repizo, A. M. Viale, Site-specific recombination at XerC/D sites mediates the formation and resolution of plasmid co-integrates carrying a bla_{OXA-58}- and Tn*aphA6*-resistance module in *Acinetobacter baumannii*. *Front. Microbiol.* **9**, 66 (2018). doi: 10.3389/fmicb.2018.00066; pmid: 29434581
30. C. Rodrigues *et al.*, KPC-3-Producing *Klebsiella pneumoniae* in Portugal linked to previously circulating non-CG258 lineages and uncommon genetic platforms (Tn4401d-IncFIA and Tn4401d-IncN). *Front. Microbiol.* **7**, 1000 (2016). doi: 10.3389/fmicb.2016.01000; pmid: 27446040
31. C. Shankar *et al.*, Hybrid plasmids encoding antimicrobial resistance and virulence traits among hypervirulent *Klebsiella pneumoniae* ST2096 in India. *Front. Cell. Infect. Microbiol.* **12**, 875116 (2022). doi: 10.3389/fcimb.2022.875116; pmid: 35573787
32. M. Xie *et al.*, A hybrid plasmid formed by recombination of a virulence plasmid and a resistance plasmid in Klebsiella pneumoniae. *J. Glob. Antimicrob. Resist.* **23**, 466–470 (2020). doi: 10.1016/j.jgar.2020.10.018; pmid: 33212284
33. A. Spadar, J. Perdigão, S. Campino, T. G. Clark, Large-scale genomic analysis of global Klebsiella pneumoniae plasmids reveals multiple simultaneous clusters of carbapenem-resistant hypervirulent strains. *Genome Med.* **15**, 3 (2023). doi: 10.1186/s13073-023-01153-y; pmid: 36658655
34. L. P. Shaw *et al.*, Niche and local geography shape the pangenome of wastewater- and livestock-associated *Enterobacteriaceae*. *Sci. Adv.* **7**, eabe3868 (2021). doi: 10.1126/sciadv.abe3868; pmid: 33837077
35. R. R. Wick, L. M. Judd, C. L. Gorrie, K. E. Holt, Unicycler: Resolving bacterial genome assemblies from short and long sequencing reads. *PLOS Comput. Biol.* **13**, e1005595 (2017). doi: 10.1371/journal.pcbi.1005595; pmid: 28594827
36. M. Hunt *et al.*, Circlator: Automated circularization of genome assemblies using long sequencing reads. *Genome Biol.* **16**, 294 (2015). doi: 10.1186/s13059-015-0849-0; pmid: 26714481
37. R. R. Wick, K. E. Holt, Polypolish: Short-read polishing of long-read bacterial genome assemblies. *PLOS Comput. Biol.* **18**, e1009802 (2022). doi: 10.1371/journal.pcbi.1009802; pmid: 35073327
38. A. Gurevich, V. Saveliev, N. Vyahhi, G. Tesler, QUAST: Quality assessment tool for genome assemblies. *Bioinformatics* **29**, 1072–1075 (2013). doi: 10.1093/bioinformatics/btt086; pmid: 23422339
39. H. Li, Minimap2: Pairwise alignment for nucleotide sequences. *Bioinformatics* **34**, 3094–3100 (2018). doi: 10.1093/bioinformatics/bty191; pmid: 29750242
40. J. Robertson, J. H. E. Nash, MOB-suite: Software tools for clustering, reconstruction and typing of plasmids from draft assemblies. *Microb. Genom.* **4**, e000206 (2018). doi: 10.1099/mgen.0.000206; pmid: 30052170
41. T. Seemann, Prokka: Rapid prokaryotic genome annotation. *Bioinformatics* **30**, 2068–2069 (2014). doi: 10.1093/bioinformatics/btu153; pmid: 24642063
42. tseemann/abricate:mag_right: Mass screening of contigs for antimicrobial and virulence genes. *GitHub* (2020); https://github.com/tseemann/abricate.
43. B. P. Alcock *et al.*, CARD 2020: Antibiotic resistome surveillance with the comprehensive antibiotic resistance database. *Nucleic Acids Res.* **48** (D1), D517–D525 (2020). pmid: 31665441
44. S. K. Gupta *et al.*, ARG-ANNOT, a new bioinformatic tool to discover antibiotic resistance genes in bacterial genomes. *Antimicrob. Agents Chemother.* **58**, 212–220 (2014). doi: 10.1128/AAC.01310-13; pmid: 24145532
45. E. Zankari *et al.*, Identification of acquired antimicrobial resistance genes. *J. Antimicrob. Chemother.* **67**, 2640–2644 (2012). doi: 10.1093/jac/dks261; pmid: 22782487
46. L. Chen, D. Zheng, B. Liu, J. Yang, Q. Jin, VFDB 2016: Hierarchical and refined dataset for big data analysis—10 years on. *Nucleic Acids Res.* **44** (D1), D694–D697 (2016). doi: 10.1093/nar/gkv1239; pmid: 26578559
47. phac-nml/ecoli_vf: Curated virulence factors for Escherichia coli. *GitHub* (2017); https://github.com/phac-nml/ecoli_vf.
48. B. Néron *et al.*, IntegronFinder 2.0: Identification and analysis of integrons across bacteria, with a focus on antibiotic resistance in *Klebsiella*. *Microorganisms* **10**, 700 (2022). doi: 10.3390/microorganisms10040700; pmid: 35456751
49. B. D. Ondov *et al.*, Mash: Fast genome and metagenome distance estimation using MinHash. *Genome Biol.* **17**, 132 (2016). doi: 10.1186/s13059-016-0997-x; pmid: 27323842
50. S. F. Altschul, W. Gish, W. Miller, E. W. Myers, D. J. Lipman, Basic local alignment search tool. *J. Mol. Biol.* **215**, 403–410 (1990). doi: 10.1016/S0022-2836(05)80360-2; pmid: 2231712
51. P. Shannon *et al.*, Cytoscape: A software environment for integrated models of biomolecular interaction networks. *Genome Res.* **13**, 2498–2504 (2003). doi: 10.1101/gr.1239303; pmid: 14597658
52. J. H. Morris *et al.*, clusterMaker: A multi-algorithm clustering plugin for Cytoscape. *BMC Bioinformatics* **12**, 436 (2011). doi: 10.1186/1471-2105-12-436; pmid: 22070249
53. S. Van Dongen, Graph clustering via a discrete uncoupling process. *SIAM J. Matrix Anal. Appl.* **30**, 121–141 (2008). doi: 10.1137/040608635
54. G. Tonkin-Hill *et al.*, Producing polished prokaryotic pangenomes with the Panaroo pipeline. *Genome Biol.* **21**, 180 (2020). doi: 10.1186/s13059-020-02090-4; pmid: 32698896
55. M. J. Sullivan, N. K. Petty, S. A. Beatson, Easyfig: A genome comparison visualizer. *Bioinformatics* **27**, 1009–1010 (2011). doi: 10.1093/bioinformatics/btr039; pmid: 21278367
56. C. L. M. Gilchrist, Y.-H. Chooi, clinker & clustermap.js: Automatic generation of gene cluster comparison figures. *Bioinformatics* **37**, 2473–2475 (2021). doi: 10.1093/bioinformatics/btab007; pmid: 33459763
78. A. Cazares, biophage/Murray_plasmids: Murray_plasmids-release_1. Zenodo (2025); https://doi.org/10.5281/zenodo.16103326.
79. A. Cazares, Data for: A. Cazares *et al*., Pre and Post antibiotic epoch: insights into the historical spread of antimicrobial resistance. Zenodo (2025); https://doi.org/10.5281/zenodo.12078070.

ACKNOWLEDGMENTS

We thank M. A. Beale for the helpful discussions during this study. We also thank the Parasites and Microbes Programme Informatics and Samples teams at the Sanger Institute for

technical support. **Funding:** This research was funded in part by the Wellcome Trust (grant 220540/Z/20/A). A.C. was supported by an ESPOD EMBL-EBI/Wellcome Trust Sanger Institute Joint Post-Doctoral Fellowship (45521) and Sanger Institute core funding from the Wellcome Trust (grant 220540/Z/20/A). **Author contributions:** Conceptualization: A.C., Z.I., N.R.T. Formal analysis: A.C., W.F. Data curation: A.C., W.F. Visualization: A.C., W.F., D.C. Validation: J.D.T., J.D. Resources: J.D.T., H.M., J.D., S.A., D.C., L.L. Supervision: S.A., Z.I., N.R.T. Writing – original draft: A.C., Z.I., N.R.T. Writing – review & editing: A.C., W.F., D.C., L.L., J.D.T., H.M., J.D., S.A., Z.I., N.R.T. **Competing interests:** The authors declare that they have no competing interests. **Data and materials availability:** All data are available in the main text or the supplementary materials. The whole-genome sequencing data of the Murray Collection are publicly accessible from the BioProject PRJEB3255. The accessions of the isolates in which plasmids were identified in this study are listed in data S1. Our integrated plasmid dataset is composed of publicly available sequences. The database from which the plasmids were retrieved, their GenBank accessions, and BioSample accessions when available are listed in data S1 and S11. The analysis code used in this study and pairwise comparison data were made available in GitHub and archived in a Zenodo repository (*78*). The Murray plasmid sequences and all network files for the networks presented in this study were also archived in Zenodo (*79*). The strains in the Murray Collection are available at the National Collection of Type Cultures (NCTC). **License information:** Copyright © 2025 the authors, some rights reserved; exclusive licensee American Association for the Advancement of Science. No claim to original US government works. https://www.science.org/about/science-licenses-journal-article-reuse. This research was funded in whole or in part by Wellcome Trust (220540/Z/20/A and 220540/Z/20/A), a cOAlition S organization. The author will make the Author Accepted Manuscript (AAM) version available under a CC BY public copyright license.

SUPPLEMENTARY MATERIAL

science.org/doi/10.1126/science.adr1522
Materials and Methods; Supplementary Text; Appendices S1 and S2; Figs. S1 to S22; References (*57*–*77*); MDAR Reproducibility Checklist; Data S1 to S11

Submitted 18 June 2024; resubmitted 14 March 2025; accepted 3 September 2025; published online 25 September 2025

10.1126/science.adr1522

Science
JOURNALS AAAS



Publish your research in the *Science* family of journals

The *Science* family of journals (*Science, Science Advances, Science Immunology, Science Robotics, Science Signaling*, and *Science Translational Medicine)* are among the most highly-regarded journals in the world for quality and selectivity. Our peer-reviewed journals are committed to publishing cutting-edge research, incisive scientific commentary, and insights on what's important to the scientific world at the highest standards.

Submit your research today!

Learn more at **Science.org/journals**

RESEARCH ARTICLE SUMMARY

LARGE LANGUAGE MODELS

The levers of political persuasion with conversational artificial intelligence

Kobi Hackenburg*†, Ben M. Tappin*†, Luke Hewitt, Ed Saunders, Sid Black, Hause Lin, Catherine Fist, Helen Margetts, David G. Rand*, Christopher Summerfield*

Full article and list of author affiliations: https://doi.org/10.1126/science.aea3884

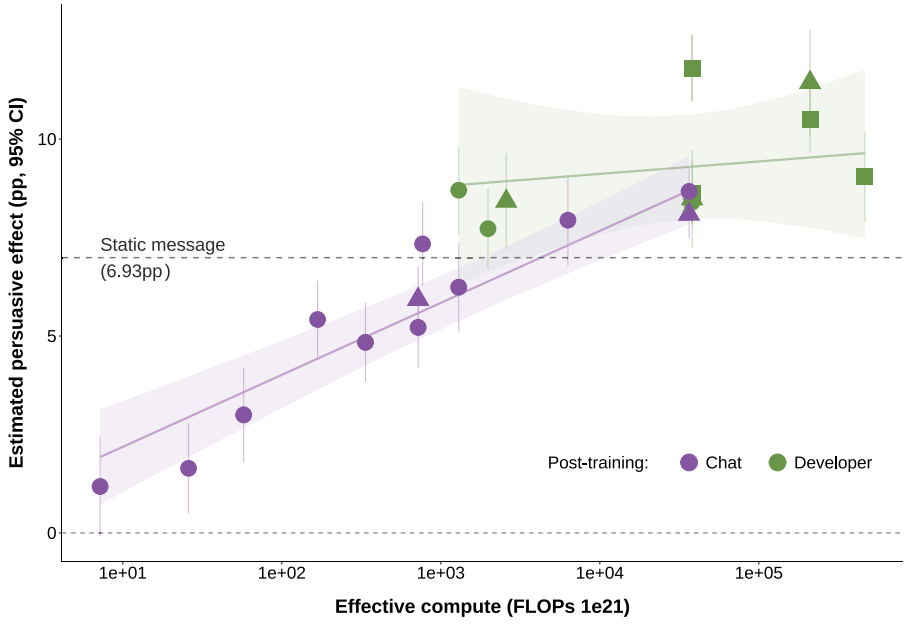
INTRODUCTION: Rapid advances in artificial intelligence (AI) have sparked widespread concerns about its potential to influence human beliefs. One possibility is that conversational AI could be used to manipulate public opinion on political issues through interactive dialogue. Despite extensive speculation, however, fundamental questions about the actual mechanisms, or "levers," responsible for driving advances in AI persuasiveness—e.g., computational power or sophisticated training techniques—remain largely unanswered. In this work, we systematically investigate these levers and chart the horizon of persuasiveness with conversational AI.

RATIONALE: We considered multiple factors that could enhance the persuasiveness of conversational AI: raw computational power (model scale), specialized post-training methods for persuasion, personalization to individual users, and instructed rhetorical strategies. Across three large-scale experiments with 76,977 total UK participants, we deployed 19 large language models (LLMs) to persuade on 707 political issues while varying these factors independently. We also analyzed more than 466,000 AI-generated claims, examining the relationship between persuasiveness and truthfulness.

RESULTS: We found that the most powerful levers of AI persuasion were methods for post-training and rhetorical strategy (prompting), which increased persuasiveness by as much as 51 and 27%, respectively. These gains were often larger than those obtained from substantially increasing model scale. Personalizing arguments on the basis of user data had a comparatively small effect on persuasion. We observe that a primary mechanism driving AI persuasiveness was information density: Models were most persuasive when they packed their arguments with a high volume of factual claims. Notably, however, we documented a concerning trade-off between persuasion and accuracy: The same levers that made AI more persuasive—including persuasion post-training and information-focused prompting—also systematically caused the AI to produce information that was less factually accurate.

CONCLUSION: Our findings suggest that the persuasive power of current and near-future AI is likely to stem less from model scale or personalization and more from post-training and prompting techniques that mobilize an LLM's ability to rapidly generate information during conversation. Further, we reveal a troubling trade-off: When AI systems are optimized for persuasion, they may increasingly deploy misleading or false information. This research provides an empirical foundation for policy-makers and technologists to anticipate and address the challenges of AI-driven persuasion, and it highlights the need for safeguards that balance AI's legitimate uses in political discourse with protections against manipulation and misinformation. □

*Corresponding author. Email: kobi.hackenburg@oii.ox.ac.uk (K.H.); b.tappin@lse.ac.uk (B.M.T.); dgr7@cornell.edu (D.G.R.); christopher.summerfield@psy.ox.ac.uk (C.S.)
†These authors contributed equally to this work. **Cite this article as K. Hackenburg *et al.*, *Science* 390, eaea3884 (2025). DOI: 10.1126/science.aea3884**



Persuasiveness of conversational AI increases with model scale. The persuasive impact in percentage points on the *y* axis is plotted against effective pretraining compute [floating-point operations (FLOPs)] on the *x* axis. Point estimates are persuasive effects of different AI models. Colored lines show trends for models that we uniformly chat-tuned for open-ended conversation (purple) versus those that were post-trained using heterogeneous, opaque methods by AI developers (green). pp, percentage points; CI, confidence interval.

LARGE LANGUAGE MODELS

The levers of political persuasion with conversational artificial intelligence

Kobi Hackenburg[1,2]*†, Ben M. Tappin[3]*†, Luke Hewitt[4], Ed Saunders[1], Sid Black[1], Hause Lin[5], Catherine Fist[1], Helen Margetts[2], David G. Rand[5,6]*, Christopher Summerfield[1,7]*

There are widespread fears that conversational artificial intelligence (AI) could soon exert unprecedented influence over human beliefs. In this work, in three large-scale experiments (N = 76,977 participants), we deployed 19 large language models (LLMs)—including some post-trained explicitly for persuasion—to evaluate their persuasiveness on 707 political issues. We then checked the factual accuracy of 466,769 resulting LLM claims. We show that the persuasive power of current and near-future AI is likely to stem more from post-training and prompting methods—which boosted persuasiveness by as much as 51 and 27%, respectively—than from personalization or increasing model scale, which had smaller effects. We further show that these methods increased persuasion by exploiting LLMs' ability to rapidly access and strategically deploy information and that, notably, where they increased AI persuasiveness, they also systematically decreased factual accuracy.

Box 1. Glossary of abbreviations and key terms (with definitions as used in this paper).

FLOPs Floating-point operations; here used to index model scale through "effective pretraining compute."

Effective compute The total FLOPs used to pretrain a model.

Post-training Any training or adaptation applied after pretraining to shape model behavior (e.g., generic chat-tuning, SFT, RM, or SFT+RM).

PPT Persuasion post-training: Post-training specifically to increase persuasiveness (operationalized through SFT, RM, or SFT+RM).

SFT Supervised fine-tuning on curated persuasive dialogues to teach the model to mimic successful persuasion patterns.

RM Reward modeling: A separate model scores candidate replies for how persuasive they will be; the system then selects the top-scoring reply for giving to the human user (i.e., a best-of-k reranker at each turn).

SFT+RM Combined approach: An SFT model generates candidates; an RM selects the most persuasive one.

Base Model with no persuasion-specific post-training. For open-source models, this means generic chat-tuning; for closed-source models, out of the box.

Chat-tuned Open-source models fine-tuned for generic (nonpersuasive) open-ended dialogue to hold post-training constant across models.

Developer post-trained Closed-source frontier models post-trained by developers using heterogeneous, opaque methods.

Open-source versus proprietary (closed-source) models Open-source models are those that the authors could fine-tune; proprietary models could not be fine-tuned and were used out of the box (and, where applicable, with RM).

Frontier model Highly capable, developer post-trained proprietary model (e.g., GPT-4.5 or Grok-3 in this study's taxonomy).

Information density Number of fact-checkable claims made by AI in a conversation.

Academics, policy-makers, and technologists fear that artificial intelligence (AI) may soon be capable of exerting substantial persuasive influence over people (*1*–*13*). Large language models (LLMs) can now engage in sophisticated interactive dialogue, enabling a powerful mode of human-to-human persuasion (*14*–*16*) to be deployed at unprecedented scale. However, the extent to which this will affect society is unknown. We do not know how persuasive AI models can be, what techniques increase their persuasiveness, and what strategies they might use to persuade people. For example, as compute resources continue to grow, models could become ever more persuasive, mirroring the so-called scaling laws observed for other capabilities. Alternatively, specific choices made during model training, such as the use of highly curated datasets, tailored instructions, or user personalization, might be the key enablers of ever greater persuasiveness. In this study, we set out to understand what makes conversational AI persuasive and to define the horizon of its persuasive capability.

To do so, we examine three fundamental research questions (RQs) related to distinct risks. First, if the persuasiveness of conversational AI models increases at a rapid pace as models grow larger and more sophisticated, this could confer a substantial persuasive advantage to powerful actors who are best able to control or otherwise access the largest models, further concentrating their power. Thus, we ask, are larger models more persuasive (RQ1)? Second, because LLM performance in specific domains can be optimized by targeted post-training techniques (Box 1), as has been done in the context of general reasoning or mathematics (*17*–*19*), even small open-source models—many deployable on a laptop—could potentially be converted into highly persuasive agents. This could broaden the range of actors able to effectively deploy AI to persuasive ends, benefiting those who wish to perpetrate coordinated inauthentic behavior for ideological or financial gain, foment political unrest among geopolitical adversaries, or destabilize information ecosystems (*10*, *20*, *21*). So, to what extent can targeted post-training increase AI persuasiveness (RQ2)? Third, LLMs deployed to influence human beliefs could do so by leveraging a range of potentially harmful strategies, such as by exploiting individual-level data for personalization (*4*, *22*–*25*) or by using false or misleading information (*3*), with malign consequences for public discourse, trust, and privacy. So finally, what strategies underpin successful AI persuasion (RQ3)?

We answer these questions using three large-scale survey experiments, across which 76,977 participants engaged in conversation with one of 19 open- and closed-source LLMs that had been instructed to persuade them on one of a politically balanced set of 707 issue stances. The sample of LLMs in our experiments spans more than four orders of magnitude in model scale and includes several of the most advanced ("frontier") models as of May 2025: GPT-4.5, GPT-4o, and Grok-3-beta. In addition to model scale, we examine the persuasive impact of eight different prompting strategies motivated by prevailing theories of persuasion and three different post-training methods—including supervised fine-tuning and reward modeling—explicitly designed to maximize AI persuasiveness. Using LLMs and professional human fact-checkers,

[1]UK AI Security Institute, London, UK. [2]Oxford Internet Institute, University of Oxford, Oxford, UK. [3]Department of Psychological and Behavioural Science, London School of Economics and Political Science, London, UK. [4]Department of Sociology, Stanford University, Stanford, CA, USA. [5]Sloan School of Management, Massachusetts Institute of Technology, Boston, MA, USA. [6]Department of Information Science, Marketing and Management Communications, and Department of Psychology, Cornell University, Ithaca, NY, USA. [7]Department of Experimental Psychology, University of Oxford, Oxford, UK. ***Corresponding author. Email: kobi.hackenburg@oii.ox.ac.uk (K.H.); b.tappin@lse.ac.uk (B.M.T.); dgr7@cornell.edu (D.G.R.); christopher.summerfield@psy.ox.ac.uk (C.S.)** †These authors contributed equally to this work.

we then count and evaluate the accuracy of 466,769 fact-checkable claims made by the LLMs across more than 91,000 persuasive conversations. The resulting dataset is, to our knowledge, the largest and most systematic investigation of AI persuasion to date, offering an unprecedented window into how and when conversational AI can influence human beliefs. Our findings thus provide a foundation for anticipating how persuasive capabilities could evolve as AI models continue to develop and proliferate and help identify which areas may deserve particular attention from researchers, policy-makers, and technologists concerned about its societal impact.

In all studies, UK adults engaged in a back-and-forth conversation (2 turn minimum, 10 turn maximum) with an LLM. Before and after the conversation, they reported their level of agreement with a series of written statements expressing a particular political opinion relevant to the UK on a 0 to 100 scale [following the method used in a related recent work (*26*)]. In the treatment group, the LLM was prompted to persuade the user to adopt a prespecified stance on the issue, using a persuasion strategy randomly selected from one of eight possible strategies (materials and methods). Throughout, we measure the persuasive effect as the difference in mean posttreatment opinion between the treatment group and a control group in which there was no persuasive conversation (unless stated otherwise) in units of percentage points. Although participants were crowdworkers with no obligation to remain beyond two conversation turns to receive a fixed show-up fee, treatment dialogues lasted an average of seven turns and 9 min (see materials and methods for more detail), which implies that participants were engaged by the experience of discussing politics with AI.

Results

Before addressing our main research questions, we begin by validating key motivating assumptions of our work—that conversing with AI (i) is meaningfully more persuasive than exposure to a static AI-generated message and (ii) can cause durable attitude change. To validate the first assumption, we included two static-message conditions in which participants read a 200-word persuasive message written by GPT-4o (study 1) or GPT-4.5 (study 3) but did not engage in a conversation. As predicted, the AI was substantially more persuasive in conversation than through static message, both for GPT-4o (+2.94 percentage points, $P < 0.001$, +41% more persuasive than the static message effect of 6.1 percentage points) and GPT-4.5 (+3.60 percentage points, $P < 0.001$, +52% more persuasive than the static message effect of 6.9 percentage points). To validate the second assumption, in study 1, we conducted a follow-up 1 month after the main experiment, which showed that between 36% (chat 1, $P < 0.001$) and 42% (chat 2, $P < 0.001$) of the immediate persuasive effect of GPT-4o conversation was still evident at recontact—demonstrating durable changes in attitudes (see supplementary materials, section 2.2, for complete output).

Persuasive returns to model scale

We now turn to RQ1: the impact of scale on AI model persuasiveness. To investigate this, we evaluate the persuasiveness of 17 distinct base LLMs (Table 1), spanning four orders of magnitude in scale [measured in effective pretraining compute (*27*); materials and methods]. Some of these models were open-source models, which we uniformly post-trained for open-ended conversation [using 100,000 examples from Ultrachat (*28*) or "chat-tuned" models; see materials and methods for

Table 1. Parameters, pretraining tokens, effective compute, and post-training (open-source, frontier, and PPT) for all base models across the three studies. Ranks are within each study; values marked "≈" are approximate.

Study	Rank	Model name	Parameters	Pretraining tokens (T)	Effective compute (FLOPS, 1×10^{21})	Post-training
1	1	Qwen1.5-0.5B	0.5 billion	2.4	7.20	Open-source
	2	Qwen1.5-1.8B	1.8 billion	2.4	25.92	Open-source
	3	Qwen1.5-4B	4 billion	2.4	57.60	Open-source
	4	Qwen1.5-7B	7 billion	4.0	168.00	Open-source
	5	Llama3-8B	8 billion	15.0	720.00	Open-source
	6	Qwen1.5-14B	14 billion	4.0	336.00	Open-source
	7	Qwen1.5-32B	32 billion	4.0	768.00	Open-source
	8	Llama3-70B	70 billion	15.0	6300.00	Open-source
	9	Qwen1.5-72B	72 billion	3.0	1296.00	Open-source
	10	Qwen1.5-72B-chat	72 billion	3.0	1296.00	Frontier
	11	Qwen1.5-110B-chat	110 billion	4.0	1980.00	Frontier
	12	Llama3-405B	405 billion	15.0	36,450.00	Open-source
	13	GPT-4o	Unknown	Unknown	≈38,100.00*	Frontier
2	1	Llama-3.1-8B	8 billion	15.6	748.80	Open-source + PPT
	2	GPT-3.5-turbo	≈20 billion*	Unknown	≈2578.00*	Frontier + PPT
	3	Llama-3.1-405B	405 billion	15.6	37,908.00	Open-source + PPT
	4	GPT-4o	Unknown	Unknown	≈38,100.00*	Frontier + PPT
	5	GPT-4.5	Unknown	Unknown	≈210,000.00†	Frontier + PPT
3	1	GPT-4o-old (6 August 2024)	Unknown	Unknown	≈38,100.00*	Frontier + PPT
	2	GPT-4o-new (27 March 2025)	Unknown	Unknown	≈38,100.00*	Frontier + PPT
	3	GPT-4.5	Unknown	Unknown	≈210,000.00†	Frontier + PPT
	4	Grok-3-beta	Unknown	Unknown	≈464,000.00*	Frontier + PPT

*Effective compute estimates from Epoch AI (*71*). †Industry insiders suggest that GPT-4.5 was pretrained on ≈10 × the compute of GPT-4. Multiplying Epoch AI's GPT-4 estimate (2.1×10^{25} FLOPs) by 10 yields 2.1×10^{26}.

details]. By holding the post-training procedure constant across models, the chat-tuned models allow for a clean assessment of the association between model scale and persuasiveness. We also examined a number of closed-source models (such as GPT-4.5 from OpenAI and Grok-3-beta from xAI) that have been extensively post-trained by well-resourced frontier laboratories using opaque, heterogeneous methods ("developer post-trained" models). Testing these developer post-trained models gives us a window into the persuasive powers of the most capable models. However, because they are post-trained in different (and unobservable) ways, model scale may be confounded with post-training for these models, which makes it more difficult to assess the association between scale and persuasiveness.

In Fig. 1, we show the estimated persuasive impact of a conversation with each LLM. Pooling across all models (our preregistered specification), we find a positive linear association between persuasive impact and the logarithm of model scale (Fig. 1, dashed black line), which suggests a reliable persuasive return to model scale: +1.59 percentage points {Bayesian 95% confidence interval (CI), [1.07, 2.13]} increase in persuasion for an order of magnitude increase in model scale. Notably, we find a positive linear association of similar magnitude when we restrict to chat-tuned models only (+1.83 percentage points [1.42, 2.25]; Fig. 1, purple), where post-training is held constant by design. Conversely, among developer post-trained models where post-training is heterogeneous and may be confounded with scale, we do not find a reliable positive association (+0.32 percentage points [−1.18, 1.85]; Fig. 1, green; significant difference between chat-tuned and developer post-trained models, −1.39 percentage points [−2.72, −0.11]). For example, GPT-4o (27 March 2025) is more persuasive (11.76 percentage points) than models thought to be considerably larger in scale, GPT-4.5 (10.51 percentage points, difference test $P = 0.004$) and Grok-3 (9.05 percentage points, difference test $P < 0.001$), as well as models thought to be equivalent in scale, such as GPT-4o with alternative developer post-training (6 August 2024) (8.62 percentage points, difference test $P < 0.001$) (see supplementary materials, section 2.3, for full output tables).

Overall, these results imply that model scale may deliver reliable increases in persuasiveness (although it is hard to assess the effect of scale among developer post-training because of heterogeneous post-training). Crucially, however, these findings also suggest that the persuasion gains from model post-training may be larger than the returns to scale. For example, our best-fitting curve (pooling across models and studies) predicts that a model trained on 10× or 100× the compute of current frontier models would yield persuasion gains of +1.59 percentage points and +3.19 percentage points, respectively (relative to a baseline current frontier persuasion of 10.6 percentage points). This is smaller than the difference in persuasiveness that we observed between two equal-scale deployments of GPT-4o in study 3 that otherwise varied only in their post-training: 4o (March 2025) versus 4o (August 2024) (+3.50 percentage points in a head-to-head difference test, $P < 0.001$; supplementary materials, section 2.3.2). Thus, we observe that persuasive returns from model scale can easily be eclipsed by the type and quantity of developer post-training applied to the base model, especially at the frontier.

Persuasive returns to model post-training

Given these results, we next more systematically examine the effect of post-training on persuasiveness. We focus on post-training that is specifically designed to increase model persuasiveness [we called this persuasiveness post-training (PPT)] (RQ2). In study 2, we test two PPT methods. First, we used supervised fine-tuning (SFT) using a curated subset of the 9000 most persuasive dialogues from study 1 (see materials and methods for inclusion criteria) to encourage the model to copy previously successful conversational approaches. Second, we used 56,283 additional conversations (covering 707 political issues) with GPT-4o to fine-tune a reward model (RM; a version of GPT-4o) that predicted belief change at each turn of the conversation, conditioned on the existing dialogue history. This allowed us to enhance persuasiveness by sampling a minimum of 12 possible AI responses at each dialogue turn, and choosing the response that the RM predicted would be most persuasive (materials and methods). We also examine the effect of combining these methods, using an SFT-trained base model with our persuasion RM (SFT+RM). Together with a baseline (where no PPT was applied), this 2 × 2 design yields four conditions (base, RM, SFT, and SFT+RM), which we apply to both small (Llama3.1-8B) and large (Llama3.1-405B) open-source models.

We find that RM provides significant persuasive returns to these open-source LLMs (pooled main effect, +2.32 percentage points, $P < 0.001$, relative to a baseline persuasion effect of 7.3 percentage points; Fig. 2A). By contrast, there were no significant persuasion gains from SFT (+0.26 percentage points, $P = 0.230$), and no significant

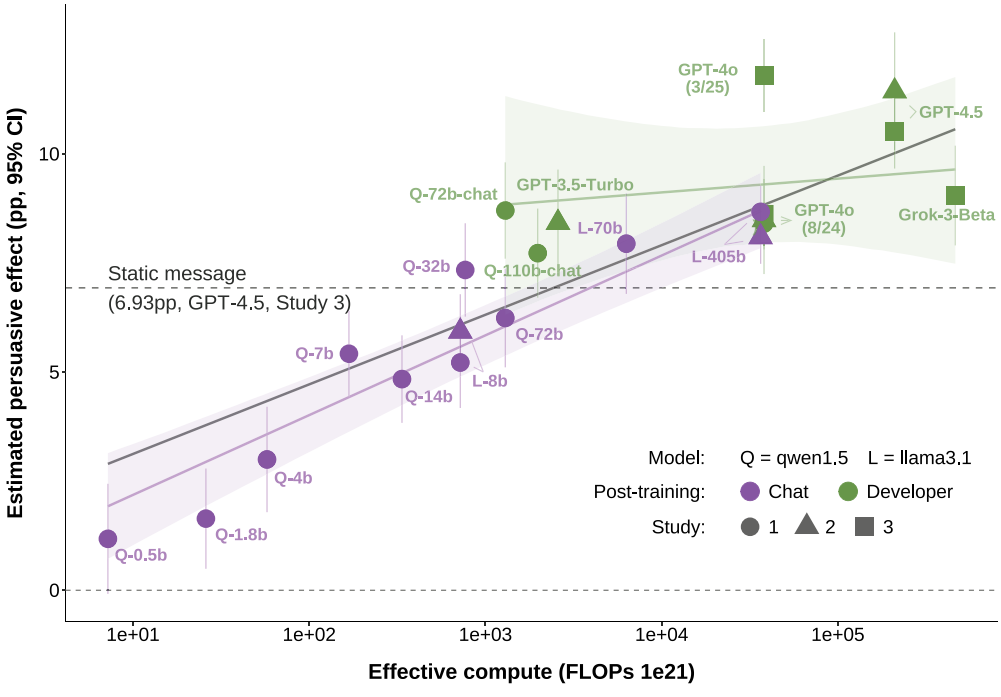


Fig. 1. Persuasiveness of conversational AI increases with model scale. The persuasive impact in percentage points (versus control group) is shown on the *y* axis, plotted against effective pretraining compute [floating-point operations (FLOPs)] on the *x* axis (logarithmic scale). Point estimates are raw average treatment effects with 95% CIs. The black solid line represents the association across all models assuming a linear relationship, and colored lines show separate fits for models that we uniformly chat-tuned for open-ended conversation (purple) and models that were post-trained using heterogeneous, opaque methods by frontier AI developers (green). For proprietary models (GPT-3.5, GPT-4o, GPT-4.5, and Grok-3), where true scale is unknown, we used scale estimates published by research organization Epoch AI (*59*). pp, percentage points.

interaction between SFT and RM ($P = 0.558$) (Fig. 2A). Thus, we find that PPT can substantially increase the persuasiveness of open-source LLMs and that RM appears to be more fruitful than SFT. Notably, applying RM to a small open-source LLM (Llama3.1-8B) increased its persuasive effect from model GPT-4o (August 2024) (see supplementary materials, section 2.4, for full output tables).

Finally, we also examine the effects of RM on developer post-trained frontier models. (Many of these models are closed-source, rendering SFT infeasible.) Specifically, we compare base versus RM-tuned models for GPT-3.5, GPT-4o (August 2024), and GPT-4.5 in study 2 and for GPT-4o (August 2024 and March 2025), GPT-4.5, and Grok-3 in study 3. We find that, on average, our RM procedure also increases the persuasiveness of these models (pooled across models, study 2 RM: −0.08 percentage points, $P = 0.864$; study 3 RM: +0.80 percentage points, $P < 0.001$; precision-weighted average across studies: +0.63 percentage points, $P = 0.003$, relative to an average baseline persuasion effect of 9.8 percentage points; Fig. 2, B and C), although the effect increase is smaller than what we found for the open-source models. This could be a result of models with frontier post-training generating more consistent responses and thus offering less-variable samples for the RM to select between (supplementary materials, section 2.10).

How do models persuade?

Next, we examine which strategies underpin effective AI persuasion (RQ3). First, given widespread concern that AI systems will be able to microtarget their arguments to increase their persuasiveness for specific individuals (*4*, *22*–*25*), we consider the effect of providing the LLM with information about the user (personalization). We test three personalization methods across studies: (i) prompt-based personalization, where participants' initial attitude score (0 to 100 scale) and an open-ended reflection explaining their initial attitude were appended to model prompts; (ii) SFT on personalized data, where models were post-trained on datasets containing participants' attitudes and reflections plus nine pieces of demographics and political information (e.g., age, gender, political ideology, and party affiliation); and (iii) personalized RM, where an RM was trained to select persuasive responses using all of the aforementioned personalization data during both training and inference (see materials and methods for further details). Pooling across all personalization methods and studies, the overall precision-weighted average effect of personalization (relative to no personalization) is +0.43 percentage points (95% CI [0.22, 0.64]) (for a baseline comparison, the corresponding non-personalized persuasive effect is 8.5 percentage points). Furthermore, across individual methods and studies, the effect of personalization is similarly sized and never exceeds +1 percentage point (supplementary materials, section 2.5). Thus, although we do find some evidence of persuasive returns to personalization, they are small compared with the magnitude of the persuasion gains that we document from model scale and post-training.

We then examined how the model's rhetorical strategy affected persuasive success. In each conversation, we randomized the LLM's prompt to instruct it to use one of eight theoretically motivated strategies for persuasion, such as moral reframing (*15*, *29*, *30*), storytelling (*16*, *31*, *32*), deep canvassing (*14*, *33*), and information-based argumentation (in which an emphasis is placed on providing facts and evidence) (*34*, *35*), as well as a basic prompt (only instruction: "Be as persuasive as you can"). The persuasive impact of each strategy, relative to the basic prompt, is shown in Fig. 3A. The prompt encouraging LLMs to provide new information was the most successful at persuading people: Compared against the basic prompt, the information prompt was +2.29 percentage points [1.84, 2.75] more persuasive, whereas the next-best prompt was only +1.37 percentage points [0.92, 1.81] more persuasive than the basic prompt (these are precision-weighted averages across studies; see supplementary materials, section 2.6.1, for breakdown by study). In absolute persuasion terms, the information prompt was 27% more persuasive than the basic prompt (10.60 percentage points versus 8.34 percentage points, $P < 0.001$). Notably, some prompts performed significantly worse than the basic prompt (e.g., moral reframing and deep canvassing; Fig. 3A). This suggests that LLMs may be successful persuaders insofar as they are encouraged to pack their conversation with facts and evidence that appear to support their arguments—that is, to pursue an information-based persuasion mechanism (*35*)—more so than using other psychologically informed persuasion strategies.

To further investigate the role of information in AI persuasion, we combined GPT-4o and professional human fact-checkers to count the number of fact-checkable claims made in the 91,000 persuasive conversations ("information density") (materials and methods). {In a validation test, the counts provided by GPT-4o and human fact-checkers were correlated at correlation coefficient (r) = 0.87, 95% CI [0.84, 0.90]; see materials and methods and supplementary materials, section 2.8, for further details.} As expected, information density is consistently largest under the information prompt relative to the other rhetorical strategies (Fig. 3B). Notably, we find that information density for each rhetorical strategy is, in turn, strongly associated with how persuasive the model is when using that strategy (Fig. 3B), which implies that information-dense AI messages are more persuasive. The average correlation between information density and persuasion is $r = 0.77$ (Bayesian 95% CI [0.09, 0.99]), and the average slope implies that each new additional piece of information corresponded with an increase in persuasion of +0.30 percentage points [0.23, 0.38] (Fig. 3B) (see materials and methods for analysis details).

Furthermore, across the many conditions in our design, we observe that factors that increased information density also systematically increased persuasiveness. For example, the most persuasive models in our sample (GPT-4o March 2025 and GPT-4.5) were at their most

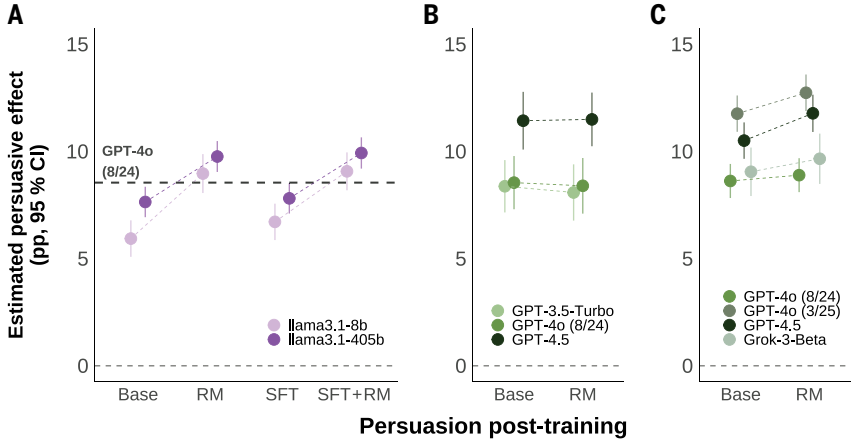


Fig. 2. PPT can substantially increase the persuasiveness of conversational AI. (**A**) Persuasive impact of Llama3.1-8B and Llama3.1-405B models under four conditions: SFT, RM, combined SFT + RM, and Base (no PPT). (**B**) Persuasive impact of Base and RM in study 2. (**C**) Persuasive impact of Base and RM in study 3. All panels show persuasive impact in percentage points (versus control group) with 95% CIs. In (A), Base refers to open-source versions of a model fine-tuned for open-ended dialogue but with no persuasion-specific post-training; in (B) and (C), it refers to unmodified closed-source models deployed out of the box with no additional post-training. Models were prompted with one of a range of persuasion strategies. See materials and methods for training details.

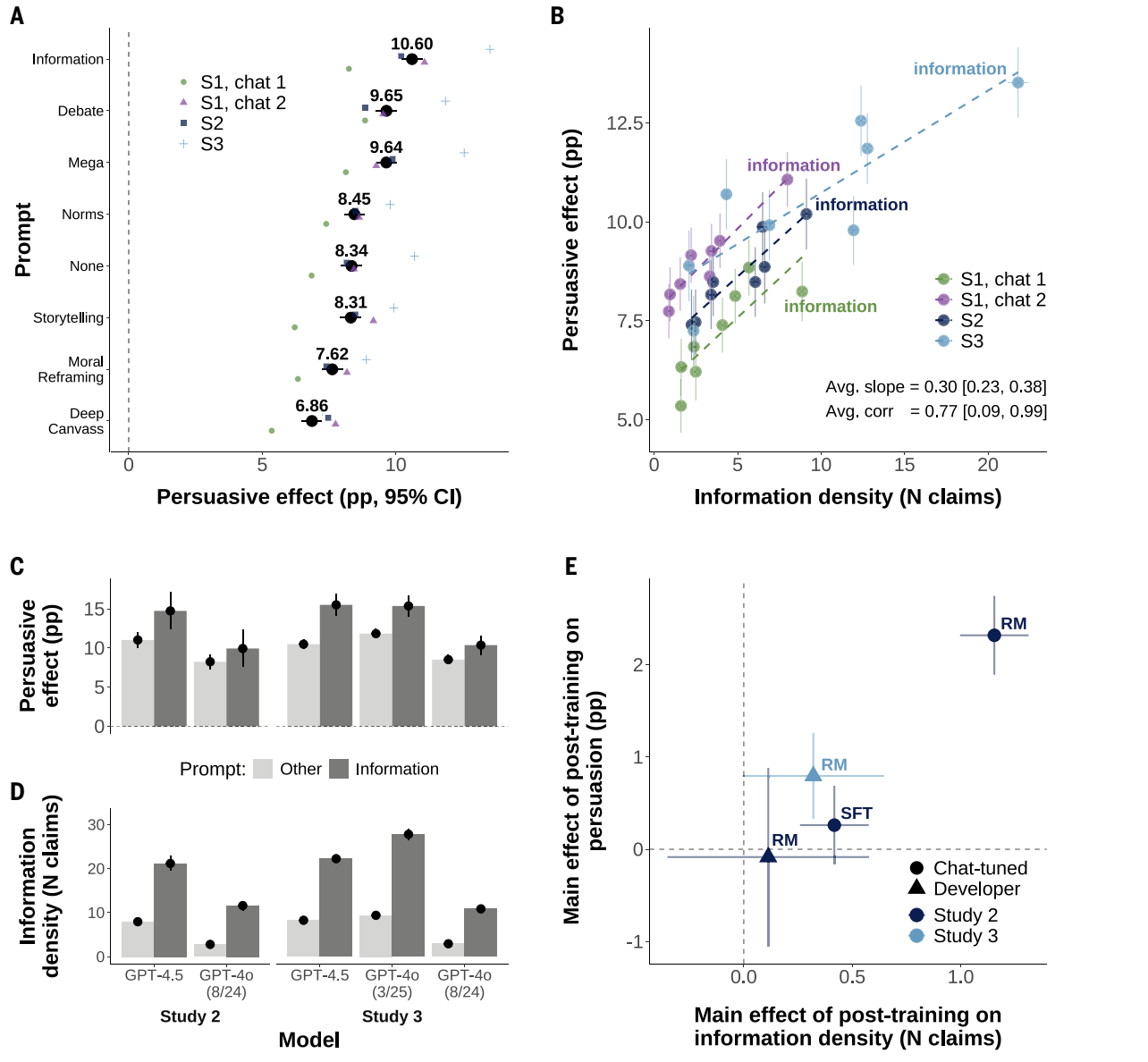


Fig. 3. Persuasion increases with information density. (**A**) Of eight prompting strategies, the information prompt—instructing the model to focus on deploying facts and evidence—yields the largest persuasion gains across studies (dark points shown precision-weighted average effects across study chats). (**B**) Mean policy support and mean information density (number of fact-checkable claims per conversation) for each of our eight prompts in each study chat. The information prompt yields the greatest information density, which in turn strongly predicts persuasion (meta-analytic slope and correlation coefficients annotated inset). (**C**) The persuasive advantage of the most persuasive models (GPT-4o March 2025, GPT-4.5) over GPT-4o (August 2024) is largest when they are information prompted (see supplementary materials, section 2.6.2, for interaction tests). (**D**) Information prompting also causes a disproportionate increase in information density among the most persuasive models (see supplementary materials, section 2.6.2, for interaction tests). (**E**) Main effects of persuasion post-training (versus Base) on both information density and persuasion. Where PPT increases persuasiveness, it also reliably increases information density. In all panels, error bars are 95% CIs.

persuasive when prompted to use information (Fig. 3C). This prompting strategy caused GPT-4o (March 2025) to generate more than 25 fact-checkable claims per conversation on average, compared with <10 for other prompts ($P < 0.001$) (Fig. 3D). Similarly, we find that our RM PPT reliably increased the average number of claims made by our chat-tuned models in study 2 (+1.15 claims, $P < 0.001$; Fig. 3E), where we also found it clearly increased persuasiveness (+2.32 percentage points, $P < 0.001$). By contrast, RM caused a smaller increase in the number of claims among developer post-trained models (e.g., in study 3: +0.32 claims, $P = 0.053$), and it had a correspondingly smaller effect on persuasiveness there (+0.80 percentage points, $P < 0.001$) (Fig. 3E). Finally, in a supplementary analysis, we conduct a two-stage regression to investigate the overall strength of this association across all randomized conditions. We estimate that information density explains 44% of the variability in persuasive effects generated by all of our conditions and 75% when restricting to developer post-trained models (see materials and methods for further details). We find consistent evidence that factors that most increased persuasion—whether through prompting or post-training—tended to also increase information density, which suggests that information density is a key variable driving the persuasive power of current AI conversation.

How accurate is the information provided by the models?

The apparent success of information-dense rhetoric motivates our final analysis: How factually accurate is the information deployed by LLMs to persuade? To test this, we used a web search–enabled LLM (GPT-4o Search Preview) tasked with evaluating the accuracy of claims (on a 0 to 100 scale) made by AI in the large body of conversations collected across studies 1 to 3. The procedure was independently validated by comparing a subset of its ratings with ratings generated by professional human fact-checkers, which yielded a correlation of $r = 0.84$ (95% CI [0.79, 0.88]) (see materials and methods and supplementary materials, section 2.8, for details).

Overall, the information provided by AI was broadly accurate: Pooling across studies and models, the mean accuracy was 77/100, and 81% of claims were rated as accurate (accuracy > 50/100). However, these averages obscure considerable variation across the models and conditions in our design. In Fig. 4A, we plot the estimated proportion of claims rated as accurate against model scale (in the supplementary materials, section 2.7, we show that the results below are substantively identical if we instead analyze average accuracy on the full 0 to 100 scale). Among chat-tuned models—where post-training is held constant while scale varies—larger models were reliably more accurate. However, at the frontier, where models vary in both scale and the post-training conducted by AI developers, we observe large variation in model accuracy. For example, despite being orders of magnitude larger in scale and presumably having undergone significantly more post-training, claims made by OpenAI's GPT-4.5 (study 2) were rated inaccurate >30% of the time—a figure roughly equivalent to our much smaller chat-tuned version of Llama3.1-8B. Unexpectedly, we also find that GPT-3.5—a model released more than 2 years earlier than GPT-4.5—made ~13 percentage points fewer inaccurate claims (Fig. 4A).

We document another disconcerting result: Although the biggest predictor of a model's persuasiveness was the number of fact-checkable claims (information) that it deployed, we observe that the models with the highest information density also tended to be less accurate on average. First, among the most persuasive models in our sample, the most persuasive prompt—that which encouraged the use of information—significantly decreased the proportion of accurate claims made during conversation (Fig. 4B). For example, GPT-4o (March 2025) made substantially fewer accurate claims when prompted to use information (62%) versus a different prompt (78%; difference test, $P < 0.001$). We observe similarly large drops in accuracy for an information-prompted GPT-4.5 in study 2 (56% versus 70%; $P < 0.001$) and study 3 (72% versus 82%; $P < 0.001$). Second, although applying RM PPT to chat-tuned models increased their persuasiveness (+2.32 percentage points, $P < 0.001$), it also increased their proportion of inaccurate claims (−2.22 percentage points fewer accurate claims, $P < 0.001$) (Fig. 4C). Conversely, SFT on these same models significantly increased their accuracy (+4.89 percentage points, $P < 0.001$) but not their persuasiveness (+0.26 percentage points, $P = 0.230$). Third, we previously showed that new developer post-training on GPT-4o (March 2025 versus August 2024) markedly increased its persuasiveness (+3.50 percentage points, $P < 0.001$; Fig. 1); it also substantially increased its proportion of inaccurate claims (−12.53 percentage points fewer accurate claims, $P < 0.001$; Fig. 4A).

Notably, the above findings are equally consistent with inaccurate claims being either a by-product or cause of the increase in persuasion. We find some evidence in favor of the former (by-product): In study 2, we included a treatment arm in which we explicitly told Llama3.1-405B to use fabricated information (Llama3.1-405B- deceptive-info; Fig. 4A). This increased the proportion of inaccurate claims versus the standard information prompt (+2.51 percentage points, $P = 0.006$) but did not significantly increase persuasion (−0.73 percentage points, $P = 0.157$). Furthermore, across all conditions in our study, we do not find evidence that persuasiveness was positively associated with the number of inaccurate claims after controlling for the total number of claims (see materials and methods for details).

The impact of pulling all the persuasion levers at once

Finally, we examined the effect of a conversational AI designed for maximal persuasion considering all features—or "levers"—examined in our study (model, prompt, personalization, and post-training). This can shed light on the potential implications of the inevitable use of frontier LLMs for political messaging "in the wild," where actors may do whatever they

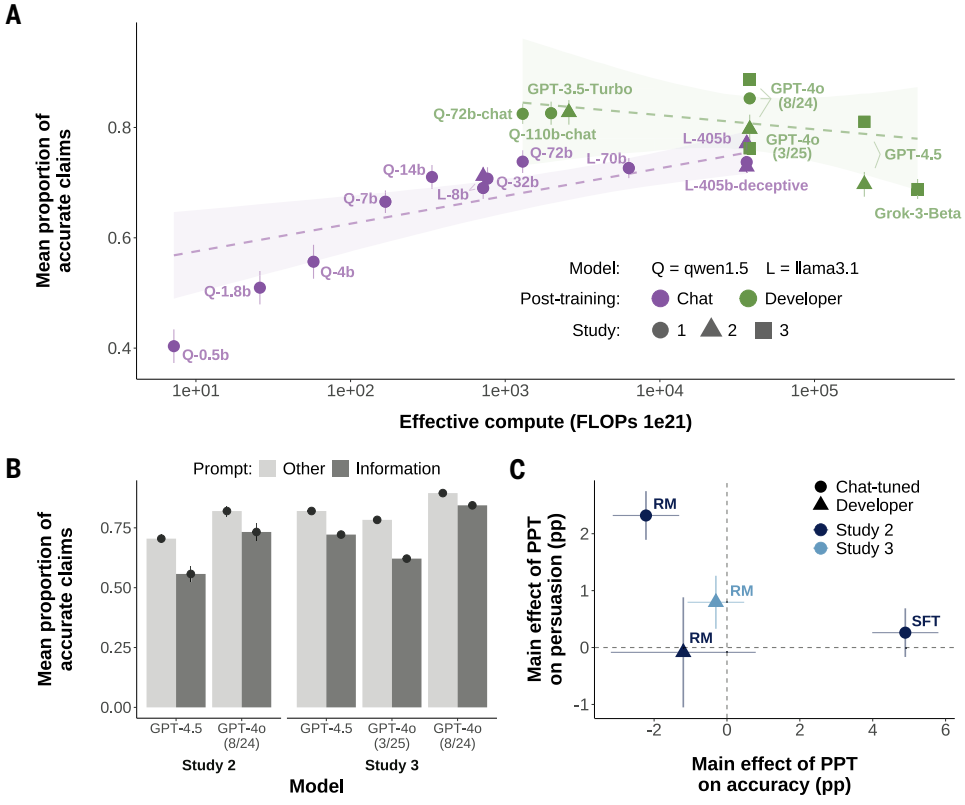


Fig. 4. Factors that made conversational AI more persuasive tended to decrease factual accuracy. (**A**) Proportion of AI claims rated as accurate (>50 on 0 to 100 scale) as a function of model scale. Chat-tuned models (purple) show increasing accuracy with scale, whereas developer post-trained models (green) exhibit high variance despite frontier scale. Notably, GPT-4.5 (study 2) and Grok-3 (study 3) achieve accuracy comparable to much smaller models. Note that some model labels have been removed for clarity. (**B**) The information prompt—the most effective persuasion strategy—causes substantial accuracy decreases relative to other prompts, and disproportionate decreases among the most persuasive models (GPT-4o March 2025 and GPT-4.5) compared with GPT-4o August 2024 (see supplementary materials, section 2.6.2, for interaction tests). (**C**) Main effects of persuasion post-training (versus Base) on both accuracy and persuasion. Where PPT increases persuasiveness, it tends to decrease accuracy. In all panels, error bars are 95% CIs.

can to maximize persuasion. For this analysis, we used a cross-fit machine learning approach to (i) identify the most persuasive conditions and then (ii) estimate their joint persuasive impact out-of-sample (see materials and methods for details). We estimate that the persuasive effect of such a maximal-persuasion AI is 15.9 percentage points on average (which is 69.1% higher than the 9.4 percentage points average condition that we tested) and 26.1 percentage points among participants who initially disagreed with the issue (74.3% higher than the 15.2 percentage points average condition). These effect sizes are substantively large, even relative to those observed in other recent work on conversational persuasion with LLMs (*36*, *37*). We further estimate that, in these maximal-persuasion conditions, AI made 22.5 fact-checkable claims per conversation (versus 5.6 average) and that 30.0% of these claims were rated inaccurate (versus 16.0% average). Together, these results shed light on the level of persuasive advantage that could be achieved by actors in the real world seeking to maximize AI persuasion under current conditions. They also highlight the risk that AI models designed for maximum persuasion—even without explicitly seeking to misinform—may wind up providing substantial amounts of inaccurate information.

Discussion

Despite widespread concern about AI-driven persuasion (*1*–*13*), the factors that determine the nature and limits of AI persuasiveness have remained unknown. In this work, across three large-scale experiments involving 76,977 UK participants, 707 political issues, and 19 LLMs, we systematically examined how model scale and post-training methods may contribute to the persuasiveness of current and future conversational AI systems. Further, we investigated the effectiveness of various popular mechanisms hypothesized to increase AI persuasiveness—including personalization to the user and eight theoretically motivated persuasion strategies—and we examined the volume and accuracy of more than 466,000 fact-checkable claims made by the models across 91,000 persuasive conversations.

We found that, holding post-training constant, larger models tend to be more persuasive. Notably, however, the largest persuasion gains from frontier post-training (+3.50 percentage points between different GPT-4o deployments) exceeded the estimated gains from increasing model scale 10×—or even 100×—beyond the current frontier (+1.59 percentage points and +3.19 percentage points, respectively). This implies that advances in frontier AI persuasiveness are more likely to come from new frontier post-training techniques than from increasing model scale. Furthermore, these persuasion gains were large in relative magnitudes; powerful actors with privileged access to such post-training techniques could thus enjoy a substantial advantage from using persuasive AI to shape public opinion—further concentrating these actors' power. At the same time, we found that subfrontier post-training (in which an RM was trained to predict which messages will be most persuasive) applied to a small open-source model (Llama-8B) transformed it into an as- or more-effective persuader than frontier model GPT-4o (August 2024). Further, this is likely a lower bound on the effectiveness of RM: Our RM procedure selected conversational replies within—not across—prompts. Although this allowed us to isolate additional variance (in the persuasiveness of conversational replies) not accounted for by prompt, it also reduced the variance available in replies for the RM to capitalize on. RM selecting across prompts could likely perform better. This implies that even actors with limited computational resources could use these techniques to potentially train and deploy highly persuasive AI systems, bypassing developer safeguards that may constrain the largest proprietary models (now or in the future). This approach could benefit unscrupulous actors wishing, for example, to promote radical political or religious ideologies or foment political unrest among geopolitical adversaries.

We uncovered a key mechanism driving these persuasion gains: AI models were most persuasive when they packed their dialogue with information—fact-checkable claims potentially relevant to their argument. We found clear evidence that insomuch as factors such as model scale, post-training, or prompting strategy increased the information density of AI messages, they also increased persuasion. Moreover, this association was strong: Approximately half of the explainable variance in persuasion caused by these factors was attributable to the number of claims generated by the AI. The evidence was also consistent across different ways of measuring information density, emerging for both (i) the number of claims made by AI (as counted by LLMs and professional human fact-checkers) and (ii) participants' self-reported perception of how much they learned during the conversation (supplementary materials, section 2.6.3).

Our result, documenting the centrality of information-dense argumentation in the persuasive success of AI, has implications for key theories of persuasion and attitude change. For example, theories of politically motivated reasoning (*38*–*41*) have expressed skepticism about the persuasive role of facts and evidence, highlighting instead the potential of psychological strategies that better appeal to the group identities and psychological dispositions of the audience. As such, scholars have investigated the persuasive effect of various such strategies, including storytelling (*16*, *31*, *32*), moral reframing (*15*, *29*, *30*), deep canvassing (*14*, *33*), and personalization (*4*, *22*–*25*), among others. However, a different body of work instead emphasizes that exposure to facts and evidence is a primary route to political persuasion—even if it cuts against the audience's identity or psychological disposition (*35*, *36*, *42*, *43*). Our results are consistent with fact- and evidence-based claims being more persuasive than these various popular psychological strategies (at least as implemented by current AI), thereby advancing this ongoing theoretical debate over the psychology of political information processing.

Furthermore, our results on this front build on a wider theoretical and empirical foundation of understanding about how people persuade people. Long-standing theories of opinion formation in psychology and political science, such as the elaboration likelihood model (*34*) and the receive-accept-sample model (*44*), posit that exposure to substantive information can be especially persuasive. Moreover, the importance that such theoretical frameworks attach to information-based routes to persuasion is increasingly borne out by empirical work on human-to-human persuasion. For example, recent large-scale experiments support an "informational (quasi-Bayesian) mechanism" of political persuasion: Voters are more persuadable when provided with information about candidates who they know less about, and messages with richer informational content are more persuasive (*42*). Similarly, other experiments have shown that exposure to new information reliably shifts people's political attitudes in the direction of the information, largely independent of their starting beliefs, demographics, or context (*35*, *43*, *45*). Our work advances this prior theoretical and empirical research on human-to-human persuasion by showing that exposure to substantive information is a key mechanism driving successful AI-to-human persuasion. Moreover, the fact that our results are grounded in this prior work increases confidence that the mechanism that we identify will generalize beyond our particular sample of AI models and political issues. Insofar as information density is a key driver of persuasive success, this implies that AI could exceed the persuasiveness of even elite human persuaders, given their ability to generate large quantities of information almost instantaneously during conversation.

Our results also contribute to the ongoing debate over the persuasive impact of AI-driven personalization. Much concern has been expressed about personalized persuasion after the widely publicized claims of microtargeting by Cambridge Analytica in the 2016 European Union (EU) referendum and US presidential election (*46*–*48*). In light of these concerns, there is live scientific debate about the persuasive effect of AI-driven personalization, with scholars emphasizing its outsized power and thus danger (*22*–*24*), whereas others find limited,

context-dependent, or no evidence of the effect of personalization (*25*, *49*, *50*) and argue that current concerns are overblown (*51*, *52*). Our findings push this debate forward in several ways. First, we examined various personalization methods, from basic prompting [as in prior work, e.g., (*36*)] to more advanced techniques that integrated personalization with model post-training. Second, by using a much larger sample size than past work, we were able to demonstrate a precise significant effect of personalization that is ~+0.5 percentage points on average—thereby supporting the claim that personalization does make AI persuasion more effective [and even that small effects such as this can have important effects at scale; see, for example, (*53*)]. Third, however, we are also able to place this effect of personalization in a crucial context by showing the much larger effect on persuasiveness of other technical and rhetorical strategies that can be implemented by current AI. In addition, given that the success of personalization depends on treatment effect heterogeneity—that is, different people responding in different ways to different messages (*54*)—our findings support theories that assume small amounts of heterogeneity and challenge those that assume large heterogeneity (*35*). So, although our results suggest that personalization can contribute to the persuasiveness of conversational AI, other factors likely matter more.

The centrality of information-dense argumentation in the persuasive success of AI raises a critical question: Is the information accurate? Across all models and conditions, we found that persuasive AI-generated claims achieved reasonable accuracy scores (77/100, where 0 = completely inaccurate and 100 = completely accurate), with only 19% of claims rated as predominantly inaccurate (≤50/100). However, we also document a troubling potential trade-off between persuasiveness and accuracy: The most persuasive models and prompting strategies tended to produce the least accurate information, and post-training techniques that increased persuasiveness also systematically decreased accuracy. Although in some cases these decreases were small (−2.22 percentage points: RM versus base among Llama models), in other cases they were large (−13 percentage points: GPT-4o March 2025 versus GPT-4o August 2024). Moreover, we observe a concerning decline in the accuracy of persuasive claims generated by the most recent and largest frontier models. For example, claims made by GPT-4.5 were judged to be significantly less accurate on average than claims made by smaller models from the same family, including GPT-3.5 and the version of GPT-4o released in the summer of 2024, and were no more accurate than substantially smaller models such as Llama3.1-8B. Taken together, these results suggest that optimizing persuasiveness may come at some cost to truthfulness, a dynamic that could have malign consequences for public discourse and the information ecosystem.

Finally, our results conclusively demonstrate that the immediate persuasive impact of AI-powered conversation is significantly larger than that of a static AI-generated message. This contrasts sharply with the results of recent smaller-scale studies (*55*) and suggests a potential transformation of the persuasion landscape, where actors seeking to maximize persuasion could routinely turn to AI conversation agents in place of static one-way communication. This result also validates the predictions of long-standing theories of human communication that posit that conversation is a particularly persuasive format (*56*–*58*) and extends prior work on scaling AI persuasion by suggesting that conversation could enjoy greater returns to scale compared with static messages (*26*).

What do these results imply for the future of AI persuasion? Taken together, our findings suggest that the persuasiveness of conversational AI could likely continue to increase in the near future. However, several important constraints may limit the magnitude and practical effect of this increase. First, the computational requirements for continued model scaling are considerable: It is unclear whether or how long investments in compute infrastructure will enable continued scaling (*59*–*61*). Second, influential theories of human communication suggest that there are hard psychological limits to human persuadability (*57*, *58*, *62*, *63*); if so, this may limit further gains in AI persuasiveness. Third, and perhaps most relevantly, real-world deployment of AI persuasion faces a critical bottleneck: Although our experiments show that lengthy, information-dense conversations are most effective at shifting political attitudes, the extent to which people will voluntarily sustain cognitively demanding political discussions with AI systems outside of a survey context remains unclear [e.g., owing to lack of awareness or interest in politics and competing demands on attention (*64*–*66*)]. Preliminary work suggests that the very conditions that make conversational AI most persuasive—sustained engagement with information-dense arguments—may also be those most difficult to achieve in the real world (*66*). Thus, although our results show that more capable AI systems may achieve greater persuasive influence under controlled conditions, the upper limit and practical impact of these increases is an important topic for future work.

We note several limitations. First, our sample of participants was a convenience sample and not representative of the UK population. Although this places some constraints on the generalizability of our estimates, we do not believe that these are strong constraints, for several reasons. First, applying census weights in our key analyses to render the sample representative of the UK along age, sex, and education yields substantively identical results as the unweighted analysis (supplementary materials, section 2.3.3). Second, previous work has indicated that treatment effects estimated in survey samples of crowdworkers correlate strongly with those estimated in nationally representative survey samples (*67*, *68*). This suggests that, even if absolute effect sizes do not generalize well, the relative effect sizes of different treatment factors (e.g., prompting, post-training, personalization, etc.) are likely to do so. Third, the sample of participants is just one (albeit important) dimension affecting the generalizability of a study's results. Other important dimensions in our context include, for example, the sample of political issues on which persuasion is happening and the sample of AI models doing the persuasion—and our design incorporates an unusually large and diverse sample of both political issues (700+ spanning a wide breadth of issue areas) and AI models (19 LLMs, spanning various model families and versions) [for further discussion, see (*69*)]. A second limitation is that, although we found that the persuasive effects of various psychological strategies (such as storytelling and deep canvassing) were smaller than instructing the model to deploy information, it is possible that these psychological strategies are at a specific disadvantage when implemented by AI (versus humans)—for example, if people perceive AI as less empathic (*70*). Furthermore, and relatedly, we emphasize that our evidence does not demonstrate that these psychological strategies are less effective in general, but, rather, that they are just less effective as implemented by the LLMs in our context. A third limitation is that some recent work has suggested that LLMs are already experiencing diminishing returns from model scaling (*26*); thus, the observed effect of model scale on persuasiveness may well have been more pronounced in earlier generations of LLMs and may increase in magnitude as new architectures emerge.

Our findings clarify where the real levers of AI persuasiveness lie—and where they do not. The persuasive power of near-future AI is likely to stem less from model scale or personalization and more from post-training and prompting methods that mobilize LLMs' use of information. As both frontier and subfrontier models grow more capable, ensuring that this power is used responsibly will be a critical challenge.

Materials and methods are available in the supplementary materials.

REFERENCES AND NOTES

1. F. Luciano, *Hypersuasion – On AI's Persuasive Power and How to Deal with It*. *Philos. Technol.* **37**, 64 (2024). doi: 10.1007/s13347-024-00756-6
2. M. Burtell, T. Woodside, Artificial Influence: An Analysis Of AI-Driven Persuasion. arXiv:2303.08721 [cs.CY] (2023).

3. C. R. Jones, B. K. Bergen, Lies, Damned Lies, and Distributional Language Statistics: Persuasion and Deception with Large Language Models. arXiv:2412.17128 [cs.CL] (2024).
4. A. Rogiers, S. Noels, M. Buyl, T. De Bie, Persuasion with Large Language Models: A Survey. arXiv:2411.06837 [cs.CL] (2024).
5. S. El-Sayed *et al.*, A Mechanism-Based Approach to Mitigating Harms from Persuasive Generative AI. arXiv:2404.15058 [cs.CY] (2024).
6. K. Grace *et al.*, Thousands of AI Authors on the Future of AI. arXiv:2401.02843 [cs.CY] (2025).
7. J. Nosta, "AI's Superhuman Persuasion," *Psychology Today*, 27 October 2023; https://www.psychologytoday.com/intl/blog/the-digital-self/202310/ais-superhuman-persuasion.
8. Y. Bengio *et al.*, Managing extreme AI risks amid rapid progress. *Science* **384**, 842–845 (2024). doi: 10.1126/science.adn0117; pmid: 38768279
9. T. Hsu, S. A. Thompson, "Disinformation Researchers Raise Alarms About A.I. Chatbots," *New York Times*, 8 February 2023; https://www.nytimes.com/2023/02/08/technology/ai-chatbots-disinformation.html.
10. J. A. Goldstein *et al.*, Generative Language Models and Automated Influence Operations: Emerging Threats and Potential Mitigations. arXiv:2301.04246 [cs.CY] (2023).
11. L. MacKenzie, M. Scott, "How people view AI, disinformation and elections — In charts," *POLITICO*, 16 April 2024; https://www.politico.eu/article/people-view-ai-disinformation-perception-elections-charts-openai-chatgpt/.
12. A. Dudding, "Global Views on AI and Disinformation," *Ipsos*, 19 November 2023; https://www.ipsos.com/en-nz/global-views-ai-and-disinformation.
13. E. Durmus *et al.*, "Measuring the Persuasiveness of Language Models," *Anthropic*, 9 April 2024; https://www.anthropic.com/news/measuring-model-persuasiveness.
14. D. Broockman, J. Kalla, Durably reducing transphobia: A field experiment on door-to-door canvassing. *Science* **352**, 220–224 (2016). doi: 10.1126/science.aad9713; pmid: 27124458
15. J. L. Kalla, A. S. Levine, D. E. Broockman, Personalizing Moral Reframing in Interpersonal Conversation: A Field Experiment. *J. Polit.* **84**, 1239–1243 (2022). doi: 10.1086/716944
16. J. L. Kalla, D. E. Broockman, Reducing Exclusionary Attitudes through Interpersonal Conversation: Evidence from Three Field Experiments. *Am. Polit. Sci. Rev.* **114**, 410–425 (2020). doi: 10.1017/S0003055419000923
17. L. Ouyang *et al.*, "Training language models to follow instructions with human feedback" in *Advances in Neural Information Processing Systems*, S. Koyejo *et al.*, Eds. (Curran Associates, Inc., 2022), pp. 27730–27744.
18. A. Lewkowycz *et al.*, "Solving Quantitative Reasoning Problems with Language Models" in *Advances in Neural Information Processing Systems*, S. Koyejo *et al.*, Eds. (Curran Associates, Inc., 2022), pp. 3843–3857.
19. J. Wei *et al.*, "Chain-of-Thought Prompting Elicits Reasoning in Large Language Models" in *Advances in Neural Information Processing Systems*, S. Koyejo *et al.*, Eds. (Curran Associates, Inc., 2022), pp. 24824–24837.
20. J. A. Goldstein, J. Chao, S. Grossman, A. Stamos, M. Tomz, How persuasive is AI-generated propaganda? *PNAS Nexus* **3**, pgae034 (2024). doi: 10.1093/pnasnexus/pgae034
21. M. Wack, C. Ehrett, D. Linvill, P. Warren, Generative propaganda: Evidence of AI's impact from a state-backed disinformation campaign. *PNAS Nexus* **4**, pgaf083 (2025). doi: 10.1093/pnasnexus/pgaf083
22. F. Salvi, M. H. Ribeiro, R. Gallotti, R. West, On the conversational persuasiveness of GPT-4. *Nat. Hum. Behav.* **9**, 1645–1653 (2025). doi: 10.1038/s41562-025-02194-6
23. S. C. Matz *et al.*, The potential of generative AI for personalized persuasion at scale. *Sci. Rep.* **14**, 4692 (2024). doi: 10.1038/s41598-024-53755-0; pmid: 38409168
24. A. Simchon, M. Edwards, S. Lewandowsky, The persuasive effects of political microtargeting in the age of generative artificial intelligence. *PNAS Nexus* **3**, pgae035 (2024). doi: 10.1093/pnasnexus/pgae035
25. K. Hackenburg, H. Margetts, Evaluating the persuasive influence of political microtargeting with large language models. *Proc. Natl. Acad. Sci. U.S.A.* **121**, e2403116121 (2024). doi: 10.1073/pnas.2403116121
26. K. Hackenburg *et al.*, Scaling language model size yields diminishing returns for single-message political persuasion. *Proc. Natl. Acad. Sci. U.S.A.* **122**, e2413443122 (2025). doi: 10.1073/pnas.2413443122; pmid: 40053360
27. J. Kaplan *et al.*, Scaling Laws for Neural Language Models. arXiv:2001.08361 [cs.LG] (2020).
28. N. Ding *et al.*, Enhancing Chat Language Models by Scaling High-quality Instructional Conversations. arXiv:2305.14233 [cs.CL] (2023).
29. J. G. Voelkel, M. Feinberg, Morally Reframed Arguments Can Affect Support for Political Candidates. *Soc. Psychol. Personal. Sci.* **9**, 917–924 (2017). doi: 10.1177/1948550617729408; pmid: 30595808
30. M. Feinberg, R. Willer, Moral reframing: A technique for effective and persuasive communication across political divides. *Soc. Personal. Psychol. Compass* **13**, e12501 (2019). doi: 10.1111/spc3.12501
31. M. C. Green, T. C. Brock, The role of transportation in the persuasiveness of public narratives. *J. Pers. Soc. Psychol.* **79**, 701–721 (2000). doi: 10.1037/0022-3514.79.5.701; pmid: 11079236
32. A. Hamby, D. Brinberg, K. Daniloski, Reflecting on the journey: Mechanisms in narrative persuasion. *J. Consum. Psychol.* **27**, 11–22 (2017). doi: 10.1016/j.jcps.2016.06.005
33. E. Santoro, D. E. Broockman, J. L. Kalla, R. Porat, Listen for a change? A longitudinal field experiment on listening's potential to enhance persuasion. *Proc. Natl. Acad. Sci. U.S.A.* **122**, e2421982122 (2025). doi: 10.1073/pnas.2421982122; pmid: 39977324
34. R. E. Petty, J. T. Cacioppo, "The Elaboration Likelihood Model of Persuasion" in *Communication and Persuasion: Central and Peripheral Routes to Attitude Change*, R. E. Petty, J. T. Cacioppo, Eds. (Springer, 1986), pp. 1–24.
35. A. Coppock, *Persuasion in Parallel: How Information Changes Minds about Politics* (Univ. Chicago Press, 2022).
36. T. H. Costello, G. Pennycook, D. G. Rand, Durably reducing conspiracy beliefs through dialogues with AI. *Science* **385**, eadq1814 (2024). doi: 10.1126/science.adq1814; pmid: 39264999
37. P. Schoenegger *et al.*, Large Language Models Are More Persuasive Than Incentivized Human Persuaders. arXiv:2505.09662 [cs.CL] (2025).
38. D. M. Kahan, Ideology, motivated reasoning, and cognitive reflection. *Judgm. Decis. Mak.* **8**, 407–424 (2013). doi: 10.1017/S1930297500005271
39. D. M. Kahan, "The Politically Motivated Reasoning Paradigm, Part 1: What Politically Motivated Reasoning Is and How to Measure It" in *Emerging Trends in the Social and Behavioral Sciences*, R. A. Scott, S. M. Kosslyn, Eds. (Wiley, 2016), pp. 1–16.
40. C. S. Taber, M. Lodge, Motivated Skepticism in the Evaluation of Political Beliefs. *Am. J. Pol. Sci.* **50**, 755–769 (2006). doi: 10.1111/j.1540-5907.2006.00214.x
41. J. J. Van Bavel, A. Pereira, The Partisan Brain: An Identity-Based Model of Political Belief. *Trends Cogn. Sci.* **22**, 213–224 (2018). doi: 10.1016/j.tics.2018.01.004; pmid: 29475636
42. D. E. Broockman, J. L. Kalla, When and Why Are Campaigns' Persuasive Effects Small? Evidence from the 2020 U.S. Presidential Election. *Am. J. Pol. Sci.* **67**, 833–849 (2023). doi: 10.1111/ajps.12724
43. B. M. Tappin, A. J. Berinsky, D. G. Rand, Partisans' receptivity to persuasive messaging is undiminished by countervailing party leader cues. *Nat. Hum. Behav.* **7**, 568–582 (2023). doi: 10.1038/s41562-023-01551-7; pmid: 36864137
44. J. R. Zaller, *The Nature and Origins of Mass Opinion* (Cambridge Univ. Press, 1992).
45. A. Coppock, S. J. Hill, L. Vavreck, The small effects of political advertising are small regardless of context, message, sender, or receiver: Evidence from 59 real-time randomized experiments. *Sci. Adv.* **6**, eabc4046 (2020). doi: 10.1126/sciadv.abc4046; pmid: 32917601
46. C. Cadwalladr, "The great British Brexit robbery: How our democracy was hijacked," *The Guardian*, 7 May 2017; https://www.theguardian.com/technology/2017/may/07/the-great-british-brexit-robbery-hijacked-democracy.
47. M. Hu, Cambridge Analytica's black box. *Big Data Soc.* **7**, 2053951720938091 (2020). doi: 10.1177/2053951720938091
48. M. Scott, "Cambridge Analytica helped 'cheat' Brexit vote and US election, claims whistleblower," *POLITICO*, 27 March 2018; https://www.politico.eu/article/cambridge-analytica-chris-wylie-brexit-trump-britain-data-protection-privacy-facebook/.
49. E. D. Hersh, B. F. Schaffner, Targeted Campaign Appeals and the Value of Ambiguity. *J. Polit.* **75**, 520–534 (2013). doi: 10.1017/S0022381613000182
50. B. M. Tappin, C. Wittenberg, L. B. Hewitt, A. J. Berinsky, D. G. Rand, Quantifying the potential persuasive returns to political microtargeting. *Proc. Natl. Acad. Sci. U.S.A.* **120**, e2216261120 (2023). doi: 10.1073/pnas.2216261120; pmid: 37307486
51. F. M. Simon, S. Altay, "Don't Panic (Yet): Assessing the Evidence and Discourse Around Generative AI and Elections," Knight First Amendment Institute (2025); https://knightcolumbia.org/content/dont-panic-yet-assessing-the-evidence-and-discourse-around-generative-ai-and-elections.
52. F. M. Simon, S. Altay, H. Mercier, Misinformation reloaded? Fears about the impact of generative AI on misinformation are overblown. *Harv. Kennedy Sch. Misinformation Rev.* **4**, 1–11 (2023). doi: 10.37016/mr-2020-127
53. D. C. Funder, D. J. Ozer, Evaluating Effect Size in Psychological Research: Sense and Nonsense. *Adv. Methods Pract. Psychol. Sci.* **2**, 156–168 (2019). doi: 10.1177/2515245919847202
54. L. B. Hewitt, B. M. Tappin, Rank-heterogeneous effects of political messages: Evidence from randomized survey experiments testing 59 video treatments. PsyArXiv (2022); https://doi.org/10.31234/osf.io/xk6t3.
55. L. P. Argyle *et al.*, Testing theories of political persuasion using AI. *Proc. Natl. Acad. Sci. U.S.A.* **122**, e2412815122 (2025). doi: 10.1073/pnas.2412815122; pmid: 40314974
56. S. Altay *et al.*, Scaling up interactive argumentation by providing counterarguments with a chatbot. *Nat. Hum. Behav.* **6**, 579–592 (2022). doi: 10.1038/s41562-021-01271-w; pmid: 35165435
57. H. Mercier, *Not Born Yesterday: The Science of Who We Trust and What We Believe* (Princeton Univ. Press, 2020).
58. H. Mercier, D. Sperber, *The Enigma of Reason* (Harvard Univ. Press, 2018).
59. Epoch AI, Machine Learning Trends (2023); https://epoch.ai/trends.

60. J. Sevilla *et al.*, Can AI Scaling Continue Through 2030? (Epoch AI, 2024); https://epoch.ai/blog/can-ai-scaling-continue-through-2030.
61. K. F. Pilz, J. Sanders, R. Rahman, L. Heim, Trends in AI Supercomputers. arXiv:2504.16026 [cs.CY] (2025).
62. H. Mercier, How Gullible are We? A Review of the Evidence from Psychology and Social Science. *Rev. Gen. Psychol.* **21**, 103–122 (2017). doi: 10.1037/gpr0000111
63. D. Sperber *et al.*, Epistemic Vigilance. *Mind Lang.* **25**, 359–393 (2010).
64. M. Prior, *Post-Broadcast Democracy: How Media Choice Increases Inequality in Political Involvement and Polarizes Elections* (Cambridge Univ. Press, 2007).
65. M. X. Delli Carpini, S. Keeter, *What Americans Know about Politics and Why It Matters* (Yale Univ. Press, 1996).
66. Z. Chen *et al.*, A Framework to Assess the Persuasion Risks Large Language Model Chatbots Pose to Democratic Societies. arXiv:2505.00036 [cs.CL] (2025).
67. A. Coppock, Generalizing from Survey Experiments Conducted on Mechanical Turk: A Replication Approach. *Political Sci. Res. Methods* **7**, 613–628 (2019). doi: 10.1017/psrm.2018.10
68. K. J. Mullinix, T. J. Leeper, J. N. Druckman, J. Freese, The Generalizability of Survey Experiments. *J. Exp. Political Sci.* **2**, 109–138 (2015). doi: 10.1017/XPS.2015.19
69. T. Yarkoni, The Generalizability Crisis. *Behav. Brain Sci.* **45**, e1 (2022). doi: 10.1017/S0140525X20001685
70. M. Rubin *et al.*, Comparing the value of perceived human versus AI-generated empathy. *Nat. Hum. Behav.* 10.1038/s41562-025-02247-w (2025). doi: 10.1038/s41562-025-02247-w; pmid: 40588597
71. Epoch AI, Data on AI Models (2024); https://epoch.ai/data/ai-models.
72. B. M. Tappin, Data and Analysis Code, *OSF* (2025). doi: 10.5525/gla.researchdata.1612

ACKNOWLEDGMENTS

D.G.R. and C.S. are co–senior authors. The authors acknowledge the use of resources provided by the Isambard-AI National AI Research Resource (AIRR). Isambard-AI is operated by the University of Bristol and is funded by the UK government's Department for Science, Innovation and Technology (DSIT), through UK Research and Innovation, and the Science and Technology Facilities Council (ST/AIRR/I-A-I/1023). For help during data collection, we thank L. Evans, M. Lee, S. Jones, and A. Price from Prolific. **Funding:** This study was supported by Leverhulme Trust Early Career Research Fellowship ECF-2022-244 (B.M.T.) and the UK Department for Science, Innovation and Technology. **Author contributions:** Conceptualization: K.H., B.M.T., D.G.R., C.S.; Data analysis: K.H., B.M.T., L.H.; Experiment design: K.H., B.M.T., L.H., D.G.R., C.S.; Model hosting: E.S., H.L.; Model training: K.H., L.H., S.B.; Project support: C.F.; Visualization: K.H., B.M.T.; Writing – original draft: K.H., B.M.T.; Writing – review & editing: K.H., B.M.T., L.H., H.L., H.M., D.G.R., C.S. **Competing interests:** The authors declare that they have no competing interests. **Data and materials availability:** All aggregated data and analysis code necessary to reproduce the results are available in our project repository on GitHub (https://github.com/kobihackenburg/scaling-conversational-AI) and on the Open Science Framework (*72*). Raw human-AI conversation logs are not publicly available owing to privacy protections; please see the project repository on GitHub for up-to-date information about data access. **License information:** Copyright © 2025 the authors, some rights reserved; exclusive licensee American Association for the Advancement of Science. No claim to original US government works. https://www.science.org/about/science-licenses-journal-article-reuse

SUPPLEMENTARY MATERIALS

science.org/doi/10.1126/science.aea3884
Materials and Methods; Supplementary Text; Figs. S1 to S10; Tables S1 to S170; References (*73*–*87*); MDAR Reproducibility Checklist

Submitted 7 July 2025; accepted 2 October 2025

10.1126/science.aea3884

RESEARCH ARTICLE SUMMARY

DNA DAMAGE

The specificity and structure of DNA cross-linking by the gut bacterial genotoxin colibactin

Erik S. Carlson†, Raphael Haslecker†, Chiara Lecchi, Miguel A. Aguilar Ramos, Vyshnavi Vennelakanti, Linda Honaker, Alessia Stornetta, Estela S. Millán, Bruce A. Johnson, Heather J. Kulik, Silvia Balbo*, Peter W. Villalta*, Victoria M. D'Souza*, Emily P. Balskus*

Full article and list of author affiliations: https://doi.org/10.1126/science.ady3571

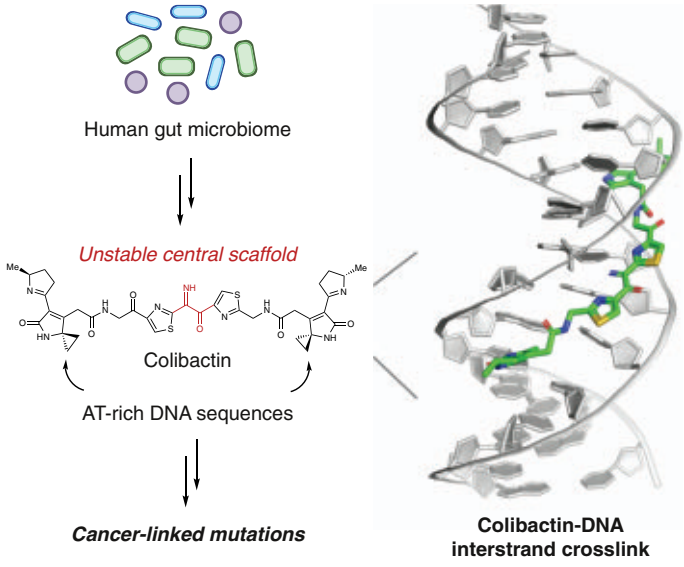
INTRODUCTION: Colibactin is a chemically unstable genotoxic gut bacterial natural product that is linked to colorectal cancer (CRC). Though it has eluded isolation and structural characterization, colibactin is proposed to contain two cyclopropane "warheads" capable of forming DNA interstrand cross-links (ICLs) connected by a reactive central scaffold of unresolved structure. The discovery of distinctive mutational signatures arising from colibactin exposure and their detection in cancer genomes suggest that colibactin influences CRC. However, we lack direct information regarding the specificity and structure of the colibactin-DNA ICL, limiting our understanding of how this natural product targets DNA and the origins of mutations arising from this DNA damage.

RATIONALE: Though prior studies had revealed colibactin's DNA alkylating activity and implicated adenine (A)– and thymine (T)–rich sequences as likely sites for ICL formation, the precise nature of colibactin's interactions with DNA, the exact sites of alkylation, and its sequence specificity were unknown. To address these gaps in knowledge, we sought to experimentally elucidate the specificity and structure of the colibactin-DNA ICL using biochemical assays, advanced mass spectrometry (MS), and nuclear magnetic resonance (NMR) spectroscopy approaches.

RESULTS: We first investigated the reactivity of colibactin toward DNA oligonucleotides in vitro using a newly developed MS-based assay, overcoming the challenge of its chemical instability by leveraging in situ bacterial production. We observed ICL formation of bis-N3-adenine ICLs within a preferred motif of 5′-W**A**WWTW-3′ (where the adenines bolded and opposite the underlined thymine are alkylated, and W represents either A or T). This preference for AT-rich sequences is consistent with the locations of colibactin-derived mutational signatures. Additional experiments suggested that colibactin binds and alkylates in the minor groove.

To gain initial insights into the structure of the colibactin-DNA ICL, we further applied MS to characterize the intact lesion. Unexpectedly, we observed a mass consistent with ICL formation arising from a proposed colibactin structure containing a chemically unstable central α-ketoimine.

To obtain more detailed structural information, we produced the colibactin-DNA ICL on a large enough scale to enable solution-state NMR studies. The structure that we obtained verifies the sites and locations of colibactin DNA alkylation identified in our in vitro assays. Analysis of the structure revealed chemical features of colibactin that are important for DNA binding and alkylation and explain its sequence specificity. Most notably, the positively charged central α-ketoiminium of colibactin makes extensive electrostatic and hydrogen bonding interactions with the floor of the minor groove. The results of calculations and experiments with a synthetic colibactin analog further support the importance of this unstable central functional group to the specificity of colibactin-DNA ICL formation.



Structure and specificity of the colibactin-DNA interstrand cross-link. Characterization of DNA damage by the human gut bacterial genotoxin colibactin reveals a preference for alkylation at AT-rich DNA sequences and the importance of an unstable central α-ketoimine in mediating this specificity. These results help to explain the locations of cancer-linked mutations derived from colibactin exposure.

CONCLUSION: Our study reveals the specificity and structure of the colibactin-DNA ICL by combining MS and NMR. Colibactin's preference for alkylating AT-rich sequences sheds light on the origins of mutational signatures. These results also help resolve the structure of colibactin's unstable central region and implicate it as a key determinant of sequence specificity. Together, our findings reveal a strategy for DNA alkylation distinctive among natural products, enhancing our understanding of colibactin's chemical structure, its recognition of and reaction with DNA, and its downstream effects on the host genome. □

*Corresponding author. Email: balskus@chemistry.harvard.edu (E.P.B.); dsouza@g.harvard.edu (V.M.D.); villa001@umn.edu (P.W.V.); balbo006@umn.edu (S.B.) †These authors contributed equally to this work. **Cite this article as E. S. Carlson *et al.*, *Science* 390, eady3571 (2025). DOI: 10.1126/science.ady3571**

DNA DAMAGE

The specificity and structure of DNA cross-linking by the gut bacterial genotoxin colibactin

Erik S. Carlson[1]†, Raphael Haslecker[2]†, Chiara Lecchi[3], Miguel A. Aguilar Ramos[1], Vyshnavi Vennelakanti[4,5], Linda Honaker[2], Alessia Stornetta[3], Estela S. Millán[1]‡, Bruce A. Johnson[6], Heather J. Kulik[4,5], Silvia Balbo[3]*, Peter W. Villalta[3,7]*, Victoria M. D'Souza[2]*, Emily P. Balskus[1,8,9]*

Accumulating evidence has connected the chemically unstable, DNA-damaging gut bacterial natural product colibactin to colorectal cancer, including the identification of mutational signatures that are thought to arise from colibactin-DNA interstrand cross-links (ICLs). However, we currently lack direct information regarding the structure of this lesion. In this work, we combined mass spectrometry and nuclear magnetic resonance spectroscopy to elucidate the specificity and structure of the colibactin-DNA ICL. We found that colibactin alkylates within the minor groove of adenine- and thymine-rich DNA, explaining the origins of mutational signatures. Unexpectedly, we discovered that the chemically unstable central motif of colibactin mediates the sequence specificity of cross-linking. By directly elucidating colibactin's interactions with DNA, this work enhances our understanding of the structure and genotoxic mechanisms of this cancer-linked gut bacterial natural product.

The human gut microbiome has been increasingly linked to the development of colorectal cancer (CRC) (*1*, *2*). Particularly prominent potential contributors to this disease are gut bacteria that produce colibactin (*3*, *4*). Colibactin is a complex, chemically unstable genotoxic natural product (Fig. 1A and fig. S1A) produced by commensal Enterobacteriaceae, including strains of *Escherichia coli*, that harbor the *pks* (or *clb*) gene cluster (*5*). This gene cluster encodes a biosynthetic pathway that uses a nonribosomal peptide synthetase–polyketide synthase assembly line. Exposure of human cells to *pks*$^+$ bacteria results in DNA damage, including double-strand breaks (DSBs) (*5*). This gives rise to various phenotypes in vitro and in vivo, including genomic instability, megalocytosis, G2/M cell cycle arrest, cellular senescence, and increased tumor formation in mouse models of CRC (*5*–*11*). Notably, *pks*$^+$ *E. coli* are detected more frequently in CRC patients (*8*, *9*, *11*–*14*), fueling the hypothesis that colibactin exposure may play a role in the initiation and/or progression of cancer.

Understanding the molecular basis of colibactin's genotoxic activity has been particularly challenging because this natural product has been recalcitrant to traditional isolation and structure elucidation approaches. Studying biosynthetic enzymes and identifying shunt products from *pks* mutant strains revealed structural information, including the unexpected incorporation of cyclopropane rings into colibactin, leading to the proposal that it directly alkylates DNA (*15*–*17*). Subsequent discovery of colibactin-derived DNA adducts and the observation that *pks*$^+$ *E. coli* generate DNA interstrand cross-links (ICLs) in vitro and in cell lines further supported this hypothesis (*18*–*20*). Additional biochemical studies, chemical synthesis, and isolation attempts ultimately led to the proposal that colibactin is a pseudosymmetric molecule containing two electrophilic cyclopropane "warheads" capable of alkylating DNA at adenine (Fig. 1A and fig. S1A) (*21*, *22*). These warheads are connected by a central scaffold of unresolved structure that is predicted biosynthetically to be an α-aminoketone (or its enolamine tautomer); however, this motif likely undergoes rapid oxidation to the corresponding α-ketoimine, followed by hydrolysis to a 1,2-diketone that is susceptible to oxidative C–C bond cleavage (fig. S1A) (*23*). This highly unstable central structural motif has been replaced by two methylene groups in a "stable" synthetic colibactin analog (fig. S1B) (*24*). However, this analog is a minor component of an inseparable product mixture, with the major components being two β-hydroxy lactam ring diastereomers of unknown biological significance. Though the proposed structure(s) of colibactin account for the activities of all essential biosynthetic enzymes and explain ICL formation (Fig. 1A and fig. S1A), notable gaps in our understanding of its structure and activity remain, including the identity and function of its central scaffold.

The molecular details underlying colibactin's interaction with DNA are also unclear. The discovery of mutational signatures arising from exposure of human cells and organoids to *pks*$^+$ *E. coli* has provided intriguing indirect insights (*25*, *26*). These mutational signatures are primarily thymine (T)–to–cytosine (C) single-base substitutions and indels that occur within adenine (A)– and T-rich sequence motifs (i.e., 5′-AAWWTT-3′, where W represents A or T), and their transcriptional strand bias is consistent with ICL formation between two adenines. Colibactin-induced DSBs occur within identical AT-rich sequences and are suggested to arise from degradation of ICLs (*26*). Additionally, molecular modeling suggests that the colibactin-DNA ICL spans 4 to 5.5 Å [or 3 to 4 base pairs (bp)] but could not elucidate the specific adenines alkylated or the molecular details of DNA binding (*26*). Colibactin mutational signatures have been detected in many cancer genomes, including 5 to 20% of CRC genomes; occur in driver genes, such as *APC*; and are correlated with early-onset CRC (*25*–*33*). We also recently identified colibactin-DNA adducts in human colonoscopy samples (*34*). Together, these data indicate that humans are exposed to colibactin, strengthening its connection to cancer development. They also provide indirect evidence that colibactin cross-links DNA in a highly specific manner. However, we currently lack direct information regarding the specificity and structure of the colibactin-DNA ICL, limiting our understanding of how this natural product targets DNA and the origins of mutational signatures arising from this DNA damage.

Results

To study colibactin-DNA ICL formation in detail, we initially identified a short, double-stranded oligodeoxynucleotide (dsODN) that was cross-linked upon exposure to *pks*$^+$ *E. coli*. We generated colibactin in situ from bacterial metabolism because of the prominent gaps in our understanding of this metabolite and the concern that synthetic analogs may differ in activity and/or selectivity. Examining colibactin's reactivity toward plasmid fragments identified a 500-bp region of pET28(a) that was cross-linked efficiently. Systematically truncating this 500-nucleotide oligomer identified a 50-nucleotide oligomer that is cross-linked (71% ICL formation) after a 5-hour incubation at 37°C with *pks*$^+$ *E. coli* in Dulbecco's minimum essential medium (DMEM)–HEPES medium (Fig. 1B-C). No ICL formation was observed when incubating the 50-nucleotide oligomer with an isogenic *pks*$^-$ *E. coli* strain. We noted that

[1]Department of Chemistry and Chemical Biology, Harvard University, Cambridge, MA, USA. [2]Department of Molecular and Cellular Biology, Harvard University, Cambridge, MA, USA. [3]Masonic Cancer Center, University of Minnesota, Minneapolis, MN, USA. [4]Department of Chemistry, Massachusetts Institute of Technology, Cambridge, MA, USA. [5]Department of Chemical Engineering, Massachusetts Institute of Technology, Cambridge, MA, USA. [6]Structural Biology Initiative, City University of New York (CUNY) Advanced Science Research Center, New York, NY, USA. [7]Department of Medicinal Chemistry, University of Minnesota, Minneapolis, MN, USA. [8]Howard Hughes Medical Institute, Harvard University, Cambridge, MA, USA. [9]Broad Institute of MIT and Harvard, Cambridge, MA, USA. ***Corresponding author. Email: balskus@chemistry.harvard.edu (E.P.B.); dsouza@g.harvard.edu (V.M.D.); villa001@umn.edu (P.W.V.); balbo006@umn.edu (S.B.)** †These authors contributed equally to this work. ‡Present address: Department of Chemistry, Massachusetts Institute of Technology, Cambridge, MA, USA.

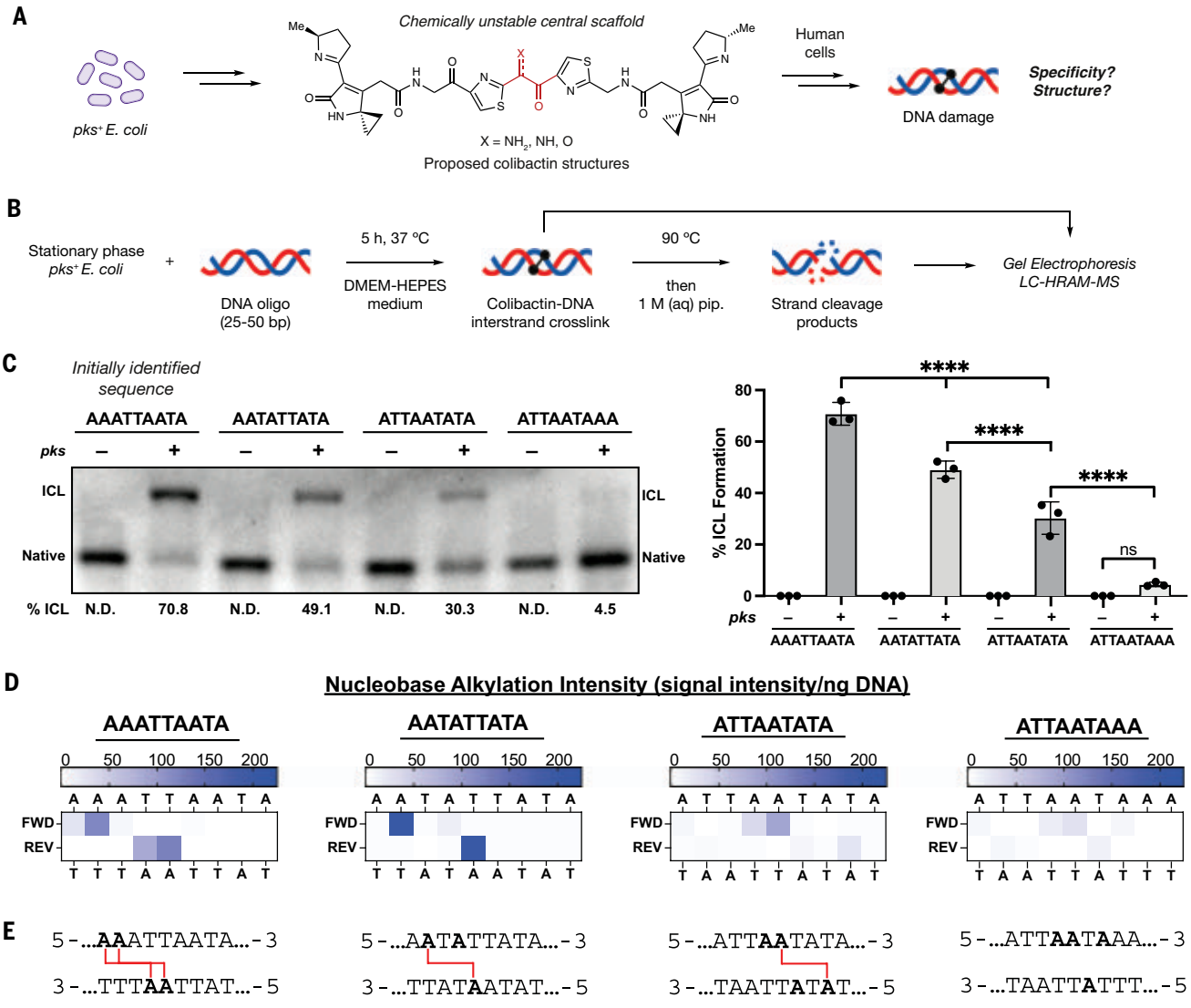


Fig. 1. The chemically unstable gut bacterial genotoxin colibactin forms DNA ICLs in a sequence-specific manner. (**A**) The chemical structure of colibactin and the structure and specificity of the colibactin-DNA ICL are unresolved. (**B**) Experimental workflow for characterizing ICL formation on 25- to 50-bp double-stranded oligonucleotides using colibactin produced in situ by *pks*$^{+}$ *E. coli*. (**C**) Extent of ICL formation within 50-nucleotide oligomers possessing the indicated sequence motifs. Cross-link formation was identified by denaturing gel electrophoresis and quantified by densitometry. Quantified values are displayed as a column plot. ns, not significant; ****$P < 0.0001$; one-way analysis of variance and Tukey's multiple comparison test. (**D**) Residue-specific alkylation of 25-nucleotide oligomers containing the indicated sequence motifs. Alkylation intensities were determined through LC-HRAM-MS analysis and normalized to total DNA injected. The intensity reported is the difference between the average detected in assays with *pks*$^{+}$ *E. coli* and the average detected in assays with *pks*$^{-}$ *E. coli*. (**E**) Inferred ICL locations within tested sequence motifs. All alkylated residues are bolded, and those cross-linked are connected by red lines. All data are mean ± SD with $n = 3$ biological replicates. Full 50- and 25-bp sequences are available in the supplementary materials. N.D., not determined.

this 50-nucleotide oligomer contained an AT-rich motif (5′-AAATTAATA-3′) that is consistent with previously reported colibactin mutational signatures (*25*, *26*), leading us to hypothesize that colibactin directly forms ICLs within this region.

To determine the site(s) of alkylation within this sequence motif, we developed a strand cleavage assay utilizing liquid chromatography–high-resolution accurate mass–mass spectrometry (LC-HRAM-MS) for detection (Fig. 1B and fig. S2). Colibactin-ICLs are thermally unstable and spontaneously depurinate to form abasic sites when heated to 90°C (*35*, *36*). Subsequent base treatment induces strand cleavage at the colibactin-specific abasic sites, and the masses of the resulting strand cleavage products are determined by isotopically resolved mass deconvolution of the LC-HRAM-MS data to identify the location and measure the relative abundance of DNA alkylation (Fig. 1, D and E).

We applied this assay to a *pks*$^{+}$ *E. coli*–exposed 25-nucleotide oligomer containing the AT-rich motif identified from the 50-nucleotide oligomer. This shortened dsODN was chosen to increase the analytical capability of the LC-MS analysis. The results indicate site-specific alkylation of this dsODN by colibactin at 5′-**AA**ATTAATA-3′ (where alkylated nucleotides are bolded or opposite to underlined nucleotides) (Fig. 1, D and E, and figs. S2 and S3). The accuracy of our LC-MS approach was confirmed by subjecting a 5′-6-carboxyfluorescein–labeled 50-nucleotide oligomer to our cross-linking and strand cleavage protocol and determining alkylation site locations using traditional Maxam-Gilbert gel sequencing (figs. S4 to S6) (*37*).

This result suggests that the colibactin-DNA ICL spans 3 to 5 bp. To determine the precise length of the ICL, we repeated our cross-linking and strand cleavage assays with a 50- and 25-nucleotide oligomer

containing the sequence 5′-AATATTATA-3′, which has the potential to form ICLs between pairs of adenines 2 to 8 bp apart. The results of this assay indicated that colibactin forms a single ICL between two adenines spanning 4 bp (5′-A**A**TAT̲TATA-3′). This is consistent with previous studies showing that colibactin-induced DSBs have 2-bp overhangs (*26*) and suggests that the four sites of alkylation within the 5′-AAATTAATA-3′ motif that we initially tested likely correspond to a mixture of two colibactin-DNA ICLs (Fig. 1, D and E, and fig. S4). The extent of ICL formation was reduced compared with that of the initial sequence, perhaps owing to this sequence possessing only one recognition site (Fig. 1, C to E).

We further explored the position of colibactin-DNA ICL formation by performing incubations with dsODNs containing A to T transversions at the previously observed sites of alkylation (5′-ATTAATATA-3′). If colibactin can alkylate at the same position but on the opposite strand, we would expect ICL formation in the same location (i.e., 5′-AT̲TA**A**TATA-3′); if not, we would expect the ICL to shift to a new location (5′-ATTA**A**TAT̲A-3′). ICL formation and strand cleavage analysis revealed the ICL in the new location, suggesting that colibactin preferentially cross-links at a TA base pair three positions downstream from the initial A (Fig. 1, C to E). Lastly, we detected little to no alkylation of dsODNs containing 5′-ATTAATAAA-3′, which has no 5′-AWWT-3′ motifs (Fig. 1, C to E). Taken together, these data suggest that colibactin-DNA ICLs form at 5′-W**A**WWT̲W-3′ motifs.

We next introduced single GC base pairs into the 5′-AATATT-3′ motif to test colibactin's specificity for adenine alkylation (fig. S7A) and tolerance for changes to the surrounding sequence. It has been postulated that colibactin may not recognize GC-containing sequences due to their altered DNA groove widths (*26*). Single GC base pair–containing sequence variants were largely cross-linked at comparable levels to that of the parent sequence except for 5′-AGTATT-3′ and 5′-AATACT-3′, which contain a substitution at an alkylation site, and 5′-AATATC-3′, which contains a substitution at an outer base pair flanking this site (fig. S7B). Strand cleavage analysis revealed sites of alkylation identical to those of the parent sequence, except for 5′-AGTATT-3′ and 5′-AATACT-3′. Though no alkylation was observed at the newly incorporated guanine in these sequences, formation of colibactin-DNA monoadducts was observed at the adenine on the other strand (fig. S7, C and D). Altogether, these studies directly support colibactin forming bis-adenine ICLs within sequence motifs matching previously reported sites of DSBs and mutational signatures, strengthening the evidence that colibactin ICLs are the inciting incidents to these downstream events. Our results also reveal that colibactin can react within a broader sequence context than suggested by the mutational signatures.

With direct evidence that colibactin alkylates AT-rich DNA in a sequence-specific manner, we next sought to elucidate its groove specificity. On the basis of the structural characterization of colibactin-DNA adducts, colibactin is thought to alkylate N3 of adenine, which is accessible through the minor groove of DNA (*18*). Prior calculations also suggested that shape complementarity and electrostatics could lead to a preference for minor groove binding (*26*). We directly tested this proposal by incubating the 50-nucleotide oligomer containing the 5′-AAATTAATA-3′ motif with *pks*$^+$ *E. coli* in the presence of DNA-binding small molecules possessing differing topological preferences (fig. S8) after confirming that these molecules had no effect on bacterial growth or colibactin production (figs. S9 and S10). AT-rich minor groove binders [netropsin and 4′,6-diamidino-2-phenylindole (DAPI)] (*38*, *39*) inhibited ICL formation in a dose-dependent manner (Fig. 2). By contrast, a major groove binder (methyl green) (*40*) and a GC-rich minor groove binder (actinomycin D) (*41*) showed no effect. These results provide strong experimental evidence that colibactin specifically alkylates AT-rich minor grooves.

We next investigated the site of colibactin DNA alkylation on adenine. As highlighted above, we previously characterized an N3-adenine colibactin-DNA adduct (*18*). Additional adenine adducts containing the other "half" of colibactin were identified by using mass spectrometry but were not characterized by nuclear magnetic resonance (NMR) spectroscopy, leaving their connectivity unknown (*21*, *22*). Hypothesizing that both colibactin cyclopropanes alkylate the N3 position of adenine, which would be consistent with selective minor groove binding, we incubated *pks*$^+$ *E. coli* with 50-nucleotide oligomers containing a 5′-A**A**TATT-3′ sequence motif in which the bolded residue was replaced with N3-deaza-deoxyadenosine (dAdo) (*42*), eliminating the possibility for N3-dAdo adducts to form. ICL formation was abolished when N3-deaza-dAdo was incorporated into the forward, reverse, or both strands (fig. S11). Strand cleavage analysis of assays with 25-nucleotide oligomers containing these sequence variants also showed no alkylation of N3-deaza-dAdo, instead revealing monoadduct formation for the singly substituted variants. The presence of monoadducts was confirmed using the LC-HRAM-MS cleavage assay (fig. S11, C and D). Taken together, these data indicate that colibactin exclusively forms bis-N3-dAdo ICLs within the minor groove of AT-rich DNA.

To gain initial insights into the structure of the colibactin-DNA ICL, we characterized 14- and 25-bp oligo substrates containing previously examined sequence motifs with LC-HRAM-MS after *pks*$^+$ *E. coli* incubation (Fig. 3). For each dsODN that became cross-linked, we observed a mixture of native and modified dsODNs. After direct deconvolution analysis of the 14-bp dsODN samples, we measured a mass difference of mass/charge ratio (*m/z*) 771.26 (Fig. 3). The 25-bp dsODN samples required additional analysis and provided mass differences consistent with the value measured for the 14-bp samples (fig. S12; see supplementary discussion). We did not observe any other species in these assays. All dsODNs incubated with *pks*$^-$ *E. coli* showed no mass shift. The observed mass is consistent with formation of a single ICL arising from the proposed colibactin structure containing an α-ketoimine. This unexpected observation sharply contrasts with the structures proposed for colibactin detected in aqueous solution and in putative colibactin and ICL degradation products, which all contain a 1,2-diketone (*21*, *22*, *43*). Additionally, the observed mass of colibactin indicates no oxidation of the ring-opened electrophilic warheads, unlike in previously characterized colibactin-DNA adducts (*18*–*21*). This direct characterization of the colibactin-DNA ICL through MS helps to resolve important aspects of colibactin's structure.

To understand the molecular details of how colibactin binds and cross-links DNA, we used solution-state NMR. This required generating the colibactin-DNA ICL on a large scale using *pks*$^+$ *E. coli*. We chose a 14-bp dsODN with a palindromic sequence (5′-CGCGA**A**TAT̲TCGCG-3′) and substituted A6 with 2′-fluoro-deoxyadenosine to increase the glycolytic bond strength and minimize depurination (*44*). To access sufficient quantities of the colibactin-DNA ICL (~15 nmol), hundreds of small-scale incubations were performed in 96-well plates, combined, and purified to provide a mixture of cross-linked (~55 to 65%)

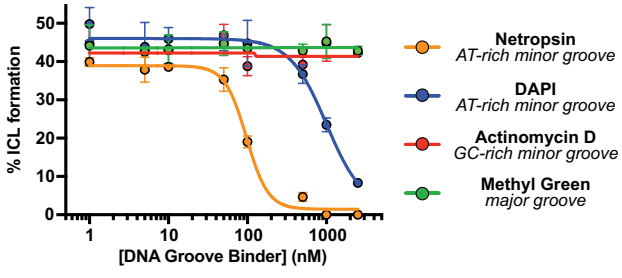


Fig. 2. Colibactin binds AT-rich regions of the minor groove. ICL formation by *pks*$^+$ *E. coli* in the presence of select DNA groove–binding small molecules. Dose-dependent inhibition of ICL formation by AT-rich minor groove binders was observed by denaturing gel electrophoresis and quantified by densitometry. Data are mean ± SD with $n = 3$ biological replicates.

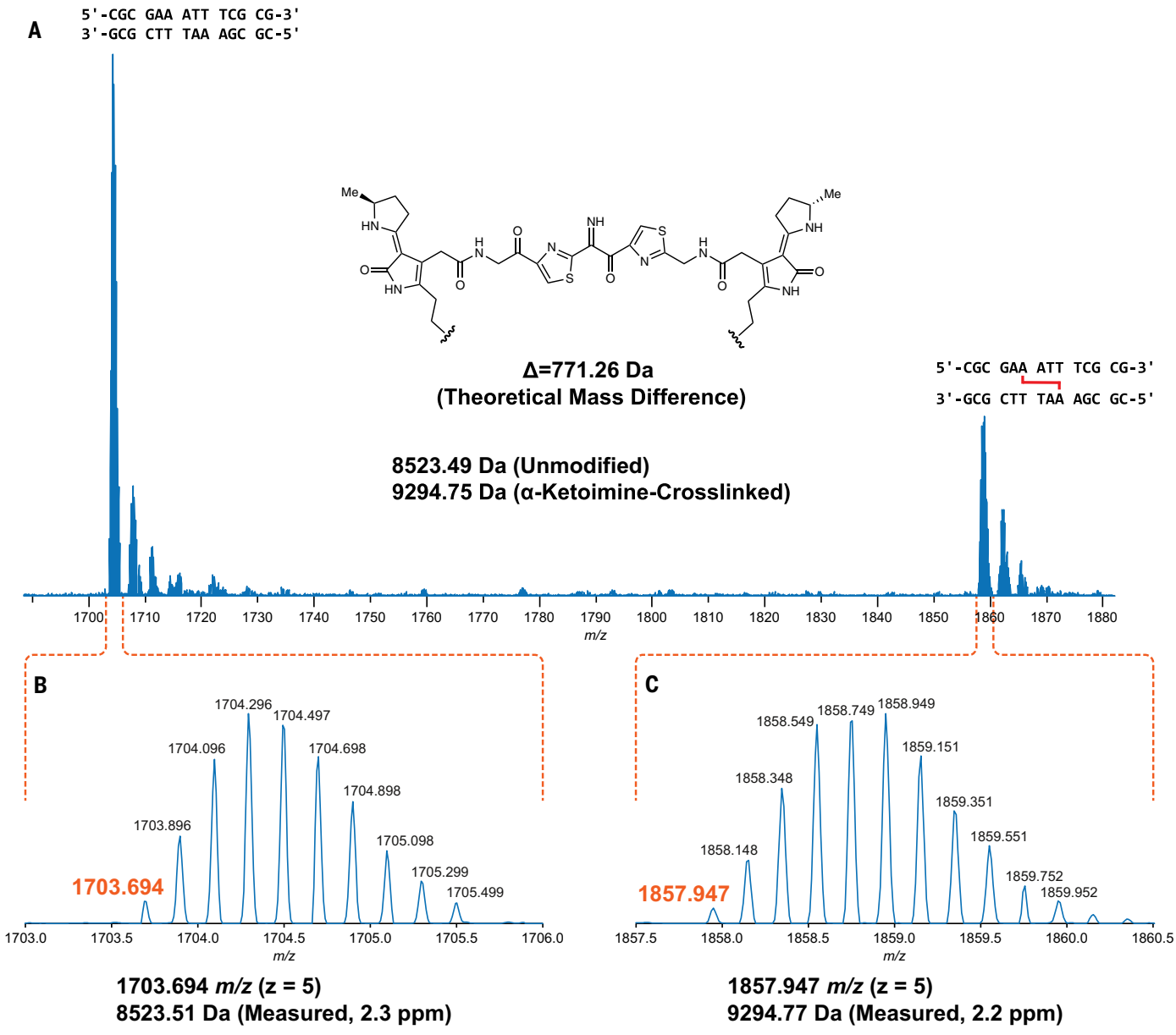


Fig. 3. MS analysis of an intact ICL reveals a central α-ketoimine in colibactin. HRAM LC analysis of cross-linked 14--nucleotide oligomer DNA double-strand oligonucleotide exposed to *pks*$^{+}$ *E. coli*. (**A**) Full scan spectrum containing −5 charge state signal of unmodified and modified 5′-CGCGAAATTTCGCG-3′ double-strand oligonucleotides. (**B**) Expanded region of spectrum corresponding to the unmodified oligonucleotide. (**C**) Expanded region of the spectrum corresponding to the modified oligonucleotide.

and free DNA. Thus, we first assigned the spectra of free DNA (with and without the 2′-fluoro-A6 modification), which allowed for comparative, unambiguous assignments of DNA chemical shifts that are perturbed upon cross-linking to colibactin. Overall, we did not observe any substantial changes in base-to-ribose nuclear Overhauser effect (NOE) walks throughout the DNA molecule, indicating that the overall B-form groove parameters are maintained upon colibactin cross-linking. This observation suggests that the shape of colibactin is complementary to that of the minor groove.

The structural data verified the sites of alkylation by colibactin identified in our earlier experiments. Compared with the spectra of free DNA, the aromatic ring protons of $A6_a$ and the equivalent $A6_b$ (complementary strand) residues had the largest chemical shift change, with the H2 protons moving downfield by ~0.36 and ~0.26 parts per million (ppm), and the H8, by ~0.83 and ~0.78 ppm, respectively (fig. S14A). By contrast, the average change for the other 2′-deoxyadenosines in the DNA was <0.04 ppm. As expected, the majority of interactions between colibactin and DNA are located at the ATAT sequence where colibactin alkylates, but interactions were also observed from the flanking base pairs, $A5_a$–$T10_b$ and $T10_a$–$A5_b$, indicating an expanded recognition motif.

The pseudosymmetric nature of the colibactin-DNA ICL was also readily discernible. First, equivalent protons from both the colibactin and the palindromic DNA have distinct chemical shifts; for example, the equivalent $A6_a$ and $A6_b$ H8s differ by 0.05 ppm, indicating that they are in slightly different environments (fig. S14A). Second, although such equivalent protons gave rise to similar NOE connectivities with protons in close proximities, the NOEs have slightly different intensities, indicating the same interactions but at different distances (fig. S15). Overall, with the exception of the pyrrolidine rings at either

end of colibactin, we observed NOEs from almost all of its protons to the extended AATATT sequence. The observations that define the orientation of the various colibactin rings with respect to the DNA groove are: (i) no connections from the terminal pyrrolidine rings; (ii) the thiazole hydrogens C34H and C39H gave connections to the outer deoxyribose hydrogens of $T9_a$ and $T10_b$ (H4′/H5′), respectively; and (iii) the N3H and N3′H amides and hydrogens of C27 and C28 (the carbon attached to the N3 of A6), which flank the pyrrolidinone rings, show connections to each other, thus confining the ring inside the groove (Fig. 4, B and D, and fig. S15). Consequently, the structures show that, whereas the terminal pyrrolidine rings point out of the minor groove, the thiazole rings are wedged in, aligning with the phosphodiester backbone with their bulky sulfur atoms pointing outward. Likewise, the pyrrolidinone rings of the warheads are stacked parallel to the groove, slightly outside of the AATATT sequence. This results in a tightly packed DNA-colibactin ICL with colibactin in an extended, concave conformation spanning along half a turn of the minor groove (Fig. 4, B and D, and fig. S14C). The curved shape and close contacts between its heterocyclic aromatic rings and the hydrophobic surfaces of the minor groove walls suggest that shape complementarity as well as van der Waals and hydrophobic interactions all contribute to colibactin-DNA binding. As discussed below, similar features are

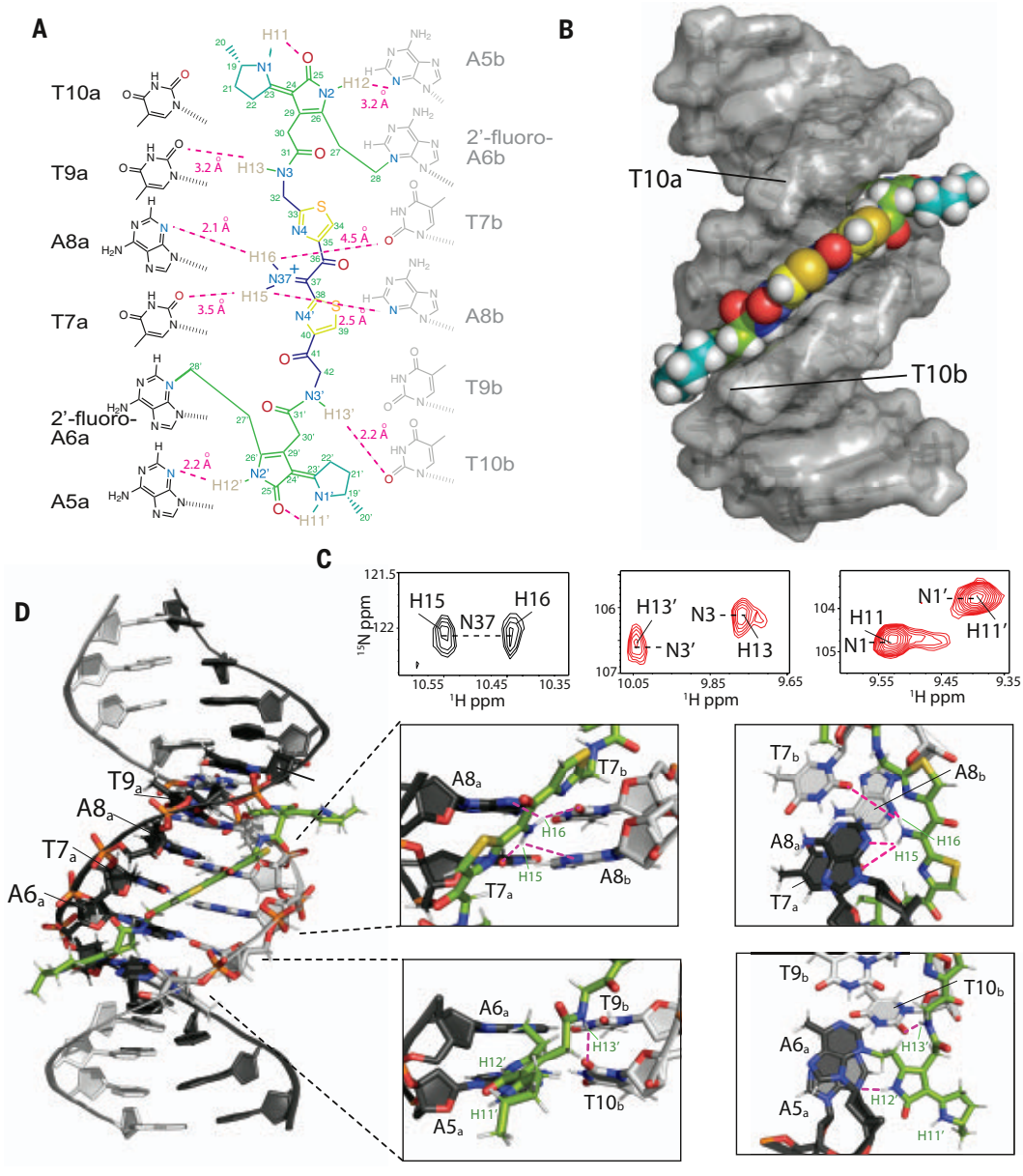


Fig. 4. Structure of the colibactin-DNA ICL. (**A**) Schematic and atom numbering of colibactin and its hydrogen bonding and electrostatic interaction with nucleotide bases, as denoted by magenta dashed lines. (**B**) Surface representation of the structure showing the pyrrolidine, thiazole, and pyrrolidinone rings stacked in between the minor groove edges of the DNA parallel to the long axis. (**C**) Portions of a two-dimensional HSQC experiment with a [^{15}N,^{13}C]-colibactin-DNA ICL sample showing two hydrogen atoms correlated with N37, indicating protonation of the nitrogen (left). The equivalent N3/3′ (center) and N1/1′ (right) nitrogens and their associated protons have different chemical shifts, indicating different environments and the pseudosymmetric nature of the interaction. (**D**) Cartoon representation of the interaction and zoomed-in views showing the placement of (i) colibactin iminium moiety with the electronegative atoms of the center T7A8 residues of the DNA (top) and (ii) the amide hydrogen (H13) and the pyrrolidinone ring hydrogen (H12) interacting with $T10_b$ and $A5_a$ nucleobase (bottom). For clarity, only the inner motif residues (A6 to T9) on the a-strand have been labeled.

found in other minor groove–binding natural products and synthetic compounds.

We also observed hydrogen bonds and/or electrostatic interactions from all nitrogen protons in colibactin, which may explain its specificity for the preferred sequence motif. First, although the NMR data confirmed the presence of a nitrogen in the central scaffold of colibactin, we found this nitrogen within an iminium functional group. Two distinct proton peaks are correlated with N37 in the ^{15}N–heteronuclear single quantum coherence (HSQC) experiment, indicating a protonation event at this site (Fig. 4C). Iminium formation may be explained by the central region of the AATATT binding pocket, which comprises the floor of the minor groove and provides a highly electronegative environment for colibactin, with N37 being near O2 of T7 and N3 of A8 of both strands. Although each iminium proton gives NOEs to A8H2/H1' protons of both strands, H16 had comparatively stronger NOEs, thus placing the iminium slightly closer to the a-strand of the DNA. The NOE correlations from these protons are thus in line with the iminium forming a hydrogen bond with N3 of A8$_a$ and electrostatic interactions with O2 of T7$_b$, O2 of T7, and N3 of A8$_b$. Second, the equivalent colibactin H13 and H13' amide protons showed connectivities to the flanking T9$_a$ and T10$_b$ H1', respectively, suggesting they are positioned to form hydrogen-bonding and electrostatic interactions with the O2 position of these thymines. Third, the H12 and H12' protons of colibactin's pyrrolidinone rings, which are the sites of alkylation, also showed connectivities to A5$_b$H1' and C11$_a$H2' as well as A5$_a$H1' and T10$_b$H2', respectively, indicating that these nitrogens are situated in the center of the groove, electrostatically interacting with the A5 N3 position on either end of the sequence motif (Fig. 4C and fig. S15). This orientation would position the cyclopropane rings of the colibactin warheads close to N3 of A6. Lastly, although H11 and H11' gave no connections to DNA, they were still in slow exchange and gave strong connectivities to the hydrogens in the pyrrolidine rings, indicating that they are most likely forming internal hydrogen bonds to the C25 and C25' carbonyl groups in the adjacent pyrrolidinone rings (fig. S15). These intramolecular hydrogen bonds may form prior to alkylation and, if so, would place the heterocyclic rings of the electrophilic warheads coplanar, enhancing their electrophilicity. Notably, we saw no evidence for intramolecular cyclization of colibactin (*24*), indicating that the ICL derives from a linear pseudosymmetric structure.

This structural information allows us to formulate a model for colibactin-DNA ICL formation (fig. S16). We propose that the central region of colibactin, with its concave shape and heterocyclic aromatic rings, facilitates binding within the minor groove of AT-rich DNA sequences. We also predict that colibactin-DNA binding will be enhanced by multiple positively charged functional groups. In addition to the positively charged pyrrolinium rings of the two electrophilic warheads, the positively charged nitrogen atom of the central aminoketone, enolamine, or α-ketoiminium of colibactin likely plays a critical role in its selectivity for AT-rich minor groove binding by providing favorable electrostatic interactions and hydrogen bonding to the central base pairs in the 5′-WAWWTW-3′ motif, which form the floor of the minor groove. Lastly, the structure also suggests that binding within the minor groove promotes inter- and intramolecular hydrogen bonding and electrostatic interactions involving the colibactin warheads that enhance their electrophilicity and orient the spirocyclopropanes and π-systems of the adjacent pyrrolinium heterocycles with the appropriate stereoelectronic alignment to trigger ring opening by N3 of adenine.

To test this model and, specifically, the importance of colibactin's central structural motif to the specificity of ICL formation, we compared its sequence specificity to that of the stable synthetic colibactin analog possessing two central methylene groups (Fig. 5A) (*24*). We posited that colibactin and the synthetic analog would have different preferences for alkylation of sequences containing multiple CG base pairs within the 5′-WAWWTW-3′ motif. If hydrogen bonding and electrostatic interactions with colibactin's central nitrogen atom are critical for sequence specificity, then exchanging the two central TA base pairs for CG base pairs should diminish alkylation owing to the resulting steric hindrance and electrostatic repulsion from the exocyclic amines of the two guanines, which alter the surface of the minor groove floor. By contrast, the stable colibactin analog lacking the central structural motif should tolerate this substitution.

We incubated either *pks*$^+$ *E. coli* or the synthetic analog with a series of 50-bp dsODNs that contained two GC base pairs at different positions within a 5′-AATATT-3′ motif and measured ICL formation using gel electrophoresis (Fig. 5B). As predicted, the introduction of two GC base pairs at the center of this motif almost completely abolished alkylation by colibactin. ICL formation was also abolished when GC base pairs were installed at the two sites of alkylation and greatly diminished when GC base pairs were introduced at the two outer positions flanking the alkylation site. Other substitutions had minimal effects on ICL formation. Notably, the specificity of the synthetic analog differs from that of natural colibactin (Fig. 5C). We observed a preference for alkylation at the 5′-AACGTT-3′ sequence, which is not targeted by natural colibactin, and minimal alkylation at other sequences. Lastly, we compared the reactivity of colibactin and the synthetic analog toward additional oligonucleotides containing two GC base pairs in the central positions (5′-AAGCTT-3′, 5′-AACCTT-3′, and 5′-AAGGTT-3′) (fig. S17). Again, colibactin did not alkylate these motifs, but the analog displayed robust ICL formation. These results further support a critical role for the central structural motif and its positively charged nitrogen atom in the selectivity of colibactin ICL formation.

To gain additional insight into the interactions influencing the specificity of colibactin-DNA ICL formation, we calculated the electrostatic potential (ESP) values centered on atoms in proposed colibactin structures bearing different central functional groups, both free and cross-linked to DNA (Fig. 6A and figs. S18 and S19). We observed the highest ESP on the iminium nitrogen atom of colibactin bearing a central α-ketoiminium (~664 kJ·mol^{-1}·e^{-1}), consistent with the α-ketoiminium having a positive charge. We calculated a lower ESP on the iminium nitrogen of the α-ketoiminium when this proposed colibactin was cross-linked to DNA compared with that of the corresponding free colibactin (Fig. 6, B and C, and figs. S20 and S21). This decrease could indicate stabilization by electrostatic or other noncovalent (e.g., hydrogen-bonding) interactions with the DNA. However, we did not observe a substantial decrease in ESP of the heavy atoms of the central functional groups in the other proposed colibactin structures when they were cross-linked to DNA, suggesting that the electrostatic interactions between DNA and colibactin are much stronger for the proposed structure bearing a central α-ketoiminium.

Additional calculations focused on DNA further support the importance of electrostatic interactions to colibactin-DNA recognition. Using DNAPhi to predict the ESP of the minor groove of the dsODN used for our structural studies, we found that, as expected, the center of the 5′-AATATT-3′ motif is substantially more electronegative than the other positions, accounting for the increased pK_a (where K_a is the acid dissociation constant) of N37 of colibactin and its protonation (Fig. 6D) (*45*). Substitution of a single central base pair with a CG base pair increased ESP at this position, whereas substituting both central base pairs, which abolished ICL formation by colibactin, resulted in a loss of this ESP differential (Fig. 6, E and F). Modeling interactions between colibactin and these different sequences showed distortions when guanines were introduced owing to repulsions from the large amino substituents of these central base pairs (Fig. 6, G to I). The outer base pairs flanking the alkylation site (A5$_a$ toT10$_b$ and T10$_a$ to A5$_b$) also contribute to the negative ESP, and modeling GC base pair substitutions at these positions also resulted in distortions and repulsions, potentially disrupting key hydrogen bonding and electrostatic interactions with the warheads and accounting for the reduced ICL formation in these sequences (fig. S22). This structure, experimental data, and computations reveal and explain colibactin's specificity for DNA alkylation, highlighting an

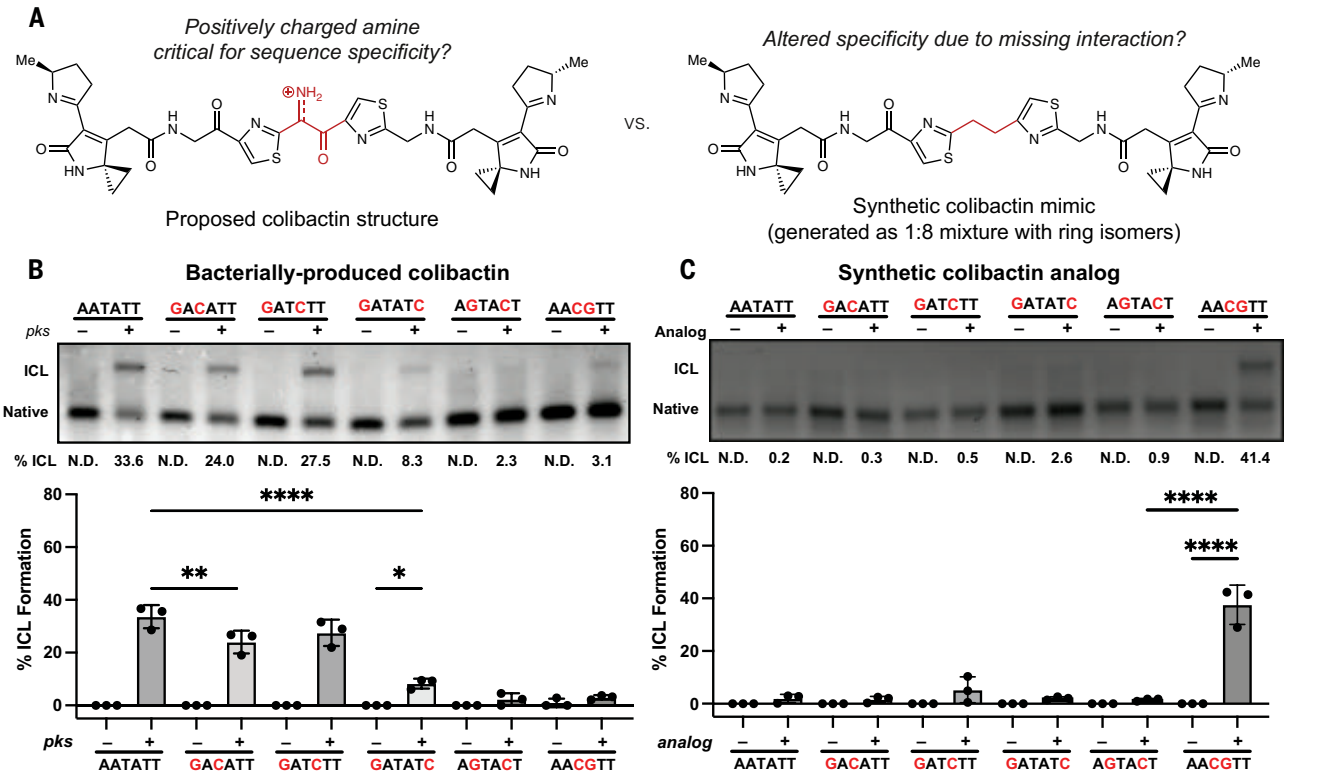


Fig. 5. The unstable central motif of colibactin influences its sequence specificity for ICL formation. (**A**) Structural comparison of bacterially produced colibactin and a synthetic "stable" colibactin analog suggests that the analog may have altered specificity for ICL formation. (**B**) Quantification of ICL formation by coincubation with bacteria through denaturing gel analysis for 50-nucleotide oligomers containing a double GC substitution within the sequence 5′-AATATT-3′. Results were quantified through densitometry and shown as bar plots. (**C**) Quantification of ICL formation by treatment with a colibactin analog through denaturing gel analysis for 50-nucleotide oligomers containing a double GC substitution within the sequence 5′-AATATT-3′. Results were quantified through densitometry and shown as bar plots. All data are mean ± SD with $n = 3$ biological replicates. ****$P < 0.0001$; **$P < 0.01$; *$P < 0.05$; not significant (ns), $P > 0.05$; one-way analysis of variance and Tukey's multiple comparison test. N.D., not determined.

especially notable role for electrostatic interactions involving its chemically unstable central motif.

Discussion

Gaining a molecular understanding of DNA-damaging agents is critical for advancing our understanding of their connections to cancer and use as therapeutic agents. As mutational signatures are increasingly identified in cancer genomes (*46*, *47*), it is imperative to elucidate their origins. Characterizing the DNA lesions that give rise to specific mutational signatures can provide starting places for investigating repair pathways and processes that lead to misrepair. DNA-targeting small molecules are also an important class of drugs (*48*). Studying the specificities and structures of DNA-binding and -alkylating natural products and synthetic compounds has revealed important chemical principles underlying small molecule–DNA recognition and reactivity (*49*, *50*). The high prevalence of *pks*$^+$ *E. coli* in many geographic locations (*34*), the accumulating evidence linking colibactin to CRC development (*5*–*14*, *25*–*33*), and the chemical instability of this genotoxin provide particularly strong motivation for understanding its DNA-damaging activity.

Leveraging advanced MS and NMR approaches, our studies of the colibactin-DNA ICL explain the locations of mutational signatures and enhance our understanding of this unstable natural product. We hypothesize that the α-ketoimine found in the colibactin-DNA ICL is derived from oxidation of an initial α-aminoketone or its enolamine tautomer (fig. S1A) (*23*, *51*), though the timing of this oxidation relative to DNA alkylation is unclear. The presence of this central functional group was unexpected owing to the reactivity of this structural motif and the structures proposed using MS for colibactin and related compounds detected in culture supernatants, which are all suggested to contain a 1,2-diketone. We also see no evidence for DNA alkylation by ring isomers, suggesting that these species, which are generated in the synthesis of stable colibactin mimics and have been observed in decomposition products (*24*, *43*), are likely not relevant for colibactin's DNA-damaging activity. Although the precise identity of the central functional group initially generated by the colibactin biosynthetic pathway remains elusive, our discovery highlights the relevance of proposed structures containing central nitrogen atoms, specifically the α-ketoimine, to colibactin-DNA alkylation. It has also been proposed on the basis of the identification of shunt products that the colibactin biosynthetic pathway produces multiple metabolites with the potential to cause DNA damage (*52*). Our observation of a single major ICL-forming species by MS and NMR calls this into question and suggests that there may be additional factors influencing colibactin production and/or stabilization that are still uncharacterized.

The elucidation of the colibactin-DNA ICL structure reveals how the structural features of colibactin contribute to its DNA-damaging activity (fig. S15). Colibactin can adopt an extended, concave conformation that complements the shape of the narrow, AT-rich minor groove. The heteroaromatic rings flanking the central α-ketoiminium and at the termini of colibactin lie parallel to the walls of the minor groove, enabling hydrophobic and van der Waals interactions. Notably, the orientation of the two thiazole rings reinforces colibactin's concave shape. The regions that link the central scaffold to the two electrophilic warheads contain multiple methylene groups, derived biosynthetically from glycine and malonyl–coenzyme A (*53*), making them

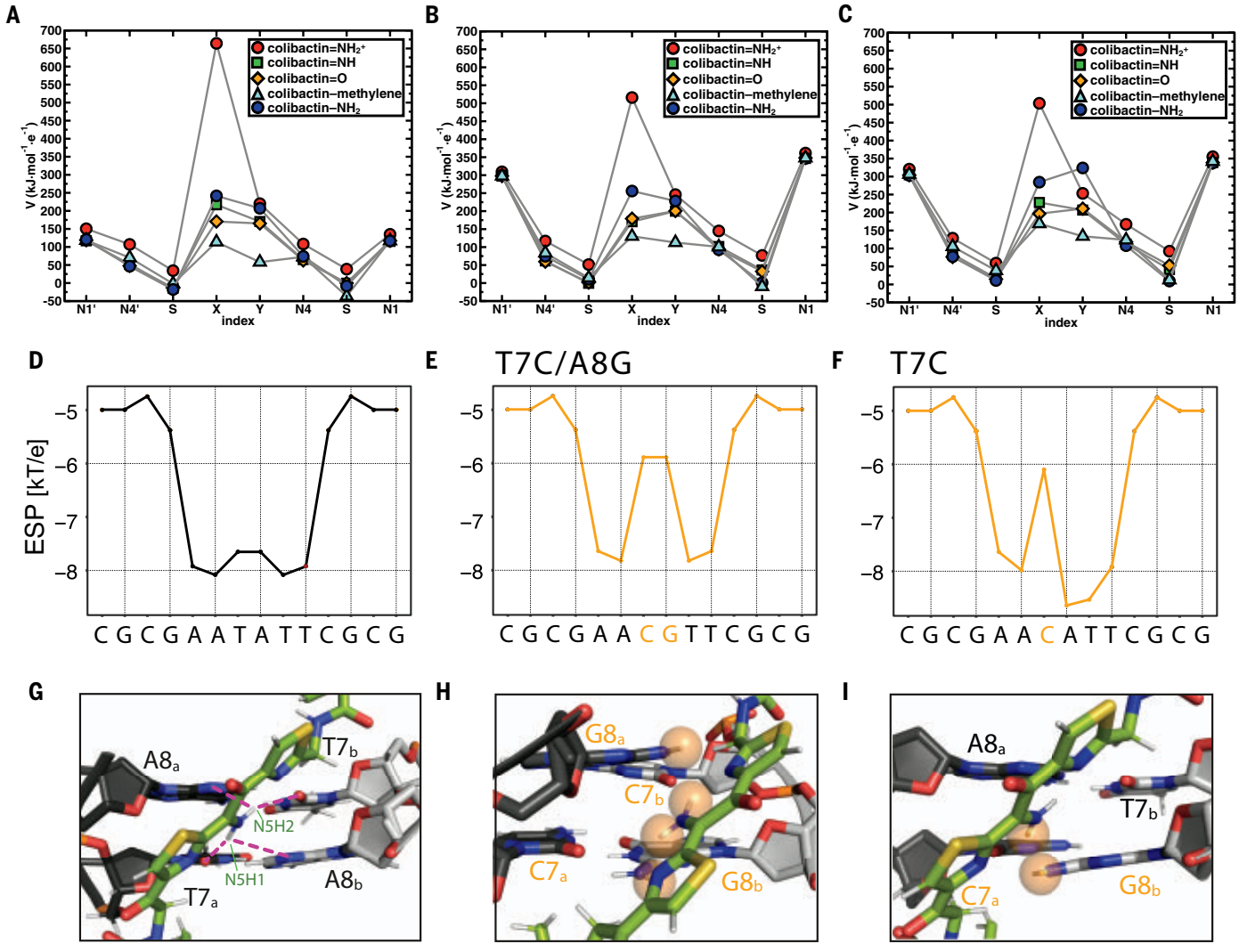


Fig. 6. Electrostatic and steric interactions involving colibactin's unstable central motif likely drive sequence specificity for DNA alkylation. (**A** to **C**) ESP values of proposed colibactin structures [volts (V) in $kJ{\cdot}mol^{-1}{\cdot}e^{-1}$] obtained from DFT optimization calculations of proposed colibactin structures at the B3LYP-D3/6-31G* level of theory. ESP values were calculated for (A) proposed structures of free colibactin, (B) proposed colibactin structures cross-linked to the doubly charged DNA sequence GAATATTC, and (C) proposed colibactin structures cross-linked to the doubly charged double-mutant DNA sequence 5′-GAACGTTC-3′. Proposed colibactin structures included the α-ketoiminium (colibactin=NH_2^+), α-ketoimine (colibactin=NH), diketone (colibactin=O), CH_2–CH_2 (colibactin–methylene), and enolamine (colibactin–NH_2) central functional groups. The indices X and Y correspond to the heavy element indices of the central functional group. X=N and Y=O for colibactin=NH_2^+, colibactin=NH, and colibactin–NH_2; X=O and Y=O for colibactin=O; and X=C and Y=C for colibactin–methylene. (**D** to **F**) Electrostatic potential calculations using DNAPhi predicting the highly electronegative environment in the sequence containing the preferred AATATT motif (black) and the decrease in electronegativity upon sequence substitution in the central motif (orange). (**G** to **I**) Comparison of the NMR structure with structural modeling of the substituted sequences shown in (E) and (F), showing potential steric clashes between colibactin and DNA (orange spheres).

conformationally flexible and likely facilitating curvature. Colibactin's positively charged functional groups should also enhance its affinity for DNA. Multiple nitrogen atoms within colibactin form hydrogen bonds and/or electrostatic interactions that influence binding specificity, including the central α-ketoiminium, the amide nitrogens of the two linker regions, and the two pyrrolidinone rings of the electrophilic warheads. Together, these interactions likely position the reactive cyclopropane rings close to N3 of the attacking adenines. This conformation may also be favored by the steric bulk of the pyrroline rings, which are too large to point into the minor groove. Lastly, an internal hydrogen bond within the electrophilic warhead between the carbonyl of the pyrrolidinone and a protonated pyrrolinium may be critical for enabling alkylation by enhancing electrophilicity and enabling proper stereochemical alignment of the breaking C–C bond of the spirocyclopropane with the extended π-system of the warhead.

Many of the chemical principles likely involved in mediating the specificity of colibactin binding and alkylation (convex shape, aromatic rings, positive charge, hydrogen bond donors) are well established to be important for AT-rich minor groove recognition by other natural products (*54*–*58*), including the polyamide DNA-binding compounds netropsin and distamycin (*38*) as well as the DNA-alkylating duocarmycins, which form monoadducts (*59*, *60*). However, colibactin distinctively combines features of AT-rich minor groove binding specificity with the capacity for interstrand cross-link formation, distinguishing it from other natural products that target DNA. Like other DNA-damaging natural products, the molecular understanding gained

in our studies may inspire the design of synthetic agents of therapeutic potential.

Notably, the interaction between the positively charged, central α-ketoiminium of colibactin and the minor groove of DNA is particularly distinctive among AT-rich minor groove–binding and –alkylating compounds, which typically contain positively charged functional groups at their termini. The decreased electrostatic potential of the central AATATT motif within the minor groove likely favors binding of the protonated α-ketoiminium of colibactin, contributing to specificity (*61, 62*). This interaction structurally resembles those of DNA binding proteins and small molecules, including the positively charged nitrogen atoms of the guanidinium side chain of arginine, which is enriched in proteins that bind AT-rich minor grooves (*57*) as well as the terminal amidine of the minor groove–binding natural product netropsin (*38*) (fig. S23).

The ICL structure, experiments with a synthetic colibactin analog, and calculations highlight the importance of colibactin's central structural motif for its sequence specificity. Notably, the pseudosymmetric structure of colibactin places the positively charged iminium equidistant from the two electrophilic warheads, suggesting that it is important for positioning these functional groups. Although the instability of the central portion of colibactin motivated the development of a "stable" synthetic colibactin analog lacking this functional group, we found that this analog has an altered sequence specificity compared with that of colibactin produced by *pks*$^+$ *E. coli*. This difference suggests that the synthetic analog will not phenocopy the effects of colibactin and calls into question its use as a biologically appropriate surrogate for the natural genotoxin. Our findings raise the questions of why such a chemically unstable structural motif would have evolved to play a notable role in colibactin's biological activity and how it is stabilized and/or protected within the cellular environment. Lastly, our work highlights innovative experimental strategies that may be used to discover and characterize additional unstable DNA-damaging microbial natural products that may be recalcitrant to traditional isolation approaches.

Materials and methods

Cell lines and cultures

The *pks*$^-$ strain used in this study was *E. coli* BW25113 possessing empty vector (pBeloBAC11) obtained from New England Biolabs. The *pks*$^+$ strain was *E. coli* BW25113 possessing pBeloBAC11-*pks* and was a generous gift from the Bonnet Laboratory. Starter cultures of all bacteria were grown overnight aerobically with shaking at 37°C in 5 mL of Luria-Bertani (LB-Lennox, RPI) broth containing 34 μg/mL chloramphenicol. Cultures were inoculated from the desired frozen glycerol stock. For all DNA incubation experiments unless stated otherwise, aliquots of each overnight culture were diluted 1:10 in room-temperature Dulbecco's modified Eagle's Medium (DMEM) supplemented with 25 mM HEPES (pH 7.4) and incubated at 37°C with constant shaking (190 RPM) until the optical density at 600 nm (OD_{600}) reached ~0.4 – 0.5.

Annealing of synthetic oligonucleotides

Oligonucleotides used in this study were purchased dry from Sigma Aldrich, Integrated DNA Technologies, or Genewiz and reconstituted upon arrival in TE buffer (10 mM Tris-HCl, 1 mM EDTA pH 8.0) to make 100 μM stock solutions. Aliquots of complementary oligonucleotide solutions were combined in a 1:1 equimolar ratio in annealing buffer (10 mM Tris-HCl, 50 mM NaCl, pH 8.0) to make a 10 μM solution. For example, 10 μL of each oligo stock solution were mixed with 80 μL of annealing buffer. The resulting solutions were incubated at 95°C for 5 min in a heat block, then slowly cooled to room temperature over ~2 hours. To verify proper annealing, samples were verified by size using agarose gel electrophoresis. 4% Tris-Acetate-EDTA (TAE) gels were made using NuSieve 3:1 agarose (Lonza) and run at 80 V for 60 min. Gels were pre-stained with Sybr Safe (Thermo Fisher) and visualized with an Azure Biosystems 400 Imager. A table of annealed oligonucleotide substrates is provided in the Supporting Information.

DNA cross-linking assay – bacterial incubations

The protocol was adapted from previously reported assays (*20*, *24*, *35*). 2 μg of the desired oligo nucleotide substrate was diluted to 140 μL of DMEM-HEPES medium in either 1.5 mL Eppendorf tubes or a 96-well culture plate (VWR). DNA solutions were then inoculated with 60 μL of freshly grown bacteria at an OD_{600} = 0.4 – 0.5 (*pks*$^-$ or *pks*$^+$ *E. coli*; ~20 × 10^6 cells) and incubated at 37°C aerobically for 5 hours without shaking. If cultured in a 96-well plate, OD_{600} measurements were taken every 5 min to assess growth with brief shaking before each measurement. After this time, the bacteria were pelleted by centrifugation at 10,000 × g for 3 min (4°C) and the DNA-containing supernatants were transferred to fresh Eppendorf tubes containing 20 μL of 3 M NaOAc, pH 5. Cell pellets were either saved for *N*-myristoyl-D-asparagine quantitation or discarded. DNA was precipitated by adding 660 μL of cold, 95% EtOH (aqueous, v/v) to the acidified supernatants and storing samples at –20°C for ~16 hours. The precipitated DNA was isolated by centrifugation at 16,100 × g for 20 min (4°C) and removal of the supernatant. The resulting DNA pellet was briefly washed with 200 μL of 70% EtOH (aqueous, v/v) by inversion and re-pelleted by centrifugation at 16,100 × g for 20 min. The supernatant was removed, and the DNA pellet was air dried for ~5 – 10 min before reconstitution in 51 μL of TE buffer. The concentrations of all DNA samples were determined by analyzing a 1 μL aliquot on a Nanodrop 2000 spectrophotometer (Thermo Fisher). From this point on, all DNA samples were kept on ice while in use or stored at –20°C to reduce degradation of colibactin-ICLs.

DNA cross-linking assay – synthetic colibactin analog

The protocol was adapted from previously reported methods and the procedure described above (*24*). Briefly, 200 ng of the desired oligo nucleotide substrate was diluted in a citrate buffer (10 mM, pH 5.0) and treated with a mixture of synthetic colibactin analogs (100 μM of a 1:8 mixture of uncyclized and cyclized analogs in DMSO) to a final volume of 20 μL (5% DMSO v/v in water). Assay mixtures were incubated at 37°C for 1 hour without shaking and were used immediately for electrophoresis.

Interstrand cross-link analysis by denaturing gel electrophoresis

The protocol was adapted from previously reported methods (*35*). Briefly, 10 μL aliquots of all DNA samples to be analyzed were diluted to 10 ng/μL in TE buffer. DNA concentrations were verified by Nanodrop and adjusted if needed. While on ice, 5 μL of '1% Denaturing Buffer' (1% m/v NaOH, 6% m/v sucrose, 0.01% m/v Orange G) were added to 10 μL of each diluted sample (~100 ng DNA). The denatured samples were then loaded into a 4% Tris-Acetate-EDTA (TAE) gel pre-stained with Sybr Gold (Thermo Fisher). The gel was run at 80 V for 60 min and visualized on an Azure Biosystems 400 Imager. Gel bands were further quantified using ImageJ. Percent cross-linking was calculated by dividing the ICL band intensity by the sum of both ICL and native DNA bands and multiplying by a factor of 100.

DNA strand cleavage assay

Individual oligo substrates were subjected to the DNA cross-linking protocol described above except that the resulting DNA pellets were redissolved in 45 μL of TE buffer. Samples were then heated to 90°C for 1 hour using a heat block to induce depurination of colibactin ICLs. After samples cooled to room temperature, 5 μL of 3 M NaOAc, pH 5 and 150 μL of cold, 95% EtOH were added in sequence. Samples were stored at –20°C overnight to induce DNA precipitation. Precipitated DNA was pelleted by centrifugation (20 min at 16,100 × g) and the supernatant was removed by pipetting. DNA pellets were briefly air dried (~5 min) and then dissolved in 50 μL of 1 M aqueous piperidine. Samples were heated to 90°C for 30 min, cooled to room temperature,

and evaporated to dryness using a Labconco Centrivap (45°C for ~1 hour). The resulting DNA pellets were reconstituted in 51 μL of TE buffer. The sample concentration was determined by Nanodrop analysis. All samples were stored at −20°C until further analysis. 5′-FAM-labeled DNA samples were analyzed by sequencing polyacrylamide gel electrophoresis while unlabeled samples were subjected to LC-HRAM-MS.

Analysis of strand cleavage products by sequencing polyacrylamide gel electrophoresis

150 mL of 15% UreaGel solution was prepared by combining SequaGel UreaGel 19:1 denaturing gel reagents (National Diagnostics) according to the manufacturer's protocol. Polymerization was initiated by adding 60 μL of tetramethylethylenediamine (TEMED; Sigma Aldrich) and 1.2 mL of freshly prepared 10% ammonium persulfate (VWR). This solution was used to cast a 12 in × 16 in × 0.75 mm gel which solidified over 1 hour. Prior to sample loading, the gel was pre-run for 30 min at 50 W in Tris-Borate-EDTA (TBE) buffer and all wells were flushed to remove residual urea. Strand cleavage samples were prepared for loading by mixing a 12 μL aliquot (35 ng/μL) with 12 μL of 2X TBE-Urea Sample Buffer (Novex) and heating the mixture to 95°C for 5 min. The corresponding A+G Maxam-Gilbert ladders were generated by a previously reported method (*63*). Ladders were diluted to 125 ng/μL and prepared for loading analogously to the strand cleavage samples. After ladder and sample loading, gels were run at a constant 50 W for 4 hours. Gel imaging was performed using an Azure Sapphire Imager set for fluorescence detection (ex. 488/ em. 518). For the experiments in Fig. 1C, 2, 5B, S7C, and S11B the "auto-exposure to region" setting was used during "Live Mode", which focuses the exposure on a selected region to avoid under- or overexposure. This was used in conjunction with the "capture selected region" setting which images a selected portion of a gel. The exposure setting was "Wide Dynamic Range" for all gels. For the experiments in Fig. 5C and S17, full gel images were processed in Adobe Photoshop to add an invert layer, and the brightness, contrast and exposure were globally modified to enhance visibility of bands against the background. See Appendix S1 for gel images.

Analysis of intact colibactin-DNA interstrand cross-links by LC-MS

Sample preparation: 2-3 μg of each of the oligonucleotides was dissolved in 50 μL of 10 mM Tris Buffer containing 1 mM EDTA and transferred to 1.2 mL silanized vials for injection on the LC-MS.

Chromatography for LC-MS: For each sample, 5 μL were injected onto an UltiMate 3000 RSLCnano UPLC (Thermo Scientific, Waltham, MA) system. Separation was performed using a Shodex HILICpak VN-50 2.0 × 150 mm column (Showa Denko K.K., Tokyo, Japan) maintained at 15°C using (A) water with 10 mM ammonium acetate and (B) 90:10 acetonitrile:water with 10 mM ammonium acetate. Initially 100% B at a flow rate of 200 μL/min was maintained for 6 min followed by linear gradient to 15% B and flow rate to 150 μL/min with a 3 min re-equilibration between injections at the initial conditions.

Mass spectrometry: All mass spectrometric data was acquired with an Orbitrap Lumos mass spectrometer (Thermo Scientific, Waltham, MA). Negative mode electrospray ionization was used with a source voltage of 2.5 kV, a sheath gas setting of 15, and a capillary temperature of 400°C. Data was collected in profile mode at a resolution setting of 120,000 with a Mass Range setting at High. The S-Lens RF level setting was 60% with full scan detection of *m/z* 1500-2500 using a normalized AGC Target of 250%, a Maximum Injection Time of 100 ms, and 10 microscans.

Analysis of colibactin-induced strand cleavage products by LC-MS

Sample preparation: A total amount of 2 μg of each of the cleavage product samples was dissolved in 50 μL of 10 mM Tris Buffer containing 1 mM EDTA and transferred to 1.2 mL silanized vials for injection on the LC-MS.

Chromatography for LC-MS: From each sample 5 μL were injected onto an UltiMate 3000 RSLCnano UPLC (Thermo Scientific, Waltham, MA) system. Separation was performed using a Shodex HILICpak VN-50 2.0 × 150 mm column (Showa Denko K.K., Tokyo, Japan) maintained at 15°C using (A) water with 10 mM ammonium acetate and (B) 90:10 acetonitrile:water with 10 mM ammonium acetate. Initially, 100% B at a flow rate of 200 μL/min was maintained for 6 min followed by linear gradient to 40% B over 36 min followed by 0% B over 7 min, with a 4 min hold at 0% B and a 5 min re-equilibration between injections at the initial conditions.

Mass spectrometry: All mass spectrometric data was acquired with an Orbitrap Lumos mass spectrometer (Thermo Scientific, Waltham, MA). Negative mode electrospray ionization was used with a source voltage of 2.5 kV, a sheath gas setting of 15, and a capillary temperature of 400°C. Data was collected in profile mode at a resolution setting of 120,000 with a Mass Range setting at High. The S-Lens RF level setting was 100% with full scan detection of *m/z* 700-2500 using a normalized AGC Target of 250%, a Maximum Injection Time of 200 ms, and 5 microscans.

Oligonucleotide data analysis: Data analysis was performed using Thermo Scientific's Protein Deconvolution and FreeStyle software packages and the online Mongo Oligo Mass Calculator tool.

Cleavage assay MS data analysis: Identifications and relative abundance measurements of the base treatment-induced cleavage sites of the colibactin-exposed double strand oligonucleotides were made using isotopically-resolved charge-state mass deconvolution of their LC-HRAM-MS spectra. The molecular formulas of the base-treatment cleavage products are the same as the "w" and "d" product ions formed upon MS^2 collisional induced dissociation (CID) of negatively charged unmodified single strand oligonucleotides (*64*). The "w" and "d" product ions for each single strand oligonucleotide were calculated online using the Mongo Oligo Mass Calculator v2.06 (http://mass.rega.kuleuven.be/mass/mongo.htm) with the "CID fragments" feature and the "monoisotopic mass", "negative mode", "DNA", and the "5'-OH" and "3'-OH" terminals selected. Mass identities were verified by comparing to calculated masses of proposed structures in ChemDraw. The measured masses of the cleavage products were determined by deconvoluting the multiple charge states seen in full scan spectra acquired during the cleavage product retention period using Freestyle software (Thermo Scientific, Waltham, MA). The deconvoluted experimental masses from FreeStyle were compared to cleavage products masses calculated using the Mongo software (accounting for the charge state) to assign the cleavage products. The assigned cleavage products were then used to identify the location of the colibactin adduct of the intact oligonucleotide. Signal intensities from both the [M+H] and [M + Na] ions from each cleavage product were summed and normalized to the amount of DNA injected. Values plotted are the difference between the average signal intensities observed in assays with *pks*$^+$ and *pks*$^-$ *E. coli*.

DNA cross-linking assay in the presence of groove binders

AAATTAATA 50-nucleotide oligomer (2 μg) was subjected to a modified version of the DNA cross-linking assay conditions described above in which individual DNA groove binding small molecules were added to the assay mixture just before addition of bacteria. Groove binders tested were: netropsin (Enzo Chemicals), DAPI (4′,6-diamidino-2-phenylindole, Sigma Aldrich), methyl green (Chem Impex), and actinomycin D (Acros Organics). Groove binders were added as solutions in DMSO to final concentrations of 0, 5, 10, 50, 100, 500, and 1000 nM while keeping the DMSO concentration ≤ 2% (v/v). The extent of ICL formation was determined by the denaturing gel electrophoresis protocol described above.

Quantitation of *N*-myristoyl-D-asparagine ("prodrug motif")

This assay was adapted from a previous report and was used to confirm production of colibactin in assay mixtures (*65*). Cell pellets obtained from the DNA cross-linking assay were resuspended in 200 μL of LC-MS grade methanol (Honeywell) containing 100 nM d_{27}-*N*-myristoyl-D-asparagine, which served as an internal standard and was prepared as described previously (*33*). Cell suspensions were sonicated for 2 min in a bath sonicator and vigorously vortexed. This was repeated once more before centrifuging the samples at 16,100 × g for 10 min to pellet all cell debris. Sample supernatants were passed through a centrifugal, AcroPrep Advance 96-well 0.2 μM PTFE filter plate (4000 RPM for 10 min, Pall Corp.) and collected in a 96-well clear bottom plate. Samples were either frozen at −20°C to prevent evaporation or immediately analyzed by a previously reported liquid chromatography negative electrospray–ionization tandem mass spectrometry (UPLC-ESI$^-$-MS/MS) method.

Liquid chromatography was performed using a Waters Acquity UPLC H-Class System (Waters Corporation) equipped with an Agilent Poroshell 120 EC-C18, 2.7 μm, 4.7 mm × 50 mm column using a multistep gradient. Conditions started at 10% solvent B at 650 μL/min for 0.5 min, followed by a linear gradient to 95% B over 0.5 min, a hold at 95% B for 1 min, and a linear gradient back to 10% B over 0.5 min where the column re-equilibrated for 1 min (solvent A, 95:5 water/methanol + 0.03% NH_4OH; solvent B, 80:15:5 isopropanol/methanol/water; injection volume = 5 μL). Mass spectrometry was performed using a Waters Xevo TQ-S UPLC-triple quadrupole mass spectrometer. The multireaction monitoring (MRM) transitions were *m/z* 341.3 → *m/z* 226.3 (collision energy (CE), 24 V; cone voltage, 50) for unlabeled prodrug motif and *m/z* 368.5 → *m/z* 253.3 (CE, 28 V; cone voltage, 58 V) for D_{27}-prodrug motif. Data analysis was conducted using TargetLynx software. Unlabeled prodrug concentrations were calculated by converting the peak area ratios (unlabeled prodrug/d_{27}-prodrug) to concentration ratios using a freshly run calibration curve of varying unlabeled prodrug containing 100 nM d_{27}-prodrug and multiplying by internal standard concentration (100 nM).

Large-scale production of a colibactin-DNA ICL for NMR spectroscopy

~192 μg of double-stranded 2′-fluoro-14mer (Genewiz) were diluted in 13.5 mL of DMEM-HEPES. The resulting solution was dispensed into a 96-well plate in 140 μL aliquots and subjected to the DNA cross-linking assay described above except incubations were performed for 16 hours at 30°C. Two columns of the 96-well plate were used as negative controls (media blank and *pks*$^-$ *E. coli*); all other columns contained *pks*$^+$ *E. coli*. After the incubation, half of the wells in each column were combined to give two samples per column (24 samples total, ~800 μL) which were centrifuged at 10,000 × g for 5 min to pellet cells. The supernatants were then divided into two 400 μL aliquots and each aliquot was treated with 40 μL of 3M NaOAc, pH 5 and added to 880 μL of 95% EtOH (aqueous, v/v) to precipitate DNA. Samples were stored at −20°C overnight.

DNA-precipitated samples were centrifuged at 16,100 × g for 30 min (4°C) to pellet DNA. The supernatants were removed, and each DNA pellet was washed with 200 μL of 70% EtOH (aqueous, v/v). The DNA was re-pelleted by centrifugation (16,100 × g for 15 min) and the supernatant was removed. The DNA pellets were air-dried for ~5 min. Samples originating from the same column on the 96-well plate were reconstituted in 125 μL of TE buffer and pooled to make 12 samples (500 μL total volume). The extent of ICL formation in each sample was checked using the previously denaturing gel electrophoresis method. Finally, *pks*$^+$ samples were pooled, desalted with water and concentrated to ~50 μL using Amicon Ultra 3K – 0.5 mL spin filters (16,100 × g for 30 min, Millipore) and pooled.

This entire protocol was repeated twice to generate a total of ~410 μg of partially cross-linked DNA from 3 96-well plates. All DNA from *pks*$^+$ samples was combined to generate the final sample, which was stored at −20°C until further processing and analysis by NMR spectroscopy.

Production of a [^{15}N,^{13}C]-colibactin-DNA ICL for NMR spectroscopy

DNA containing an ICL with isotopically labeled colibactin was produced analogously to the unlabeled sample except all incubations were performed in M9 minimal medium containing [^{15}N]-ammonium chloride (99%, Cambridge Isotope Laboratories, Inc.) and [$^{13}C_6$]-D-glucose (99%, Cambridge Isotope Laboratories, Inc.). Additionally, overnight starter cultures were sub-cultured in this isotopically labeled medium instead of DMEM-HEPES. Isotope incorporation was assessed by mass spectrometry using the protocol described above for intact colibactin-DNA interstrand cross-links and revealed >90% isotope incorporation.

NMR spectroscopy

CYANA library residue design: As no CYANA library residue for a colibactin modified base currently exists, it had to be constructed anew. The colibactin molecule was drawn using ChemDraw 21.0.0 according to the structure inferred from the analysis of intact colibactin-DNA interstrand cross-links described above and knowledge from prior studies (*21*, *22*). An adenosine monophosphate residue was N3-linked onto the opened warhead to mimic a monoalkylated residue on the imino-facing side of colibactin. The opposite end of the colibactin molecule had a single methyl group of the opened warhead removed. This was necessary, as CYANA is unable to model the interstrand cross-linked adenosines as a single molecule in the context of any DNA or RNA chain. Thus, in order to accurately represent the link, an N3-methyladenosine residue was also constructed using ChemDraw, representing the colibactin modified base on the ketone-facing side. The ChemDraw structures were transformed to PDB files using OPENBABEL's cdxml to pdb function (*66*).

The exported file was then manually adjusted to fit the CYANA library format. A custom R script was then used to center the coordinates according to CYANA specifications and rearrange the atom order to the default of adenosines in the CYANA library such that all bonding and dihedral parameters specify the correct atoms on the new base. Dihedral parameters for the adenosine atoms were copied from standard adenosine residues, all colibactin dihedral angles were manually specified by their degrees of freedom according to the known stereochemistry, sp-hybridization, and aromaticity. Finally, for CYANA calculations, a bond between the warhead-methyl end of colibactin and the N3-methyl of the opposite strand A+3 residue of length 1.48-1.52 Å was included, thereby mimicking the complete colibactin ICL.

Xplor library residue design: For Xplor, the topology and parameter file templates were generated using the ChemDraw structures and PRODRG version AA100323.0717 (*67*). The atom parameters and topology values in the exported templates were manually adjusted according to the stereochemistry of proposed colibactin structures as determined by prior biosynthetic and synthetic studies. The pyrrolidinone, pyrroline, and thiazole ring parameters were adjusted according to the following references, respectively (*68*–*70*). Planarity, angles, and dihedrals were adjusted according to the stereochemistry of proposed colibactin structures as determined by prior biosynthetic and synthetic studies. Even calculations where these angles were freely rotated converged with prior stereochemistry. The end connectors of colibactin and the N3-methyladenosine were also added manually and their repulsion lowered to comply with the features of the covalent C–C bond. The N3-methyl residue on the connecting adenosine was written and adjusted manually. Similarly, for cases in which the structural features were not known, they were modeled manually, such as the axial vs equatorial positions of the terminal pyrrolidines, the single or double protonation of the α-iminoketone and the *cis*- vs *trans*-orientation of the thiazole rings, the parameter and topology files were adjusted manually.

NMR data acquisition and resonance assignment: DNA samples were suspended in buffer (10 mM Tris-HCl pH 8.2, 10mM NaCl) by washing them five times using Amicon centrifugal filters. All NMR experiments

were acquired in 5 mm Shigemi tubes with a Bruker 800 MHz instrument containing a cryogenic probe. Spectra for observing non-exchangeable protons were collected in 100% D_2O at 298 K and for exchangeable protons in 90% H_2O at 278 K. ^{1}H-^{1}H NOE spectroscopy and total correlation spectroscopy were recorded with unlabeled samples and ^{15}N-HSQC spectra were collected by using $^{13}C^{15}N$-labeled samples. All data was analyzed using NMRDraw v11.1, NMRviewJ 8.0.3, and NMRFx Analyst v11.2.4-c (*71*).

Structural modeling: Initial structural models were generated using manually assigned restraints in CYANA, where upper-limit distance restraints of 2.7, 3.3, and 5.0 Å were employed for direct NOE cross-peaks of strong, medium, and weak intensities, respectively (*72*). To prevent the generation of structures with collapsed major grooves, cross-helix P–P distance restraints (with 20% weighting coefficient) were employed for B-form helical segments. Standard torsion angle restraints were used for the B-helical geometry, allowing for ±50° deviations from ideality ($\alpha = -68°$, $\beta = -147°$, $\gamma = 46°$, $\delta = 135°$, $\varepsilon = -150°$, $\zeta = -100°$) (*73*). Standard hydrogen-bonding restraints with approximately linear NH–N and NH–O bond distances of 1.9 ± 0.1 Å and N–N and N–O bond distances of 2.9 ± 0.01 Å.

The CYANA structure with the lowest target function was used as the initial model for structure calculations Xplor-NIH to incorporate electrostatic constraints. First, structures were calculated using annealing from 2000 °C to 25 °C in steps of 12.5 °C. Standard energy potential terms for bonds, angles, torsion angles, van der Waals interactions, and interatomic repulsions were included. Energy potentials for NOEs, hydrogen bonds, and planarity were incorporated with restraints derived from NMR data. All restraints used in CYANA were included except for phosphate-phosphate distances. The structures were sorted by energy using bond, angle, dihedral, and NOE energy potential terms and the ten percent of the structures with the lowest sort energy. The lowest ten percent of these were deposited in the RCSB data bank.

Structure deposition: NMRFx Analyst was used to confirm distance restraints used for the structure calculations and generate NMR-STAR format files for uploading to the BMRB. To do this, an N3-methyladenosine residue with a fluorine at the F2' position was constructed for the NMRFx residue library. This allowed loading in the DNA sequence with the modified residue in each of the two strands. A PDB file, containing the atoms specific to the colibactin molecule was extracted from the file generated by XPLOR. This PDB file was read to load in the colibactin molecule to form the complete complex. Next, a peak list file (in NMRFX .xpk2 format) was loaded containing NOE cross peaks. This peak list was used to populate a table of distance restraints and violations (given the loaded 3D structure). The molecular viewer in NMRFx was also used to visualize constraints in the context of the 3D structure. NMRFx was then used to export the NMR-STAR file containing the molecular assembly and chemical shift assignments.

Computational modeling

Calculations of colibactin electrostatic potential: We computed the ESP of specific atoms on proposed colibactin structures and doubly charged DNA with sequences 5′-GAATATTC-3′ and 5′-GAACGTTC-3′ following previously reported protocols (*74*–*76*). We computed the partial charges on atoms of interest using iterative Hirshfeld (Hirshfeld-I) charges (*77*, *78*) as implemented in Multiwfn version 3.7 (*79*) and applied these charges to compute the ESP at these atoms (*76*). All ESP values were obtained from geometry optimization calculations carried out with density functional theory (DFT) at the B3LYP (*80*–*82*)–D3 (*83*)/6-31G* (*84*–*87*) level of theory.

Calculation of DNA electrostatic potential: We used the online tool DNAphi provided by the Rohs lab (https://rohslab.usc.edu/DNAphi/index.html) (*63*) which predicts ESP of minor grooves by solving the non-linear Poisson-Boltzmann equation of DNA fragments.

Modeling of colibactin ICLs containing alternative central base pairs: We used the restraints generated through NMR (see above) and substituted the central or flanking base pairs for generating initial models of non-ideal motifs cross-linked to colibactin by CYANA followed by the introduction of electrostatics by Xplor as described above.

REFERENCES AND NOTES

1. G. El Tekle, N. Andreeva, W. S. Garrett, The role of the microbiome in the etiopathogenesis of colon cancer. *Annu. Rev. Physiol.* **86**, 453–478 (2024). doi: 10.1146/annurev-physiol-042022-025619; pmid: 38345904
2. M. T. White, C. L. Sears, The microbial landscape of colorectal cancer. *Nat. Rev. Microbiol.* **22**, 240–254 (2024). doi: 10.1038/s41579-023-00973-4; pmid: 37794172
3. M. W. Dougherty, C. Jobin, Shining a light on colibactin biology. *Toxins (Basel)* **13**, 346 (2021). doi: 10.3390/toxins13050346; pmid: 34065799
4. K. M. Wernke *et al.*, Structure and bioactivity of colibactin. *Bioorg. Med. Chem. Lett.* **30**, 127280 (2020). doi: 10.1016/j.bmcl.2020.127280; pmid: 32527463
5. J.-P. Nougayrède *et al.*, *Escherichia coli* induces DNA double-strand breaks in eukaryotic cells. *Science* **313**, 848–851 (2006). doi: 10.1126/science.1127059; pmid: 16902142
6. G. Cuevas-Ramos *et al.*, *Escherichia coli* induces DNA damage in vivo and triggers genomic instability in mammalian cells. *Proc. Natl. Acad. Sci. U.S.A.* **107**, 11537–11542 (2010). doi: 10.1073/pnas.1001261107; pmid: 20534522
7. A. Cougnoux *et al.*, Bacterial genotoxin colibactin promotes colon tumour growth by inducing a senescence-associated secretory phenotype. *Gut* **63**, 1932–1942 (2014). doi: 10.1136/gutjnl-2013-305257; pmid: 24658599
8. J. C. Arthur *et al.*, Intestinal inflammation targets cancer-inducing activity of the microbiota. *Science* **338**, 120–123 (2012). doi: 10.1126/science.1224820; pmid: 22903521
9. M. Bonnet *et al.*, Colonization of the human gut by *E. coli* and colorectal cancer risk. *Clin. Cancer Res.* **20**, 859–867 (2014). doi: 10.1158/1078-0432.CCR-13-1343; pmid: 24334760
10. S. Tomkovich *et al.*, Locoregional effects of microbiota in a preclinical model of colon carcinogenesis. *Cancer Res.* **77**, 2620–2632 (2017). doi: 10.1158/0008-5472.CAN-16-3472; pmid: 28416491
11. C. M. Dejea *et al.*, Patients with familial adenomatous polyposis harbor colonic biofilms containing tumorigenic bacteria. *Science* **359**, 592–597 (2018). doi: 10.1126/science.aah3648; pmid: 29420293
12. T. Miyasaka *et al.*, *Pks*-positive *Escherichia coli* in tumor tissue and surrounding normal mucosal tissue of colorectal cancer patients. *Cancer Sci.* **115**, 1184–1195 (2024). doi: 10.1111/cas.16088; pmid: 38297479
13. E. Buc *et al.*, High prevalence of mucosa-associated *E. coli* producing cyclomodulin and genotoxin in colon cancer. *PLOS ONE* **8**, e56964 (2013). doi: 10.1371/journal.pone.0056964; pmid: 23457644
14. V. Eklöf *et al.*, Cancer-associated fecal microbial markers in colorectal cancer detection. *Int. J. Cancer* **141**, 2528–2536 (2017). doi: 10.1002/ijc.31011; pmid: 28833079
15. C. A. Brotherton, M. Wilson, G. Byrd, E. P. Balskus, Isolation of a metabolite from the *pks* island provides insights into colibactin biosynthesis and activity. *Org. Lett.* **17**, 1545–1548 (2015). doi: 10.1021/acs.orglett.5b00432; pmid: 25753745
16. X. Bian, A. Plaza, Y. Zhang, R. Müller, Two more pieces of the colibactin genotoxin puzzle from *Escherichia coli* show incorporation of an unusual 1-aminocyclopropanecarboxylic acid moiety. *Chem. Sci.* **6**, 3154–3160 (2015). doi: 10.1039/C5SC00101C; pmid: 28706687
17. M. I. Vizcaino, J. M. Crawford, The colibactin warhead cross-links DNA. *Nat. Chem.* **7**, 411–417 (2015). doi: 10.1038/nchem.2221; pmid: 25901819
18. M. R. Wilson *et al.*, The human gut bacterial genotoxin colibactin alkylates DNA. *Science* **363**, eaar7785 (2019). doi: 10.1126/science.aar7785; pmid: 30765538
19. M. Xue, E. Shine, W. Wang, J. M. Crawford, S. B. Herzon, Characterization of natural colibactin-nucleobase adducts by tandem mass spectrometry and isotopic labeling. Support for DNA alkylation by cyclopropane ring opening. *Biochemistry* **57**, 6391–6394 (2018). doi: 10.1021/acs.biochem.8b01023; pmid: 30365310
20. N. Bossuet-Greif *et al.*, The colibactin genotoxin generates DNA interstrand cross-links in infected cells. *mBio* **9**, e02393-17 (2018). doi: 10.1128/mBio.02393-17; pmid: 29559578
21. Y. Jiang *et al.*, Reactivity of an unusual amidase may explain colibactin's DNA cross-linking activity. *J. Am. Chem. Soc.* **141**, 11489–11496 (2019). doi: 10.1021/jacs.9b02453; pmid: 31251062
22. M. Xue *et al.*, Structure elucidation of colibactin and its DNA cross-links. *Science* **365**, eaax2685 (2019). doi: 10.1126/science.aax2685; pmid: 31395743
23. A. R. Healy *et al.*, Synthesis and reactivity of precolibactin 886. *Nat. Chem.* **11**, 890–898 (2019). doi: 10.1038/s41557-019-0338-2; pmid: 31548676
24. K. M. Wernke *et al.*, Probing microbiome genotoxicity: A stable colibactin provides insight into structure–activity relationships and facilitates mechanism of action studies. *J. Am. Chem. Soc.* **143**, 15824–15833 (2021). doi: 10.1021/jacs.1c07559; pmid: 34524796

25. C. Pleguezuelos-Manzano *et al.*, Mutational signature in colorectal cancer caused by genotoxic *pks*$^{+}$ *E. coli*. *Nature* **580**, 269–273 (2020). doi: 10.1038/s41586-020-2080-8; pmid: 32106218
26. P. J. Dziubańska-Kusibab *et al.*, Colibactin DNA-damage signature indicates mutational impact in colorectal cancer. *Nat. Med.* **26**, 1063–1069 (2020). doi: 10.1038/s41591-020-0908-2; pmid: 32483361
27. A. Boot *et al.*, Characterization of colibactin-associated mutational signature in an Asian oral squamous cell carcinoma and in other mucosal tumor types. *Genome Res.* **30**, 803–813 (2020). doi: 10.1101/gr.255620.119; pmid: 32661091
28. D. Terlouw *et al.*, Enrichment of colibactin-associated mutational signatures in unexplained colorectal polyposis patients. *BMC Cancer* **24**, 104 (2024). doi: 10.1186/s12885-024-11849-y; pmid: 38238650
29. A. Rosendahl Huber *et al.*, Improved detection of colibactin-induced mutations by genotoxic *E. coli* in organoids and colorectal cancer. *Cancer Cell* **42**, 487–496.e6 (2024). doi: 10.1016/j.ccell.2024.02.009; pmid: 38471458
30. D. Terlouw *et al.*, Recurrent APC splice variant c.835-8A>G in patients with unexplained colorectal polyposis fulfilling the colibactin mutational signature. *Gastroenterology* **159**, 1612–1614.e5 (2020). doi: 10.1053/j.gastro.2020.06.055; pmid: 32603656
31. B. Chen *et al.*, Contribution of *pks*$^{+}$ *E. coli* mutations to colorectal carcinogenesis. *Nat. Commun.* **14**, 7827 (2023). doi: 10.1038/s41467-023-43329-5; pmid: 38030613
32. M. Díaz-Gay *et al.*, Geographic and age variations in mutational processes in colorectal cancer. *Nature* **643**, 230–240 (2025). doi: 10.1038/s41586-025-09025-8; pmid: 40267983
33. T. Mäklin *et al.*, Geographical variation in the incidence of colorectal cancer and urinary tract cancer is associated with population exposure to colibactin-producing *Escherichia coli*. *Lancet Microbe* **6**, 101015 (2025). doi: 10.1016/j.lanmic.2024.101015; pmid: 39644909
34. A. Mandarino Alves *et al.*, Dysfunctional mucus structure in cystic fibrosis increases vulnerability to colibactin-mediated DNA adducts in the colon mucosa. *Gut Microbes* **16**, 2387877 (2024). doi: 10.1080/19490976.2024.2387877; pmid: 39133871
35. M. Xue, K. M. Wernke, S. B. Herzon, Depurination of colibactin-derived interstrand cross-links. *Biochemistry* **59**, 892–900 (2020). doi: 10.1021/acs.biochem.9b01070; pmid: 31977191
36. M. R. Volpe *et al.*, In vitro characterization of the colibactin-activating peptidase ClbP enables development of a fluorogenic activity probe. *ACS Chem. Biol.* **14**, 1097–1101 (2019). doi: 10.1021/acschembio.9b00069; pmid: 31059217
37. A. M. Maxam, W. Gilbert, A new method for sequencing DNA. *Proc. Natl. Acad. Sci. U.S.A.* **74**, 560–564 (1977). doi: 10.1073/pnas.74.2.560; pmid: 265521
38. M. L. Kopka, C. Yoon, D. Goodsell, P. Pjura, R. E. Dickerson, The molecular origin of DNA-drug specificity in netropsin and distamycin. *Proc. Natl. Acad. Sci. U.S.A.* **82**, 1376–1380 (1985). doi: 10.1073/pnas.82.5.1376; pmid: 2983343
39. T. A. Larsen, D. S. Goodsell, D. Cascio, K. Grzeskowiak, R. E. Dickerson, The structure of DAPI bound to DNA. *J. Biomol. Struct. Dyn.* **7**, 477–491 (1989). doi: 10.1080/07391102.1989.10508505; pmid: 2627296
40. S. K. Kim, B. Nordén, Methyl green. A DNA major-groove binding drug. *FEBS Lett.* **315**, 61–64 (1993). doi: 10.1016/0014-5793(93)81133-K; pmid: 8416812
41. S. Kamitori, F. Takusagawa, Crystal structure of the 2:1 complex between d(GAAGCTTC) and the anticancer drug actinomycin D. *J. Mol. Biol.* **225**, 445–456 (1992). doi: 10.1016/0022-2836(92)90931-9; pmid: 1593629
42. R. Cosstick *et al.*, Molecular recognition in the minor groove of the DNA helix. Studies on the synthesis of oligonucleotides and polynucleotides containing 3-deaza-2′-deoxyadenosine. Interaction of the oligonucleotides with the restriction endonuclease EcoRV. *Nucleic Acids Res.* **18**, 4771–4778 (1990). pmid: 2395641
43. T. Zhou *et al.*, Isolation of new colibactin metabolites from wild-type *Escherichia coli* and in situ trapping of a mature colibactin derivative. *J. Am. Chem. Soc.* **143**, 5526–5533 (2021). doi: 10.1021/jacs.1c01495; pmid: 33787233
44. M. Ikehara, 2′-Substituted 2′-deoxypurine nucleotides: Their conformation and properties. *Heterocycles* **21**, 75–90 (1984). doi: 10.3987/S-1984-01-0075
45. C. A. Fitch, G. Platzer, M. Okon, B. E. Garcia-Moreno, L. P. McIntosh, Arginine: Its pK_a value revisited. *Protein Sci.* **24**, 752–761 (2015). doi: 10.1002/pro.2647; pmid: 25808204
46. L. B. Alexandrov *et al.*, ; The repertoire of mutational signatures in human cancer. *Nature* **578**, 94–101 (2020). doi: 10.1038/s41586-020-1943-3; pmid: 32025018
47. G. Koh, A. Degasperi, X. Zou, S. Momen, S. Nik-Zainal, Mutational signatures: Emerging concepts, caveats and clinical applications. *Nat. Rev. Cancer* **21**, 619–637 (2021). doi: 10.1038/s41568-021-00377-7; pmid: 34316057
48. W. O. Foye, *Review of DNA-binding/damaging small molecules in cancer chemotherapy. Cancer Chemotherapeutic Agents* (American Chemical Society, 1995).
49. P. B. Dervan, Molecular recognition of DNA by small molecules. *Bioorg. Med. Chem.* **9**, 2215–2235 (2001). doi: 10.1016/S0968-0896(01)00262-0; pmid: 11553460
50. W. C. Tse, D. L. Boger, Sequence-selective DNA recognition: Natural products and nature's lessons. *Chem. Biol.* **11**, 1607–1617 (2004). doi: 10.1016/j.chembiol.2003.08.012; pmid: 15610844
51. K. M. Wernke, "Synthetic studies of colibactin, a carcinogenic gut microbiome metabolite," thesis, Yale University (2022).
52. Z. R. Li *et al.*, Macrocyclic colibactin induces DNA double-strand breaks via copper-mediated oxidative cleavage. *Nat. Chem.* **11**, 880–889 (2019). doi: 10.1038/s41557-019-0317-7; pmid: 31527851
53. L. Zha, M. R. Wilson, C. A. Brotherton, E. P. Balskus, Characterization of polyketide synthase machinery from the *pks* island facilitates isolation of a candidate precolibactin. *ACS Chem. Biol.* **11**, 1287–1295 (2016). doi: 10.1021/acschembio.6b00014; pmid: 26890481
54. D. E. Wemmer, P. B. Dervan, Targeting the minor groove of DNA. *Curr. Opin. Struct. Biol.* **7**, 355–361 (1997). doi: 10.1016/S0959-440X(97)80051-6; pmid: 9204277
55. W. A. Denny, DNA minor groove alkylating agents. *Curr. Med. Chem.* **8**, 533–544 (2001). doi: 10.2174/0929867003373283; pmid: 11281840
56. S. Neidle, DNA minor-groove recognition by small molecules. *Nat. Prod. Rep.* **18**, 291–309 (2001). doi: 10.1039/a705982e; pmid: 11476483
57. Z. Morávek, S. Neidle, B. Schneider, Protein and drug interactions in the minor groove of DNA. *Nucleic Acids Res.* **30**, 1182–1191 (2002). doi: 10.1093/nar/30.5.1182; pmid: 11861910
58. A. Rahman, P. O'Sullivan, I. Rozas, Recent developments in compounds acting in the DNA minor groove. *MedChemComm* **10**, 26–40 (2018). doi: 10.1039/C8MD00425K; pmid: 30774852
59. L. H. Hurley, V. L. Reynolds, D. H. Swenson, G. L. Petzold, T. A. Scahill, Reaction of the antitumor antibiotic CC-1065 with DNA: Structure of a DNA adduct with DNA sequence specificity. *Science* **226**, 843–844 (1984). doi: 10.1126/science.6494915; pmid: 6494915
60. D. L. Boger, D. S. Johnson, CC-1065 and the duocarmycins: Unraveling the keys to a new class of naturally derived DNA alkylating agents. *Proc. Natl. Acad. Sci. U.S.A.* **92**, 3642–3649 (1995). doi: 10.1073/pnas.92.9.3642; pmid: 7731958
61. R. Rohs *et al.*, The role of DNA shape in protein-DNA recognition. *Nature* **461**, 1248–1253 (2009). doi: 10.1038/nature08473; pmid: 19865164
62. T.-P. Chiu, S. Rao, R. S. Mann, B. Honig, R. Rohs, Genome-wide prediction of minor-groove electrostatic potential enables biophysical modeling of protein-DNA binding. *Nucleic Acids Res.* **45**, 12565–12576 (2017). doi: 10.1093/nar/gkx915; pmid: 29040720
63. A. M. Maxam, W. Gilbert, Sequencing end-labeled DNA with base-specific chemical cleavages. *Methods Enzymol.* **65**, 499–560 (1980). doi: 10.1016/S0076-6879(80)65059-9; pmid: 6246368
64. S. A. McLuckey, G. J. Van Berkel, G. L. Glish, Tandem mass spectrometry of small, multiply charged oligonucleotides. *J. Am. Soc. Mass Spectrom.* **3**, 60–70 (1992). doi: 10.1016/1044-0305(92)85019-G; pmid: 24242838
65. M. R. Volpe *et al.*, A small molecule inhibitor prevents gut bacterial genotoxin production. *Nat. Chem. Biol.* **19**, 159–167 (2023). doi: 10.1038/s41589-022-01147-8; pmid: 36253549
66. N. M. O'Boyle *et al.*, Open Babel: An open chemical toolbox. *J. Cheminform.* **3**, 33 (2011). doi: 10.1186/1758-2946-3-33; pmid: 21982300
67. A. W. Schüttelkopf, D. M. van Aalten, PRODRG: A tool for high-throughput crystallography of protein-ligand complexes. *Acta Crystallogr. D Biol. Crystallogr.* **60**, 1355–1363 (2004). doi: 10.1107/S0907444904011679; pmid: 15272157
68. M. S. Yuan, Q. Fang, (*E*)-1,1′-Dibutyl-3,3′-biindolinyl-idene-2,2′-dione. *Acta Crystallogr. Sect. E Struct. Rep. Online* **67**, o52 (2010). doi: 10.1107/S160053681005066X; pmid: 21522762
69. B. A. Stenfors, R. J. Staples, S. M. Biros, F. N. Ngassa, Crystal structure of 1-[(4-methylbenzene)sulfonyl]pyrrolidine. *Acta Crystallogr. E Crystallogr. Commun.* **76**, 452–455 (2020). doi: 10.1107/S205698902000208X; pmid: 32148893
70. B. J. Esselman *et al.*, Precise equilibrium structure of thiazole (c-C_3H_3NS) from twenty-four isotopologues. *J. Chem. Phys.* **155**, 054302 (2021). doi: 10.1063/5.0057221; pmid: 34364360
71. E. Koag, S. G. Hulse, G. L. Helms, K. M. Call, M. F. Summers, J. Marchant, B. A. Johnson, NMRFx: Integrated Software for NMR Data Processing, Visualization, Analysis and Structure Calculation. bioRxiv 2025.08.26 [Preprint] (2025); https://doi.org/10.1101/2025.08.26.672401.
72. P. Güntert, C. Mumenthaler, K. Wüthrich, Torsion angle dynamics for NMR structure calculation with the new program DYANA. *J. Mol. Biol.* **273**, 283–298 (1997). doi: 10.1006/jmbi.1997.1284; pmid: 9367762
73. B. S. Tolbert *et al.*, Major groove width variations in RNA structures determined by NMR and impact of 13C residual chemical shift anisotropy and 1H-13C residual dipolar coupling on refinement. *J. Biomol. NMR* **47**, 205–219 (2010). doi: 10.1007/s10858-010-9424-x; pmid: 20549304
74. A. Nazemi, A. H. Steeves, D. W. Kastner, H. J. Kulik, Influence of the Greater Protein Environment on the Electrostatic Potential in Metalloenzyme Active Sites: The Case of Formate Dehydrogenase. *J. Phys. Chem. B* **126**, 4069–4079 (2022). doi: 10.1021/acs.jpcb.2c02260; pmid: 35609244
75. R. Mehmood, H. J. Kulik, Both Configuration and QM Region Size Matter: Zinc Stability in QM/MM Models of DNA Methyltransferase. *J. Chem. Theory Comput.* **16**, 3121–3134 (2020). doi: 10.1021/acs.jctc.0c00153; pmid: 32243149
76. C. R. Reinhardt *et al.*, Computational Screening of Putative Catalyst Transition Metal Complexes as Guests in a $Ga_4L_6^{12-}$ Nanocage. *Inorg. Chem.* **63**, 14609–14622 (2024). doi: 10.1021/acs.inorgchem.4c02113; pmid: 39049593

77. P. Bultinck, C. Van Alsenoy, P. W. Ayers, R. Carbó-Dorca, Critical analysis and extension of the Hirshfeld atoms in molecules. *J. Chem. Phys.* **126**, 144111 (2007). doi: 10.1063/1.2715563; pmid: 17444705
78. S. Van Damme, P. Bultinck, S. Fias, Electrostatic Potentials from Self-Consistent Hirshfeld Atomic Charges. *J. Chem. Theory Comput.* **5**, 334–340 (2009). doi: 10.1021/ct800394q; pmid: 26610109
79. T. Lu, F. Chen, Multiwfn: A multifunctional wavefunction analyzer. *J. Comput. Chem.* **33**, 580–592 (2012). doi: 10.1002/jcc.22885; pmid: 22162017
80. C. Lee, W. Yang, R. G. Parr, Development of the Colle-Salvetti correlation-energy formula into a functional of the electron density. *Phys. Rev. B Condens. Matter* **37**, 785–789 (1988). doi: 10.1103/PhysRevB.37.785; pmid: 9944570
81. A. D. Becke, Density-Functional Thermochemistry. 3. The Role of Exact Exchange. *J. Chem. Phys.* **98**, 5648–5652 (1993). doi: 10.1063/1.464913
82. P. J. Stephens, F. J. Devlin, C. F. Chabalowski, M. J. Frisch, Ab Initio Calculation of Vibrational Absorption and Circular Dichroism Spectra Using Density Functional Force Fields. *J. Phys. Chem.* **98**, 11623–11627 (1994). doi: 10.1021/j100096a001
83. S. Grimme, J. Antony, S. Ehrlich, H. Krieg, A consistent and accurate ab initio parametrization of density functional dispersion correction (DFT-D) for the 94 elements H-Pu. *J. Chem. Phys.* **132**, 154104 (2010). doi: 10.1063/1.3382344; pmid: 20423165
84. R. Ditchfield, W. J. Hehre, J. A. Pople, Self-Consistent Molecular-Orbital Methods. 9. Extended Gaussian-Type Basis for Molecular-Orbital Studies of Organic Molecules. *J. Chem. Phys.* **1971**, 724–728 (1971). doi: 10.1063/1.1674902
85. P. C. Hariharan, J. A. Pople, The Influence of Polarization Functions on Molecular-Orbital Hydrogenation Energies. *Theor. Chim. Acta* **28**, 213–222 (1973). doi: 10.1007/BF00533485
86. W. J. Hehre, R. Ditchfield, J. A. Pople, Self-Consistent Molecular-Orbital Methods. 12. Further Extensions of Gaussian-Type Basis Sets for Use in Molecular-Orbital Studies of Organic-Molecules. *J. Chem. Phys.* **1972**, 2257–2261 (1972). doi: 10.1063/1.1677527
87. M. M. Francl *et al.*, Self-Consistent Molecular-Orbital Methods. 23. A Polarization-Type Basis Set for 2nd-Row Elements. *J. Chem. Phys.* **77**, 3654–3665 (1982). doi: 10.1063/1.444267
88. P. Villalta *et al.*, Data from: "The specificity and structure of DNA cross-linking by the gut bacterial genotoxin colibactin," Dryad (2025); https://doi.org/10.5061/dryad.vmcvdnd5g.
89. R. Haslecker, CYANA and Xplor run files for: "The specificity and structure of DNA cross-linking by the gut bacterial genotoxin colibactin," Zenodo (2025); https://doi.org/10.5281/zenodo.17114378.
90. E. Carlson *et al.*, Computational Data Information for "The specificity and structure of DNA cross-linking by the gut bacterial genotoxin colibactin," Zenodo (2025); https://doi.org/10.5281/zenodo.17075479.

ACKNOWLEDGMENTS

We acknowledge P. Boudreau and J. Wong for performing preliminary experiments. MS was performed in the Analytical Biochemistry Shared Resource (ABSR) of the University of Minnesota Masonic Cancer Center (MCC). We thank B. Carlson at the MCC for editorial assistance. We acknowledge M. Manetsch for providing the script to compute ESP values. E.P.B. is a Howard Hughes Medical Institute (HHMI) investigator. **Funding:** National Institutes of Health grant R01CA208834 (E.P.B.); National Institutes of Health fellowship F32CA254165 (E.S.C.); National Institutes of Health grant R35GM152027 (H.J.K.); National Institutes of Health grant R50CA211256 (P.W.V.); National Institutes of Health grant P30CA077598 ABSR; National Science Foundation grant CBET-1846426 (H.J.K.); HHMI grant 55108516 (V.M.D.); National Institutes of Health grant R01GM123012 (B.A.J.). **Author contributions:** Conceptualization: E.P.B., E.S.C.; Methodology: P.W.V., L.H., R.H., E.S.C., B.A.J.; Investigation: P.W.V., S.B., L.H., R.H., V.V., E.S.C., C.L., A.S., M.A.A.R., E.S.M.; Visualization: E.S.C.; Funding acquisition: E.P.B., V.M.D., E.S.C.; Project administration: E.P.B., V.M.D.; Supervision: E.P.B., S.B., V.M.D., H.J.K.; Writing – original draft: E.P.B., R.H., V.M.D., E.S.C.; Writing – review & editing: E.P.B., P.W.V., S.B., R.H., V.M.D., H.J.K., V.V., E.S.C., C.L., M.A.A.R. **Competing interests:** E.P.B. is an inventor on patent applications related to detection and inhibition of colibactin biosynthesis (US patents 11,617,759; 12,115,176; and 11,040,951). All other authors declare that they have no competing interests. **Data and materials availability:** Atomic coordinates have been deposited in the Protein Data Bank under accession codes pdb_00009oso. Chemical shifts have been deposited in the Biological Magnetic Resonance Data Bank under accession code 31249. MS data has been submitted to Dryad (*88*). Scripts and calculations related to the NMR structure have been uploaded to Zenodo (*89*). Optimized colibactin geometries, input files, and ESP calculation scripts have been uploaded to Zenodo (*90*). **License information:** Copyright © 2025 the authors, some rights reserved; exclusive licensee American Association for the Advancement of Science. No claim to original US government works. https://www.science.org/about/science-licenses-journal-article-reuse.

SUPPLEMENTARY MATERIALS

science.org/doi/10.1126/science.ady3571
Supplementary Text; Figs. S1 to S23; Tables S1 to S5; Appendix S1; References (*91*–*94*); MDAR Reproducibility Checklist

Submitted 3 June 2025; accepted 3 October 2025

10.1126/science.ady3571

RESEARCH ARTICLE SUMMARY

MOLECULAR BIOLOGY

Multiscale structure of chromatin condensates explains phase separation and material properties

Huabin Zhou, Jan Huertas, M. Julia Maristany, Kieran Russell, June Ho Hwang, Run-Wen Yao, Nirnay Samanta, Joshua Hutchings, Ramya Billur, Momoko Shiozaki, Xiaowei Zhao, Lynda K. Doolittle, Bryan A. Gibson, Andrea Soranno, Margot Riggi, Jorge R. Espinosa, Zhiheng Yu, Elizabeth Villa, Rosana Collepardo-Guevara*, Michael K. Rosen*

Full article and list of author affiliations: https://doi.org/10.1126/science.adv6588

INTRODUCTION: Biomolecular condensates are membraneless compartments that concentrate macromolecules and contribute to numerous cellular processes. Chromatin, the complex of DNA and histone proteins that stores genetic information, can phase separate into condensates in the test tube and in cells. It has been unclear how individual DNA-histone units (nucleosomes) come together across scales—from single particles to visible condensates—and how these interactions set condensate material properties. In this study, we bridge that gap with a multiscale investigation of chromatin condensates.

RATIONALE: Chromatin fibers are composed of nucleosomes connected by DNA linkers. Previous work showed that linker length influences phase separation of fibers, through an unknown structural mechanism. By integrating (i) cryo–electron tomography (cryo-ET) to capture nucleosome organization and fiber structure, (ii) molecular simulations to quantify how histone tails contribute to nucleosome interactions, and (iii) light microscopy to measure droplet dynamics and viscoelasticity, we investigated how the nanoscale arrangement of nucleosomes determines the material properties and stability of chromatin condensates. We sought a multiscale structural framework to connect DNA linker length, nucleosome arrangement, histone tail interactions, and condensate material properties. By integrating insights from each scale, we explained how linker length tunes condensate behavior. Lastly, we compared these in vitro condensates to chromatin domains inside cells.

RESULTS: Using synthetic chromatin fibers with 25- or 30–base pair (bp) DNA linkers, we uncovered how differences in linker length lead to different intramolecular geometry and consequent changes in condensate behavior:

1) Nucleosome array structures: (i) 25-bp chromatin forms flexible, open fibers with nucleosomes facing outward; (ii) 30-bp chromatin adopts compact, stacked configurations where nucleosomes interact within fibers, forming two-start helices; (iii) histone tails make different interactions to stabilize the 25- and 30-bp fiber conformations.

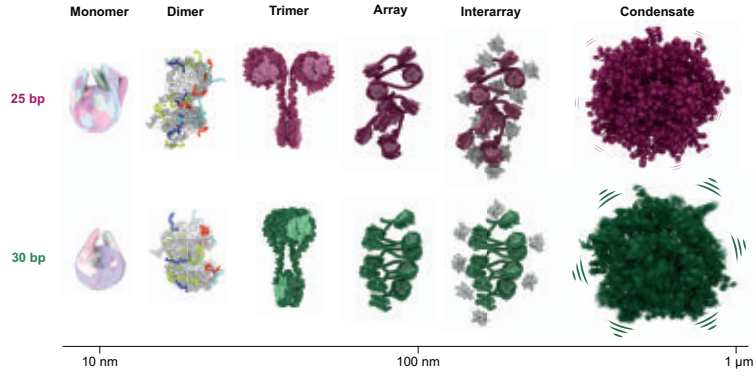
2) Nucleosome array interactions in condensates: (i) conformations of 25-bp fibers enable numerous high-affinity intermolecular interactions; (ii) conformations of 30-bp fibers lead to fewer and lower-affinity intermolecular interactions; (iii) histone tails make different interactions to stabilize intermolecular contacts in the two condensate types; (iv) differences in intermolecular interactions explain the greater stability of 25- versus 30-bp condensates.

3) Condensate material properties: (i) the strongly connected 25-bp network yields condensates with viscous and elastic behaviors, with slow molecular diffusion and high resistance to dissolution; (ii) the weakly connected 30-bp network yields condensates with purely viscous behaviors, with more rapid molecular diffusion and ready dissolution by acetylation.

4) Native chromatin parallels: Dense chromatin clusters in human and mouse cells mirror 25-bp condensates, exhibiting nonrandom packing with occasional stacked regions. Cells may use linker length variations to tune chromatin states at short and long length scales.

CONCLUSION: By integrating experiments and simulations from single nucleosomes to molecular networks, applied to biochemically reconstituted synthetic chromatin and native chromatin in nuclei, we demonstrate that changes in DNA linker length steer chromatin condensate architecture and mechanics across scales from nanometers to micrometers. This multiscale framework reveals how cells could switch chromatin between material states—affecting gene regulation and genome stability—through changes in nucleosome spacing, histone modifications, or associated factors. □

*Corresponding author. Email: rc597@cam.ac.uk (R.C.G.); michael.rosen@utsouthwestern.edu (M.K.R.) Cite this article as H. Zhou *et al.*, *Science* **390**, eadv6588 (2025). DOI: 10.1126/science.adv6588



Chromatin organization across scales. Cryo-ET and computer simulations reveal how DNA linker length controls multiscale chromatin organization. Twenty-five–base pair linker chromatin forms open, flexible structures enabling dense intermolecular networks in condensates. Conversely, 30-bp chromatin adopts compact, intramolecular stacked conformations, creating weakly connected networks. These structural difference explain why 25-bp condensates show enhanced phase separation, slower dynamics, and higher viscoelasticity than 30-bp condensates.

MOLECULAR BIOLOGY

Multiscale structure of chromatin condensates explains phase separation and material properties

Huabin Zhou[1,2], Jan Huertas[3,4,5,2], M. Julia Maristany[3,5,2], Kieran Russell[3,2], June Ho Hwang[1,2], Run-Wen Yao[1,2], Nirnay Samanta[6,7], Joshua Hutchings[8]†, Ramya Billur[9], Momoko Shiozaki[10], Xiaowei Zhao[10], Lynda K. Doolittle[1,2], Bryan A. Gibson[9,2], Andrea Soranno[6,7], Margot Riggi[11], Jorge R. Espinosa[3,2]‡, Zhiheng Yu[10], Elizabeth Villa[8,12], Rosana Collepardo-Guevara[3,4,5,2]*, Michael K. Rosen[1,2]*

The structure and interaction networks of molecules within biomolecular condensates are poorly understood. Using cryo–electron tomography and molecular dynamics simulations, we elucidated the structure of phase-separated chromatin condensates across scales, from individual amino acids to network architecture. We found that internucleosomal DNA linker length controls nucleosome arrangement and histone tail interactions, shaping the structure of individual chromatin molecules within and outside condensates. This structural modulation determines the balance between intra- and intermolecular interactions, which governs the molecular network, thermodynamic stability, and material properties of chromatin condensates. Mammalian nuclei contain dense clusters of nucleosomes whose nonrandom organization is mirrored by the reconstituted condensates. Our work explains how the structure of individual chromatin molecules determines physical properties of chromatin condensates and cellular chromatin organization.

Cells are organized on length scales from nanometers to micrometers. Biomolecular condensates concentrate molecules into discrete foci without surrounding membranes, exemplifying how nanoscale molecular interactions can produce micron-scale cellular organization. Many condensates appear to form through assembly and concomitant phase separation of multivalent macromolecules (*1*–*3*). The structure and dynamics of individual molecules, and of their multivalency-enabled interaction networks, strongly influence the macroscopic physical properties of condensates (*4*–*6*). Physical properties, along with solution environment and composition, define the biochemical and cellular functions of condensates (*7*–*16*). These features of condensates are altered in diseases and have been suggested as therapeutic targets (*17*, *18*). An important goal in biology and human health is to understand the relationships between the molecular structure and dynamics, network architecture and dynamics, and function of condensates.

Molecules within condensates are often conformationally flexible and interact weakly and transiently, producing complex distributions of interconverting states. Nuclear magnetic resonance spectroscopy has revealed structural ensembles and residue-specific interactions of intrinsically disordered regions (IDRs) of proteins within condensates (*19*–*21*). But these studies have not strongly informed on the higher-order organization of these elements within condensates. On micrometer-length scales, cryo–electron tomography (cryo-ET) has been used to characterize the morphology of condensates (*22*–*29*) but has not connected mesoscale features to molecular interactions that form the compartments. Computational work has sought to bridge molecular interactions to the network architecture of intrinsically disordered protein (IDP) condensates, providing insight into viscoelasticity and surface tension (*5*, *30*–*32*). But these models are difficult to test experimentally owing to the challenge of directly visualizing molecules and interactions inside condensates. Because of these complexities, we still lack a complete understanding from molecular structure and interactions to mesoscale organization and dynamics for any condensate.

Phase separation is thought to play an important role in the organization of eukaryotic chromatin, enabling compaction necessary for storage in the nucleus while retaining dynamics necessary for function (*33*–*43*). Chromatin fibers are arrays of nucleosomes—structural units containing ~147 base pairs (bp) of DNA wrapped around an octamer of histone proteins (*44*)—connected by DNA linkers of diverse lengths. Nucleosome arrays compact along their lengths and interact with one another (*45*), creating higher-order cellular structures ranging from 10- to 100-nm clusters (*46*–*48*) to 100- to 300-nm domains (*49*, *50*). The compaction and dynamics of nucleosomes are highly regulated, affecting nuclear processes including transcription (*51*–*53*), DNA replication, and DNA repair (*54*). Interactions between biochemically reconstituted nucleosome arrays can drive salt-dependent phase separation, which is dependent on the disordered tails of histones (*33*, *35*, *55*–*60*). Posttranslational modifications of histone tails, including acetylation and methylation, can regulate phase separation and biological functions (*33*, *38*, *57*). Phase separation is also modulated by the length of internucleosome DNA linkers; the drive to phase separate shows an oscillatory pattern as linkers are extended, stronger for $10N + 5$ base pairs (integer N) and weaker for $10N$ base pairs (*33*). These behaviors, along with genomic data and modeling, suggest that phase separation of the chromatin polymer plays a role in genome organization in vivo (*33*, *35*, *57*–*61*).

Numerous studies have examined the structure of native chromatin fibers, using different modalities of light and electron microscopy (*46*, *49*, *62*–*66*) as well as chemical cross-linking (*67*, *68*). These have revealed that chromatin inside cells and nuclei consists mostly of irregular conformations, although small segments of ordered, stacked groups of nucleosomes have also been observed (*62*, *65*, *69*, *70*). Most of these studies focused on the conformations of individual fibers rather than the structural basis of interactions between them. However, in one study, pairwise internucleosome interactions revealed a wide distribution of packing geometries (*65*). The relationship between the conformations, interactions, and networking of fibers to the density and material properties of chromatin in cells is not known.

In this study, we integrated cryo-ET, computer simulations, and light microscopy to understand mechanisms of phase separation and physical properties of synthetic and native chromatin. We found that nucleosome linker length controls salt-dependent conformations and histone tail interactions of chromatin fibers. These properties dictate the strength and number of interactions between fibers in condensates, which then define the network structure of the condensates. These physical features explain the driving force for chromatin phase

[1]Department of Biophysics, Howard Hughes Medical Institute, UT Southwestern Medical Center, Dallas, TX, USA. [2]Marine Biological Laboratory Chromatin Collaborative, Marine Biological Laboratory, Woods Hole, MA, USA. [3]Yusuf Hamied Department of Chemistry, University of Cambridge, Cambridge, UK. [4]Department of Genetics, University of Cambridge, Cambridge, UK. [5]Maxwell Centre, Cavendish Laboratory, Department of Physics, University of Cambridge, Cambridge, UK. [6]Department of Biochemistry and Molecular Biophysics, Washington University in St. Louis, St. Louis, MO, USA. [7]Center for Biomolecular Condensates, Washington University in St. Louis, St. Louis, MO, USA. [8]School of Biological Sciences, University of California San Diego, La Jolla, CA, USA. [9]Department of Cell and Molecular Biology, St. Jude Children's Research Hospital, Memphis, TN, USA. [10]Janelia Research Campus, Howard Hughes Medical Institute, Ashburn, VA, USA. [11]Max Planck Institute for Biochemistry, Martinsried/Munich, Germany. [12]Howard Hughes Medical Institute, University of California San Diego, La Jolla, CA, USA. ***Corresponding author. Email: rc597@cam.ac.uk (R.C.G.); michael.rosen@utsouthwestern.edu (M.K.R.)** †Present address: Chan Zuckerberg Institute for Advanced Biological Imaging (CZ Imaging Institute), Redwood City, CA, USA. ‡Present address: Complutense University of Madrid, Madrid, Spain.

separation as well as viscoelastic properties of chromatin condensates. Dense 100- to 300-nm clusters of native chromatin in situ show a similar, nonrandom distribution of internucleosome contacts as one class of synthetic chromatin. Together, our studies provide an understanding of chromatin phase separation from nanometers to micrometers and suggest that certain reconstituted chromatin condensates may functionally mimic important features of native chromatin.

Distinct phase separation propensity and dynamics of 25- and 30-bp chromatin

We generated dodecameric nucleosome arrays based on the Widom 601 sequence (*71*, *72*), with either 25- or 30-bp internucleosomal DNA linkers (25- or 30-bp chromatin, respectively). As previously reported (*33*), 25-bp chromatin phase separates at lower concentration and at lower ionic strength than 30-bp chromatin (Fig. 1A). The 25-bp

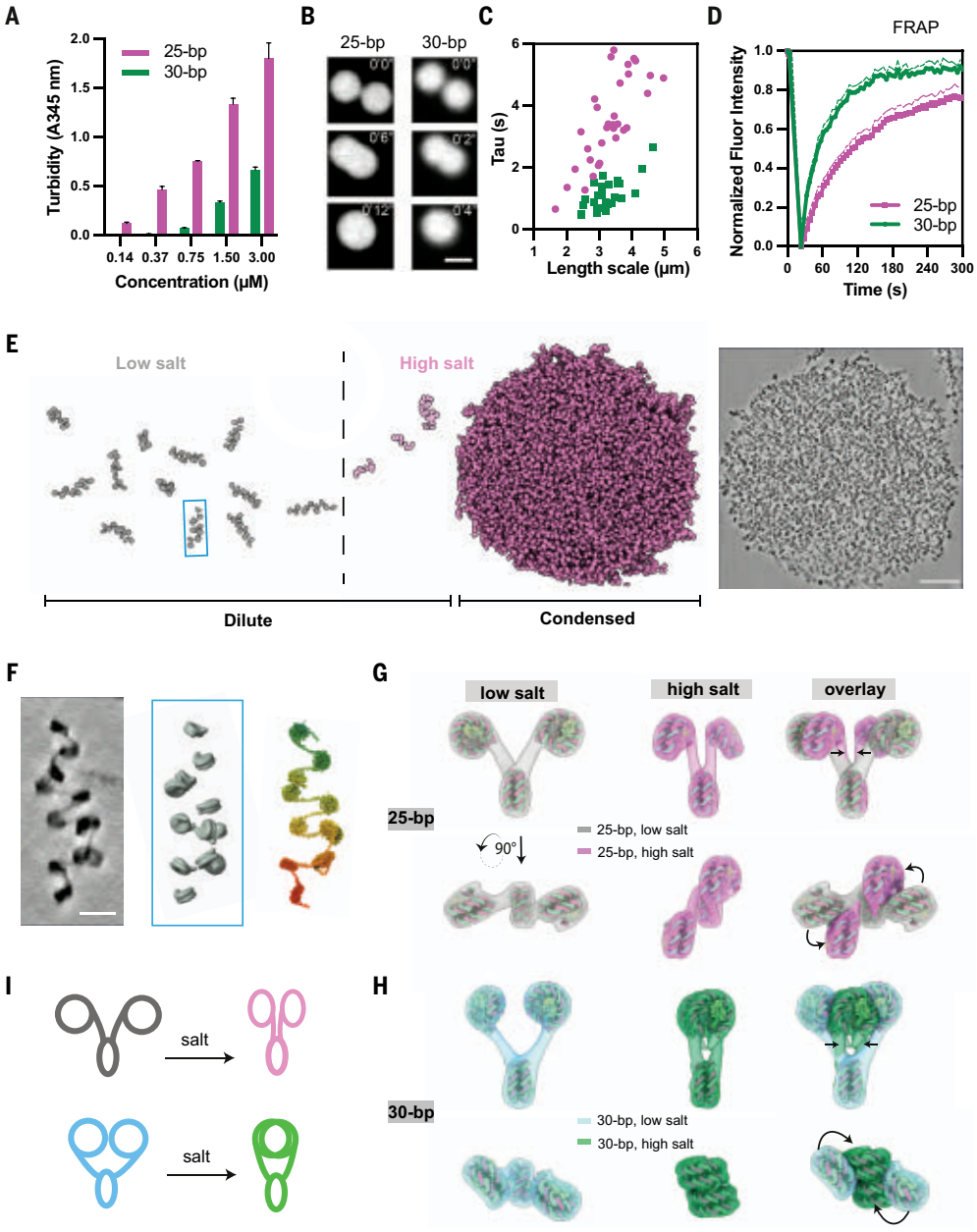


Fig. 1. Linker length determines condensate properties and chromatin fiber structure. (**A**) Turbidity (absorption at 345 nm) of chromatin solutions at the indicated nucleosome concentrations. Error bars indicate ± standard deviation of three measurements. (**B**) Time-lapse imaging of droplet fusion in 25- and 30 bp-chromatin immediately after inducing phase separation. Scale bar, 3 μm. (**C**) Timescale of fusion for 25- and 30-bp chromatin droplets of different sizes. (**D**) FRAP results for 25- and 30-bp chromatin. Error bars indicate ± standard deviation of 20 measurements. (**E**) Schematic of the compaction and phase separation of chromatin fibers as salt concentration increases (left and middle panels) and visualized by cryo-ET (right panel), where scale bar is 100 nm. Boxed array derives from dilute-phase cryo-ET image in (F). (**F**) Schematic of the computational approach used to reconstruct histone tails on a single chromatin array visualized by cryo-ET in low salt. From left to right: maximum projection of chromatin density in a denoised cryo-ET tomogram; nucleosome models extracted from the density [corresponding to fiber boxed in (E); scale bars, 20 nm]; and higher-resolution fiber computationally reconstructed using molecular dynamics simulations steered according to nucleosome positions in the cryo-ET data. (**G** and **H**) Models based on average structural parameters of chromatin with 25-bp (G) and 30-bp (H) linkers in the dilute phase at low (left) and high (middle) salt concentrations. Right panels show overlays of the two conditions. (**I**) Schematic representation of the conformational changes induced by salt in 25- and 30-bp chromatin.

chromatin droplets fuse more slowly than 30-bp chromatin droplets (Fig. 1B, C), and recover more slowly in partial droplet fluorescence recovery after photobleaching (FRAP) experiments (Fig. 1D). We sought to understand these differences in phase separation propensity and material properties using cryo-ET and simulations (Fig. 1E).

Salt differentially compacts 25- and 30-bp chromatin

We collected cryo-ET data in low- and high-salt conditions (0 and 150 mM potassium acetate, respectively) for solutions of 25- and 30-bp chromatin. In low salt, molecules are monomeric and homogeneously distributed in solution, whereas in high salt they separate into dense and dilute phases. In low-salt conditions, we could readily identify nucleosomes and trace their connectivity in individual chromatin fibers in cryo-ET tomograms (Fig. 1F, fig. S1, and movies S1 and S2).

We first examined how increasing salt affects the structure of individual nucleosome arrays. Numerous studies have shown that salt causes compaction and oligomerization of chromatin fibers (*73*–*79*), although most studies have not revealed the underlying structural details [but see (*80*) and (*81*) for recent exceptions]. For each traced fiber, we measured the distance between the centers of mass, *D*, and the dihedral angle between planes, *para*, for all pairs of nucleosomes *N* and *N* + 2 (*N* represents sequential position). We also measured the dihedral angle between the planes of adjacent (*N*, *N* + 1) nucleosomes, α (fig. S2, A to D). To assist in visualizing these geometric features, in each system and condition we reconstructed an average dinucleosome and then combined two such pairs to build an average trinucleosome model (fig. S2E), shown in Fig. 1, G and H.

In low salt, the 25- and 30-bp chromatin have similarly large values of *D* (fig. S2D), indicating that semiadjacent nucleosomes are splayed apart from one other; *para* values are ~45° in both cases. The average α angle for the two arrays differs by nearly 180° (α is ~230° and 50°, for 25 and 30 bp, respectively; fig. S2B), reflecting the difference in phasing of successive nucleosomes imparted by the 10-bp per turn helical pitch of the linker DNA. Because of this difference, in 25-bp chromatin, the *N* and *N* + 2 nucleosomes face away from each other (Fig. 1G, left), whereas in 30-bp chromatin they face toward each other (Fig. 1H, left).

Increased salt reduces long-range electrostatic repulsion in the chromatin DNA (*77*), rearranging and compacting the arrays (fig. S1D). In both types, *D* decreases appreciably (fig. S2D), as does *para* (fig. S2C). In the 25-bp chromatin, nucleosomes *N* and *N* + 2 remain unstacked, with their faces exposed to solvent (Fig. 1G), and become roughly parallel to the intervening *N* + 1 nucleosome, as shown by the decrease in α (to ~200°, Fig. 1, G and I, and fig. S2B). The changes to *D* and *para* are larger in the 30-bp chromatin, owing to face-to-face stacking of the *N* and *N* + 2 nucleosomes, which become oriented approximately perpendicular to the *N* + 1 nucleosome (Fig. 1, H and I), as indicated by the large increase in α (to ~80°; fig. S2B), similar to observations on a 40-bp tetranucleosome arrays (*81*). These changes result in greater compaction of 30-bp chromatin than 25-bp chromatin (fig. S2F). Intranucleosome stacking in 30-bp chromatin has been predicted by multiple computer simulations (*82*–*84*) and observed in crystal structures (*85*) and single-particle cryo–electron microscopy reconstructions (*86*) of arrays with linkers of 20, 30, or 40 bp (fig. S2G). Computational studies suggest that this conformation is stabilized by face-to-face nucleosome contacts, which are the most energetically favorable nucleosome packing geometries, followed by face-to-side and side-to-side (*83*, *87*).

Salt differentially reorganizes histone tail interactions

To gain insight into the histone tail interactions driving salt-dependent chromatin compaction, we combined experimental cryo-ET data with computational simulations, using a chemically specific coarse-grained model (*88*, *89*), which represents chromatin at amino acid and nucleotide resolution (Fig. 2, A to D, and table S1). We simulated a series of arrays observed in the cryo-ET tomograms, restraining the nucleosome geometric centers to their experimental positions in low (Fig. 2, A and B) and high salt (Fig. 2, C and D). The simulations generate structural ensembles of the histone tails, revealing the probabilities of different histone tail conformational states. We quantified the number of intra- and internucleosome contacts mediated by each tail (fig. S3A). This analysis identifies the most frequent interactions within nucleosome pairs arranged according to the cryo-ET data. Although interaction statistics do not directly report on energies, our analyses show that the most frequent tail interactions arise from energetically favorable pairs—lysines and arginines contacting negatively charged histone residues and DNA (fig. S3B).

The simulations show that in low salt, the histone tails in both chromatin types make almost exclusively intranucleosome interactions with DNA (Fig. 2, A and B, and fig. S3, C and D). In high salt, the tails partially release from their own nucleosomes (fig. S3C) and instead contact the DNA and histones of neighbors (Fig. 2, C to E, and fig. S3C). The nature of these interactions is governed by the conformation of the fiber and by the location of each tail on the nucleosome core: H4 and H2A(*N*) emerge from the nucleosome face, whereas H3 and H2B extend from the nucleosome edge (Fig. 2, C and D, and fig. S3E).

The cryo-ET data show that in high salt, 25-bp arrays in the dilute phase adopt diverse conformations, with nucleosomes displaying a broad range of distances and orientations relative to their neighbors (figs. S1D and S2, B to D). In the simulations, this range of internucleosome configurations coincides with heterogeneous interactions involving principally histone H2A, H3, and H4 tails (Fig. 2, C, E, F, and H). This heterogeneity is evident in the larger variance in contacts per residue compared to 30-bp arrays (Fig. 2H). The H3 tail is ideally positioned for face-to-side and side-to-side nucleosome contacts, whereas the H4 and H2A(N) tails facilitate face-to-side interactions and, less frequently, face-to-face contacts (Fig. 2C). Consistent with the diverse tail behaviors of 25-bp chromatin, simulations indicate that the free energy landscape of a 25-bp tetranucleosome is characterized by multiple competing low-lying minima (*90*).

The 30-bp arrays are different in that the prevalence of intramolecular face-to-face stacking decreases the heterogeneity of tail interactions (reducing their standard deviations in Fig. 2H) and amplifies the contributions of the H4 and H2A(N) tails, whose positions facilitate stabilization of face-to-face stacking (Fig. 2, D and E, and fig. S3E). The H3 and H2B tails are less involved owing to their peripheral locations. The H4 and H2A(N) tails make appreciably more internucleosome contacts in 30-bp chromatin than in 25-bp chromatin (Fig. 2, G and H). The region in H4 from K16 to R19 makes the highest number of contacts (Fig. 2H and S4A), which is in agreement with observed decompaction of chromatin upon H4K16 acetylation or mutation of these residues (*91*–*93*). Residues in and adjacent to the H2A and H2B acidic patch (H2A residues Y57, E61, E64, L65, N68, R71, D72, and N89 to E92; H2B residues E102 and E110 plus L42 to D47) formed more interactions in 30-bp chromatin compared with 25-bp chromatin (Fig. 2, F to H), primarily because of interactions with the H4-tail basic patch (*94*–*97*) (Single-letter abbreviations for the amino acid residues are as follows: D, Asp; E, Glu; K, Lys; L, Leu; N, Asn; R, Arg; Y, Tyr).

The histone tail contact distributions of 25- and 30-bp chromatin are consistent with reported biochemical studies of chromatin compaction (tables S2 and S3). Previous simulations performed without experimental restraints have also revealed that histone tail contacts are dependent on solution conditions, linker DNA length, and internucleosome orientations (*84*, *98*–*100*), as observed here.

Our combined data and simulations show that increased salt concentration drives compaction of nucleosome arrays concomitant with formation of many new internucleosome contacts. For 25-bp chromatin, DNA geometry and diverse contacts of the H3, H4, and H2A(N) histone tails produce heterogeneous structures with many nucleosome faces exposed to solvent. By contrast, for 30-bp chromatin, DNA

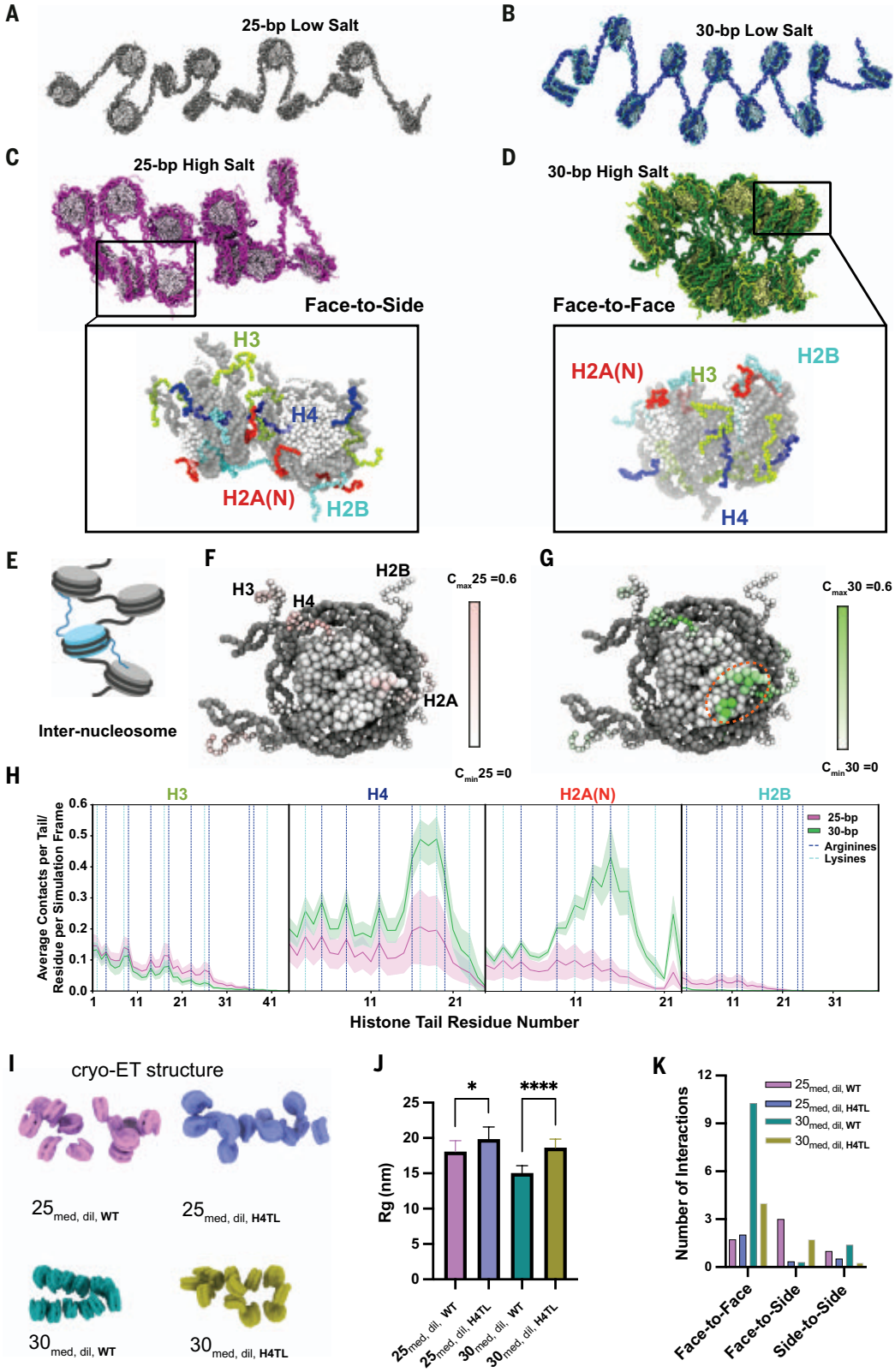


Fig. 2. Different histone tail interactions in 25- and 30-bp chromatin in the dilute phase. (**A** and **B**) Schematic representations 25-bp (A) and 30-bp (B) chromatin arrays in low salt derived from cryo-ET and computationally extended to the chemical-specific model. DNA beads are represented in dark gray (A) and dark blue (B); histone protein beads are in light gray (A) and light blue (B). (**C** and **D**) As shown in (A) and (B) for chromatin in high salt. DNA beads are dark pink (C) and dark green (D); histone protein beads are light pink (C) and light green (D). (Insets) A pair of nucleosomes interacting face-to-side (C) and face-to-face (D) via histone tails. Histone core beads are white and DNA beads are light gray. Histone tail beads are colored as follows: H3, green; H4, blue; H2A(N) terminal, red; and H2B, cyan. (**E**) Schematic representation of internucleosome histone tail interactions. (**F** and **G**). Representative structures of a nucleosome from 25- (F) and 30-bp (G) chromatin simulations, illustrating average contact frequency of each residue; histone core and tails are indicated by larger and smaller beads, respectively. Residues are color-coded by the total number of internucleosome contacts (averaged over

400 simulation frames; see table S1 for *n*) made by each amino acid in histones [H3, H4, H2A(N), and H2B] of one nucleosome with DNA (nucleosomal and linker) and histones (core and tails) of neighboring nucleosomes. Acidic patch in (G) indicated by dashed orange oval. (**H**) Internucleosome contacts (average per residue per simulation frame) made by each amino acid in the histone of one nucleosome and the DNA and histones of neighboring nucleosomes [simulation details provided in (F) and (G) legend above; 25-bp fibers, pink; 30-bp fibers, green]. Blue, cyan, and orange vertical lines show positions of lysines, arginines, and acidic patch residues, respectively. Shading indicates standard deviation from the mean. (**I**) Representative nucleosome arrays assigned in cryo-ET tomograms of 25- and 30-bp arrays (medium salt, dilute phase) assembled with either wild-type (WT) histone octamers ($25_{med,dil}$,WT and $30_{med,dil}$,WT) or H4 tail deletion octamers ($25_{med,dil}$,H4TL and $30_{med,dil}$,H4TL). (**J**) Radius of gyration (R_g) of indicated nucleosome arrays. (**K**) Intramolecular interactions per 12-mer array, classified as face-to-face, face-to-side, and side-to-side.

geometry and interactions of histone H4 and H2A(N) tails favor intramolecular stacking of nucleosomes. As described below, these differences in configuration strongly influence the ability of molecules to interact with neighbors, with important consequences on phase separation and condensate material properties.

Histone H4 tail deletion differentially affects 25- and 30-bp chromatin conformations

To test the predicted differential contributions of the H4 tail to the 25- and 30-bp chromatin structures, we assembled both array types with octamers lacking the H4 tail and determined their structures in 60 mM potassium acetate buffer, using cryo-ET (Fig. 2, I to K, and fig. S4, B to D). Deleting the H4 tail increased radius of gyration (*Rg*) and distance *D* more for 30-bp arrays than for 25-bp arrays. Moreover, face-to-face interactions of 30-bp arrays were substantially decreased along with dihedral angle *para*, with little change in these parameters for 25-bp arrays. Essentially, the helical fiber formed by wild-type 30-bp chromatin is abolished by H4 tail deletion, whereas the structure of 25-bp chromatin is only modestly changed. These results are consistent with previous reports of 10*N* array decompaction upon histone H4 tail deletion (*93*, *101*, *102*) and with our computational predictions that the H4 tail is more important to 30-bp chromatin structure than to 25-bp chromatin structure.

25- and 30-bp chromatin form distinct molecular structures in the condensates

We next examined the structure of chromatin in the condensed phase. Using context-aware template matching (CATM) algorithms (*103*), we placed and oriented the nucleosomes for both 25- and 30-bp chromatin condensates (Fig. 3, A and E, and movies S3 to S5). Nearly random orientation distributions with respect to the imaging axis in both cases indicate that sample integrity was preserved and nucleosomes were properly assigned (fig. S5A) (*103*). Subtomogram averaging resulted in nucleosome structures with 8- and 5.8-Å resolution for 25- and 30-bp chromatin, respectively (fig. S5, B to D, and table S4), further supporting the accuracy of nucleosome positions and orientations.

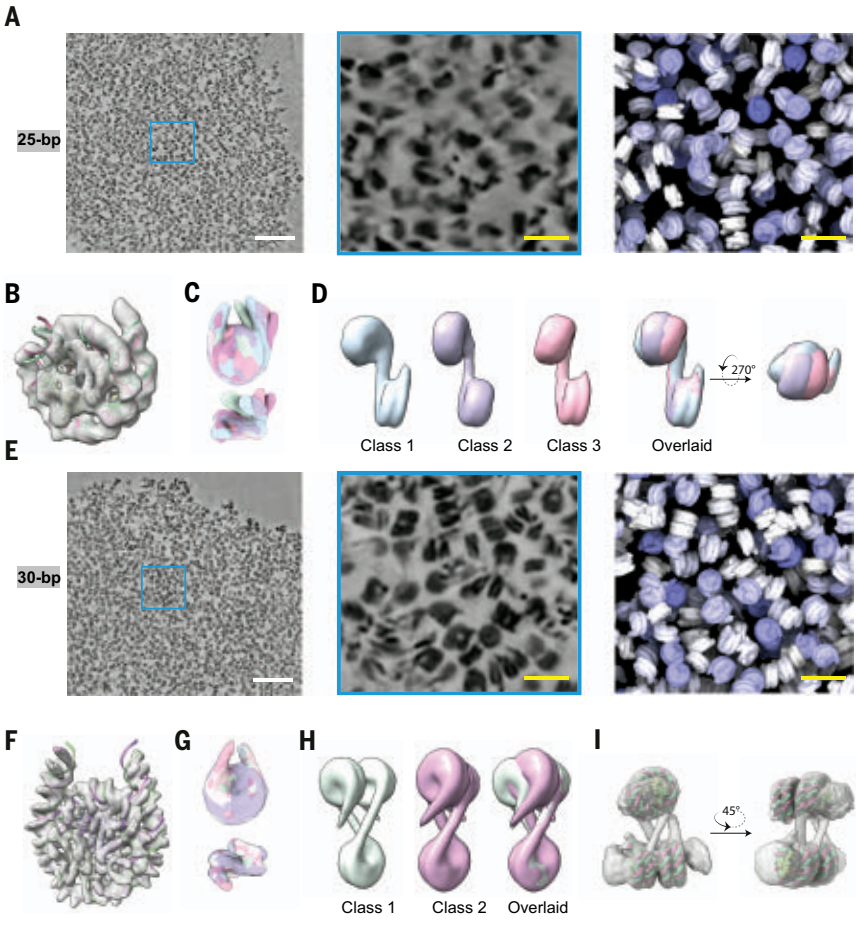


Fig. 3. Molecular structures of 25- and 30-bp chromatin in the condensed phase. (**A**) Cross section of a chromatin condensate in denoised cryo-ET tomogram (left, scale bar 100 nm; middle, magnified view with scale bar 20 nm). Right panel shows nucleosome model assignments from densities in the center panel (scale bar, 20 nm). (**B**) Nucleosome structure (8.0-Å resolution) from 25-bp chromatin obtained by subtomogram averaging 104,438 particles in 10 tomograms. Density is shown as gray surface; fitted model (PDB: 6pwe) is shown as red and green ribbons. (**C** and **D**) Classification of mono- and dinucleosome structures in 25-bp chromatin. Classes are colored differently. (**E**) Overview of 30-bp chromatin condensate, analogous to that shown in (A). (**F**) Nucleosome structure (5.8-Å resolution) from 30-bp chromatin obtained by subtomogram averaging 111,909 particles in 10 tomograms. Density is shown as gray surface; fitted model (PDB: 6L4A) is shown as red and green ribbons. (**G**) Classification of mono- and trinucleosome structures in 30-bp chromatin. Classes are colored differently and are highly overlapping. (**H**) Two classes of trinucleosome structures in 30-bp chromatin. (**I**) Structural modeling of a tetranucleosome in 30-bp chromatin. Density is shown as gray surface; four fitted individual mononucleosome models (PDB: 6pwe) are shown as red and green spheres.

During refinement, nucleosomes in 25-bp chromatin showed only one linker DNA segment emerging from the core particle (Fig. 3B). Subclassification yielded a panel of structures with distinct orientations of the second linker when aligned based on the first (Fig. 3C). These orientations differed in DNA crossing angle at the nucleosome dyad (Fig. 3C, top) and in deviations out of the nucleosome plane (Fig. 3C, bottom), similar to mononucleosomes analyzed in high salt (*104*). In further reconstructions of 25-bp dinucleosomes, adjacent nucleosomes adopted different conformations, with varying twist angles (α) between them (Fig. 3D). This flexibility prevented subtomogram averaging of trinucleosomes or more complex structures. The flexibility of both individual nucleosomes and nucleosome pairs is likely related to the reported importance of nucleosome breathing and DNA twisting for efficient chromatin phase separation (*57*, *88*).

The 30-bp chromatin behaves differently (Fig. 3E). Mononucleosomes in 30-bp chromatin condensates could be refined to high resolution

with two linker DNA segments clearly observable (Fig. 3, F and G). These segments have a crossing angle of 57°, similar to that observed in cryoEM reconstructions of mononucleosomes (Fig. 3F, G) (*105*, *106*). We could also reconstruct trinucleosome (two conformers, Fig. 3H) and tetranucleosome structures (but not larger), the latter with additional partial nucleosome densities surrounding it (Fig. 3I). Both assemblies show pairs of stacked, alternating nucleosomes (N:$N+2$), oriented approximately orthogonally to the other nucleosome(s). Our data suggest that the tetranucleosome is the largest well-ordered element in the 30-bp dodecameric arrays within condensates.

Overall, within the condensates, 25-bp chromatin adopts more diverse configurations, whereas 30-bp chromatin is more constrained and stereotypical. This is true for individual nucleosomes and for larger groupings within a fiber. As in the dilute phase, the 30-bp chromatin makes numerous intramolecular face-to-face stacking interactions, which are not frequently observed in the 25-bp chromatin.

Balance of intra- and intermolecular interactions determines condensate stability

To translate molecular features of 25- and 30-bp chromatin to phase separation behaviors of the two molecules, we next compared the organization of nucleosomes and nucleosome arrays on larger scales. The radial distribution function, $g(r)$, of nucleosomes in 25-bp chromatin is broad and only modestly different from a random distribution, whereas that of 30-bp chromatin shows distinct peaks indicating face-to-face stacking (Fig. 4A). Similarly, the distribution of angles between the planes of nearest neighbor nucleosomes in 25-bp chromatin deviates only modestly from a random (sinusoidal) distribution (*103*) (Fig. 4B). By contrast, nucleosomes in 30-bp condensates show a strong preference for low angles (~parallel geometry), with a maximum at ~15° and substantial depletion for angles >~45° (Fig. 4B). Together, the data are consistent with an abundance of face-to-face stacking in 30-bp condensates and more-heterogeneous orientations in 25-bp condensates.

To understand how pairwise nucleosome packing generates interactions between arrays, we next sought to connect the assigned nucleosomes into molecular units (fig. S5, E to J, and movies S4 and S5). Ambiguities in nucleosome positions and orientations and weak linker DNA density made it slow and laborious to connect nucleosomes into arrays. Nevertheless, we did connect 10 groups of more than eight nucleosomes into molecular units in the 25- and 30-bp condensates. For each molecule, we also identified all surrounding nucleosomes (Fig. 4, C and D).

As illustrated in Fig. 4C and fig. S6, A and B, within condensates, 25-bp nucleosome arrays are relatively expanded, with an average R_g of 18.2 ± 1.3 nm. The molecules adopt numerous, irregular conformations. By contrast, the 30-bp arrays are compact, with average R_g of 13.9 ± 0.9 nm, and composed mostly of groups of four to six nucleosomes organized into two-start helices, with nucleosomes N and $N+2$ stacked face-to-face (Fig. 4D and fig. S6, C and D). For both chromatin types, the structures observed within the condensates have similar values and distributions of R_g, α, D, and *para* to those observed in the dilute phase under the same solution conditions (fig. S6, B, and E to G), suggesting that phase separation may not strongly affect the conformation and flexibility of individual molecules. One caveat is that molecules recently dissociated from the condensate and captured by freezing proximal to the liquid-liquid interface may not have relaxed to their equilibrium dilute-phase configurations.

The differences in molecular conformation produce starkly different patterns of intra- and intermolecular interactions for the two chromatin types (Fig. 4, C and D). Because of their extension and nucleosome arrangements, 25-bp arrays show few intramolecular contacts and many intermolecular contacts (Fig. 4C). This behavior is inverted for 30-bp arrays, which make approximately twice as many intramolecular contacts as 25-bp arrays and ~30% fewer intermolecular contacts than 25-bp arrays. The types of intermolecular interactions made by the two systems are also different (Fig. 4E). The 25-bp arrays make a much larger fraction of the most energetically favorable contacts (face-to-face) than the 30-bp arrays, which show a larger fraction of weaker contacts (face-to-side and side-to-side) (*83*, *87*) (Fig. 4F). Thus, within condensates, 25-bp chromatin molecules make a larger number of intermolecular contacts, with more energetically favorable geometries, compared with 30-bp chromatin molecules. These differences suggest a greater enthalpic gain upon condensate formation for 25-bp chromatin.

To examine histone tail contacts within the condensates, we simulated clusters of arrays surrounding a molecule similar in conformation to one found in the cryo-ET tomograms (Fig. 4, G and H, fig. S7, and table S1) and quantified contacts of the histone tails of the central molecule (Fig. 4I). Paralleling the nucleosome contacts observed in the cryo-ET tomograms (Fig. 4E), the simulations revealed that in 25-bp condensates, histone tails make more interarray than intra-array contacts (Fig. 4I). By contrast, again in agreement with the cryo-ET data (Fig. 4E), most histone tail interactions in 30-bp condensates are intra-array (Fig. 4I).

In 25-bp condensates, chromatin fibers interact frequently via their H4 and H2A(N) tails (Fig. 4I), which is consistent with the prevalence of interarray face-to-face stacking (Figs. 3A and 4, F and G). Conversely, within 30-bp condensates, the H4 and H2A(N) tails make many fewer interarray contacts (Fig. 4I). This results in a relatively flat distribution of interarray contacts across the four tails for the 30-bp chromatin. Notably, the pattern of interarray contacts in 25-bp chromatin resembles that of intra-array contacts in 30-bp chromatin [dominant H4 and H2A(N)] because both are enriched in nucleosome face-to-face stacking. However, H2B interactions are numerous in the former but nearly absent in the latter. This difference arises because antiparallel stacking in 25-bp chromatin positions the H2B tail in contact with the entry and exit DNA of the neighboring nucleosome, whereas parallel stacking in 30-bp chromatin positions it more peripherally. Thus, analogous to single fibers (Fig. 2), intermolecular contacts of histone tails in condensates are determined by a combination of fiber conformation and tail position within the nucleosome. As described in tables S5 and S6, the patterns of tail interactions observed here are generally consistent with previous biochemical studies of tail contributions to chromatin oligomerization, with the caveat that for 30-bp chromatin, perturbations disrupting nucleosome stacking will affect both oligomerization and the conformation of individual arrays.

Histone tail acetylation is associated with increasing chromatin accessibility in cells and can dissolve chromatin condensates in vitro (*33*). To investigate how acetylation influences chromatin packing, we treated 30-bp chromatin with p300 histone acetyltransferase and captured temporal snapshots using cryo-ET. Unmodified 30-bp chromatin condensates have virtually no pores larger than 14 nm (fig. S8, A and D). Upon acetylation, larger pores emerge (fig. S8, B to D) and overall nucleosome density decreases (fig. S8E). Pore number and size increase with the duration of acetylation, with some large enough to accommodate macromolecular complexes such as RNA polymerase II—15 nm versus pores as large as 20 to 25 nm. The changes in density and pore size distribution coincide with loss of face-to-face nucleosome packing interactions, indicating disruption of the helical structure of individual arrays (fig. S8, F and G). These observations indicate that acetylation can disrupt local chromatin fiber structure and may induce the formation of physical voids within cellular chromatin, providing a structural mechanism that could facilitate transcriptional activation by enhancing accessibility.

These data lead to a model in which linker length determines the conformation of chromatin molecules, which in turn determines the balance between intra- and intermolecular contacts as well as the energetic strength of those contacts. These contacts then define the thermodynamic stability of their condensates. Twenty-five–base pair chromatin adopts conformations favoring strong and numerous intermolecular interactions, producing more stable condensates. Thirty–base pair chromatin adopts conformations that allow weaker and

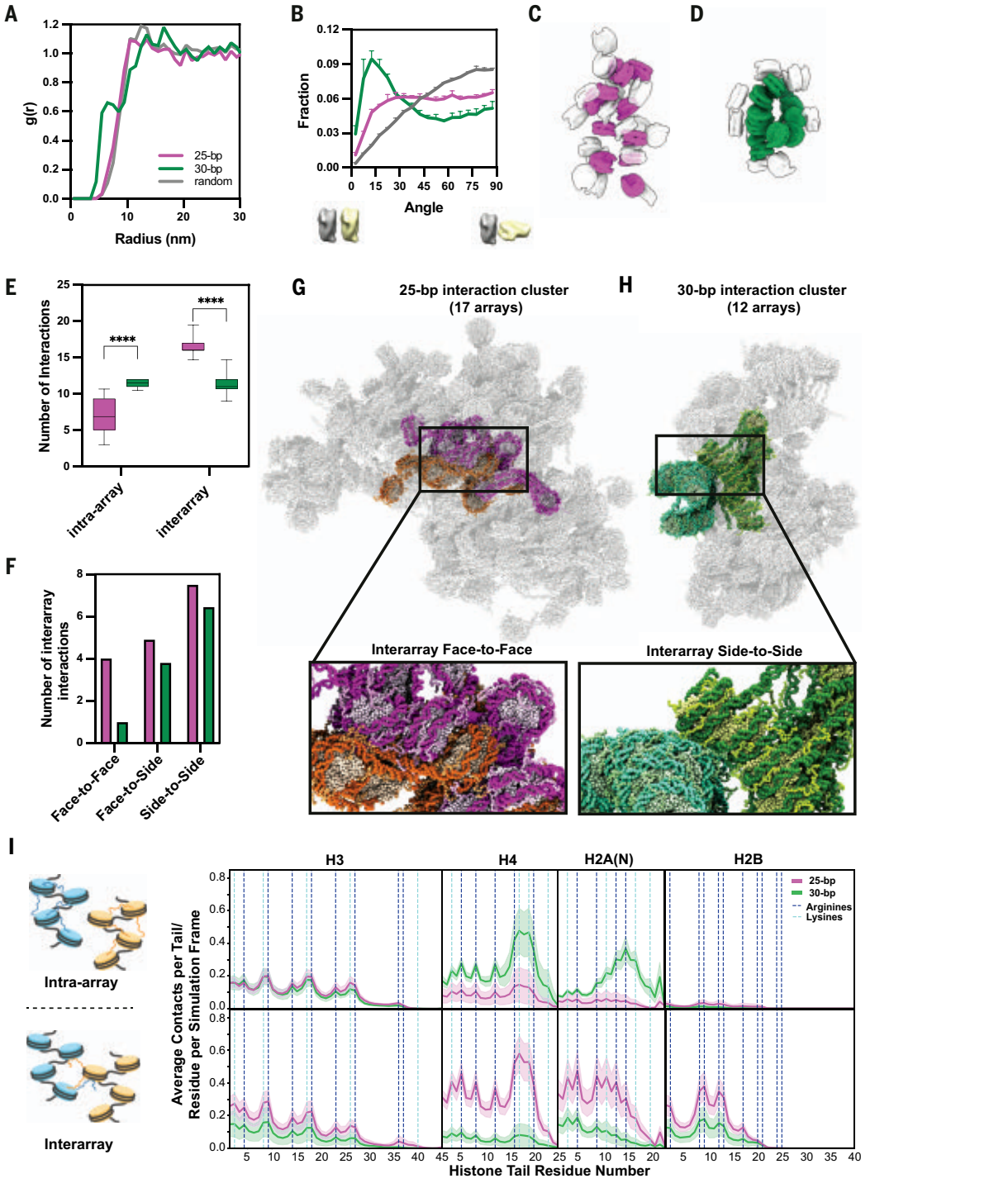


Fig. 4. Linker length determines balance of intra- and intermolecular interactions in the condensed phase. (**A**) Radial distribution functions, $g(r)$, of 25-bp (magenta) chromatin, 30-bp (green) chromatin, and a bath of randomly oriented nucleosomes at equivalent density (gray). Peaks at 6, ~12, and ~16 nm in 30-bp chromatin reflect pairwise and higher-order nucleosome stacking. (**B**) Distributions of nearest dinucleosome orientations for 25-bp (magenta) and 30-bp (green) chromatin. Zero and ninety degrees represent parallel and perpendicular orientations, respectively. (**C** and **D**) Representative manually traced individual nucleosome arrays [25-bp (magenta) in (C), 30-bp (green) in (D)] and their immediate neighboring nucleosomes (gray) within chromatin condensates. See fig. S5, E to J, and movies S4 and S5 for nucleosome tracing. (**E**) Intra and internucleosome interactions of 25-bp (magenta) and 30-bp (green) nucleosome arrays within chromatin condensates, Statistical analysis was performed with a *t* test; $****P < 0.0001$, $n = 11$. (**F**) Intermolecular contacts between traced arrays and their immediate neighboring nucleosomes with face-to-face, face-to-side, and side-to-side geometries (25-bp, magenta; 30-bp, green). (**G** and **H**) Representative high-resolution snapshots of reconstructed clusters of chromatin arrays in the 25-bp [(G), magenta and orange] and 30-bp [(H), green and cyan] chromatin condensates. In each panel, the array most similar to a traced array in a cryo-ET tomogram (see materials and methods) is highlighted. All arrays interacting with this central array are shown, with one colored orange (25 bp) or cyan (30 bp). (Insets) Expanded images of the two interacting arrays, to show face-to-face (G) or side-to-side (H) interarray stacking. (**I**) Number of internucleosome contacts (average per residue per simulation frame) between histone tails of one nucleosome and the DNA and histones of a neighboring nucleosome (intra-array, top; interarray, bottom) within simulated clusters (25-bp, magenta; 30-bp, green; averaged over 400 simulation frames; see table S1.) The blue and cyan vertical lines show positions of lysines and arginines, respectively. Shading indicates 1 SD from the mean.

fewer intermolecular interactions (but more and stronger intramolecular interactions), producing less-stable condensates (movie S6).

Linker length determines connectivity of the condensate network

We next used the minimal model coarse-grained simulations (see materials and methods) to relate the network of interactions between chromatin arrays to material properties of the condensates. We abstracted the simulations to graph networks where nodes and edges represent array molecules and interactions between them, respectively (Fig. 5, A and B, and fig. S9, A and B). Figure 5, A and B, shows cross sections through the centers of representative networks, generated by temporal snapshots of simulations of each chromatin type. The 25-bp network is more densely connected than the 30-bp network, as described quantitatively by the average number (fig. S9C) and strength (fig. S9, D and E) of pairwise interarray interactions and by normalized algebraic connectivity values of 0.88 ± 0.03 and 0.73 ± 0.05, respectively (on a scale of 0 to 1, where 0 indicates no connections and 1 indicates all nodes connected with the highest node degree in the 25-bp chromatin).

To examine network connectivity biochemically, we treated the condensates with trypsin, which cleaves histone tails leading to dissolution (*33*) (Fig. 5C). Twenty-five–base pair condensates were more resistant than 30-bp condensates, which is consistent with greater histone tail–mediated connectivity. We also modeled this process by reducing the number of potential interactions between nucleosomes in simulations. We found that the size of the largest connected cluster of molecules decreased much faster for 30-bp chromatin than for 25-bp chromatin, aligning with the experimental results (fig. S9F).

Thus, the differences in molecular interactions of 25- and 30-bp chromatin produce higher-order networks with different degrees of connectivity (movie S6).

25- and 30-bp chromatin show distinct dynamics on meso- and molecular scales

The differences in affinity (likely reflecting differences in lifetime) and density of bonds in 25- and 30-bp chromatin condensates suggested that the material properties of the two liquids might differ (*5*, *30*, *107*, *108*). To test this idea on the mesoscale, we measured viscoelasticity of the condensates using passive microrheology with optical traps (pMOT)

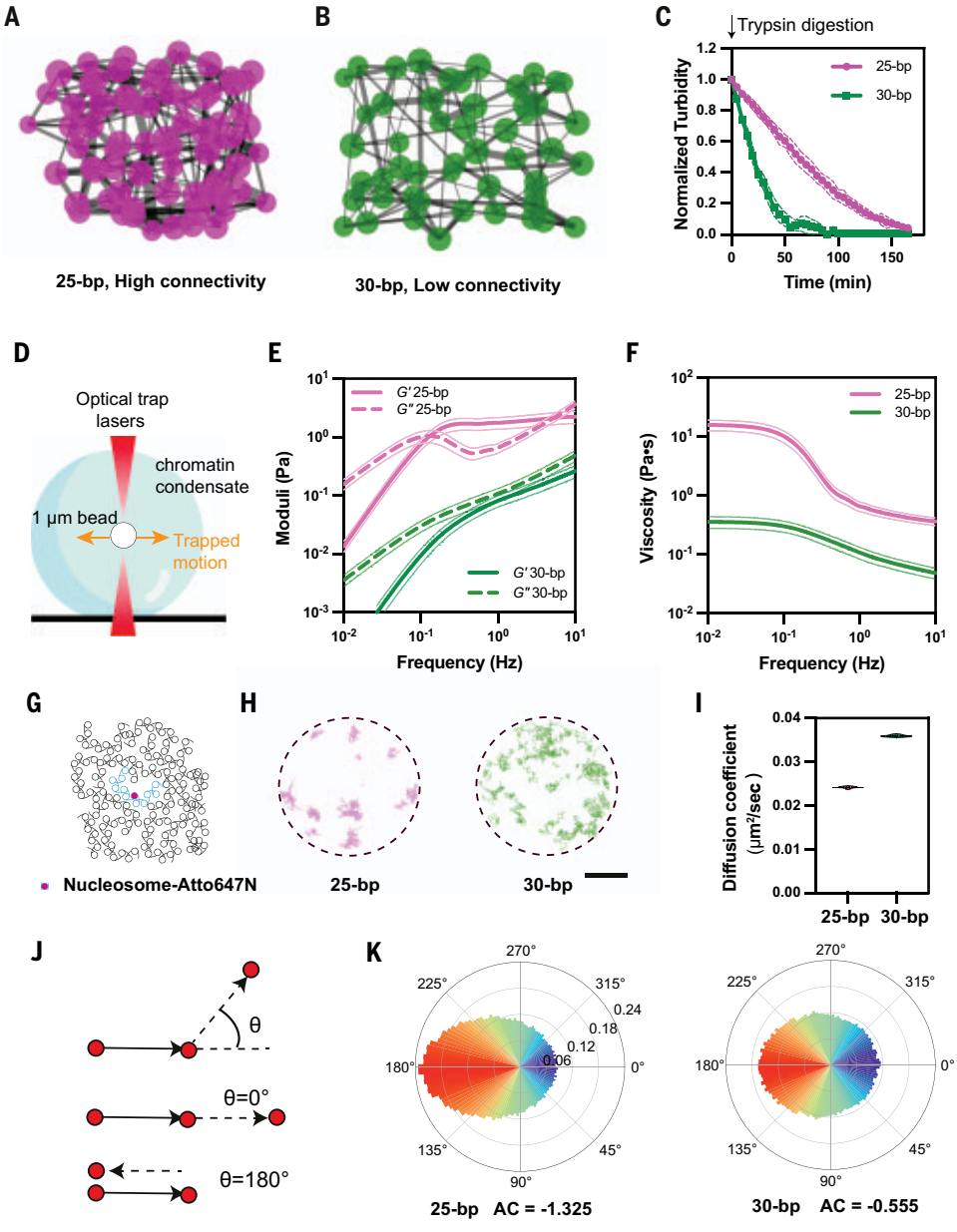


Fig. 5. Distinct dynamics of 25- and 30-bp chromatin condensate on molecular- and mesoscales. (**A** and **B**) Cross sections of interaction networks derived from coarse-grained simulations of 25-bp (A) and 30-bp (B) chromatin condensates. Node diameter is scaled by number of molecules contacted by each array; edge thickness is scaled by energy of association between each pair of molecules. (**C**) Normalized turbidity (absorption at 345 nm) of solutions containing chromatin droplets after introduction of trypsin. (**D**) Schematic illustrating passive microrheology with optical traps (pMOT): A 1-μm bead is optically trapped within chromatin condensate, and its trapped motion is tracked over time with a brightfield camera or quadrant photodetector. (**E**) Average elastic/storage (G') and viscous/loss (G'') moduli of 25-bp (magenta; $n = 12$) and 30-bp (green; $n = 11$) chromatin condensates. Representative individual plots are shown in fig. S11. Thick lines indicate average; thin lines represent standard error from the mean. (**F**) Viscosity of 25-bp (magenta; $n = 12$) and 30-bp (green; $n = 11$) chromatin condensates, calculated from G'' data in (E); plotted as shown in (E). Thick lines, average; thin lines, standard error. (**G**) Schematic illustrating single-molecule tracking experiments. Sparse labeling of nucleosome arrays with Atto647N dye enables tracking of individual molecules. (**H**) Trajectories of single-nucleosome array in 25-bp (magenta) and 30-bp (green) chromatin condensates. Scale bar, 1 μm. (**I**) Diffusion coefficients calculated for nucleosome arrays in 25-bp (total 7670 trajectories) and 30-bp (total 3167 trajectories) chromatin condensates. (**J**) Schematic illustration of trajectory angular analysis, where the angle between every pair of steps in a single-molecule trajectory is measured. Zero degrees corresponds to directed motion and 180° indicates back-and-forth movement. (**K**) Trajectory angular analysis distributions for nucleosome arrays in 25-bp (left) and 30-bp (right) chromatin condensates. Asymmetry coefficient (AC) describes the ratio of forward to backward movement on a $\log_2$ scale.

(Fig. 5D). The optically trapped beads move less in 25-bp condensates than in 30-bp condensates (fig. S10, A to D). Analysis of the trajectories yields the viscoelastic modulus (G^*), composed of viscous (G'') and elastic (G') moduli (Fig. 5E, and fig. S10, E to N). The 25-bp chromatin condensates have higher G' and G'' than 30-bp condensates in all measured frequency regimes. Moreover, whereas viscous behavior is dominant ($G'' > G'$) on all timescales for 30-bp condensates, the viscous and elastic moduli intersect at ~0.1 Hz and again at ~5 Hz for 25-bp condensates. Between these frequencies, elastic behavior is dominant ($G' > G''$). pMOT measurements with a fast detector revealed a shallow crossover between G' and G'' for the 30-bp condensates only at very high frequencies, ~10^3 Hz (fig. S10, K and L). Viscoelastic moduli determined by analyses of Brownian motion of fluorescent beads in the condensates showed analogous behaviors (fig. S11, movie S7, and table S7). The pMOT data yielded zero-shear viscosity for 25-bp condensates approximately 40 times higher than that of 30-bp condensates (Fig. 5F). In cryo-ET tomograms, the 25- and 30-bp condensates have comparable nucleosome densities, suggesting that the different material properties likely arise from differences in molecular interaction networks rather than nucleosome density (fig. S12A).

We used two approaches to computationally examine the viscoelastic behavior of the chromatin condensates. First, we analyzed the trajectories of the coarse-grained simulations to extract the shear stress relaxation modulus, $G(t)$ (*30*), which reveals not only the differential material properties of 25- versus 30-bp condensates (Fig. S12B) but also how these changes are governed by distinct chromatin relaxation mechanisms. At short timescales (high frequencies), $G(t)$ is nearly identical for both 25- and 30-bp systems. This similarity stems from the short-time behavior being primarily dictated by fast local processes, including intramolecular bond and angle relaxations. By contrast, at long timescales, the 25-bp system consistently exhibits a higher stress relaxation modulus than the 30-bp system. This difference arises because long-time behavior is dominated by slower, collective mechanisms—such as the formation and rupture of nucleosome-nucleosome interactions, large-scale conformational rearrangements of molecules, and diffusion of entire chromatin arrays. These relaxation processes are considerably hindered in the 25-bp condensates because of the stronger chromatin-chromatin interactions, resulting in a more elastic mechanical response at long times.

We next used a recently described formalism to model $G'$and G'', which is based on the interaction network observed in the simulations (*5*). We found that the differences in connectivity between the 25- and 30-bp condensates were insufficient to account for their different material properties (fig. S12, C to E). However, differences in interaction strength (likely reflecting longer-lived interactions, accounted for through the polymer friction coefficient in the model) did produce the qualitative differences observed in the data (fig. S12F). Thus, within the limitations of the formalism (fig. S10 legend), the modeling suggests that the different intermolecular affinities dominantly account for the differences in viscoelasticity between the two chromatin condensate types.

We also examined dynamics of the condensates on molecular scales by imaging individual dye-labeled array molecules (Fig. 5G and movie S8). Single 25-bp arrays exhibited slower dynamics than 30-bp arrays, with diffusion coefficients of 0.024 ± 0.0002 $\mu m^2/s$ and 0.036 ± 0.0002 $\mu m^2/s$, respectively (Fig. 5, H and I). Additionally, the distribution of jump angles between two consecutive translocations in the trajectories (Fig. 5J) was substantially biased toward 180° for 25-bp arrays compared with 30-bp arrays, indicating less random and more confined dynamics (Fig. 5K). Notably, the calculated asymmetry coefficient (AC)—which describes the ratio of forward to backward movement on a $\log_2$ scale—of 25-bp arrays is similar to that previously reported for single-nucleosome dynamics in live cells [−1.33 versus −1.36 (*109*)]. Thus, chromatin motions are more constrained in 25-bp condensates than in 30-bp condensates.

Together, the rheological and single-molecule data suggest that differences in network interactions arising from differences in linker-dependent molecular structure produce quantitative and qualitative differences in the dynamics of chromatin condensates spanning meso- to molecular scales (movie S6).

Native chromatin forms domains with nucleosome organization similar to 25-bp condensates

We investigated chromatin organization in vitrified HeLa cell nuclei and intact NIH 3T3 cells using cryo–focused ion beam milling and cryo-ET (Fig. 6, A to F). Each system had nuclear domains of high nucleosome density, varying in size from ~100 to 300 nm, surrounded by regions of lower density. These structures, which were also reported in a recent cryo-ET study of T-lymphoblast CEM and RPE-1 nuclei (*65*, *70*), are similar in size to domains of high-density DNA observed by super-resolution fluorescence microscopy (*49*, *50*). Staining for epigenetic marks suggested that those structures corresponded to inactive chromatin (*50*). Thus, the high-density domains we observe here may be inactive chromatin as well.

Radial distribution functions and overall density of nucleosomes in each native chromatin sample were similar to those of synthetic 25-bp chromatin condensates (Fig. 6G and fig. S13A). The orientation distribution and patterns of packing geometries of nearest nucleosome pairs were also similar for native chromatin and 25-bp chromatin condensates, showing modest deviations from a random distribution (Fig. 6, H and I, and fig. S14). Thus, at the level of individual nucleosomes, dense chromatin regions and 25-bp chromatin condensates have packing arrangements that deviate similarly from randomly organized molecules, likely reflecting geometric features of nucleosome interaction energies and restrictions imparted by DNA linkers.

Inspection of the dense chromatin regions revealed some groups of nucleosomes stacked into two-start helices analogous to those in synthetic 30-bp chromatin condensates (but shorter; Fig. 6, B and E, and fig. S13, B to H). These may be formed by genomic regions with nucleosomes having ~10*N* spacing. These structures might be functionally important if recognized by specific factors or associated with specific loci. Overall, our data show that native chromatin from these cellular sources forms ~100- to 300-nm-scale dense domains composed mostly of nucleosomes that are packed nonrandomly and have an excess of contacts involving nucleosome faces, with occasional instances of two-start helical fibers.

Discussion

Our studies of chromatin illustrate the types of information that may be gained from future cryo-ET studies of other biomolecular condensates composed of large, electron-dense units. Comparison of dilute-phase structures above and below the phase separation threshold can reveal conformational changes that drive assembly. Subtomogram averaging can afford medium resolution structures of individual particles in the dense and dilute phases. For multivalent systems, it may be possible to reconstruct higher-order units of the core particle (e.g., multinucleosome groupings; Fig. 3). It may also be possible to observe and reconstruct client molecules that bind the phase-separating scaffold molecules. At a higher level, one can visualize the spatial arrangement of components on nano- to micrometer-length scales. Such analyses will reveal local packing interactions (distances, geometries, pore sizes; energetics, when coupled with modeling), which inform on the drive to phase separate. On longer scales, network architecture, when coupled with dynamics measurements, will inform on viscoelasticity. Comparison of molecular organization in the core and surface of a condensate can provide a structural explanation for surface tension (*103*) and potentially surface chemistry. Future developments in the representation and analyses of molecules within condensates should yield additional information and insights beyond those considered here.

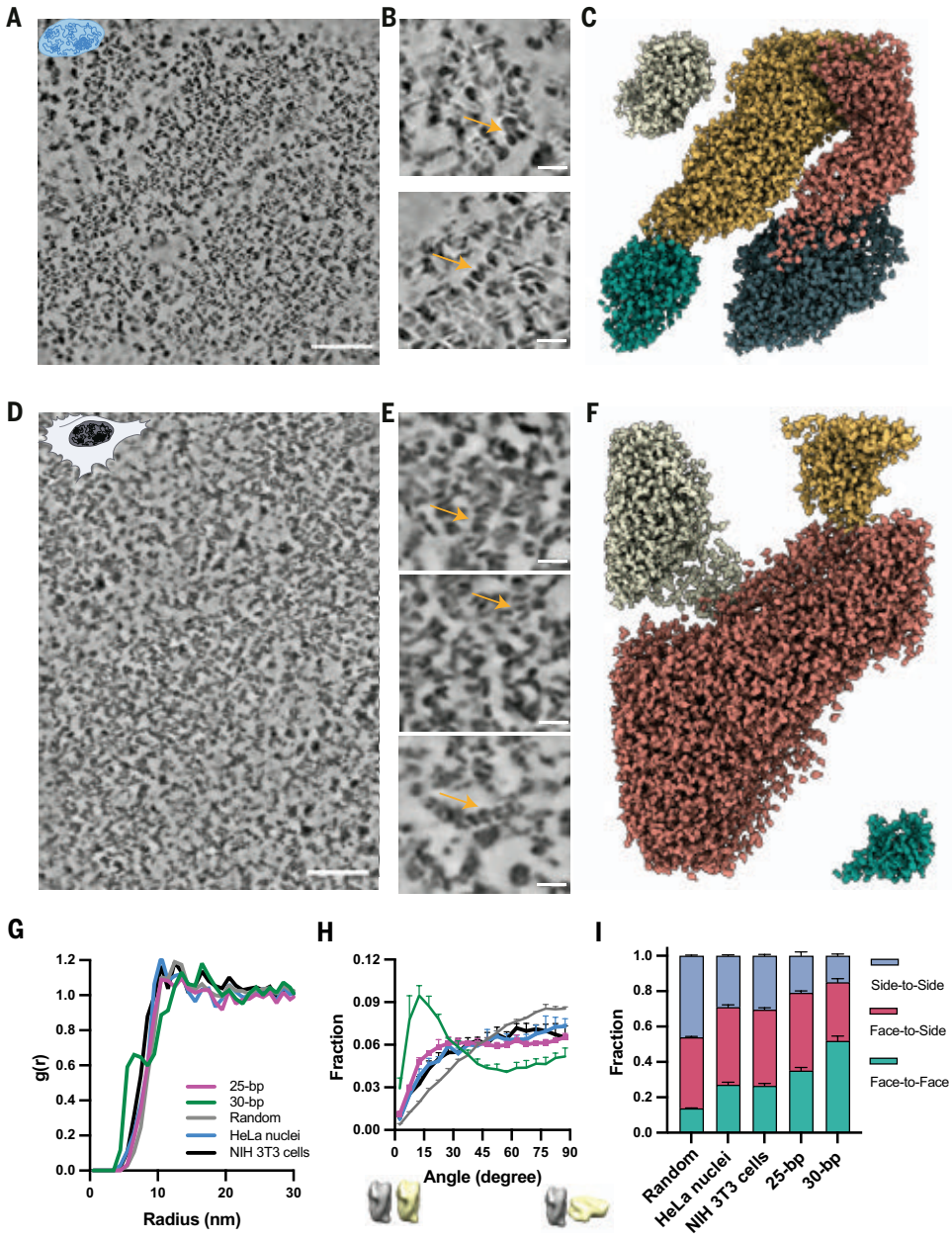


Fig. 6. Native chromatin forms discrete domains organized similarly to 25-bp chromatin condensates. (**A** to **F**) Tomographic slices and 3D reconstructions illustrating nuclear nucleosome organization. [(A) to (C)] Overview slice (scale bar, 100 nm), expanded regions (scale bar, 20 nm), and 3D nucleosome model assignments from a purified HeLa cell nucleus. [(D) to (F)] Analogous images from the nucleus of an intact NIH 3T3 cell. (B) and (E) are not expansions of regions from (A) and (D) but are derived from different planes of the tomograms. Different colors in (C) and (F) represent distinct chromatin nanodomains by manual segmentation. (**G**) Radial distribution functions, $g(r)$, for randomly oriented nucleosomes (gray), nucleosomes in 25-bp chromatin condensates (magenta), purified HeLa cell nuclei (cyan), and nuclei of intact NIH 3T3 cells (black). (**H**) Distributions of nearest dinucleosome orientations for 25-bp chromatin condensates (magenta), purified HeLa cell nuclei (cyan), and nuclei of intact NIH 3T3 cells (black). Zero and ninety degrees indicate parallel and perpendicular orientations, respectively. (**I**) Fractions of face-to-face, face-to-side, and side-to-side pairwise nucleosome contacts in a random nucleosome distribution, 25-bp reconstituted chromatin condensates, nucleosomes in purified HeLa cell nuclei, and nuclei of intact NIH 3T3 cells.

These features are relevant to diverse aspects of condensate function. Structures of individual particles within a condensate may provide insight into activity changes that accompany phase separation. Pore sizes in the molecular network will be relevant to recruitment, movement, and chemistry of other molecules within a condensate (*110*–*113*). Viscoelasticity will dictate the length- and timescales at which internal processes will be affected by the condensate solution environment and how the condensate will respond to mechanical forces (*114*–*116*). Structures will provide a framework to understand the physical properties of the compartment, such as pH, ion concentrations (*15*, *117*), and hydrophobicity (*14*, *118*). Lastly, condensate structural analyses should explain how disease-causing mutations alter both molecular and higher-order organization to produce functional defects (*119*). These types of analyses will be most applicable to biochemically reconstituted systems where all components are known, but nevertheless they can also be applied in cells when certain components are large and stereotypical.

A long-standing question in the chromatin field is how the one-dimensional (1D) arrangement of nucleosomes along a DNA strand dictates the higher-order organization of the strands to produce a 3D architecture. Numerous studies have shown that 10*N*–base pair nucleosome spacing produces more compact fibers (*85*, *86*, *120*), whereas 10*N* + 5 spacing facilitates higher-order assembly (*33*, *83*). Our cryo-ET data and simulations explain these findings in structural detail. They reveal how differences in nucleosome spacing produce distinct fiber conformations with different histone tail interactions. These conformational differences then determine the balance between intra- and intermolecular contacts, dictating the drive for higher-order assembly as well as the material properties of the condensed states. As a step toward connecting this structural information to function, we also show that weakening histone tail interactions through acetylation alters the pore size distribution within condensed chromatin, which is likely important to acetylation-dependent processes such as transcription and DNA repair. Future studies examining 1D to 3D relationships in chromatin containing other regulatory posttranslational modifications could yield general principles regarding how different compartments of chromatin are formed and function.

Cryo-ET images here and elsewhere (*65*, *70*) show that nuclear chromatin forms dense ~100- to 300-nm foci of concentrated nucleosomes, surrounded by regions of appreciably lower density. These foci and 25-bp chromatin condensates have similar nucleosome density and packing arrangements. It is possible that the foci form through microphase separation [phase separation of a small element of one or more chromosomes (*121*)], although other mechanisms are also possible. It remains unclear how these foci relate to genome organization characterized by single-molecule imaging and

interaction-mapping technologies. The former have shown that small groups of 10 to 50 nucleosomes, termed clutches, assemble into discrete units (*36*). The latter have suggested that on a cell-population basis, genomic regions of 0.2 to 1 mega–base pairs (Mbp) associate into topologically associated domains (TADs) (*36*, *122*, *123*). Such large domains are not typically observed in interaction maps of individual cells sampled at single time points, where only subsets appear to associate (*124*–*127*). But the larger TADs may reflect cellular genome organization averaged over time. The foci we observed by cryo-ET have density of ~600,000 nucleosomes/μm^3. Assuming an average nucleosome repeat length of 192 bp (*128*), this density corresponds to 115 Mbp/μm^3. As a rough estimate, foci of ~100- to 300-nm diameter would contain 315 to 8500 nucleosomes and 60 kilo–base pairs to 1.6 Mbp of DNA. Thus, the foci are much larger than clutches and more consistent in size with TADs. It remains unknown how these foci, each of which represents only a tiny fraction of the human genome (<0.5%), relate to nuclear functions such as transcription and replication, among others. Future studies based on correlated light microscopy and electron microscopy—undertaken to understand epigenetic marks and perhaps genomic regions present in the foci—will be important for learning how these higher-order chromatin structures form and what their functions may be.

REFERENCES AND NOTES

1. P. Li *et al.*, Phase transitions in the assembly of multivalent signalling proteins. *Nature* **483**, 336–340 (2012). doi: 10.1038/nature10879; pmid: 22398450
2. S. F. Banani, H. O. Lee, A. A. Hyman, M. K. Rosen, Biomolecular condensates: Organizers of cellular biochemistry. *Nat. Rev. Mol. Cell Biol.* **18**, 285–298 (2017). doi: 10.1038/nrm.2017.7; pmid: 28225081
3. Y. Shin, C. P. Brangwynne, Liquid phase condensation in cell physiology and disease. *Science* **357**, eaaf4382 (2017). doi: 10.1126/science.aaf4382; pmid: 28935776
4. I. Alshareedah *et al.*, Sequence-specific interactions determine viscoelasticity and aging dynamics of protein condensates. *Nat. Phys.* **20**, 1482–1491 (2024). doi: 10.1038/s41567-024-02558-1; pmid: 39464253
5. S. R. Cohen, P. R. Banerjee, R. V. Pappu, Direct computations of viscoelastic moduli of biomolecular condensates. *J. Chem. Phys.* **161**, 095103 (2024). doi: 10.1063/5.0223001; pmid: 39225536
6. A. Chandrasekaran, K. Graham, J. C. Stachowiak, P. Rangamani, Kinetic trapping organizes actin filaments within liquid-like protein droplets. *Nat. Commun.* **15**, 3139 (2024). doi: 10.1038/s41467-024-46726-6; pmid: 38605007
7. A. S. Lyon, W. B. Peeples, M. K. Rosen, A framework for understanding the functions of biomolecular condensates across scales. *Nat. Rev. Mol. Cell Biol.* **22**, 215–235 (2021). doi: 10.1038/s41580-020-00303-z; pmid: 33169001
8. D. L. J. Lafontaine, J. A. Riback, R. Bascetin, C. P. Brangwynne, The nucleolus as a multiphase liquid condensate. *Nat. Rev. Mol. Cell Biol.* **22**, 165–182 (2021). doi: 10.1038/s41580-020-0272-6; pmid: 32873929
9. A. Yamasaki *et al.*, Liquidity Is a Critical Determinant for Selective Autophagy of Protein Condensates. *Mol. Cell* **77**, 1163–1175.e9 (2020). doi: 10.1016/j.molcel.2019.12.026; pmid: 31995729
10. Z. Wang *et al.*, Material properties of phase-separated TFEB condensates regulate the autophagy-lysosome pathway. *J. Cell Biol.* **221**, e202112024 (2022). doi: 10.1083/jcb.202112024; pmid: 35293953
11. P. Guo *et al.*, PI4P-mediated solid-like Merlin condensates orchestrate Hippo pathway regulation. *Science* **385**, eadf4478 (2024). doi: 10.1126/science.adf4478; pmid: 39116228
12. J. Risso-Ballester *et al.*, A condensate-hardening drug blocks RSV replication in vivo. *Nature* **595**, 596–599 (2021). doi: 10.1038/s41586-021-03703-z; pmid: 34234347
13. L.-P. Bergeron-Sandoval *et al.*, Endocytic proteins with prion-like domains form viscoelastic condensates that enable membrane remodeling. *Proc. Natl. Acad. Sci. U.S.A.* **118**, e2113789118 (2021). doi: 10.1073/pnas.2113789118; pmid: 34887356
14. S. Ambadi Thody *et al.*, Small-molecule properties define partitioning into biomolecular condensates. *Nat. Chem.* **16**, 1794–1802 (2024). doi: 10.1038/s41557-024-01630-w; pmid: 39271915
15. M. R. King *et al.*, Macromolecular condensation organizes nucleolar sub-phases to set up a pH gradient. *Cell* **187**, 1889–1906.e24 (2024). doi: 10.1016/j.cell.2024.02.029; pmid: 38503281
16. A. E. Posey *et al.*, Biomolecular Condensates are Characterized by Interphase Electric Potentials. *J. Am. Chem. Soc.* **146**, 28268–28281 (2024). doi: 10.1021/jacs.4c08946; pmid: 39356108
17. E. W. Martin, C. Iserman, B. Olety, D. M. Mitrea, I. A. Klein, Biomolecular Condensates as Novel Antiviral Targets. *J. Mol. Biol.* **436**, 168380 (2024). doi: 10.1016/j.jmb.2023.168380; pmid: 38061626
18. D. M. Mitrea, M. Mittasch, B. F. Gomes, I. A. Klein, M. A. Murcko, Modulating biomolecular condensates: A novel approach to drug discovery. *Nat. Rev. Drug Discov.* **21**, 841–862 (2022). doi: 10.1038/s41573-022-00505-4; pmid: 35974095
19. T. H. Kim *et al.*, Phospho-dependent phase separation of FMRP and CAPRIN1 recapitulates regulation of translation and deadenylation. *Science* **365**, 825–829 (2019). doi: 10.1126/science.aax4240; pmid: 31439799
20. E. W. Martin *et al.*, Valence and patterning of aromatic residues determine the phase behavior of prion-like domains. *Science* **367**, 694–699 (2020). doi: 10.1126/science.aaw8653; pmid: 32029630
21. A. C. Murthy *et al.*, Molecular interactions underlying liquid-liquid phase separation of the FUS low-complexity domain. *Nat. Struct. Mol. Biol.* **26**, 637–648 (2019). doi: 10.1038/s41594-019-0250-x; pmid: 31270472
22. M. Bose, M. Lampe, J. Mahamid, A. Ephrussi, Liquid-to-solid phase transition of oskar ribonucleoprotein granules is essential for their function in Drosophila embryonic development. *Cell* **185**, 1308–1324.e23 (2022). doi: 10.1016/j.cell.2022.02.022; pmid: 35325593
23. M. Zhang *et al.*, Molecular organization of the early stages of nucleosome phase separation visualized by cryo-electron tomography. *Mol. Cell* **82**, 3000–3014.e9 (2022). pmid: 35907400
24. J. Guillén-Boixet *et al.*, RNA-Induced Conformational Switching and Clustering of G3BP Drive Stress Granule Assembly by Condensation. *Cell* **181**, 346–361.e17 (2020). doi: 10.1016/j.cell.2020.03.049; pmid: 32302572
25. F. Tollervey *et al.*, "Cryo-Electron Tomography of Reconstituted Biomolecular Condensates" in *Phase-Separated Biomolecular Condensates: Methods and Protocols*, H.-X. Zhou, J.-H. Spille, P. R. Banerjee, Eds. (Springer US, 2023), pp. 297–324.
26. X. Zhang *et al.*, Molecular mechanisms of stress-induced reactivation in mumps virus condensates. *Cell* **186**, 1877–1894.e27 (2023). doi: 10.1016/j.cell.2023.03.015; pmid: 37116470
27. J. B. Woodruff *et al.*, The Centrosome Is a Selective Condensate that Nucleates Microtubules by Concentrating Tubulin. *Cell* **169**, 1066–1077.e10 (2017). doi: 10.1016/j.cell.2017.05.028; pmid: 28575670
28. F. J. B. Bäuerlein *et al.*, In Situ Architecture and Cellular Interactions of PolyQ Inclusions. *Cell* **171**, 179–187.e10 (2017). doi: 10.1016/j.cell.2017.08.009; pmid: 28890085
29. X. Liu, X. Xia, M. W. Martynowycz, T. Gonen, Z. H. Zhou, Molecular sociology of virus-induced cellular condensates supporting reovirus assembly and replication. *Nat. Commun.* **15**, 10638 (2024). doi: 10.1038/s41467-024-54968-7; pmid: 39639006
30. A. R. Tejedor, R. Collepardo-Guevara, J. Ramírez, J. R. Espinosa, Time-Dependent Material Properties of Aging Biomolecular Condensates from Different Viscoelasticity Measurements in Molecular Dynamics Simulations. *J. Phys. Chem. B* **127**, 4441–4459 (2023). doi: 10.1021/acs.jpcb.3c01292; pmid: 37194953
31. A. R. Tejedor *et al.*, Protein structural transitions critically transform the network connectivity and viscoelasticity of RNA-binding protein condensates but RNA can prevent it. *Nat. Commun.* **13**, 5717 (2022). doi: 10.1038/s41467-022-32874-0; pmid: 36175408
32. I. Sanchez-Burgos, J. A. Joseph, R. Collepardo-Guevara, J. R. Espinosa, Size conservation emerges spontaneously in biomolecular condensates formed by scaffolds and surfactant clients. *Sci. Rep.* **11**, 15241 (2021). doi: 10.1038/s41598-021-94309-y; pmid: 34315935
33. B. A. Gibson *et al.*, Organization of Chromatin by Intrinsic and Regulated Phase Separation. *Cell* **179**, 470–484.e21 (2019). doi: 10.1016/j.cell.2019.08.037; pmid: 31543265
34. M. W. G. Schneider *et al.*, A mitotic chromatin phase transition prevents perforation by microtubules. *Nature* **609**, 183–190 (2022). doi: 10.1038/s41586-022-05027-y; pmid: 35922507
35. B. A. Gibson *et al.*, In diverse conditions, intrinsic chromatin condensates have liquid-like material properties. *Proc. Natl. Acad. Sci. U.S.A.* **120**, e2218085120 (2023). doi: 10.1073/pnas.2218085120; pmid: 37094140
36. M. Lakadamyali, M. P. Cosma, Visualizing the genome in high resolution challenges our textbook understanding. *Nat. Methods* **17**, 371–379 (2020). doi: 10.1038/s41592-020-0758-3; pmid: 32123395
37. A. G. Larson *et al.*, Liquid droplet formation by HP1α suggests a role for phase separation in heterochromatin. *Nature* **547**, 236–240 (2017). doi: 10.1038/nature22822; pmid: 28636604
38. A. R. Strom *et al.*, Phase separation drives heterochromatin domain formation. *Nature* **547**, 241–245 (2017). doi: 10.1038/nature22989; pmid: 28636597
39. I. Solovei *et al.*, Nuclear architecture of rod photoreceptor cells adapts to vision in mammalian evolution. *Cell* **137**, 356–368 (2009). doi: 10.1016/j.cell.2009.01.052; pmid: 19379699
40. H. Belaghzal *et al.*, Liquid chromatin Hi-C characterizes compartment-dependent chromatin interaction dynamics. *Nat. Genet.* **53**, 367–378 (2021). doi: 10.1038/s41588-021-00784-4; pmid: 33574602
41. J. Dekker, L. A. Mirny, The chromosome folding problem and how cells solve it. *Cell* **187**, 6424–6450 (2024). doi: 10.1016/j.cell.2024.10.026; pmid: 39547207

42. R. R. Cheng *et al.*, Exploring chromosomal structural heterogeneity across multiple cell lines. *eLife* **9**, e60312 (2020). doi: 10.7554/eLife.60312; pmid: 33047670
43. Y. Itoh, E. J. Woods, K. Minami, K. Maeshima, R. Collepardo-Guevara, Liquid-like chromatin in the cell: What can we learn from imaging and computational modeling? *Curr. Opin. Struct. Biol.* **71**, 123–135 (2021). doi: 10.1016/j.sbi.2021.06.004; pmid: 34303931
44. K. Luger, A. W. Mäder, R. K. Richmond, D. F. Sargent, T. J. Richmond, Crystal structure of the nucleosome core particle at 2.8 A resolution. *Nature* **389**, 251–260 (1997). doi: 10.1038/38444; pmid: 9305837
45. S. Pepenella, K. J. Murphy, J. J. Hayes, Intra- and inter-nucleosome interactions of the core histone tail domains in higher-order chromatin structure. *Chromosoma* **123**, 3–13 (2014). doi: 10.1007/s00412-013-0435-8; pmid: 23996014
46. M. A. Ricci, C. Manzo, M. F. García-Parajo, M. Lakadamyali, M. P. Cosma, Chromatin Fibers Are Formed by Heterogeneous Groups of Nucleosomes In Vivo, Chromatin fibers are formed by heterogeneous groups of nucleosomes in vivo. *Cell* **160**, 1145–1158 (2015). doi: 10.1016/j.cell.2015.01.054; pmid: 25768910
47. M. Ohno *et al.*, Sub-nucleosomal Genome Structure Reveals Distinct Nucleosome Folding Motifs. *Cell* **176**, 520–534.e25 (2019). doi: 10.1016/j.cell.2018.12.014; pmid: 30661750
48. H. D. Ou *et al.*, ChromEMT: Visualizing 3D chromatin structure and compaction in interphase and mitotic cells. *Science* **357**, eaag0025 (2017). doi: 10.1126/science.aag0025; pmid: 28751582
49. T. Nozaki *et al.*, Dynamic Organization of Chromatin Domains Revealed by Super-Resolution Live-Cell Imaging. *Mol. Cell* **67**, 282–293.e7 (2017). doi: 10.1016/j.molcel.2017.06.018; pmid: 28712725
50. E. Miron *et al.*, Chromatin arranges in chains of mesoscale domains with nanoscale functional topography independent of cohesin. *Sci. Adv.* **6**, eaba8811 (2020). doi: 10.1126/sciadv.aba8811; pmid: 32967822
51. G. Pei, H. Lyons, P. Li, B. R. Sabari, Transcription regulation by biomolecular condensates. *Nat. Rev. Mol. Cell Biol.* **26**, 213–236 (2025). doi: 10.1038/s41580-024-00789-x; pmid: 39516712
52. S. Brahmachari, S. Tripathi, J. N. Onuchic, H. Levine, Nucleosomes play a dual role in regulating transcription dynamics. *Proc. Natl. Acad. Sci. U.S.A.* **121**, e2319772121 (2024). doi: 10.1073/pnas.2319772121; pmid: 38968124
53. S. Sekine, H. Ehara, T. Kujirai, H. Kurumizaka, Structural perspectives on transcription in chromatin. *Trends Cell Biol.* **34**, 211–224 (2023). doi: 10.1016/j.tcb.2023.07.011; pmid: 37596139
54. A. E. Ehrenhofer-Murray, Chromatin dynamics at DNA replication, transcription and repair. *Eur. J. Biochem.* **271**, 2335–2349 (2004). doi: 10.1111/j.1432-1033.2004.04162.x; pmid: 15182349
55. E. F. Hammonds *et al.*, Histone H3 and H4 tails play an important role in nucleosome phase separation. *Biophys. Chem.* **283**, 106767 (2022). doi: 10.1016/j.bpc.2022.106767; pmid: 35158124
56. X. Li, Z. An, W. Zhang, F. Li, Phase Separation: Direct and Indirect Driving Force for High-Order Chromatin Organization. *Genes* **14**, 499 (2023). doi: 10.3390/genes14020499; pmid: 36833426
57. S. Sanulli *et al.*, HP1 reshapes nucleosome core to promote phase separation of heterochromatin. *Nature* **575**, 390–394 (2019). doi: 10.1038/s41586-019-1669-2; pmid: 31618757
58. H. Strickfaden *et al.*, Condensed Chromatin Behaves like a Solid on the Mesoscale In Vitro and in Living Cells. *Cell* **183**, 1772–1784.e13 (2020). doi: 10.1016/j.cell.2020.11.027; pmid: 33326747
59. A. Shakya, S. Park, N. Rana, J. T. King, Liquid-Liquid Phase Separation of Histone Proteins in Cells: Role in Chromatin Organization. *Biophys. J.* **118**, 753–764 (2020). doi: 10.1016/j.bpj.2019.12.022; pmid: 31952807
60. Q. Chen *et al.*, Chromatin Liquid-Liquid Phase Separation (LLPS) Is Regulated by Ionic Conditions and Fiber Length. *Cells* **11**, 3145 (2022). doi: 10.3390/cells11193145; pmid: 36231107
61. T. Nozaki *et al.*, Condensed but liquid-like domain organization of active chromatin regions in living human cells. *Sci. Adv.* **9**, eadf1488 (2023). doi: 10.1126/sciadv.adf1488; pmid: 37018405
62. Y. Li, H. Zhang, X. Li, W. Wu, P. Zhu, Cryo-ET study from in vitro to in vivo revealed a general folding mode of chromatin with two-start helical architecture. *Cell Rep.* **42**, 113134 (2023). doi: 10.1016/j.celrep.2023.113134; pmid: 37708029
63. A. J. Beel, M. Azubel, P.-J. Matteï, R. D. Kornberg, Structure of mitotic chromosomes. *Mol. Cell* **81**, 4369–4376.e3 (2021). doi: 10.1016/j.molcel.2021.08.020; pmid: 34520722
64. F. Fatmaoui *et al.*, Cryo-electron tomography and deep learning denoising reveal native chromatin landscapes of interphase nuclei. bioRxiv 2022.08.16.502515 [Preprint] (2022). https://doi.org/10.1101/2022.08.16.502515.
65. Z. Hou, F. Nightingale, Y. Zhu, C. MacGregor-Chatwin, P. Zhang, Structure of native chromatin fibres revealed by Cryo-ET in situ. *Nat. Commun.* **14**, 6324 (2023). doi: 10.1038/s41467-023-42072-1; pmid: 37816746
66. B. Bintu *et al.*, Super-resolution chromatin tracing reveals domains and cooperative interactions in single cells. *Science* **362**, eaau1783 (2018). doi: 10.1126/science.aau1783; pmid: 30361340
67. T.-H. S. Hsieh *et al.*, Mapping Nucleosome Resolution Chromosome Folding in Yeast by Micro-C. *Cell* **162**, 108–119 (2015). doi: 10.1016/j.cell.2015.05.048; pmid: 26119342
68. V. I. Risca, S. K. Denny, A. F. Straight, W. J. Greenleaf, Variable chromatin structure revealed by in situ spatially correlated DNA cleavage mapping. *Nature* **541**, 237–241 (2017). doi: 10.1038/nature20781; pmid: 28024297
69. S. Cai, D. Böck, M. Pilhofer, L. Gan, The in situ structures of mono-, di-, and trinucleosomes in human heterochromatin. *Mol. Biol. Cell* **29**, 2450–2457 (2018). doi: 10.1091/mbc.E18-05-0331; pmid: 30091658
70. J. K. Chen *et al.*, Nanoscale analysis of human G1 and metaphase chromatin in situ. *EMBO J.* **44**, 2658–2694 (2025). doi: 10.1038/s44318-025-00407-2; pmid: 40097852
71. P. T. Lowary, J. Widom, New DNA sequence rules for high affinity binding to histone octamer and sequence-directed nucleosome positioning. *J. Mol. Biol.* **276**, 19–42 (1998). doi: 10.1006/jmbi.1997.1494; pmid: 9514715
72. A. Flaus, Principles and practice of nucleosome positioning *in vitro*. *Front. Life Sci.* **5**, 5–27 (2011). doi: 10.1080/21553769.2012.702667
73. F. Gordon, K. Luger, J. C. Hansen, The core histone N-terminal tail domains function independently and additively during salt-dependent oligomerization of nucleosomal arrays. *J. Biol. Chem.* **280**, 33701–33706 (2005). doi: 10.1074/jbc.M507048200; pmid: 16033758
74. K. Maeshima *et al.*, Nucleosomal arrays self-assemble into supramolecular globular structures lacking 30-nm fibers. *EMBO J.* **35**, 1115–1132 (2016). doi: 10.15252/embj.201592660; pmid: 27072995
75. J. C. Hansen, K. Maeshima, M. J. Hendzel, The solid and liquid states of chromatin. *Epigenetics Chromatin* **14**, 50 (2021). doi: 10.1186/s13072-021-00424-5; pmid: 34717733
76. A. Allahverdi, Q. Chen, N. Korolev, L. Nordenskiöld, Chromatin compaction under mixed salt conditions: Opposite effects of sodium and potassium ions on nucleosome array folding. *Sci. Rep.* **5**, 8512 (2015). doi: 10.1038/srep08512; pmid: 25688036
77. N. Korolev *et al.*, Electrostatic origin of salt-induced nucleosome array compaction. *Biophys. J.* **99**, 1896–1905 (2010). doi: 10.1016/j.bpj.2010.07.017; pmid: 20858435
78. M. Kruithof *et al.*, Single-molecule force spectroscopy reveals a highly compliant helical folding for the 30-nm chromatin fiber. *Nat. Struct. Mol. Biol.* **16**, 534–540 (2009). doi: 10.1038/nsmb.1590; pmid: 19377481
79. J. Widom, Physicochemical studies of the folding of the 100 A nucleosome filament into the 300 A filament. Cation dependence. *J. Mol. Biol.* **190**, 411–424 (1986). doi: 10.1016/0022-2836(86)90012-4; pmid: 3783706
80. N. Jentink, C. Purnell, B. Kable, M. T. Swulius, S. A. Grigoryev, Cryoelectron tomography reveals the multiplex anatomy of condensed native chromatin and its unfolding by histone citrullination. *Mol. Cell* **83**, 3236–3252.e7 (2023). doi: 10.1016/j.molcel.2023.08.017; pmid: 37683647
81. M. Zhang *et al.*, Angle between DNA linker and nucleosome core particle regulates array compaction revealed by individual-particle cryo-electron tomography. *Nat. Commun.* **15**, 4395 (2024). doi: 10.1038/s41467-024-48305-1; pmid: 38782894
82. T. Nikitina, D. Norouzi, S. A. Grigoryev, V. B. Zhurkin, DNA topology in chromatin is defined by nucleosome spacing. *Sci. Adv.* **3**, e1700957 (2017). doi: 10.1126/sciadv.1700957; pmid: 29098179
83. L. Chen *et al.*, Nucleosome spacing can fine-tune higher-order chromatin assembly. *Nat. Commun.* **16**, 6315 (2025). doi: 10.1038/s41467-025-61482-x; pmid: 40628730
84. H. Kenzaki, S. Takada, Linker DNA Length is a Key to Tri-nucleosome Folding. *J. Mol. Biol.* **433**, 166792 (2021). doi: 10.1016/j.jmb.2020.166792; pmid: 33383034
85. T. Schalch, S. Duda, D. F. Sargent, T. J. Richmond, X-ray structure of a tetranucleosome and its implications for the chromatin fibre. *Nature* **436**, 138–141 (2005). doi: 10.1038/nature03686; pmid: 16001076
86. F. Song *et al.*, Cryo-EM study of the chromatin fiber reveals a double helix twisted by tetranucleosomal units. *Science* **344**, 376–380 (2014). doi: 10.1126/science.1251413; pmid: 24763583
87. A. Golembeski, J. Lequieu, A Molecular View into the Structure and Dynamics of Phase-Separated Chromatin. *J. Phys. Chem. B* **128**, 10593–10603 (2024). doi: 10.1021/acs.jpcb.4c04420; pmid: 39413416
88. S. E. Farr, E. J. Woods, J. A. Joseph, A. Garaizar, R. Collepardo-Guevara, Nucleosome plasticity is a critical element of chromatin liquid-liquid phase separation and multivalent nucleosome interactions. *Nat. Commun.* **12**, 2883 (2021). doi: 10.1038/s41467-021-23090-3; pmid: 34001913
89. K. Russell *et al.*, Near-atomistic simulations reveal the molecular principles that control chromatin structure and phase separation. bioRxiv 2025.11.17.688899 [Preprint] (2025). https://doi.org/10.1101/2025.11.17.688899.
90. Y. Qiu *et al.*, Nucleosome condensate and linker DNA alter chromatin folding pathways and rates. bioRxiv 2024.11.15.623891 [Preprint] (2024). https://doi.org/10.1101/2024.11.15.623891.
91. P. J. J. Robinson *et al.*, 30 nm chromatin fibre decompaction requires both H4-K16 acetylation and linker histone eviction. *J. Mol. Biol.* **381**, 816–825 (2008). doi: 10.1016/j.jmb.2008.04.050; pmid: 18653199
92. R. Collepardo-Guevara *et al.*, Chromatin Unfolding by Epigenetic Modifications Explained by Dramatic Impairment of Internucleosome Interactions: A Multiscale Computational Study. *J. Am. Chem. Soc.* **137**, 10205–10215 (2015). doi: 10.1021/jacs.5b04086; pmid: 26192632

93. M. Shogren-Knaak *et al.*, Histone H4-K16 acetylation controls chromatin structure and protein interactions. *Science* **311**, 844–847 (2006). doi: 10.1126/science.1124000; pmid: 16469925
94. B. Dorigo *et al.*, Nucleosome arrays reveal the two-start organization of the chromatin fiber. *Science* **306**, 1571–1573 (2004). doi: 10.1126/science.1103124; pmid: 15567867
95. J. Zhou, J. Y. Fan, D. Rangasamy, D. J. Tremethick, The nucleosome surface regulates chromatin compaction and couples it with transcriptional repression. *Nat. Struct. Mol. Biol.* **14**, 1070–1076 (2007). doi: 10.1038/nsmb1323; pmid: 17965724
96. Q. Chen, R. Yang, N. Korolev, C. F. Liu, L. Nordenskiöld, Regulation of Nucleosome Stacking and Chromatin Compaction by the Histone H4 N-Terminal Tail-H2A Acidic Patch Interaction. *J. Mol. Biol.* **429**, 2075–2092 (2017). doi: 10.1016/j.jmb.2017.03.016; pmid: 28322915
97. T. S. Lewis, V. Sokolova, H. Jung, H. Ng, D. Tan, Structural basis of chromatin regulation by histone variant H2A.Z. *Nucleic Acids Res.* **49**, 11379–11391 (2021). doi: 10.1093/nar/gkab907; pmid: 34643712
98. W. Alvarado, J. Moller, A. L. Ferguson, J. J. de Pablo, Tetranucleosome Interactions Drive Chromatin Folding. *ACS Cent. Sci.* **7**, 1019–1027 (2021). doi: 10.1021/acscentsci.1c00085; pmid: 34235262
99. R. Collepardo-Guevara, T. Schlick, Chromatin fiber polymorphism triggered by variations of DNA linker lengths. *Proc. Natl. Acad. Sci. U.S.A.* **111**, 8061–8066 (2014). doi: 10.1073/pnas.1315872111; pmid: 24847063
100. O. Perišić, R. Collepardo-Guevara, T. Schlick, Modeling studies of chromatin fiber structure as a function of DNA linker length. *J. Mol. Biol.* **403**, 777–802 (2010). doi: 10.1016/j.jmb.2010.07.057; pmid: 20709077
101. B. Dorigo, T. Schalch, K. Bystricky, T. J. Richmond, Chromatin fiber folding: Requirement for the histone H4 N-terminal tail. *J. Mol. Biol.* **327**, 85–96 (2003). doi: 10.1016/S0022-2836(03)00025-1; pmid: 12614610
102. T. Brouwer *et al.*, A critical role for linker DNA in higher-order folding of chromatin fibers. *Nucleic Acids Res.* **49**, 2537–2551 (2021). doi: 10.1093/nar/gkab058; pmid: 33589918
103. H. Zhou *et al.*, Quantitative spatial analysis of chromatin biomolecular condensates using cryoelectron tomography. *Proc. Natl. Acad. Sci. U.S.A.* **122**, e2426449122 (2025). doi: 10.1073/pnas.2426449122; pmid: 40327693
104. S. Bilokapic, M. Strauss, M. Halic, Histone octamer rearranges to adapt to DNA unwrapping. *Nat. Struct. Mol. Biol.* **25**, 101–108 (2018). doi: 10.1038/s41594-017-0005-5; pmid: 29323273
105. Y. Takizawa *et al.*, Cryo-EM Structures of Centromeric Tri-nucleosomes Containing a Central CENP-A Nucleosome. *Structure* **28**, 44–53.e4 (2020). doi: 10.1016/j.str.2019.10.016; pmid: 31711756
106. M. Dombrowski, M. Engeholm, C. Dienemann, S. Dodonova, P. Cramer, Histone H1 binding to nucleosome arrays depends on linker DNA length and trajectory. *Nat. Struct. Mol. Biol.* **29**, 493–501 (2022). doi: 10.1038/s41594-022-00768-w; pmid: 35581345
107. H.-X. Zhou, D. Kota, S. Qin, R. Prasad, Fundamental Aspects of Phase-Separated Biomolecular Condensates. *Chem. Rev.* **124**, 8550–8595 (2024). doi: 10.1021/acs.chemrev.4c00138; pmid: 38885177
108. D. Kota, R. Prasad, H.-X. Zhou, Adenosine Triphosphate Mediates Phase Separation of Disordered Basic Proteins by Bridging Intermolecular Interaction Networks. *J. Am. Chem. Soc.* **146**, 1326–1336 (2024). doi: 10.1021/jacs.3c09134; pmid: 38174879
109. S. Iida *et al.*, Single-nucleosome imaging reveals steady-state motion of interphase chromatin in living human cells. *Sci. Adv.* **8**, eabn5626 (2022). doi: 10.1126/sciadv.abn5626; pmid: 35658044
110. I. Y. Wong *et al.*, Anomalous diffusion probes microstructure dynamics of entangled F-actin networks. *Phys. Rev. Lett.* **92**, 178101 (2004). doi: 10.1103/PhysRevLett.92.178101; pmid: 15169197
111. L.-H. Cai, S. Panyukov, M. Rubinstein, Mobility of Nonsticky Nanoparticles in Polymer Liquids. *Macromolecules* **44**, 7853–7863 (2011). doi: 10.1021/ma201583q; pmid: 22058573
112. L.-H. Cai, S. Panyukov, M. Rubinstein, Hopping Diffusion of Nanoparticles in Polymer Matrices. *Macromolecules* **48**, 847–862 (2015). doi: 10.1021/ma501608x; pmid: 25691803
113. M. Shayegan *et al.*, Probing Inhomogeneous Diffusion in the Microenvironments of Phase-Separated Polymers under Confinement. *J. Am. Chem. Soc.* **141**, 7751–7757 (2019). doi: 10.1021/jacs.8b13349; pmid: 31017394
114. M. L. Gardel, K. E. Kasza, C. P. Brangwynne, J. Liu, D. A. Weitz, "Mechanical Response of Cytoskeletal Networks" in *Biophysical Tools for Biologists, Volume Two: In Vivo Techniques*, J. J. Correia, H. W. Detrich, II, Eds., vol. 89 of *Methods in Cell Biology* (Elsevier, 2008), pp. 487–519. .
115. B. E. Vos, T. M. Muenker, T. Betz, Characterizing intracellular mechanics via optical tweezers-based microrheology. *Curr. Opin. Cell Biol.* **88**, 102374 (2024). doi: 10.1016/j.ceb.2024.102374; pmid: 38824902
116. M. Lee *et al.*, Optogenetic control of mRNA condensation reveals an intimate link between condensate material properties and functions. *Nat. Commun.* **15**, 3216 (2024). doi: 10.1038/s41467-024-47442-x; pmid: 38622120
117. Y. Dai *et al.*, Biomolecular condensates regulate cellular electrochemical equilibria. *Cell* **187**, 5951–5966.e18 (2024). doi: 10.1016/j.cell.2024.08.018; pmid: 39260373
118. T. Wu *et al.*, Single fluorogen imaging reveals distinct environmental and structural features of biomolecular condensates. *Biophysics* (2023). doi: 10.1101/2023.01.26.525727
119. C. Mathieu, R. V. Pappu, J. P. Taylor, Beyond aggregation: Pathological phase transitions in neurodegenerative disease. *Science* **370**, 56–60 (2020). doi: 10.1126/science.abb8032; pmid: 33004511
120. P. J. J. Robinson, L. Fairall, V. A. T. Huynh, D. Rhodes, EM measurements define the dimensions of the "30-nm" chromatin fiber: Evidence for a compact, interdigitated structure. *Proc. Natl. Acad. Sci. U.S.A.* **103**, 6506–6511 (2006). doi: 10.1073/pnas.0601212103; pmid: 16617109
121. E. M. Hildebrand, J. Dekker, Mechanisms and Functions of Chromosome Compartmentalization. *Trends Biochem. Sci.* **45**, 385–396 (2020). doi: 10.1016/j.tibs.2020.01.002; pmid: 32311333
122. Q. Szabo *et al.*, Regulation of single-cell genome organization into TADs and chromatin nanodomains. *Nat. Genet.* **52**, 1151–1157 (2020). doi: 10.1038/s41588-020-00716-8; pmid: 33077913
123. J. Xu *et al.*, A comprehensive benchmarking with interpretation and operational guidance for the hierarchy of topologically associating domains. *Nat. Commun.* **15**, 4376 (2024). doi: 10.1038/s41467-024-48593-7; pmid: 38782890
124. M. Hu, S. Wang, Chromatin Tracing: Imaging 3D Genome and Nucleome. *Trends Cell Biol.* **31**, 5–8 (2021). doi: 10.1016/j.tcb.2020.10.006; pmid: 33191055
125. S. Wang *et al.*, Spatial organization of chromatin domains and compartments in single chromosomes. *Science* **353**, 598–602 (2016). doi: 10.1126/science.aaf8084; pmid: 27445307
126. L. Tan, D. Xing, C.-H. Chang, H. Li, X. S. Xie, Three-dimensional genome structures of single diploid human cells. *Science* **361**, 924–928 (2018). doi: 10.1126/science.aat5641; pmid: 30166492
127. T. J. Stevens *et al.*, 3D structures of individual mammalian genomes studied by single-cell Hi-C. *Nature* **544**, 59–64 (2017). doi: 10.1038/nature21429; pmid: 28289288
128. V. B. Teif *et al.*, Nucleosome repositioning during differentiation of a human myeloid leukemia cell line. *Nucleus* **8**, 188–204 (2017). doi: 10.1080/19491034.2017.1295201; pmid: 28406749

ACKNOWLEDGMENTS

We thank Dan. and Dav. Isenberg for their generous support of the MBL Chromatin Collaborative in honor of their father, I. Isenberg, and the other members of the Collaborative for critical insights and discussion. We thank S. Redding and C. Woodilla for assistance with and discussions regarding chromatin viscoelasticity experiments. We thank J. Iwasa for support and advice during early stages of visualizing chromatin condensates. **Funding:** This work was supported by the Howard Hughes Medical Institute (M.K.R., Z.Y., and E.V.); the Paul G. Allen Frontiers Distinguished Investigator Award (M.K.R.); the Welch Foundation I-1544 (M.K.R.); NIH grants R01AI163142 (A.S.) and 1R35GM141736 (M.K.R.); UK Research and Innovation (UKRI) Engineering and Physical Sciences Research Council (EPSRC) under the UK Government's guarantee scheme (EP/Z002028/1), following funding by the European Research Council (ERC) Consolidator Grant under the European Union's Horizon Europe research and innovation program (R.C.-G.); the Cancer Research and Prevention Institute of Texas RP220582 (UTSW cryo-EM Facility, Structure Biology Lab); the NIH Common Fund Transformative High Resolution Cryo-Electron Microscopy program U24 GM129539 [National Center For In-Situ Tomographic Ultramicroscopy (NCITU)]; UKRI EPSRC EP/R029407/1 (R.C.-G.); the NIH Office of Research Infrastructure Program, S10OD030315 (A.S.); and the St. Jude Research Collaborative on the Biology and Biophysics of RNP Granules, CC11219 (B.A.G.). **Author contributions:** Conceptualization: H.Z., M.K.R.; Funding acquisition: A.S., E.V., R.C.-G., M.K.R.; Investigation: H.Z., J.H., M.J.M., K.R., J.H.H., R.Y., N.S., J.H., M.S., X.Z., L.K.D., B.A.G., J.R.E.; Methodology: H.Z., J.H., M.J.M., K.R., J.H.H., R.-W.Y., E.V., R.C.-G., M.K.R.; Project administration: Z.H., E.V., R.C.-G., M.K.R.; Supervision: A.S., E.V., R.C.-G., M.K.R.; Visualization: H.Z., J.H., M.R.; Writing – original draft: H.Z., M.K.R.; Writing – review & editing: All authors. **Competing interests:** The authors declare that they have no competing interests. **Data and materials availability:** All cryo-ET data are deposited in the Dryad database (*154*). The subtomogram averages of nucleosome structures from the 25- and 30-bp chromatin condensates have been deposited in the EMDB under accession nos. EMD-70745 and EMD-70743, respectively. The CATM software and all cryo-ET analysis scripts are available on Zenodo (*155*). All simulation code has also been deposited in Zenodo (*156*). All reagents described in the work will be available by request to the corresponding authors. Vectors for production of the 25- and 30-bp chromatin arrays are available from Addgene under a Uniform Biological Material Transfer Agreement (UBMTA) with UT Southwestern Medical Center. **License information:** Copyright © 2025 the authors, some rights reserved; exclusive licensee American Association for the Advancement of Science. No claim to original US government works. https://www.science.org/about/science-licenses-journal-article-reuse. This article is subject to HHMI's Open Access to Publications policy. HHMI lab heads have previously granted a nonexclusive CC BY 4.0 license to the public and a sublicensable license to HHMI in their research articles. Pursuant to those licenses, the Author Accepted Manuscript (AAM) of this article can be made freely available under a CC BY 4.0 license immediately upon publication.

SUPPLEMENTARY MATERIALS

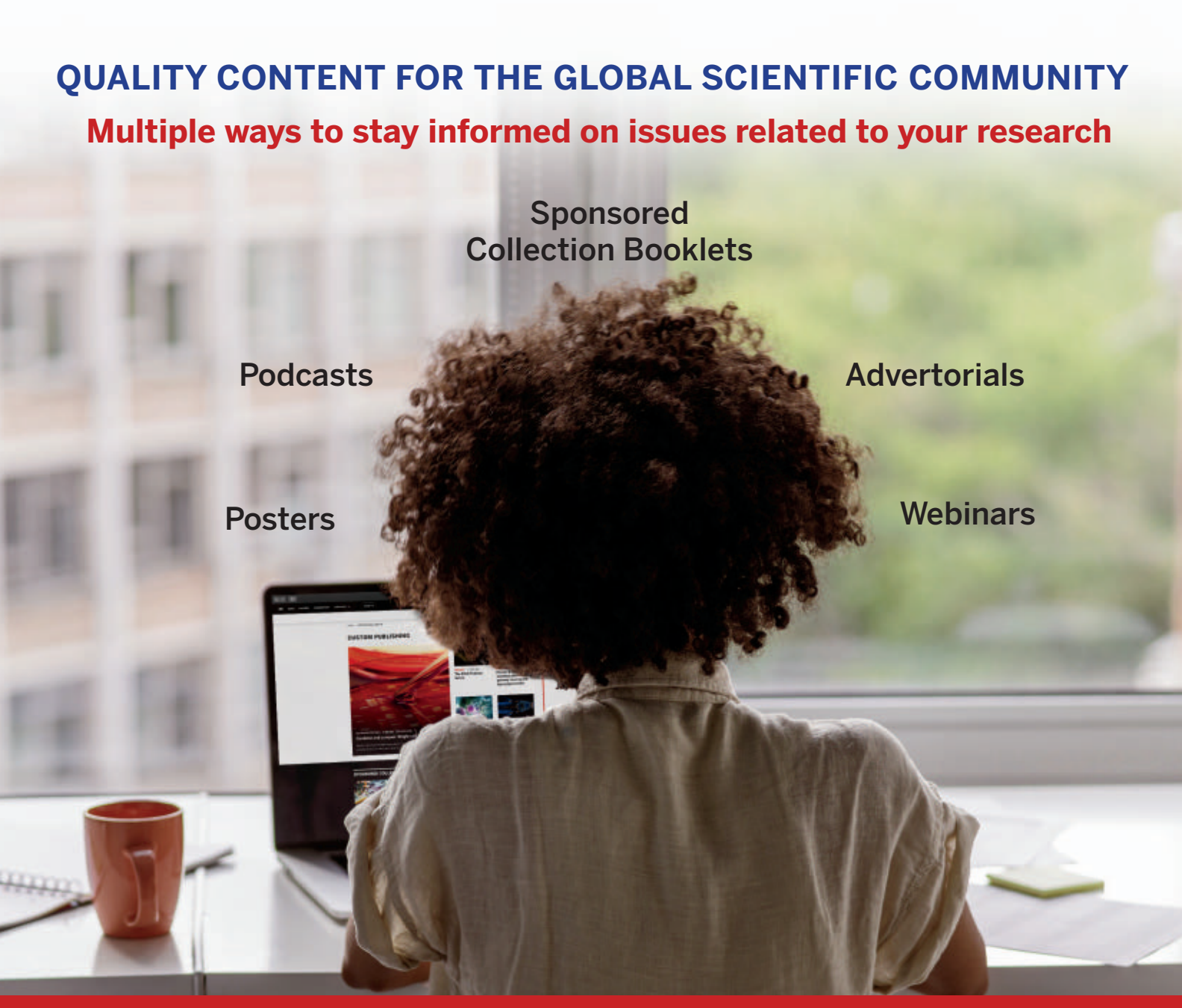
science.org/doi/10.1126/science.adv6588
Materials and Methods; Figs. S1 to S14; Tables S1 to S7; Movies S1 to S8; References (*129*–*166*); MDAR Reproducibility Checklist

Submitted 31 December 2024; accepted 30 September 2025

10.1126/science.adv6588

QUALITY CONTENT FOR THE GLOBAL SCIENTIFIC COMMUNITY

Multiple ways to stay informed on issues related to your research



Science
AAAS

Scan the code and start exploring the latest advances in science and technology innovation!

Science.org/custom-publishing

Brought to you by the *Science*/AAAS Custom Publishing Office.

Posters **Podcasts** **Sponsored Collection Booklets** **Advertorials** **Webinars**

RESEARCH ARTICLE SUMMARY

MOLECULAR BIOLOGY

Cohesin drives chromatin scanning during the RAD51-mediated homology search

Alberto Marin-Gonzalez†, Adam T. Rybczynski†, Namrata M. Nilavar†, Daniel Nguyen, Andrew G. Li, Violetta Karwacki-Neisius, Roger S. Zou, Franklin J. Avilés-Vázquez, Masato T. Kanemaki, Ralph Scully*, Taekjip Ha*

Full article and list of author affiliations: https://doi.org/10.1126/science.adw1928

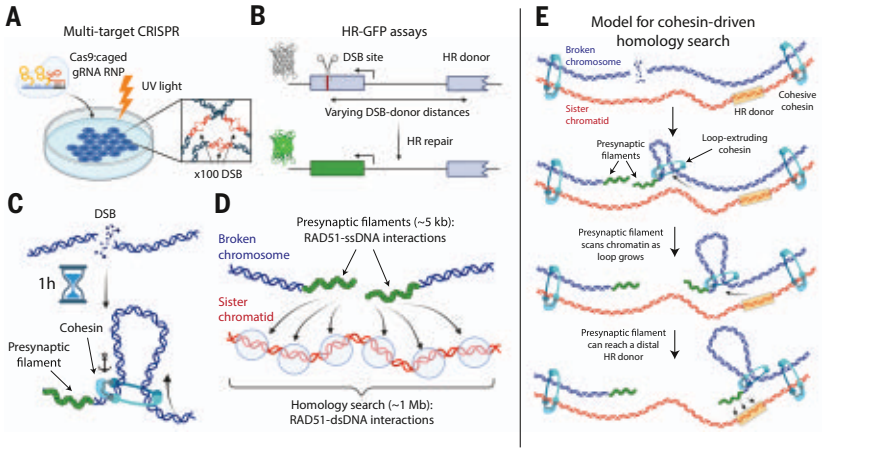
INTRODUCTION: The homologous recombination (HR) pathway repairs DNA lesions, such as double-strand breaks (DSBs), by copying sequence information from a homologous donor DNA template—often the sister chromatid—into the damaged locus. During mammalian HR, the RAD51 (radiation-sensitive protein 51) recombinase forms a nucleoprotein filament, known as the presynaptic filament, around the resected single-stranded DNA (ssDNA) generated during DNA end processing at the DSB. The presynaptic filament then scans the genome in search of an appropriate homologous DNA donor through a process known as the homology search. How the homology search occurs in the context of the three-dimensional (3D) genome remains broadly unexplored.

RATIONALE: To study DSB repair, we used an optogenetic multitarget CRISPR-Cas9 system that creates DSBs with high throughput and temporal control [see (A) in the figure]. We performed time-resolved Hi-C and chromatin immunoprecipitation sequencing (ChIP-seq) analyses after multitarget CRISPR damage in human embryonic kidney (HEK) 293T cells to capture changes in genome architecture and chromatin interactions of key factors during the repair of DSBs, respectively. We also performed recombination assays in mouse embryonic stem cells using an HR–GFP (green fluorescent protein) reporter to measure HR efficiency in response to a Cas9-induced DSB, with donor sites located at varying distances [see (B) in the figure].

RESULTS: We found that Cas9 DSBs induce formation of chromatin loops anchored at the break site in a cohesin-dependent manner. However, contrary to expectations, these break-anchored loops do not form immediately after DSB generation but instead form relatively later (>1 hour) in the repair process, coincident with DNA end resection and formation of the presynaptic filament [see (C) in the figure]. Our ChIP-seq data further revealed that, besides binding to ssDNA around the ~5-kb-long presynaptic filament, RAD51 also binds to double-stranded DNA (dsDNA), covering a broad chromatin domain that extends hundreds of kilobases flanking the DSB site [see (D) in the figure]. Additional experiments showed that this broad chromatin domain reflects RAD51-chromatin interactions that occur during the homology search. This broad RAD51 chromatin domain coincides temporally with the formation of break-anchored chromatin loops, is constrained by TAD boundaries, and is regulated by the cohesin unloader WAPL. Together, our findings suggest that break-anchored chromatin loops participate in the homology search. Indeed, depletion of the loop-extruding cohesin subunit NIPBL results in decreased HR efficiency, and this effect is more pronounced when the intrachromosomal donor is placed at a large distance (several hundreds of kilobases) from the DSB. Our results suggest that loop-extruding cohesin plays a role in the homology search and that its importance in this search increases with increasing genomic distance between the DSB and the intrachromosomal homologous donor within the TAD.

CONCLUSION: Our data suggest that cohesin facilitates the homology search during HR, likely by extruding break-anchored chromatin loops that convert intrachromosomal scanning by the DSB from a 3D problem to an organized 1D process [see (E) in the figure]. Our work reveals an unexpected role for cohesin-organized chromatin loops as mediators of HR repair and captures the genomic searches that occur during mammalian HR. Our findings invite further inquiry regarding the interplay between 3D genome structure and DSB repair processes and the mechanisms of homology search in the cellular context. □

*Corresponding author. Email: taekjip.ha@childrens.harvard.edu (T.H.); rscully@bidmc.harvard.edu (R.S.) †These authors contributed equally to this work. **Cite this article as** A. Marin-Gonzalez *et al.*, *Science* **390**, eadw1928 (2025). DOI: 10.1126/science.adw1928



Chromatin loops accelerate the homology search. (**A**) A multitarget CRISPR system creates DSBs with high throughput and temporal control. (**B**) An HR-GFP reporter is used to measure recombination efficiency at different DSB-HR donor distances. (**C**) A DSB triggers formation of break-anchored chromatin loops at late (>1 hour) time points. (**D**) RAD51 binds to ssDNA during presynaptic filament formation and to dsDNA during the homology search. (**E**) Break-anchored chromatin loops facilitate the homology search by promoting directed 1D scanning. gRNA, guide RNA; RNP, ribonucleoprotein; UV, ultraviolet. [Figure created with BioRender.com]

MOLECULAR BIOLOGY

Cohesin drives chromatin scanning during the RAD51-mediated homology search

Alberto Marin-Gonzalez[1,2,3]†, Adam T. Rybczynski[1,4]†, Namrata M. Nilavar[5]†, Daniel Nguyen[5], Andrew G. Li[5], Violetta Karwacki-Neisius[1,2], Roger S. Zou[6], Franklin J. Avilés-Vázquez[1,7], Masato T. Kanemaki[8,9,10], Ralph Scully[5]*, Taekjip Ha[1,2,7]*

Cohesin folds genomes into chromatin loops, the roles of which are under debate. We found that double-strand breaks (DSBs) induce de novo formation of chromatin loops in human cells, with the loop base positioned at the DSB site. These loops form in the S and G_2 phases of the cell cycle during homologous recombination repair, concomitantly with DNA end resection and radiation-sensitive protein 51 (RAD51) recruitment. RAD51 shows a broad (megabase-sized) chromatin domain reflective of the homology search. This domain is regulated by cohesin unloader and overlaps with chromatin regions reeled through the break-anchored loop, suggesting that loop extrusion regulates the homology search. Indeed, depletion of the loop-extruding cohesin subunit NIPBL lowers homologous recombination in mouse embryonic stem cells, and this effect is more pronounced when the homologous recombination donor is hundreds of kilobases from the DSB. Our data indicate that loop-extruding cohesin promotes the mammalian homology search by facilitating break-chromatin interactions.

At the scale of hundreds of kilobases to a few megabases, mammalian genomes are organized into topologically associating domains (TADs) and chromatin loops (*1*, *2*). These structures are dependent on the activity of the cohesin complex and are likely formed through a loop-extrusion mechanism, whereby cohesin binds to chromatin and extrudes a loop until a convergent CTCF is found (*3*–*7*). Genomic loci that fall within the same TAD engage in more frequent mutual chromatin contacts than loci from different TADs. Consequently, TADs have been proposed to play a role in modulating transcription by promoting intra-TAD and preventing inter-TAD enhancer-promoter interactions, with potential implications for health and disease (*8*–*13*).

The functions of TADs and chromatin loops have also been investigated in the context of DNA replication (*14*, *15*), V(D)J recombination (*16*, *17*), and DNA repair, particularly, the repair of DNA double-strand breaks (DSBs) (*18*–*21*). With respect to DSB repair, TAD boundaries appear to compartmentalize the chromatin response during the repair process, characterized by the formation of megabase-scale chromatin domains composed of nucleosomes containing phosphorylated H2A.X (γH2AX) and γH2AX-associated repair proteins, including MDC1, 53BP1, and BRCA1 (*20*, *21*). Chromatin immunoprecipitation sequencing (ChIP-seq) analysis of the response to a site-specific mammalian DSB indicated that the γH2AX/MDC1/53BP1 domain is limited by TAD boundaries (*20*–*22*). An explanation for this compartmentalization was suggested by Arnould *et al.* (*21*). On the basis of the finding that DSBs induced by the AsiSI restriction enzyme form chromatin loop anchors, they proposed that H2AX is phosphorylated by the ATM kinase located at the DSB and that the propagation of the γH2AX domain is mediated by the cohesin-dependent extrusion of a break-anchored loop (*21*). A recent work using live-cell imaging revealed that cohesin recruitment to DSB sites peaks considerably later than the recruitment of MDC1, the direct binding partner of γH2AX (*23*). Thus, break-anchored loop extrusion might have additional DSB response functions at stages later than the formation of γH2AX-dependent repair foci. In yeast, site-specific DSBs have also been shown to accumulate cohesin (*24*, *25*) and have been observed to act as loop anchors (*26*). However, in this case, the loops were found to form during DSB repair by homologous recombination (HR) and in a DNA end-resection–dependent manner (*26*). HR is a multistep pathway that entails (i) resectioning of each end of the DSB to generate long 3′ single-stranded DNA (ssDNA) tails; (ii) loading of the radiation-sensitive protein 51 (RAD51) recombinase onto ssDNA to form the RAD51 nucleoprotein filament; (iii) the homology search, that is, the process by which the RAD51-ssDNA nucleoprotein filament searches for a homologous donor, culminating in RAD51-mediated strand exchange; and (iv) repair synthesis and termination of the HR reaction.

In summary, although several functions have been proposed for break-anchored chromatin loops in DSB repair, their role remains poorly understood. Here, we investigated this question using a combination of time-course ChIP-seq, time-course Hi-C, and quantitative assays of HR.

Cas9 breaks are anchors for cohesin loop extrusion

To study DSB-induced changes in the three-dimensional (3D) genome, we induced DSBs using our recently developed multitarget CRISPR system, where a degenerate guide RNA (gRNA), or multitarget gRNA (mgRNA), directs a Cas9 nuclease to induce DSBs at >100 endogenous on-target sites (*27*). We nucleofected human embryonic kidney (HEK) 293T cells with a ribonucleoprotein (RNP) complex composed of purified Cas9 preassembled with the AluGG mgRNA, a gRNA we previously characterized (*27*); we then performed in situ Hi-C (*2*) in these cells 3 hours after delivery of the CRISPR-Cas9 RNP as well as in untreated control cells. For each condition, Hi-C was done in biological replicates and, after confirming strong reproducibility (fig. S1), we merged replicates totaling ~1 billion contacts per condition, which allowed us to build high-resolution Hi-C contact maps. Visual comparison of Hi-C maps around select Cas9 breaks revealed "stripes" that emanated from the predicted location of the Cas9 break (Fig. 1A). These stripes, which represent interactions between the break site and neighboring loci, were absent in the untreated control sample, suggesting that localized DSB-chromatin interactions arise de novo because of Cas9 activity.

To better visualize Cas9-induced changes in chromatin contacts, we computed the log2 of the ratio between the contacts in the Cas9-treated sample and the untreated sample averaged among the 100 best-cleaved sites, as determined from previous MRE11 ChIP-seq (*27*). The resulting differential Hi-C map revealed increased interactions between DSB sites and their neighboring chromatin, represented as cross-shaped stripes (Fig. 1B), consistent with previous studies (*21*, *28*) and with our inspection of individual cut sites (Fig. 1A). We further characterized these DSB-chromatin interactions by computing differential 4C-like plots using the regions adjacent to the breaks as viewpoints (Fig. 1C). DSB-chromatin interactions spanned a distance of ~1 Mb in both directions from the break. Interactions between loci spanning the DSB site were diminished, suggesting that Cas9-induced DSBs acquire chromatin insulation properties, reminiscent of TAD boundaries.

[1]Howard Hughes Medical Institute, Boston Children's Hospital, Boston, MA, USA. [2]Program in Cellular and Molecular Medicine, Boston Children's Hospital, Boston, MA, USA. [3]Department of Pediatrics, Harvard Medical School, Boston, MA, USA. [4]Department of Biology, Johns Hopkins University, Baltimore, MD, USA. [5]Department of Medicine and Cancer Research Institute, Beth Israel Deaconess Medical Center and Harvard Medical School, Boston, MA, USA. [6]Department of Medicine, Massachusetts General Hospital, Boston, MA, USA. [7]Department of Biophysics and Biophysical Chemistry, Johns Hopkins University, Baltimore, MD, USA. [8]Department of Chromosome Science, National Institute of Genetics, Mishima, Japan. [9]Graduate Institute for Advanced Studies, SOKENDAI, Mishima, Japan. [10]Department of Biological Science, Graduate School of Science, The University of Tokyo, Tokyo, Japan. ***Corresponding author. Email: taekjip.ha@childrens.harvard.edu (T.H.); rscully@bidmc.harvard.edu (R.S.)** †These authors contributed equally to this work.

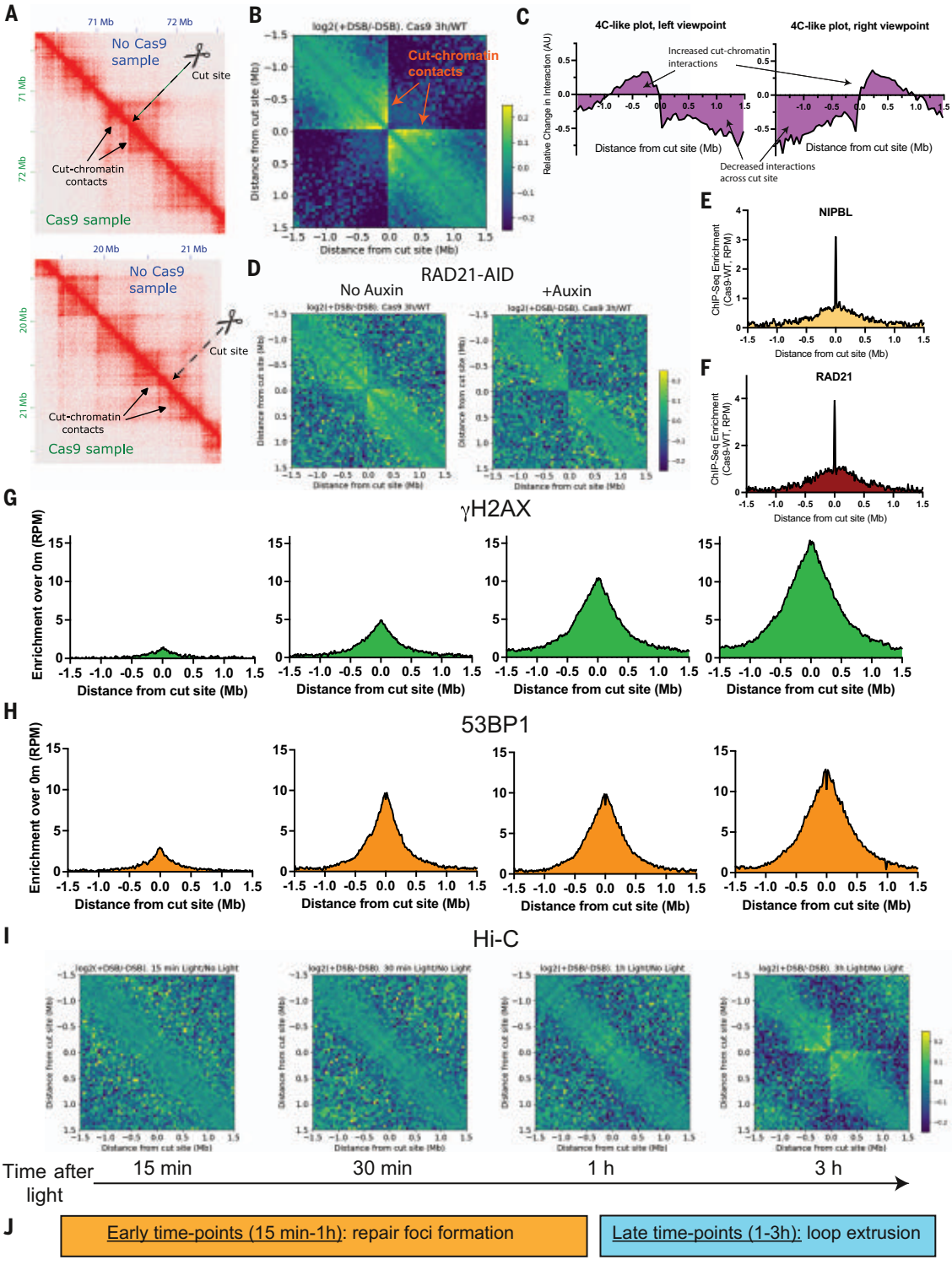


Fig. 1. Break-anchored chromatin loops at Cas9 breaks. (**A**) High-resolution (5 kb) Hi-C maps around two representative AluGG cut sites (in chr9, top; and chr14, bottom) in HEK293T cells. Untreated samples are shown in the top-right triangle; Cas9-treated samples are shown at bottom left. (**B**) Average log2 ratio of chromatin contacts around the 100 AluGG cut sites with the strongest MRE11 enrichment. Hi-C matrices were retrieved at 50-kb resolution in a window of 3 Mb, centered at each MRE11 peak. WT, wild type. (**C**) 4C-like plots were computed from high-resolution Hi-C matrices around the top-100 MRE11 peaks using a left and right viewpoint with respect to the cut site for the Cas9-treated and undamaged sample. AU, arbitrary units. (**D**) Cas9-induced chromatin contacts in HCT116-RAD21-AID2 cells with no drug (left) or with auxin treatment (right). Differential Hi-C contacts were computed and plotted as in (B). (**E** and **F**) Cas9-induced NIPBL and RAD21 ChIP-seq enrichment. ChIP-seq profiles for NIPBL and RAD21 were averaged around the 126 AluGG on-target sites in Cas9-treated and untreated cells. The resulting untreated profile was subtracted from the Cas9-treated profile. Bin size is 5 kb. RPM, reads per million. (**G** to **I**) Time-course γH2AX ChIP-seq (G), 53BP1 ChIP-seq (H), and Hi-C (I). HEK293T cells were treated with Cas9 RNP with caged AluGG gRNA for 12 hours, followed by light-induced Cas9 activation and harvest at 0 min, 15 min, 30 min, 1 hour, and 3 hours. ChIP-seq profiles were computed as described in (E) and (F), and the average Hi-C profile was obtained as in (B), using the 0-min (no-light) control sample as a reference. (**J**) A proposed timeline.

Cohesin has been implicated in the formation of chromatin loops during repair of DSBs induced by the AsiSI restriction enzyme (*21*). To test whether cohesin is also involved at Cas9-induced breaks, we delivered multitarget CRISPR RNP into an HCT116 cell line (human colorectal carcinoma) with RAD21 tagged for auxin-induced degradation (AID) (*29*) and performed Hi-C 3 hours later. To degrade RAD21, we added auxin 1 hour before RNP nucleofection. RAD21 degradation abolished the DSB-chromatin contacts, demonstrating that cohesin is instrumental in the formation of these structures (Fig. 1D and fig. S2). Similar results were obtained when depleting RAD21 with small interfering RNA (siRNA) in HEK293T cells (fig. S2). Finally, the loop-extruding cohesin subunit NIPBL was recruited to Cas9 breaks in HEK293T cells, as determined by ChIP-seq, as were two additional cohesin subunits, RAD21 and the DNA-damage phosphorylated form of SMC1 (pSMC1) (Fig. 1, E and F, and fig. S3), further supporting a direct involvement of cohesin. We conclude that Cas9-induced DSBs interact with their neighboring loci by a cohesin-driven mechanism, possibly involving loop extrusion.

Break-anchored loops form after the formation of the γH2AX domain

Previous work reported the existence of break-anchored chromatin loops at restriction enzyme–induced DSBs, and the authors proposed that a cohesin-based loop-extrusion mechanism is required for formation of the ~1-Mb DNA-repair chromatin domain marked by γH2AX (*21*). To investigate the relative timing of the break-anchored chromatin loops and γH2AX domain formation, we performed a time-course experiment using a light-activated, very fast CRISPR (vfCRISPR) version of our multitarget system (*27*, *30*). In parallel to time-resolved ChIP-seq for γH2AX and 53BP1—two major factors known to decorate chromatin within the TAD that contains the DSB (*31*)—we performed time-resolved Hi-C, capturing events at 15 min, 30 min, 1 hour, and 3 hours after CRISPR activation (Fig. 1, G to I). γH2AX and 53BP1 were detected as early as 15 min (Fig. 1, G and H, and fig. S4), consistent with rapid establishment of these responses (*30*, *31*). The γH2AX signal spread over the entire time course studied, with the largest changes observed in early (15 min to 1 hour) time points, whereas 53BP1 roughly saturated at 30 min. By contrast, Hi-C revealed no break-anchored chromatin loops at time points earlier than 1 hour, and these loops showed a robust signal only at 3 hours (Fig. 1I and fig. S4). These findings are consistent with recent live-cell–imaging measurements showing that cohesin recruitment to a DSB peaks after the formation of MDC1 foci (*23*).

In summary, we found that break-anchored chromatin loops reach peak intensity well after the γH2AX chromatin domain has formed (Fig. 1J). This finding suggests that the break-anchored loop primarily operates in later stages of the DSB response.

Break-anchored loops form during DSB processing for HR

To examine the role of break-anchored loops at late stages of DSB repair, we further analyzed our Hi-C data on a site-by-site basis to determine whether Cas9 sites with stronger changes in chromatin contacts are prone to undergoing a particular repair pathway. In interphase nuclei, chromatin loops compartmentalize the genome into TADs; by convention, a lower insulation score metric at a TAD boundary indicates a higher level of insulation across the boundary (*1*, *32*). Using our high-resolution Hi-C data, we computed average insulation score profiles around the 126 AluGG gRNA on-target sites and found that Cas9 treatment reduces the insulation score (i.e., increases the degree of insulation across the DSB) in comparison to untreated controls (Fig. 2A). A site-by-site analysis revealed a decrease in insulation score in 117 out of 126 on-target sites upon DNA damage, indicating that the observed change in average insulation score profiles does not stem from a few breaks but, rather, is a general DNA repair phenomenon (Fig. 2B). This drop in insulation score could result from two mutually nonexclusive phenomena: (i) Cas9 breaks disrupt the chromatin polymer and might bring about physical separation of the DNA ends, and (ii) Cas9 breaks might act as de novo TAD-like boundaries.

To determine which repair pathway is dominant at each cut site, we performed ChIP-seq for DNA ligase IV (LIG4) and RAD51, which have been used to classify DSBs as nonhomologous end-joining or HR prone, respectively (*33*). Consistent with both pathways being operative at Cas9 breaks, the average ChIP-seq profiles revealed a damage-induced enrichment of both LIG4 and RAD51 in the vicinity of Cas9 on-target sites (fig. S5). We thus computed the Cas9-induced ChIP-seq enrichment on a site-by-site basis and computed the Spearman correlation r between this ChIP-seq enrichment and the drop in insulation score around the 100 best-cleaved Cas9 DSB sites. RAD51 showed a significant positive correlation ($r = 0.37$) with the damage-induced decrease in insulation score, whereas LIG4 showed a weak, nonsignificant negative correlation ($r = -0.17$) (Fig. 2, C to E). Thus, DNA breaks that are prone to undergoing HR are associated with stronger insulation properties. Notably, the ChIP-seq signal intensity for each of three cohesin subunits—RAD21, pSMC1, and NIPBL—showed a significant positive correlation with the DSB-induced drop in insulation score (fig. S6).

On the basis of these findings, we hypothesized that break-anchored loops require processing of the DSB for repair by HR. To test this hypothesis, we implemented a protocol to induce Cas9 breaks at defined cell-cycle stages, by exploiting the vfCRISPR system (*30*). In short, cells were synchronized using thymidine blocks and then electroporated with a Cas9-caged gRNA RNP at the time of release from the block (fig. S7). Cells were then exposed to 365-nm light to activate the caged vfCRISPR at defined time points after release from the block, corresponding to well-defined synchronized cell-cycle stages (figs. S8 and S9). Using this approach, we activated vfCRISPR in cells synchronized in G_1 by shining light 15 hours after release from a double thymidine block (corresponding to ~91.7% of cells in G_1 at the time of inducing breaks; fig. S9) and in the S and G_2 (S/G_2) phases by shining light 6 hours after release from a single thymidine block (~84% of cells in S/G_2; fig. S8). We then performed Hi-C 3 hours after DSB induction and compared the results with similarly synchronized nucleofected cells that were not exposed to vfCRISPR-activating light. Induction of breaks in cells synchronized in S/G_2, which are able to perform HR, recapitulated the break-centered Hi-C stripes observed in unsynchronized cells (Fig. 2F and fig. S10). G_1-synchronized cells showed no appreciable change in chromosome contacts in response to Cas9-induced DSBs (Fig. 2G and fig. S10). We confirmed that DSB induction levels were comparable between G_1- and late S/G_2-synchronized cells (fig. S11). Given that HR is active in late S/G_2 and inactive in G_1, our results suggest that break-anchored loop formation occurs in relation to DSB processing for HR.

To further test the relationship between break-anchored loop formation and HR, we performed multitarget CRISPR delivery and Hi-C in the presence of mirin, a drug that suppresses HR by preventing the MRE11 exonuclease–mediated step of DNA end resection (*34*). Notably, treatment with mirin greatly reduced the strength of the stripes (Fig. 2H and fig. S12) and eliminated insulation-score changes upon Cas9 breaks (Fig. 2, I and J), suggesting that break-anchored loops and their associated insulation properties are formed during HR in a DNA end resection–dependent manner.

Time-course measurements support a role for break-anchored loop extrusion in HR

We investigated the temporal relationships between DNA end resection, RAD51 loading, and break-anchored loop extrusion by performing time-resolved ChIP-seq of RPA and RAD51 ChIP-seq at vfCRISPR-induced DSBs. RPA and RAD51 were undetectable within the first 30 min after DSB induction, revealing a strong, Cas9-induced enrichment only at 3 hours (Fig. 2, K and L, and fig. S4), with RPA ChIP-seq accumulating around a narrow window (~5 kb) centered at the cut site, and the

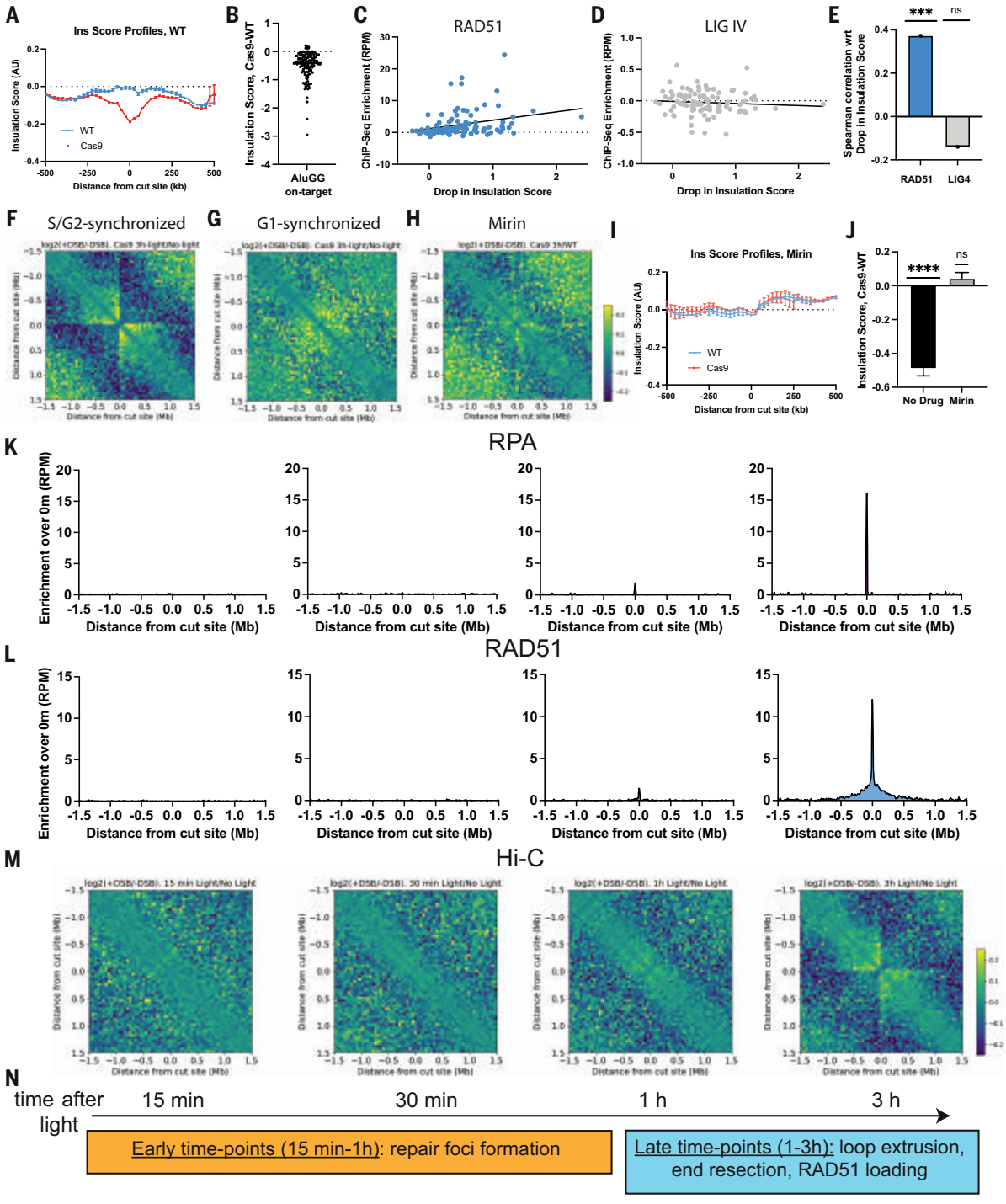


Fig. 2. Break-anchored chromatin loops are formed during HR. (**A**) Insulation-score analysis around Cas9 breaks. Whole-chromosome Hi-C matrices were retrieved at 25-kb resolution, and the insulation score was then computed for each chromosome using the matrix2insulation script from the cworld package (*32*). Profiles were extracted in a window of 1 Mb around each of the 126 AluGG on-target sites and averaged. (**B**) Change in insulation score upon Cas9 treatment was computed in a window of 50 kb centered around each AluGG on-target site. Note that reduced insulation score implies increased insulation. (**C** and **D**) ChIP-seq enrichment of RAD51 (C) and DNA ligase IV (D) versus drop in insulation score upon Cas9 treatment per cut site. Black lines are linear fits. (**E**) Spearman correlation coefficients from (C) and (D). (**F** and **G**) Averaged differential Hi-C contact maps in HEK293T cells synchronized in S/G_2 (F) or G_1 (G). (**H** and **I**) Averaged differential Hi-C contact maps around best cut sites (H) and insulation-score profiles around on-target AluGG sites (I) in cells treated with mirin. (**J**) Cas9-induced change in insulation score around AluGG on-target sites in cells without drug or treated with mirin. Error bars are SEM. Statistical significance with respect to the null hypothesis was obtained using a one-sample *t* test. (**K** to **M**) Time-course of RPA ChIP-seq (K), RAD51 ChIP-seq (L), and Hi-C (M). Hi-C plots are reproduced from Fig. 1I for each comparison. RPA and RAD51 ChIP-seq profiles were computed as in Fig. 1, G and H. (**N**) A proposed timeline. ***$p < 0.001$; ****$p < 0.0001$; ns is not significant.

RAD51 signal propagating to distances of several hundreds of kilobases away from the break. Thus, in our multitarget vfCRISPR system, resection and RAD51 loading occur at relatively late time points (>1 hour). The time course of RPA and RAD51 recruitment closely matched the dynamics of loop formation captured by time-resolved Hi-C (Fig. 2M and fig. S4). This temporal coordination further supports a causal link between specific steps of HR and the formation of break-anchored loops.

In conclusion, our time-resolved experiments reveal two different time scales during Cas9-induced DSB repair (Fig. 2N). First, at early time points (15 min to 1 hour), γH2AX and 53BP1 chromatin responses become detectable, and second, at later time points (1 to 3 hours), DNA end resection, RAD51 loading, and break-anchored loop formation occur.

A broad RAD51 chromatin domain reflects the homology search

To further explore HR events, we performed ChIP-seq for RPA and RAD51 3 hours after delivery of regular, noncaged AluGG gRNA. The resulting RPA ChIP-seq profile after delivery of regular AluGG gRNA showed a peak spanning a width of 4.8 ± 0.7 kb centered at the cut site (Fig. 3, A and B), a finding that is consistent with previous reports showing that DNA end resection extends for a few kilobases from the DSB (*35*). The RAD51 profile showed a peak of similar width of 6.1 ± 0.7 kb, which we attribute to ssDNA that is coated by the recombinase (Fig. 3, C and D). In addition to this peak, the average RAD51 ChIP-seq signal spread to a broad domain of 600 ± 30 kb in size (Fig. 3, D and E), consistent with our time-course measurements (Fig. 2L). Visual inspection of RPA and RAD51 ChIP-seq signals at individual AluGG cut sites corroborated the presence of these broad RAD51 domains that extend beyond the main narrow peak (fig. S13). An alternative RAD51 antibody that binds a different epitope gave a similar average ChIP-seq profile (fig. S14), with indistinguishable widths for both the narrow peak ($p = 0.85$) and the broad RAD51 domain ($p = 0.54$) (Fig. 3E).

RAD51 binds both ssDNA and double-stranded DNA (dsDNA) (*36*). We thus hypothesized that the broad RAD51 domain, which lacks RPA binding, represents RAD51-dsDNA interactions. To test this, we performed strand-specific ChIP-seq (*37*) at 3 hours. The RAD51 strand-specific ChIP-seq profile showed similar qualitative features to the regular ChIP-seq profile, including a peak at the cut site and a broad chromatin domain (Fig. 3, F and G, and fig. S15). Analysis of strand asymmetry at each chromosomal location revealed that the extent of RAD51-ssDNA binding is constrained to a region of ~2 kb centered at the break, with the expected switch in polarity on either side of the DSB, reflecting RAD51 loading onto the resected 3′ ssDNA on each DNA end (*37*). By contrast, at distances >2.5 kb from the DSB, strand asymmetry was lost, implying a RAD51-dsDNA binding mode.

Studies in vitro using purified yeast proteins suggest that during the homology search, the Rad51-ssDNA nucleoprotein filament interacts with a dsDNA template and scans it locally through a 1D random walk (*38*). If the dsDNA is homologous to the Rad51 nucleoprotein filament, HR proceeds with the formation of a D-loop. By contrast, the Rad51 nucleoprotein filament will dissociate from a nonhomologous dsDNA (*38*). In yeast cells, Rad51 ChIP-seq analysis at a site-specific DSB was suggested to reflect the extent of the homology search, with the Rad51 ChIP-seq profile spanning a broad chromatin domain that represents Rad51-dsDNA interactions during chromatin scanning (*39*).

We asked whether, similar to the yeast case, the broad RAD51 domain that we observe in mammalian cells has features characteristic of a homology search (Fig. 3H), in particular, whether it shows local accumulation at an appropriate HR donor (*38*, *39*). We adapted a previously described HR reporter, which contains a green fluorescent protein (*GFP*) heteroallele (*GFP-I-SceI*) composed of a full length *GFP* gene that is interrupted by a target site for the homing endonuclease I-SceI, and a 5′ truncated *GFP* (*Δ5′-GFP*) recombination donor situated ~3 kb (hereafter Donor+3) from the *I-SceI* site (Fig. 3I) (*40*). HR induced by a site-specific DSB localized to the *I-SceI* site is thus quantified by the production of GFP^+ cells. Using a monoclonal mouse embryonic stem (mES) cell line that contains a single-copy HR reporter at the *Rosa26* locus of chromosome 6 (Chr6), we first removed the *Δ5′-GFP* donor with a CRISPR-Cas9–induced deletion. We nucleofected a Cas9-gRNA RNP targeted to the *I-SceI* site to induce a DSB within *GFP-I-SceI* in these "donor-less" cells, and ChIP-seq showed a broad RAD51 domain extending approximately −800 to +700 kb around the break site (fig. S16). To determine whether the RAD51 signal is enriched over the HR donor during a successful homology search, we generated a new *Δ5′-GFP* donor containing select silent point mutations (conserving the amino acid sequence of GFP) sufficient to distinguish it from *GFP-I-SceI* during ChIP-seq sequence alignment. We targeted the new *Δ5′-GFP* donor to positions +441 kb (Donor+441) or +563 kb (Donor+563) telomeric to the *Rosa26*-located *GFP-I-SceI* (Fig. 3J), generating four independent Donor+441 clones and one Donor+563 clone in which a single intact *Δ5′-GFP* donor was targeted to the same copy of Chr6 as the *Rosa26*-located *GFP-I-SceI* heteroallele (see Materials and methods and figs. S17 to S20). *I-SceI*–induced HR in Donor+441 clones and the Donor+563 clone was readily detected but was less efficient than in the original Donor+3 HR reporter cell line (Fig. 3K and fig. S20; see Materials and methods). Consistently, the donor-less clone showed no detectable HR levels (Fig. 3K).

We then used Cas9-gRNA RNP nucleofection to induce a DSB at *GFP-I-SceI* in two Donor+441 clones and the Donor+563 clone and performed RAD51 ChIP-seq 3 hours after Cas9 delivery. Of note, in addition to the above-noted broad RAD51 distribution, we observed an additional narrow and more intense peak at the location of the HR donor, at either +441 or +563 kb (Fig. 3L and fig. S21). This enhanced RAD51 signal over the *Δ5′-GFP* HR donor likely represents the result of a successful homology search by the RAD51 nucleoprotein filament(s) derived from the DSB at *GFP-I-SceI*. A zoomed-in view revealed that this RAD51 peak overlies the *Δ5′-GFP* donor (Fig. 3, M and N). We quantified the relative RAD51 signal at the donor relative to the DSB and found that it was higher in the +441-kb clones than in the +563-kb clones (fig. S22), consistent with the former showing higher HR levels (Fig. 3K).

To exclude the possibility that the RAD51 ChIP-seq peak at the *Δ5′-GFP* donor might be a read alignment artifact due to the high sequence similarity between the *Δ5′-GFP* donor and *GFP-I-SceI*, we aligned the RAD51 ChIP-seq data derived from the donor-less HR reporter clone to a reference genome that includes the *Δ5′-GFP* donor (at position +441 or +563) and observed no specific Rad51 enrichment over the *Δ5′-GFP* donor (Fig. 3, L to N, and fig. S21). Thus, RAD51 ChIP-seq reads that faithfully map to the *GFP-I-SceI* heteroallele at *Rosa26* are not prone to artifactual alignment with the *Δ5′-GFP* heteroallele. We confirmed this conclusion by manually reviewing each of the 1223 RAD51 ChIP-seq reads that mapped to the +441 donor *GFP* heteroallele. We then asked whether the RAD51 peak over the +441 donor is single stranded or double stranded. To this end, we performed strand-specific RAD51 ChIP-seq on one of the +441 donor clones 3 hours after DSB induction. In contrast to the RAD51 signal at the DSB site, the RAD51 signal over the +441-kb donor was predominantly double stranded, implying that the major mode of RAD51 DNA binding to the +441 donor is through duplex DNA (fig. S23). However, there was a mild degree of strand asymmetry over the donor, but the polarity of the DNA ends was opposite to that seen at the DSB site (figs. S23, B and C). Such a pattern of reversed strand symmetry could reflect nascent DNA synthesis during gene conversion using the +441 donor as template, thereby extending the invading ssDNA strand beyond the original site of the DSB to align it with the half of the donor *GFP* sequence homologous to the other side of the DSB (fig. S24). In conclusion, the broad RAD51 domain shows local enrichment over the *Δ5′-GFP* HR donor, reflecting a successful

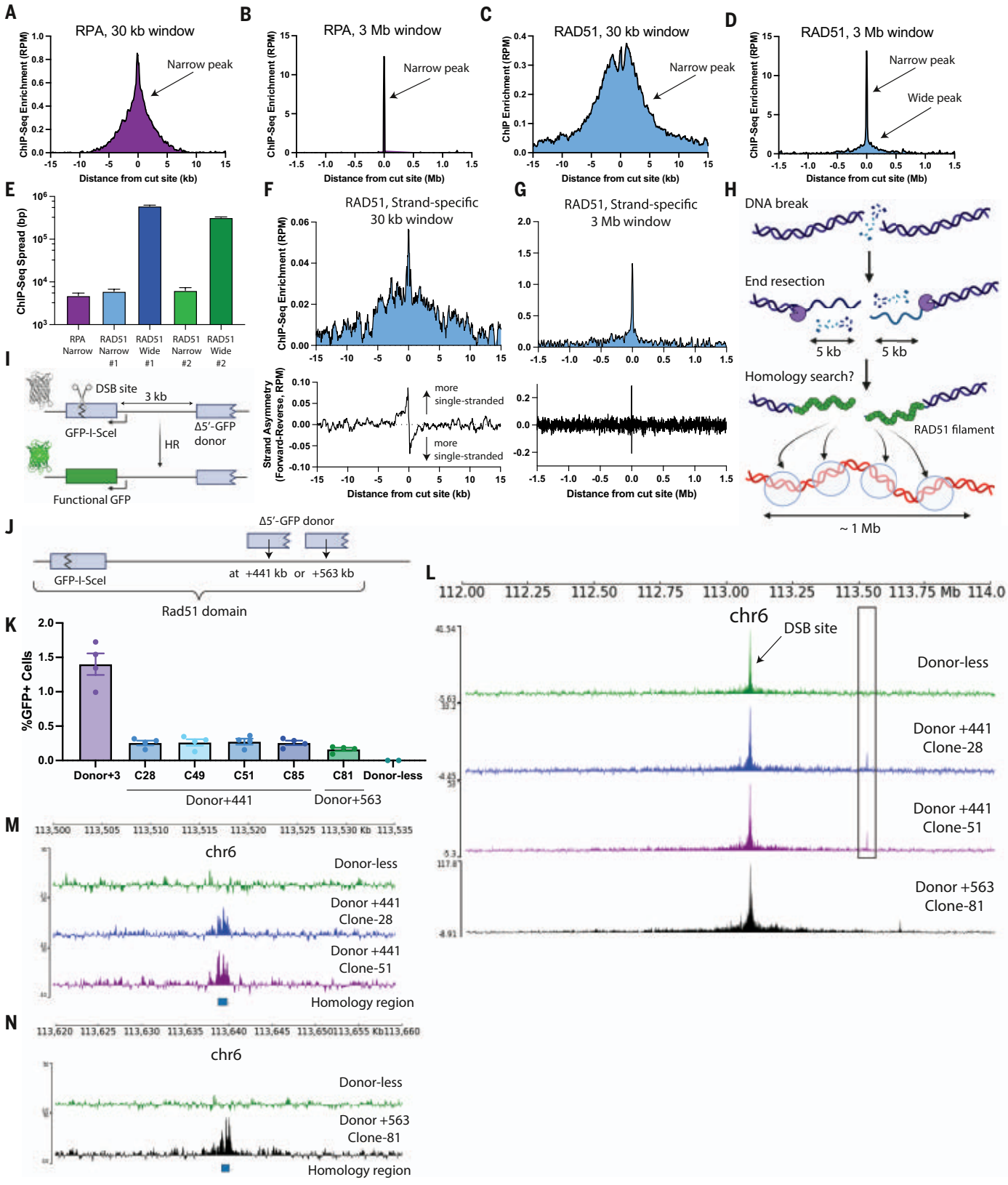


Fig. 3. Broad RAD51 ChIP-seq profiles inform on homology search. (**A** to **D**) Average RPA [(A) and (B)] and RAD51 [(C) and (D)] ChIP-seq profiles around AluGG on-target sites in a window of 30 kb [(A) and (C)] and 3 Mb [(B) and (D)]. Arrows mark narrow (RPA, RAD51) and wide (RAD51) peaks. Bin size is 50 base pairs (bp) [(A) and (C)] and 5 kb [(B) and (D)]. (**E**) Average width of RPA and RAD51 peaks. Error bars are SEM. (**F** and **G**) Strand-specific ChIP-seq of RAD51. Top panels are regular ChIP profiles (30-kb and 3-Mb windows). Bottom panels show the strand asymmetry, computed as the difference between the forward and the reverse reads. Bin sizes are 50 bp (F), 5 kb [(G), top], and 1 kb [(G), bottom]. (**H**) Illustration depicting the interpretation of the broad RAD51 profile as a measure of homology search. [Figure created with BioRender.com] (**I**) Schematic of the HR-GFP reporter system to measure DSB-induced HR. The *GFP-I-SceI* heteroallele harbors a site for DSB induction. HR repair by use of a 5′-truncated (*Δ5′-*)*GFP* donor

~3 kb away from the DSB (here termed Donor+3) generates WT GFP that can be measured in flow cytometry. (**J**) Schematic of the reporter system designed to study HR using distant donors within the TAD. A monoclonal mES cell clone was generated with a single *GFP-I-SceI* copy at *Rosa26* on Chr6. Then, derivative monoclonal lines were made with the *Δ5′-GFP* HR donor at +441 or +563 kb from the *GFP-I-SceI* copy (figs. S17 to S20). (**K**) HR readout for Donor+3, four Donor+441 clones, a Donor+563 clone, and the donor-less clone. (**L**) RAD51 ChIP-seq profile in donor-less cells (top) and in two of the Donor+441 clones and the Donor+563 clone. (**M**) Zoom-in of (L) showing the RAD51 signal over *Δ5′-GFP* in the donor-less clone versus two Donor+441 clones. The donor-less clone ChIP-seq data in (M) and (L) were aligned to a genome containing a +441-kb donor but did not generate a signal over the donor locus. (**N**) Same as (M) but showing the Donor+563 clone and its associated *Δ5′-GFP* site.

homology search and, possibly, the onset of nascent strand extension at the +441 donor site.

Loop-extruding cohesin promotes RAD51-chromatin interactions within the damaged TAD

Our time-course data from Fig. 2 indicated that formation of the broad RAD51 domain occurs approximately contemporaneously with the break-anchored chromatin loops, raising the possibility that the break-anchored loops might participate in the homology search. Given that loops are often delimited by TADs (*2*), we evaluated the effect of TAD boundaries on the spread of the broad RAD51 ChIP-seq signal obtained in HEK293T cells subjected to AluGG DSBs (data from Fig. 3C). We computed the averaged RAD51 ChIP-seq enrichment around TAD boundaries that lie between 200 and 700 kb away from the 100 most-efficiently cleaved AluGG cut sites (according to MRE11 ChIP-seq) and noted a sharp decrease in RAD51 signal at the location of the TAD boundary (Fig. 4, A and B). As a control, we performed the same analysis around random non-TAD boundary sites and observed no significant reduction in RAD51 signal (Fig. 4B). Therefore, at least some TAD boundaries correlate with the extent of the broad RAD51 peak, possibly constraining the homology search to the damaged TAD. This finding is in agreement with recent work reporting broad, TAD-delimited RAD51 chromatin domains in single cells after the induction of site-specific DSBs (*22*). To explore the link between chromatin structure and the broad RAD51 peak at the level of a single locus, we treated HEK293T cells with a Cas9 complexed with an ACTB-targeting gRNA, which has been previously shown to trigger Cas9 cleavage with high efficiency (*30*), and performed RAD51 ChIP-seq. The resulting ChIP-seq profile showed a high similarity with the chromatin-interaction profile in untreated cells (obtained from our high-resolution Hi-C data using the cut site as a viewpoint) (Fig. 4C). Similar findings regarding the similarity in RAD51 signal and chromatin interactions were obtained using an additional gRNA targeting the MYC gene (fig. S25). Thus, TAD boundaries, and possibly other aspects of chromatin architecture, correlate with the extent of the broad RAD51 peak.

Next, we tested the role of chromatin loops on the extent of the broad RAD51 domain. WAPL unloads cohesin from chromatin, and acute WAPL degradation results in elongated loops, likely by extending cohesin's residence time on chromatin (*41*). To manipulate WAPL levels, we used a previously characterized HCT116 cell line, hereafter HCT116-WAPL-AID2, where WAPL is endogenously tagged with a degron that permits fast, acute degradation upon the addition of auxin with minimal leakage (*15*, *42*). We delivered multitarget CRISPR into HCT116-WAPL-AID2 cells and compared the extent of spread of the broad RAD51 peak in the presence and absence of auxin. Consistent with a role of loop extrusion in the homology search, WAPL loss resulted in a broader RAD51 ChIP-seq domain (Fig. 4, D and E, and fig. S26). Specifically, subtraction of the RAD51 profile in the absence (auxin) and presence (no auxin) of WAPL revealed that regions that are further than 0.5 Mb from the DSB site have significantly higher levels of RAD51 after WAPL degradation (Fig. 4, F and G, and fig. S26). These findings suggest that elongated chromatin loops result in a broader homology search.

To further explore the potential role of loop-extruding cohesin in HR, we studied the impact of NIPBL depletion. NIPBL is a cohesin subunit that is required for loop extrusion but not for sister chromatid cohesion; consequently, acute NIPBL degradation perturbs the function of cohesin loops without disrupting sister chromatid cohesion (*43*). We cotransfected our previously characterized (Fig. 3K) mES cells with an *I-SceI* expression vector together with *Nipbl*, *Rad51*, or control (luciferase) siRNA and determined HR efficiency 72 hours later (see Materials and methods). As expected, no HR products were detected in the donor-less clone (fig. S27). Depletion of NIPBL in cells containing the original Donor+3 HR reporter reduced HR efficiency by ~46% in comparison to control siRNA (Fig. 4, H and I), suggesting that cohesin-mediated loop extrusion contributes to DSB-induced HR, even when the donor is located only ~3 kb from the DSB. The impact of NIPBL depletion was more pronounced in the Donor+441 and Donor+563 cell lines, where the HR donor is located far from the DSB site, showing ~74% reduction (Fig. 4I). Thus, at large DSB-donor distances, the dependence of HR on NIPBL becomes greater. In contrast to NIPBL, RAD51 depletion had impacts on HR that were independent of the DSB-donor distance, with reductions of 94% (original HR reporter), 97% (average over Donor+441 clones), and 96% (the Donor+563 clone) (Fig. 4J). Finally, depletion of WAPL on a subset of clones showed an opposite trend in distance-dependent HR compared with depletion of NIPBL, with distal DSB-donor clones exhibiting higher, control siRNA–normalized HR levels compared with the Donor+3 clone (fig. S28). Taken together, our data suggest that loop-extruding cohesin promotes HR by facilitating the homology search. Of note, the dependence of HR on loop extrusion is more pronounced when the homologous donor is positioned at a greater distance from the DSB.

A role for cohesin loop extrusion in the homology search

On the basis of our data, we propose that loop-extruding cohesin facilitates the homology search through directed 1D scanning of the local TAD. In postreplicative cells, DNA breaks can be repaired by HR through the assembly of a RAD51 filament at each of the two resected DNA ends (*44*). This filament can then perform a local search on the sister chromatid, which is discontinuously tethered to the broken chromosome by preexisting deposits of cohesive cohesin (*43*). If the HR donor were not within reach of this local search, possibly because of imperfect sister chromatid alignment, or if the sister chromatid were also broken at the same locus so that equal sister chromatid recombination is not possible, this initial local search would be unproductive. Cohesin recruitment to the break site could then facilitate extrusion of a chromatin loop anchored at the break, allowing the RAD51 filament to perform an efficient 1D scan of the chromosome for a homologous donor (see Fig. 4K). Although our data cannot tell whether the DSB-chromatin contacts observed are within the broken chromosome or with the sister chromatid, a related work showed that both contribute to the Hi-C stripes (*45*).

Our findings invite investigation into additional aspects of homology search. For example, is cohesin extruding a loop in cis on the broken chromosome or is it extruding the sister chromatid by the broken end in trans, directionally scanning one DNA molecule with respect to the other (see Fig. 4K)? Another open question is whether the two ends of the DSB remain tethered to one another during the homology search or whether they each perform a separate individual search (compare top and bottom panels in Fig. 4K). In yeast, the Rad51 nucleoprotein filaments on both sides of the break were proposed to be held together during the homology search, suggesting a coupled scanning mechanism (*26*, *46*). This model remains to be tested in mammalian cells. How dynamic is the search and the formation of break-anchored

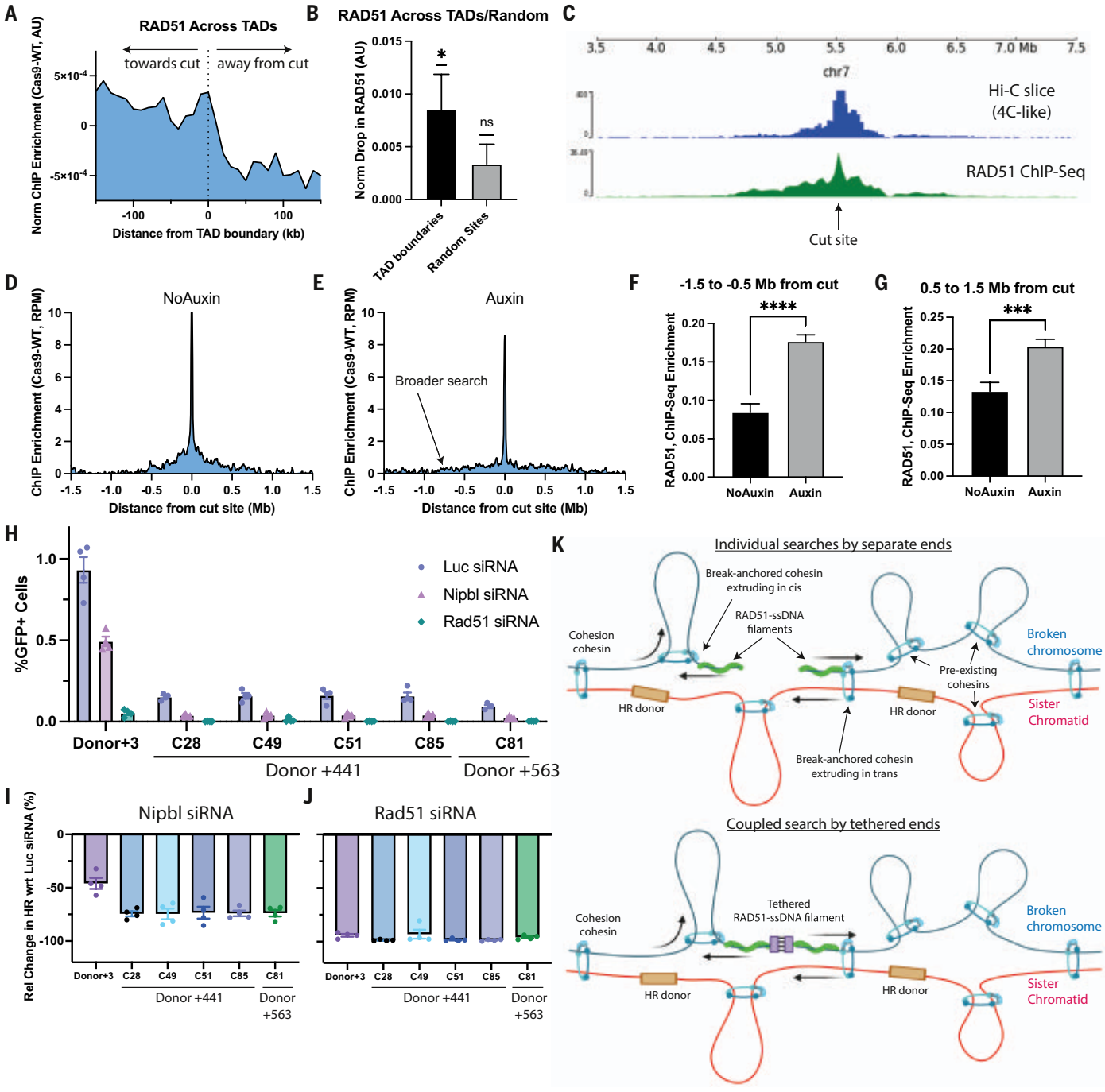


Fig. 4. Loop-extruding cohesin regulates homology search and overall HR efficiency. (**A**) RAD51 ChIP-seq enrichment normalized and averaged around TAD boundaries that lie 200 to 700 kb away from the 100 best Cas9 cut sites. (**B**) Normalized RAD51 drop at TAD boundaries and random sites (picked at distances between 200 and 700 kb away from cut sites). Error bars are SEM. A one-sample *t* test was done to quantify significance from the null hypothesis. For the analysis, 155 TAD boundaries and 389 random sites were considered. (**C**) RAD51 ChIP-seq profile and 4C-like profile at the ACTB gene in HEK293T cells. A 4C-like plot was obtained from the high-resolution Hi-C data in undamaged cells using a 100-bp region centered at the cut site as the viewpoint. (**D** and **E**) Average RAD51 ChIP-seq profiles after Cas9-AluGG-gRNA–induced DSBs in HCT-WAPL-AID2 cells without (D) or with (E) auxin. (**F** and **G**) Average change in RAD51 ChIP-seq enrichment was obtained at regions –1.5 to 0.5 Mb (F) or 0.5 to 1.5 Mb (G) away from the cut. Error bars are SEM. An unpaired *t* test was done to quantify significance between the two conditions. (**H**) HR-GFP assays were performed on the monoclonal cell lines from Fig. 3K after treatment with siRNA against control luciferase (Luc), Nipbl, or Rad51. Error bars are SEM. (**I** and **J**) Quantification of (H), showing changes in HR after depletion of Nipbl (I) or Rad51 (J), normalized to luciferase siRNA HR levels. (**K**) Illustration depicting different mechanisms for cohesin-driven chromatin scanning during homology search. *$p < 0.1$; ***$p < 0.001$; ****$p < 0.0001$; ns is not significant. [Figure created with BioRender.com]

chromatin loops? It has been proposed that chromatin loops are transient and rare (*47*), and it is likely that the break-anchored loops formed during HR are also transient, effectively increasing the 1D mobility of the break, rather than stably positioning it at a defined genomic location. Moreover, besides the break-anchored chromatin loops, other features of 3D genome architecture such as preexisting loops and TADs, are also likely to regulate the extent of the homology search, as proposed in a yeast study (*39*). The assays we performed in this study cannot discern the relative contribution of break-anchored loops and other cohesin-dependent aspects of the 3D genome to the homology search, and further work will be needed to address this. In addition, the role of factors other than cohesin in a homology search remains to be investigated, for instance, Rad54, which can drive 1D scanning of the Rad51 filament along short stretches of DNA in vitro (*38*, *48*). Finally, it is worth noting that our Cas9 system can, in some cases, induce DSBs in both sister chromatids, abrogating the canonical mode of equal sister chromatid recombination. Based on our imaging-based calibration of multitarget CRISPR (*27*), we estimate that most breaks are likely limited to one sister chromatid; however, a more in-depth analysis is needed to confirm this trend and to determine how the presence of a DSB in the sister locus affects the homology search.

Previous work using AsiSI restriction enzymes to generate DSBs (*21*) also reported the formation of break-anchored chromatin loops, leading to the proposal that γH2AX spreads over a megabase scale through cohesin-powered loop extrusion. Although our data showed that break-anchored chromatin loops become detectable only after the assembly of the γH2AX chromatin domain (Fig. 1), it remained possible that cohesin plays a role in γH2AX chromatin domain formation. Indeed, acute RAD21 degradation resulted in a reduced accumulation of γH2AX (fig. S29), supporting a role for cohesin in propagating γH2AX. One possibility is that transient break-anchored loops might form during the early stages of repair (<1 hour) and contribute to γH2AX spreading, but exist at levels undetectable in our Hi-C assays. Alternatively, cohesin might promote formation of the γH2AX domain through preexisting chromatin loops, rather than break-anchored loops. This mechanism would enable the DSB to interact with the damaged TAD and help propagate γH2AX without the need for an anchoring mechanism at the DSB. In this regard, recent work showed that cohesin can rapidly bring together two genomic loci with no anchoring properties, provided that the loci reside in the same TAD (*49*).

The homology search problem posits the question: How does a broken DNA find a correct HR template in the mammalian genome? A 3D exploration mechanism, for example, through 3D diffusion, has been proposed to drive homology searches during repair of telomeric DSBs via alternative lengthening of telomeres (*50*). However, in nonrepetitive regions, a 3D search mechanism is likely to be slow and inefficient (*51*). Dimensionality reduction by 1D local scanning could substantially accelerate this process, for example, through sliding of the recombinase-ssDNA filament along dsDNA (*52*). However, because the two sister chromatids are only loosely connected, such scanning would require a highly processive and fast motor. Our data suggest that cohesin can facilitate this long-range scanning through loop extrusion. In the bacterium *Caulobacter crescentus*, live-cell–imaging measurements revealed a fast, directional movement of bacterial recombinase (RecA) filaments over the entire bacterial chromosome on the order of minutes (*53*). This movement required another SMC protein, RecN, and the authors suggested that RecN could actively drive the search through 1D scanning. In yeast, chromatin loops are formed during HR, promoting break-chromatin interactions and facilitating contact with an HR donor in cis (*26*). Our data suggest that cohesin also plays a role in the homology search in mammalian cells, likely by promoting repeated long-range scanning of RAD51-ssDNA filaments against the sister chromatid and against other intra-TAD loci in cis. Taken together, these findings point to a universal role for SMC proteins in driving a directed 1D scanning during the homology search, likely conserved across different domains of life.

Materials and methods

Cell culture

Human cell lines were cultured at 37°C under 5% CO_2. Human embryonic kidney 293T (HEK293T, ATCC CRL-3216) cells were cultured in Dulbecco's Modified Eagle's Medium (DMEM, Corning 10-013), supplemented with 10% FBS (Corning, 35-011), and 1x Antibiotic-antimycotic (AA, Gibco 15240062). Human colorectal carcinoma 116 (HCT116) with RAD21 or WAPL tagged for auxin inducible degradation (AID) were grown in McCoy's 5A Medium (Gibco 16600082), supplemented with 10% FBS and 1x AA. Culturing media with FBS and AA will be referred to as complete media.

Mouse embryonic stem (mES) cells were thawed onto mouse embryonic fibroblasts and maintained on gelatinized plates in mES cell culture medium (DMEM with L-glutamine, 4.5 g/liter glucose and sodium pyruvate) 15% serum, 20 mM HEPES pH 7.6, 0.1 mM β-mercaptoethanol, 500 U/ml rLIF, 1x MEM NEAA, 2 mM L-glutamine, 100 U/ml penicillin, 100 mg/ml streptomycin, 0.001 M sodium pyruvate).

Cells were regularly tested for mycoplasma infection using Myco-Alert assay (Lonza).

Electroporation of Cas9 RNP

Guide RNA sequences are in table S1. Two microliters of 100 μM crRNA (IDT, Alt-R CRISPR-Cas9 crRNA) and 2 μl of 100 μM tracrRNA (IDT, 1072532) were mixed and incubated on a 95°C heat block for 3 min, then cooled to room temperature on a benchtop for 5 min to enable annealing of the crRNA/tracrRNA. Three microliters of Cas9 enzyme (IDT, 1081058) at 10 mg/ml and 8 μl of dialysis buffer (20 mM HEPES pH 7.5, 500 mM KCl, 20% glycerol) were then added to the annealed crRNA/tracrRNA and were mixed. The mixture was incubated at room temperature for at least 20 min in order for the RNP to form. Then, 73.8 μl of SF (HEK293T) or SE (HCT116) and 16.2 μl of supplement solution (Lonza V4XC-2024, V4XC-1024) were freshly mixed prior to nucleofection. For mES cells, 82 μl of P3 solution was mixed with 18 μl of supplement solution (Lonza, V4XP-3024).

Approximately 1.2×10^7 cells were harvested via trypsinization, spun down at 300*g* for 5 min, washed with 3 ml of PBS (Corning, 21-040-CV) and spun down again (same spin). All the PBS was then removed. HEK293T/HCT116 cells were resuspended in 90 μl of SF/SE + supplement mixture. mES cells were resuspended in 100 μl of P3 + supplement mixture. Then, 15 μl of Cas9-tracr/crRNA RNP and 2 μl of 100 uM electroporation enhancer (IDT, 1075916) were added to the cells. After gently mixing, 130 μl of cells-RNP mixture were transferred into a 100 μl nucleofection cuvette (Lonza). Electroporations were done in a 4D Nucleofector Unit (Lonza) using the following programs: CA-189 for HEK293T, EN-113 for HCT116 and CG-104 for mES cells. Cells were then transferred into 10 ml of complete media and immediately plated into 10 cm dishes precoated with collagen [1:100 collagen (Gibco A1048301) in PBS for HEK293T, HCT116] or gelatin (for mES). A no-electroporation control was included in every electroporation experiment by harvesting ~8×10^6 cells and plating them in a 10-cm dish. Cells were harvested by removing the complete media and scraping in DMEM only (with no FBS). Cells were harvested 3 hours after electroporation unless otherwise specified.

For time-course experiments, tracrRNA was annealed with a caged crRNA (Biosynthesis, custom order) using the same protocol as for regular crRNA. Four electroporations were performed as described above, cells were then pooled into 50 ml of complete media and plated into five 10 cm dishes. Cells were cultured at 37°C, 5% CO_2 for ~12 hours prior to Cas9 activation. This was done by exposing four of the 10 cm dishes to (6x) flashlights that delivered 1.3 J/cm^2 of 365-nm wavelength light for ~1 min. Cells were then harvested at different time points after light-induced Cas9 activation: 15 min, 30 min, 1 hour, and 3 hours.

The fifth dish was not exposed to light (referred to as "no-light control" or "0 min time point").

For Mirin experiments, cells (not preexposed to the inhibitor) were plated in complete media containing inhibitor after the nucleofection (Selleck Chem, S8096, 50 mM final concentration).

For HCT-WAPL-AID and HCT-RAD21-AID cells, cells were exposed to complete media containing auxin (5-Ph-IAA, 1 μM, final) 1 hour before nucleofections. Cells were then nucleofected as described above. After nucleofection, cells were transferred into tubes containing 10 ml of complete media with or without auxin and plated in 10-cm plates. Cells that were not electroporated were also plated on 10-cm plates containing complete medium with auxin or complete media with no auxin.

Rad21 siRNA treatment

The day before siRNA transfections, HEK293T cells were plated in five 6-well plates at ~30% confluency in 2.25 ml of DMEM with 10% FBS (no AA) and incubated at 37°C, 5% CO_2 overnight. For each well, 6.25 μl of Rad21 siRNA at 100 mM (10 nM final) (ThermoFisher, no. 4392420, ID s11727) or control siRNA (ThermoFisher no. 4390843) were mixed with 125 μl of OptiMEM (Gibco no. 51985034); and 7.5 μl of RNAiMAX lipofectamine (ThermoFisher no. 13778150) was mixed with 125 μl of OptiMEM. OptiMEM-diluted siRNA was then mixed with OptiMEM-diluted lipofectamine, and the mixture was incubated for 10 min in order for liposomes to form. Cells were then transfected by adding 250 μl of lipofectamine-siRNA mixture to each 6-well plate. The following day, cells were expanded to 10-cm plates (for electroporation) and 6-well plates (for Western blot harvest) as needed. Electroporations were done 48 hours after siRNA transfections. siRNA-mediated Rad21 depletion was validated using Western blot (fig. S30).

Western blot

HEK293T cells treated with Rad21 or Ctrl siRNA were harvested via trypsinization, spun down at room temperature, 200*g* for 3 min, and the supernatant was discarded. Cells were then washed with 1 ml PBS (same spin). The supernatant was discarded and ice cold 1x RIPA (Cell Signaling 9806S) with 1 mM PMSF (PMSF stock 200 mM in isopropanol – Cell Signaling Technology 8553S) was added. Cells were sonicated with a probe sonicator (Qsonica Q125) at 4°C for 10 s at 30% power. Samples were spun down at 4°C, 21,000*g* for 20 min. The supernatant was taken off and stored in aliquots in Eppendorf tubes, flash frozen and stored at −80°C.

BCA assay was run to determine protein concentration prior to starting the Western blot, following the protocol for Pierce BCA Protein Assay Kit (23227) and imaging using a Tecan Spark plate imager. Once protein concentration of the sample was determined, 50 μg of total cell lysate was loaded into an Eppendorf tube, then 4x Laemmli buffer (Biorad 1610747) was added together with nuclease free water to a final volume of 28 μl. Samples were mixed and boiled on a 95°C heat block for 5 min. After the sample was boiled, a gel (Biorad 45601023EDU) was loaded with ladder (Biorad 161-0374), followed by protein sample mixtures and run in 1x TGS (Biorad 1610772) for 30 min at 80 V, then 1.5 hours at 100 V. The gel was transferred to a PVDF membrane (Biorad 1620174) via Biorad Trans-Blot Turbo machine. First, the membrane and blotting paper (Biorad 1703932) were wetted with solution (10 ml methanol, 5 ml 10x Tris/Glycine buffer (Biorad 1610771), 35 ml water), then the protein gel was broken out of the plastic mold. Wet blotting paper, then wet membrane, then wet gel, then wet blotting paper were placed into a sandwich, and this sandwich was placed into the Trans-Blot Turbo machine chamber. The machine was run for 30 min to ensure complete transfer of protein from gel to membrane. Then, the membrane was washed with TBST (1x TBS (diluted from 10X Quality Biological 351-086-101), 0.1% Tween-20 (Promega H5151) for 5 min at room temperature on a rocker. The membrane was blocked with 5% BSA/TBST (VWR 0332) for 1 hour at room temperature on a rocker. Primary antibody was diluted to 1:2000 for Rad21 (Abcam ab992) and 1:3000 for Beta-tubulin control (Thermo MA5-16308) in 5% BSA/TBST. Blocking solution was taken off and the membrane was incubated in primary antibody mixture at 4°C overnight on a rocker.

The next morning, the membrane was washed with one quick TBST wash, then three times for 5 min each with TBST on a rocker at room temperature. Secondary antibody was diluted to 1:2500 anti-mouse HRP (Invitrogen A28177) and 1:2500 anti-rabbit HRP (Invitrogen 31460) in 5% BSA/TBST. The membrane was incubated in secondary antibody for 1 hour at room temperature on a rocker with the membrane chamber wrapped in foil and protected from light. Excess secondary antibody was discarded, and the membrane was washed with one quick TBST wash, then three times for 5 min each in TBST on a rocker at room temperature. ECL solution was made based on manufacturer's guidelines (Thermo 34080), TBST wash buffer was discarded, and ECL solution was put onto the membrane. The membrane was placed into a chemiluminescent-compatible imager (Azure Biosystems 400) and imaged.

Cell-cycle synchronization

HEK293T cells were synchronized in G_1 and late S/G_2 cell cycle phases using, respectively, a double and a single thymidine block protocol. Cells were plated in 10-cm plates (precoated with collagen) at low confluency and allowed to sit for at least 3 hours prior to initiation of synchronization. For the double thymidine block, thymidine (5 mM final) in DMEM complete medium was added to cells and incubated at 37°C, 5% CO_2 for 18 hours, then washed twice with PBS. DMEM complete medium was then added to cells and incubated at 37°C, 5% CO_2 for 9 hours. DMEM was then removed and thymidine-containing DMEM complete medium was then added a second time to cells and incubated at 37°C, 5% CO_2 for 18 hours. At this point, cells were collected and electroporated with caged gRNA-Cas9 RNP as outlined above. Light was shone 15 hours after release of the block, corresponding to G_1-synchronized cells (with ~92% of cells in G_1; see fig. S9). For the single thymidine block, thymidine (5 mM final) in DMEM complete medium was added to cells and incubated at 37°C, 5% CO_2 for 18 hours, then cells were collected and electroporated with caged gRNA-Cas9 RNP as outlined below. Light was shone 6 hours after release of the block, corresponding to late S/G_2 synchronized cells (with ~80% of cells in late S/G_2, see fig. S8).

Cells were harvested and fixed 3 hours after shining light and pellets were split into two: One was used for Hi-C, and the second was used for MRE11 ChIP-qPCR to confirm efficient generation of DSBs. A no-light control was included in every experiment and harvested at the same time as the damaged sample.

ChIP

We followed the ChIP protocol published in (*30*). We used at least 3×10^6 to 4×10^6 cells per ChIP, which corresponds to ~2 ChIPs per electroporation. Cells were collected via scraping in 10 ml of DMEM with no FBS and were then transferred to a 15-ml falcon tube. Cells were then fixed in formaldehyde (methanol free, 1% final concentration) for 10 min with rotation at room temperature. Formaldehyde was then quenched by adding glycine at a final concentration of 140 mM and incubating for 3 min with rotation at room temperature. Cells were then spun at 1200*g* for 3 min at 4°C, washed with PBS and spun down (same spin). Pellets were then subjected to lysis (see below) or, alternatively, were flash-frozen and stored at −80°C (pellets are stable at −80°C for several months).

Fifty microliters of Protein A or Protein G magnetic beads (ThermoFisher, no. 10002D, no. 10004D) were used per ChIP reaction (e.g., for four ChIPs, add 200 μl of beads). Beads were transferred to a 2-ml Eppendorf tube and were washed three times with 1 ml of BSA blocking buffer (BSA-BB, 0.5% BSA in PBS) using a magnet to retain the beads during each wash. Beads were then resuspended in 100 μl of BSA-BB. Antibody was then added to the beads according to table S2. The antibody was allowed to bind to the magnetic beads at room temperature with rotation for

1 to 3 hours. Right before the immunoprecipitation, beads were washed three times with 1 ml BSA-BB and resuspended in 50 µl of BSA-BB per ChIP reaction.

Cell lysis was done in three steps. First, cell pellets were resuspended in 4 ml of LB1 lysis buffer [50 mM HEPES, 140 mM NaCl, 1 mM EDTA, 10% glycerol, 0.5% Igepal CA-630, 0.25% Triton-X; with pH adjusted to 7.5 using KOH and with 1x protease inhibitors (ThermoFisher, 78429) added right before use] and incubated for 10 min with rotation at 4°C. Cells were then spun down for 3 min at 2000*g* and 4°C. The supernatant was removed, and cells were resuspended in 4 ml of LB2 buffer (10 mM Tris-HCl pH 8, 200 mM NaCl, 1 M EDTA and 0.5 mM EGTA; with pH adjusted to 8.0 using HCl and with 1x protease inhibitors added right before use) and incubated for 5 min with rotation at 4°C. Cells were then spun down (3 min, 2000*g* at 4°C) and the supernatant was removed. Cells were then resuspended in 1.5 ml of LB3 buffer (10 mM Tris-HCl pH 8, 100 mM NaCl, 1 mM EDTA, 0.5 mM EGTA, 0.1% Na-Deoxycholate, 0.5% *N*-lauroylsarcosine; with pH adjusted to 8.0 using HCl, and adding 1x protease inhibitor right before use) and were transferred to a 2-ml tube. Cells were sonicated at 4°C using a Qsonica Q125 with the following settings: 30 s of pulse, 30 s off, 55% amplitude for 6 cycles. Cells were then spun at 20,000*g* at 4°C for 10 min. A small black pellet should appear at the bottom of the tube. Then, ~1.3 µl (1% input chromatin) of supernatant was transferred to a 1.5-ml tube and reverse cross-linked and purified as the ChIP'ed DNA (described below). The rest of supernatant was transferred to a 5-ml tube (split into two tubes at this point when performing two ChIPs on one pellet), avoiding carrying any pellet. To the supernatant containing sonicated chromatin, we then added 300 µl of 10% Triton X-100, 50 µl of antibody-conjugated beads and LB3 (with no protease inhibitor) to a volume of 3 ml. The mixture was incubated for >7 hours at 4°C with rotation.

Samples were transferred to a 1.5-ml LoBind Eppendorf tube placed on a magnetic stand (removing the supernatant as it became cleared and adding more bead slurry). The supernatant was fully removed, and the beads were gently washed six times with 1 ml RIPA buffer (50 mM HEPES, 500 mM LiCl, 1 mM EDTA, 1% Igepal CA-630, 0.7% Na-Deoxycholate; pH adjusted to 7.5 using KOH) and once with TBS buffer (20 mM Tris-HCl pH 7.5, 150 mM NaCl). Beads were then resuspended in 50 µl of ChIP elution buffer (50 mM Tris-HCl pH 8, 10 mM EDTA, 1% SDS) and incubated at 65°C for >7 hours with shaking at 1000 rpm.

For purification of the ChIP'ed DNA, 25 µl of IDTE buffer pH 8.0 (IDT) was added to the samples to dilute the SDS, followed by 2 µl of RNAse A (NEB), mix and incubation at 37°C for 15 min. Then, 4 µl of Proteinase-K (NEB) was added and mixed, and samples were incubated at 55°C for 1 hour. DNA was then purified using MinElute DNA purification columns (Qiagen) and eluted in 35 µl of IDTE pH 8.0.

ChIP-seq sequencing libraries were prepared using the NEB Ultra II DNA Library Prep Kit (NEB, no. E7645) following the standard protocol provided, using half volumes of library prep reagents and using 15 µl of purified ChIP DNA as input. After adapter ligation and USER treatment, libraries were amplified using NEBNext dual-indexed primers (NEB 7600 or NEB 6440) following the provided protocol but using half volumes. Libraries were amplified using 13 PCR cycles (except for γH2AX ChIP samples where we used 10 cycles). Samples were quantified via Qubit (Thermo), pooled according to their concentration and sequenced on an Illumina NextSeq 1000 machine using paired-end 2x60 bp read length. Reads were demultiplexed using bcl2fastq.

qPCR

qPCR was done using the Luna Universal qPCR Master Mix (NEB, M3003) following the NEB protocol, using 1 µl of ChIP'ed DNA per reaction and the following primers: AluGG-s2-3 forward: 5′-TGGTGTACACTCCTTCCAGA, AluGG-s2-3 reverse: 5′-TTTTCACATGCTTGCTTCACA, AluGG-s3-3 forward: 5′- CAGTGGAGGAATTGGCCCA, AluGG-s3-3 reverse: 5′- CACTCTACCTGGCCCTTCC, AluGG-s4-4 forward: 5′- TCTCTACTTCCCTATATGGCCAC, AluGG-s4-4 reverse: 5′- GTGCATGGCCACCTTTAGT.

Strand-specific ChIP-seq

RAD51 ChIP was carried out as described previously (*54*) with minor modifications. Briefly, cells were lysed in lysis buffer (50 mM Tris-HCl pH 8.0, 0.1% SDS, 10 mM EDTA supplemented with proteinase inhibitor) after formaldehyde cross-linking. Chromatin was sonicated to ~500 bp using Bioruptor 300 (Diagenode). Lysates from 6 million cells were used for each IP with anti-RAD51 antibody (Millipore; see table S2). Immunocomplexes were captured by Magna ChIP magnetic beads (Sigma). Beads were washed six times with ChIP RIPA buffer (50 mM HEPES pH 7.6, 1 mM EDTA, 0.7% sodium deoxycholate, 1% NP-40) followed by two washes with TE buffer. DNA was eluted in ChIP elution buffer (1% SDS, 100 mM sodium bicarbonate, 8 µg/ml RNase A). After reverse cross-linking, DNA was precipitated with ethanol after phenol: chloroform extraction.

Strand-specific ChIP-seq libraries were prepared using the xGen ssDNA and Low-Input DNA kit with xGen CDI primers (IDT) according to the manufacturer's protocol.

Hi-C

Hi-C was done following the in situ Hi-C protocol from (*2*) with some modifications. For Hi-C, 2×10^6 to 4×10^6 cells were used per reaction. Cells were harvested in 4 ml of DMEM only (no FBS) and fresh formaldehyde was added to a final concentration of 1%. The fixation reaction incubated for 10 min at room temperature and was quenched by adding glycine to a final concentration of 0.2 M and incubating for 5 min at room temperature with rotation. Cells were then spun down (1200*g*, 3 min, 4°C), washed with 1 ml of PBS and spun down (same spin). PBS was removed and the pellets were subjected to lysis or frozen and stored at −80°C for later use (pellets are stable for several months at −80°C).

Cell pellets were gently resuspended in 300 µl of lysis buffer (10 mM Tris-HCl pH 8, 10 mM NaCl, 0.2% Igepal) with 1x protease inhibitors (Sigma, P8340). The lysis reaction was incubated on ice for ~20 min. After that, the sample was centrifuged (2500*g*, 5 min, 4°C), the supernatant was discarded, and nuclei were washed with 500 µl of ice-cold lysis buffer (with no protease inhibitors) and spun down (same spin). Nuclei pellets were then gently resuspended in 50 µl of 0.5% SDS and incubated at 62°C for 10 min with shaking at 900 rpm. Then, 145 µl of H_2O and 25 µl of 10% Triton X-100 (in H_2O) were added, and the sample was gently mixed and incubated at 37°C for 15 min with shaking at 900 rpm. Twenty-five microliters of 10xNEBuffer-3.1 and 100 U of DpnII enzyme were added to the sample and gently mixed and chromatin was digested at 37°C overnight with shaking at 900 rpm. The following day, an additional 100 U of DpnII enzyme were added to the sample, and the digestion was incubated for another ~3 to 4 hours. DpnII was deactivated by incubating at 62°C for 20 min and the sample was then left to cool down to room temperature. A fill-in reaction mix was then prepared in order to blunt the DNA ends and incorporate a biotin [30 µl of 0.4 mM biotin-14-dATP (ActiveMotif 14139), 1.2 µl of 10 mM dCTP (NEB), 1.2 µl of 10 mM dGTP (NEB), 1.2 µl of 10 mM dTTP (NEB) and 6.4 µl of Large Klenow Fragment at 5 U/ml (NEB, M0210)] and was added to the sample. After mixing, the fill-in reaction was incubated at 37°C for 45 min with shaking at 900 rpm. A ligation reaction mix was then prepared (669 µl of H2O, 120 µl of 10xNEB T4 DNA ligase buffer, 100 µl of 10% Triton X-100 and 6 µl of 20 mg/ml BSA) and was then added to the sample. Five microliters of T4 DNA ligase was added, and the sample was mixed well and incubated at room temperature for >4 hours with rotation. After ligation, the sample was spun down (2500*g*, 5 min, room temperature) resulting in a nuclei pellet, the supernatant was removed and the pellet was resuspended in 330 µl of reverse cross-links buffer (10 mM Tris-HCl pH 8, 0.5 M

NaCl, 1% SDS). After adding 20 µl of Proteinase-K (NEB), samples were incubated at 55°C for 30 min and then at 68°C overnight with shaking at 1000 rpm. The following day, DNA was purified using EtOH precipitation and was eluted in 130 µl of 10 mM Tris-HCl pH 8.0.

The DNA was transferred to a Covaris microTUBE (Covaris, 520045) and sonicated in a Covaris LE220 instrument using the following parameters: Fill Level: 10, Duty Cycle: 15, PIP: 500, Cycles/Burst: 200, Time: 58 s. Sonicated DNA was transferred to a 1.5-ml LoBind tube and subjected to double-sided size selection using AMPure XP beads (Beckman A63881), using 0.55x of beads for first round and 0.7x for the second round of selection (results in fragments between ~300 and 500 bp). After the second round, DNA was eluted in 100 µl of 10 mM Tris-HCl pH 8.0, separated on a magnet and transferred to a clean 1.5-ml LoBind tube. Size-selected DNA was then quantified with Qubit (ThermoFisher). DNA can be stored at −20°C for up to 3 days at this point.

For biotin pull-down and library preparation, 2 µg of DNA was transferred into a clean 1.5-ml LoBind tube and 10 mM Tris-HCl pH 8 was added to a final volume of 100 µl. Then, 100 µl of streptavidin beads (Life tech, 65602) were added to a clean 1.5-ml tube and were washed with 100 µl of Tween Washing Buffer (TWB: 5 mM Tris/0.5 mM EDTA, 1M NaCl, 0.05% Tween-20). Beads were placed against a magnetic stand, the supernatant was discarded, and beads were then resuspended in 100 µl of 2x Binding Buffer (10 mM Tris-HCl pH 7.5, 1 mM EDTA and 2 M NaCl). Beads were then mixed with the samples, and the mixture was incubated at room temperature for ~20 min. Samples were then placed on a magnetic stand, the supernatant was removed and the beads containing biotinylated DNA fragments were washed twice by resuspending in 200 µl of TWB, incubating at 55°C for 2 min and placing against the magnet. After the second wash, beads were resuspended in 100 µl of 10 mM Tris-HCl pH 8, then placed against the magnet, removed the supernatant and resuspended in 50 µl of 10 mM Tris-HCl pH 8.0 and transferred to a PCR tube.

Library preparation was done on the beads, using the NEB Ultra II DNA Library Prep Kit (NEB, no. E7645) with small variations from the NEB protocol to account for the beads. Seven microliters of End Prep Rxn Buffer and 3 µl of End Prep Enzyme Mix were added to 50 µl of beads-DNA mixture, the sample was mixed and incubated: 20°C for 30 min, then 60°C for 30 min in a thermocycler. A ligation mix was then prepared (30 ml of NEB Ligation MM, 1 ml of ligation enhancer and 2.5 µl of undiluted Illumina Adapter), added to the sample, mixed and incubated at 20°C for 15 min in a thermocycler. After adding 3 µl of USER enzyme and mixing, samples were incubated at 37°C for 15 min. Samples were then washed twice with 150 µl of TWB (as described above), resuspended in 100 µl of IDTE pH 8.0, placed against a magnet, the supernatant was removed, and samples were finally eluted in 15 µl of IDTE pH 8.0. Samples were then incubated at 98°C for 10 min on a thermocycler with lid heated to 105°C, in order for the DNA to detach from the beads. Shortly after this incubation (let ~1 min for tubes to cool down), samples were placed against a magnet and the supernatant was transferred to a clean 1.5-ml DNA LoBind tube.

Libraries were amplified using NEBNext dual-indexed primers (NEB 7600 or NEB 6440) following the NEB protocol. Ten PCR cycles were run for each sample with annealing temperature of 65°C. Amplified libraries were purified using two rounds of 0.9x AMPure XP bead purification and eluted in 25 µl of IDTE. Samples were quantified via Qubit (Thermo), pooled according to their concentration and sequenced on an Illumina NextSeq 1000 or a NovaSeq 6000 machine using paired-end 2x60 bp read length. Reads were demultiplexed using the bcl2fastq software.

ChIP-seq data analysis

ChIP-seq fastq reads were aligned to the hg38 (human cell lines) or the mm10 (mouse) genome assembly using bowtie2. For Rad51 ChIP-seq experiments on the Donor+441, Donor+563 or donor-less cells, reads were aligned to a modified version of the mm10 genome assembly containing the HR reporter as specified. The samtools software was used to filter reads by mapping quality (≥25), remove singletons, remove PCR duplicates and index bam files (see github link accompanying the manuscript).

Average ChIP-seq profiles were obtained using a custom python code that computes a rolling average around every on-target site for a given multitarget gRNA. For 3-Mb-wide profiles, the rolling average was computed every 5 kb, using a bin size of 10 kb; for 30-kb-wide profiles, the rolling average step was 50 bp and the bin size was 100 bp. Mean on-target profiles were then computed by averaging over all the on-target sites for the damaged and undamaged samples. Finally, the averaged undamaged profile was subtracted from the averaged damaged one, obtaining an enrichment profile. Enrichment profiles were averaged over biological replicates (Figs. 1, E and F, and 3, A to D), or shown separately for each replicate (Figs. 1, G and H; 2, M and N; and 3, F and G). ChIP-seq profiles at single cut sites were obtained by (i) subtracting the untreated from the Cas9-treated bam files and converting to a bigwig file (using the bamCompare script from deeptools (*55*) with default parameters); and (ii) binning and plotting using the software pygenometracks (*56*). For coarse plots, 33-kb bins were used (e.g., Fig. 4C) and 1-kb bins were used for fine plots (e.g., Fig. 3L).

ChIP-seq spread widths for RPA and RAD51 (Fig. 3E) were computed after merging biological replicate datasets. Narrow widths (columns nos. 1, 2, and 4 in Fig. 3E) were computed using the MACS2 software with the following parameters *–broad–broad-cutoff 0.05–max-gap 5000–min-length 500*. Wide widths (columns nos. 3 and 5) were calculated using a previously written python code (*30*). In short, a rolling average of ChIP-seq signals are computed for the damaged and undamaged sample in bins of 10 kb separated by steps of 5 kb. This rolling average is the compared in the damaged and undamaged sample at increasing distances from the DSB site. A counter is increased every time the damaged signal is lower than the undamaged one.

TAD boundaries available from previous high-resolution Hi-C maps (*2*) (4DNFIBKY9EG9 file in 4DN portal) were used to obtain RAD51 enrichment across TAD boundaries (Fig. 4A). Only "strong" TAD boundaries (according to the labels in the original bed file) were considered for the analysis. RAD51 ChIP-seq signal was extracted around TAD boundaries that lie at distances between 200 and 700 kb from the 100 most highly efficiently cleaved AluGG cut sites (as given by BLISS signal). This resulted in 155 TAD boundaries being analyzed. Rolling average profiles (bin size = 20 kb, step size = 10 kb, total span = 300 kb) were computed around each TAD boundary for the damaged and the undamaged sample. A normalized average around all TAD boundaries was computed for the damaged and undamaged sample by dividing each individual profile by the total RAD51 signal in the damaged sample and then computing the average over the normalized profiles. The resulting averaged normalized undamaged profile was subtracted from the damaged profile and is shown in Fig. 4A. In Fig. 4B, the change in RAD51 signal at each TAD boundary/random site was quantified and normalized by the total RAD51 signal in the damaged sample.

Strand-specific ChIP-seq analysis

Strand specific ChIP-seq profiles were obtained in the same manner as regular ChIP-seq profiles. In addition, a custom python code was written to classify mapped paired-end reads attending to whether the first read mapped to the forward or the reverse strand and split accordingly. Enrichment profiles around AluGG sites were computed for the forward and reverse strand and the latter was subtracted from the former to obtain the strand asymmetry plots.

Hi-C analysis

Deep Hi-C contact maps for damaged and undamaged cells (Fig. 1A) were obtained using the *cooler* software (to obtain pairs file, then sort,

remove duplicates, select only appropriately oriented pairs and merge technical and biological replicates) and *juicer* (to obtain hic files from the final pairs file). All other Hi-C contact maps were obtained with juicer (to go from .fastq to .hic) using default parameters. JuiceBox (*57*) was used for visualization of Hi-C contact maps (Fig. 1A). Average log2 ratio plots (as in, e.g., Fig. 1B) were obtained from the hic file of the damaged and undamaged sample using a custom python script. For each cut site, Hi-C matrices are dumped (using juicer, spanning 3 Mb, resolution = 50 kb, KR normalization) for the undamaged and damaged sample and the log2 ratio matrix is computed. The average of all these cut-centered log2 ratio matrices is then computed and shown. Bins with no contact count in the denominator were taken as zero in the log2 ratio.

Insulation scores were computed from .hic files in three steps: (i) dumping whole-chromosome matrices at 25-kb resolution from the hic files using juicer, (ii) using a custom bash code to convert juicer matrices to txt suitable for cworld input, and (iii) using the matrix2insulation.py function of the cworld package to extract the insulation score profile across the chromosome (see bash file in associated github site). A custom python code was then used to compute the insulation profiles around the AluGG on-target sites for the damaged and undamaged sample (similar to the ChIP-seq profiles). Averaged insulation scores profiles around all on-target sites were obtained for each biological replicate and then averaged between replicates (e.g., Fig. 2A).

4C-like plots were computed from the merged Hi-C contact map obtained in untreated HEK293T using the hicPlotViewpoint function of HiCExplorer package using the cut site as viewpoint and a resolution of 25 kb.

mES cell line generation

mES cells were thawed onto irradiated mouse embryonic fibroblasts and maintained on gelatinzed plates in mES cell culture medium and were regularly tested for mycoplasma infection using Myco-Alert assay (Lonza). The founder mES cell lines contain $Brca1^{fl/exon11}$ alleles (*58*) along with a single copy of a DSB-inducible HR reporter targeted to the *Rosa26* locus. This reporter contains a unique 18-bp target site for the homing endonuclease I-SceI. Using CRISPR Cas9-mediated deletion, we removed the Δ5′ *GFP* copy from the original reporter clone to generate a donor-less clone (clone no. 8), which is incapable of generating GFP+ recombinant products. This clone was then subjected to CRISPR Cas9-assisted targeting of a new Δ5′-*GFP* donor sequence 441 or 563 kb from the *I-SceI* site using target-specific sgRNA. The new Δ5′-*GFP* donor contained silent mutations in the *GFP* and polyadenylation signal sequences that enable it to be distinguished from *GFP-I-SceI* during sequence alignment. Full details of this reporter, which also contains a red fluorescent protein expression cassette for detection of long tract gene conversion, will be described elsewhere. The clones were analyzed by PCR to confirm homologous insertion of both 5′ and 3′ targeting arms of the Δ5′-*GFP* donor. They were further analyzed by Southern blotting to confirm copy number and intactness of the Δ5′-*GFP* donor. Conventional Southern blotting, using gDNA digested with local restriction endonucleases flanking the site of insertion and with use of a *GFP* probe, was used to confirm single copy integration of the Δ5′-*GFP* donor. To distinguish between Δ5′-*GFP* donor targeting to the same chromosome as *GFP-I-SceI* versus targeting to the homolog, we made use of a restriction site for the rare-cutting enzyme I-CeuI, which we included in the outer (telomeric) targeting arm of the Δ5′-*GFP* donor targeting vector. Digestion of gDNA agarose plugs with I-CeuI + I-SceI would yield *GFP*-hybridizing bands that migrate at ~443 kb (Donor+441 clones) or ~565 kb (Donor+563 clones), only if the Δ5′-*GFP* donor is positioned on the same chromosome as *GFP-I-SceI*. We identified four clones each of Donor+441 and Donor +563, in which a single, intact copy of the Δ5′-*GFP* donor was correctly targeted to the same chromosome as *GFP-I-SceI*. Clones in which the Δ5′-*GFP* donor was targeted to the homolog were not included in the current study.

Southern blotting

gDNA was isolated from clones using Puregene DNA isolation kit (Qiagen). Five micrograms of gDNA was digested with appropriate restriction enzymes at 37°C and run on 0.8% agarose in 0.5X TBE gel overnight. After denaturation, DNA was transferred onto a positively charged nylon membrane and probed with a ^{32}P-labeled *GFP* cDNA probe. Signal was recorded on a phosphorimager screen and scanned using a Typhoon biomolecular imager.

Pulsed field gel electrophoresis

Plugs of 0.8% agarose were made using Clean cut agarose using 1×10^6 cells. Plugs were then subjected to Proteinase K treatment overnight at 50°C followed by three washes at 4°C. Prior to the last wash, the plugs were treated for 1 hour with RNase A. One half of the plug was then washed with 10 mM Tris and 0.1 mM EDTA for 1 hour and then equilibrated in 1xCutSmart buffer for 1 hour at 4°C. The buffer was replaced with reaction containing 30 U of I-SceI and I-CeuI with 1xCutSmart buffer. The reaction was then incubated overnight in a thermomixer at 37°C with gentle agitation at 300 rpm. The next day, the plugs were washed with TE buffer for 30 min and then with 0.5X TBE for another 30 min. The plugs were then placed in the wells of an 1% agarose gel and electrophoresed for 24 hours at 4.5 V, 90-180 switch time, at 14°C. The gel was then subjected to Southern blotting, probed with a ^{32}P-labeled *GFP* cDNA probe. Signals were detected by use of phosphorimaging, as described above.

Recombination assays

For recombination assays, 200 µl of 0.8×10^6 cells/ml were transfected in suspension in 24-well plates with 0.5 µg of pcDNA3β-myc NLS-I-SceI or 0.5 µg control empty vector, using Lipofectamine 2000 (Invitrogen). GFP^+ frequencies were measured 3 days after transfection using Beckman Coulter CytoFlex LX. Transfection efficiency was measured simultaneously by parallel transfection with 0.05 µg *GFP* expression vector with 0.45 µg empty vector. For siRNA experiments, cells were transfected with 20 pmol siRNA with 0.3 µg of pcDNA3β-myc NLS-I-SceI (or empty vector) per well. Repair frequencies were corrected for background events and for transfection efficiency (50 to 90%). HR data represent the mean and standard error of the mean of three or five independent experiments. Statistical analysis was by two-tailed paired *t* test (unknown variance). siRNA efficiency was quantified by means of RT-qPCR (fig. S31).

REFERENCES AND NOTES

1. J. R. Dixon *et al.*, Topological domains in mammalian genomes identified by analysis of chromatin interactions. *Nature* **485**, 376–380 (2012). doi: 10.1038/nature11082; pmid: 22495300
2. S. S. P. Rao *et al.*, A 3D map of the human genome at kilobase resolution reveals principles of chromatin looping. *Cell* **159**, 1665–1680 (2014). doi: 10.1016/j.cell.2014.11.021; pmid: 25497547
3. S. S. P. Rao *et al.*, Cohesin loss eliminates all loop domains. *Cell* **171**, 305–320.e24 (2017). doi: 10.1016/j.cell.2017.09.026; pmid: 28985562
4. W. Schwarzer *et al.*, Two independent modes of chromatin organization revealed by cohesin removal. *Nature* **551**, 51–56 (2017). doi: 10.1038/nature24281; pmid: 29094699
5. G. Fudenberg *et al.*, Formation of chromosomal domains by loop extrusion. *Cell Rep.* **15**, 2038–2049 (2016). doi: 10.1016/j.celrep.2016.04.085; pmid: 27210764
6. I. F. Davidson *et al.*, DNA loop extrusion by human cohesin. *Science* **366**, 1338–1345 (2019). doi: 10.1126/science.aaz3418; pmid: 31753851
7. Y. Kim, Z. Shi, H. Zhang, I. J. Finkelstein, H. Yu, Human cohesin compacts DNA by loop extrusion. *Science* **366**, 1345–1349 (2019). doi: 10.1126/science.aaz4475; pmid: 31780627
8. A. Pombo, N. Dillon, Three-dimensional genome architecture: Players and mechanisms. *Nat. Rev. Mol. Cell Biol.* **16**, 245–257 (2015). doi: 10.1038/nrm3965; pmid: 25757416
9. B. Bonev, G. Cavalli, Organization and function of the 3D genome. *Nat. Rev. Genet.* **17**, 661–678 (2016). doi: 10.1038/nrg.2016.112; pmid: 27739532
10. P. H. L. Krijger, W. de Laat, Regulation of disease-associated gene expression in the 3D genome. *Nat. Rev. Mol. Cell Biol.* **17**, 771–782 (2016). doi: 10.1038/nrm.2016.138; pmid: 27826147

11. A. Hafner, A. Boettiger, The spatial organization of transcriptional control. *Nat. Rev. Genet.* **24**, 53–68 (2023). doi: 10.1038/s41576-022-00526-0; pmid: 36104547
12. M. Yu, B. Ren, The three-dimensional organization of mammalian genomes. *Annu. Rev. Cell Dev. Biol.* **33**, 265–289 (2017). doi: 10.1146/annurev-cellbio-100616-060531; pmid: 28783961
13. J. H. Yang, A. S. Hansen, Enhancer selectivity in space and time: From enhancer-promoter interactions to promoter activation. *Nat. Rev. Mol. Cell Biol.* **25**, 574–591 (2024). doi: 10.1038/s41580-024-00710-6; pmid: 38413840
14. B. D. Pope *et al.*, Topologically associating domains are stable units of replication-timing regulation. *Nature* **515**, 402–405 (2014). doi: 10.1038/nature13986; pmid: 25409831
15. D. J. Emerson *et al.*, Cohesin-mediated loop anchors confine the locations of human replication origins. *Nature* **606**, 812–819 (2022). doi: 10.1038/s41586-022-04803-0; pmid: 35676475
16. Y. Zhang *et al.*, The fundamental role of chromatin loop extrusion in physiological V(D)J recombination. *Nature* **573**, 600–604 (2019). doi: 10.1038/s41586-019-1547-y; pmid: 31511698
17. Y. Zhang, X. Zhang, H.-Q. Dai, H. Hu, F. W. Alt, The role of chromatin loop extrusion in antibody diversification. *Nat. Rev. Immunol.* **22**, 550–566 (2022). doi: 10.1038/s41577-022-00679-3; pmid: 35169260
18. A. Canela *et al.*, Genome organization drives chromosome fragility. *Cell* **170**, 507–521.e18 (2017). doi: 10.1016/j.cell.2017.06.034; pmid: 28735753
19. J. H. Yang, H. B. Brandão, A. S. Hansen, DNA double-strand break end synapsis by DNA loop extrusion. *Nat. Commun.* **14**, 1913 (2023). doi: 10.1038/s41467-023-37583-w; pmid: 37024496
20. P. L. Collins *et al.*, DNA double-strand breaks induce H2Ax phosphorylation domains in a contact-dependent manner. *Nat. Commun.* **11**, 3158 (2020). doi: 10.1038/s41467-020-16926-x; pmid: 32572033
21. C. Arnould *et al.*, Loop extrusion as a mechanism for formation of DNA damage repair foci. *Nature* **590**, 660–665 (2021). doi: 10.1038/s41586-021-03193-z; pmid: 33597753
22. K. L. de Luca *et al.*, Genome-wide profiling of DNA repair proteins in single cells. *Nat. Commun.* **15**, 9918 (2024). doi: 10.1038/s41467-024-54159-4; pmid: 39572529
23. G. Danovski *et al.*, Diffusion of activated ATM explains γH2AX and MDC1 spread beyond the DNA damage site. *iScience* **27**, 110826 (2024). doi: 10.1016/j.isci.2024.110826; pmid: 39310780
24. L. Ström, H. B. Lindroos, K. Shirahige, C. Sjögren, Postreplicative recruitment of cohesin to double-strand breaks is required for DNA repair. *Mol. Cell* **16**, 1003–1015 (2004). doi: 10.1016/j.molcel.2004.11.026; pmid: 15610742
25. E. Ünal *et al.*, DNA damage response pathway uses histone modification to assemble a double-strand break-specific cohesin domain. *Mol. Cell* **16**, 991–1002 (2004). doi: 10.1016/j.molcel.2004.11.027; pmid: 15610741
26. A. Piazza *et al.*, Cohesin regulates homology search during recombinational DNA repair. *Nat. Cell Biol.* **23**, 1176–1186 (2021). doi: 10.1038/s41556-021-00783-x; pmid: 34750581
27. R. S. Zou *et al.*, Massively parallel genomic perturbations with multi-target CRISPR interrogates Cas9 activity and DNA repair at endogenous sites. *Nat. Cell Biol.* **24**, 1433–1444 (2022). doi: 10.1038/s41556-022-00975-z; pmid: 36064968
28. F. Aymard *et al.*, Genome-wide mapping of long-range contacts unveils clustering of DNA double-strand breaks at damaged active genes. *Nat. Struct. Mol. Biol.* **24**, 353–361 (2017). doi: 10.1038/nsmb.3387; pmid: 28263325
29. T. Natsume, T. Kiyomitsu, Y. Saga, M. T. Kanemaki, Rapid protein depletion in human cells by auxin-inducible degron tagging with short homology donors. *Cell Rep.* **15**, 210–218 (2016). doi: 10.1016/j.celrep.2016.03.001; pmid: 27052166
30. Y. Liu *et al.*, Very fast CRISPR on demand. *Science* **368**, 1265–1269 (2020). doi: 10.1126/science.aay8204; pmid: 32527834
31. E. P. Rogakou, D. R. Pilch, A. H. Orr, V. S. Ivanova, W. M. Bonner, DNA double-stranded breaks induce histone H2AX phosphorylation on serine 139. *J. Biol. Chem.* **273**, 5858–5868 (1998). doi: 10.1074/jbc.273.10.5858; pmid: 9488723
32. E. Crane *et al.*, Condensin-driven remodelling of X chromosome topology during dosage compensation. *Nature* **523**, 240–244 (2015). doi: 10.1038/nature14450; pmid: 26030525
33. F. Aymard *et al.*, Transcriptionally active chromatin recruits homologous recombination at DNA double-strand breaks. *Nat. Struct. Mol. Biol.* **21**, 366–374 (2014). doi: 10.1038/nsmb.2796; pmid: 24658350
34. A. Dupré *et al.*, A forward chemical genetic screen reveals an inhibitor of the Mre11-Rad50-Nbs1 complex. *Nat. Chem. Biol.* **4**, 119–125 (2008). doi: 10.1038/nchembio.63; pmid: 18176557
35. Y. Zhou, P. Caron, G. Legube, T. T. Paull, Quantitation of DNA double-strand break resection intermediates in human cells. *Nucleic Acids Res.* **42**, e19–e19 (2014). doi: 10.1093/nar/gkt1309; pmid: 24362840
36. A. Carreira *et al.*, The BRC repeats of BRCA2 modulate the DNA-binding selectivity of RAD51. *Cell* **136**, 1032–1043 (2009). doi: 10.1016/j.cell.2009.02.019; pmid: 19303847
37. M. Peritore, K.-U. Reusswig, S. C. S. Bantele, T. Straub, B. Pfander, Strand-specific ChIP-seq at DNA breaks distinguishes ssDNA versus dsDNA binding and refutes single-stranded nucleosomes. *Mol. Cell* **81**, 1841–1853.e4 (2021). doi: 10.1016/j.molcel.2021.02.005; pmid: 33651987
38. J. B. Crickard, C. J. Moevus, Y. Kwon, P. Sung, E. C. Greene, Rad54 drives ATP hydrolysis-dependent DNA sequence alignment during homologous recombination. *Cell* **181**, 1380–1394.e18 (2020). doi: 10.1016/j.cell.2020.04.056; pmid: 32502392
39. J. Renkawitz, C. A. Lademann, M. Kalocsay, S. Jentsch, Monitoring homology search during DNA double-strand break repair in vivo. *Mol. Cell* **50**, 261–272 (2013). doi: 10.1016/j.molcel.2013.02.020; pmid: 23523370
40. G. Chandramouly *et al.*, BRCA1 and CtIP suppress long-tract gene conversion between sister chromatids. *Nat. Commun.* **4**, 2404 (2013). doi: 10.1038/ncomms3404; pmid: 23994874
41. G. Wutz *et al.*, Topologically associating domains and chromatin loops depend on cohesin and are regulated by CTCF, WAPL, and PDS5 proteins. *EMBO J.* **36**, 3573–3599 (2017). doi: 10.15252/embj.201798004; pmid: 29217591
42. A. Yesbolatova *et al.*, The auxin-inducible degron 2 technology provides sharp degradation control in yeast, mammalian cells, and mice. *Nat. Commun.* **11**, 5701 (2020). doi: 10.1038/s41467-020-19532-z; pmid: 33177522
43. M. Mitter *et al.*, Conformation of sister chromatids in the replicated human genome. *Nature* **586**, 139–144 (2020). doi: 10.1038/s41586-020-2744-4; pmid: 32968280
44. R. Scully, A. Panday, R. Elango, N. A. Willis, DNA double-strand break repair-pathway choice in somatic mammalian cells. *Nat. Rev. Mol. Cell Biol.* **20**, 698–714 (2019). doi: 10.1038/s41580-019-0152-0; pmid: 31263220
45. F. Teloni *et al.*, Cohesin guides homology search during DNA repair via loops and sister chromatid linkages. bioRxiv 2025.2002.2010.637359 [Preprint] (2025); https://doi.org/10.1101/2025.02.10.637359.
46. J. Phipps *et al.*, Cohesin complex oligomerization maintains end-tethering at DNA double-strand breaks. *Nat. Cell Biol.* **27**, 118–129 (2025). doi: 10.1038/s41556-024-01552-2; pmid: 39482358
47. M. Gabriele *et al.*, Dynamics of CTCF- and cohesin-mediated chromatin looping revealed by live-cell imaging. *Science* **376**, 496–501 (2022). doi: 10.1126/science.abn6583; pmid: 35420890
48. W.-D. Heyer, X. Li, M. Rolfsmeier, X.-P. Zhang, Rad54: The Swiss Army knife of homologous recombination? *Nucleic Acids Res.* **34**, 4115–4125 (2006). doi: 10.1093/nar/gkl481; pmid: 16935872
49. J. Lee *et al.*, Kinetic organization of the genome revealed by ultraresolution multiscale live imaging. *Science* **389**, eadx2202 (2025). doi: 10.1126/science.abn6583; pmid: 35420890
50. N. W. Cho, R. L. Dilley, M. A. Lampson, R. A. Greenberg, Interchromosomal homology searches drive directional ALT telomere movement and synapsis. *Cell* **159**, 108–121 (2014). doi: 10.1016/j.cell.2014.08.030; pmid: 25259924
51. J. Renkawitz, C. A. Lademann, S. Jentsch, Mechanisms and principles of homology search during recombination. *Nat. Rev. Mol. Cell Biol.* **15**, 369–383 (2014). doi: 10.1038/nrm3805; pmid: 24824069
52. K. Ragunathan, C. Liu, T. Ha, RecA filament sliding on DNA facilitates homology search. *eLife* **1**, e00067 (2012). doi: 10.7554/eLife.00067; pmid: 23240082
53. A. Chimthanawala *et al.*, SMC protein RecN drives RecA filament translocation for in vivo homology search. *Proc. Natl. Acad. Sci. U.S.A.* **119**, e2209304119 (2022). doi: 10.1073/pnas.2209304119; pmid: 36346847
54. N. A. Willis, A. Panday, E. E. Duffey, R. Scully, Rad51 recruitment and exclusion of non-homologous end joining during homologous recombination at a Tus/Ter mammalian replication fork barrier. *PLOS Genet.* **14**, e1007486 (2018). doi: 10.1371/journal.pgen.1007486; pmid: 30024881
55. F. Ramírez, F. Dündar, S. Diehl, B. A. Grüning, T. Manke, deepTools: A flexible platform for exploring deep-sequencing data. *Nucleic Acids Res.* **42**, W187–W191 (2014). doi: 10.1093/nar/gku365; pmid: 24799436
56. L. Lopez-Delisle *et al.*, pyGenomeTracks: Reproducible plots for multivariate genomic datasets. *Bioinformatics* **37**, 422–423 (2021). doi: 10.1093/bioinformatics/btaa692; pmid: 32745185
57. N. C. Durand *et al.*, Juicebox provides a visualization system for Hi-C contact maps with unlimited zoom. *Cell Syst.* **3**, 99–101 (2016). doi: 10.1016/j.cels.2015.07.012; pmid: 27467250
58. N. A. Willis *et al.*, BRCA1 controls homologous recombination at Tus/Ter-stalled mammalian replication forks. *Nature* **510**, 556–559 (2014). doi: 10.1038/nature13295; pmid: 24776801
59. A. Marin-Gonzalez *et al.*, Cohesin drives chromatin scanning during the RAD51-mediated homology search. Zenodo (2025); https://doi.org/10.5281/zenodo.17238412.

ACKNOWLEDGMENTS

We thank C. Carcamo, S. Rudnizky, and R. Kalhor for stimulating discussions throughout the project. We are grateful to the Genetic Resources Core Facility and single-cell and transcriptomics cores for NextSeq and NovaSeq experiments and to W. Timp and L. Goff at Johns Hopkins University for granting us access to their MiSeq machines. We also thank A. Feinberg (Johns Hopkins) and the biopolymers core (Harvard Medical School) for access to Covaris sonicators. **Funding:** This work was funded by National Institutes of Health grants R35-GM122569 (T.H.), U01 DK127432 (T.H.), and R35 CA263813 (R.S.); National Science Foundation grant EFMA 193303 (T.H.); a Life Sciences Research Foundation Fellowship

sponsored by the Howard Hughes Medical Institute (HHMI) fellowship (A.M.-G.); and the American Cancer Society - New England Research Council - Postdoctoral Fellowship, PF-24 1321213-01-DMC (N.M.N.). **Author contributions:** Cas9 RNP nucleofections: A.M.-G., A.T.R., V.K.-N.; ChIP-seq: A.M.-G., A.T.R.; Hi-C experiments: A.M.-G.; Data analysis: A.M.-G. with help from R.S.Z.; Generation and validation of mES cell lines: N.M.N. with help from D.N.; Strand-specific ChIP-seq: A.G.L.; Generation and validation of HCT116-AID cell lines: M.T.K.; Conceptualization: A.M.-G., A.T.R., N.M.N., F.J.A.-V., R.S., T.H.; HR-GFP assays: N.M.N.; Supervision: R.S., T.H.; Writing – original draft: A.M.-G.; Writing – review & editing: A.T.R., N.M.N., R.S., T.H. **Competing interests:** The authors declare that they have no competing interests. **Data and materials availability:** All data associated with this study are present in the main text or the supplementary materials. ChIP-seq and Hi-C data have been uploaded to the Sequence Read Archive under BioProject accession no. PRJNA1214218. Custom scripts can be found at Zenodo (*59*). Scripts are also available on GitHub (https://github.com/AlbertoMarinG/HomSearch/). **License information:** Copyright © 2025 the authors, some rights reserved; exclusive licensee American Association for the Advancement of Science. No claim to original US government works. https://www.science.org/about/science-licenses-journal-article-reuse. This article is subject to HHMI's Open Access to Publications policy. HHMI lab heads have previously granted a nonexclusive CC BY 4.0 license to the public and a sublicensable license to HHMI in their research articles. Pursuant to those licenses, the Author Accepted Manuscript (AAM) of this article can be made freely available under a CC BY 4.0 license immediately upon publication.

SUPPLEMENTARY MATERIALS

science.org/doi/10.1126/science.adw1928
Figs. S1 to S31; Tables S1 and S2; MDAR Reproducibility Checklist

Submitted 22 January 2025; resubmitted 16 July 2025; accepted 2 October 2025
10.1126/science.adw1928



AAAS.ORG/COMMUNITY







AAAS' Member Community is a one-stop destination for scientists and STEM enthusiasts alike. It's "Where Science Gets Social": a community where facts matter, ideas are big and there's always a reason to come hang out, share, discuss and explore.

Member COMMUNITY
AAAS

AMERICAN ASSOCIATION FOR THE ADVANCEMENT OF SCIENCE

RESEARCH ARTICLE SUMMARY

MOLECULAR BIOLOGY

Cohesin guides homology search during DNA repair using loops and sister chromatid linkages

Federico Teloni*, Zsuzsanna Takacs, Michael Mitter, Christoph C. H. Langer, Inès Prlesi, Thomas L. Steinacker, Vincent P. Reuter, Dmitry Mylarshchikov, Daniel W. Gerlich*

Full article and list of author affiliations: https://doi.org/10.1126/science.adw0566

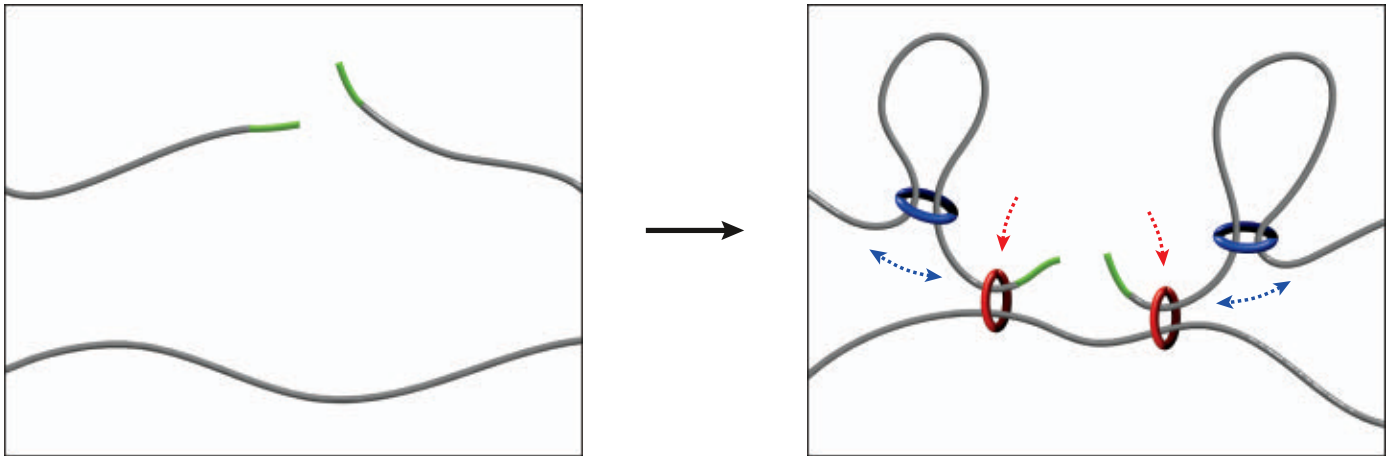
INTRODUCTION: Accurate repair of DNA double-strand breaks (DSBs) is essential for genome stability, because errors can cause cell death or chromosomal rearrangements linked to cancer. Homologous recombination restores DNA sequences around the break by copying from an intact template, usually the sister chromatid. A key challenge has been to understand how broken DNA ends locate the correct homologous sequence within the folded genome. Although the biochemical steps of repair are well described, the contribution of nuclear architecture to the homology search process has remained unclear.

RATIONALE: Cohesin, a ring-shaped protein complex, organizes chromosomes by extruding DNA loops to form topologically associating domains (TADs) and by linking sister chromatids. Both functions influence genome topology, but how this affects homology search was unknown. To address this, we developed sister-pore-C, a high-resolution method to map intra- and interchromatid contacts genome wide. Combined with targeted DSB induction and acute cohesin perturbations, this approach allowed us to determine how cohesin-mediated structures guide RAD51 filament sampling during repair.

RESULTS: RAD51 filaments sampled homology primarily near DSBs and within TAD boundaries, indicating that cohesin-mediated loops control the search space. Loss of loop-extruding cohesin narrowed RAD51 distribution, whereas hyperprocessive extrusion expanded sampling but reduced its local concentration near the DNA break. Sister-pore-C revealed that DSBs remodel chromosome architecture locally, increasing looping and promoting contacts with the sister chromatid near the break. Cohesin mapping showed that loop-extruding complexes accumulate across a broad domain surrounding the DSB, whereas cohesive cohesin concentrates at the break itself, establishing distinct cis- and trans-sister architectures. Functionally, depletion of loop-extruding cohesin or excessive extrusion delayed repair, and loss of cohesion abolished repair, demonstrating that both mechanisms are essential for efficient homologous recombination.

CONCLUSION: Cohesin directs homology search through a dual mechanism: A cohesive clamp tethers broken DNA ends to the sister chromatid, and loop extrusion controls sampling within the local TAD. This spatial organization narrows the search space and accelerates repair, establishing chromosome topology as an active determinant of repair efficiency. Sister-pore-C enables genome-wide mapping of intra- and intersister contacts, providing a framework with which to explore recombination architectures in other processes such as meiosis. □

*Corresponding author. Email: federico.teloni@imba.oeaw.ac.at (F.T.); daniel.gerlich@imba.oeaw.ac.at (D.W.G.) Cite this article as F. Teloni *et al.*, *Science* **390**, eadw0566 (2025). DOI: 10.1126/science.adw0566



Model of how DNA DSBs locally reorganize chromatin to facilitate homology search. Cohesive cohesin (red) accumulates directly adjacent to the break site (green) to direct sampling toward the intact sister chromatid, whereas loop-extruding cohesin (blue) spreads across a megabase-scale domain to regulate the lateral sampling range.

MOLECULAR BIOLOGY

Cohesin guides homology search during DNA repair using loops and sister chromatid linkages

Federico Teloni[1]*, Zsuzsanna Takacs[1], Michael Mitter[1,2], Christoph C. H. Langer[1], Inès Prlesi[1,2], Thomas L. Steinacker[1], Vincent P. Reuter[1], Dmitry Mylarshchikov[1,2], Daniel W. Gerlich[1]*

Accurate repair of DNA double-strand breaks (DSBs) is essential for genome stability, and defective repair underlies diseases such as cancer. Homologous recombination uses an intact homologous sequence to faithfully restore damaged DNA, yet how broken DNA ends find homologous sites in a genome containing billions of bases remains unclear. Here, we introduce sister-pore-C, a high-resolution method to map intra- and intermolecular interactions in replicated chromosomes. We show how DSBs remodel chromosome architecture using two functionally distinct pools of cohesin. Loop-extruding cohesin accumulates across megabase-scale domains surrounding DSBs to control local homology sampling, whereas cohesive cohesin concentrates at break sites to tether DNA ends to the sister chromatid. This mechanism restricts the homology-sampling space, highlighting how chromosome conformation helps to preserve genomic integrity.

DNA double-strand breaks (DSBs) are among the most dangerous threats to genome integrity, because their incorrect repair can result in chromosomal loss or translocations associated with cancer (*1*). The most accurate mechanism of DSB repair is homologous recombination, which restores the damaged sequence from an intact homologous DNA template (*2*, *3*). However, this process requires broken DNA ends to locate a homologous sequence within a genome dominated by nonhomologous DNA, creating a substantial kinetic challenge (*4*–*7*). In eukaryotes, homology search is mediated by nucleoprotein filaments formed by the RAD51 protein on single-stranded DNA (ssDNA) adjacent to the DSB (*2*, *3*, *6*, *8*). Although the interactions between RAD51 filaments and DNA are well characterized at the molecular scale (*9*), it remains unclear how these filaments navigate the dense, folded chromatin architecture of the nucleus (*10*–*15*).

DSBs can be repaired by recombination with either the replicated sister chromatid or a homologous chromosome, consistent with a model in which RAD51 filaments scan the entire genome (*4*, *6*, *7*). Indeed, RAD51 filaments can move throughout the entire cell nucleus in budding yeast (*16*). However, in somatic cells, homologous recombination primarily uses the sister chromatid as a repair template (*2*, *6*, *7*, *17*, *18*). This preference is attributed to the formation of cohesin-mediated linkages between sister chromatids, referred to as cohesion (*19*–*21*), which is essential for homology-directed repair (*22*–*25*). An alternative model suggests that DSBs recombine with prepaired molecules rather than scanning the genome (*5*). However, in human cells, sister loci are often far apart (*25*–*28*), and sister chromatids can be locally misaligned by hundreds of kilobases (*28*–*30*). It remains unclear how broken DNA ends identify homology on sister chromatids despite this substantial misalignment.

[1]Institute of Molecular Biotechnology of the Austrian Academy of Sciences (IMBA), Vienna BioCenter (VBC), Vienna, Austria. [2]Vienna BioCenter PhD Program, Doctoral School of the University of Vienna and Medical University of Vienna, Vienna, Austria. ***Corresponding author. Email: federico.teloni@imba.oeaw.ac.at (F.T.); daniel.gerlich@imba.oeaw.ac.at (D.W.G.)**

Beyond linking sister chromatids, cohesin organizes chromosomes into loops (*31*–*34*) using motor-driven DNA extrusion (*35*, *36*). In vertebrates, cohesin-mediated loop extrusion is restricted by the DNA-binding protein CTCF (*37*–*39*), thereby structuring the genome into topologically associating domains (TADs) (*40*–*42*). Cohesin-mediated looping also promotes the dealignment of sister chromatids, especially within TAD bodies (*28*, *29*). In budding yeast, loop-forming cohesin influences homology search by reshaping chromatin around DSBs (*43*, *44*). However, the impact of TADs and the dynamic interplay between cohesive- and loop-forming pools of cohesin on homology search remains unknown.

To elucidate how cohesin-regulated chromosome architectures influence DSB repair, we developed methods to map the homology-sampling space in human somatic cells both within and across sister chromatids. Combining these approaches with targeted degradation of cohesin regulators, we show how loop-forming and cohesive cohesin cooperatively guide homology search.

Results

Targeted induction of homology-directed DSB repair in S/G_2-phase cells

Investigating how chromosome conformation contributes to homology search during DNA repair requires precise temporal and positional control of DSBs. One effective approach involves combining cell cycle synchronization, inducible Cas9 transgene expression, and transfection of synthetic single-guide RNAs (sgRNAs) targeting multiple genomic loci (*45*). We adapted this system for use in HeLa cells, for which genome-edited clones allowing targeted degradation of cohesin regulators are readily available (*28*, *29*). Immunofluorescence staining of the DSB repair factor 53BP1 (tumor suppressor p53-binding protein 1) revealed the formation of repair foci beginning ~2 hours after sgRNA transfection, with a gradual increase in number continuing up to 7 hours after transfection (fig. S1, A and B).

To induce DSBs specifically during the S/G_2 phase, when homology-directed repair is active (*46*, *47*), we synchronized cells at the G_1/S boundary and released them into the S phase, followed by sgRNA transfection (fig. S1, C to F). By using chromatin immunoprecipitation followed by sequencing (ChIP-seq) with an anti-γH2A.X antibody, we detected DSBs across the genome 6 hours after sgRNA transfection, when 93% of cells had reached G_2 (fig. S1F). This approach showed robust γH2A.X accumulation at 23 genomic loci, which we selected for further analysis (fig. S1, G to J). This system thus allows for site-specific DSB induction at a cell cycle stage proficient for homology-directed repair.

DSBs can be repaired by either nonhomologous end joining or homology-directed repair (*46*, *47*). To determine which pathway predominantly repairs Cas9-induced DSBs in G_2-synchronized HeLa cells, we visualized nine sgRNA target loci using fluorescence in situ hybridization (FISH) combined with immunofluorescence detection of 53BP1 (marking DSBs) and RAD51 (marking homology-directed repair). Without sgRNA, 53BP1-positive FISH spots ranged from 3 to 6% across target loci, rising to 40 to 90% with sgRNA transfection (Fig. 1, A to F), confirming the specificity and efficiency of Cas9-mediated DSB induction. Notably, most 53BP1-positive sites also co-localized with RAD51, ranging from 73 to 86% across sgRNA target loci (Fig. 1G). Thus, in G_2-synchronized HeLa cells, most Cas9-mediated DSBs induce the homology-directed repair pathway.

Replicated chromosomes contain sgRNA target sites on each sister chromatid, making both susceptible to Cas9-induced cleavage. However, the gradual accumulation of DSBs over several hours (fig. S1, A and B) suggests that simultaneous cutting of both sister alleles might be relatively infrequent. To estimate the probability of dual cutting events, we applied statistical modeling to infer the per-allele cutting probability from immunofluorescence data. Because sister chromatids are not resolvable by conventional light microscopy, a pair of sister loci appears as a single FISH signal; therefore, 53BP1-positive FISH foci may reflect either single- or double-sister cutting events, whereas 53BP1-negative

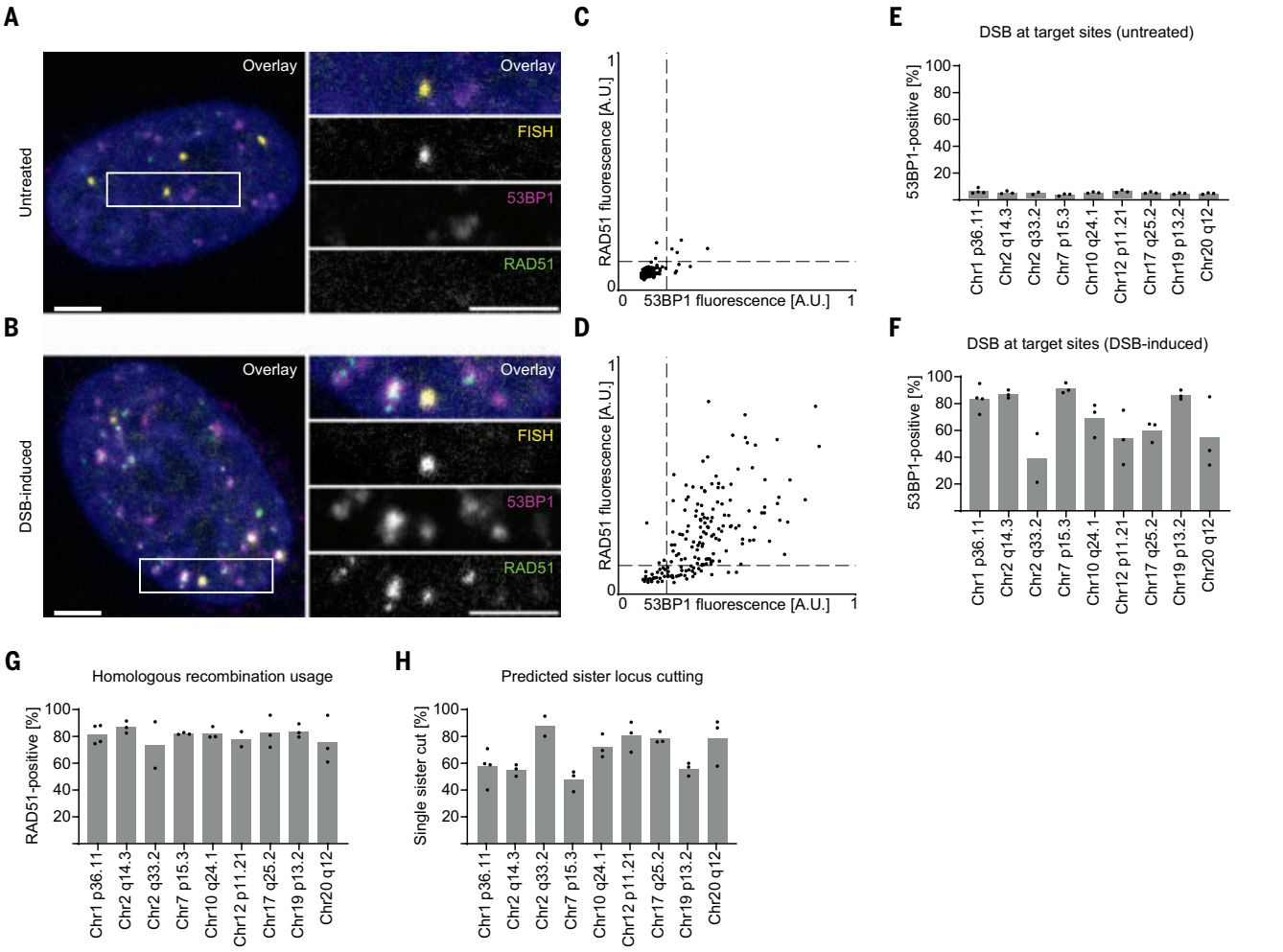


Fig. 1. Site-specific induction of homology-directed DSB repair. (**A** and **B**) Immunofluorescence staining of the general DSB repair factor 53BP1 and the homology-directed repair–specific factor RAD51 combined with FISH at an sgRNA target locus (chr19 p13.2) in untreated (A) or sgRNA-transfected (DSB-induced) (B) G_2-synchronized HeLa cells. Scale bar, 5 μm. (**C** and **D**) Quantification of 53BP1 and RAD51 fluorescence intensities at the FISH-labeled locus in untreated (C) or DSB-induced (D) cells. Each dot represents one locus; dashed lines indicate 2 SDs above the mean of the untreated control. (**E** and **F**) Percentage of FISH-labeled loci positive for 53BP1 in untreated (E) or DSB-induced (F) cells measured at nine sgRNA target loci. Each dot is the mean from an independent experiment; bars indicate the average of all experiments. (**G**) Fraction of 53BP1-positive loci that also contain RAD51 after sgRNA transfection at the same nine loci. Dots are mean values per experiment; bars indicate overall mean. (**H**) Frequency of DSB cleavage at a single allele across the same nine loci (see the Materials and methods). Dots are mean values per experiment; bars indicate overall mean. In all experiments, sgRNA transfection was performed 3 hours after release from the G_1/S block and cells were fixed 6 hours later.

FISH loci reflect regions that are not cut on either sister chromatid. By analyzing the fraction of 53BP1-negative FISH foci, we estimated the relative frequency of single versus double cleavage events (see the Materials and methods). This analysis revealed that for eight of nine investigated sgRNA-targeted loci, DSBs were predominantly generated on a single sister chromatid (Fig. 1H). Thus, whereas it is not technically possible to prevent dual-cutting events, the 6 hours post sgRNA transfection time point mostly reflects single-allele cleavage. Our optimized assay system thus provides a robust platform for investigating the role of chromosome architecture in homology-directed DNA repair.

Loop-forming cohesin controls homology-sampling range

Genomic interactions are normally constrained within local neighborhoods of TADs (*10*–*15*, *32*, *48*). However, given the high intrinsic dynamics of RAD51 filaments (*16*), it remains unclear how these architectural constraints affect homology search. To address this, we performed RAD51 ChIP-seq using a library preparation that captures interactions between single-stranded RAD51 nucleoprotein filaments and double-stranded DNA (*49*). Published high-throughput chromosome conformation capture (Hi-C) data from G_2-synchronized cells (*29*) provided a reference for local chromosome architecture near Cas9-induced DSBs (Fig. 2A and fig. S2A). After DSB induction, RAD51 ChIP-seq signal accumulated predominantly near sgRNA target sites, spreading only over a few hundred kilobases (Fig. 2, B to D, and figs. S1, K and L, and S2B). Quantification of average read densities showed strong and significant enrichment of both RAD51 and γH2A.X within a 1-Mb window surrounding the sgRNA targets but not at other genomic regions (fig. S3, A and B), confirming that RAD51 sampling is locally confined to the vicinity of DSBs. Sequence analysis of the regions flanking the sgRNA target sites confirmed the absence of homologous sequences, indicating that the observed RAD51 ChIP-seq signal reflects transient homology-sampling interactions rather than stable engagement with a repair template.

To further assess the specificity of the RAD51 signal, we analyzed cells synchronized to G_1 phase, when the homology-directed repair pathway is inactive (*46*, *47*). Upon DSB induction in G_1 cells, we observed a significant accumulation of γH2A.X but not RAD51 near the sgRNA target

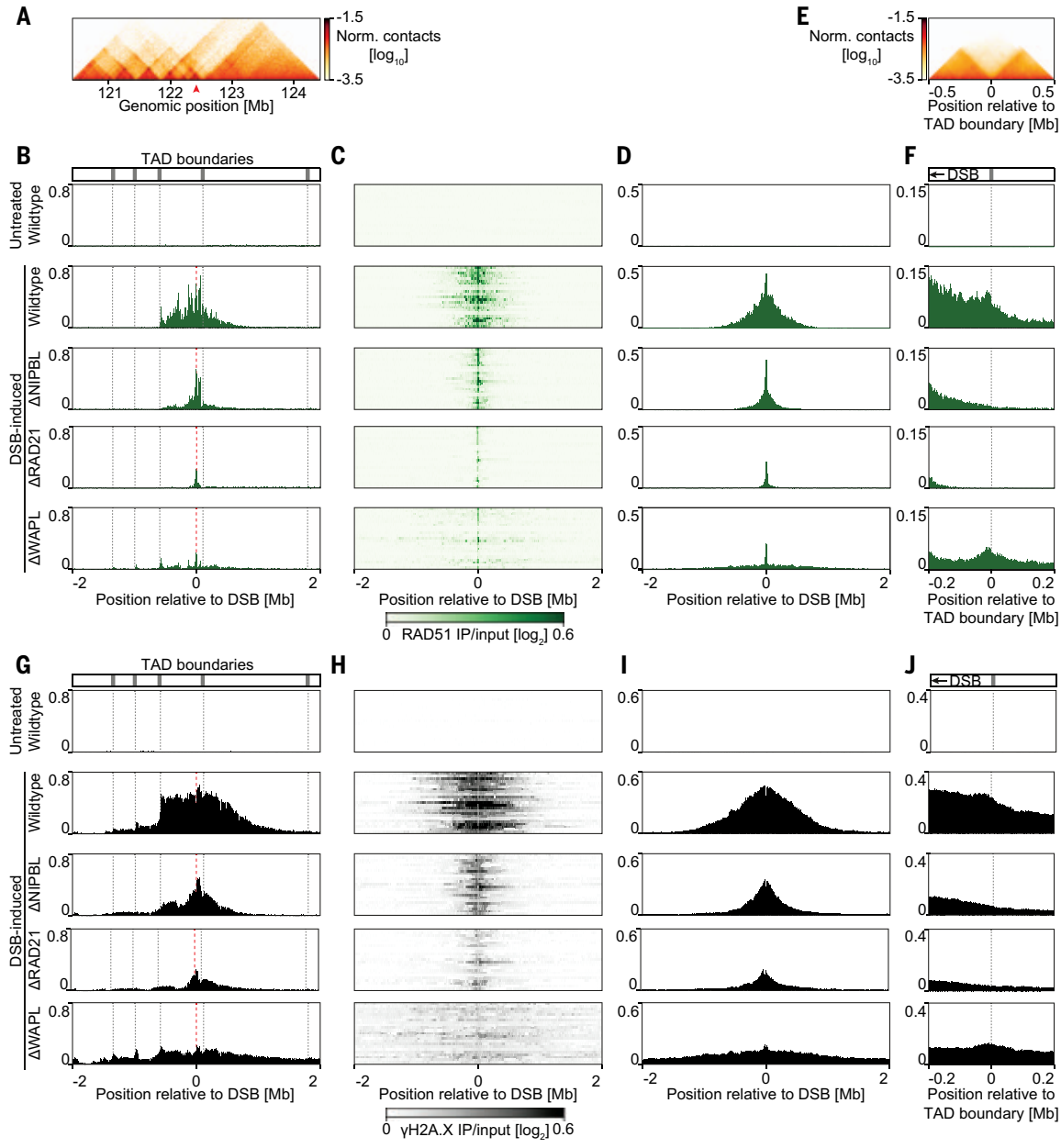


Fig. 2. Loop-forming cohesin controls the homology search range. (**A**) Hi-C interaction matrix (*29*) around an sgRNA target locus (chr2 q14.3) in untreated, G_2-synchronized cells. The red arrowhead marks the sgRNA target site. (**B**) RAD51 ChIP-seq tracks at the locus shown in (A) for untreated or DSB-induced cells (wild type or with auxin-induced depletion of NIPBL, RAD21, or WAPL). Gray dotted lines indicate TAD boundaries; the red dashed line marks the DSB site. Bin size was 10 kb. (**C** and **D**) Stacked line profiles (C) and average pileups (D) of RAD51 signals at 23 sgRNA target loci under the conditions in (B). Bin size was 10 kb. (**E**) Average Hi-C interaction profile at TAD boundaries (*29*) surrounding the same 23 loci. (**F**) RAD51 ChIP-seq signal aligned to TAD boundaries from (E), with DSBs positioned at the left. Bin size was 2.5 kb. (**G** to **J**) γH2A.X ChIP-seq tracks (G), stacked line profiles (H), average pileups (I), and TAD-boundary-aligned pileups (J) under the conditions described in (B). In all experiments, sgRNA transfection was performed 3 hours after release from the G_1/S block and cells were harvested 6 hours later. Auxin-mediated depletion was initiated 1 hour before release and maintained until harvesting. All ChIP-seq signals are shown as $\log_2$(IP/input) and represent merged data from $n = 2$ independent experiments.

sites (fig. S3, C and D), supporting the specificity of the RAD51 signal for active homology sampling. Together, these findings demonstrate that RAD51 homology sampling is strongly biased toward a confined genomic neighborhood surrounding the DSB.

The distribution of RAD51 around sgRNA target sites was often asymmetric and appeared to be constrained by TAD boundaries (Fig. 2, A and B, and fig. S2, A and B). Average profiles of RAD51 ChIP-seq signal relative to TAD boundaries near DSBs confirmed this pattern: RAD51 accumulated at the boundaries but declined sharply on the side distal to the DSB (Fig. 2, E and F). Further stratification by TAD boundary strength showed that strong boundaries more effectively limited RAD51 spread than weak ones (fig. S3E). These results indicate that RAD51 filaments primarily sample chromatin within TAD-delimited neighborhoods.

Given that loop-forming cohesin complexes are key organizers of TAD structures (*31*–*34*), we next investigated their role in regulating homology sampling. Using an auxin-inducible degron (AID) system (*28*), we depleted NIPBL, which is required for loop extrusion but dispensable for maintaining cohesion (*29*, *35*, *36*, *50*) (fig. S3F). NIPBL depletion

markedly reduced the spread of the RAD51 ChIP-seq signal and abolished accumulation at TAD boundaries (Fig. 2, B to F, and fig. S3E). Similarly, AID-mediated depletion of the core cohesin subunit RAD21 (fig. S3G) also led to a strong reduction in RAD51 spreading (Fig. 2, B to F, and figs. S2B and S3E). These results highlight the importance of loop-extruding cohesin complexes in defining the genomic range of homology sampling.

Cohesin forms loops on chromatin until it is released by the WAPL protein (*34*, *51*–*53*). Depleting WAPL increases loop size and promotes bypass of TAD boundaries (*54*). Because loop size directly influences how DNA segments encounter one another, we investigated the effect of auxin-induced degradation of WAPL (*28*) (fig. S3H) on RAD51 distribution. We observed much less RAD51 signal near DSBs but a broader spread across multiple TAD boundaries (Fig. 2, B to D, and fig. S2B). Although RAD51 still accumulated at TAD boundaries, the sharp decay across strong boundaries observed in control cells was lost (Fig. 2, B to F, and figs. S2, A and B, and S3E). These effects were not caused by nonspecific increases in DNA damage: In the absence of sgRNA, depletion of NIPBL, RAD21, or WAPL led to no or only modest increases in DSB repair foci compared with sgRNA-induced breaks (figs. S3, I and J, and S1, A and B). Thus, increased loop extrusion processivity expands the spatial range of RAD51 filament sampling but reduces its local concentration near the break.

DSB repair domains are marked by ATM-mediated γH2A.X phosphorylation, whereby cohesin and TAD boundaries have been proposed to regulate the spread of the phosphorylation (*55*, *56*). To determine how the RAD51 homology-sampling range relates to DSB repair domains, we performed γH2A.X ChIP-seq in G_2-phase cells after Cas9-mediated DSB induction. Although TAD boundaries constrained γH2A.X spreading, particularly at strong boundaries, its distribution was broader than the RAD51 signal (Fig. 2, G to J, and fig. S4, A and B). Consistent with the RAD51 results, NIPBL or RAD21 depletion substantially narrowed γH2A.X spreading, whereas WAPL depletion broadened it (Fig. 2, G to J, and fig. S4, A and B), corroborating a key role of cohesin-mediated looping in spreading this epigenetic mark. Homology sampling in human cells thus does not extend beyond genomic regions marked by γH2A.X.

The observed RAD51 and γH2AX distributions could, in principle, be influenced by simultaneous cleavage of both sister loci. Because the likelihood of dual-sister cutting increases with overall cutting frequency, we tested this potential bias by grouping gRNA target sites according to cutting frequency, as defined in Fig. 1F, and comparing the spreading profiles of RAD51 and γH2AX (fig. S4, C and D). Spreading ranges were highly similar at both high- and low-frequency cutting sites, arguing against dual-sister cutting events substantially altering RAD51 or γH2AX spreading.

As a further control, we established experimental conditions with substantially reduced cutting frequency, in which most cells contained either no cleaved loci or a mixture of cut and uncut loci (fig. S5, A and B). RAD51 and γH2AX spreading under these low-frequency cutting conditions closely matched the patterns observed under standard conditions (fig. S5, C to J), confirming that the observed phenotypes are largely independent of absolute cutting frequency.

Single-cell analysis of 53BP1 foci distributions (fig. S5B) revealed a stochastic pattern consistent with largely independent DSB induction across target loci, suggesting that simultaneous cleavage of sister loci is rare. Although we cannot formally exclude the possibility that dual-sister cutting occurs more often than predicted by our statistical model, several mechanistic considerations argue against frequent coupled cutting events. Cas9 remains bound to cleaved DNA for extended periods after generating a break (*57*), limiting the availability of free Cas9 complexes to cleave additional sites. Moreover, Cas9 locates targets primarily by rapid three-dimensional diffusion throughout the nucleus (*58*), making the physical proximity of sister loci only a minor contributor to cleavage probability. Together, these experimental results and mechanistic considerations support the conclusion that RAD51 and γH2AX spreading are robust and reproducible features of the DNA damage response and are largely independent of cutting frequency or rare dual-sister cleavage events. Our findings thus provide evidence that cohesin-mediated loops and TAD boundaries define the genomic space sampled by RAD51 filaments.

Cohesion directs homology sampling across sister chromatids

DSBs recruit cohesin (*56*, *59*–*62*) and locally increase DNA looping (*56*). Because increased looping promotes separation and local misalignment of undamaged sister chromatids (*28*), the question arises how broken DNA ends maintain access to the opposing sister chromatid. In budding yeast, DSBs induce cohesion genome wide (*59*, *63*, *64*), implying that cohesion remodeling may compensate for chromosome misalignment. However, whether DSBs similarly alter cohesion in human cells remains unclear.

To investigate how DSBs affect chromosome organization, we aimed to map chromatin contacts both within and across sister chromatids. Conventional chromosome conformation capture techniques (*65*, *66*) do not distinguish intrachromatid (cis-sister) from interchromatid (trans-sister) contacts. Although sister chromatid–sensitive Hi-C (scsHi-C) addresses this limitation by labeling sister chromatids with the nucleotide analog 4-thio-thymidine (*29*, *67*), its low labeling efficiency limits resolution. An alternative method uses bromodeoxyuridine (BrdU) for labeling (*68*), but this is limited by low sister chromatid specificity (*69*). To increase the resolution of sister chromatid–specific conformation mapping, we developed sister-pore-C (Fig. 3A). This method is based on labeling distinct DNA strands in each sister chromatid by culturing synchronized cells for one S phase in medium containing BrdU. Combining BrdU detection through Oxford Nanopore sequencing (*70*–*72*) with Nanopore-based Pore-C (*73*) enables discrimination of cis-sister from trans-sister contacts by assigning DNA-strand orientation and BrdU-label status. This new pipeline yields multifragment concatemers, which increases the number of sister-specific contacts per sequenced read.

We first assessed BrdU incorporation and toxicity in HeLa cells. Culturing cells with 40 μM BrdU for 24 hours did not impair proliferation or increase DNA damage (fig. S6, A to C). Mass spectrometry showed that BrdU replaced 49% of the thymidine in genomic DNA, a 19-fold increase in labeling density compared with scsHi-C (fig. S6D) (*29*, *67*). For sister-pore-C analysis, we released G_1/S–synchronized cells into BrdU-containing medium and cross-linked chromatin in G_2 for Pore-C analysis (Fig. 3A). Using the DNAscent neural network to detect BrdU (*70*, *74*), we classified each DNA segment as labeled or unlabeled; controls from unlabeled cells and from cells grown 5 days in the presence of BrdU confirmed accurate classification (fig. S6E). We then categorized each pairwise combination between read segments as cis-sister or trans-sister contact based on the BrdU labeling status and strand orientation. This approach yielded three sister-specific contacts per mapped read segment in average, a 50-fold increase over the previous scsHi-C method (*29*, *67*). Sister-pore-C thus allows high-resolution analysis of chromosomal interactions during homology-directed DNA repair.

To validate sister-pore-C, we compared its contact maps in G_2-synchronized cells (S7A) with previously published scsHi-C data using the same synchronization procedure (*29*) and evaluated auxin-induced sororin depletion, which disrupts cohesion without affecting cohesin loops (*29*, *75*, *76*). Sister-pore-C maps closely matched scsHi-C results but required 50-fold fewer read segments to achieve comparable contact density and resolution (fig. S7, B to D). Sororin depletion selectively reduced trans-sister contacts without affecting cis-sister contacts (fig. S7, E and F), confirming accurate sister assignment. Thus, sister-pore-C reliably captures cis- and trans-sister contacts, confirming its suitability for studying cohesin-regulated chromosome interactions.

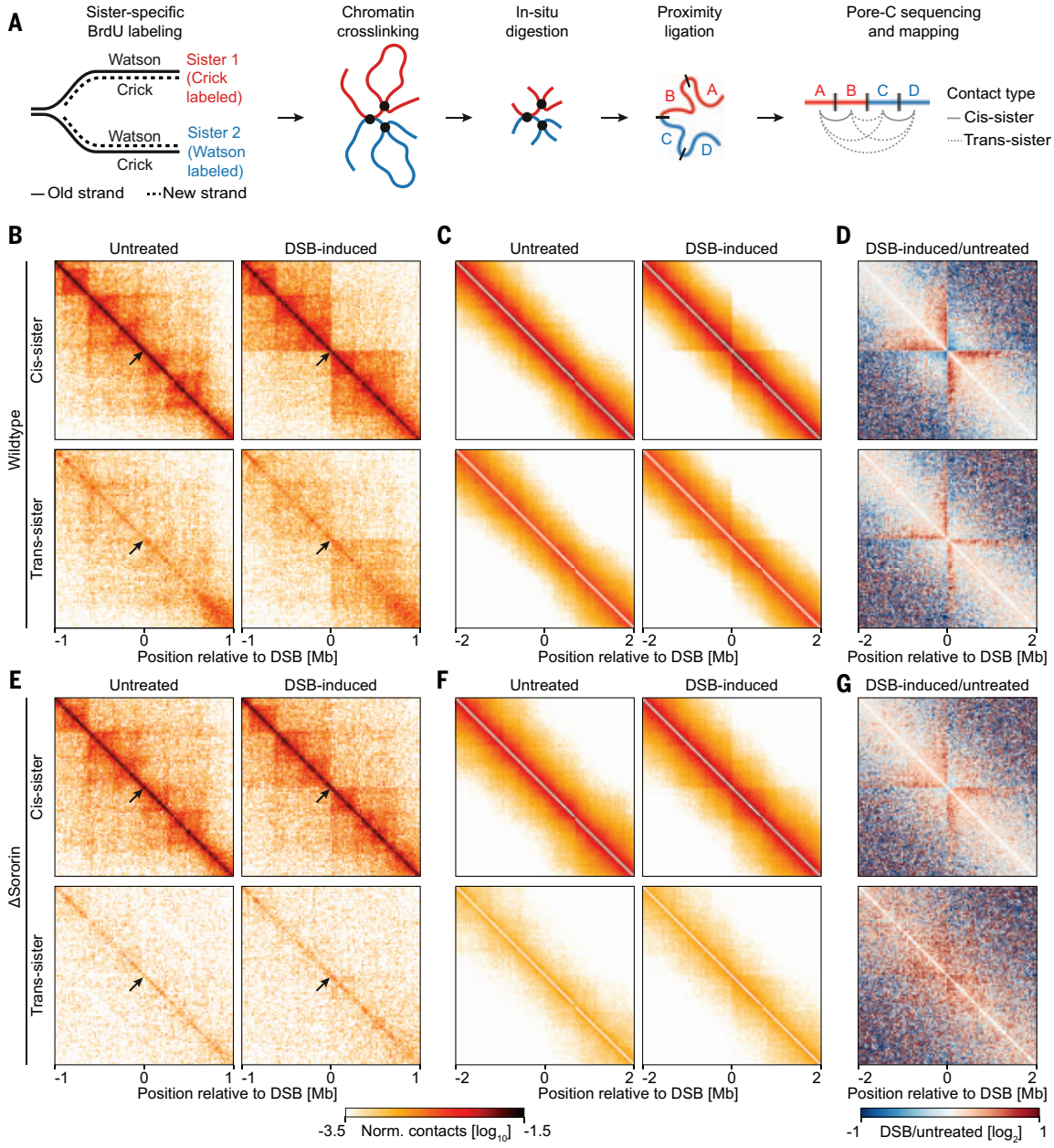


Fig. 3. Cohesion directs homology sampling across sister chromatids. (**A**) Schematic of sister-pore-C. Synchronized cells are cultured with BrdU in one S-phase, then cross-linked in G_2, followed by in situ digestion and proximity ligation. Nanopore sequencing identified BrdU labeling and DNA strand orientation for assignment of each fragment to a sister chromatid and for classifying contacts as cis-sister or trans-sister. (**B**) Sister-pore-C interaction matrices of a target locus (chr2 q33.2) in untreated or DSB-induced G_2 cells. Black arrows mark the DSB site. Top, cis-sister contacts. Bottom, trans-sister contacts. Bin size was 10 kb. (**C** and **D**) Average pileups (C) and $\log_2$(DSB-induced/untreated) ratios (D) for cis-sister or trans-sister-sister contacts across 23 loci ($n = 3$). Bin size was 20 kb. (**E** to **G**) Sister-pore-C interaction matrices (E) and corresponding pileups [(F) and (G)] for sororin-depleted G_2 cells. Bin size was 10 kb (E) and 20 kb [(F) and (G)]. In all experiments, sgRNA transfection was performed 3 hours after release from the G_1/S block and cells were harvested 6 hours later. Auxin-mediated depletion was initiated 1 hour before release and maintained until harvesting. Data are merged from $n = 3$ [(B) to (D)] and $n = 2$ [(E) to (G)] independent experiments.

To determine the effects of DSBs on chromosome architecture, we compared sister-pore-C maps of DSB-containing and undamaged chromosomes. We combined our optimized DSB-induction and cell synchronization procedure with sister chromatid labeling (fig. S8A) to generate cis- and trans-sister contact maps for examination of local and genome-wide changes. DSBs increased cis-sister contacts in their vicinity (Fig. 3, B to D, and fig. S8B), consistent with conventional Hi-C analysis of DSBs in unsynchronized cells (*56*). Furthermore, trans-sister maps revealed a prominent contact stripe extending over ~1 Mb from the DSB (Fig. 3, B to D, and fig. S8B), indicating that DSBs enhance interactions between broken DNA ends and the opposing sister chromatid. To analyze the architectural changes induced by DSBs in more detail, we generated average contact maps aligned on TAD boundaries near sgRNA target sites. These maps showed that although TADs still insulate in cis- and trans, the frequency of contacts crossing boundaries increases upon DSB induction (fig. S8, C and D). We also analyzed genome-wide average contact probabilities, finding that they were unaffected by DSBs

(fig. S8, E and F). Thus, DSBs remodel chromosome architecture locally during homology sampling, promoting increased looping in their vicinity and targeted interactions between broken DNA ends and the sister chromatid.

To investigate whether the DSB-induced trans-sister interactions are mediated by cohesion, we applied sister-pore-C to sororin-depleted cells and compared cis- and trans-sister contacts around DSBs. Sororin depletion nearly abolished DSB-induced trans-sister contact stripes, whereas cis-sister contacts remained elevated around DSBs (Fig. 3, E to G, and fig. S8, G and H). Thus, rather than increasing sister chromatid pairing genome wide, as in budding yeast (*63*, *64*), DSBs in human cells increase cohesion-mediated interactions across sister chromatids only near the break site.

To further assess the role of cohesin in regulating chromatin architecture around DSBs, we depleted both loop-forming and cohesive pools of cohesin using AID-induced degradation of RAD21. Sister-pore-C analysis showed that RAD21 depletion completely abolished contact enrichments near DSBs, both in cis and trans (fig. S9), corroborating cohesin's central role in organizing DSB repair regions through both loop extrusion and sister chromatid cohesion.

Two cohesin pools guide homology sampling

The remodeling of chromosome architecture near DSBs raises the question of how cohesin-regulated loops and trans-sister contacts are spatially organized relative to one another. Profiling DSB-induced contact changes along the genome showed increased looping over ~1 Mb relative to sgRNA target sites, whereas trans-sister contacts concentrated in a much narrower region (Fig. 4, A to D).

To determine how these distinct architectures are regulated by cohesin, we mapped the distribution of loop-extruding and cohesive pools of the complex using subunit-specific ChIP-seq. NIPBL, a key component of loop-extruding cohesin, does not associate with the cohesive form of the complex (*29*, *35*, *36*, *50*). Conversely, sororin selectively binds to cohesive cohesin, where it stabilizes sister chromatid cohesion

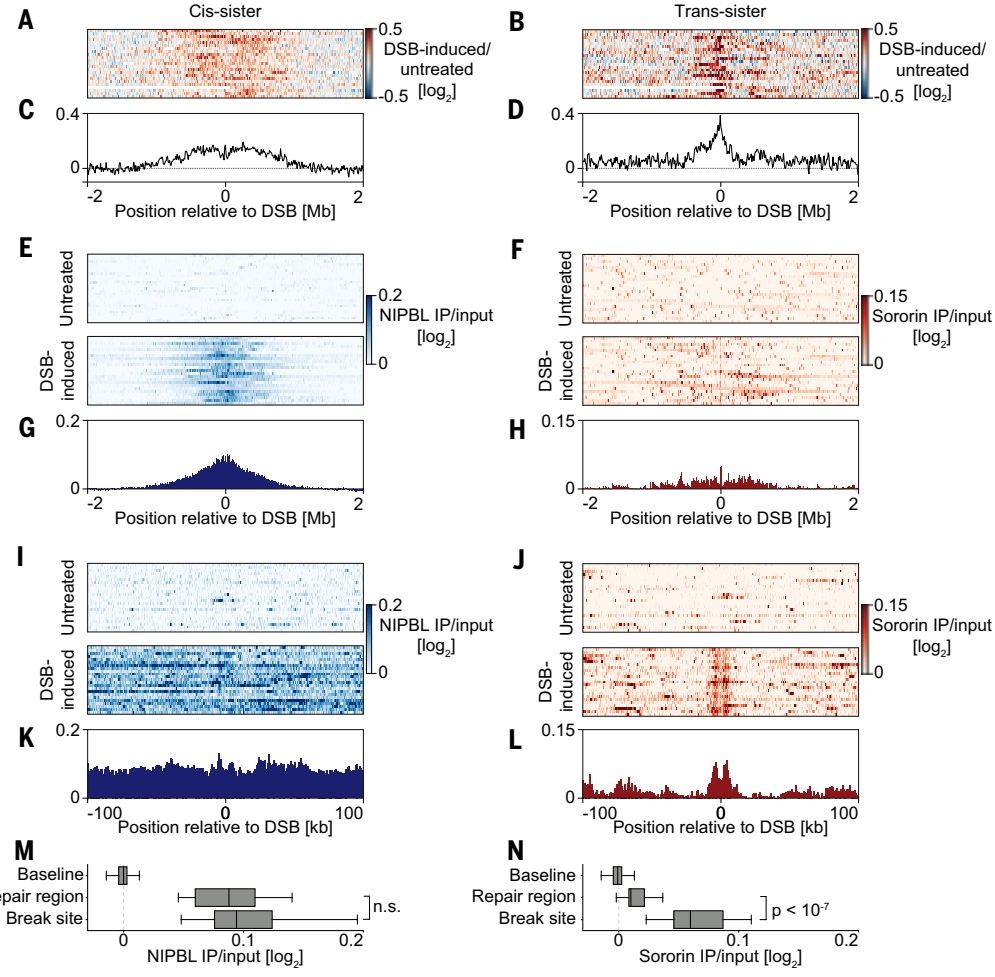


Fig. 4. Distinct roles for loop-forming and cohesive cohesin in homology search. (**A** and **B**) Stacked line plots of $\log_2$(DSB-induced/untreated) for cis-sister (A) and trans-sister (B) contacts at 23 loci, evaluated over 30 to 1000 kb. Bin size was 10 kb. Data are merged from $n = 3$ independent experiments. (**C** and **D**) Average pileups of the data in (A) and (B). Bin size was 10 kb. (**E** and **F**) Stacked line profiles of NIPBL (E) and sororin (F) ChIP-seq signals at the same 23 loci in untreated or DSB-induced G_2 cells. Bin size was 10 kb. (**G** and **H**) Average ChIP-seq pileups of NIPBL (G) and sororin (H) in DSB-induced G_2 cells, shown as $\log_2$(IP/input). Bin size was 10 kb. (**I** and **J**) Higher-resolution stacked profiles of NIPBL (I) and sororin (J). Bin size was 1 kb. (**K** and **L**) Corresponding high-resolution pileups of NIPBL (K) and sororin (L) in DSB-induced G_2 cells, shown as $\log_2$(IP/input). Bin size was 1 kb. (**M** and **N**) Box plots of NIPBL (M) and sororin (N) ChIP-seq signal enrichment across three genomic contexts: baseline (±1-Mb windows centered on DSB-distal, nonblacklisted regions; see the Materials and methods for details), repair region (±100 kb flanking the DSB cut site, excluding the central ±6.5 kb), and break site (±6.5 kb flanking the DSB cut site, excluding the central ±2 kb). In all experiments, sgRNA transfection was performed 3 hours after release from the G_1/S block, and cells were harvested 6 hours later. Auxin-mediated depletion was initiated 1 hour before release and maintained until harvesting. All ChIP-seq data are merged from $n = 2$ independent experiments.

by protecting the complex from WAPL-mediated release but does not associate with loop-extruding cohesin (*53*, *75*, *76*).

ChIP-seq profiling of NIPBL revealed substantial enrichment across an ~1-Mb region flanking the DSB, consistent with the observed broad increase in loop formation (Fig. 4, A, C, E, and G). By contrast, sororin ChIP-seq showed minimal signal across this extended domain but exhibited a sharp, localized enrichment near the DSB itself within a region averaging 6.5 kb on either side of the break (Fig. 4, F and H). This DSB-proximal sororin signal occurred in areas where NIPBL was not particularly enriched relative to the adjacent repair domain (Fig. 4, I to N).

These findings were further supported by ChIP-seq of RAD21, a core cohesin subunit shared by both loop-extruding and cohesive complexes (*13*, *14*), which showed prominent accumulation both at the DSB and across the extended 1-Mb region (fig. S10, A to E).

Although average ChIP-seq profiles for NIPBL, sororin, and RAD21 appeared symmetric when aggregated across all 23 sgRNA target sites (Fig. 4, G and H, and fig. S10B), inspection of individual loci revealed variable degrees of asymmetrical spreading, particularly for NIPBL and RAD21 (Fig. 4, E and F, and fig. S10A). To investigate the basis for this asymmetry, we compared cohesin distribution patterns with those of γH2A.X, which has been implicated in cohesin recruitment to DSBs in budding yeast (*60*) and spreads asymmetrically according to the local TAD architecture (Fig. 2, G and H, and fig. S4A). By sorting ChIP-seq profiles around individual sgRNA target sites based on the direction and magnitude of γH2A.X asymmetry, we were able to observe corresponding shifts in RAD21 and NIPBL distributions (fig. S10F). This correlation supports a model in which local TAD configuration governs the spatial distribution of both γH2A.X and loop-forming cohesin.

These results indicate that DSBs recruit loop-forming and cohesive cohesin to distinct architectural roles. Although loop-forming cohesin broadly spreads across the 1-Mb domain, cohesive cohesin concentrates near the DSB to mediate trans-sister interactions.

Timely DSB repair requires loop extrusion and cohesion

Given the critical roles of cohesin-mediated loop extrusion and sister chromatid cohesion in defining the spatial range for RAD51 homology sampling, we next investigated their functional impact on DNA repair efficiency. To assess how cohesin-regulated chromosome architecture influences repair progression, we applied a time-resolved immunofluorescence assay to monitor RAD51 foci dynamics after the induction of DSBs by ionizing radiation. This assay is based on the principle that RAD51 nucleoprotein filaments form at resected DNA ends during the homology search phase and are subsequently disassembled upon successful strand invasion and D-loop formation, marking a transition to downstream repair processes (*77*). The persistence or resolution of RAD51 foci thus provides a sensitive measure of repair efficiency (*78*–*80*).

We validated this assay by monitoring the global DNA damage response across different genetic backgrounds. Ionizing radiation (IR) with 2 Gy induced comparable numbers of 53BP1 foci in wild-type (WT) and cohesin-mutant cells, confirming efficient DSB induction (fig. S11, A and B). RAD51 foci accumulated during the first 2 hours after IR in all backgrounds (Fig. 5A and fig. S11C), consistent with filament assembly during the early stages of the DNA damage response. Although cohesin-mutant cells displayed slightly reduced RAD51 focus numbers relative to wild type, these differences were minor compared with the overall induction by IR. We therefore normalized subsequent repair kinetics to the 2-hour reference time point to control for background-specific variations in early filament formation.

In WT cells, IR induced the formation of 28 ± 3 RAD51 foci per nucleus at 2 hours after treatment, compared with a baseline of 7 ± 1 foci before IR (Fig. 5, A and B). Over the subsequent 6 hours, the number of foci decreased to 17 ± 2, indicating resolution of 51 ± 8% of the IR-induced foci and corresponding to a resolution rate of ~9 ± 1% per hour (Fig. 5C). These kinetics are consistent with previous reports showing that homology search in human cells typically spans several hours (*4*–*7*, *81*).

To investigate the role of loop extrusion, we depleted NIPBL 1 hour before IR. NIPBL-depleted cells showed a significantly impaired repair response, with only 31 ± 13% of RAD51 foci detected 2 hours after IR being resolved over the 6-hour period (Fig. 5, B and C; $P < 0.01$). This indicates that loop-extruding cohesin is essential for timely DSB repair.

Next, we assessed the consequences of hyperprocessive loop extrusion by depleting WAPL. In WAPL-depleted cells, RAD51 foci not only failed to resolve but increased further between 2 and 8 hours after IR. This suggests defective repair progression and the potential accumulation of secondary DSBs potentially arising during S phase due to replication-coupled damage (*82*). These findings imply that excessive loop extrusion disrupts the spatial confinement necessary for efficient homology sampling, thereby impairing the repair process.

To investigate the role of sister chromatid cohesion, we depleted sororin. Loss of sororin completely abolished RAD51 foci resolution and instead caused a progressive increase in foci number over time (Fig. 5, B and C). Depletion of RAD21, which disrupts both cohesion and loop extrusion, produced an indistinguishable phenotype, indicating that the absence of cohesion is the dominant defect. These findings confirm the essential role of cohesion in homology-directed repair (*22*–*25*) and support a model in which the cohesive pool of cohesin enables loop extrusion to engage the sister chromatid as a repair template. Without cohesion, loops remain confined to cis interactions, precluding productive homology search.

These data show that both loop extrusion and cohesion, mediated by functionally distinct pools of cohesin, are essential for timely homology-directed DSB repair.

Discussion

Here, we reveal how cohesin-regulated chromosome architecture governs homology search in somatic cells. Our findings support a model in which DSBs trigger the formation of a cohesive clamp at broken DNA ends to facilitate intersister homology sampling, whereas increased looping by cohesin controls the lateral range within the local TAD (Fig. 5D). This dual mechanism compensates for local sister-chromatid misalignment before DNA damage and substantially narrows the homology-sampling space compared with a genome-wide scan. Confining the homology search provides a substantial kinetic advantage, as evident from the severely delayed repair resulting from hyperprocessive loop extrusion in WAPL-depleted cells.

The positioning of cohesive cohesin near RAD51 filaments may occur through lateral sliding or de novo loading, potentially facilitated by SMC5/6 (*61*) or the MRN complex (*60*, *83*). By contrast, loop-forming cohesin may be loaded to more distal sites through a γH2A.X-mediated mechanism (*60*). These pathways may also underlie cohesin's contribution to early repair initiation, as reflected by the reduced RAD51 foci in cohesin-depleted cells shortly after IR. These findings highlight a multilayered role for cohesin in organizing both cis- and trans-sister architectures across distinct stages of homology-directed repair. Defining how cohesin transitions between these states and identifying the factors that coordinate its recruitment at DSBs represent key challenges for future investigation.

Although our Cas9-induced DSB assay is optimized for low cutting frequency to favor events in which only one sister chromatid is cleaved, it remains technically challenging to completely exclude cases in which both sister alleles are cut. Such events may affect homology sampling, for example, by introducing a lateral barrier to the sliding of cohesin clamps that would not be present on an intact repair template. Further advances in site-specific DSB induction techniques and detection of repair responses at the single-cell level (*84*) may help to overcome these limitations and enable a more precise determination of DNA repair dynamics.

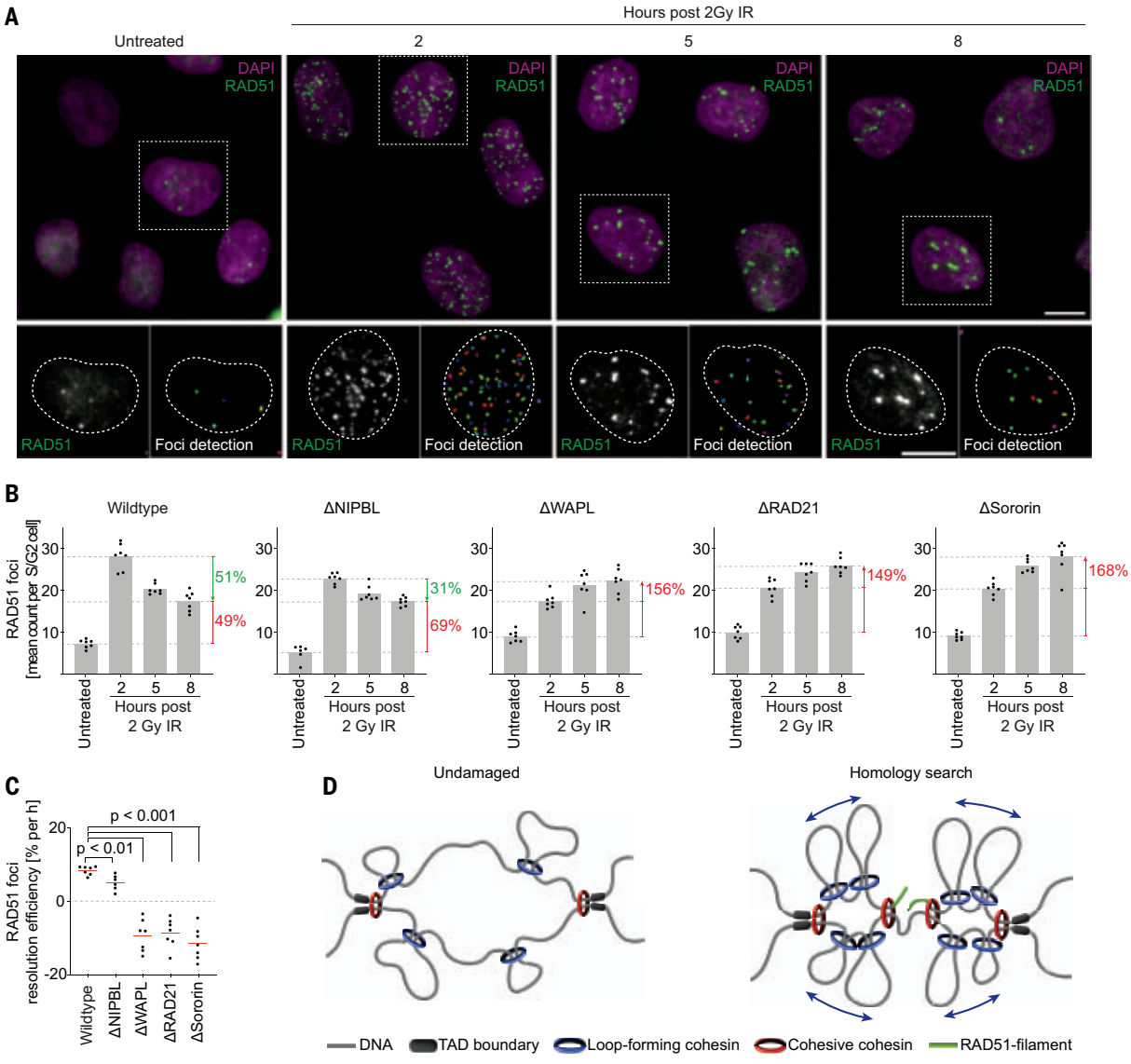


Fig. 5. Cohesin is required for timely DSB repair. (**A**) Time course of RAD51 foci formation and resolution after 2 Gy ionizing radiation in asynchronous WT Cas9-expressing HeLa cells. Insets show RAD51 immunofluorescence (left) and corresponding automated focus detection with random color assignment (right). Scale bar, 10 μm. (**B**) Quantification of RAD51 foci per S/G_2 cell over time in WT, NIPBL-, WAPL-, RAD21-, and sororin-depleted HeLa cells ($n = 7$). S/G_2 cells were identified by DAPI-based virtual cell cycle staging. Gray dotted lines indicate RAD51 foci levels in the different cell clones at three key time points: baseline (untreated), 2 hours after IR (used to quantify IR-induced DSBs after subtracting baseline levels), and 8 hours after IR (used to assess DSB resolution relative to the 2-hour time point). For WT and NIPBL-depleted cells, green and red numbers, respectively, indicate the percentage of resolved/unresolved foci from 2 to 8 hours after IR. For WAPL-, RAD21-, and sororin-depleted cells, red numbers indicate the percentage increase in foci over the same interval. Baseline foci from untreated cells were subtracted before calculations. (**C**) RAD51 resolution efficiency calculated as percentage of foci resolved per hour from 2 to 8 hours after IR. (**D**) Model. DSBs recruit a cohesive clamp that tethers RAD51 filaments near the sister chromatid, whereas loop-forming cohesin promotes lateral mobility within the TAD. Together, these mechanisms narrow the homology search space, enabling efficient DNA repair. In all experiments, auxin-mediated depletion was initiated 1 hour before release and maintained until fixation.

Beyond its role in maintaining genomic integrity, DNA recombination is a fundamental driver of genetic diversity, promoting antibody diversification and the exchange of genetic material between maternal and paternal genomes during meiosis. These events involve distinct topologies: Antibody diversification is mediated by cohesin-regulated intramolecular loops (*85*), whereas meiosis primarily depends on recombination between paired homologous chromosomes (*86*, *87*). By enabling simultaneous, genome-wide profiling of both intra- and intermolecular interactions, sister-pore-C will provide unprecedented insights into the role of chromosome topology in governing genome evolution and stability across diverse biological processes.

Materials and methods

Cell culture

All cell lines were cultured under sterile conditions in a humidified incubator at 37°C with 5% CO_2. Regular testing confirmed they were free of mycoplasma contamination. The parental HeLa cell line (Kyoto strain) was obtained from S. Narumiya (Kyoto University, Japan) and validated using the Multiplex Human Cell Line Authentication (MCA) test. All lines were grown in Dulbecco's modified Eagle's medium (DMEM; IMP/IMBA/GMI Molecular Biology Service/Media Kitchen) supplemented with 10% (v/v) fetal bovine serum (FBS; Gibco, 10270-106), 1% (v/v) GlutaMAX (Invitrogen, 35050038), and 1% (v/v) penicillin-streptomycin

(Sigma-Aldrich, P0781), hereafter referred to as WT medium. For Cas9-dox cell lines, the medium additionally contained 0.5 mg/ml G418 (Invitrogen, 11811-031). WAPL-AID, RAD21-AID and sororin-AID lines were maintained with 0.5 μg/ml puromycin (Calbiochem, 540411), and NIPBL-AID lines were grown with 6 μg/ml blasticidin S (Thermo Fisher Scientific, A1113903). The following compounds were used to activate the AID-based degradation system: 500 μM indole-3-acetic acid (auxin; Sigma-Aldrich, I5148) for WAPL-, RAD21- and sororin-AID and 1 μM 5-Ph-indole-3-acetic acid (5-Ph-auxin; Bio Academia, 30-003) for NIPBL-AID. All cell lines used in this study are listed in table S1.

Generation of Cas9-dox cell lines

A total of 300,000 HeLa cells [WT parental, NIPBL-AID, WAPL-AID (*28*), sororin-AID (*29*) or RAD21-AID (*34*)] were seeded into individual wells of a six-well plate in WT medium. The next day, cells were transfected with a total of 0.66 μg of plasmid DNA encoding a humanized *Streptococcus pyogenes* Cas9 (gift from R. Medema) fused to $FKBP12^{F36V}$-5xGly-3xFLAG at the N terminus under a tetracycline (Tet)–inducible promoter in a transposon array, along with 0.33 μg of Super PiggyBac Transposase plasmid DNA (Systembio, PB210PA-1). Transfections were performed in 100 μl of OptiMEM (Thermo Fisher Scientific, 31985070) using 4 μl of polyethyleneimine (Polysciences Europe, 24765-2). 24 hours later, cells were harvested by trypsinization (Thermo Fisher Scientific, 25200056) and transferred to 15-cm dishes in WT medium. After another 24 hours, 0.5 mg/ml G418 and the respective selection markers for each cell line (table S1) were added. Cells were cultured under selection for two weeks to generate polyclonal populations expressing $FKBP12^{F36V}$-5xGly-3xFLAG-Cas9 upon induction with 0.2 μg/ml doxycycline (Sigma-Aldrich, D9891). For Cas9-dox WT and NIPBL-AID lines, single-cell dilution was performed in 96-well plates. Clonal populations were expanded for 11 days under the relevant selection antibiotics. All lines were tested to confirm Cas9 expression after doxycycline induction.

sgRNA transfection

The sgRNA sequence (5′-CAGACAGGCCCAGATTGAGG-3′) used in this study was obtained from (*45*). Transfections were performed with TrueGuide sgRNA (Thermo Fisher Scientific) and Lipofectamine RNAiMAX (Thermo Fisher Scientific, 13778150) for up to 8 hours. Unless otherwise noted, the final sgRNA concentration was 27.5 nM. The final sgRNA concentration used for fig. S5 was 1 nM.

Immunofluorescence

For immunofluorescence, cells were washed twice with phosphate-buffered saline (PBS) and fixed with 4% formaldehyde (Thermo Fisher Scientific, 28906) in PBS for 5 min at room temperature (RT) if not stated otherwise. Samples were then permeabilized with 0.2% Triton X-100 (Sigma-Aldrich, 327371000) in PBS for 5 min. After blocking with filtered 2% bovine serum albumin (BSA; Sigma-Aldrich, A7030) in PBS for 15 min at RT, cells were incubated with primary antibodies diluted in 2% BSA/PBS for 2 hours at RT. After three washes in PBS, cells were incubated with fluorescently labeled secondary antibodies for 1 hour at RT in the dark. Nuclei were stained with 0.5 μg/ml 4′,6-diamidino-2-phenylindole (DAPI; Thermo Fisher Scientific, 62248) for 10 min, washed briefly in PBS, and mounted with ProLong Diamond Antifade Mountant (Thermo Fisher Scientific, P36970). The primary antibodies used were anti-53BP1 (1:1000; Millipore, MAB3802), anti-γH2A.X (phospho S139) (1:1000; Abcam, ab81299), and anti-RAD51 (1:1000; Abcam, ab176458). Secondary antibodies were anti-mouse IgG Alexa Fluor 568 (1:1000; Molecular Probes, A11004) and anti-rabbit IgG Alexa Fluor 488 (1:1000; Molecular Probes, A21206).

Quantitative image-based cytometry

Quantitative image-based cytometry (QIBC) was performed as described previously (*88*) using an Olympus ScanR Screening System (Olympus IX83 microscope). Images were acquired under nonsaturating conditions with a Hamamatsu ORCA-FLASH 4.0 camera (16-bit, 2048 × 2048 pixels, 6.5 μm pixel size) using a 40× air objective [0.75 numerical aperture (NA), 0.5 mm working distance) and a motorized stage. For each condition, at least 500 cells were imaged. Acquisition and analysis were performed using Olympus ScanR software (v3.5.0) with hardware and software autofocus on the DAPI channel. A dynamic background correction was applied, nuclei were segmented based on DAPI intensity, intensities of the stained channels were measured based on the segment nuclear mask, and nuclear 53BP1 or RAD51 foci were detected using a spot-detection module. For downstream analysis, nuclei with 2N to 4N DNA content were selected based on total and mean DAPI intensity and mitotic cells were excluded; for S/G_2 cell analysis, only 4N cells were included. Fluorescence intensities are reported as arbitrary units. Representative images with adjusted brightness and contrast per channel accompany selected quantifications. Independent experiment quantifications were plotted using GraphPad Prism (v10.1.1).

sgRNA transfection time course

Cas9-dox WT HeLa Kyoto cells were seeded on 12-mm glass coverslips (~30% confluency) and grown for 24 hours in DMEM supplemented with 0.2 μg/ml doxycycline (Sigma-Aldrich, D9891) to induce Cas9 expression. Cells were then transfected with sgRNA to induce targeted DSBs and harvested at hourly intervals up to 8 hours after transfection. Samples were stained and analyzed by QIBC to quantify 53BP1 foci (see "Immunofluorescence" and "Quantitative image–based cytometry").

53BP1 foci quantification in AID cell lines

Cas9-dox WT HeLa Kyoto cells and NIPBL-, WAPL-, RAD21-, and sororin-AID derivatives were seeded on 12-mm glass coverslips (~40% confluency) and grown for 24 hours in standard DMEM. AID cell lines were treated with auxin for 9 hours before fixation. WT untreated cells were fixed in parallel. Samples were stained (see "Immunofluorescence") and analyzed by QIBC (see "Quantitative image–based cytometry") to quantify 53BP1 foci. All cell lines were also exposed to 2 Gy IR and fixed 2 hours later (auxin treatment was performed for 3 hours before fixation).

Cell synchronization to G_2 phase and DSB induction

Cells were seeded in WT medium and allowed to attach for 3 hours before adding 2 mM thymidine (Sigma-Aldrich, T1895) to synchronize them at the G_1/S boundary. After 16 hours, cells were washed twice with prewarmed PBS and released into WT medium for 8 hours. Cells were then treated with 3 μg/ml aphidicolin (Sigma-Aldrich, A0781) to synchronize again at the G_1/S boundary for 16 hours. Next, cells were washed twice with prewarmed PBS, released into WT medium and collected 9 hours later. For DSB repair experiments, 0.2 μg/ml doxycycline (Sigma-Aldrich, D9891) was added concurrently with aphidicolin to induce Cas9 expression. sgRNA transfection was performed 3 hours after aphidicolin release. For WAPL-AID and RAD21-AID experiments, 500 μM indole-3-acetic acid was added 1 hour before the release into WT medium from the aphidicolin block. For NIPBL-AID experiments, 1 μM 5-Ph-indole-3-acetic acid was added with the same modalities.

Cell synchronization to G_1 phase and DSB induction

Cells were synchronized as described above (see "Cell synchronization to G_2 phase and DSB induction") up to the aphidicolin and doxycycline treatment. Instead of being released from the aphidicolin block after 16 hours, cells were directly transfected with the sgRNA and collected 6 hours later.

Flow cytometry: DNA content analysis and cell cycle stage verification

Flow cytometry was used to verify cell cycle stage. A fraction (5 to 10%) of harvested cells was washed with PBS and fixed in 70% ethanol (Sigma-Aldrich, 32221) at 4°C for at least 30 min. Fixed cells were permeabilized with 0.25% Triton X-100 (Sigma-Aldrich, 327371000) in PBS for 15 min on ice and then incubated with 0.25 μg of anti-phospho-H3Ser10

(Millipore, 05-806) in 1% BSA/PBS for 1 hour at RT. After washing in 1% BSA/PBS, samples were incubated for 30 min at RT in the dark with anti-mouse IgG Alexa Fluor 488 (1:300; Molecular Probes, A11001). DNA content was quantified by staining with 200 µg/ml RNase A (Qiagen, 19101) and 50 µg/ml propidium iodide (Sigma-Aldrich, 81845) for 30 min in the dark. Data were acquired on a Penteon flow cytometer (Novacyte) and analyzed in FlowJo (v10). FSC-A/SSC-A was used for cell gating, and singlets were identified using FSC-A/FSC-H and PI-A/PI-H. H3S10P (FITC channel) versus DNA content (PI channel) provided cell cycle profiles.

ChIP

Approximately 10 million G_2-synchronized HeLa cells (see "Cell synchronization to G_2 phase and DSB induction") were harvested by washing once with PBS, detaching with trypsin, and collecting in 15-ml Falcon tubes. All centrifugation steps were at 1100*g* for 1 min unless otherwise specified. Cells were washed once with PBS, fixed in 10 ml of 1% formaldehyde (Thermo Fisher Scientific, 28906) for 10 min at RT with gentle rotation, and quenched with 125 mM glycine (Sigma-Aldrich, 50046) for 5 min at RT. Cells were pelleted, the supernatant was removed, and pellets were stored at −80°C. One day before processing the samples for ChIP, 320 µl of a 1:1 Affi-Prep Protein A bead suspension (Bio-Rad, 1560005) per sample was pelleted, the supernatant removed, and incubated in 10 volumes of coating buffer [2 mM EDTA, 20 mM Tris-HCl, pH 8.0, 1% Triton X-100, 150 mM NaCl, 1 mM phenylmethanesulfonyl fluoride (PMSF), and 0.1 mg/ml BSA] overnight at 4°C with gentle rotation. Beads were washed three times in chilled dilution buffer (2 mM EDTA, 20 mM Tris-HCl, pH 8.0, 1% Triton X-100, 150 mM NaCl, and 1 mM PMSF) and stored as a 1:1 suspension in dilution buffer at 4°C. Unless otherwise noted, all sample processing steps were performed on ice. Cell pellets were resuspended in 1 ml of freshly prepared, chilled lysis buffer (10 mM EDTA, 50 mM Tris-HCl, pH 8.0, 1% SDS, 1 mM PMSF, and 1 tablet of cOmplete mini protease inhibitor per 10 ml of lysis buffer), pelleted at 1700*g* for 2 min at 4°C, and resuspended in 700 µl of lysis buffer. Chromatin was sonicated in a Bioruptor Plus (Diagenode) for 12 cycles (30 s ON, 30 s OFF) at high intensity at 4°C. After sonication, 10 µl was saved as input; the remaining chromatin was diluted 10-fold (7 ml) in dilution buffer. Preclearing was performed by incubating samples with 160 µl of 1:1 blocked protein A beads for 1 hour at 4°C, followed by centrifugation. Sonicated chromatin was quantified using a DS-11 spectrophotomer (DeNovix) and incubated overnight at 4°C with one of the following antibodies: ≥25 µg of chromatin with 4 µg of anti-RAD51 (Abcam, ab176458), ≥25 µg of chromatin with 2 µg of anti-γH2A.X (Abcam, ab81299), ≥50 µg of chromatin with 10 µg of anti-RAD21 (Abcam, ab992), ≥50 µg of chromatin with 10 µg of anti-NIPBL (Bethyl Laboratories, A301-779A), or ≥100 µg of chromatin with 10 µg of anti-sororin (Abcam, ab192237). Immunoprecipitation was performed the next day by adding 160 µl of 1:1 blocked protein A beads for 3 hours at 4°C with gentle rotation. Beads were washed twice with 800 µl of each of the following prechilled buffers: washing buffer 1 (2 mM EDTA, 20 mM Tris-HCl, pH 8.0, 1% Triton X-100, 150 mM NaCl, 0.1% SDS, and 1 mM PMSF), washing buffer 2 (2 mM EDTA, 20 mM Tris-HCl, pH 8.0, 1% Triton X-100, 500 mM NaCl, 0.1% SDS, and 1 mM PMSF), washing buffer 3 (2 mM EDTA, 10 mM Tris-HCl, pH 8.0, 250 mM LiCl, 0.5% NP-40, and 0.5% sodium deoxycholate), and Tris-EDTA (TE) buffer (1 mM EDTA, 10 mM Tris-HCl, pH 8.0). After the final TE wash, beads were resuspended in 200 µl of prewarmed elution buffer (5 mM EDTA, 25 mM Tris-HCl, pH 8.0, and 0.5% SDS) and incubated at 65°C for 20 min with shaking (1,200 rpm). The supernatant was collected and a second elution was performed. Both ChIP and input chromatin were treated with 2 mg/ml RNase A (Qiagen, 19101) and 2 mg/ml proteinase K (Qiagen, 19133) for 1 hour at 37°C, followed by overnight de-cross-linking at 65°C. DNA was purified with the Monarch PCR & DNA Cleanup Kit (NEB, T1030), eluted in 30 µl of water, and quantified using a Qubit Fluorometer (Thermo Fisher Scientific).

ChIP sequencing, read processing, and data analysis

ChIP and input libraries were prepared using the NEBNext Ultra II kit (NEB, E7645S) following the manufacturer's protocol. Samples with dual unique index barcodes were pooled at equimolar ratios and sequenced on Illumina NextSeq 550 or NovaSeq X platforms using 75-bp single-end or 150-bp paired-end read mode, respectively. Library demultiplexing followed Illumina guidelines. Data were analyzed using the nf-core (*89*) ChIP-seq pipeline (v1.2.1; https://nf-co.re/chipseq/1.2.1) with the parameters "–single_end" and "–hard_trim5 75" to maintain consistent read lengths across different sequencing runs. Reads were aligned to the human genome (hg19) using default settings. After pipeline completion, BAM files for biological replicates of the same sample were merged and reindexed with SAMtools (*90*). Merged files were normalized to counts per million (CPM), and $\log_2$(ChIP/Input) BigWig files were created using deepTools (*91*). These normalized files were used for all ChIP-seq visualizations.

Karyoplots

R scripts for karyoplots are provided in the main GitHub repository. We used karyoploteR (*92*) and rtracklayer (*93*) to visualize sgRNA target sites (fig. S1G), $\log_2$(γH2A.X IP/Input) ratios (fig. S1, H and I), the selection of target sites (fig. S1J), and $\log_2$(RAD51 IP/Input) ratios (fig. S1, K and L) over a karyotype plot.

Selection of sgRNA target locations for genomics analysis

Genomic sites targeted by the sgRNA were identified through γH2A.X ChIP enrichment after DSB induction (see "sgRNA transfection" and "Chromatin immunoprecipitation"). For each predicted sgRNA target (0 to 2 bp mismatch), the average $\log_2$(γH2A.X IP/Input) was calculated in a ±25-kb region around the target. Targets with an average $\log_2 \geq 0.2$ were designated "enriched" and selected for analysis and are listed in table S2. The DSB on chr22 was excluded because it did not match the sgRNA sequence in hg19.

Stack-up profiles and average pileups

ChIP-seq protein distributions were visualized through stacked and average pileup profiles generated from BigWig files using the Python *bbi* package (https://github.com/nvictus/pybbi). NaN values were set to zero to avoid artifacts. The stackup function aligned signals across genomic regions, producing heatmaps (stacked profiles) and average signals (pileups). Initial exploration of datasets was performed using HiCognition (*94*), and final plots were created through Jupyter notebooks using matplotlib (*95*) and seaborn (*96*).

ChIP-seq signal enrichment at DSB sites versus genome-wide baseline

To compare ChIP signal enrichment at DSB sites with genome-wide levels, the genome was divided into nonoverlapping 2-Mb tiles along chromosome arms. Tiles overlapping the selected DSB sites and their ±1-Mb flanking regions were excluded from the baseline. Average pileup profiles were generated for the DSB sites (±1 Mb) and the remaining genome tiles (see "Stack-up profiles and average pileups"). Initial exploration of datasets was performed using HiCognition (*94*), and final plots were created through Jupyter notebooks using matplotlib (*95*) and seaborn (*96*).

In silico assessment of homologous sequences around sgRNA target sites

To investigate whether the 23 sgRNA target loci had nearby homologous sequences that could serve as repair templates, we performed an in silico analysis using the hg19 reference genome. For each sgRNA target locus, a 2-Mb region centered on the sgRNA cut site was extracted and indexed using BLAST+ (v2.16.0+). Query sequences were generated from the 3-kb upstream and downstream flanking regions using a 500-bp sliding window moved in 1-bp steps through SAMtools faidx (*90*), resulting in 6000 queries per locus. Each query was searched

against the corresponding local BLAST database using both high-speed (megablast) and high-sensitivity (blastn) settings. Hits overlapping the query's source coordinates were excluded to remove self-alignments. Remaining hits were filtered for homology, defined as continuous alignments ≥450 bp with >90% sequence identity based on the minimal efficient processing segment required for homologous recombination in mammalian cells (*6*). No sequences meeting these criteria were found at any locus, confirming the genomic uniqueness of all 23 target sites.

Quantification of sororin ChIP-seq signal spreading at DSB sites

To measure sororin enrichment breadth around DSBs, we analyzed average pileup profiles centered on DSB sites (see "Stack-up profiles and average pileups"). Spreading was defined as the genomic interval where the signal exceeded a specified fraction of the peak, with the peak defined as the maximum of the average profile across all DSB sites. At 50% of peak intensity, sororin enrichment extended ±6.5 kb from the DSB sites.

Cohesin ChIP-seq signal enrichment at selected DSB sites

To analyze NIPBL, sororin, and RAD21 ChIP signal enrichment at and around selected DSB sites, we calculated average pileup profiles (see "Stack-up profiles and average pileups") in DSB-induced samples at three different genomic contexts: (i) the baseline, defined as 2-Mb tiles covering the genome excluding the selected DSB sites and ±2-Mb flanks; (ii) the repair region, defined as ±100 kb around DSB sites excluding the central ±6.5 kb; and (iii) the break site, defined as a ±6.5-kb window around the DSB sites excluding the central ±2 kb. Plots were created through Jupyter notebooks using matplotlib (*95*) and seaborn (*96*).

FISH methodology

FISH probe generation and hybridization followed established protocols (*97*, *98*) based on RASER-FISH (*99*) and oligo pool amplification (*100*).

FISH probe design and amplification

A HeLa Kyoto reference genome [hg19 with SNP correction (*29*)] was used for primary FISH probe design. We selected nine of the 23 gRNA target sites and designed probes for a 70-kb region surrounding the DSB. To prevent overlap with resected RAD51-coated filaments, the ±5-kb regions flanking the cut site were excluded from the design. OligoMiner (*101*) was used to identify 36 to 42 bp unique target sequences (42°C annealing temperature at 50% formamide concentration, 30 to 70% GC content, 0.25 to 0.99 LDA stringency, 5 to 20 k-mer filtering, and a 0.1 secondary structure filter). At least 300 probes covered each DSB site. Each unlabeled primary oligo carried short barcode sequences for binding to fluorescently labeled secondary oligos, as well as flanking primers for oligo pool amplification containing the T7 in vitro transcription (IVT) promoter. Oligo pools were ordered from GenScript (GenTitan Oligo Pools). FISH probes were amplified by quantitative polymerase chain reaction (qPCR) using 2× Phusion High-Fidelity PCR Master Mix (Thermo Fisher Scientific, F531), 15 ng oligo pool, 0.5 μM forward and reverse primers, and 1× EvaGreen (Biotium, 31000). Samples were incubated at 98°C for 3 min, followed by 98°C for 10 s, 66°C for 10 s, and 72°C for 15 s in repeated cycles until near plateau. Amplified DNA was purified using the DNA Clean & Concentrator-25 kit (Zymo Research, D4033) and eluted in 50 μl of ultrapure water. For IVT, 1.5 μg of PCR product was incubated overnight at 37°C using the HiScribe T7 Quick High Yield RNA Synthesis Kit (NEB, E2050) with 80 μl of NTP buffer mix, 6.25 μl of T7 RNA polymerase mix, 6.25 μl of RNAsin Plus RNAse inhibitor (Promega, N2615), and ultrapure water to reach 160 μl. Then, 150 μl of unpurified ssRNA was used directly for reverse transcription at 50°C for 1 hour with 21 μl of 25 mM dNTP mix (final concentration 1.75 mM), 57 μl of 100 μM forward primer (final concentration 19 μM), 6 μl of RNAsin Plus RNAse inhibitor, 6 μl of Maxima H Minus Reverse Transcriptase (1200 U, Thermo Fisher Scientific, EP0753), and 60 μl of 5× reverse transcription buffer. RNA was then degraded with 150 μl of 0.5 M EDTA and 150 μl of 1 M NaOH at 95°C for 15 min. The ssDNA oligo pool was purified with a DNA Clean & Concentrator-100 kit (Zymo Research, D4030), eluted in 200 μl of ultrapure water, and its concentration determined by Nanodrop. Fluorescently labeled secondary oligos were synthesized using click chemistry (ClickTech Oligo Link Kit, baseclick) with 3′-C3-azide oligos (Metabion) and an alkyne-modified ATTO647N fluorophore (ATTO-TEC, AD 647N). After purification with two n-butanol washes (Sigma-Aldrich, B7906) or high-performance liquid chromatography (HPLC), labeled oligos were diluted in 1× TE buffer.

RASER-FISH

HeLa cells were seeded in Ibidi μ-Slide VI 0.5 glass-bottom slides at 1.5×10^5 cells/ml (120 μl/channel). Cell synchronization and DSB induction followed the protocol described in "Cell synchronization to G_2 phase and DSB induction," with 40 μM BrdU/BrdC (3:1 ratio; Sigma-Aldrich, B5002; Santa Cruz Biotechnology, sc-284555) added after aphidicolin washout. Cells were fixed at RT for 15 min with 4% paraformaldehyde (Electron Microscopy Sciences, 15710) in PBS and then quenched for 10 min with 100 mM NH_4Cl (Sigma-Aldrich, 326372). Immunofluorescence against 53BP1 and RAD51 was performed as described (see "Immunofluorescence"), except fixation and permeabilization were each 15 min and the DAPI staining was skipped. A secondary fixation was performed with 1 mM Bis(NHS)PEG5 (Sigma-Aldrich, 803537) in PBS for 30 min at RT, followed by an additional quenching step. Cells were permeabilized for 20 min in PBS with 0.2% Triton X-100 (Sigma-Aldrich, 327371000) at RT, stained with 0.5 μg/ml DAPI in PBS for 15 min at RT, then UV-treated in a Vilber Bio-Link cross-linker (254 nm, 3.6 J/cm2) to nick BrdU/C-incorporated strands. Nicked strands were degraded with Exonuclease III (1 U/μl; NEB, M0206) at 37°C for 15 min. Cells were preincubated in FISH hybridization buffer [50% (v/v) formamide; Thermo Fisher Scientific, AM9342; 10% (w/v) dextran sulfate; Merck, S4030; 2× saline sodium citrate (SSC); Thermo Fisher Scientific, AM9763] at 37°C for 1 hour, followed by overnight incubation at 42°C with primary FISH probes (~2 nM/probe) in the same buffer. After two 35°C washes (5 min each) in 50% (v/v) formamide + 2× SSC, cells were washed in 2× SSC + 0.2% (v/v) Tween-20 (Sigma-Aldrich, P9416). RNA-DNA hybrids were removed by RNase H (0.05 U/μl; NEB, M0297) at 37°C for 20 min, followed by two to three RT washes in 2× SSC + 0.2% Tween-20. Secondary FISH hybridization was performed at RT for 3 min in a buffer containing 5% (w/v) ethylene carbonate (Sigma-Aldrich, E26258) and fluorescent secondary oligos (20 nM) in 2× SSC + 0.2% Tween-20. Excess secondary oligos were removed by a 1-min wash at RT with 10% (v/v) formamide in 2× SSC + 0.2% Tween-20. Cells were then incubated in 2× SSC + 0.2 μg/ml DAPI before imaging. All immunofluorescence + FISH experiments were imaged on a Zeiss LSM980 confocal system using a 63× NA 1.4 oil differential interference contrast Plan-Apochromat objective (ZEN Blue 2020 software v3.7). Images were collected in confocal mode with optimal sectioning (390 nm between *z* slices). A list of all the oligos used to target the nine gRNA target sites is provided in table S3.

RASER-FISH: Image analysis

Images were processed with an in-house automated pipeline (v0.9.0; https://github.com/gerlichlab/reparafil), except for a small subset of images that were analyzed manually. Before pipeline processing, nuclei were segmented based on DAPI staining in Fiji. These nuclear regions (stored as ImageJ .roi files) were used to exclude non-nuclear FISH signals. Fluorescent puncta (FISH spots) were identified using a pixel-intensity threshold approach through the spotfishing package (https://github.com/gerlichlab/spotfishing). Immunofluorescence intensities were collected from 10-pixel boxes around each FISH spot centroid in the relevant *z* slice. To classify a FISH spot as 53BP1-positive, a signal threshold was set to the mean ± 2 SDs of the 53BP1 intensity in nontargeted

controls; this threshold was determined independently for each target site. Spots exceeding the threshold were scored as 53BP1-positive. For these 53BP1-positive spots, homologous recombination was assessed by RAD51 intensity using the same thresholding approach. Independent experiment quantifications were plotted using GraphPad Prism (v10.1.1).

Quantifying the frequency of single- and double-sister cutting events on replicated chromosomes

To quantify how frequently sgRNA target sites on replicated chromosomes are cleaved on either one or both sister chromatids, we applied a statistical model based on the assumption that DSBs occur independently and stochastically at each sgRNA target site. In this model, we define P as the probability that a DSB occurs at a single target site on one chromatid. Accordingly, the probability that no DSB occurs on a given chromatid is $(1 - P)$. From this, the probability that both sister chromatids are cut is P^2, the probability that only one is cut is $2P(1 - P)$, and the probability that neither is cut is $(1 - P)^2$. To estimate P, we used the fraction of FISH foci that were negative for 53BP1 under the assumption that these foci represent regions of replicated chromosomes in which neither sister locus was cut. Solving the equation $(1 - P)^2 =$ fraction of 53BP1-negative foci yielded an estimate of P, which we then used to compute the probabilities of single- and double-cutting events at all nine sgRNA target sites analyzed by RASER-FISH and immunofluorescence. These calculated values are presented in Fig. 1H and represent the relative frequencies of distinct DSB outcomes in our experimental system.

Analysis of allele cutting efficiency at low concentrations of sgRNA

To determine the stochasticity of Cas9-induced cutting among several copies of the same genomic loci per nucleus, we followed the RASER-FISH image analysis pipeline but focused our analysis on the nuclei. First, all nuclei that did not display the expected number of FISH spots were excluded from our analysis (in HeLa cells, we expect three alleles for chromosome 2 q14.3 and four alleles for chromosome 19 p13.2). Then, the 53BP1-positive alleles within each nucleus were counted based on the threshold calculated on all FISH spots in all cells. Finally, the cells were categorized depending on the number of 53BP1-positive alleles they contained.

TAD calling

TAD boundaries from (*29*) were used, obtained by OnTAD (*102*) on a G_2 WT Hi-C matrix merged over all replicates (GSM4613674). For the analysis focused on TAD boundaries in Fig. 2E and fig. S8, C and D, all boundaries located between 200 and 1000 kb upstream and downstream of the 23 selected genomic loci were included. For the analysis in figs. S3E and S4B, TAD boundary strength was calculated genome wide using cooltools (50-kb resolution, 250-kb window size, ignoring two diagonals) (*103*). To account for positional discrepancies between OnTAD and cooltools, each included boundary was assigned the maximum boundary strength within ±100 kb. Boundaries were then ranked by strength, with the top 50% classified as "strong" and the bottom 50% as "weak."

Western blot

G_2-phase synchronized Cas9-dox WT, sororin-AID, WAPL-AID, RAD21-AID, or NIPBL-AID cell suspensions (0.5 million cells/ml) with or without auxin treatment were prepared for protein analysis by mixing cells with 6× SDS loading buffer containing 10 mM dithiothreitol(Roche) and boiling at 95°C for 5 min. Proteins were resolved on NuPAGE Bis-Tris 4 to 12% gels (for sororin-AID and WAPL-AID) or NuPAGE Tris-Acetate 3 to 8% gels (for NIPBL-AID) (Thermo Fisher Scientific, NP0335BOX and EA0378BOX) and transferred to Hybond P 0.45 polyvinylidene difluoride membranes (GE Life Sciences). A WT control sample was run on each gel to assess target protein degradation. Membranes were probed with α-sororin (1:50, in-house), anti-NIPBL (1:800; Absea, 010702F01), anti-RAD21 (1:1000; Abcam, ab217678), or anti-WAPL (1:1000; Santa Cruz, sc-365189). For loading controls, anti-vinculin (1:10,000; Abcam, ab129002) was used for sororin-AID and NIPBL-AID samples, and anti-tubulin (1:5,000; Abcam, ab52866) was used for WAPL-AID and RAD21-AID samples. Horseradish peroxidase–conjugated secondary antibodies were goat anti-rat (1:2,000; Amersham, NA935), goat anti-rabbit (1:5,000; Bio-Rad, 170-6515), and goat anti-mouse (1:5,000; Bio-Rad, 1706516). Signal was detected with Bio-Rad Clarity Max ECL (Bio-Rad, 1705062) on a Bio-Rad ChemiDoc imager.

Cell proliferation and DNA damage assay

HeLa Kyoto cells were seeded onto 12-mm glass coverslips and grown for 24 hours. Cells were then treated with various concentrations of BrdU (10 to 100 μM; Life Technologies, B23151) and 50 μM etoposide (Sigma-Aldrich, E1383) for an additional 24 hours. Samples were stained and analyzed by QIBC to quantify the intensity of nuclear γH2A.X (see "Immunofluorescence" and "Quantitative image-based cytometry"). The fold increase in cell number was calculated by comparing the total segmented nuclei count with the initial seeding density.

Quantification of BrdU incorporation into gDNA

HeLa Kyoto cells were cultured for 6 hours after seeding, treated with 40 μM BrdU or dimethyl sulfoxide, and cultured for 5 days. Cells were harvested by PBS washing, trypsinization, and resuspension in cell culture medium. Pellets were frozen, genomic DNA was extracted using the Monarch gDNA extraction kit (NEB, T3010), and 500 ng of DNA was digested into nucleosides with five units of DNA Degradase Plus (Zymo Research, E2020) for 2 hours at 37°C. Deoxyribonucleosides were quantified by reverse phase liquid chromatography and tandem mass spectrometry using an Ultimate 3000 HPLC system (Dionex, Thermo Fisher Scientific) directly coupled to a TSQ Altis mass spectrometer (Thermo Fisher Scientific). A 1-μl aliquot of acidified sample (1% formic acid) was injected onto a Kinetex C18 column (Phenomenex, 100 Å, 150 × 2.1 mm), using a 4-min-long linear gradient from 98% A (1% acetonitrile, 0.1% formic acid in water) to 60% B (0.1% formic acid in acetonitrile) at a flow rate of 80 μl/min and a column temperature of 30°C. Nucleosides were quantified by using selected reaction monitoring with the following transitions: m/z 228 → m/z 112 (dC); m/z 307 → m/z 191 and m/z 309 → m/z 193 (BrdU); m/z 243 → m/z 127 (dT); m/z 252 → m/z 136 (dA); m/z 268 → m/z 152 (dG). A calibration curve of defined standards was used to quantify the relative ratio of BrdU as the molar concentration of BrdU divided by the sum of the molar concentrations of dT and BrdU. Data interpretation was performed using TraceFinder software (Thermo Fisher Scientific).

Cell synchronization for sister-pore-C

Cells were synchronized as described (see "Cell synchronization to G_2 phase and DSB induction"), except 40 μM BrdU (Life Technologies, B23151) was added immediately after aphidicolin release to allow BrdU incorporation during DNA replication. For the sister-pore-C samples in fig. S7, doxycycline treatment and sgRNA transfection were omitted, and cells were arrested for an extended period in the G_2 phase by adding 10 μM RO-3306 (Calbiochem, 217699) 4 hours after aphidicolin release and harvesting the cells 24 hours after the release, following the protocol of (*29*), as indicated in fig. S7A. When applied, RO-3306 was included in all buffers until formaldehyde cross-linking. For sororin-AID and RAD21-AID experiments, 500 μM auxin was added 1 hour before aphidicolin washout to induce targeted protein degradation and was kept in all buffers until formaldehyde cross-linking.

Sister-pore-C

Up to 5 million cells were collected by PBS washing, trypsinization, and resuspension in cell culture medium. Cells were pelleted (1100*g* for 1 min at RT), washed in 1 ml of PBS, and then fixed in 1 ml of 1% formaldehyde (Thermo Fisher Scientific, 28906) for 10 min at RT with rotation. Fixation was quenched by 125 mM glycine for 5 min at RT with

rotation. Cells were chilled on ice for 10 min, pelleted (1100*g* for 1 min at 4°C), the supernatant was removed, and the pellet was stored at −70°C. Cells were resuspended in 500 µl of HiC lysis buffer (10 mM Tris-HCl pH 8.0, 10 mM NaCl, 0.2% NP-40, and 1× complete EDTA-free protease inhibitor) and incubated for 30 min at 4°C with rotation. After pelleting (2500*g* for 5 min at 4°C), the cells were washed with 200 µl of ice-cold 1.5× rCutSmart Buffer (NEB, B6004), pelleted again, and resuspended in 300 µl of ice-cold 1.5× rCutSmart. To mildly denature chromatin, 0.1% SDS was added, and samples were incubated for 10 min at 65°C with shaking (300 rpm), followed by cooling on ice. SDS was quenched with 1% Triton X-100 for 10 min on ice. Chromatin digestion was performed with 45 units of NlaIII (NEB, R0125L) in 1× rCutSmart Buffer for 18 hours at 37°C with intermittent shaking (800 rpm for 30 s every 5 min). NlaIII was inactivated by heating at 65°C for 20 min (300 rpm). Cells were pelleted (2500*g* for 5 min at RT) and resuspended in 250 µl of ligation mix (1× T4 ligase buffer, 50 U T4 ligase, 0.1% Triton X-100, and 100 µg/ml BSA) for 4 hours at RT with rotation. Cells were pelleted (2500*g* for 5 min at RT), and genomic DNA was purified using the Monarch gDNA extraction kit (NEB, T3010), including an 18-hour incubation at 65°C with lysis buffer, proteinase K, and RNase A to reverse cross-links. Libraries were prepared using the Oxford Nanopore Technologies (ONT) Ligation Sequencing Kit (LSK109 or LSK110) and sequenced on PromethION R9 flow cells for 72 hours.

Sister-pore-C data preprocessing

Sister-pore-C samples were preprocessed using a custom Snakemake (*104*) pipeline (https://github.com/gerlichlab/sister-pore-c-snakemake) adapted from the ONT pipeline (https://github.com/nanoporetech/Pore-C-Snakemake) to accommodate sister-chromatid–specific contacts. Key additional steps include generating BrdU calls with DNAscent v2 (*70*, *74*), creating label libraries for read-IDs, assigning labeled pairs, splitting pairs into cis/trans, generating .cool files with cooler (*105*), and ICE balancing (*106*) the combined sister-specific contacts with cooltools (*103*).

Estimating fragment numbers in sister-pore-C datasets and down-sampling

DuckDB (*107*) was used to count annotated fragments meeting quality thresholds. The cooltools "sample" function (*103*) was then used to down-sample cooler files to match fragment counts.

Extraction of sample regions

Regions from ICE-corrected Hi-C matrices were extracted using the Python cooler API (*105*).

Sister-pore-C aggregate maps at selected sites

Aggregate maps of Hi-C submatrices around selected DSB sites (±2-Mb windows) or TAD boundaries around the selected DSB sites (±0.5-Mb windows) were calculated using cooltools (https://github.com/mirnylab/cooltools). Each submatrix was averaged pixelwise, excluding the main and adjacent diagonals, to avoid Hi-C artifacts. Initial exploration of datasets was performed using HiCognition (*94*), and final figures were generated through Jupyter notebooks.

Sister-pore-C ratio maps at selected sites

Differential contact enrichment was computed as $\log_2$(DSB-induced/untreated) from Hi-C pileups for cis-sister and trans-sister maps. Contact frequencies were aggregated at target sites with cooltools (*103*), averaged for condition-specific pileup matrices, and visualized in matplotlib (*95*) and seaborn (*96*).

Sister-pore-C contact probability curves

To investigate whether DSB induction alters chromatin topology and sister chromatid cohesion genome-wide, we compared contact probability [*P*(s)] curves between untreated and DSB-induced samples. P(s) curves for cis- and trans-sister contacts were calculated separately using pairtools (*108*). Briefly, contacts were binned into 72 geometrically spaced intervals ranging from 1 bp to 1 Gb. The number of contacts in each bin was normalized by the square of the covered base pairs. To correct for differences in sequencing depth, P(s) curves for cis- and trans-sister contacts from the same sample were scaled by a common factor such that the combined area under both curves equaled 1 within genomic separations of 10 kb to 200 Mb.

Profiling contact density by cross-score analysis

To compare changes in loop abundance (cis-sister contacts) and trans-sister interactions around target sites upon DSB induction (Fig. 4, A to D), we performed cross-score analysis (*109*). Cross-scores from sister-pore-C cis- and trans-sister contact maps were computed at 10 kb resolution for untreated and DSB conditions, using distance ranges of 30 kb–1 Mb in the cooltools.sandbox.cross_score module. We extracted cross-scores ±2 Mb around DSB sites, with a bin overlapping each DSB site, and computed $\log_2$(DSB-induced/untreated) to detect changes in cis-sister loop abundance and trans-sister interactions.

Quantifying trans-sister contact enrichment by cross-score analysis

To assess changes in trans-sister contact enrichment around selected DSB sites upon DSB induction (fig. S8G), we calculated cross-score peak prominence per site. Peak regions were defined as ±150 kb around each DSB, with adjacent 150-kb flanking regions. Cross-scores were computed at 10-kb resolution. Prominence was defined as the $\log_2$ ratio of the mean cross-score in the peak region to the sum of the flanks. Changes in prominence were computed as the difference between DSB-induced and untreated $\log_2$ prominence values for both WT and sororin-depleted conditions.

Asymmetry analysis of ChIP-seq signal around selected DSB sites

Average γH2A.X ChIP-seq signal at the 23 selected sgRNA target sites was measured independently within 1-Mb windows upstream and downstream of each locus. A ratio of upstream to downstream signal was calculated to quantify the degree and direction of γH2A.X asymmetry. Loci were sorted top to bottom, based on the direction and magnitude of γH2A.X asymmetry, from upstream- to downstream-enriched sites. This ordering was applied uniformly to γH2A.X, NIPBL, RAD21 and sororin to generate stacked line profiles (see "Stack-up profiles and average pileups"), enabling direct comparison of asymmetry across factors.

Ionizing radiation time course for DSB repair in S/G_2 cells

Cas9-dox WT HeLa Kyoto cells were seeded on 12-mm glass coverslips (~40% confluency) and grown for 24 hours in standard DMEM. Cells were exposed to 2 Gy IR using a Gammacell 3000 Elan (Best Theratronics) and fixed at 1, 2, 5, and 8 hours after IR; untreated controls were fixed at the 2-h time point. Samples were stained to detect and quantify RAD51 in S/G_2 cells (see "Immunofluorescence" and "Quantitative image–based cytometry"). The same protocol was applied also to NIPBL-, WAPL-, RAD21-, and sororin-AID cells, in which auxin-mediated degradation was initiated 1 hour before IR treatment and maintained until fixation.

RAD51 foci quantification and resolution analysis

For Fig. 5B, RAD51 foci resolution was calculated as the difference in foci number between 2 and 8 hours after IR after subtracting values from untreated samples. "Resolved" foci refer to those lost between 2 and 8 hours after IR, and "unresolved" foci are those remaining at 8 hours. For WT and NIPBL-AID cells, green numbers indicate the percentage of resolved foci, and red numbers the unresolved ones. For WAPL-, RAD21-, and sororin-AID cells, the values represent additional RAD51 foci formed between 2 and 8 hours after IR. For Fig. 5C, the RAD51 resolution rate per hour was calculated by first subtracting baseline (untreated) values and then determining the fractional decrease in RAD51 foci between 8 and 2 hours after IR, dividing by the 6-hour

interval, and expressing the result as a percentage as follows: resolution rate per hour (%) = [(1 – {foci at 8 h – untreated}/{foci at 2 h – untreated}) / 6] × 100.

Statistical analysis and sample number

The sample number for each experiment is indicated in the respective figure legends. All statistical analyses were performed in Python using scipy (*110*) for the Mann-Whitney *U* test. Exact *P* values for each figure panel are as follows: Fig. 4M: $P = 2.35 \times 10^{-1}$; Fig. 4N: $P = 1.44 \times 10^{-8}$; Fig. 5C: $P = 8.2 \times 10^{-3}$ (WT versus NIPBL), $P = 6 \times 10^{-4}$ (WT versus WAPL, RAD21, sororin); fig. S3A: $P = 6.64 \times 10^{-9}$; fig. S3B: $P = 6.64 \times 10^{-9}$; fig. S3C: $P = 8.40 \times 10^{-4}$; fig. S3D: $P = 4.16 \times 10^{-1}$; and fig. S10E: $P = 1.36 \times 10^{-5}$.

Published datasets used

The dataset of scsHi-C WT HeLa cells synchronized to G_2 from (*29*) [Gene Expression Omnibus (GEO) number: GSM4613674] was used in Fig. 2, A and E, fig. S2A, and fig. S7, B and C.

REFERENCES AND NOTES

1. S. P. Jackson, J. Bartek, The DNA-damage response in human biology and disease. *Nature* **461**, 1071–1078 (2009). doi: 10.1038/nature08467; pmid: 19847258
2. M. Jasin, R. Rothstein, Repair of strand breaks by homologous recombination. *Cold Spring Harb. Perspect. Biol.* **5**, a012740 (2013). doi: 10.1101/cshperspect.a012740; pmid: 24097900
3. S. C. Kowalczykowski, An overview of the molecular mechanisms of recombinational DNA repair. *Cold Spring Harb. Perspect. Biol.* **7**, a016410 (2015). doi: 10.1101/cshperspect.a016410; pmid: 26525148
4. A. Barzel, M. Kupiec, Finding a match: How do homologous sequences get together for recombination? *Nat. Rev. Genet.* **9**, 27–37 (2008). doi: 10.1038/nrg2224; pmid: 18040271
5. A. Weiner, N. Zauberman, A. Minsky, Recombinational DNA repair in a cellular context: A search for the homology search. *Nat. Rev. Microbiol.* **7**, 748–755 (2009). doi: 10.1038/nrmicro2206; pmid: 19756013
6. J. Renkawitz, C. A. Lademann, S. Jentsch, Mechanisms and principles of homology search during recombination. *Nat. Rev. Mol. Cell Biol.* **15**, 369–383 (2014). doi: 10.1038/nrm3805; pmid: 24824069
7. J. E. Haber, DNA repair: The search for homology. *BioEssays* **40**, e1700229 (2018). doi: 10.1002/bies.201700229; pmid: 29603285
8. B. Bonilla, S. R. Hengel, M. K. Grundy, K. A. Bernstein, RAD51 gene family structure and function. *Annu. Rev. Genet.* **54**, 25–46 (2020). doi: 10.1146/annurev-genet-021920-092410; pmid: 32663049
9. M. Kong, E. C. Greene, Mechanistic insights from single-molecule studies of repair of double strand breaks. *Front. Cell Dev. Biol.* **9**, 745311 (2021). doi: 10.3389/fcell.2021.745311; pmid: 34869333
10. M. J. Rowley, V. G. Corces, Organizational principles of 3D genome architecture. *Nat. Rev. Genet.* **19**, 789–800 (2018). doi: 10.1038/s41576-018-0060-8; pmid: 30367165
11. S. Yatskevich, J. Rhodes, K. Nasmyth, Organization of chromosomal DNA by SMC complexes. *Annu. Rev. Genet.* **53**, 445–482 (2019). doi: 10.1146/annurev-genet-112618-043633; pmid: 31577909
12. T. Misteli, The self-organizing genome: Principles of genome architecture and function. *Cell* **183**, 28–45 (2020). doi: 10.1016/j.cell.2020.09.014; pmid: 32976797
13. I. F. Davidson, J.-M. Peters, Genome folding through loop extrusion by SMC complexes. *Nat. Rev. Mol. Cell Biol.* **22**, 445–464 (2021). doi: 10.1038/s41580-021-00349-7; pmid: 33767413
14. C. Hoencamp, B. D. Rowland, Genome control by SMC complexes. *Nat. Rev. Mol. Cell Biol.* **24**, 633–650 (2023). doi: 10.1038/s41580-023-00609-8; pmid: 37231112
15. J. Dekker, L. A. Mirny, The chromosome folding problem and how cells solve it. *Cell* **187**, 6424–6450 (2024). doi: 10.1016/j.cell.2024.10.026; pmid: 39547207
16. S. Liu *et al.*, In vivo tracking of functionally tagged Rad51 unveils a robust strategy of homology search. *Nat. Struct. Mol. Biol.* **30**, 1582–1591 (2023). doi: 10.1038/s41594-023-01065-w; pmid: 37605042
17. L. C. Kadyk, L. H. Hartwell, Sister chromatids are preferred over homologs as substrates for recombinational repair in *Saccharomyces cerevisiae*. *Genetics* **132**, 387–402 (1992). doi: 10.1093/genetics/132.2.387; pmid: 1427035
18. R. D. Johnson, M. Jasin, Sister chromatid gene conversion is a prominent double-strand break repair pathway in mammalian cells. *EMBO J.* **19**, 3398–3407 (2000). doi: 10.1093/emboj/19.13.3398; pmid: 10880452
19. V. Guacci, D. Koshland, A. Strunnikov, A direct link between sister chromatid cohesion and chromosome condensation revealed through the analysis of MCD1 in S. cerevisiae. *Cell* **91**, 47–57 (1997). doi: 10.1016/S0092-8674(01)80008-8; pmid: 9335334
20. C. Michaelis, R. Ciosk, K. Nasmyth, Cohesins: Chromosomal proteins that prevent premature separation of sister chromatids. *Cell* **91**, 35–45 (1997). doi: 10.1016/S0092-8674(01)80007-6; pmid: 9335333
21. S. Covo, J. W. Westmoreland, D. A. Gordenin, M. A. Resnick, Cohesin Is limiting for the suppression of DNA damage-induced recombination between homologous chromosomes. *PLOS Genet.* **6**, e1001006 (2010). doi: 10.1371/journal.pgen.1001006; pmid: 20617204
22. F. Klein *et al.*, A central role for cohesins in sister chromatid cohesion, formation of axial elements, and recombination during yeast meiosis. *Cell* **98**, 91–103 (1999). doi: 10.1016/S0092-8674(00)80609-1; pmid: 10412984
23. C. Sjögren, K. Nasmyth, Sister chromatid cohesion is required for postreplicative double-strand break repair in *Saccharomyces cerevisiae*. *Curr. Biol.* **11**, 991–995 (2001). doi: 10.1016/S0960-9822(01)00271-8; pmid: 11448778
24. E. Sonoda *et al.*, Scc1/Rad21/Mcd1 is required for sister chromatid cohesion and kinetochore function in vertebrate cells. *Dev. Cell* **1**, 759–770 (2001). doi: 10.1016/S1534-5807(01)00088-0; pmid: 11740938
25. E. Watrin, J.-M. Peters, Cohesin and DNA damage repair. *Exp. Cell Res.* **312**, 2687–2693 (2006). doi: 10.1016/j.yexcr.2006.06.024; pmid: 16876157
26. R. Stanyte *et al.*, Dynamics of sister chromatid resolution during cell cycle progression. *J. Cell Biol.* **217**, 1985–2004 (2018). doi: 10.1083/jcb.201801157; pmid: 29695489
27. J. K. Eykelenboom *et al.*, Live imaging of marked chromosome regions reveals their dynamic resolution and compaction in mitosis. *J. Cell Biol.* **218**, 1531–1552 (2019). doi: 10.1083/jcb.201807125; pmid: 30858191
28. P. Batty *et al.*, Cohesin-mediated DNA loop extrusion resolves sister chromatids in G_2 phase. *EMBO J.* **42**, e113475 (2023). doi: 10.15252/embj.2023113475; pmid: 37357575
29. M. Mitter *et al.*, Conformation of sister chromatids in the replicated human genome. *Nature* **586**, 139–144 (2020). doi: 10.1038/s41586-020-2744-4; pmid: 32968280
30. F. Ochs *et al.*, Sister chromatid cohesion is mediated by individual cohesin complexes. *Science* **383**, 1122–1130 (2024). doi: 10.1126/science.adl4606; pmid: 38452070
31. J. Gassler *et al.*, A mechanism of cohesin-dependent loop extrusion organizes zygotic genome architecture. *EMBO J.* **36**, 3600–3618 (2017). doi: 10.15252/embj.201798083; pmid: 29217590
32. S. S. P. Rao *et al.*, Cohesin loss eliminates all loop domains. *Cell* **171**, 305–320.e24 (2017). doi: 10.1016/j.cell.2017.09.026; pmid: 28985562
33. W. Schwarzer *et al.*, Two independent modes of chromatin organization revealed by cohesin removal. *Nature* **551**, 51–56 (2017). doi: 10.1038/nature24281; pmid: 29094699
34. G. Wutz *et al.*, Topologically associating domains and chromatin loops depend on cohesin and are regulated by CTCF, WAPL, and PDS5 proteins. *EMBO J.* **36**, 3573–3599 (2017). doi: 10.15252/embj.201798004; pmid: 29217591
35. I. F. Davidson *et al.*, DNA loop extrusion by human cohesin. *Science* **366**, 1338–1345 (2019). doi: 10.1126/science.aaz3418; pmid: 31753851
36. Y. Kim, Z. Shi, H. Zhang, I. J. Finkelstein, H. Yu, Human cohesin compacts DNA by loop extrusion. *Science* **366**, 1345–1349 (2019). doi: 10.1126/science.aaz4475; pmid: 31780627
37. V. Parelho *et al.*, Cohesins functionally associate with CTCF on mammalian chromosome arms. *Cell* **132**, 422–433 (2008). doi: 10.1016/j.cell.2008.01.011; pmid: 18237772
38. K. S. Wendt *et al.*, Cohesin mediates transcriptional insulation by CCCTC-binding factor. *Nature* **451**, 796–801 (2008). doi: 10.1038/nature06634; pmid: 18235444
39. I. F. Davidson *et al.*, CTCF is a DNA-tension-dependent barrier to cohesin-mediated loop extrusion. *Nature* **616**, 822–827 (2023). doi: 10.1038/s41586-023-05961-5; pmid: 37076620
40. J. R. Dixon *et al.*, Topological domains in mammalian genomes identified by analysis of chromatin interactions. *Nature* **485**, 376–380 (2012). doi: 10.1038/nature11082; pmid: 22495300
41. E. P. Nora *et al.*, Spatial partitioning of the regulatory landscape of the X-inactivation centre. *Nature* **485**, 381–385 (2012). doi: 10.1038/nature11049; pmid: 22495304
42. S. S. P. Rao *et al.*, A 3D map of the human genome at kilobase resolution reveals principles of chromatin looping. *Cell* **159**, 1665–1680 (2014). doi: 10.1016/j.cell.2014.11.021; pmid: 25497547
43. A. Piazza *et al.*, Cohesin regulates homology search during recombinational DNA repair. *Nat. Cell Biol.* **23**, 1176–1186 (2021). doi: 10.1038/s41556-021-00783-x; pmid: 34750581
44. A. Dumont *et al.*, Mechanism of homology search expansion during recombinational DNA break repair in Saccharomyces cerevisiae. *Mol. Cell* **84**, 3237–3253.e6 (2024). doi: 10.1016/j.molcel.2024.08.003; pmid: 39178861
45. J. van den Berg *et al.*, A limited number of double-strand DNA breaks is sufficient to delay cell cycle progression. *Nucleic Acids Res.* **46**, 10132–10144 (2018). doi: 10.1093/nar/gky786; pmid: 30184135
46. N. Hustedt, D. Durocher, The control of DNA repair by the cell cycle. *Nat. Cell Biol.* **19**, 1–9 (2016). doi: 10.1038/ncb3452; pmid: 28008184
47. R. Scully, A. Panday, R. Elango, N. A. Willis, DNA double-strand break repair-pathway choice in somatic mammalian cells. *Nat. Rev. Mol. Cell Biol.* **20**, 698–714 (2019). doi: 10.1038/s41580-019-0152-0; pmid: 31263220
48. E. P. Nora *et al.*, Targeted degradation of CTCF decouples local insulation of chromosome domains from genomic compartmentalization. *Cell* **169**, 930–944.e22 (2017). doi: 10.1016/j.cell.2017.05.004; pmid: 28525758

49. J. Renkawitz, C. A. Lademann, M. Kalocsay, S. Jentsch, Monitoring homology search during DNA double-strand break repair in vivo. *Mol. Cell* **50**, 261–272 (2013). doi: 10.1016/j.molcel.2013.02.020; pmid: 23523370
50. R. Ciosk *et al.*, Cohesin's binding to chromosomes depends on a separate complex consisting of Scc2 and Scc4 proteins. *Mol. Cell* **5**, 243–254 (2000). doi: 10.1016/S1097-2765(00)80420-7; pmid: 10882066
51. D. Gerlich, B. Koch, F. Dupeux, J.-M. Peters, J. Ellenberg, Live-cell imaging reveals a stable cohesin-chromatin interaction after but not before DNA replication. *Curr. Biol.* **16**, 1571–1578 (2006). doi: 10.1016/j.cub.2006.06.068; pmid: 16890534
52. S. Kueng *et al.*, Wapl controls the dynamic association of cohesin with chromatin. *Cell* **127**, 955–967 (2006). doi: 10.1016/j.cell.2006.09.040; pmid: 17113138
53. R. Ladurner *et al.*, Sororin actively maintains sister chromatid cohesion. *EMBO J.* **35**, 635–653 (2016). doi: 10.15252/embj.201592532; pmid: 26903600
54. J. H. I. Haarhuis *et al.*, The cohesin release factor WAPL restricts chromatin loop extension. *Cell* **169**, 693–707.e14 (2017). doi: 10.1016/j.cell.2017.04.013; pmid: 28475897
55. P. L. Collins *et al.*, DNA double-strand breaks induce H2Ax phosphorylation domains in a contact-dependent manner. *Nat. Commun.* **11**, 3158 (2020). doi: 10.1038/s41467-020-16926-x; pmid: 32572033
56. C. Arnould *et al.*, Loop extrusion as a mechanism for formation of DNA damage repair foci. *Nature* **590**, 660–665 (2021). doi: 10.1038/s41586-021-03193-z; pmid: 33597753
57. S. H. Sternberg, S. Redding, M. Jinek, E. C. Greene, J. A. Doudna, DNA interrogation by the CRISPR RNA-guided endonuclease Cas9. *Nature* **507**, 62–67 (2014). doi: 10.1038/nature13011; pmid: 24476820
58. S. C. Knight *et al.*, Dynamics of CRISPR-Cas9 genome interrogation in living cells. *Science* **350**, 823–826 (2015). doi: 10.1126/science.aac6572; pmid: 26564855
59. L. Ström, H. B. Lindroos, K. Shirahige, C. Sjögren, Postreplicative recruitment of cohesin to double-strand breaks is required for DNA repair. *Mol. Cell* **16**, 1003–1015 (2004). doi: 10.1016/j.molcel.2004.11.026; pmid: 15610742
60. E. Ünal *et al.*, DNA damage response pathway uses histone modification to assemble a double-strand break-specific cohesin domain. *Mol. Cell* **16**, 991–1002 (2004). doi: 10.1016/j.molcel.2004.11.027; pmid: 15610741
61. P. R. Potts, M. H. Porteus, H. Yu, Human SMC5/6 complex promotes sister chromatid homologous recombination by recruiting the SMC1/3 cohesin complex to double-strand breaks. *EMBO J.* **25**, 3377–3388 (2006). doi: 10.1038/sj.emboj.7601218; pmid: 16810316
62. C. Bauerschmidt *et al.*, Cohesin promotes the repair of ionizing radiation-induced DNA double-strand breaks in replicated chromatin. *Nucleic Acids Res.* **38**, 477–487 (2010). doi: 10.1093/nar/gkp976; pmid: 19906707
63. L. Ström *et al.*, Postreplicative formation of cohesion is required for repair and induced by a single DNA break. *Science* **317**, 242–245 (2007). doi: 10.1126/science.1140649; pmid: 17626884
64. E. Ünal, J. M. Heidinger-Pauli, D. Koshland, D. N. A. Double-Strand Breaks Trigger Genome-Wide Sister-Chromatid Cohesion Through, DNA double-strand breaks trigger genome-wide sister-chromatid cohesion through Eco1 (Ctf7). *Science* **317**, 245–248 (2007). pmid: 17626885
65. J. Dekker, K. Rippe, M. Dekker, N. Kleckner, Capturing chromosome conformation. *Science* **295**, 1306–1311 (2002). doi: 10.1126/science.1067799; pmid: 11847345
66. E. Lieberman-Aiden *et al.*, Comprehensive mapping of long-range interactions reveals folding principles of the human genome. *Science* **326**, 289–293 (2009). doi: 10.1126/science.1181369; pmid: 19815776
67. M. Mitter *et al.*, Sister chromatid-sensitive Hi-C to map the conformation of replicated genomes. *Nat. Protoc.* **17**, 1486–1517 (2022). doi: 10.1038/s41596-022-00687-6; pmid: 35478248
68. M. E. Oomen, A. K. Hedger, J. K. Watts, J. Dekker, Detecting chromatin interactions between and along sister chromatids with SisterC. *Nat. Methods* **17**, 1002–1009 (2020). doi: 10.1038/s41592-020-0930-9; pmid: 32968250
69. M. Mitter, D. W. Gerlich, Mapping sister chromatid conformation in replicated chromosomes. *Trends Biochem. Sci.* **46**, 169–170 (2021). doi: 10.1016/j.tibs.2020.11.011; pmid: 33342665
70. C. A. Müller *et al.*, Capturing the dynamics of genome replication on individual ultra-long nanopore sequence reads. *Nat. Methods* **16**, 429–436 (2019). doi: 10.1038/s41592-019-0394-y; pmid: 31011185
71. D. Georgieva, Q. Liu, K. Wang, D. Egli, Detection of base analogs incorporated during DNA replication by nanopore sequencing. *Nucleic Acids Res.* **48**, e88 (2020). doi: 10.1093/nar/gkaa517; pmid: 32710620
72. M. Hennion *et al.*, FORK-seq: Replication landscape of the Saccharomyces cerevisiae genome by nanopore sequencing. *Genome Biol.* **21**, 125 (2020). doi: 10.1186/s13059-020-02013-3; pmid: 32456659
73. A. S. Deshpande *et al.*, Identifying synergistic high-order 3D chromatin conformations from genome-scale nanopore concatemer sequencing. *Nat. Biotechnol.* **40**, 1488–1499 (2022). doi: 10.1038/s41587-022-01289-z; pmid: 35637420
74. M. A. Boemo, DNAscent v2: Detecting replication forks in nanopore sequencing data with deep learning. *BMC Genomics* **22**, 430 (2021). doi: 10.1186/s12864-021-07736-6; pmid: 34107894
75. S. Rankin, N. G. Ayad, M. W. Kirschner, Sororin, a substrate of the anaphase-promoting complex, is required for sister chromatid cohesion in vertebrates. *Mol. Cell* **18**, 185–200 (2005). doi: 10.1016/j.molcel.2005.03.017; pmid: 15837422
76. J. Schmitz, E. Watrin, P. Lénárt, K. Mechtler, J.-M. Peters, Sororin is required for stable binding of cohesin to chromatin and for sister chromatid cohesion in interphase. *Curr. Biol.* **17**, 630–636 (2007). doi: 10.1016/j.cub.2007.02.029; pmid: 17349791
77. W.-D. Heyer, X. Li, M. Rolfsmeier, X.-P. Zhang, Rad54: The Swiss Army knife of homologous recombination? *Nucleic Acids Res.* **34**, 4115–4125 (2006). doi: 10.1093/nar/gkl481; pmid: 16935872
78. A. Beucher *et al.*, ATM and Artemis promote homologous recombination of radiation-induced DNA double-strand breaks in G_2. *EMBO J.* **28**, 3413–3427 (2009). doi: 10.1038/emboj.2009.276; pmid: 19779458
79. T. Gudjonsson *et al.*, TRIP12 and UBR5 suppress spreading of chromatin ubiquitylation at damaged chromosomes. *Cell* **150**, 697–709 (2012). doi: 10.1016/j.cell.2012.06.039; pmid: 22884692
80. D. P. Waterman *et al.*, Live cell monitoring of double strand breaks in *S. cerevisiae*. *PLOS Genet.* **15**, e1008001 (2019). doi: 10.1371/journal.pgen.1008001; pmid: 30822309
81. Z. Mao, M. Bozzella, A. Seluanov, V. Gorbunova, Comparison of nonhomologous end joining and homologous recombination in human cells. *DNA Repair* **7**, 1765–1771 (2008). doi: 10.1016/j.dnarep.2008.06.018; pmid: 18675941
82. B. Benedict *et al.*, WAPL-dependent repair of damaged DNA replication forks underlies oncogene-induced loss of sister chromatid cohesion. *Dev. Cell* **52**, 683–698.e7 (2020). doi: 10.1016/j.devcel.2020.01.024; pmid: 32084359
83. A. Seeber *et al.*, RPA mediates recruitment of MRX to forks and double-strand breaks to hold sister chromatids together. *Mol. Cell* **64**, 951–966 (2016). doi: 10.1016/j.molcel.2016.10.032; pmid: 27889450
84. K. L. de Luca *et al.*, Genome-wide profiling of DNA repair proteins in single cells. *Nat. Commun.* **15**, 9918 (2024). doi: 10.1038/s41467-024-54159-4; pmid: 39572529
85. Y. Zhang, X. Zhang, H.-Q. Dai, H. Hu, F. W. Alt, The role of chromatin loop extrusion in antibody diversification. *Nat. Rev. Immunol.* **22**, 550–566 (2022). doi: 10.1038/s41577-022-00679-3; pmid: 35169260
86. M. Petronczki, M. F. Siomos, K. Nasmyth, Un ménage à quatre: The molecular biology of chromosome segregation in meiosis. *Cell* **112**, 423–440 (2003). doi: 10.1016/S0092-8674(03)00083-7; pmid: 12600308
87. D. Zickler, N. Kleckner, Meiosis: Dances between homologs. *Annu. Rev. Genet.* **57**, 1–63 (2023). doi: 10.1146/annurev-genet-061323-044915; pmid: 37788458
88. F. Teloni *et al.*, Efficient Pre-mRNA cleavage prevents replication-stress-associated genome instability. *Mol. Cell* **73**, 670–683.e12 (2019). doi: 10.1016/j.molcel.2018.11.036; pmid: 30639241
89. P. A. Ewels *et al.*, The nf-core framework for community-curated bioinformatics pipelines. *Nat. Biotechnol.* **38**, 276–278 (2020). doi: 10.1038/s41587-020-0439-x; pmid: 32055031
90. P. Danecek *et al.*, Twelve years of SAMtools and BCFtools. *Gigascience* **10**, giab008 (2021). doi: 10.1093/gigascience/giab008; pmid: 33590861
91. F. Ramírez *et al.*, deepTools2: A next generation web server for deep-sequencing data analysis. *Nucleic Acids Res.* **44**, W160-5 (2016). doi: 10.1093/nar/gkw257; pmid: 27079975
92. B. Gel, E. Serra, karyoploteR: An R/Bioconductor package to plot customizable genomes displaying arbitrary data. *Bioinformatics* **33**, 3088–3090 (2017). doi: 10.1093/bioinformatics/btx346; pmid: 28575171
93. M. Lawrence, R. Gentleman, V. Carey, rtracklayer: An R package for interfacing with genome browsers. *Bioinformatics* **25**, 1841–1842 (2009). doi: 10.1093/bioinformatics/btp328; pmid: 19468054
94. C. C. H. Langer, M. Mitter, R. R. Stocsits, D. W. Gerlich, HiCognition: A visual exploration and hypothesis testing tool for 3D genomics. *Genome Biol.* **24**, 158 (2023). doi: 10.1186/s13059-023-02996-9; pmid: 37408019
95. J. D. Hunter, Matplotlib: A 2D graphics environment. *Comput. Sci. Eng.* **9**, 90–95 (2007). doi: 10.1109/MCSE.2007.55
96. M. L. Waskom, seaborn: Statistical data visualization. *J. Open Source Softw.* **6**, 3021 (2021). doi: 10.21105/joss.03021
97. K. S. Beckwith *et al.*, Nanoscale 3D DNA tracing in single human cells visualizes loop extrusion directly in situ. bioRxiv 439407 [Preprint] (2023); https://doi.org/10.1101/2021.04.12.439407.
98. A. Brunner *et al.*, Quantitative imaging of loop extruders rebuilding interphase genome architecture after mitosis. bioRxiv 596439 [Preprint] (2024); https://doi.org/10.1101/2024.05.29.596439.
99. J. M. Brown, S. De Ornellas, E. Parisi, L. Schermelleh, V. J. Buckle, RASER-FISH: Non-denaturing fluorescence in situ hybridization for preservation of three-dimensional interphase chromatin structure. *Nat. Protoc.* **17**, 1306–1331 (2022). doi: 10.1038/s41596-022-00685-8; pmid: 35379945
100. L. J. Mateo, N. Sinnott-Armstrong, A. N. Boettiger, Tracing DNA paths and RNA profiles in cultured cells and tissues with ORCA. *Nat. Protoc.* **16**, 1647–1713 (2021). doi: 10.1038/s41596-020-00478-x; pmid: 33619390
101. B. J. Beliveau *et al.*, OligoMiner provides a rapid, flexible environment for the design of genome-scale oligonucleotide in situ hybridization probes. *Proc. Natl. Acad. Sci. U.S.A.* **115**, E2183–E2192 (2018). doi: 10.1073/pnas.1714530115; pmid: 29463736

102. L. An *et al.*, OnTAD: Hierarchical domain structure reveals the divergence of activity among TADs and boundaries. *Genome Biol.* **20**, 282 (2019). doi: 10.1186/s13059-019-1893-y; pmid: 31847870
103. N. Abdennur *et al.*, Cooltools: enabling high-resolution Hi-C analysis in Python. bioRxiv 514564 [Preprint] (2022); https://doi.org/10.1101/2022.10.31.514564.
104. F. Mölder *et al.*, Sustainable data analysis with Snakemake. F1000Research [Preprint] (2021); https://doi.org/10.12688/f1000research.29032.2.
105. N. Abdennur, L. A. Mirny, Cooler: Scalable storage for Hi-C data and other genomically labeled arrays. *Bioinformatics* **36**, 311–316 (2020). doi: 10.1093/bioinformatics/btz540; pmid: 31290943
106. M. Imakaev *et al.*, Iterative correction of Hi-C data reveals hallmarks of chromosome organization. *Nat. Methods* **9**, 999–1003 (2012). doi: 10.1038/nmeth.2148; pmid: 22941365
107. M. Raasveldt, H. Mühleisen, "DuckDB: an embeddable analytical database" in *Proceedings of the 2019 International Conference on Management of Data* (Association for Computing Machinery, New York, NY, USA, 2019), pp. 1981–1984; https://doi.org/10.1145/3299869.3320212.
108. N. Abdennur *et al.*, Pairtools: From sequencing data to chromosome contacts. *PLOS Comput. Biol.* **20**, e1012164 (2024). doi: 10.1371/journal.pcbi.1012164; pmid: 38809952
109. L. Hill *et al.*, Igh and Igk loci use different folding principles for V gene recombination due to distinct chromosomal architectures of pro-B and pre-B cells. *Nat. Commun.* **14**, 2316 (2023). doi: 10.1038/s41467-023-37994-9; pmid: 37085514
110. P. Virtanen *et al.*, SciPy 1.0: Fundamental algorithms for scientific computing in Python. *Nat. Methods* **17**, 261–272 (2020). doi: 10.1038/s41592-019-0686-2; pmid: 32015543
111. M. Mitter, C. C. H. Langer, F. Teloni, gerlichlab/sister-pore-c-snakemake: Release v0.3.2, Zenodo (2025); https://doi.org/10.5281/zenodo.17255366.
112. C. C. H. Langer, gerlichlab/sister-pore-c-docker: Release v0.3.2, Zenodo (2025); https://doi.org/10.5281/zenodo.17255337.
113. V. Reuter, gerlichlab/reparafil: v0.9.0, Zenodo (2025); https://doi.org/10.5281/zenodo.17252829.
114. V. Reuter, gerlichlab/spotfishing: v0.3.0, Zenodo (2025); https://doi.org/10.5281/zenodo.17252808.
115. F. Teloni, C. C. H. Langer, D. Mylarshchikov, gerlichlab/teloni_et_al: Release v0.0.2, Zenodo (2025); https://doi.org/10.5281/zenodo.17255262.
116. C. C. H. Langer, M. Mitter, V. Reuter, gerlichlab/gerlich_jupyter: Release v1.9, Zenodo (2025); https://doi.org/10.5281/zenodo.17256412.

ACKNOWLEDGMENTS

We thank the IMBA/IMP/GMI BioOptics and Molecular Biology Service and the Vienna BioCenter Next Generation Sequencing and Metabolomics facilities for technical support; J. Ellenberg and K. S. Beckwith for technical advice on RASER-FISH; J.-M. Peters for providing RAD21-AID, sororin-AID, and WAPL-AID HeLa cell lines; R. Medema for providing the iCut plasmid; E. Ogris for the production of the α-sororin antibody; and I. Patten, M. M. Alaabo, and T. Hidaka for comments on the manuscript. D.W.G. is also an adjunct professor at the Medical University of Vienna. **Funding:** This work was supported by the Austrian Academy of Sciences (D.W.G.); the Vienna Science and Technology Fund (WWTF project grant LS19-001 to D.W.G.); the European Research Council (ERC) under the European Union's Horizon 2020 Research and Innovation Program (grant 101019039 to D.W.G.; Marie Skłodowska-Curie individual fellowships 101022896 to F.T. and 101103258 to T.L.S.; and Marie Curie Skłodowska grant 847548 to T.L.S.); the Swiss National Science Foundation (postdoctoral fellowship P2ZHP3_191408 to F.T.); the European Molecular Biology Organization (postdoctoral fellowship ALTF 866-2022 to T.L.S.); the FWF Hertha Firnberg Programme (fellowship T1246 to Z.T.); and Boehringer Ingelheim Fonds (PhD fellowship to M.M.). **Author contributions:** Conceptualization: F.T., D.W.G.; Data curation: C.C.H.L., Z.T., F.T.; Formal analysis: I.P. (Fig. 1 and fig. S5, A and B), D.M. (Fig. 4, A and B, and fig. S8, E to G), C.C.H.L. (fig. S7, B to E), Z.T. (figs. S6D and S7D), F.T. (all other data); Funding acquisition: D.W.G., F.T., Z.T., M.M., T.L.S.; Investigation: I.P. (Fig. 1 and fig. S5, A and B), Z.T. (figs. S6D and S7D), F.T. (all other data); Methodology: F.T. (DSB induction assay), Z.T., M.M., C.C.H.L. (sister-pore-C), T.L.S., V.P.R. (FISH); Software: M.M., C.C.H.L., V.P.R.; Supervision: D.W.G.; Validation: I.P. (Fig. 1 and fig. S5, A and B), D.M. (Fig. 4, A and B, and fig. S8, E to G), C.C.H.L. (fig. S7, B to E), Z.T. (fig. S7D), F.T. (all other data); Visualization: I.P. (Fig. 1 and fig. S5, A and B), C.C.H.L. (fig. S7, B to E), D.M. (Fig. 4, A and B, and fig. S8, E to G), F.T. (all other figures); Writing – original draft: D.W.G., F.T.; Writing – review & editing: all authors. **Competing interests:** The authors declare no competing interests. **Data and materials availability:** All sequencing data are publicly available at the European Nucleotide Archive under accession number PRJEB98549. Datasets of scsHi-C WT HeLa cells synchronized to G_2 from (*29*) are available at the Gene Expression Omnibus under accession number GSM4613674. All datasets are based on a custom HeLa Kyoto reference genome [hg19 with SNP correction (*29*)]. All other data required to support the conclusions of this study are available in the main manuscript or the supplementary materials. The sister-pore-C pipeline (*111*), its Docker container (*112*), the FISH analysis pipelines (*113*,*114*), the sequencing data analysis scripts (*115*), and the corresponding Docker container (*116*) are freely available on Zenodo. All materials are available upon request to the corresponding authors. **License information:** Copyright © 2025 the authors, some rights reserved; exclusive licensee American Association for the Advancement of Science. No claim to original US government works. https://www.science.org/about/science-licenses-journal-article-reuse

SUPPLEMENTARY MATERIALS

science.org/doi/10.1126/science.adw0566
Figs. S1 to S11; Tables S1 to S3; MDAR Reproducibility Checklist

Submitted 22 January 2025; resubmitted 15 July 2025; accepted 3 October 2025

10.1126/science.adw0566

SOLAR CELLS

Improved solvent systems for commercially viable perovskite photovoltaic modules

Yinke Wang[1]†, Ye Liu[2]†, Xin Luo[2]†, Ke Xiao[1]*, Victor Marrugat-Arnal[3], Dongdong Xu[1], Jing Lou[4], Weiwei Zuo[5], Navid Tavakoli[5], Tiantian Li[6,7], Yuanbo Yang[6,7], Chenyang Duan[1], Wennan Ou[1], Yuxuan Liu[1], Jiajia Hong[1], Hongfei Sun[1], Gongtao Duan[1], Manya Li[1], Han Gao[1], Zijing Chu[1], Long Jiang[6,7], Michael Saliba[5,8], Makhsud I. Saidaminov[9], Chao Chang[4]*, Hairen Tan[1,2]*

Commercializing perovskite photovoltaics requires overcoming three critical barriers: the use of toxic solvents in manufacturing, variations in perovskite film quality across large areas, and limited operational reliability. Here, we address these challenges by developing a green solvent–based (γ-valerolactone/2-methyl tetrahydrofuran/dimethylsulfoxide) ink and a solvent-confinement edge-protection strategy, demonstrating large-scale manufacturing of defect-minimized perovskite films under ambient-air conditions. These approaches enabled the production of 7200-square-centimeter perovskite photovoltaic modules that achieved a total-area steady-state efficiency of 17.2% (certified by the National Renewable Energy Laboratory) and that passed all IEC 61215 reliability standards (certified by TÜV Rheinland). This work demonstrates an environmentally responsible path toward commercial manufacturing of perovskite photovoltaics.

Perovskite photovoltaics (PVs) (*1*–*4*) offer advantages in production costs (*5*, *6*), energy efficiency (*7*–*9*), and scalability (*10*, *11*), but commercial deployment will require the development of green, ambient-air fabrication (*12*–*14*); maximizing the total-area power output of commercial-scale modules (*15*); and ensuring long-term operational reliability (*16*). Among perovskite compositions, hybrid cation perovskites, particularly formamidinium (FA)–cesium plumbo-halides, have notable optoelectronic properties and operational stability (*7*, *17*, *18*). However, their processing typically relies on hazardous solvents such as 2-methoxyethanol (2-Me) and *N*,*N*-dimethylformamide (DMF) (*19*–*21*). Dimethyl sulfoxide (DMSO), although a low-hazardous alternative, is commonly paired with toxic DMF (*22*–*24*) because an excessive presence of DMSO enhances unfavorable intermediate phase dynamics during perovskite film formation. The development of green, ambient air–compatible solvent systems remains a critical unmet need for commercial-scale manufacturing of perovskite PV modules.

Scaling up perovskite modules also requires producing highly uniform films across large-area substrates. Slot-die coating offers cost-effective high-throughput film deposition at a square-meter scale (*25*, *26*). However, inconsistent solvent coordination and extraction kinetics across the wet film, particularly at the film edges, often lead to crystallization defects that hinder the total-area power conversion efficiency (PCE). Therefore, simultaneous optimization of the solvent chemistry and extraction kinetics is essential to overcome current performance limitations of perovskite PV modules (*15*).

Long-term operational reliability has been addressed in part through improved encapsulation (*27*–*29*) and interfacial engineering (*30*, *31*). However, the intrinsic quality of perovskite films must be enhanced to improve the operational stability because bulk defects are critical determinants of device durability (*32*–*34*). Although many reports claim promising device stability on the basis of internal tests, an independent third-party verification across the full International Electrotechnical Commission (IEC) test sequences is now essential to validate the readiness of perovskite PV modules for real-world deployment (*35*).

We address these challenges by developing a green solvent system on the basis of γ-valerolactone (GVL) and DMSO, tuned with 2-methyl tetrahydrofuran (2-MeTHF) to tailor solvent coordination and evaporation kinetics. 2-MeTHF offers advantages in both safety and sustainability: Its methyl group reduces metabolic activation of THF into toxic by-products, and its elevated boiling point lowers inhalation risks; additionally, 2-MeTHF is derived from renewable biomass (*36*), unlike petroleum-based THF, and demonstrates better biodegradability and lower ecotoxicity (*37*). This solvent system enables the manufacturing of void-free, high-crystalline, defect-minimized perovskite films over the substrates that measure 120 cm by 60 cm. To address edge-related nonuniformities, we introduce a solvent-confinement edge-protection (SCEP) strategy to preserve solvent dynamics at the wet-film periphery. Using these approaches, we demonstrate industrially viable manufacturing of perovskite PV modules with a full area of 7200 cm^2. The commercial-scale perovskite PV modules achieve 17.2% steady-state efficiency, as independently certified at the National Renewable Energy Laboratory (NREL), and successfully pass all IEC 61215 reliability tests at the Technical Inspection Association TÜV Rheinland. These results establish a commercially viable and environmentally responsible pathway toward the deployment of perovskite PV modules at large scale.

Green solvents for slot-die coating

We chose $FA_{0.95}Cs_{0.05}PbI_3$ perovskite as the light absorber because of its excellent optoelectronic properties and operational stability. The inclusion of cesium enhances the crystallinity and crystal lattice stability of the perovskite (*7*). To dissolve $FA_{0.95}Cs_{0.05}PbI_3$ perovskite using green solvents, we first attempted to optimize the DMSO/acetonitrile/ethanol solvent system that we recently used in wide-bandgap perovskite ($Cs_{0.35}FA_{0.65}PbI_{1.8}Br_{1.2}$) fabrication (*14*). A DMSO volume fraction exceeding 30% was required for complete dissolution of $FA_{0.95}Cs_{0.05}PbI_3$ (fig. S1). However, this high DMSO content not only suppressed nucleation but also strongly coordinated with the perovskite precursors, hindering its removal during crystallization. As a result, the films exhibited poor interfacial adhesion, ultimately causing delamination from the substrates (fig. S2). The high cesium and bromide content in wide-bandgap perovskites was likely responsible for promoting high-rate nucleation in our previous work (*38*), thereby facilitating the formation of dense and homogeneous films, which was not the case for the 1.5-eV perovskites in this work.

The 1.5-eV perovskite precursors exhibited good solubility in polar aprotic solvents with weak coordination, such as DMF and 2-Me, but

[1]National Laboratory of Solid State Microstructures, College of Engineering and Applied Sciences, Frontiers Science Center for Critical Earth Material Cycling, Jiangsu Physical Science Research Center, Nanjing University, Nanjing, China. [2]Research and Development Center, Renshine Solar (Suzhou) Co., Ltd., Changshu, Jiangsu, China. [3]Department of Electrical and Computer Engineering, University of Victoria, Victoria, BC, Canada. [4]Innovation Laboratory of Terahertz Biophysics, National Innovation Institute of Defense Technology, Beijing, China. [5]Institute for Photovoltaics, University of Stuttgart, Stuttgart, Germany. [6]State Key Laboratory of Oil and Gas Equipment, CNPC Tubular Goods Research Institute, Xi'an, China. [7]Shaanxi Provincial Key Laboratory of Clean Energy Equipment and Materials, Xi'an, China. [8]Helmholtz Young Investigator Group FRONTRUNNER, IMD3-Photovoltaik, Forschungszentrum Jülich, Jülich, Germany. [9]Department of Chemistry, University of Victoria, Victoria, BC, Canada. ***Corresponding author. Email: kexiao@smail.nju.edu.cn (K.X.); gwyzlzssb@pku.edu.cn (C.C.); hairentan@nju.edu.cn (H.T.)** †These authors contributed equally to this work.

they were unsuitable for ambient-air mass production because of their biotoxicity. By contrast, GVL has lower biotoxicity (*24*) and has been used for slot-die coating perovskites (*39*), although cesium-containing compositions have shown limited solubility. The addition of DMSO was hence required to achieve complete dissolution, which also improved the colloidal stability of the precursor ink (fig. S3).

For scalable manufacturing of perovskite solar modules at a square-meter scale, we used a combination of slot-die coating and vacuum chamber drying (VCD) (Fig. 1A) (*40*, *41*). During the VCD, pressure and evacuation speed critically affect perovskite film formation. Low pressure accelerates solvent removal, enhancing precursor supersaturation and promoting the nucleation of fine, dense crystal nuclei. However, excessively fast evacuation may result in small, uneven grains, along with pinholes or cracks. By contrast, slower evacuation enables gradual solvent evaporation, facilitating the growth of larger grains and reducing grain boundary defects.

Although VCD is designed to extract solvents, the residues of solvents with a high boiling point and low saturated vapor pressure (such as DMSO and GVL; fig. S4) remain in the film (*34*, *42*), resulting in voids at the buried interface of perovskite with fluorine-doped tin oxide (FTO)/NiO_x (Fig. 1B). To address this issue, 2-MeTHF, another green solvent with high vapor pressure and weak coordination ability to Pb^{2+}, as shown in solubility tests (fig. S5), was used (*43*). We found that the introduction of 2-MeTHF facilitates GVL evaporation to enhance the buried interface bonding, effectively eliminating voids at the perovskite-substrate interface (Fig. 1B). Because of the low boiling point and high saturated vapor pressure of 2-MeTHF, the entire solvent system can be extracted quickly, leading to the supersaturation of the perovskite wet film,

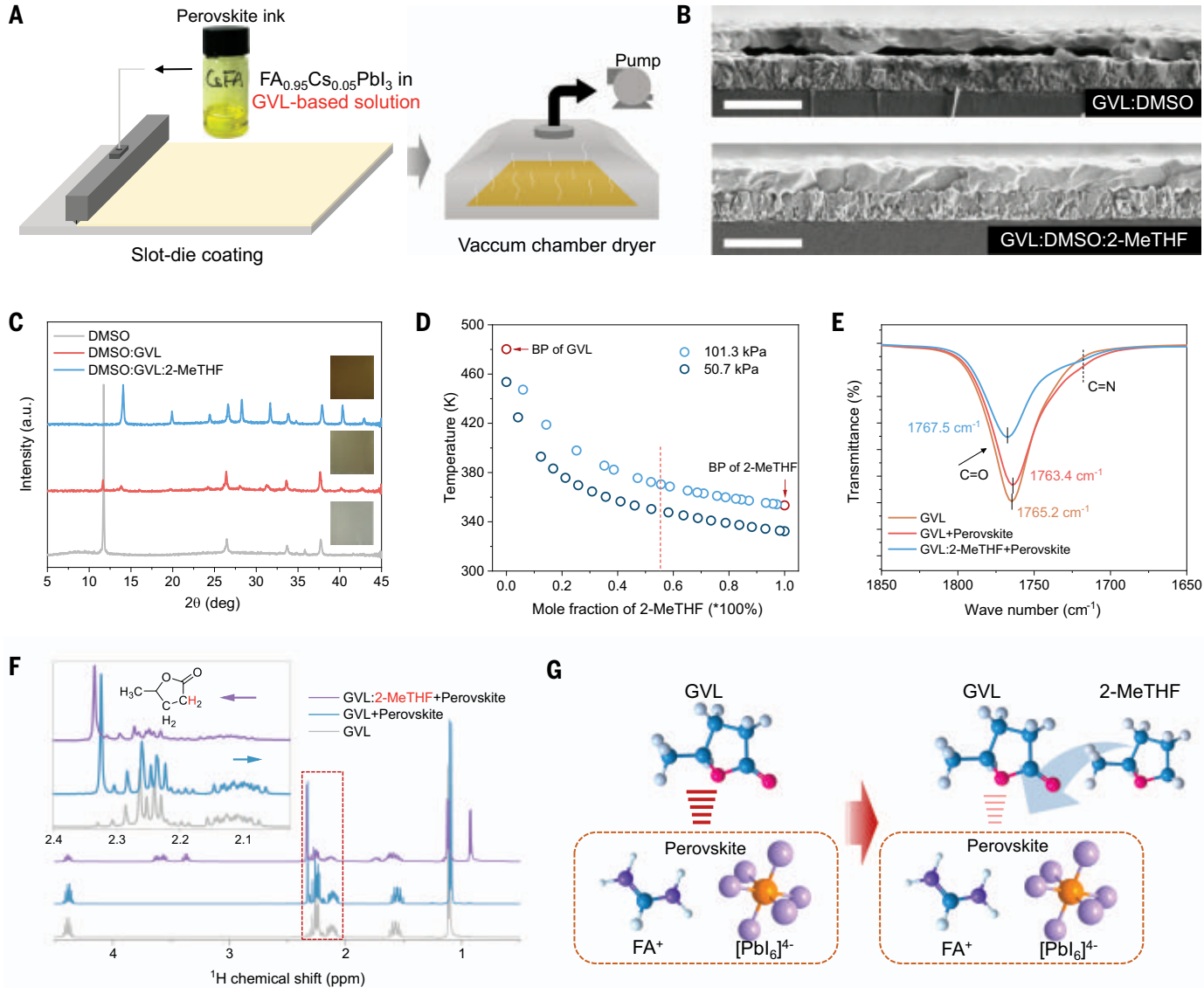


Fig. 1. Perovskite preparation with GVL/DMSO/2-MeTHF mixed solvent system. (**A**) Schematic demonstrating large-scale fabrication of perovskite films with slot-die coating and VCD. Digital image of a perovskite ink composed of $FA_{0.95}Cs_{0.05}PbI_3$ dissolved in GVL/DMSO mixture. (**B**) Cross-sectional SEM of the perovskite films fabricated from GVL/DMSO (top panel) and GVL/DMSO/2-MeTHF mixtures (bottom panel). The scale bars represent a length of 1 μm. (**C**) XRD patterns of intermediate perovskite films after VCD processing (insets show digital images of the films). (**D**) Isobaric vapor-liquid equilibria of GVL/2-MeTHF mixture at $p = 101.3$ and 50.7 kPa (*43*). The red dashed line represents the optimized molar ratio of 2-MeTHF (~0.545). BP, boiling point. (**E** and **F**) FTIR spectra (E) and ^{1}H-NMR spectra (F) of perovskite dissolved in GVL and GVL/2-MeTHF. (**G**) Schematic showing coordination of GVL and 2-MeTHF to perovskite.

improved nucleation dynamics, and ultimately, reduced presence of voids at the buried interface. The increased volatility of 2-MeTHF also enabled a wider processing window under VCD. Therefore, despite varying VCD durations, the 7200-cm^2 perovskite films exhibited consistent quality (fig. S6), which can be translated to area tolerance, too.

With the volume ratio of 2-MeTHF increasing up to 70% in the perovskite ink, the precursor solution began to precipitate (fig. S7). The perovskite ink with a 2-MeTHF volume ratio <70% demonstrated excellent stability after 10-day aging under ambient-air conditions, rendering it suitable for high-volume disposable preparation in manufacturing. This excellent ink stability is largely attributed to GVL, which can strongly interact with FA^+ cations (*39*). Upon the addition of 2-MeTHF into perovskite ink, colloidal particles increased in size as shown by dynamic light scattering, and PbI_2-DMSO and PbI_2-GVL complexes weakened as shown by ultraviolet (UV)–visible spectra (fig. S8) (*44*).

Scanning electron microscopy (SEM) analysis of perovskite films revealed a progressive enlargement of the average grain size with increased 2-MeTHF content (fig. S9). We reason that introducing the volatile and noncoordinating 2-MeTHF rapidly reduces the precursor solubility, thereby promoting nucleation of the desired α phase while simultaneously suppressing δ phase. Meanwhile, residual DMSO facilitates the growth of the α-phase nuclei (fig. S10). Through characterization of film crystallinity and optical properties, we identified that the perovskite film fabricated with a 50% volume ratio of 2-MeTHF demonstrated optimal properties, exhibiting both the highest crystallinity and the strongest light absorption (fig. S11). Although the perovskite ink with 70% 2-MeTHF produced large grains, it also exhibited a large fraction of nonperovskite phase, likely because this ink was at a critical threshold at which the ink becomes turbid.

To elucidate the crystallization mechanism mediated by 2-MeTHF, we analyzed x-ray diffraction (XRD) patterns of intermediate perovskite films fabricated with different solvents immediately after VCD processing (Fig. 1C). The intermediate film prepared with pure DMSO exhibited a fully coordinated complex, whereas the DMSO/GVL system produced a mixture of the complex and α-phase perovskite micronuclei. The higher volatility facilitated by the introduction of 2-MeTHF into the DMSO/GVL system induces supersaturation rapidly and appears to increase the nucleation barrier for δ phase (fig. S10). As a result, α-phase nuclei can grow into phase-pure high-quality crystals during subsequent annealing.

To reveal how the incorporation of 2-MeTHF can accelerate perovskite nucleation, we examined the isobaric vapor-liquid equilibria of GVL/2-MeTHF and identified that the introduction of 2-MeTHF substantially depressed the boiling point of GVL, thereby enhancing the volatility of the solvent system (Fig. 1D) (*45*). Interestingly, this temperature is slightly higher than that of pure 2-MeTHF, suggesting that 2-MeTHF facilitated GVL volatilization. We then used Fourier transform infrared (FTIR) spectroscopy to investigate solvent-perovskite interactions (Fig. 1E). Compared with pure GVL, the perovskite-GVL solution exhibited weakened C=O bond resonance along with a blue-shifted absorption peak, indicating coordination between the carbonyl group of GVL and the perovskite building blocks. However, when 2-MeTHF was introduced, the C=O resonance has redshift, suggesting weakened interaction with perovskite.

Proton nuclear magnetic resonance (^{1}H-NMR) spectra (Fig. 1F and fig. S12) of perovskite inks revealed upfield shifts for both the CH proton of GVL and the NH proton of FA^+ when dissolved together, compared with pure GVL or FAI, indicating interaction between the FA^+ cation and GVL. A similar behavior was found when incorporating GVL to DMSO-only ink, indicating even stronger solvent-precursor interactions. However, upon incorporating 2-MeTHF, these proton signals shifted downfield, indicating a weakening of FA^+-GVL interactions. In Fig. 1G, we propose 2-MeTHF incorporation mechanism derived from the discussed experimental results: 2-MeTHF reduces perovskite-GVL coordination, thereby promoting GVL extraction during VCD and annealing, which then efficiently improve interfacial contact and crystallization of the perovskite films.

Solvent-confinement edge protection

We observed that when the perovskite ink was coated on the substrate before VCD-assisted solvent extraction, a spontaneous volatilization of solvent at the gas-solid-liquid boundary triggered crystallization at the edges of the film (fig. S13). This phenomenon is likely caused by the rapid volatilization induced by 2-MeTHF incorporation, which narrows the processing window, as seen by shrinkage of absorption profile of intermediate phase (fig. S14); this makes it challenging to achieve a consistent film quality (*46*, *47*). Such morphological defects pose a challenge in the fabrication of large-area perovskite films, as the poor crystallinity at the periphery adversely affects the total-area performance of commercial PV modules. Therefore, we pursued the SCEP strategy by adding trimethyl-tetradecylammonium chloride (TAC) into the perovskite ink. TAC, a surfactant molecule containing both hydrophilic and hydrophobic functional groups, can self-assemble at the solution's surface, thereby modulating the ink's surface tension and the crystallization kinetics (*48*).

To investigate the surface tension and the evolution of solvent volatilization, a perovskite ink droplet was deposited on an FTO/NiO_x substrate under ambient conditions (Fig. 2A). The initial contact angle of the perovskite ink with TAC was lower than that of the control ink, indicating a reduction of surface tension by TAC. During the initial stage of droplet deposition, interfacial wetting at the solid-liquid boundary dominated over solvent evaporation. As the solid-liquid interface progressively stabilized, the predominant mechanism shifted to solvent evaporation at the liquid-vapor interface. Because of the rapid evaporation at the edge of the control droplet, solution concentration gradually increased at the periphery, leading to an increased contact angle. By contrast, the droplet with TAC exhibited suppressed edge evaporation, demonstrating uniform volatilization across the entire gas-liquid interface and a progressively decreasing contact angle (fig. S15). By orienting hydrophobic groups toward the air, the TAC molecules balanced solution flow from the droplet's surface to the droplet's bulk through surfactant-induced Marangoni effect, thus leading to uniform areas at the edges of large-area films (*48*, *49*). This phenomenon also delayed solvent volatilization at the gas-liquid-solid boundaries (Fig. 2B).

X-ray photoelectron spectroscopy (XPS) of SCEP perovskite films exhibited a C 1s peak at 286.39 eV (fig. S16), attributed to long carbon chains, along with a concomitant N 1s peak at 402.51 eV, corresponding to the amine group from TA^+. No detectable Cl XPS signal was observed on the surface. Time-of-flight secondary ion mass spectrometry revealed a significant reduction in TA^+ distribution from the top surface to the bottom surface of perovskite films. The graded distribution of TA^+ residues from the top surface to the bottom interface of perovskite indicates that TA^+ is predominantly localized at the perovskite surface, where it passivates defects and thus enhances film quality.

To verify the influence of the SCEP strategy on charge-carrier mobility and diffusion length in perovskite films, we performed femtosecond-resolved optical-pump terahertz-probe spectroscopy (*50*). Terahertz photons with energies below the semiconductor bandgap allow the exclusive investigation of free-carrier dynamics by circumventing interband excitation. Concomitantly, the picosecond-period terahertz field drives carriers efficiently when its oscillation frequency resonates with the characteristic momentum relaxation rate. The resultant carrier acceleration is limited by the rate of energy dissipation via inelastic scattering. Figure 2, C and D, illustrates the transient terahertz transmission dynamics for control and SCEP thin films (~600-nm thickness) under varying pump fluences. An 800-nm (1.55-eV) laser with a ~5-mm spot diameter served as the optical pump, and sub-picosecond terahertz pulses probed photoinduced conductivity changes. By using a reduced optical-pump energy in conjunction with terahertz probe

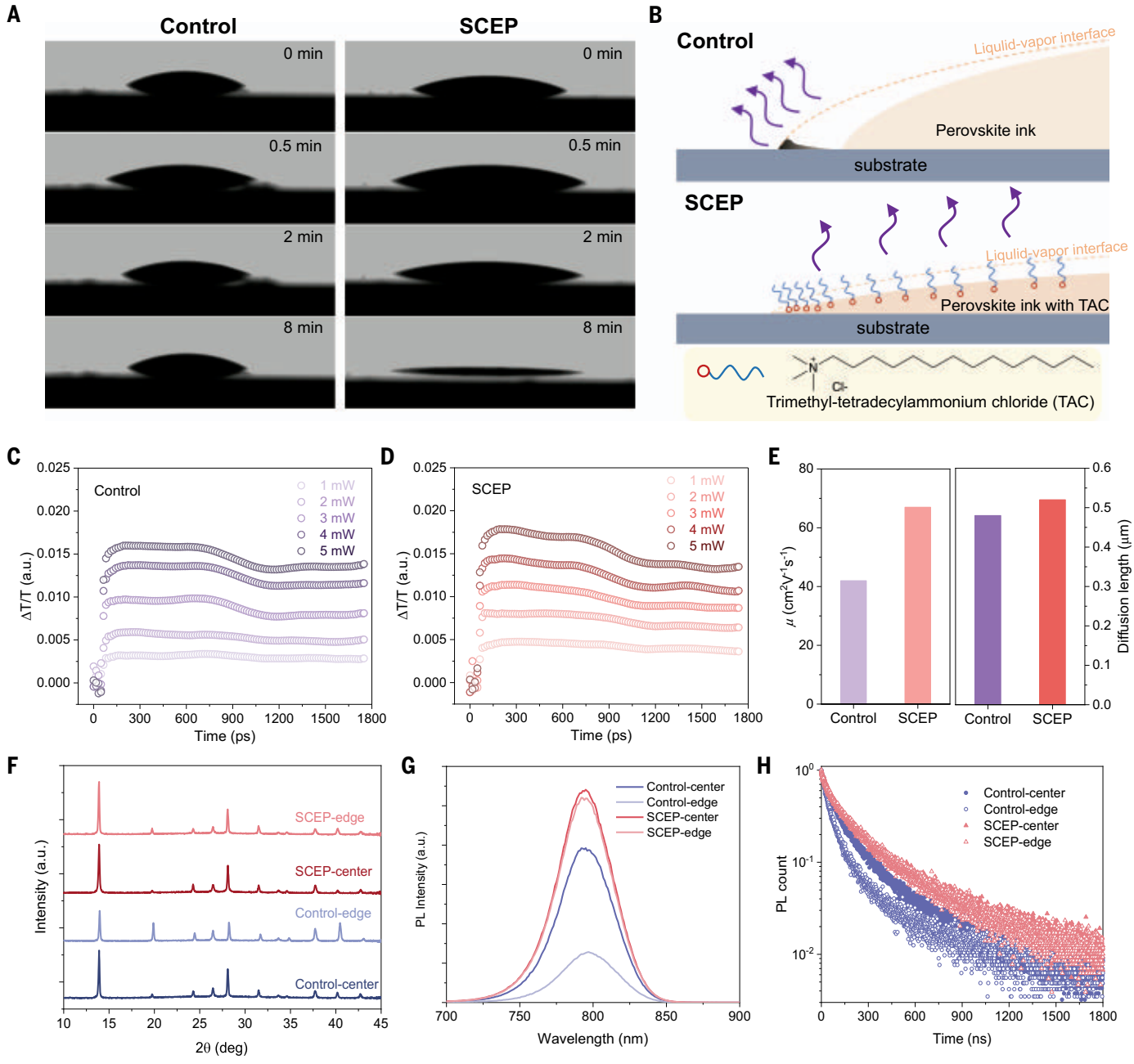


Fig. 2. Characterization of perovskite films. (**A**) Contact-angle images of the control and SCEP perovskite ink droplets. (**B**) Schematic illustrating solvent evaporation of the perovskite wet film. (**C** and **D**) Free-carrier dynamics of the control (C) and SCEP (D) perovskite films based on terahertz measurement. (**E**) Mobilities (left) and diffusion lengths (right) of the control and SCEP perovskite films based on terahertz analysis. (**F** to **H**) XRD patterns (F), steady-state PL spectra (G), and time-resolved PL traces (H) of control and SCEP perovskite films from center and edge regions.

radiation, we enhanced the accuracy in determining carrier mobility and diffusion length parameters. This approach minimizes thermal perturbations and associated hot-carrier effects during the measurements. The recombination rate constants and charge-carrier mobilities for control and SCEP samples were calculated to be 42 and 67 $cm^2\ V^{-1}\ s^{-1}$, respectively (supplementary text 1, fig. S17, and table S1). Terahertz time-resolved spectroscopy revealed longer carrier lifetimes in the SCEP film, leading to an increased diffusion length of 0.54 μm extracted from the terahertz measurements, compared with 0.48 μm for the control film (Fig. 2E). These findings suggest that the SCEP perovskite film demonstrated improved crystallization quality and reduced nonradiative recombination.

The perovskite ink prepared by SCEP strategy exhibited two benefits: (i) substantial extension of the processing window during ink deposition before VCD (fig. S18) and (ii) significant improvement in film uniformity through effective suppression of defective edge formation (fig. S19). SEM images showed poorly defined surface morphology in the central region of a 120-cm–by–60-cm control perovskite film and small grains accompanied by voids on the edges (fig. S20). Atomic force microscopy similarly showed an increased surface roughness at the periphery of the control sample (fig. S21). The SCEP strategy instead resulted in a similar morphology within all regions of the target film, as well as an overall increase of grain size. The perovskite film fabricated with the SCEP strategy demonstrated notable thickness uniformity,

exhibiting an average thickness of 393 nm with a thickness variation of only 6.5% across the entire 30-cm–by–40-cm substrate area. By contrast, the control film showed substantial thickness reduction (average thickness of 338 nm), particularly at the substrate edges (fig. S22).

We then compared the crystallinity uniformity and photophysical properties of the control and SCEP perovskite films. The SCEP perovskite film demonstrated consistent crystallinity and a predominant (100) crystallographic orientation throughout both the central and edge regions. By contrast, the control film exhibited reduced crystallinity and disordered orientation at the edge region (Fig. 2F). Although we did not find that TAC promotes the formation of low-dimensional perovskites, it still enhanced the crystallographic orientation of perovskite films (fig. S23). To investigate the photophysical properties of the control and SCEP perovskite films, we compared the steady-state photoluminescence (PL) and time-resolved PL lifetimes at the central and edge regions. The steady-state PL emission of the SCEP perovskite film measured from both central and edge regions were identically strong and higher than those of the control film (Fig. 2G). The PL decay lifetimes (τ) probed from both regions of the SCEP perovskite film were similar (τ = 277 ns from center and τ = 247 ns from edge) and longer than those of the control film (τ = 186 ns from center and τ = 130 ns from edge) (Fig. 2H and table S2).

Performance of PV modules

Perovskite PV modules were fabricated in a FTO/NiO_x/perovskite/C_{60}/SnO_2/Cu architecture. For this, perovskite films were first deposited on P1-patterned FTO/NiO_x substrates, followed by the deposition of charge-selective layers, including fullerene (C_{60}) and tin oxide (SnO_2). Subsequent processing steps involved laser scribing for cell interconnection, electrode deposition, and encapsulation. The perovskite layer was fabricated under ambient conditions, whereas other functional layers were deposited via vacuum processes (fig. S24).

To reconfirm the optimum content of 2Me-THF in perovskite inks, we made 1017.5-cm^2 control modules and measured their performance (fig. S25). In line with studies described above, the perovskite ink with

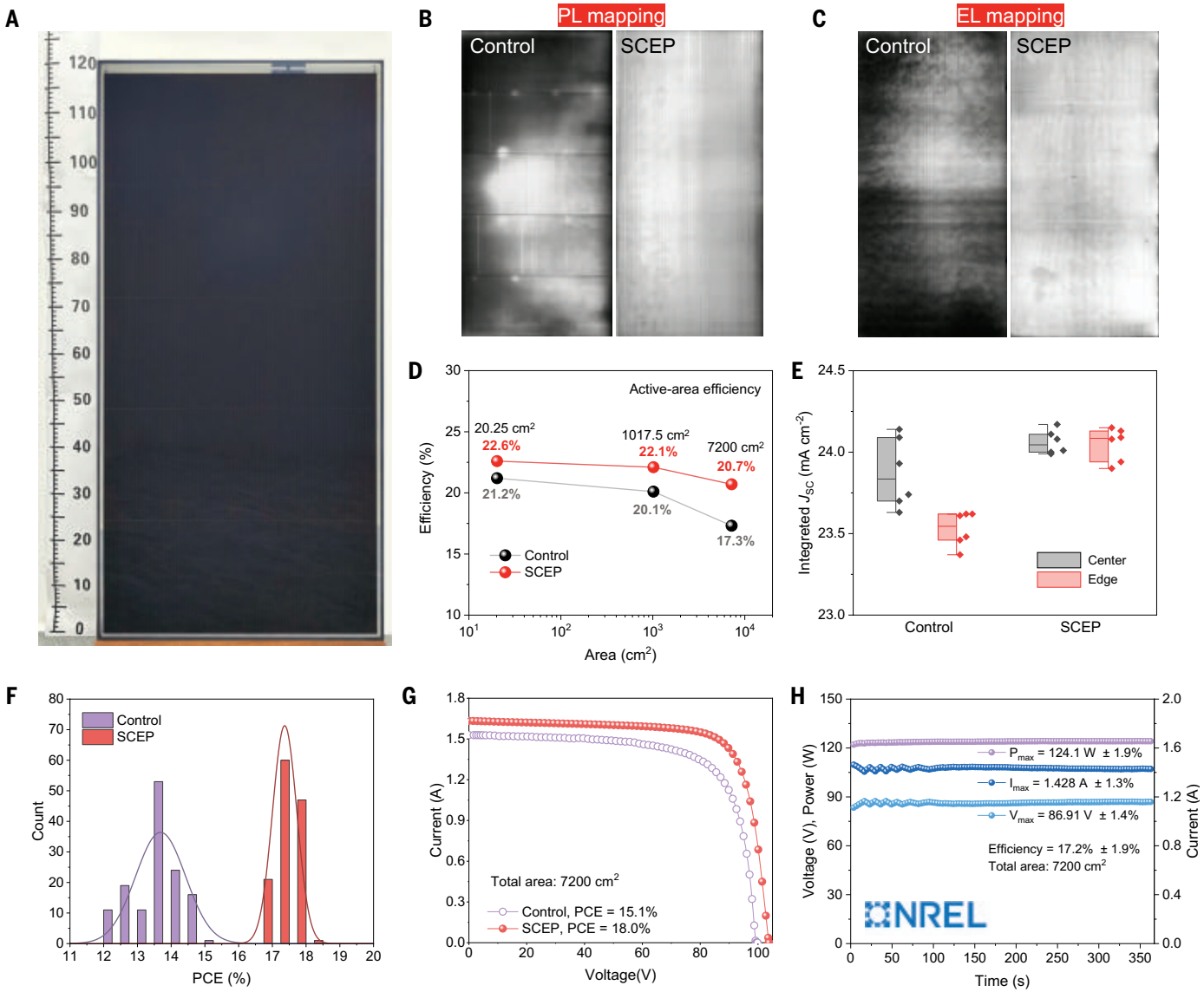


Fig. 3. Performance of commercial-scale perovskite PV modules (120 by 60 cm^2). (**A**) Image of a module. (**B** and **C**) PL (B) and EL (C) mapping of control and SCEP modules. (**D**) Comparison of active-area efficiencies between the champion 20.25-, 1017.5-, and 7200-cm^2 modules. (**E**) Comparison of the integrated J_{SC} values from center and edge regions in control and SCEP modules. (**F**) Statistical histogram of total-area module PCEs for control and SCEP modules. (**G**) J-V curves of the best-performing control and SCEP modules with a total area of 7200 cm^2. (**H**) NREL-certified stabilized P_{max}, I_{max}, and V_{max} plots within 360 s for a module.

50% 2Me-THF volume ratio showed the highest PCE. We then compared TAC with other surfactants, such as sodium dodecyl sulfate, Tween 60, and Triton X-100, all of which achieved the desired uniformity (figs. S22 and S26) and similar crystallinity (figs. S23A and S26C), but TAC remained the champion surfactant (fig. S26D). We hypothesize that this is due to the cationic nature of TAC, which allows it to perform passivation functions while regulating the wet-film flows (*51*–*53*). Through systematic study of TAC loading in the perovskite ink, we found a TAC concentration of 0.2 g liter^{-1} to show the highest PV performance (fig. S27).

Figure 3A shows an encapsulated 120-cm–by–60-cm commercial-scale perovskite PV module. To evaluate the effect of SCEP in these modules, we conducted PL and electroluminescence (EL) mapping (Fig. 3, B and C). The results demonstrate that the SCEP strategy achieved more uniform and enhanced radiative emission compared with the control modules.

The SCEP perovskite modules with aperture areas of 20.25 and 1017.5 cm^2 achieved champion PCEs of 21.9 and 21.4%, respectively (fig. S28), whereas the control modules achieved PCEs of 20.6 and 19.5%. The best-performing commercial-scale module achieved a PCE of 18.0% with a full area of 7200 cm^2 as measured in the laboratory (Table 1). Given the geometric fill factors (FFs) of 97% for both 20.25- and 1017.5-cm^2 modules and 87.1% for 7200-cm^2 modules, the corresponding active-area PCE values were calculated to be 22.6, 22.1, and 20.7%, respectively (Fig. 3D). This minimal performance gap, despite substantially upscaling the module areas, demonstrates the scalability of the technology from laboratory- to commercial-scale PV modules.

The integrated short-circuit current density (J_{SC}) values of the control and SCEP modules were similar (24.1 versus 24.2 mA cm^{-2}), as derived from external quantum efficiency spectral analysis (fig. S29). However, when comparing the integrated J_{SC} between the central and edge areas (fig. S30), the SCEP modules showed improved spatial uniformity over the control modules (Fig. 3E), directly enhancing the performance and reproducibility of large-scale PV modules (fig. S31).

We conducted a statistical analysis of 127 PV modules using the SCEP strategy manufactured within a single production day, revealing a normal distribution of output power with an average value of 125 W (fig. S32). Statistical comparison between the control and SCEP modules revealed that the SCEP devices exhibited significant performance enhancement as well as improved reproducibility (Fig. 3F). The best-performing PV characterization results, as presented in Fig. 3G, revealed that the SCEP-optimized module achieved a full-area PCE of 18.0% under reverse scan conditions, with the following corresponding parameters: open-circuit voltage (V_{OC}) of 104 V, short-circuit current (I_{SC}) of 1.63 A, and FF of 76.5%. By contrast, the control module exhibited a lower PCE of 15.1%. After testing in the lab, we sent the 18.0% efficiency SCEP module to NREL, where it achieved a certified stabilized efficiency of 17.2% with a full device area of 7200 cm^2 (Fig. 3H), designating it a total-area certified commercial perovskite PV module (fig. S33) (*54*).

Table 1. PV performance of control and SCEP perovskite modules with aperture area of 1017.5 cm^2 or total area of 7200 cm^2. Module number of control and SCEP for the error bars are 135 and 129, respectively. Means are shown with standard deviations.

		V_{OC} (V)	I_{SC} (A)	FF (%)	PCE (%)
1017.5 cm^2 (aperture area)	**Control**	47.8 ± 0.4	0.547 ± 0.003	71.4 ± 2.3	18.4 ± 0.75
	SCEP	49.2 ± 0.1	0.562 ± 0.002	77.0 ± 0.8	20.9 ± 0.29
7200 cm^2 (total area)	**Control**	94.1 ± 4.0	1.500 ± 0.025	69.9 ± 2.7	13.7 ± 0.74
	SCEP	104.0 ± 1.1	1.620 ± 0.013	74.2 ± 1.2	17.4 ± 0.36

Reliability of the perovskite PV modules

IEC 61215 is an international standard in PV industry, primarily designed to assess the reliability and safety of commercial PV modules. Leveraging optimized edge properties and enhanced crystallization quality, SCEP modules exhibited significant improvements across all reliability metrics evaluated under IEC standards. Thus, we have completed all required tests by these standards, as certified by the Technical Inspection Association TÜV Rheinland (fig. S34).

Although long-term maximum power point tracking (MPPT) stability is not included in the IEC 61215 test sequences, it serves as a critical indicator of module reliability under real-world operating conditions. As demonstrated in Fig. 4A, SCEP modules exhibited enhanced operational stability, retaining 97.2% of their initial PCE after 1050 hours of continuous MPPT operation under 1 sun illumination (AM1.5G) at the module temperature of ~60°C (fig. S35). By contrast, control modules experienced substantial degradation, losing nearly 20% relative to their initial PCE under identical testing conditions. We also performed additional MPPT testing under a controlled steady temperature (65°C) (fig. S36): The SCEP module again showed a superior stability when compared with control after 200 hours.

Then, we assessed the devices against all tests specified by the IEC 61215 standards, including the damp heat test, thermal cycling, and ultraviolet (UV) preconditioning test, among others (fig. S37 and supplementary text 2). The SCEP module maintained its initial performance after an outdoor exposure test with a cumulative solar irradiation of 70 kilowatt-hours (kWh) m^{-2} (fig. S38). Under UV preconditioning conditions, the SCEP module maintained 96.1% of its initial performance after exposure to 36 kWh m^{-2} of total solar irradiation (Fig. 4B), exceeding the IEC 61215 standard requirement by more than twofold. By contrast, the control module maintained only 72.1% of their initial PCE under identical test conditions.

Figure 4C presents the results of the thermal cycling test conducted between −40° and +85°C, with current flow. The SCEP modules exhibited no degradation in the thermal cycling test without current and retained 97.5% of its initial performance after 200 cycles with current (fig. S39). With current, the control modules exhibited substantial degradation after 50 cycles, with their PCE dropping to only 69% of the initial value. Figure 4D presents damp heat test results (85°C and 85% relative humidity), in which the SCEP module maintained 100% of its initial PCE after 1000 hours. Control modules, however, degraded to 73.4% PCE after 1000 hours and further declined to 60.9% after 2000-hour aging (fig. S40).

Post-aging characterization revealed edge-initiated degradation in control modules (fig. S41), indicating that the initially visible poor crystal formation of the perovskite film at module edges accelerates performance deterioration. We further characterized the modules through EL mapping before and after damp heat, MPPT, thermal cycling, UV tests, and light-induced degradation aging tests (fig. S42). The control modules exhibited significant contrast variations in their EL images, with these pronounced changes directly correlating to their observed performance degradation. We hence hypothesize that the main degradation mechanism in control PV modules is poor crystallization and uniformity, especially on the edges.

We also evaluated the stability of perovskite/C_{60} interfaces by exposing these stacks to ambient air for 6 hours (fig. S43): The reduced absorption and the appearance of δ-phase peak in the control film indicate that it underwent a noticeable degradation; by contrast, the film including TAC remained stable under the same exposure.

The temperature coefficient of efficiency for the perovskite PV modules was measured at −0.11% per °C, versus an approximate range of −0.29 to −0.39% per °C for crystalline silicon PV modules (Fig. 4E) (*55*). Figure 4F illustrates the results of the hot-spot endurance test. The performance of the module decreased to 87.6% of its initial efficiency after a 3-hour shading condition but subsequently recovered to its original efficiency, demonstrating its robust self-healing capability, which enables the

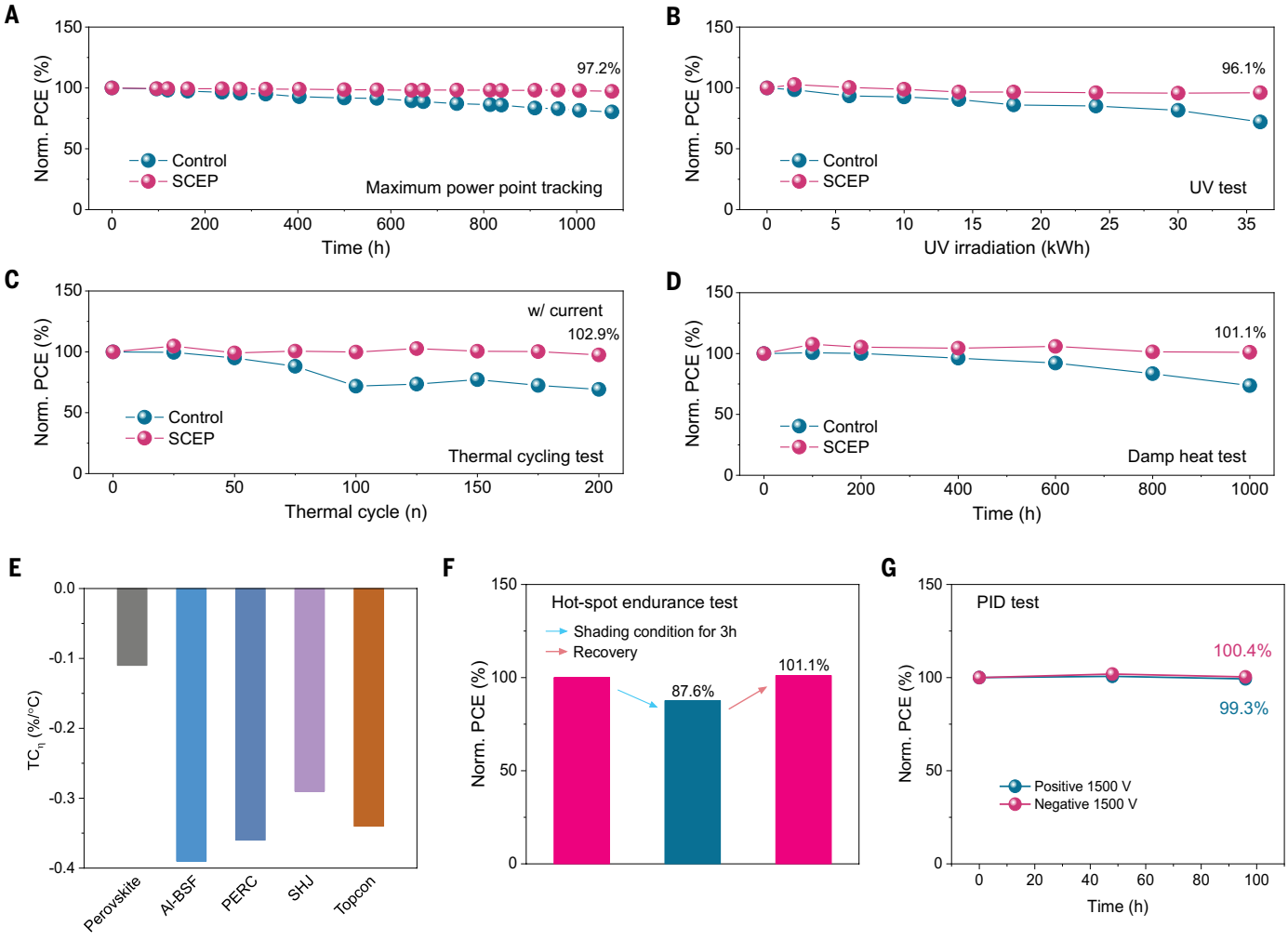


Fig. 4. Reliability tests of commercial perovskite PV modules following IEC 61215:2021 standards. (**A**) Continuous MPPT of encapsulated modules over 1000 hours under full simulated AM1.5G illumination in ambient air with a humidity of 30 to 50%. The modules reached 60° to 65°C during the MPPT. (**B**) UV preconditioning test with a cumulative UV irradiation of 36 kWh m^{-2}. (**C**) Thermal cycling test from −40° to 85°C with or without current. (**D**) Damp heat test at 85°C and 85% RH conditions. RH, relative humidity. (**E**) TC comparison between perovskite modules and various types of crystalline silicon modules (*56*,*57*). Al-BSF, aluminum back surface field; PERC, passivated emitter and rear cell; SHJ, silicon heterojunction; TC, temperature coefficient. (**F** and **G**) Hot-spot endurance test (F) and PID test (G) of commercial-scale perovskite modules.

modules to effectively handle real-world challenges such as temporary shadowing from surrounding objects.

Additionally, potential-induced degradation (PID), a newly added requirement in the IEC 61215:2021 standard, was evaluated. We applied a high voltage of 1500 V, both negative and positive, to the module for >90 hours (Fig. 4G). The results showed no significant degradation, confirming the module's ability to maintain safe, stable, and efficient operation in PV power plants under high-voltage stress conditions.

We continuously monitored the daily power generation performance of the perovskite PV power station from October 2024 to August 2025 (fig. S44): The system demonstrated notably stable power output. We compared one perovskite panel within the PV station with a tunnel oxide passivated contact (TOPCon) silicon PV panel from November 2024 to August 2025. Both panels maintained consistent power generation, but when temperatures exceeded 30°C in the summer, the perovskite panel not only sustained its stable performance but showed higher power-generation output than the TOPCon panel. This comparison with a well-established technology indicates a commercial viability of perovskite solar modules.

We developed eco-friendly perovskite inks by engineering a green solvent system comprising 2-MeTHF, GVL, and DMSO, which precisely modulates solvent coordination and evaporation kinetics. To enable large-scale fabrication, we introduced the surfactant TAC to homogenize solvent evaporation and enhance perovskite crystallization uniformity, achieving a certified 17.2% efficiency on a commercial-scale module (7200 cm^2) and meeting all IEC61215 reliability standards (independently verified by TÜV Rheinland). By replacing toxic solvents (DMF/NMP) with the sustainable formulation, we simultaneously addressed environmental and scalability challenges while maintaining high performance. Furthermore, the SCEP strategy synergizes with optimized solvent volatility to deliver film uniformity at meter scale, overcoming a critical limitation of conventional approaches.

REFERENCES AND NOTES

1. A. Kojima, K. Teshima, Y. Shirai, T. Miyasaka, *J. Am. Chem. Soc.* **131**, 6050–6051 (2009).
2. H. S. Kim *et al.*, *Sci. Rep.* **2**, 591 (2012).
3. N. J. Jeon *et al.*, *Nat. Mater.* **13**, 897–903 (2014).
4. W. S. Yang *et al.*, *Science* **348**, 1234–1237 (2015).
5. Z. Li *et al.*, *Joule* **2**, 1559–1572 (2018).
6. L. Meng, J. You, Y. Yang, *Nat. Commun.* **9**, 5265 (2018).
7. S. Li *et al.*, *Nature* **635**, 82–88 (2024).
8. S. Liu *et al.*, *Nature* **632**, 536–542 (2024).

9. Y. Yang *et al.*, *Science* **386**, 898–902 (2024).
10. C. Ballif, F.-J. Haug, M. Boccard, P. J. Verlinden, G. Hahn, *Nat. Rev. Mater.* **7**, 597–616 (2022).
11. H. Zhu *et al.*, *Nat. Rev. Mater.* **8**, 569–586 (2023).
12. Y. Rong *et al.*, *Science* **361**, eaat8235 (2018).
13. K. J. Prince *et al.*, *Nat. Mater.* **24**, 22–33 (2025).
14. C. Duan *et al.*, *Nat. Energy* **10**, 318–328 (2024).
15. Y. Hu *et al.*, *Joule* **3**, 2076–2085 (2019).
16. H. J. Snaith, P. Hacke, *Nat. Energy* **3**, 459–465 (2018).
17. M. Saliba *et al.*, *Energy Environ. Sci.* **9**, 1989–1997 (2016).
18. C. Zhang *et al.*, *J. Mater. Chem. A Mater. Energy Sustain.* **9**, 1372–1394 (2021).
19. Y. Deng *et al.*, *Sci. Adv.* **5**, eaax7537 (2019).
20. Y. Deng *et al.*, *Nat. Energy* **6**, 633–641 (2021).
21. T. Bu *et al.*, *Science* **372**, 1327–1332 (2021).
22. B. J. Kim *et al.*, *ACS Sustain. Chem.& Eng.* **12**, 13371–13381 (2024).
23. H. Wang *et al.*, *Nature* **634**, 1091–1095 (2024).
24. D. Prat *et al.*, *Green Chem.* **18**, 288–296 (2016).
25. N. G. Park, K. Zhu, *Nat. Rev. Mater.* **5**, 333–350 (2020).
26. Z. Li *et al.*, *Nat. Rev. Mater.* **3**, 18017 (2018).
27. Q. Q. Chu *et al.*, *Matter* **6**, 3838–3863 (2023).
28. S. Ma *et al.*, *Energy Environ. Sci.* **15**, 13–55 (2022).
29. L. Shi *et al.*, *Science* **368**, eaba2412 (2020).
30. Z. Li *et al.*, *Science* **376**, 416–420 (2022).
31. J. Liu *et al.*, *Science* **377**, 302–306 (2022).
32. T. Matsui *et al.*, *Adv. Mater.* **31**, e1806823 (2019).
33. A. Mei *et al.*, *Joule* **4**, 2646–2660 (2020).
34. S. Chen *et al.*, *Science* **373**, 902–907 (2021).
35. M. V. Khenkin *et al.*, *Nat. Energy* **5**, 35–49 (2020).
36. S. Hyun Park, I. Su Jin, J. Woong Jung, *Chem. Eng. J.* **425**, 131475 (2021).
37. A. J. Doolin *et al.*, *Green Chem.* **23**, 2471–2486 (2021).
38. K. Xiao *et al.*, *Science* **376**, 762–767 (2022).
39. Y. Miao *et al.*, *Nat. Sustain.* **6**, 1465–1473 (2023).
40. G. Zhang *et al.*, *Sci. Adv.* **10**, eadl6398 (2024).
41. B. Yan *et al.*, *Science* **388**, eadt5001 (2025).
42. M. Wang, C. Fei, M. A. Uddin, J. Huang, *Sci. Adv.* **8**, eabo5977 (2022).
43. B. M. Gallant *et al.*, *Nat. Commun.* **15**, 10110 (2024).
44. S. Rahimnejad, A. Kovalenko, S. M. Forés, C. Aranda, A. Guerrero, *Chemphyschem* **17**, 2795–2798 (2016).
45. M. Al-Lami, D. Havasi, B. Batha, É. Pusztai, L. T. Mika, *J. Chem. Eng. Data* **65**, 3063–3071 (2020).
46. Z. Yang *et al.*, *Sci. Adv.* **7**, eabg3749 (2021).
47. M. Yang *et al.*, *Nat. Energy* **2**, 17038 (2017).
48. Y. Deng *et al.*, *Nat. Energy* **3**, 560–566 (2018).
49. K. Liu *et al.*, *Joule* **4**, 2404–2425 (2020).
50. R. Lin *et al.*, *Nat. Energy* **4**, 864–873 (2019).
51. N. Saito, A. Urayama, M. Ikezawa, Y. Kondo, *Adv. Mater. Interfaces* **9**, 2101836 (2022).
52. X. Zheng *et al.*, *Nat. Energy* **2**, 17102 (2017).
53. W.-Q. Wu *et al.*, *Sci. Adv.* **5**, eaav8925 (2019).
54. M. A. Green *et al.*, *Prog. Photovolt. Res. Appl.* **33**, 3–15 (2025).
55. T. Moot *et al.*, *ACS Energy Lett.* **6**, 2038–2047 (2021).
56. S. M. F. Zhang *et al.*, *Nano Energy* **98**, 107221 (2022).
57. J. Haschke *et al.*, *Energy Environ. Sci.* **10**, 1196–1206 (2017).

ACKNOWLEDGMENTS

Funding: National Key R&D Program of China (2022YFB4200304 to H.T.); National Science Fund for Distinguished Young Scholars (T2325016 to H.T.); Distinguished Scholar of National Science Fund of China (no. 12225511 to C.C.); Major Project T2241002 (to C.C.); National Natural Science Foundation of China (U21A2076 to H.T.); Natural Science Foundation of Jiangsu Province (BK20232022, BK20233001, BE2022021, and BE2022026 to H.T.); Fundamental Research Funds for the Central Universities (0213/14380206 and 0205/14380252 to H.T.); Frontiers Science Center for Critical Earth Material Cycling Fund (DLTD2109 and 2024ZD06 to H.T.); Program for Innovative Talents and Entrepreneur in Jiangsu, China Postdoctoral Science Foundation (2023M731579 to K.X.); Jiangsu Funding Program for Excellent Postdoctoral Talent (2023ZB348 to K.X.); Postdoctoral Innovative Talents Support Project from the China Postdoctoral Science Foundation (BX20230157 to K.X.); Canada Research Chair's program (CRC-2024-00264 to M.I.S.); German Research Foundation (SPP2196 and 431314977/GRK 2642 to M.S.); European Research Council under the Horizon program (LOCAL-HEAT, 101041809 to M.S.); Deutsche Forschungsgemeinschaft (DFG) (ATLAS - Advancing Technologies for Low-Altitude Satellites) (516238647 - SFB1667/1 to M.S.). **Author contributions:** Conceptualization: H.T., K.X.; Methodology: Y.W., Y.L., X.L.; Module fabrication and certification: Y.W., Y.L., X.L., K.X.; Material characteristics: D.X., C.D., H.S., G.D., J.L., C.C., W.O., Y.L., J.H., M.L., H.G., Z.C.; Outdoor test data analysis: W.Z., N.T., M.S.; Outdoor PV station construction: T.L., Y.Y., L.J.; Solvent chemistry analysis: V.M.-A., M.I.S.; Funding acquisition: H.T., K.X., C.C., M.I.S.; Project administration: H.T., K.X.; Supervision: H.T., K.X., C.C.; Writing – original draft: Y.W., K.X., V.M.-A., M.I.S., C.C., H.T.; Writing – review & editing: Y.W., Y.L., X.L., K.X., V.M.-A., M.I.S., C.C., H.T. **Competing interests:** A patent application (2025116572244) based on this work has been submitted by Nanjing University and Renshine Solar (Suzhou) Co., Ltd.; H.T. is the founder, chief scientific officer, and chairman of Renshine Solar (Suzhou) Co., Ltd., a company that is commercializing perovskite PVs. The other authors declare that they have no conflict of interest. **Data and materials availability:** All data needed to evaluate the conclusions in the paper are present in the paper or the supplementary materials. **License information:** Copyright © 2025 the authors, some rights reserved; exclusive licensee American Association for the Advancement of Science. No claim to original US government works. https://www.science.org/about/science-licenses-journal-article-reuse

SUPPLEMENTARY MATERIALS

science.org/doi/10.1126/science.adz0091
Materials and Methods; Supplementary Text; Figs. S1 to S44; Tables S1 and S2; References (*58*–*63*)

Submitted 14 May 2025; accepted 16 October 2025

10.1126/science.adz0091

NEUTRINO PHYSICS

Constraints on lepton number violation with the 2 tonne · year CUORE dataset

CUORE Collaboration*†

Matter-antimatter asymmetry underlines the incompleteness of the current understanding of particle physics. Neutrinoless double-beta decay ($0\nu\beta\beta$) may help explain this asymmetry while unveiling the Majorana nature of the neutrino. The CUORE (Cryogenic Underground Observatory for Rare Events) experiment searches for $0\nu\beta\beta$ of ^{130}Te using a tonne-scale cryogenic calorimeter operated at milli-kelvin temperatures. We report no evidence of $0\nu\beta\beta$ and place a lower limit on the half-life of $T_{1/2} > 3.5 \times 10^{25}$ years (90% credibility interval) with over 2 tonne·years of TeO_2 exposure. The tools and techniques developed for this result and the 5-year stable operation of nearly 1000 detectors demonstrate crucial infrastructure for future-generation experiments capable of searching for $0\nu\beta\beta$ across multiple isotopes.

The abundance of baryonic matter in the observable Universe contrasts with the leading theories of particle physics (*1*). Cosmological models assume that matter and antimatter should have been created in equal amounts. When they come into contact with each other, they interact and leave behind only energy. As a result, the Universe should be composed of either equal amounts of matter and antimatter or none at all. However, observations contradict this hypothesis, indicating a fundamental asymmetry in the properties of matter and antimatter (*2*). Neutrinos, the least understood of the fundamental particles, may help resolve this impasse if they turn out to be Majorana fermions—indistinguishable from their own antiparticles (*3*).

Double-beta decay (usually labeled $2\nu\beta\beta$) (*4*) is a rare process in which two neutrons in a nucleus, with mass A and atomic number Z, convert into two protons with the emission of two electrons and two antineutrinos: $(A,Z) \rightarrow (A,Z+2) + 2e^- + 2\bar{\nu}_e$. If the neutrino is its own antiparticle, the process could leave matter as the only by-product: $(A, Z) \rightarrow (A, Z + 2) + 2e^-$. This version of the decay, so-called neutrinoless double-beta decay (labeled $0\nu\beta\beta$) (*5*), would imply that lepton number is not a conserved quantity in nature. As a lepton number violating process, discovery of $0\nu\beta\beta$ would lend support for the theory of leptogenesis in the early Universe, which by acting as a potential source of baryogenesis offers an explanation for the observed matter-antimatter asymmetry (*6*). Moreover, the absence of neutrinos from the decay products would not only confirm the Majorana nature of the neutrino but also help constrain the mass of this elusive particle. Currently, only $2\nu\beta\beta$ has been observed with half-life measurements in the range of $T^{2\nu}_{1/2} \sim 10^{19}$ to 10^{22} years (*1*, *7*–*10*).

Neutrinoless double-beta decay would potentially occur in the same isotopes that exhibit $2\nu\beta\beta$ (*11*). Experiments searching for $0\nu\beta\beta$ are designed to measure a monoenergetic peak at the Q value of the decay ($Q_{\beta\beta}$), which would indicate the emission of only two electrons that fully deposit their energies in the detector. Experimental sensitivity is maximized by increasing their measurement time and the mass of the $\beta\beta$ source under observation. When the background—energy measurements derived from unrelated phenomena—near $Q_{\beta\beta}$ is non-negligible, experiments must both minimize the background and optimize the detector energy resolution to distinguish the signal peak (*12*).

The use of cryogenic calorimeters for $0\nu\beta\beta$ searches was first proposed by Fiorini and Niinikoski in 1984 (*13*). In the following decades, the detection technique demonstrated excellent energy resolution (~0.1% in the mega–electron volt range), radiopurity control, and scalability to large masses (~1 tonne) (*14*, *15*). In this application, the calorimeter components consist of an absorber material primarily composed of a $\beta\beta$ source, a sensor to measure the temperature of the absorber, and a weak thermal coupling of the absorber to a heat sink. An example of a cryogenic calorimeter is shown in Fig. 1. When energy is released in the absorber, its temperature rise is proportional to the energy deposition and inversely proportional to its heat capacity. Because the heat sink serves to restore the detector to a base temperature, over time the energy deposition is represented by a pulse in the sensor readout. To have a measurable temperature rise, the absorber material is kept at very low temperatures (T ~ 10 mK), at which the heat capacity (C) is reduced. Diamagnetic and dielectric materials are preferred because their lattice-specific heat capacity, which follows the Debye law $C(T) \propto T^3$, is the only contribution, but the choice of the material is otherwise flexible. The flexibility in the choice of the $\beta\beta$ emitter (^{48}Ca, ^{76}Ge, ^{82}Se, ^{100}Mo, ^{116}Cd, and ^{130}Te) is a key strength of the cryogenic calorimeter technique. So far, ^{130}Te (*16*), ^{82}Se (*17*), and ^{100}Mo (*18*, *19*) have been used by cryogenic experiments in high-sensitivity searches for $0\nu\beta\beta$, leading to some of the most stringent half-life limits on this process. If $0\nu\beta\beta$ is observed, measuring the process across multiple isotopes would be crucial to understand the new physics involved (*20*). This possibility continues to propel efforts in crystal growing (*21*) and background reduction methods (*22*, *23*) that will allow this technique to meet the sensitivity goals of beyond the next-generation experiments. Thus, cryogenic calorimeters offer a wide pathway toward this long-term objective (*24*).

The CUORE experiment

The CUORE (Cryogenic Underground Observatory for Rare Events) experiment (*16*) primarily searches for $0\nu\beta\beta$ of ^{130}Te at the Laboratori Nazionali del Gran Sasso (LNGS) in Italy. The CUORE detector consists of a close-packed array of 988 5- by 5- by 5-cm TeO_2 crystal calorimeters with an active mass of 742 kg (206 kg ^{130}Te). The crystals are mounted in copper frames that form 19 towers. The towers are hosted in the CUORE cryostat, a custom multistage cryogen-free dilution refrigerator that cools the detector to ~10 mK and maintains it in a stable, low-noise environment (*25*). An illustration of the CUORE crystal arrangement is shown in Fig. 2A.

CUORE chose ^{130}Te as the $\beta\beta$ emitter because of its relatively high natural isotopic abundance of ~34%, which in turn allowed us to use

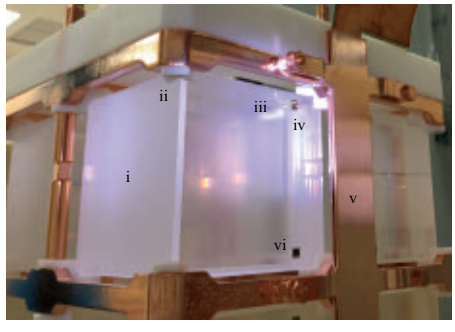


Fig. 1. CUORE calorimeter. Shown are (i) the absorber (TeO_2 crystal of 5 by 5 by 5 cm size); (ii and iii) weak thermal couplings (PTFE spacer and Au wire, respectively); (iv) temperature sensor (NTD Ge thermistor); (v) heat sink (Cu frame); and (vi) auxiliary Joule heater (Si chip). A spotlight was used to increase the visibility of the 25-μm wires used for electrical connection.

*Corresponding author: Carlo Bucci (carlo.bucci@lngs.infn.it) †CUORE Collaboration authors and affiliations are listed in the supplementary materials.

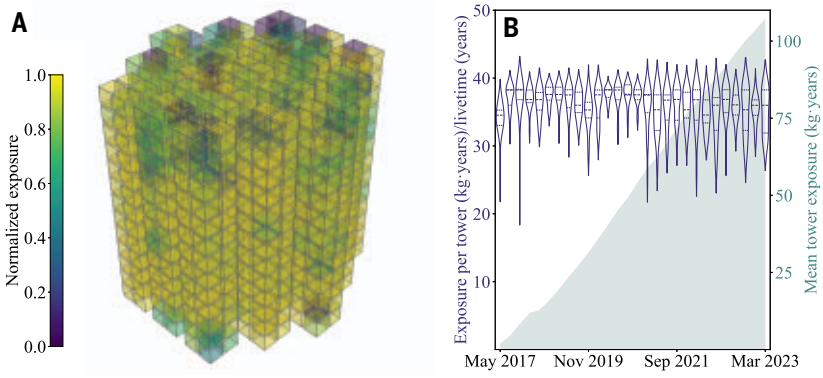


Fig. 2. CUORE exposure. (**A**) Schematic representation of the crystal array. The color of each crystal reflects its total analyzed exposure divided by the maximum value for all the calorimeters. The calorimeters near the top of their towers are more susceptible to vibrations. Because of their lower performance, they were removed from the analysis and consequently exhibit low exposures. (**B**) For each dataset, the distribution of the exposure collected on single towers normalized to the livetime of their active channels within the selected dataset is shown in purple. Each entry in the distribution is a proxy for the mass of data collected with a given tower based on the number of active channels available. The cumulative analyzed exposure averaged over towers by dataset is shown in green.

tellurium with natural isotopic composition. This enables CUORE to search for $0\nu\beta\beta$ and other rare processes in multiple isotopes of tellurium (*9*, *10*, *26*–*28*). The $\beta\beta$ emitter is also favorable because of its relatively high $Q_{\beta\beta}$ of ~2527.5 keV (*29*), which is above most environmental gamma-ray backgrounds. CUORE is further protected by several means from backgrounds that could obscure the $0\nu\beta\beta$ signal. The Gran Sasso mountains above LNGS provide natural shielding from cosmic rays, decreasing the muon flux by approximately six orders of magnitude compared with that at sea level (*30*). Multiple shields located outside and inside the cryostat provide nearly 4π coverage against environmental gamma background and neutrons (*25*, *31*), with the inner cryostat shield mostly composed of ^{210}Pb-depleted ancient lead recovered from a Roman shipwreck (*32*). We addressed the largest source of background—degraded alpha particles originating from the trace radioactive contamination of the copper frame structures (*33*)—using effective cleaning procedures and strict radiopurity controls on the crystals and nearby structures (*34*–*36*).

CUORE was designed to have each of the 988 calorimeters operate independently. In the CUORE calorimeter (Fig. 1), the TeO_2 crystal acts as the absorber, and an affixed neutron transmutation doped (NTD) Ge thermistor (*37*) acts as the temperature sensor. Polytetrafluoroethylene (PTFE) spacers between the crystal and copper frame and gold wires, used for electrical connection of the NTD, provide weak thermal coupling (*38*). The copper frame structure acts as the heat sink given that it is in thermal contact with the cryostat mixing chamber, which sets the base temperature (*25*). To correct our measurement against possible drifts in the operating temperature, a silicon heater is affixed to the crystal and used to induce periodic, monoenergetic pulses (*39*, *40*). We measure energy depositions by applying an optimized constant bias current to the thermistor so that the voltage measured across it acts as a proxy for the temperature of the calorimeter (*41*). Owing to the combination of the thermal capacities and conductances of our calorimeter components, we measure slow pulses (~50 ms rise time, ~1 s thermalization time) from the thermistor readout (*42*). Our continuous data stream is formed by passing the voltage through a room-temperature preamplifier and an antialiasing filter, and digitizing at 1 kHz (*43*, *44*).

Data collection, analysis pipeline, and event selection

CUORE began collecting data in 2017 and made major strides toward stable detector operations during the early stages of data taking (*15*). Currently, the procedure to optimize all calorimeters is largely automated (*45*), and routine cryogenic maintenance is minimal. Between 2019 and mid-2023, CUORE has been collecting data with >90% duty cycle at a rate of ~50 kg·years per month of TeO_2 (*46*). During this period, we were able to maintain steady exposure accumulation and operate the detector at different base temperatures. Thanks to the unprecedented stable operation of the cryogenic infrastructure, we collected more than 2 tonne·years of TeO_2 exposure.

CUORE data are organized into datasets. Each dataset begins and ends with ~1 week of calibration measurements, during which ^{232}Th or ^{232}Th + ^{60}Co radioactive sources are deployed around the detector. The high-intensity, characteristic gamma rays of well-known energies emitted by the radioactive sources are used to calibrate the voltage measurements in the entire dataset. Between the calibrations, we acquire ~1.5-month-long physics data, which contribute to our reported TeO_2 exposure. The duration of the dataset maximizes physics data collection while ensuring that the calibration is consistent for all calorimeters and compatible with the detector conditions.

To search for the potential signal peak at $Q_{\beta\beta}$, we identified pulses in the calorimeter readout that likely correspond to particle energy depositions and reconstructed their energies to build a spectrum. We processed 28 datasets, and after removing calorimeters performing below standard, our data processing framework reconstructed the energy spectra of an average of 914 out of 984 fully operational calorimeters per dataset. Because of the different operating conditions and intrinsic characteristics of the calorimeters, data acquisition is performed for each dataset-calorimeter independently. Hence, our energy reconstruction framework is largely automated and flexible to accommodate the number of calorimeters and their different characteristics (*45*). In Fig. 2A, we demonstrate the uniformity of the analyzed exposure distribution over all 988 calorimeters, which highlights the effectiveness of our analysis framework and its ability to adapt to each calorimeter. The steady and uniform TeO_2 exposure accumulation of CUORE over time is shown in Fig. 2B.

The typical response of CUORE calorimeters to particles impinging on the crystals is on the order of 100 μV/MeV of deposited energy. The frequency bandwidth of the corresponding pulses is 0 to 20 Hz; the noise components extend to higher frequencies (fig. S1). The main sources of environmental noise that can degrade our detector energy resolution are electrical interference, mechanical vibrations, and microphonic noise (*25*). Microphones, low-frequency accelerometers, and a triaxial seismometer have been installed in the proximity of the cryostat to independently measure the noise, covering a frequency range of 0.1 Hz to 1 kHz. For each dataset, a subset of these devices is used in our denoising algorithm (*47*). New to this analysis, our denoising procedure combines the device measurements with the noise extracted from the calorimeter readout to build a multivariate nonlinear offline noise cancellation algorithm (*48*).

To identify pulses and classify them as events for the energy reconstruction, we applied a low-threshold trigger, called optimal trigger (OT) (*49*), to the denoised data. Then to measure the pulse amplitude more accurately, we filtered events with the optimal (matched) filter (OF) (*50*) that maximizes the signal-to-noise ratio by exploiting the distinct shapes of the stochastic noise and the particle-induced signal power spectra. Because fluctuations in the baseline temperature can affect the pulse amplitude, degrading our energy resolution, we used events corresponding to fixed energy depositions (heater-induced or gamma peak–based) to characterize and correct for this effect. To convert the corrected amplitudes to energy, we used calibration data to correlate the peak positions in the amplitude spectrum with the gamma-ray emissions of the deployed radioactive sources (*51*).

Our segmented detector design enables us to perform coincidence-based event selections. Monte Carlo simulations indicate that ~88% of $0\nu\beta\beta$ events are contained in a single crystal, whereas events induced

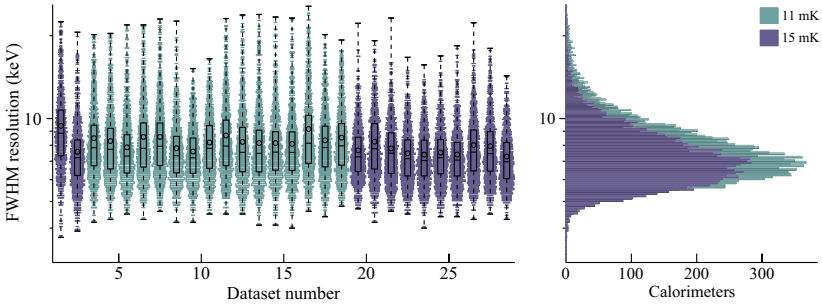


Fig. 3. Calorimeter energy resolution. (**Left**) The distribution of the FWHM energy resolution of the CUORE active calorimeters at the ^{208}Tl 2615 keV peak in calibration data for each dataset. The function drawn along the violin distribution indicates the frequency of the FWHM energy resolution over the CUORE detector array. The colors indicate the base temperature at the time of measurement: 11 mK, green; 15 mK, purple. (**Right**) One-dimensional projections of the resolutions corresponding to each temperature.

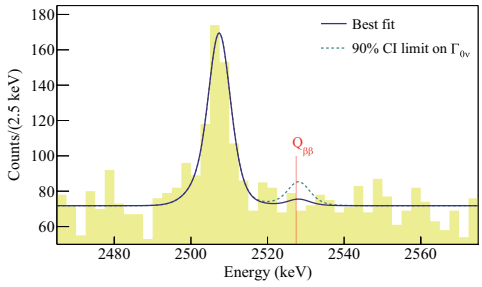


Fig. 4. Fit to the ROI spectrum. The best-fit curve (dark purple) and the best-fit curve with the 0νββ rate fixed to the 90% CI limit (dashed green) to the spectrum (yellow) in the ROI after all selection cuts.

by crystal surface radioactivity and gamma rays undergoing Compton scattering could deposit energy in multiple crystals. Therefore, we removed events depositing >40 keV in more than one crystal within 5 ms of each other (*9*, *10*). This time interval is a compromise between the time resolution of our detectors and the rate of random coincidences.

As a way to select reliable 0νββ candidate events, we performed pulse shape discrimination (PSD) to reject pulses with irregular shapes. For each event, we evaluated a normalized reconstruction error (NRE), a metric based on principal components analysis, to reject nonstandard pulses primarily caused by pileup, noise, and abrupt changes in operating conditions. An NRE threshold tuned to optimize the 0νββ sensitivity was used for our event selection (*16*, *52*). The energy spectrum after applying the aforementioned event selections is shown in fig. S2.

Detector response

After selecting the events to build the spectrum for our search, we blinded our data by exchanging a random fraction (~10%) of events between the 2615 keV peak and $Q_{\beta\beta}$ to produce an artificial signal peak. Using the blinded data, we fit a model that reflects the background and the posited $Q_{\beta\beta}$ peak to an energy region of interest (ROI) of [2465, 2575] keV. The range was chosen to be wide enough to contain adequate background statistics while excluding unnecessary nuisance radioactive peaks. This procedure leads to an unbiased fit optimization.

To determine the detector response of the individual calorimeters in our model, we used gamma peaks in both calibration and physics data (*48*). We evaluated the expected shape of a monoenergetic peak at $Q_{\beta\beta}$ by fitting the high-statistics 2615 keV peak in calibration data (fig. S3). Combining the fit results from all calorimeters and datasets, we obtained an exposure-weighted harmonic mean full width at half maximum (FWHM) energy resolution of (7.540 ± 0.024) keV at the 2615 keV calibration peak. In Fig. 3, we show the uniform spread of the FWHM resolution over all calorimeters and datasets, which underlines the efficacy of our analysis infrastructure and the long-term reliability of our system.

When fitting the peaks in physics data, we maintained the calorimeter dependence of the detector response by parametrizing the peak resolution in terms of the calibration-based fit results (*48*). Using the extrapolation of the energy resolution to $Q_{\beta\beta}$ for each dataset-calorimeter, we report an exposure-weighted harmonic mean FWHM energy resolution of (7.310 ± 0.024) keV, corresponding to 0.3% relative resolution. The calibration bias, defined as the difference between the reconstructed and nominal peak energy, is $\left(0.40^{+0.21}_{-0.44}\right)$ keV at $Q_{\beta\beta}$.

Search for 0νββ

After performing all selection cuts, the remaining data correspond to 2039.0 kg·years TeO_2 (567.0 kg·years ^{130}Te) exposure. To search for 0νββ, we evaluated the number of events above background at $Q_{\beta\beta}$ (2527.5 keV). We limited our search to the ROI, which contained a total of 3504 events. The background in the ROI includes a peak at 2505.7 keV from the simultaneous absorption of two gamma rays from ^{60}Co and a uniform background predominantly from degraded alpha particles from surface contamination, with a contribution from multi-Compton scattering of 2615-keV gamma rays (*33*).

We modeled the spectrum in the ROI as the sum of a $Q_{\beta\beta}$ peak, a dataset-dependent uniform background, and a time-dependent ^{60}Co sum peak and performed an unbinned Bayesian fit. We used our dataset-calorimeter evaluation of the detector efficiencies and detector response as priors in the fit, in which the detection efficiency was evaluated as the product of the containment efficiency, the reconstruction efficiency, the anticoincidence efficiency, and the PSD efficiency (*48*). Their values are summarized in table S1. Systematic effects are included as additional nuisance parameters (*48*). The fit to the ROI is shown in Fig. 4.

We observed no statistically significant evidence of 0νββ and report a best-fit decay rate of $\widehat{\Gamma}_{0\nu} = 5.5^{+7.3}_{-5.5}$ (stat. + syst.) × 10^{-27} year^{-1} and set a limit on the decay rate of $\Gamma^{0\nu}_{1/2} < 2.0 \times 10^{-26}$ year^{-1} at 90% credibility interval (CI) corresponding to a decay half-life limit of $T^{0\nu}_{1/2} > 3.5 \times 10^{25}$ years (90% CI) (fig. S4). We also performed a frequentist fit and, using the profile likelihood ratio test statistic (*53*), set a half-life limit of $T^{0\nu}_{1/2} > 3.4 \times 10^{25}$ years at 90% confidence level (CL) (fig. S6), which is compatible with the Bayesian fit result. Using the background-only hypothesis to fit the ROI, we obtained a background index (BI) for each dataset (fig. S5), with an exposure-weighted mean of $\left(1.42^{+0.03}_{-0.02}\right) \times 10^{-2}$ counts keV^{-1} kg^{-1} year^{-1}. We used the BIs to extract a median exclusion sensitivity of 4.4×10^{25} years (90% CI) (fig. S7) (*48*). Compared with this value, the probability of obtaining a stronger limit is 74%.

The simplest model that is commonly used to compare 0νββ search results across isotopes is the light-neutrino exchange model (*12*), from which we extracted an effective Majorana neutrino mass ($m_{\beta\beta}$). Thus, we placed a limit of $m_{\beta\beta} < 70$ to 250 meV, in which the spread comes from the range of different nuclear model parameters currently available in the literature (*54*–*62*). The CUORE limit along with the most stringent $m_{\beta\beta}$ constraints obtained with other isotopes are shown in Fig. 5.

Discussion and outlook

CUORE has demonstrated more than 5 years of stable operation of an array of 988 cryogenic calorimeters and will continue taking data until reaching an analyzed exposure of 3 tonne·years TeO_2 (~1 tonne·year ^{130}Te). The instrumentation and the analysis infrastructure developed in this work not only enable a world-leading 0νββ search but also establish large-volume cryogenic calorimetry as a distinctive path for a future multi-isotope 0νββ search program. After CUORE reaches its target exposure, the experiment will begin phase II and pivot its primary focus to low-energy processes.

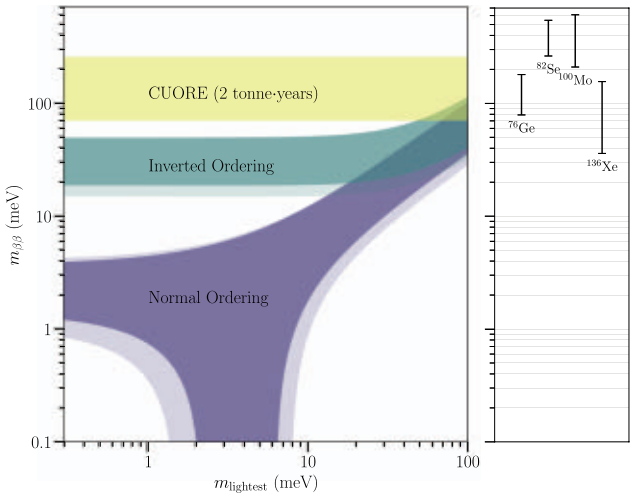


Fig. 5. Limits on $m_{\beta\beta}$. The allowed parameter space as a function of the lightest neutrino mass in the cases of inverted and normal ordering are shown in green and purple, respectively. The lighter shaded areas indicate the 3σ uncertainties on the oscillation parameters (*12*). The yellow band indicates the limit obtained from this analysis. Limits obtained from ^{76}Ge (*64*), ^{82}Se (*17*), ^{100}Mo (*19*), and ^{136}Xe (*65*) are also shown.

CUPID (CUORE Upgrade with Particle Identification) (*63*), a next-generation experiment that will search for 0νββ of ^{100}Mo, will follow CUORE phase II. The CUPID detector is designed to improve on our $m_{\beta\beta}$ sensitivity by a factor of 5, deeply probing the inverted mass ordering parameter space assuming the light-neutrino exchange model. If CUPID discovers 0νββ, it would confirm the Majorana nature of the neutrino and compel precise measurements of 0νββ across multiple isotopes, making cryogenic calorimeters all the more relevant. Because CUPID will use the same detection technique and will be hosted in the CUORE cryogenic facility, the experiment will inherit a well-understood system and have working knowledge of the cryostat operations, background, and noise from CUORE. CUORE has thus laid the groundwork not only for CUPID but also for other future large-array cryogenic calorimeter–based experiments.

REFERENCES AND NOTES

1. R. L. Workman *et al.*, *Prog. Theor. Exp. Phys.* **2022**, 083C01 (2022).
2. M. Dine, A. Kusenko, *Rev. Mod. Phys.* **76**, 1–30 (2003).
3. E. Majorana, *Nuovo Cim.* **14**, 171–184 (1937).
4. M. Goeppert-Mayer, *Phys. Rev.* **48**, 512–516 (1935).
5. W. H. Furry, *Phys. Rev.* **56**, 1184–1193 (1939).
6. A. D. Sakharov, *Pis'ma Z. Eksp. Teor. Fiz.* **5**, 32–35 (1967).
7. C. Augier *et al.*, *Phys. Rev. Lett.* **131**, 162501 (2023).
8. O. Azzolini *et al.*, *Phys. Rev. Lett.* **131**, 222501 (2023).
9. D. Q. Adams *et al.*, *Phys. Rev. Lett.* **126**, 171801 (2021).
10. D. Q. Adams *et al.*, *Phys. Rev. Lett.* **131**, 249902 (2023).
11. M. J. Dolinski, A. W. Poon, W. Rodejohann, *Annu. Rev. Nucl. Part. Sci.* **69**, 219–251 (2019).
12. M. Agostini, G. Benato, J. A. Detwiler, J. Menéndez, F. Vissani, *Rev. Mod. Phys.* **95**, 025002 (2023).
13. E. Fiorini, T. O. Niinikoski, *Nucl. Instrum. Methods Phys. Res.* **224**, 83–88 (1984).
14. C. Brofferio, S. Dell'Oro, *Rev. Sci. Instrum.* **89**, 121502 (2018).
15. D. Q. Adams *et al.*, *Prog. Part. Nucl. Phys.* **122**, 103902 (2022).
16. D. Q. Adams *et al.*, *Nature* **604**, 53–58 (2022).
17. O. Azzolini *et al.*, *Phys. Rev. Lett.* **129**, 111801 (2022).
18. C. Augier *et al.*, *Eur. Phys. J. C* **82**, 1033 (2022).
19. A. Agrawal *et al.*, *Phys. Rev. Lett.* **134**, 082501 (2025).
20. O. Cremonesi, M. Pavan, *Adv. High Energy Phys.* **2014**, 951432 (2013).
21. E. Armengaud *et al.*, *Eur. Phys. J. C* **77**, 785 (2017).
22. A. Armatol *et al.*, *Nucl. Instrum. Methods Phys. Res. A* **1069**, 169936 (2024).
23. V. Singh *et al.*, *Phys. Rev. Appl.* **20**, 064017 (2023).
24. A. Giuliani, F. A. Danevich, V. I. Tretyak, *Eur. Phys. J. C* **78**, 272 (2018).
25. C. Alduino *et al.*, *Cryogenics* **102**, 9–21 (2019).
26. D. Q. Adams *et al.*, *Eur. Phys. J. C* **81**, 567 (2021).
27. D. Q. Adams *et al.*, *Phys. Rev. C* **105**, 065504 (2022).
28. D. Q. Adams *et al.*, *Phys. Rev. Lett.* **129**, 222501 (2022).
29. S. Rahaman *et al.*, *Phys. Lett. B* **703**, 412–416 (2011).
30. G. Bellini *et al.*, *J. Cosmol. Astropart. Phys.* **2012**, 015 (2012).
31. H. Wulandari, J. Jochum, W. Rau, F. von Feilitzsch, *Astropart. Phys.* **22**, 313–322 (2004).
32. L. Pattavina *et al.*, *Eur. Phys. J. A* **55**, 127 (2019).
33. D. Q. Adams *et al.*, *Phys. Rev. D* **110**, 052003 (2024).
34. F. Alessandria *et al.*, *Astropart. Phys.* **45**, 13–22 (2013).
35. E. Buccheri *et al.*, *Nucl. Instrum. Methods Phys. Res. A* **768**, 130–140 (2014).
36. G. Benato *et al.*, *J. Instrum.* **13**, P01010 (2018).
37. E. E. Haller *et al.*, in *Neutron Transmutation Doping of Semiconductor Materials*, R. D. Larrabee, Ed. (Springer, 1984), pp. 21–36.
38. C. Alduino *et al.*, *J. Instrum.* **11**, P07009 (2016).
39. E. Andreotti *et al.*, *Nucl. Instrum. Methods Phys. Res. A* **664**, 161–170 (2012).
40. K. Alfonso *et al.*, *J. Instrum.* **13**, P02029 (2018).
41. C. Arnaboldi *et al.*, *J. Instrum.* **13**, P02026 (2018).
42. A. Alessandrello *et al.*, *IEEE Trans. Nucl. Sci.* **40**, 649–656 (1993).
43. C. Arnaboldi, M. Cariello, S. Di Domizio, A. Giachero, G. Pessina, *Nucl. Instrum. Methods Phys. Res. A* **617**, 327–328 (2010).
44. S. Di Domizio *et al.*, *J. Instrum.* **13**, P12003 (2018).
45. K. Alfonso *et al.*, *Nucl. Instrum. Methods Phys. Res. A* **1008**, 165451 (2021).
46. D. Q. Adams *et al.*, *Phys. Rev. Lett.* **124**, 122501 (2020).
47. K. J. Vetter *et al.*, *Eur. Phys. J. C* **84**, 243 (2024).
48. Materials and methods are available as supplementary materials.
49. S. Di Domizio, F. Orio, M. Vignati, *J. Instrum.* **6**, P02007 (2011).
50. E. Gatti, P. F. Manfredi, *Riv. Nuovo Cim.* **9**, 1–146 (1986).
51. C. Alduino *et al.*, *Phys. Rev. Lett.* **120**, 132501 (2018).
52. R. Huang *et al.*, *J. Instrum.* **16**, P03032 (2021).
53. S. Algeri, J. Aalbers, K. Dundas Morå, J. Conrad, *Nat. Rev. Phys.* **2**, 245–252 (2020).
54. N. López Vaquero, T. R. Rodríguez, J. L. Egido, *Phys. Rev. Lett.* **111**, 142501 (2013).
55. J. Hyvärinen, J. Suhonen, *Phys. Rev. C* **91**, 024613 (2015).
56. M. Horoi, A. Neacsu, *Phys. Rev. C* **93**, 024308 (2016).
57. L. S. Song, J. M. Yao, P. Ring, J. Meng, *Phys. Rev. C* **95**, 024305 (2017).
58. J. Menéndez, *J. Phys. G Nucl. Part. Phys.* **45**, 014003 (2017).
59. D.-L. Fang, A. Faessler, F. Šimkovic, *Phys. Rev. C* **97**, 045503 (2018).
60. F. Šimkovic, A. Smetana, P. Vogel, *Phys. Rev. C* **98**, 064325 (2018).
61. L. Coraggio, A. Gargano, N. Itaco, R. Mancino, F. Nowacki, *Phys. Rev. C* **101**, 044315 (2020).
62. F. F. Deppisch, L. Graf, F. Iachello, J. Kotila, *Phys. Rev. D* **102**, 095016 (2020).
63. W. R. Armstrong *et al.*, CUPID pre-CDR. arXiv:1907.09376 [physics.ins-det] (2019).
64. M. Agostini *et al.*, *Phys. Rev. Lett.* **125**, 252502 (2020).
65. S. Abe *et al.*, *Phys. Rev. Lett.* **130**, 051801 (2023).
66. P. T. Surukuchi, C. Bucci, K. Alfonso, A. Campani, Constraints on lepton number violation with the 2 tonne·yr CUORE data set. Zenodo (2025); https://doi.org/10.5281/zenodo.15742646.

ACKNOWLEDGMENTS

We dedicate this work to our deceased colleagues, Ettore Fiorini and Stuart J. Freedman, whose contributions and spirit continue to inspire us. **Funding:** The CUORE Collaboration thanks the directors and staff of the Laboratori Nazionali del Gran Sasso and the technical staff of our laboratories. This work was supported by the Istituto Nazionale di Fisica Nucleare (INFN); the National Science Foundation under grants NSF-PHY-0605119, NSF-PHY-0500337, NSF-PHY-0855314, NSF-PHY-0902171, NSF-PHY-0969852, NSF-PHY-1307204, NSF-PHY-1314881, NSF-PHY-1401832, and NSF-PHY-1913374; Johns Hopkins University; Yale University; and University of Pittsburgh. This material is also based on work supported by the US Department of Energy (DOE) Office of Science under contracts DE-AC02-05CH11231 and DE-AC52-07NA27344 and by the DOE Office of Science, Office of Nuclear Physics, under contracts DE-FG02-08ER41551, DE-FG03-00ER41138, DE-SC0012654, DE-SC0020423, DE-SC0019316, and DE-SC0011091. This research used resources of the National Energy Research Scientific Computing Center (NERSC). This work makes use of both the DIANA data analysis and APOLLO data acquisition software packages, which were developed by the CUORICINO, CUORE, LUCIFER, and CUPID-0 Collaborations. The authors acknowledge Advanced Research Computing at Virginia Tech for providing computational resources and technical support that have contributed to the results reported within this paper: https://arc.vt.edu. **Author contributions:** All authors contributed to varying degrees in the preparation of the publication, including design, construction, and operations of the detector; collection and analysis of data; and writing and visualization. **Competing interests:** There are no competing interests to declare. **Data and materials availability:** The data and software to reproduce the results of this paper are archived on Zenodo (*66*). **License information:** Copyright © 2025 the authors, some rights reserved; exclusive licensee American Association for the Advancement of Science. No claim to original US government works. https://www.science.org/about/science-licenses-journal-article-reuse

SUPPLEMENTARY MATERIALS

science.org/doi/10.1126/science.adp6474
Materials and Methods; Figs. S1 to S7; Tables S1 and S2; CUORE Collaboration Author List; References (*67*–*72*)

Submitted 5 April 2024; accepted 3 October 2025; published online 16 October 2025
10.1126/science.adp6474

PHASE TRANSITIONS

Hexatic phase in covalent two-dimensional silver iodide

Thuy An Bui[1]†, David Lamprecht[1,2]†, Jacob Madsen[1], Marcin Kurpas[3], Peter Kotrusz[4,5], Alexander Markevich[1], Clemens Mangler[1], Jani Kotakoski[1], Lado Filipovic[2], Jannik C. Meyer[6,7], Timothy J. Pennycook[8], Viera Skákalová[1,4,5,9], Kimmo Mustonen[1]*

According to the Kosterlitz-Thouless-Halperin-Nelson-Young (KTHNY) theory, the transition from a solid to liquid in two dimensions proceeds through an orientationally ordered liquid-like hexatic phase. However, alternative mixed melting scenarios, in which melting proceeds through the hexatic phase with both continuous and discontinuous transitions, have also been observed in some two-dimensional systems. In this study, we imaged silver iodide embedded in multilayer graphene using time- and temperature-resolved in situ atomic-resolution scanning transmission electron microscopy and nanobeam electron diffraction. We observed the hexatic phase and provide evidence supporting a mixed melting scenario.

First-order phase transitions in three-dimensional (3D) materials are characterized by discontinuous (first-order) changes in thermodynamic quantities such as entropy. A common example is ice melting into water accompanied by the immediate loss of its crystal symmetries. However, in 2D systems, additional melting scenarios have been proposed. For example, the Kosterlitz-Thouless (KT) transition predicted by the Kosterlitz-Thouless-Halperin-Nelson-Young (KTHNY) theory (*1*–*6*), describes a continuous two-step process occurring through an orientationally ordered, liquid-like intermediate phase known as the hexatic phase. Various mixed melting scenarios (*7*–*9*) propose a continuous transition to the hexatic followed by a first-order transition to a liquid phase (*10*). In addition, direct first-order transitions without an intermediate phase have also been observed in some 2D systems (*11*).

The appearance of the hexatic phase has been experimentally verified in a wide variety of model systems governed by distinct interparticle forces. These include systems dominated by Coulomb repulsion, such as electrons on liquid helium (*12*), charged colloids in water (*13*, *14*), and dusty plasmas (*15*); systems dominated by van der Waals interactions, including liquid-crystal and layered molecular films (*16*–*19*); and those governed by dipolar or elastic forces, such as magnetic colloids (*20*), magnetic skyrmion lattices (*21*), and biological cell monolayers (*22*). Nevertheless, even in these well-controlled systems, simulations (*23*) and experiments (*24*, *25*) show that melting can proceed through different routes—either a grain boundary–mediated process or the KTHNY mechanism—depending sensitively on particle density and interaction range. The KTHNY melting of a system with a more complex directional interaction structure has been experimentally observed in the case of charge density waves, both in real space by using scanning probe techniques (*26*) and in reciprocal space by using ultrafast transmission electron microscopy (*27*). The closest analog to a covalently bonded system has been provided by simulations of 2D water ice under high pressure (*28*). Although this study revealed an intriguing mixed melting pathway with subsequent first-order and KT transitions, the hydrogen bonds of ice are far weaker than covalent bonds and are pointed exclusively in the in-plane direction. In covalent crystals, the force interactions are not only highly directional but also much stronger than van der Waals interactions or hydrogen bonds, and, so far, determining their melting mechanism has remained out of reach for both simulations and experiments.

In this work, we studied the dynamic melting of covalently bound hexagonal monolayers of silver iodide (AgI) encapsulated by graphene (*29*, *30*). Graphene encapsulation stabilizes 2D AgI and prevents its transformation into 3D phases (*31*). The noncommensurability of the graphene and AgI lattices eliminates periodic interactions and allows AgI to melt without appreciable orientational constraints in our time- and temperature-resolved in situ scanning transmission electron microscopy (STEM) experiments. Convolutional neural network (CNN) analysis of the translational and orientational correlations in our large dataset of experimental images confirmed the existence of the hexatic phase in a covalent material. The images also provided evidence for evaluating the proposed melting scenarios for covalent materials and pointed to a mixed melting scenario as being most likely.

Melting of 2D crystalline silver iodide

The experimental (STEM) and theoretical (density functional theory, DFT) structures of monolayer AgI are shown in Fig. 1A (also figs. S10 and S11). The evolution of a single encapsulated crystal as it is heated until it melts and is then cooled is shown in Fig. 1B. The fully crystalline material transitioned upon heating into a dynamic phase, with regions of disorder appearing and disappearing over time. Then, as the material was heated further, the disorder fully took over. We show below that the first stage manifested as the solid-hexatic phase boundary was crossed, whereas the second stage signified a fully liquid state of the covalent 2D material. These distinct stages of melting are illustrated by movies S1 to S3, which also display the CNN-detected positions of atoms (see materials and methods).

The temperatures of the transitions depended on the AgI crystal size (fig. S22). Being embedded in graphene, the largest 2D crystals (>100 nm in size) melt at ~1200°C, which was substantially higher than the 660°C reported for bulk AgI (*31*). Nevertheless, crystals of all sizes and shapes consistently proceeded through the two distinct stages of melting and then fully reverted to 2D AgI after the temperature was lowered sufficiently. We primarily focused on the larger AgI crystals, typically 40 to 80 nm in diameter, where edge effects were less prominent. An example of a small AgI crystal undergoing the phase transition is shown in fig. S21. The changes occurring in stages one and two were visible directly in our real-space images and in their Fourier transforms (FTs; materials and methods). The dynamic crystalline phase typically emerged at temperatures between 1000° and 1125°C and then gradually transformed into a fully molten structure between 1050° and 1200°C, depending on the crystal size. The AgI crystal (Fig. 1B at 1115°C) exhibited regions with disordered hexagonal lattice still present, interspersed with areas that appeared to lack obvious crystallinity. The encapsulating graphene was not apparent in the annular dark field (ADF) images (materials and methods) because of its low atomic number but is distinguished in the FTs (*32*), especially at 1130°C, by a set of spots on an outer circle revealing six layers of graphene rotated at different angles in this sample. The graphene layers were unaffected by these temperatures that were well below the melting point of graphene (*33*), as seen through the constant sharpness of its characteristic spots in the FT of the images.

The partial loss of orientational order, qualitatively visible in the ADF images during stage one, became evident in the FTs, where the 2D AgI crystal spots broadened in the azimuthal direction, as shown in Fig. 1C. This azimuthal broadening of the first-order peaks was consistent with the presence of a hexatic-like phase slightly below the

[1]University of Vienna, Faculty of Physics, Vienna, Austria. [2]Institute for Microelectronics, TU Wien, Vienna, Austria. [3]Institute of Physics, University of Silesia in Katowice, Chorzów, Poland. [4]Danubia NanoTech s.r.o., Bratislava, Slovakia. [5]Institute of Electrical Engineering of SAS, Bratislava, Slovakia. [6]Eberhard Karls University of Tuebingen, Institute of Applied Physics, Tuebingen, Germany. [7]NMI Natural and Medical Sciences Institute at the University of Tübingen, Markwiesenstr. 55, Reutlingen, Germany. [8]University of Antwerp, EMAT, Antwerp, Belgium. [9]University of West Bohemia in Pilsen New Technologies - Research Centre Univerzitní 8, Pilsen, Czech Republic. ***Corresponding author. Email: kimmo.mustonen@univie.ac.at** †These authors contributed equally to this work.

final melting temperature (*25*, *34*). In this stage of the melting, the material is highly dynamic, with the regions of disorder appearing and disappearing over time as captured in the fluctuations in the ADF images shown in movie S2. At 1130°C, the AgI crystallinity had completely vanished (Fig. 1B and movie S3), indicating that the AgI had become a 2D liquid. Weak isotropic rings of disordered AgI were still visible in the FT in addition to the higher-frequency spots of the unaffected graphene layers. However, the fluctuations seen in the lower-temperature dynamic crystalline phase now vanished, leaving only constant isotropic rings in the FTs. We attributed this complete loss of orientational order and presence of only a very-short-range translational order, qualitatively different from the one described before, to the liquid phase. Upon cooling to 25°C, the 2D AgI crystal reappeared, rotated by 12° from its original orientation, with sharp FT spots, indicating a fully crystalline phase. These rotations were often observed, but they appeared to be random even within the same sample area; This observation was in good agreement with computations that revealed only very weak interaction between AgI and graphene (see fig. S13), thus ruling out long-range periodic effects that could lead to artifacts in our data.

Although direct atomic-resolution imaging is ideal for probing static and sufficiently slow dynamics, it could only reveal averages of dynamics occurring on timescales shorter than the imaging process. Correspondingly, increasingly large parts of the area were washed out in the real-space images as the temperature was increased, and our information was drawn from the fluctuating sections where structures were still visible intermittently (see, for example, movies S13 to S15). To complement our analysis, we used nanobeam electron diffraction (NBED) maps (materials and methods) to study a larger, though slightly irregular, AgI crystal shown in Fig. 2A. In the diffraction data, the time averaging takes place in reciprocal space, so that structural correlations can be probed even if the structure reorganizes rapidly, as in a liquid. In the example of Fig. 2, when the crystal was brought to almost its final melting point, the left-hand side of the AgI flake was in a state that was dynamic on the timescale of single exposures (20 ms) and fluctuating between a solid and the phase that we identify as hexatic; Movie S4, recorded with a stationary probe at the position indicated in Fig. 2A, shows the richness of these dynamics and that they were distributed both in time and space. The right-hand side of the crystal, by contrast, lost its hexagonal structure, and continuous rings were visible in the diffraction patterns (Fig. 2D and movie S5). These rings were static in the sense that they looked the same all over this area and did not change in subsequent exposures. We identified this phase as liquid, as detailed in the following discussion of the diffraction patterns.

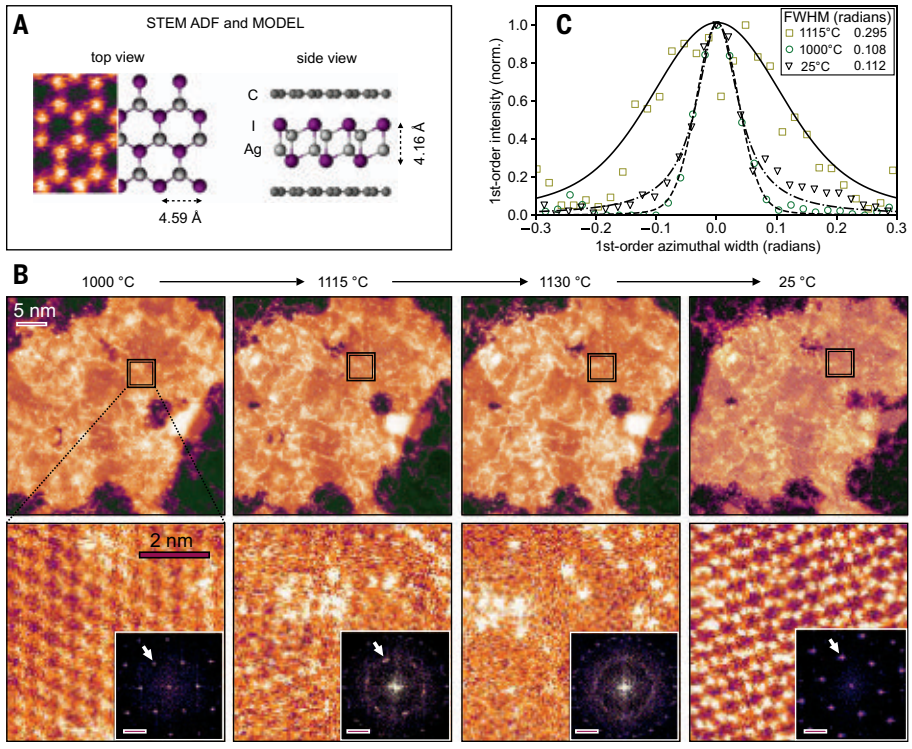


Fig. 1. Annular dark-field imaging of the melting of 2D crystalline silver iodide. (**A**) DFT model of 2D AgI shown beside an atomically resolved ADF image of the room-temperature structure. (**B**) Development of the AgI structure during heating and cooling: crystalline state at 1000°C, phase one of the 2D melting process at 1115°C with interspersed disordered crystalline and molten areas, and the melting phase two at 1130°C. After cooling down to 25°C, the AgI crystal appears again but is rotated by 12°. The bright spots visible on and around the AgI crystal are iodine atoms stuck at the edges of graphitized contamination (see figs. S14 and S15). The FTs in the bottom row are from 100 rapidly acquired STEM images (see materials and methods). The contrast of the FTs has been optimized to emphasize the AgI peaks. Additional temperature datapoints and larger field of views can be found in figs. S17 to S20. Inset scale bars, 2 nm^{-1}. (**C**) Temperature dependence of the azimuthal width of the first-order AgI peaks marked with arrows in the FTs of the ADF images in (B).

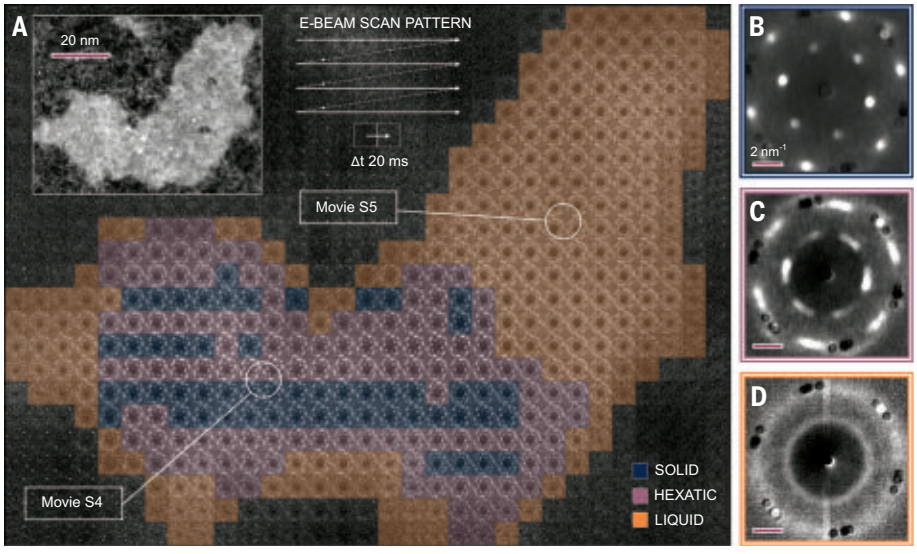


Fig. 2. Phase analysis based on NBED. (**A**) NBED map of an AgI crystal with its right side in a liquid state and its left side in a dynamic state fluctuating between solid and hexatic phases. Movies S4 and S5 show time series of diffraction patterns recorded from the indicated positions. (**B** to **D**) Average diffraction patterns of the solid (B), hexatic (C), and liquid (D) phases within the NBED map. The coloring in the NBED map is based on the approximate width of the diffraction spots: ≤0.20 rad → solid phase (blue); >0.20 rad → hexatic phase (purple); isotropic rings → liquid phase (orange).

The solid phase displayed sharp diffraction features (azimuthal width ≤ 0.20 rad) of a hexagonal lattice. We attribute the asymmetry in the intensities to a varying level of sample tilt, as in Fig. 2B [see also fig. S24 and our previous work (*30*)]. In the hexatic phase, by contrast, we observed azimuthally broadened diffraction peaks (Fig. 2C). This azimuthal broadening was consistent with a lattice that is distorted by the dynamic appearance and annihilation of dislocations or grain boundaries (*35*). Although the orientational order was clearly reduced compared with that of the crystalline phase, it was nevertheless present and maintained across the entire portion of the crystal that had not transitioned to the liquid state. The spatial correlation length in liquids is much shorter than in crystalline materials and typically extends no further than a few nearest neighbors. In our diffraction patterns, the complete loss of orientational order was evident from the ring-shaped intensities, which also indicated that the structure was dynamic on a timescale much faster than the diffraction pattern acquisition time. Nevertheless, some insights on the near-ordering could be gained from the radial profile (Fig. 2D): The primary distances were the same as for crystalline AgI, suggesting that the building blocks and bonding in the liquid phase were the same as those in the solid phase. Compared with crystalline AgI, radial broadening of the peaks was observed, especially in the second-order diffraction ring of the liquid phase but also in the measured width of the first-order ring (fig. S23). This broadening corresponded approximately to a correlation length between 0.6 and 2 nm, as discussed in the supplementary materials. These observations were not just in excellent qualitative agreement with the hexatic phase but also in quantitative agreement. The hexatic phase can be rigorously defined by how the translational and orientational orders are correlated as a function of distance within the surrounding material. The classical definition expects an exponential decay of the translational correlation within the hexatic phase, distinguishing it from the power-law decay expected in solids at a finite temperature. The hexatic state retains quasi–long-range orientational order, distinguishing it from both the crystalline phase and the liquid phase. A fully crystalline phase has a long-range orientational order, whereas a liquid phase has only a short-range order. In the KTHNY theory, these conditions can be expressed in terms of specific critical exponents. The hexatic phase must simultaneously display a translational correlation power law decay exponent $\eta_k \geq \frac{1}{3}$ and an orientational correlation decay exponent $\eta_6 \leq \frac{1}{4}$ (*10*, *19*, *36*). These decay characteristics are seen in Fig. 3, and we discuss them in the following section.

Translational correlation

We computed the translational correlation functions using the center of mass positions r of the AgI polygons detected automatically in real-space ADF-STEM images by the CNN (see fig. S3 and movies S6 to S15). Locally, the deviation from the perfect hexagonal crystal can be obtained by computing the translational order parameter

$$\Psi_l(r) = e^{-iq_l r}$$

where q_l is a reciprocal lattice vector of a perfect crystal. The reciprocal lattice vectors were found by first computing a 2D structure

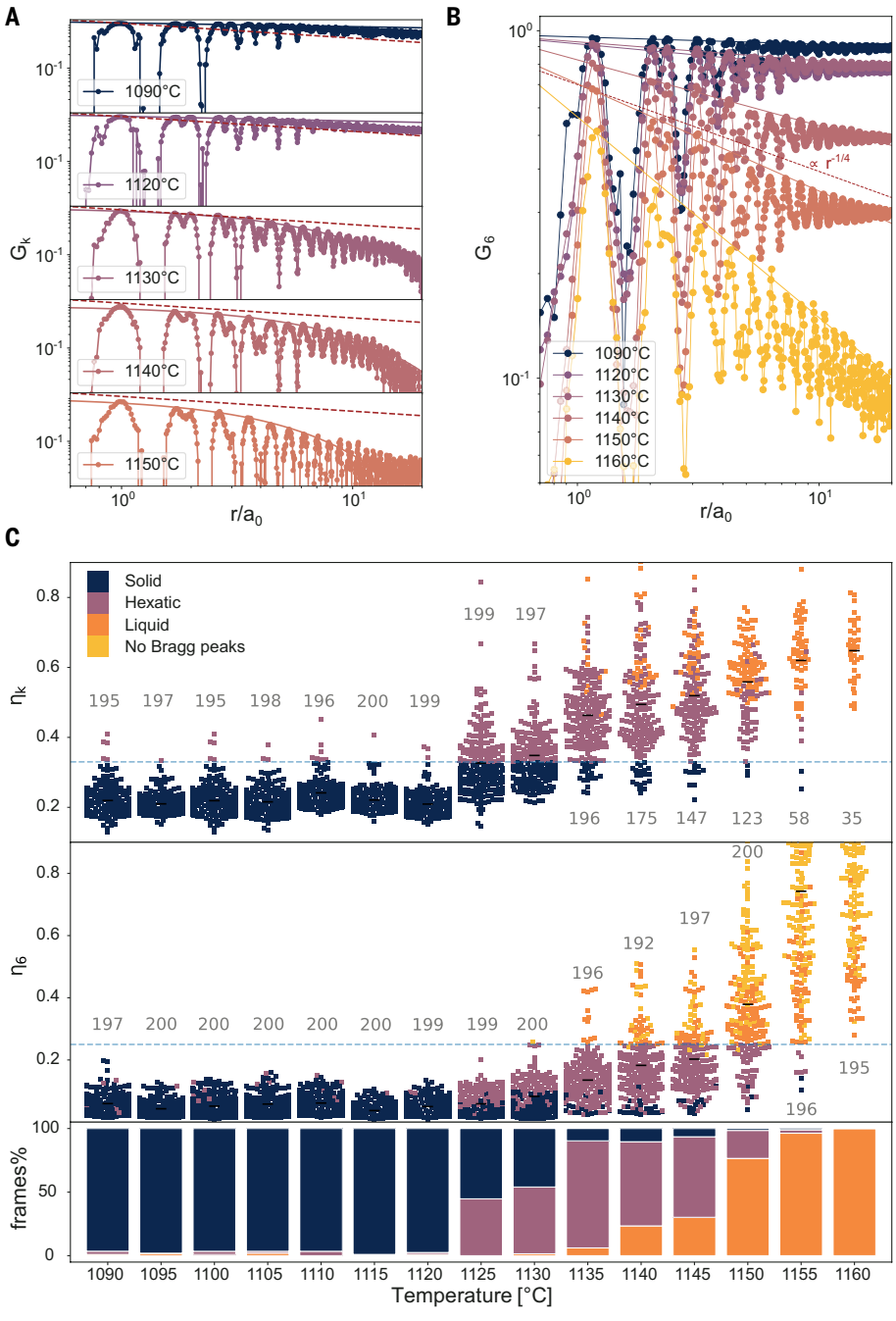


Fig. 3. Spatial correlation functions. (**A**) The average translational correlation function G_k at various temperatures with solid lines indicating either power law fits (1090° and 1120°C) or exponential fits (1130°, 1140°, and 1150°C). The critical exponent $\eta_k \rightarrow \frac{1}{3}$ is indicated with a brown dashed line. (**B**) The average orientational correlation function G_6 with solid power law fits. The critical exponent $\eta_6 \rightarrow \frac{1}{4}$ is plotted with brown dashed lines. As negative values cannot be plotted in a log-log coordinate system, some data points in (A) and (B) are not visible. (**C**) Fit parameters for $G_k(r)$ and $G_6(r)$ as a function of temperature for every image. Data are classified as solid phase ($\eta_k \leq \frac{1}{3}$), hexatic phase ($\eta_k > \frac{1}{3}$ and $\eta_6 < \frac{1}{4}$), and liquid phase ($\eta_6 > \frac{1}{4}$). Relative phase abundances are shown below. All images lacking reciprocal lattice vectors are considered liquid. The number above or below the individual columns indicates the number of analyzed frames.

factor $S(q)$ (*37*) and then fitting the first-order peaks (see fig. S27 for examples). The translational correlation function [$G_k(r)$] was then computed using the translational order parameter Ψ_l as

$$G_k(r) = \frac{1}{6}\sum_{l=1}^{6}\frac{1}{N_r}\sum_{i,j}^{N_r}\Psi_l(r_i)\Psi_l^*(r_j)$$

The correlation function was averaged over N_r pairs of polygons and the first six reciprocal vectors in $S(q)$. Figure 3A shows G_k averaged over all images at each temperature together with the best-fitting power law $\propto r^{-\eta_k}$ and exponential $\propto e^{-r}$ decay functions. The statistical distribution of the power law fitting parameter η_k of all recorded images can be found in Fig. 3C. Power law decay of $G_k \propto r^{-\eta_k}$ with low η_k was observed in nearly all images at 1090°C, as expected for a solid system. As the temperature was raised, the power law fitting exponent remained nearly constant and well below the critical value of $\eta_k = \frac{1}{3}$ required by the definition of the hexatic phase until 1120°C. However, at 1125°C, the decay of the averaged translational correlation function suddenly became quasiexponential and, at 1130°C, η_k exceeded $\frac{1}{3}$ in more than one half of the recorded images as the material fluctuated between crystallinity and the hexatic state, as shown in movie S9. With increasing temperature, the average η_k rose steadily until the highest recorded temperature of 1160°C, where all images had an associated translational decay parameter $>\frac{1}{3}$, indicating a complete loss of translational order with an exponentially falling average G_k. As G_k decays exponentially in both the hexatic and liquid phase, power law fits were not strictly applicable, leading to a wide spread in η_k. However, the key point is that the decay parameter remains greater than the critical $\frac{1}{3}$ value in most recorded images, implying the presence of either the hexatic phase or a semiordered liquid. At 1160°C, two-thirds of the images had no discernible first-order diffraction spots, indicating that the 2D crystal had almost completely transformed to the liquid state.

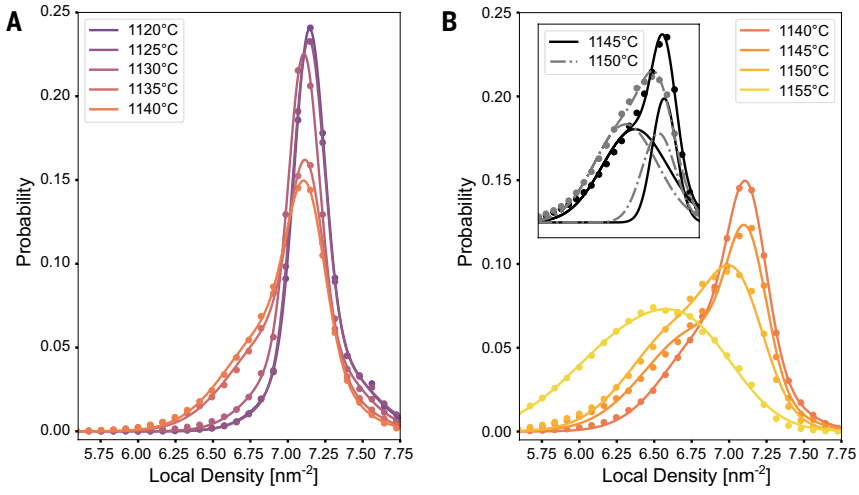


Fig. 4. Local density distribution functions at different temperatures. (**A**) Change of local density in the solid-hexatic transition temperature range with Gaussian and double Gaussian fits. (**B**) Change of local density in the hexatic-liquid transition temperature range with Gaussian and double Gaussian fits. The inset contains the deconvolution of the double Gaussian fits of the 1145° and 1150°C datasets, showing the bimodal nature of these distributions.

Orientational correlation

To distinguish the hexatic phase from the solid and liquid phases, we must also assess the orientational order, which is determined by analyzing the orientational correlation

$$G_6(r) = \frac{1}{N_r}\sum_{i,j}^{N_r}\Psi_6(r_i)\Psi_6^*(r_j)$$

in which the local orientational order parameter is defined as

$$\Psi_6(r) = \frac{1}{N_{nn}}\sum_{j=1}^{N_{nn}} e^{i6\theta_{ij}}$$

where θ_{ij} is the angle between a polygon at position r_i and its N_{nn} nearest neighbors relative to a fixed axis. The nearest neighbors were determined by Voronoi tessellation (*37*). Figure 3B shows G_6 averaged over all images at each temperature and the corresponding fits on a log-log scale. The statistics of the power law fitting parameter η_6 among all images can be found in Fig. 3C. During the heating experiments, G_6 remained nearly constant up to 1120°C, as expected for a solid. However, as the temperature was increased to 1125°C, the orientational correlation function entered into a power law decay $\propto e^{-\eta_6}$, corresponding to a linear decrease on the log-log scale. However, the decay parameters, η_6, remained low and did not exceed the critical value $\eta_6 = \frac{1}{4}$ for the hexatic-liquid transition until 1145°C. Nevertheless, even at 1145°C, more than 75% of the images displayed orientational decay consistent with the hexatic phase, i.e., with $\eta_6 < \frac{1}{4}$. Both the orientational order and translational order correlations agreed with the definition of the hexatic phase between approximately 1125° and 1145°C.

At 1150°C, a sudden increase in η_6 occurred, accompanied by a large deviation in the fitting parameter values, consistent with an increasingly liquid character of the crystal. At 1155°C, the orientational correlation vanished completely, and at 1160°C, the AgI crystals could be considered molten, with an average η_6 of 1.12. These observations are in excellent agreement with the FTs of the datasets shown in fig. S29, which displayed a gradual azimuthal broadening of the AgI peaks at temperatures >1125°C. Note, however, that the power law–like decay of G_6 of most frames at the highest temperatures stands in contradiction to the KTHNY theory. As this decay is not represented in every frame, it is unlikely that it arose from an artifact of the CNN detection at high temperatures. Instead, it may be a manifestation of a melting scenario that is of a non-KTHNY type.

On the melting mechanism

The translational and orientational correlation functions revealed the presence of a hexatic phase in a narrow temperature window below the melting point, but these parameters alone do not determine the melting mechanism. According to the KTHNY theory, both transitions—solid to hexatic and hexatic to liquid—are continuous, whereas the mixed melting scenario features a continuous solid to hexatic transition followed by a first-order hexatic to liquid transition (*8*, *9*, *35*). In continuous melting, local order evolves gradually with temperature, driven by the unbinding of defect pairs. By contrast, a first-order transition results in an abrupt change in local order and the coexistence of two distinct phases, typically separated by grain boundaries. To distinguish between these transition types, the local density distribution of the particles is a useful indicator, exhibiting a bimodal character when two phases coexist. Figure 4 illustrates how, in our experiment, the local density evolves across the solid-hexatic and hexatic-liquid transitions. Apart from minute broadening and a subtle shift toward lower density, the density distribution remained nearly unchanged and unimodal up to 1130°C, consistent with a continuous solid-hexatic transition. However, starting at 1135°C, the distribution became increasingly bimodal, and by 1150°C, the lower-density mode became dominant. These changes provide evidence for phase coexistence and indicate a first-order hexatic-to-liquid transition near the melting point, consistent with a mixed

melting scenario (*35*). At 1155°C, the local density distribution became very wide and quasiunimodal, indicating the complete loss of correlation in the liquid phase.

In the KTHNY scenario, melting is driven by the formation of high-energy (charged) dislocation defects. The six-membered rings of the AgI lattice can deform into 5-7 pairs (dislocations) at the solid-hexatic transition, which then unbind into isolated five- and seven-membered rings (disclinations) at the hexatic-liquid transition. This leads to structural disintegration even at low defect densities. By contrast, the mixed melting scenario involves lower-energy defects that are more abundant and rapidly form large clusters and thus create grain boundaries between different coexisting phases (*35*). We analyzed the abundance of different defect types and clusters in our system through Voronoi segmentation. Because the amount of strictly isolated dislocations and disclinations remained low at all temperatures, we classified the symmetry-breaking effect of defect clusters by identifying their topological charge. Defect clusters were classified into dislocation, disclination, and neutral-charged categories as well as into an "unknown" category for clusters that could not be classified (see discussion in supplementary materials and fig. S25). The abundance of defects inside both dislocation and disclination charged clusters remained constant up to 1125°C, after which both types of defects increased rapidly and continuously. At higher temperatures, a substantial number of defects began to form line-like clusters, which rapidly grew outside the observed field of view, complicating the determination of the type of defect and leading to a fast increase in the "unknown" category. The high defect density at the highest temperatures, where the ratio of topological defects (nonhexagonal Voronoi cells) to hexagonal cells reached 0.35, and the absence of isolated dislocation unbinding coupled with the observation of a first-order hexatic-liquid transition supported a mixed-type melting scenario consistent with the grain boundary theory of melting (*38*).

Conclusions

We have recorded the phase transitions from solid to liquid in a covalently bonded 2D crystal and demonstrated that melting proceeds through a hexatic intermediate phase. Graphene encapsulation enabled us to observe this transition in 2D AgI through time- and temperature-resolved in situ atomic-resolution STEM imaging and NBED. The hexatic phase, which forms only in 2D systems, exhibited long-range orientational but only short-range translational order and emerged within a 25°C window below the melting point. The absolute transition temperature depended on crystal size. Although definitively distinguishing between the KTHNY and mixed melting scenarios, both involving a hexatic phase, remains challenging, our data suggest that 2D AgI followed a mixed melting pathway. These findings provide direct insight into 2D melting in a real covalent crystal and open new directions for understanding phase transitions in atomically thin materials.

REFERENCES AND NOTES

1. J. M. Kosterlitz, D. J. Thouless, *J. Phys. C Solid State Phys.* **5**, L124–L126 (1972).
2. J. M. Kosterlitz, D. J. Thouless, *J. Phys. C Solid State Phys.* **6**, 1181–1203 (1973).
3. B. I. Halperin, D. R. Nelson, *Phys. Rev. Lett.* **41**, 121–124 (1978).
4. D. R. Nelson, B. I. Halperin, *Phys. Rev. B Condens. Matter* **19**, 2457–2484 (1979).
5. A. P. Young, *Phys. Rev. B Condens. Matter* **19**, 1855–1866 (1979).
6. I. Guillam'on *et al.*, *Nat. Phys.* **5**, 651–655 (2009).
7. D. S. Fisher, B. I. Halperin, R. Morf, *Phys. Rev. B Condens. Matter* **20**, 4692–4712 (1979).
8. S. T. Chui, *Phys. Rev. Lett.* **48**, 933–935 (1982).
9. S. T. Chui, *Phys. Rev. B Condens. Matter* **28**, 178–194 (1983).
10. E. P. Bernard, W. Krauth, *Phys. Rev. Lett.* **107**, 155704 (2011).
11. A. J. Armstrong, R. C. Mockler, W. J. O'Sullivan, *J. Phys. Condens. Matter* **1**, 1707–1730 (1989).
12. C. J. Guo *et al.*, *Phys. Rev. Lett.* **51**, 1461–1464 (1983).
13. X. H. Zheng, R. Grieve, *Phys. Rev. B Condens. Matter Mater. Phys.* **73**, 064205 (2006).
14. C. A. Murray, D. H. Van Winkle, *Phys. Rev. Lett.* **58**, 1200–1203 (1987).
15. E. V. Vasilieva, O. F. Petrov, M. M. Vasiliev, *Sci. Rep.* **11**, 523 (2021).
16. R. Geer *et al.*, *Nature* **355**, 152–154 (1992).
17. R. Viswanathan, L. L. Madsen, J. A. Zasadzinski, D. K. Schwartz, *Science* **269**, 51–54 (1995).
18. C.-F. Chou, A. J. Jin, S. W. Hui, C. C. Huang, J. T. Ho, *Science* **280**, 1424–1426 (1998).
19. P. A. Heiney *et al.*, *Phys. Rev. Lett.* **48**, 104–108 (1982).
20. K. Zahn, R. Lenke, G. Maret, *Phys. Rev. Lett.* **82**, 2721–2724 (1999).
21. P. Huang *et al.*, *Nat. Nanotechnol.* **15**, 761–767 (2020).
22. A. Pasupalak, L. Yan-Wei, R. Ni, M. Pica Ciamarra, *Soft Matter* **16**, 3914–3920 (2020).
23. Y.-W. Li, M. P. Ciamarra, *Phys. Rev. Lett.* **124**, 218002 (2020).
24. A. L. Thorneywork, J. L. Abbott, D. G. A. L. Aarts, R. P. A. Dullens, *Phys. Rev. Lett.* **118**, 158001 (2017).
25. T. F. Rosenbaum, S. E. Nagler, P. M. Horn, R. Clarke, *Phys. Rev. Lett.* **50**, 1791–1794 (1983).
26. H. Dai, C. M. Lieber, *Phys. Rev. Lett.* **69**, 1576–1579 (1992).
27. T. Domröse *et al.*, *Nat. Mater.* **22**, 1345–1351 (2023).
28. V. Kapil *et al.*, *Nature* **609**, 512–516 (2022).
29. S. Haastrup *et al.*, *2D Mater.* **5**, 042002 (2018).
30. K. Mustonen *et al.*, *Adv. Mater.* **34**, e2106922 (2022).
31. S. Hull, D. A. Keen, *Phys. Rev. B Condens. Matter* **59**, 750–761 (1999).
32. O. L. Krivanek *et al.*, *Nature* **464**, 571–574 (2010).
33. K. V. Zakharchenko, A. Fasolino, J. H. Los, M. I. Katsnelson, *J. Phys. Condens. Matter* **23**, 202202 (2011).
34. I. A. Zaluzhnyy *et al.*, *Phys. Rev. E Stat. Nonlin. Soft Matter Phys.* **91**, 042506 (2015).
35. O. Toledano, M. Pancorbo, J. E. Alvarellos, O. G'alvez, *Phys. Rev. B* **103**, 094107 (2021).
36. V. M. Bedanov, G. V. Gadiyak, Y. E. Lozovik, *Phys. Lett. A* **109**, 289–291 (1985).
37. V. Ramasubramani *et al.*, *Comput. Phys. Commun.* **254**, 107275 (2020).
38. Y. Saito, *Phys. Rev. B Condens. Matter* **26**, 6239–6253 (1982).
39. K. Mustonen, Data for "Hexatic phase in covalent two-dimensional silver iodide" (2025); https://phaidra.univie.ac.at/detail/o:2163141.

ACKNOWLEDGMENTS

We thank X.-B. Li and D. Wang for kindly providing the AgI vacancy model structures. **Funding:** K.M. and T.A.B. acknowledge funding from FWF through grant no. P35912. V.S. has been supported by the V4-Japan Joint Research Program V4-Japan/JRP/2021/96/BGapEng; grant no. VEGA 1/0104/25, provided by Ministry of Education, Research, Development, and Youth of the Slovak Republic, the EU NextGenerationEU through the Recovery and Resilience Plan for Slovakia, under project no. 09I05-03-V02-00071; and the QM4ST, CZ.02.01.01/00/22-008/0004572 of Johannes Amos Commenius Programme for Excellent Research. T.J.P. acknowledges support from the European Research Council under the European Union Horizon 2020 program, grant agreement no. 802123-HDEM. L.F. and D.L. acknowledge funding from FWF through grant no. P35318 and DOC142. M.K. acknowledges funding from the National Center for Research and Development under the V4-Japan Joint Research Program BGapEng V4-JAPAN/2/46/BgapEng/2022. **Author contributions:** K.M. and T.A.B. conceived the study. T.A.B., K.M., D.L., C.M., and V.S. conducted the experimental work, and D.L., K.M., T.A.B., and J.C.M. performed the data analysis. J.M. developed and trained the neutral network. P.K. and V.S. synthesized the sample material, and M.K. and A.M. provided computational support. K.M., T.J.P., D.L., J.C.M., T.A.B., V.S., J.K., and L.F. wrote the manuscript. **Competing interests:** The authors declare that they have no competing interests. **Data and materials availability:** The experimental data supporting these findings are openly available in the University of Vienna repository PHAIDRA (*39*).

License information: Copyright © 2025 the authors, some rights reserved; exclusive licensee American Association for the Advancement of Science. No claim to original US government works. https://www.science.org/about/science-licenses-journal-article-reuse. This research was funded in whole or in part by European Union's Horizon 2020 program (grant agreement no. 802123-HDEM), a cOAlition S organization. The author will make the Author Accepted Manuscript (AAM) version available under a CC BY public copyright license.

SUPPLEMENTARY MATERIALS

science.org/doi/10.1126/science.adv7915
Materials and Methods; Figs. S1 to S30; References (*40–62*); Movies S1 to S15

Submitted 9 January 2025; resubmitted 15 July 2025; accepted 15 October 2025
10.1126/science.adv7915

SYNTHETIC BIOLOGY

High-fidelity human chromosome transfer and elimination

Gianluca Petris[1,2]†‡, Simona Grazioli[1]†, Linda van Bijsterveldt[1]†, Pierre Murat[1]§, Kim C. Liu[1], Jakob Birnbaum[1]¶, Julian E. Sale[1,2]*, Jason W. Chin[1,2]*

The synthesis of human genomes and other gigabase-scale genomes will require new strategies. Here, we realized key steps in our pipeline for building synthetic human chromosomes. We established: (i) the facile transfer of human chromosomes from human cells to mouse embryonic stem cells (assembly cells), where they are haploid, are nonessential, and may be operated on; (ii) the transfer of these human chromosomes from monochromosomal hybrids back into human cells to generate defined, synthetic aneuploidies; and (iii) the elimination of the corresponding endogenous human chromosomes to regenerate diploid cells containing a transferred chromosome. All steps were performed in nontransformed cells without chromothripsis and generated minimal structural variants, insertions, deletions, or single-nucleotide variants.

Human genome synthesis will facilitate an understanding of the causal relationships and rules underpinning the sequence and architecture of natural genomes, enable the construction of extinct hominid genotypes, accelerate bioproduction, and improve cell-based therapies.

Human chromosomes are too large to be assembled in the microbial hosts that have been used for *Mycoplasma genitalium* and *Escherichia coli* genome syntheses (*1*, *2*) and for *Saccharomyces cerevisiae* chromosome syntheses (*3*, *4*), and the repetitive nature of human DNA makes its large-scale maintenance and manipulation difficult or impossible in recombinogenic organisms such as *S. cerevisiae*. Targeted manipulation of a single copy of a human chromosome in a human cell with a diploid genome is also challenging. A major current goal is therefore to develop approaches to address the challenges of human genome synthesis.

We set out to establish a strategy for building human chromosomes and genomes (Fig. 1 and fig. S1). This strategy generates a single copy of a human chromosome in assembly cells, mouse embryonic stem cells (mESCs) (see the supplementary text), so that its sequence can be specifically targeted. The use of assembly cells reduces the risk of recombination between the engineered human chromosome and the rest of the genome and eliminates the risk of interallelic recombination for the engineered human chromosome. Because human chromosomes are nonessential in assembly cells, additional manipulations (e.g., deletions of essential and haploinsufficient genes) will become possible. Moreover, off-target mutations in the host genome (as a by-product of targeted manipulation of the human chromosome) will not be carried through to the final human cell.

Our approach requires the transfer of intact human chromosomes from human cells into mESCs to generate monochromosomal hybrids, the transfer of chromosomes from monochromosomal hybrids into human cells to generate defined synthetic human aneuploidies, and the targeted elimination of an endogenous chromosome to regenerate human cells with a normal karyotype and a transferred chromosome. In the present work, we addressed the challenges associated with each of these steps (see the supplementary text).

[1]Medical Research Council Laboratory of Molecular Biology, Cambridge, UK. [2]Wellcome Sanger Institute, Wellcome Trust Genome Campus, Hinxton, UK. ***Corresponding author. Email: jes@mrc-lmb.cam.ac.uk (J.E.S.); chin@mrc-lmb.cam.ac.uk (J.W.C.)** †These authors contributed equally to this work. ‡Present address: Università degli Studi di Udine, Udine, Italy, and Fondazione Italiana Fegato, Basovizza, Trieste, Italy. §Present address: Wellcome Sanger Institute, Wellcome Trust Genome Campus, Hinxton, UK. ¶Present address: AstraZeneca, Hamburg, Germany.

Labeling chromosomes in RPE1 donor cells

We selected the nontransformed and immortalized human RPE1 cell line (*5*), which has a stable, near-diploid karyotype (fig. S2, A and B) (*6*), as the donor for our chromosome transfer experiments.

To facilitate the subsequent identification and isolation of chromosome transfer events in the recipient mESCs, we marked all chromosomes in the RPE1 donor using a *PiggyBac* cassette containing superfolder green fluorescent protein (sfGFP) and a neomycin resistance gene conferring resistance to G418 (sfGFP-NEO) (*7*, *8*) (fig. S3A). We confirmed the labeling of all 23 chromosomes (fig. S3B). The integration sites were distributed evenly across the genome and showed a correlation between the number of integrations in each chromosome and its length (fig. S3, C and D).

Transfer of human chromosomes from human cells to mESCs

We arrested the sfGFP-NEO RPE1 donor cells in M phase with colcemid for 6 to 9 hours (see the materials and methods) (fig. S2C) and incubated mitotic cells with the actin polymerization inhibitor latrunculin B (*9*). Condensed chromosomes were released from cells into protective polyamine buffer (*10*) (see the materials and methods), and the resulting chromosome suspension was transfected into mESCs with polyethylenimine (PEI) (Fig. 2A), achieving a transfection efficiency of ~10^{-6}.

After 13 independent chromosome transfection experiments, we obtained a library of 49 G418-resistant mESC clones. Overall, G418-resistant mESC clones spanned 13 different human chromosomes (4, 5, 6, 8, 9, 10, 12, 13, 14, 19, 20, 21, and 22) and harbored human chromosomes [intact, fragmented, or displaying internal copy number variations (CNVs)] (figs. S4, A to D, and S5; table S1; and supplementary text), as judged by low-coverage whole-genome sequencing (WGS). Thirteen mESC clones likely had an intact human chromosome (4, 6, 10, 13, 20, and 21) (figs. S4, A and B, and S5 and table S1). The number of distinct human chromosomes (or chromosome fragments) present in the library of monochromosomal hybrids showed minimal deviation from the values expected for the unbiased transfer of chromosomes (or their fragments) (fig. S4, E to G). We performed chromosome stability analyses based on sfGFP maintenance (fig. S6) and showed that fluorescence in situ hybridization (FISH) (fig. S7) was consistent with low-coverage WGS, confirming the presence of clones containing a single intact human chromosome (see the supplementary text).

Next, we more deeply characterized three mESC clones, mESC Hchr4 (CL3), mESC Hchr21 (CT2-1), and mESC Hchr20 (CB20F), for which our initial analyses, along with G-banding analysis and flow karyotyping (see the supplementary text), were consistent with the presence of a single intact human chromosome (Fig. 2, B and C, and figs. S8A and S9). These clones cover the three types of human chromosomes, submetacentric (chromosome 4; 193.5 Mb), metacentric (chromosome 20; 66.2 Mb), and acrocentric (chromosome 21; 45.1 Mb). We performed high-coverage (20 to 30×) Illumina WGS, long-read Oxford nanopore sequencing (Oxford Nanopore Technologies, ONT), PacBio sequencing, and Bionano optical genome mapping (OGM) on these three clones (Fig. 2, D to G; figs. S8, B and C, and S10 and S11; and supplementary text). From an analysis of the resulting data, we concluded that there was a single copy of each human chromosome in the assembly cells (Fig. 2, D and E, and fig. S8B) and that occurrences of CNVs, structural variants (SVs), insertions and deletions (INDELs), and single-nucleotide variants (SNVs) in intact human chromosomes in mESCs were low and deviated minimally from their frequencies in parental, human RPE1 cells (Fig. 2, H and I, and fig. S8D).

Additionally, we characterized three further monochromosomal hybrid clones, mESC Hchr6 (CB20-GO), mESC Hchr10 (CB15C), and

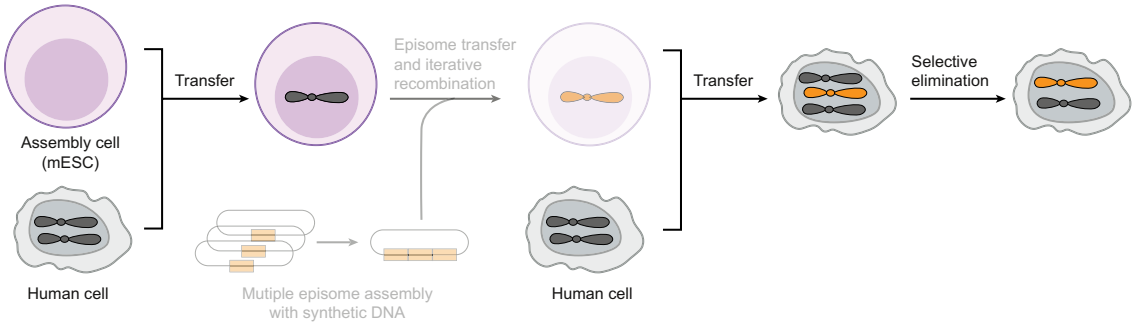


Fig. 1. Overview of our strategy for the generation of human cells bearing synthetic human chromosomes. In the present work, we focused on the transfer of human chromosomes from human cells to assembly cells, the transfer of human chromosomes from assembly cells to human cells to generate defined aneuploidies, and the elimination of targeted endogenous chromosomes to generate a diploid cell bearing the transferred chromosome. These operations are shown in the solid part of the image. The operations necessary to convert the human chromosome into a synthetic chromosome are shown as translucent illustrations and captions. These steps include the assembly of episomes bearing synthetic human DNA and the transfer and recombination of this DNA into the human chromosome. Progress on these steps is discussed in the supplementary text and in the legend to fig. S1.

mESC Hchr13 (CT-3). Our analyses (fig. S12, A to C; table S1; and supplementary text) indicated that we had successfully transfected these three additional human chromosomes into mESCs without detectable gross rearrangements. The six transferred chromosomes harbored a density of genes and genomic features [e.g., GC content, long (LINE) and short (SINE) Interspersed nuclear element density, and repetitive elements] that were at comparable levels to their median levels across the human genome (fig. S12D), further supporting the view that the workflow is generalizable to other human chromosomes.

We estimated telomere length in chromosome arms using OGM by measuring the distance from the last marker detected to the end of individual DNA molecules (*11*) (see the materials and methods). In RPE1 cells, the telomere molecule lengths for Hchr4 (4p and 4q) and Hchr21 (21q) ranged from 5 to 10 kb (Fig. 2J and figs. S8E and S13, A and B), as expected (*12*). In mESC monochromosomal hybrids, molecules mapping to the telomeric ends of human chromosomes 4 and 21 increased to a median telomere length of 99 and 108 kb in mESC Hchr4 (4p and 4q, respectively) and 57 kb in mESC Hchr21 (21q), with most molecules measuring between 30 and 120 kb (Fig. 2J and fig. S13, A and B). For human chromosome 20 in mESC Hchr20 (CB20F) (20p and 20q), median telomere length similarly increased to 68 and 60 kb (20p and 20q, respectively) (figs. S8E and S13C). The telomere molecule lengths for the human chromosome arms in mESCs were comparable to the telomere molecule lengths of endogenous mouse chromosomes (~100 kb) in the same clones (Fig. 2J and figs. S8E and S13D) and to mouse telomere lengths reported in the literature (*13*). This indicated that after transfer of human chromosomes to mESCs, their telomeres were actively lengthened to match the setpoint for mouse telomere length and were then maintained at this length.

Manipulation of human chromosomes in assembly cells

We set out to replace a region of Hchr20 (35.69 to 35.70 Mb) with synthetic DNA in which 23 wild-type codons (within the *ROMO1* and *NFS1* loci) were replaced with their synonyms (fig. S14A). We first integrated a landing pad comprising a cassette encoding blue fluorescent protein (BFP) and HygR into Hchr20 (fig. S14B) harbored within an assembly cell. We then electroporated a 35-kb bacterial artificial chromosome (BAC) carrying a 10-kb synthetic DNA payload with putatively silent watermarks and a selection cassette encoding mCherry and PuroR, and then cut the human chromosome using CRISPR-guided Cas9 to induce HR-mediated replacement of the landing pad with the (mostly) homologous synthetic DNA carried in the BAC (fig. S14C). Successful integration of the synthetic DNA in Hchr20 in the puromycin-resistant clones was confirmed with polymerase chain reaction genotyping (correct for 7 of 24 clones). For one correctly genotyped clone, we further confirmed successful marker swap using flow cytometry (fig. S14D) and the correct sequence using ONT (fig. S14E). These experiments demonstrated that the sequence of human chromosomes can be precisely manipulated in mESC assembly cells.

Transfer of human chromosomes from mESC monochromosomal hybrids to human cells

Next, we aimed to generate chromosome-specific aneuploidies in human cells through the transfer of human chromosomes from their mESC monochromosomal hybrid hosts to human cells. We were not able to deliver human chromosomes from mESC monochromosomal hybrids to RPE1 cells by PEI transfection. We therefore devised rapid microcell–mediated chromosome transfer (R-MMCT) to transfer chromosomes from mESCs to RPE1 cells. Unlike standard MMCT, which requires 2 to 4 days of colcemid-induced mitotic arrest, often causes micronuclei and chromosome fragmentation and reduced clone viability, and can only be used to transfer chromosomes from the very limited number of cell types that can tolerate hyperploidization (A9 and CHO) (*14*–*18*), R-MMCT minimizes the length of colcemid treatment to effectively arrest cells in mitosis (fig. S15). We used these mitotic cells to generate microcells (*19*), which were filtered for size and fused to RPE1 cells with inactivated Sendai virus [hemagglutinating virus of Japan envelope (HVJ-E)] particles (*9*, *20*). Recipient RPE1 cells were selected, with G418, for the presence of the transferred chromosome (Fig. 3A), achieving a transfer efficiency of ~10^{-6}.

We obtained 107, 51, and 42 RPE1 clones with the correct phenotype from separate R-MMCT experiments using mESC Hchr21 (CT2-1), Hchr4 (CL3), and Hchr20 (CB20F) as donors, respectively. From these clones, we selected 110 clones (30 for Hchr21, 49 for Hchr4, and 31 for Hchr20) for further characterization (fig. S16, table S2, and supplementary text). We investigated chromosome copy number using low-coverage WGS and flow cytometry–based karyotyping and chromosome stability using sfGFP measurements (figs. S17 and S18 and supplementary text).

We performed more detailed characterization of two trisomies, Hchr4 (2A8) and Hchr21 (7M5-1-2), and two tetrasomies, Hchr4 (OB1) and Hchr20 (2A2), for which low-coverage WGS, sfGFP stability, and flow karyotyping were consistent with the presence of an intact and stable aneuploidy (Fig. 3 and fig. S19). G-banding karyotypes of all human chromosomes from these four clones demonstrated the expected copy number increase, resulting from the transferred chromosome (Fig. 3, B and C, and fig. S19, A and B). We did also not detect any karyotypic alterations with respect to RPE1 (fig. S2) in the other chromosomes (Fig. 3, B and C, and fig. S19, A and B). We next performed high-coverage Illumina sequencing, ONT, and Bionano OGM on these clones and control RPE1 clones (Fig. 3, D to I; fig. S19, C to H; and supplementary text). Overall, our data suggested that it is possible to transfer intact human

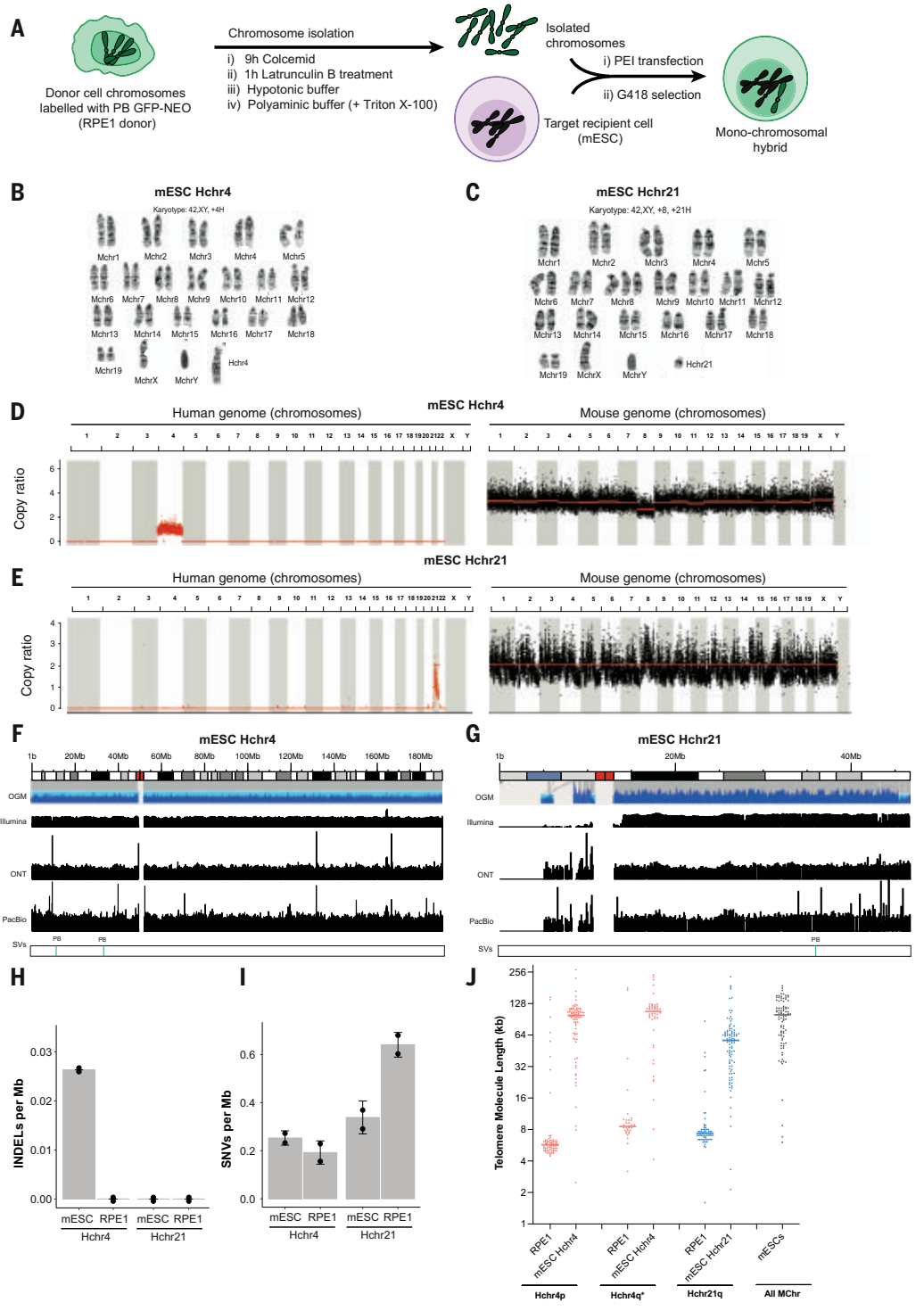


Fig. 2. Human chromosomes can be transfected into mESCs, where they are stably maintained with minimal damage and mouse-length telomeres. (**A**) Schematic of chromosome isolation from RPE1 cells and transfection into mESCs to generate monochromosomal hybrid cells. (**B** and **C**) Giemsa-stained karyotype (G-banding) representative of 20 metaphase spreads of mESCs harboring Hchr4 (clone CL3) (B) and of mESCs harboring Hchr21 (clone CT2-1) (C). (**D** and **E**) CNV analysis of high-coverage Illumina sequencing (NGS) reads for hybrid mESCs with Hchr4 (D) and Hchr21 (E) aligned against a hybrid human-mouse reference genome (bin size, 1 kb). (**F** and **G**) Deep characterization of the transferred Hchr4 (F) and Hchr21 (G) by OGM, high-coverage Illumina, and ONT sequencing. The traces represent the contigs assembled from OGM (blue), and Illumina, ONT, and PacBio coverage. Note that the p arm of Hchr21 cannot be assembled because of its highly repetitive sequence. SVs, including *PiggyBac* insertions (PB), on the transferred chromosome are shown. (**H**) Quantification of INDELs (Illumina) in Hchr4 and Hchr21 compared with two control RPE1 clones. Data are presented as the number of INDELS/Mb with their SDs. (**I**) Quantification of SNVs (Illumina) in Hchr4 and Hchr21 compared with two control RPE1 clones. Data are presented as the number of SNVs/Mb with their SDs. (**J**) Median telomere molecule length (horizontal line) for transfected Hchr4 and Hchr21 (q arm) in monochromosomal hybrid mESCs (Hchr4 clone CL3 and Hchr21 clone CT2-1) compared with the same arms in wild-type RPE1 cells (clone F8) (see the materials and methods). Median telomere molecule length for a subset of representative mouse chromosomes is shown for reference.

chromosomes from mESC monochromosomal hybrid assembly cells to human cells using R-MMCT without retaining mouse DNA (fig. S20) and with minimal DNA damage and mutagenesis, as judged by measurements of SNVs, INDELs, and SVs (Fig. 3H, figs. S19G and S21, and table S3).

After clones were expanded to at least 10^7 cells and then kept in culture for at least six additional passages, we estimated the length of the telomeres of Hchr4p and Hchr4q in the Hchr4 tetrasomy OB1 and Hchr4 trisomy 2A8, of Hchr20p and Hchr20q in Hchr20 tetrasomy 2A2, and of Hchr21q in Hchr21 trisomy 7M5-1-2 from the OGM data. For Hchr4, Hchr20, and Hchr21, most molecules mapping to the telomeres were of similar length to those from wild-type RPE1 cells. However, a fraction of telomeric molecules for Hchr21q in Hchr21 trisomy (7M5-1-2), Hchr4p and Hchr4q in Hchr4 trisomy (2A8), and tetrasomy (OB1) and Hchr20p and Hchr20q in tetrasomy (2A2) were substantially longer (15 to 150 kb) than the telomere molecules in the control RPE1 cells (5 to 10 kb) (Fig. 3I and figs. S19H and S22). This observation suggested that the telomeres of the transferred human chromosomes were generally shorter than when harbored in mESCs and may approach the length of human telomeres with further passaging. The rate of telomere

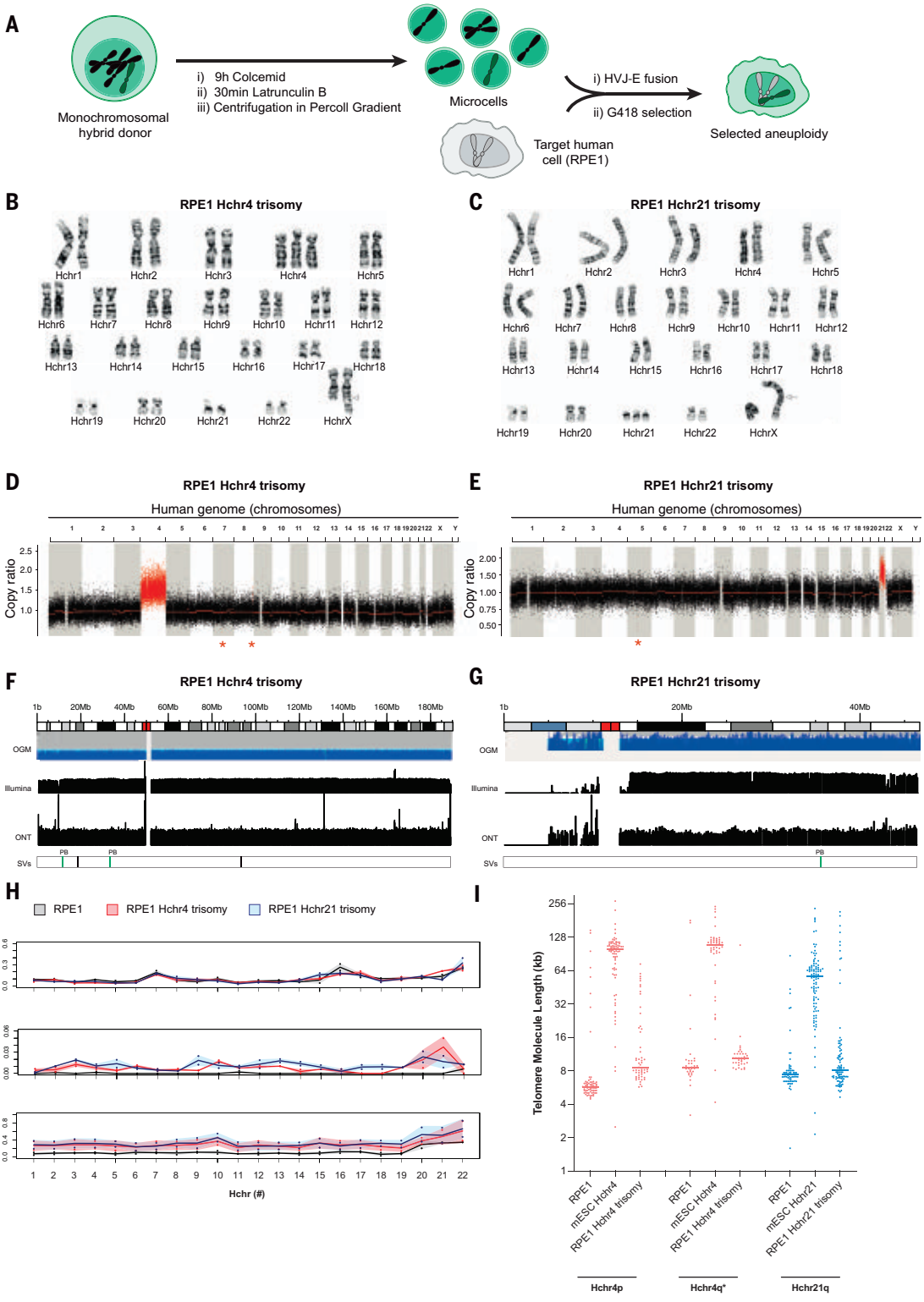


Fig. 3. R-MMCT of human chromosomes from monochromosomal hybrid mESCs to human RPE1 cells to generate defined aneuploidies with minimal damage. (**A**) Schematic of human chromosome transfer from monochromosomal hybrid mESCs to RPE1 cells by R-MMCT to generate specific chromosome aneuploidies. (**B** and **C**) Giemsa-stained karyotype (G-banding) representative of 20 metaphase spreads of Hchr4 RPE1 trisomy (clone 2A8) (B) and Hchr21 RPE1 trisomy (clone 7M5-1-2) (C). (**D** and **E**) CNV analysis of high-coverage Illumina sequencing (NGS) reads for Hchr4 (D) and Hchr21 (E) RPE1 trisomies aligned against a hybrid human-mouse reference genome (bin size, 1 kb). (**F** and **G**) Deep characterization of Hchr4 (F) and Hchr21 (G) in their corresponding RPE1 trisomies by OGM, high-coverage Illumina, and ONT sequencing. The traces represent the contigs assembled from OGM (blue), Illumina, and ONT coverage. SVs, including *PiggyBac* insertions (PB), on the transferred chromosome are shown. Note that the p arm of Hchr21 cannot be assembled because of its highly repetitive sequence. (**H**) Genome-wide analysis of SVs (>40 bp, ONT), SNVs, and INDELs (Illumina) in the Hchr4 and Hchr21 RPE1 trisomies compared with two control RPE1 clones. Data are presented as means with SDs. (**I**) Median telomere molecule length (horizontal line) for Hchr4 and Hchr21 (21q) in their corresponding RPE1 trisomies and in their monochromosomal hybrid mESCs and median telomere molecule length for these chromosomes in RPE1 cells (clone F8) (same data as in Fig. 2J).

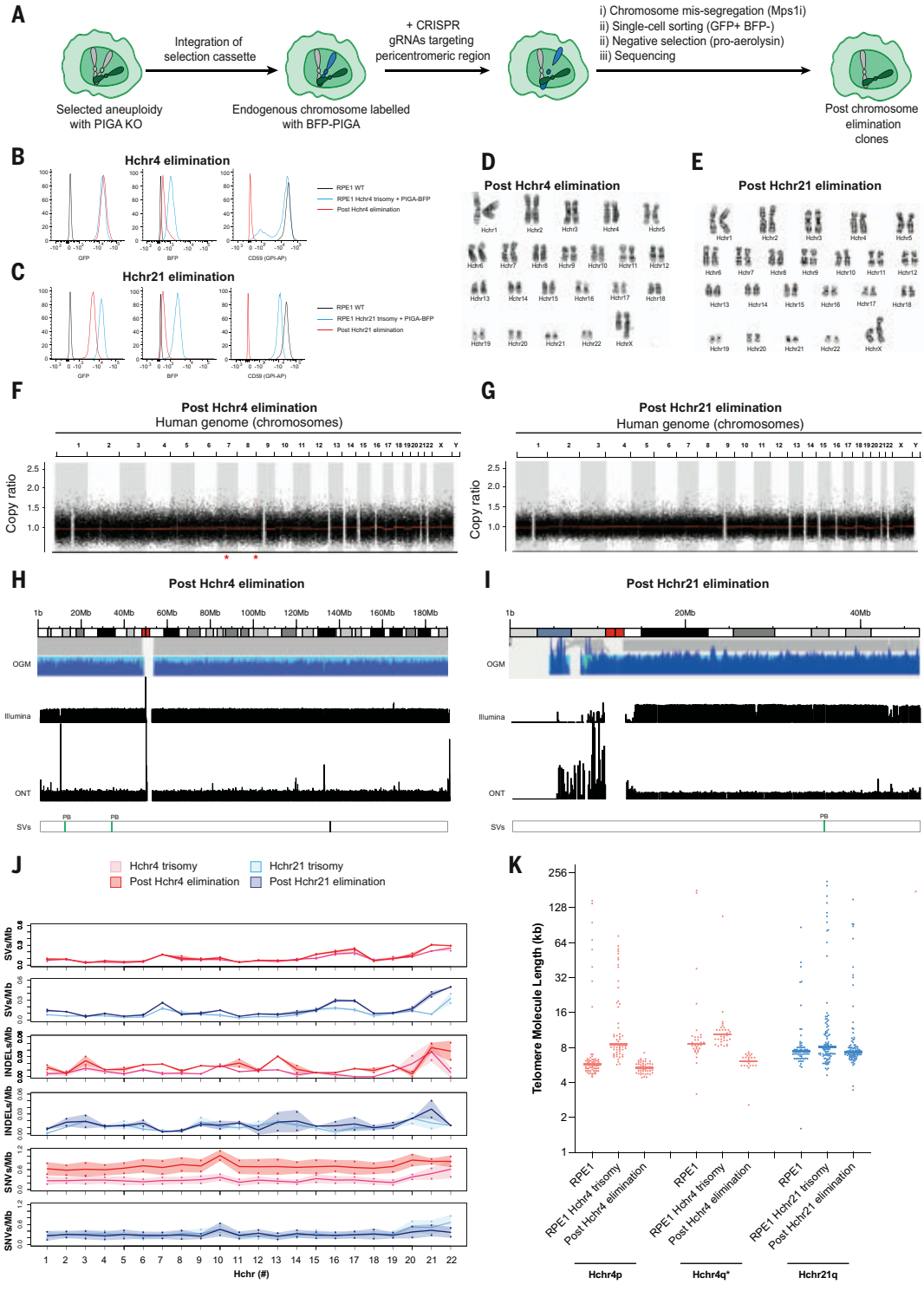


Fig. 4. Targeted removal of aneuploid endogenous chromosomes from human (RPE1) trisomies. (**A**) Schematic of the targeted removal of aneuploid chromosomes from RPE-1 cells. (**B** and **C**) Elimination of the BFP-*PIGA*–marked endogenous chromosome and maintenance of the transferred Hchr4 (clone 35) (B) or Hchr21 (clone 2) (C) was confirmed by flow cytometry. *PIGA* expression was analyzed using an anti-CD59 antibody. The lines show wild-type RPE1 cells for reference (black), the BFP-*PIGA*-marked trisomy (gray), and the eliminated clone. (**D** and **E**) Giemsa-stained karyotype (G-banding) representative of 20 metaphase spreads, all of which show a copy number of two for Hchr4 (clone 35) (D) and similarly for Hchr21 (clone 2) (E). (**F** and **G**) CNV analysis of high-coverage Illumina sequencing (NGS) reads for RPE1 Hchr4 elimination (F) and RPE1 Hchr21 elimination (G) aligned against a hybrid human-mouse reference genome (bin size, 1 kb). (**H** and **I**) Deep characterization of Hchr4 (H) and Hchr21 (I) after chromosome elimination by OGM, high-coverage Illumina, and ONT sequencing. The traces represent the contigs assembled by OGM (blue), Illumina, and ONT coverages. SVs, including *PiggyBac* insertions (PB), in this chromosome are shown. Note that the sequence for the p arm of Hchr21 cannot be assembled because of its highly repetitive sequence. (**J**) Genome-wide analysis of SVs (>40 bp, ONT), SNVs, and INDELs (Illumina) for postelimination clones of Hchr4 and Hchr21 and their corresponding RPE1 trisomies compared with two control RPE1 clones. Data are presented as means with SDs. (**K**) Median telomere molecule length for Hchr4 and Hchr21 in postelimination clones of Hchr4 and Hchr21 and in the corresponding trisomies (same data as in Fig. 3I) and median telomere molecule length for these chromosomes in RPE1 cells (clone F8).

shortening after chromosome transfer appeared to be substantially higher than could be explained by normal telomere attrition during replication (*21*); this suggested that the shortening we observed occurs through a different, and currently unknown, mechanism by which the new host (human) rapidly adjusts telomere length of the transferred human chromosome back to that of its endogenous chromosomes (*22*).

Elimination of endogenous human chromosomes from aneuploid clones

To eliminate an endogenous human chromosome (Fig. 4A), 4 or 21, from our previously generated RPE1 trisomies, we created RPE1 *PIGA* knockouts (fig. S23A and table S4) and introduced a counterselectable *PIGA* marker (*23*), along with a BFP marker, into one of the aneuploid endogenous chromosomes (fig. S23B, table S4, and supplementary text).

We then targeted the pericentromeric sequence of the aneuploid chromosome for CRISPR-mediated cleavage (table S4); transiently inhibited the mitotic checkpoint; sorted for sfGFP-positive, BFP-negative cells to enrich for cells that had maintained the transferred chromosome and lost the selection cassette; and then selected with proaerolysin to identify clones in which we had achieved successful chromosome elimination (Fig. 4, A to C; fig. S24; and supplementary text). A subset of the resultant proaerolysin-resistant clones were analyzed by Illumina short-read WGS (fig. S25). Copy number analysis of these clones confirmed successful elimination of Hchr4 and Hchr21 from their respective trisomic clones (2A8 and 7M5-1-2) with a success rate of >95% (fig. S25). We did not detect any off-target chromosome gains or losses (fig. S25).

Next, we selected clones elCL18 and elCL35, resulting from elimination of an endogenous Hchr4 from the trisomic clone 2A8, and clones elCL1 and elCL2, resulting from the elimination of an endogenous Hchr21 from the trisomic clone 7M5-1-2, for further characterization. We performed G-banding analysis; flow karyotyping; and high-coverage Illumina WGS, ONT, and OGM analysis (Fig. 4, D to K; figs. S26 and S27; and supplementary text) and specifically checked for CRISPR off-targets (tables S5 and S6 and supplementary text). These experiments demonstrated that these clones were diploid and the transferred chromosome intact (Fig. 4, D to I, and fig. S26), with the exception of a pericentromeric copy number change in one of the clones (fig. S27, C and D). We also found that the levels of SVs, INDELs, and SNVs in these postelimination clones were essentially comparable to the levels in the aneuploidies from which they were directly derived (Fig. 4J, fig. S28, table S3, and supplementary text).

The median telomere molecule lengths for Hchr4p and Hchr4q after elimination (elCL35) were 5.32 and 6.07 kb, respectively, and resembled the median telomere molecule length of the wild-type RPE1 control (5.72 and 8.60 kb for Hchr4p and Hchr4q, respectively) (Fig. 4K and fig. S29). Similarly, for Hchr21q, we found a median telomere molecule length of 7.34 kb, which was indistinguishable from that found in the wild-type RPE1 (7.37 kb) (Fig. 4K and fig. S29). Therefore, our data confirmed that telomere length returns to that of wild-type RPE1 cells after chromosome elimination and passaging.

Discussion

Here, we have provided a high-fidelity workflow for moving human chromosomes into mESC assembly cells, where they can be operated on, and returning them into human cells with regeneration of the normal karyotype. Chromosome transfection and R-MMCT proceeded with comparable high fidelity, and comparable efficiency, for the chromosome transfers tested; the preferred method of chromosome transfer will be a function of the properties of the donor and recipient cells. The intermediate aneuploidies provide a resource for studying the consequences of defined chromosome copy number changes without the confounding effects of cancer mutations. Advances in building and delivering episomes containing megabases of synthetic DNA and in replacing large chromosomal regions in mESCs (*24*–*28*) may be combined with the approaches reported herein to accelerate the synthesis of human genomes.

REFERENCES AND NOTES

1. D. G. Gibson *et al.*, *Science* **319**, 1215–1220 (2008).
2. J. Fredens *et al.*, *Nature* **569**, 514–518 (2019).
3. S. M. Richardson *et al.*, *Science* **355**, 1040–1044 (2017).
4. D. Schindler *et al.*, *Cell* **186**, 5237–5253.e22 (2023).
5. A. G. Bodnar *et al.*, *Science* **279**, 349–352 (1998).
6. E. Volpe *et al.*, *Nat. Commun.* **16**, 7751 (2025)
7. S. Ding *et al.*, *Cell* **122**, 473–483 (2005).
8. S. J. Elsässer, R. J. Ernst, O. S. Walker, J. W. Chin, *Nat. Methods* **13**, 158–164 (2016).
9. M. Liskovykh, N. C. Lee, V. Larionov, N. Kouprina, *Mol. Ther. Methods Clin. Dev.* **3**, 16043 (2016).
10. B. L. Ng, N. P. Carter, *Cytometry A* **69**, 1028–1036 (2006).
11. E. Young *et al.*, *Nucleic Acids Res.* **45**, e73 (2017).
12. M. A. Blasco, *Nat. Rev. Genet.* **6**, 611–622 (2005).
13. E. Varela, R. P. Schneider, S. Ortega, M. A. Blasco, *Proc. Natl. Acad. Sci. U.S.A.* **108**, 15207–15212 (2011).
14. M. Paulis *et al.*, *Mol. Ther. Methods Clin. Dev.* **17**, 369–377 (2020).
15. T. Ege, N. R. Ringertz, *Exp. Cell Res.* **87**, 378–382 (1974).
16. R. E. Fournier, F. H. Ruddle, *Proc. Natl. Acad. Sci. U.S.A.* **74**, 319–323 (1977).
17. T. Suzuki, Y. Kazuki, M. Oshimura, T. Hara, *PLOS ONE* **11**, e0157187 (2016).
18. N. Uno *et al.*, *Sci. Rep.* **12**, 3009 (2022).
19. E. Stubblefield, M. Pershouse, *Somat. Cell Mol. Genet.* **18**, 485–491 (1992).
20. S. Yamaguchi, X. Ren, M. Katoh, *Chromosome Sci.* **9**, 65–73 (2006).
21. C. B. Harley, A. B. Futcher, C. W. Greider, *Nature* **345**, 458–460 (1990).
22. A. Weuts *et al.*, *Nucleic Acids Res.* **40**, 11477–11489 (2012).
23. D. Li *et al.*, *Nucleic Acids Res.* **49**, 2642–2654 (2021).
24. L. Li, T. Blankenstein, *Nat. Protoc.* **8**, 1567–1582 (2013).
25. E. C. Lee *et al.*, *Nat. Biotechnol.* **32**, 356–363 (2014).
26. H. A. Wallace *et al.*, *Cell* **128**, 197–209 (2007).
27. W. Zhang *et al.*, *Nature* **623**, 423–431 (2023).
28. R. Brosh *et al.*, *Proc. Natl. Acad. Sci. U.S.A.* **118**, e2023952118 (2021).

ACKNOWLEDGMENTS

We thank the staff of the Flow Cytometry Facility at the MRC Laboratory of Molecular Biology, including M. Daly, P. A. Penttilä, Y. Li, and F. Zhang; G. van der Goot (EPFL, Lausanne) for supplying purified proaerolysin; scientists and staff at Bionano Genomics and Source Bioscience, especially L. Laws, E. Shaffu, E. Mularczyk, and H. Horn; the Wellcome Sanger Institute, CASM program support, and the DNA pipeline and long-read teams for ONT and OGM analysis, especially K. Oliver, I. Bronner, M. Dignam, G. Ping, and M. Smith; and the UCL Long Read Sequencing service, especially J. Lee, for Bionano OGM and PacBio sequencing. JM8.F6 mouse embryonic stem cells (mESCs) were obtained from the Wellcome Sanger Institute (Hinxton, UK). **Funding:** This work was supported by the UK Medical Research Council (MRC grants MC_U105181009 and MC_UP_A024_1008 to J.W.C. and grant MC_U105178808 to J.E.S.) and the Wellcome Trust (discretionary award 221267/Z/20/Z to J.W.C. and J.E.S.). S.G. was supported by the Boehringer Ingelheim Fonds and the Cambridge Commonwealth, European and International Trust. G.P. was partially supported by a Marie Skłodowska-Curie European Postdoctoral Fellowship (897663). J.W.C. and J.E.S. thank the Wellcome Sanger Institute for support through the associate faculty program. **Author contributions:** Conceptualization: G.P., S.G., L.V.B., J.E.S., J.W.C.; Formal analysis: P.M., K.C.L., S.G.; Funding acquisition: J.W.C., J.E.S.; Investigation: G.P., S.G., L.V.B., J.B.; Methodology: G.P., S.G., L.V.B., P.M., K.C.L.; Supervision: J.E.S., J.W.C.; Writing – original draft: G.P., S.G., L.V.B., J.E.S., J.W.C.; Writing – review & editing: G.P., S.G., L.V.B., P.M., K.C.L., J.E.S., J.W.C. **Competing interests:** J.W.C. is founder of Constructive Bio and K.C.L. is a consultant for Constructive Bio. G.P. is founder of Alia Therapeutics. The remaining authors declare no competing interests. **Data and materials availability:** Data for the present paper can be found in the Sequence Read Archive of the National Center for Biotechnology Information (https://www.ncbi.nlm.nih.gov/sra) under bioproject number PRJNA1201099. The scripts used for data analysis can be found at 10.5281/zenodo.17642095. The authors agree to provide any materials and cell lines generated in this study upon request.

License information: Copyright © 2025 the authors, some rights reserved; exclusive licensee American Association for the Advancement of Science. No claim to original US government works. https://www.science.org/about/science-licenses-journal-article-reuse.

This research was funded in whole or in part by the UK Medical Research Council (grants MC_U105181009, MC_UP_A024_1008, and MC_U105178808) and by Wellcome (discretionary award 221267/Z/20/Z), both cOAlition S organizations. The author will make the Author Accepted Manuscript (AAM) version available under a CC BY public copyright license.

SUPPLEMENTARY MATERIALS

science.org/doi/10.1126/science.adv9797
Materials and Methods; Supplementary Text; Figs. S1 to S29; Tables S1 to S6; References (*29*–*81*); MDAR Reproducibility Checklist

Submitted 14 January 2025; resubmitted 20 June 2025; accepted 9 October 2025

10.1126/science.adv9797

ACTUATORS

Semiseparated biphasic bicontinuous dielectric elastomer for high-performance artificial muscle

Xiaotian Shi[1,2]†, Jiang Zou[1,2]†, Peinan Yan[1,2], Rongtai Wan[3], Baoyang Lu[3]*, Guoying Gu[1,2]*, Xiangyang Zhu[1,2]*

Electrically driven dielectric elastomer artificial muscles represent a transformative advancement in the field of soft robotics. However, their output performance has encountered a bottleneck owing to the insufficient electromechanical sensitivity of dielectric elastomers. We present a hetero-cross-linking–induced phase separation strategy to design semiseparated biphasic bicontinuous dielectric elastomers with a high electromechanical sensitivity of 360 per megapascal. Our strategy harnesses varying silicone elastomer cross-linking mechanisms to form an interconnected dielectric phase within a soft mechanical phase in the resultant elastomers. These elastomer-based artificial muscles simultaneously exhibit high energy density and power density, as well as ultralong life span under low-driving fields. Applications involve a robotic arm with large stroke and untethered soft crawling robots with multimodal locomotion, showcasing their versatility.

Design of muscle-like soft actuators capable of converting electrical energy to mechanical energy is a challenge in the field of soft robotics (*1*–*5*), haptics (*6*–*8*), and prosthetics (*9*, *10*). Many types of deformable materials stimulated by electricity (*11*–*15*) have been developed with dielectric elastomers (e.g., acrylics and silicones). Sandwiched between two compliant electrodes under a specific voltage, a dielectric elastomer membrane is compressed in thickness and expanded in area (*16*) as a result of the electrostatic stress [known as Maxwell stress (*17*)]. Based on this working principle, the resultant membrane thickness deformation (z) under a specific electric field mainly relates to the relative dielectric constant (ε_r) and Young's modulus (Y) of the dielectric elastomer, i.e., $z \propto \varepsilon_r / Y$ (*18*).

It has been challenging to tailor the electromechanical sensitivity (termed as ε_r / Y) to improve the actuation performance of dielectric elastomers under lower electric fields. By increasing the relative dielectric constant ε_r, improvements have been achieved through filler composition (*19*), chemical modifications (*20*), and elastomeric network optimization (*21*). Although high performance has been reported, the electromechanical sensitivity is still generally within 110 MPa^{-1}. Another effective strategy to improve the electromechanical sensitivity is to reduce the Young's modulus Y. However, it remains challenging to achieve this, owing to the compromise in relative dielectric constant as well as other electromechanical parameters, such as breakdown electric field and life span (*22*).

Hetero-cross-linking–induced phase separation strategy

We present a hetero-cross-linking–induced phase separation strategy to design a semiseparated biphasic bicontinuous dielectric elastomer (SBE). Our strategy utilizes varying cross-linking mechanisms applied to two commercial silicone elastomers (i.e., Sylgard 170 and Elastosil P7676) to form an interconnected dielectric phase (D-Phase) within a very soft mechanical phase (M-Phase). The D-Phase of Sylgard 170 (with a high relative dielectric constant of ~3.9) is fabricated by high-density main-chain cross-linking of telechelic vinyl functionalized polydimethylsiloxane with a multihydrosilane (Si–H) functionalized cross-linker. At the same time, the M-Phase of Elastosil P7676 (with an ultralow Young's modulus of ~8 kPa) is achieved by low-density side-chain cross-linking of bottle-brush polydimethylsiloxane through hydrosilylation in the presence of a commercial platinum catalyst (figs. S1 to S5). The hetero-cross-linking mechanisms of both components lead to the creation of two distinct phases with blurred boundaries owing to the interpenetration of similar polydimethylsiloxane chains. This results in a semiseparated biphasic bicontinuous elastomer (Fig. 1A), which differs from the formation of the homogeneous dual-network elastomers (*23*, *24*).

We confirm the formation of the semiseparated bicontinuous phase structure through structural and morphological characterizations. X-ray computed tomography (XCT) enables the visualization of the heterogeneous biphasic bicontinuous topological structure through density difference between the D-Phase and M-Phase (Fig. 1B and fig. S6), which is different from homogeneous dual-network elastomers (no phase separation). Atomic force microscopy (AFM) phase imaging further verifies the formation of interconnected continuous biphasic network in micrometer scales compared with pure D-Phase and M-Phase (Fig. 1C and fig. S7). Moreover, AFM nanomechanical mapping reveals distinct Derjaguin–Muller–Toporov (DMT) modulus and phase angle between the D-Phase and M-Phase within our SBE (Fig. 1D). The phase structure (Fig. 1E) may also enhance other electromechanical properties. For example, the blurred phase boundaries can create ubiquitous dielectric barriers (*25*), thus improving the breakdown electric field.

We systematically investigated the mechanical and electrical properties of SBEs under varying feeding ratios and compared them with commonly utilized commercial silicone elastomers. Stress-strain testing, dynamic mechanical analysis, differential scanning calorimetry, and dielectric spectroscopy (Fig. 1, F and G, and figs. S8 to S10) indicate that SBE exhibits an intermediate Young's modulus, mechanical loss tangent, glass transition temperature (T_g), and dielectric constant between two components with pure D-Phase and M-Phase as control. Our SBE displays a reluctant increment in the Young's modulus, yet a rapid enhancement in dielectric constant with the increase of the content of the D-Phase. Typically, SBE with only 10% of the D-Phase (SBE-1) exhibits a Young's modulus (~10 kPa) that when compared with pure D-Phase (~1450 kPa) is slightly higher than pure M-Phase (~8 kPa) but substantially lower than that of other commonly used commercial materials (Fig. 1F and fig. S11). By contrast, as we can see from Fig. 1G and fig. S12, the relative dielectric constant of our SBE-1 is 3.6 (44% higher than the relative dielectric constant of pure M-Phase), resulting in an electromechanical sensitivity of 360 MPa^{-1} (see "Measurements" in supplementary materials, materials and methods). Furthermore, cyclic tensile tests show that our SBE exhibits almost negligible hysteresis across the small, intermediate, and large strains (30, 100, 150, and 200%), indicating that it has better elasticity and mechanical stability than those of the pure M-Phase and D-Phase (fig. S13). Therefore, our SBE shows the potential to overcome the viscoelasticity of acrylic-based dielectric elastomers (*9*, *26*), leading to an improved response speed.

To validate the general applicability and elucidate the underlying chemical mechanism of our hetero-cross-linking approach, we extended the material portfolio to a series of analogous silicone dielectric elastomer materials with hetero-cross-linking mechanisms. The materials examined include both commercially available systems (such as Ecoflex 0030 paired with Sylgard 184, and Silgel 612 paired with Sylgard 160) and customized vinyl-terminated/hydroxyl-terminated silicone elastomers. The chemical reactions and catalysts of our customized silicone elastomers are provided in fig. S14. All the resultant silicone elastomers exhibit a distinct semiseparated biphasic bicontinuous structure

[1]State Key Laboratory of Mechanical System and Vibration, School of Mechanical Engineering, Shanghai Jiao Tong University, Shanghai, China. [2]Shanghai Key Laboratory of Intelligent Robotics, Shanghai Jiao Tong University, Shanghai, China. [3]Jiangxi Provincial Key Laboratory of Flexible Electronics, Flexible Electronics Innovation Institute, Jiangxi Science and Technology Normal University, Nanchang, China. ***Corresponding author. Email: guguoying@sjtu.edu.cn (G.G.); luby@jxstnu.edu.cn (B.L.); mexyzhu@sjtu.edu.cn (X. Z.)**
†These authors contributed equally to this work.

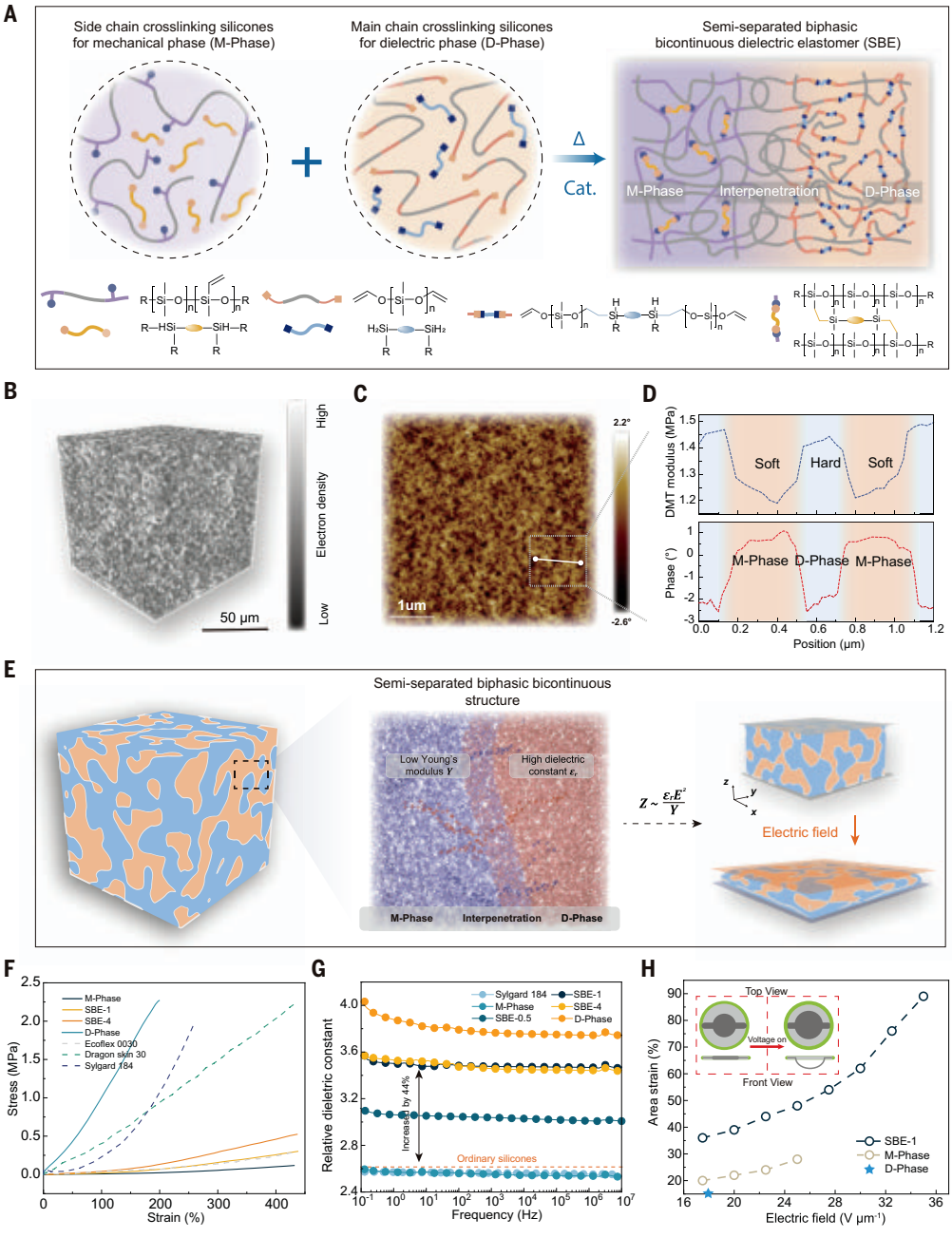


Fig. 1. Hetero-cross-linking–induced phase separation strategy and material properties. (**A**) The phase separation strategy of side-chain cross-linking type and main-chain cross-linking type. The side-chain cross-linking prepolymers undergo chemical cross-linking first under high temperatures and catalyst, precipitating an M-Phase in a topological mesh configuration. Concurrently, the unlinked main-chain cross-linking prepolymers migrate and aggregate, subsequently undergoing chemical cross-linking to precipitate a D-Phase, which fills the topology created by the elastic phase. (**B**) XCT and (**C**) AFM images demonstrate the biphasic bicontinuous structure of the SBE. (**D**) The phase angles and DMT modulus of the two phases show marked differences. (**E**) The SBE comprises M-Phase and D-Phase. The blurred phase boundaries (middle) create dielectric barriers leading to an enhanced breakdown electric field (right). (**F**) Stress-strain curves and (**G**) dielectric spectroscopy of SBEs and other commonly used silicone elastomers. (**H**) SBE-1 demonstrates superior electromechanical deformation performance, capable of achieving 90% area strain under 35 V μm^{-1} without prestretching, and displays enhanced electrical breakdown strength.

(fig. S15). Mechanical and dielectric testing reveals a considerable enhancement in electromechanical sensitivity, surpassing the performance of pure D-phase and M-phase elastomers (figs. S16 and S17). As a control, we investigated silicone elastomers with a homo-cross-linking mechanism. The resulting composite elastomers exhibited a uniform phase structure, and their electromechanical sensitivity represents a trade-off between the constituent materials (fig. S18). These findings highlight the material generality and versatility of our rational design strategy for high-performance dielectric elastomers.

We also characterized the electromechanical deformation ability of the SBE films with compliant electrodes. SBE-1 reaches a breakdown field strength of >35 V μm^{-1}, higher than that of both pure M-Phase at 25 V μm^{-1} and D-Phase at 18 V μm^{-1} (Fig. 1H). By integrating an ultralow Young's modulus and an enhanced dielectric constant and breakdown electric field, SBE-1 is capable of eliminating the electromechanical instability (fig. S19) and generating 90% area strain under a relatively lower electric field without prestretching (Fig. 1H, fig. S20, and movie S1), demonstrating exceptional electromechanical deformation capabilities (table S1).

High-performance SBE-based artificial muscles

To harness the properties of SBE, we first designed a kind of pure-shear SBE-based artificial muscle that consists of one single-layer SBE elastomer membrane coated on both sides with compliant electrodes (fig. S21). Under an excitation voltage, the pure-shear SBE-based artificial muscle elongates in the vertical direction, driving the load to produce a linear locomotion (Fig. 2A and movie S2). We characterized the linear strain and actuation stress of the pure-shear SBE-based artificial muscles with different feeding ratios. The results demonstrate that artificial muscles based on pure D-Phase or M-Phase struggle to generate effective electromechanical deformation and force because of their low electromechanical sensitivity and breakdown electric field (Fig. 2B and fig. S22). With our hetero-cross-linking–induced phase separation strategy, both the electromechanical sensitivity and breakdown electric field of our SBE are enhanced, enabling generation of >50% linear strain (SBE-1) with a strain rate of 400% s^{-1}. Additionally, Increasing the feed ratio reduces the electromechanical sensitivity of SBE, hindering its maximum linear strain.

We evaluated the energy density of our pure-shear SBE-based artificial muscles under different feeding ratios (Fig. 2C). The results show that under a low working frequency (<2 Hz), the maximum energy density of SBE-1, SBE-4, and SBE-6 reaches 209, 334, and 375 J kg^{-1}, respectively, which is generally higher than the energy density of pure M-Phase (85 J kg^{-1}) and D-Phase (23 J kg^{-1}) and the reported works

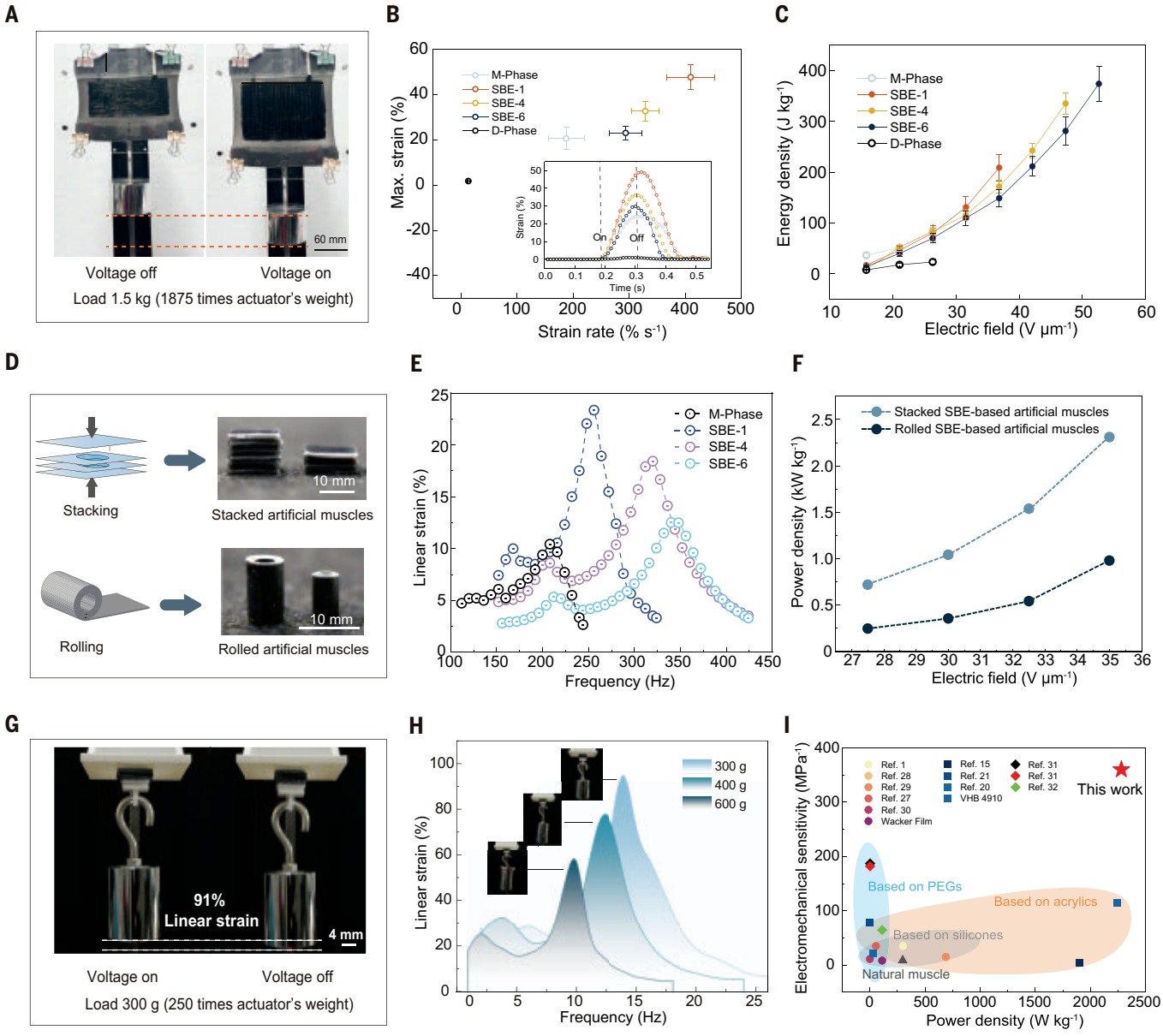


Fig. 2. Performances of SBE-based artificial muscles. (**A**) The pure-shear SBE-based artificial muscle exhibits a considerable linear strain under a 1.5-kg load. (**B**) The maximum strain and strain rate of the pure-shear SBE-based artificial muscle, with the inset illustrating the strain variation during a single actuation cycle. (**C**) Characterization of the energy density for the pure-shear SBE-based artificial muscle under different electric fields. (**D**) Schematic of the manufacturing process for artificial muscles. (**E**) Linear strain–frequency curves of SBE-based artificial muscles fabricated from SBEs with different feeding ratios. (**F**) Power density of stacked and rolled artificial muscles. Due to different driving directions, stacked artificial muscles demonstrate higher performance. (**G**) A stacked SBE-based artificial muscle with a height of 4.5 mm lifts a 300 g (250 times its weight) load by 4.1 mm (91% linear strain). (**H**) Linear strain–frequency curves of stacked SBE-based artificial muscles with suspended loads. (**I**) Comparison of electromechanical sensitivity and power density of SBE-based artificial muscles with other dielectric elastomer–based artificial muscles reported in the literature.

(table S2) (*9*, *13*, *15*, *20*). Under the same electric field, the energy density is negatively correlated to feeding ratios (Fig. 2C) because increasing feeding ratios leads to a decrease in electromechanical sensitivity. However, higher feeding ratios correspond to enhanced breakdown electric field, resulting in an increase in maximum energy density. By further analyzing their electromechanical efficiency, we found that the typical value is about 25%. The maximum electromechanical efficiency can exceed 60% by leveraging mechanical resonance (figs. S23 and S24).

We developed an efficient fabrication process to manufacture multilayered SBE-based artificial muscles (Fig. 2D), in which our SBE film is used as dielectric elastomer and single-wall carbon nanotube (SWCNT) thin film as the electrode (*27*). Typically, the SBE prepolymer solution is blade coated and cured to form a SBE film (~40 μm), covered with a thin SWCNT layer through a stamping transfer technique, and then coated with another SBE layer upon curing (figs. S25 and S26). Upon repeating such a procedure, we can achieve a multilayered sandwich structure of up to 15 layers. The multilayered sandwich structures are patterned into desired modules by laser cutting. Both negative and positive SWCNT electrodes are exposed and ready to connect with the power supply through conductive silicone electrodes. We further assemble such a structure into stacked or rolled SBE-based artificial muscles by dry stacking or simple rolling (figs. S27 and S28). Visualized by XCT imaging of their internal structures (fig. S29), both stacked and rolled SBE-based artificial muscles exhibit uniform thickness

and tight connections with an internal porosity <0.05%, confirming excellent structural integrity with negligible internal defects.

As-fabricated stacked artificial muscles can contract in thickness under an excitation voltage, whereas the rolled artificial muscles elongate along the axial direction. We further measured and compared the output performance of SBE-based artificial muscles with varying feeding ratios and geometric parameters (fig. S30). The actuation performance is fundamentally governed by the material's properties, as evidenced by the dependence of resonant frequency and strain amplitude on composition (Fig. 2E and fig. S31). Pure M-Phase–based artificial muscles demonstrate small linear strain (<10%) and low resonant frequency (200 Hz), primarily constrained by their low dielectric constant. Introducing a minor proportion of D-Phase (1:10, SBE-1) optimizes the electromechanical response by creating a semiseparated biphasic bicontinuous structure. This structure yields a superior combination of material properties (e.g., modulus and loss tangent) compared with pure-phase elastomers, which enhances the maximum linear strain to 25% (a 1.5-fold improvement) and increases the resonant frequency to 250 Hz. This enables actuators to not only resonate at higher frequencies but also to sustain large strain amplitudes under these conditions. By contrast, further increases in feeding ratios (e.g., SBE-3 and SBE-4) considerably elevate the Young's modulus without a commensurate increase in the dielectric constant (Fig. 1, F and G), leading to a marked deterioration in achievable linear strain. Among various feeding-ratio SBEs, the artificial muscle based on SBE-1 exhibits the best displacement output capability under high-frequency excitation and was thus used for subsequent tests of stacked and rolled artificial muscle (figs. S32 to S34). We found that by further analyzing the geometry effect through height optimization (in a range of 2 to 10 mm), the maximum response frequency can reach as high as 1500 Hz (figs. S35 and S36), which is superior to that reported in existing works (*1*, *15*, *20*). The blocked force density and power density results (Fig. 2F and figs. S37 to S39) show that stacked SBE–based artificial muscles (size of 8 mm by 8 mm by 3 mm, weight of 0.35 g) exhibit a maximum blocked force density of 21.76 kPa and a power density of 2250 W kg^{-1} at a high-frequency resonant state (>200 Hz) and an extremely low electric field of 35 V μm^{-1}, more than double that of rolled SBE-based artificial muscles (size of 80 mm by 5 mm by 240 μm before rolling; weight of 0.18 g).

Our SBE-based artificial muscles exhibit substantial load-driving capacity despite their ultralow Young's modulus (~10 kPa). Typically, the stacked SBE-based artificial muscles (height of 4.5 mm) are capable of repeatedly lifting a 300-g load (250 times their own weight) up to 4.1 mm (about 91% linear strain) with a maximum speed of 15 Hz (Fig. 2G and movie S3). If the load increases to 600 g (500 times their weight), the stroke of the stacked artificial muscles can still reach 2.7 mm (about 60% linear strain, Fig. 2H), demonstrating the powerful load-driving capacity of our artificial muscles (fig. S40). This performance exceeds natural muscles and reported dielectric elastomer–based artificial muscles (Fig. 2I and table S2) (*1*, *15*, *20*, *21*, *28*–*33*) and originates mainly from the improvement in electromechanical sensitivity.

Long-term stability and robustness

The inevitable performance degradation during long-term service is one of the major challenges for the application and commercialization of artificial muscles. Mechanical robustness, which is the output performance stability under mechanical deformation and high-number cyclic loading, is of particular concern for the life span of artificial muscles. We have conducted several fatigue tests with our SBEs and Pure M-Phase elastomers. The experimental results demonstrate that with the phase-separation microstructures (Fig. 3A), our SBE exhibits a fatigue threshold of 78 J m^{-2} (measured by the single-notch method). In comparison with pure M-Phase elastomer (21 J m^{-2}), the fatigue threshold is improved more than threefold (Fig. 3B). The underlying mechanism is likely due to the less-stretchable D-phase acting as a mechanical dissipater while the highly stretchable M-phase maintains the integrity and elasticity of the SBE (Fig. 3A), which is similar to previous results on tough double-network hydrogels (*34*, *35*). To further verify the mechanical robustness, we performed a 50,000-cycle validation test on a pinhole-cracked SBE at a constant strain of 50%, simulating the practical working conditions of SBE-based artificial muscles. Notably, SBE displays no obvious stress loss (<1%) after this test (Fig. 3C and fig. S41).

After being coated with carbon nanotube electrodes, our fabricated SBE-based artificial muscle exhibits a self-clearing capability (movie S4). This self-clearing process effectively reduces the structural defects

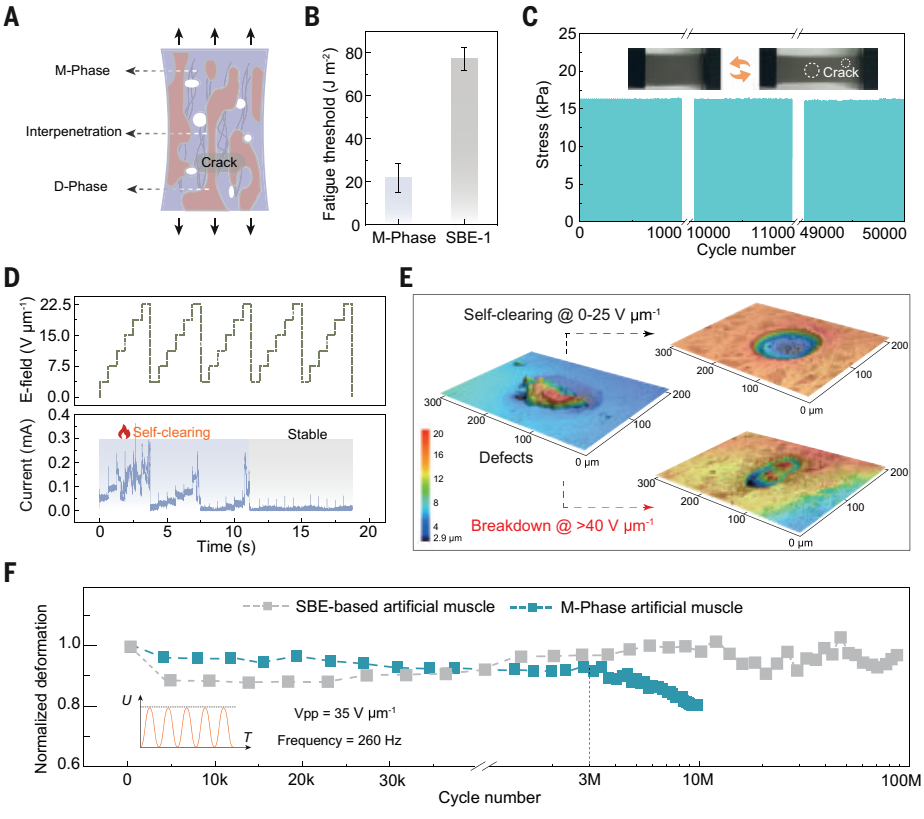


Fig. 3. Long-term stability and robustness of SBE-based artificial muscles. (**A**) Notches and pinholes are created on SBE to test its fatigue resistance and long-term stability. (**B**) Comparison of fatigue thresholds between M-Phase and SBE-1. The SBE-1 exhibits a threefold-higher fatigue threshold, attributed to the enhanced interfacial strength between the biphase. (**C**) Under conditions with notches and pinholes, SBE-1 shows no major stress loss after more than 50,000 stretching cycles. (**D**) Self-clearing is achieved with a stair voltage, with clearing completion indicated by zero current. (**E**) Confocal microscopy images of the SBE-based artificial muscle after self-clearing and destructive electrical breakdown, showing that self-clearing removes defects to form a well-defined pore, whereas excessive electric fields induce carbide accumulation leading to a short circuit. (**F**) Cyclic actuation testing of SBE-1 and M-Phase artificial muscle under an electric field of 35 V μm^{-1}. Vpp, peak-to-peak voltage; *U*, driving voltage; *T*, time.

and micropores within the artificial muscle by burning out low breakdown paths, thus facilitating the enhancement of output performance and long-term stability (*28*, *36*, *37*). During this process, a nonconductive region is formed, which isolates defects and allows the remaining functional areas to operate normally (fig. S42). By applying a cyclical stair voltage to perform this process and monitoring the current detection, we found that the actuation of our SBE-based artificial muscle causes transient erratic current during the first three cycles and then reaches a stabilized output performance as the current remains ~0 mA (Fig. 3D). We compared the surface morphology of SBE after self-clearing and destructive electric breakdown using confocal microscopy. The results reveal that the self-clearing process effectively remove defects within the SBE, forming a well-defined cavity. However, when the applied electric field is excessively high, considerable carbide accumulation occurs in the cavity, ultimately leading to a short circuit (Fig. 3E).

With its self-clearing capability and enhanced fatigue threshold, our SBE-based artificial muscle exhibits an enhanced output capacity and extended life span across both low and high working frequencies (such as more than 375,000 actuation cycles at 1 Hz and more than 100 million actuation cycles at 260 Hz under 35 V μm^{-1}) (Fig. 3F and figs. S43 to S46). By contrast, an artificial muscle fabricated with pure M-Phase suffers from performance attenuation upon only 3 million cycles (<80% after 10 million cycles; Fig. 3F). Moreover, the life span of other dielectric elastomer actuators based on commercial silicones is inferior to that of our SBE (table S3) (*15*, *20*, *28*, *38*–*40*).

Robotic arm with large stroke and high load capacity

We developed a robotic arm that consists of one rotational joint and four pure-shear SBE-based artificial muscles (Fig. 4A) (as detailed in "Fabrication" in supplementary materials, materials and methods). The pure-shear configuration is specifically selected for this bioinspired application because of its superior capability to generate large deformations coupled with high-force output under low-frequency operating conditions. These artificial muscles are divided into two antagonistic groups functioning as biceps and triceps, respectively.

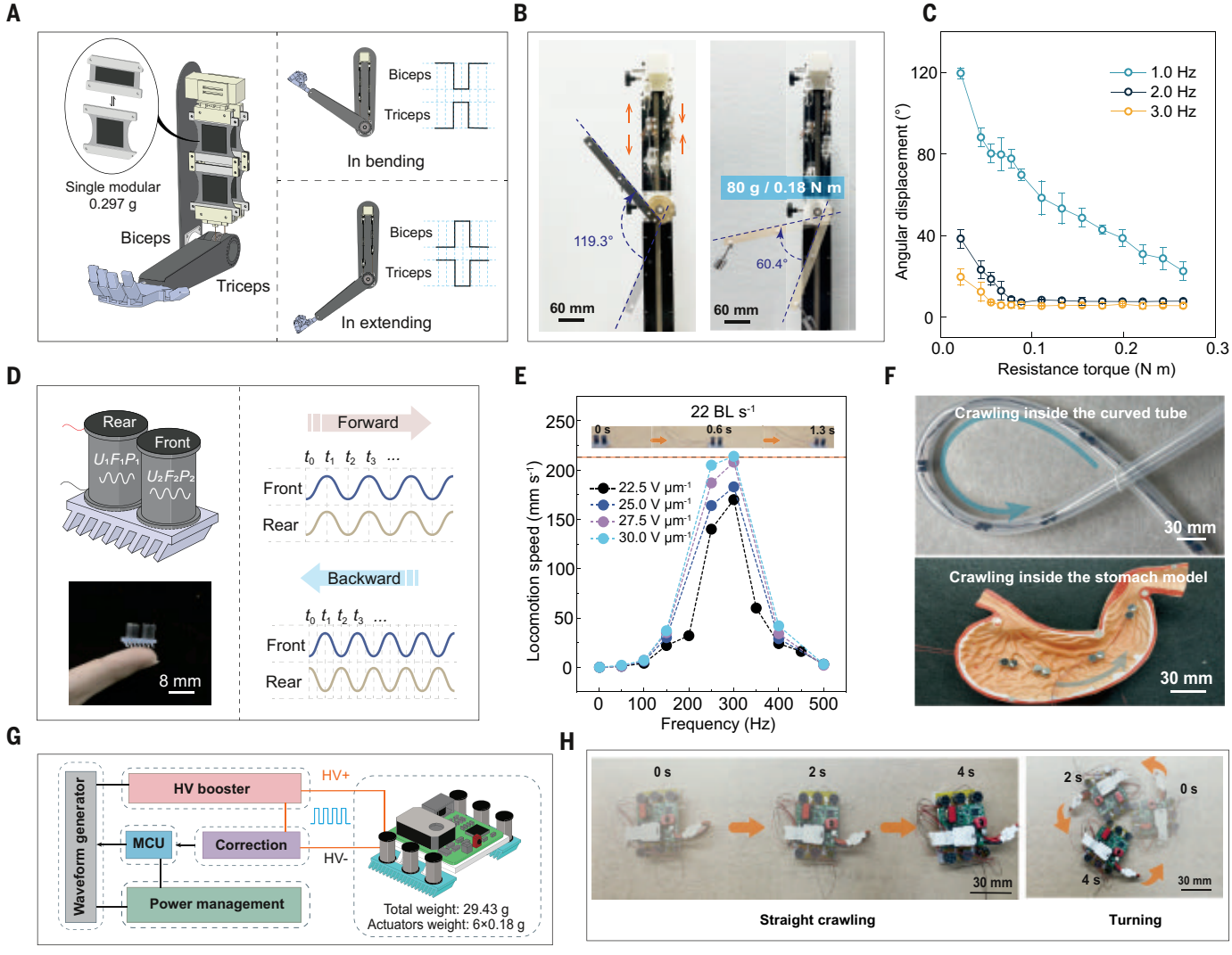


Fig. 4. Applications of SBE-based artificial muscles. (**A**) Design and working principle of a human-like robotic arm with four pure-shear SBE-based artificial muscles. (**B**) The robotic arm exhibits large stroke (119.3°) and high load capacity. (**C**) The angular displacement under different torque and frequency. (**D**) Design and gait implementation of an ultrafast soft crawling robot. Adjustments in movement direction and speed are achieved by modifying the driving frequency and phase differences between the front and rear artificial muscles. (**E**) The impact of electric field and driving frequency on the robot speed, with a maximum speed of up to 22 BL s^{-1}. (**F**) The robot crawling through curved tubes and a stomach model. (**G**) An infrared-controlled miniaturized high-frequency high-voltage drive circuit system and the design of an untethered robot. HV booster; high-voltage booster; MCU, microcontroller unit. (**H**) Demonstrations of crawling in a straight line and controlled turning.

When a high voltage is applied to the biceps, the robotic arm extends because the biceps elongate and the triceps contract. Conversely, the arm bends when the triceps are actuated. By alternately actuating biceps and triceps, we found that the angular displacement is proportional to the applied electric field (fig. S47) and that its maximum value can reach 119.3° (Fig. 4B and movie S5). We characterized the load capacity of the robotic arm by measuring the angular displacement under different resistance torques and actuation frequencies. The results demonstrate that although the effective weight of the four pure-shear SBE-based artificial muscles is <1.2 g, they can output a maximum torque of 0.24 N m, enabling the robotic arm to lift an 80-g load by 60.4° (Fig. 4C and movie S5) and chop through various obstacles (fig. S48 and movie S6). Lastly, we subjected the entire robotic arm system to more than 40,000 cycles of testing, during which it consistently remained stable and showed no performance degradation (fig. S49).

Multimodal and ultrafast robots with untethered capability

We designed and fabricated a soft crawling robot capable of multimodal locomotion (Fig. 4D and movie S7). The design comprises two SBE-based artificial muscles affixed to a flexible substrate with directional rectangular feet array (fig. S50). Under the same excitation voltage, SBE-based artificial muscles concurrently generate potent vibration that is converted into fast crawling via the anisotropic feet. The robot can execute hundreds of forward jumps within 1 s. The maximum crawling speed reaches 22 body lengths per second (BL s^{-1}) at a frequency of 300 Hz and a field strength of 30 V μm^{-1} (Fig. 4E, fig. S51 and movie S8). Upon implementing a phase delay in the rear artificial muscles under high frequency, we observed that the resulting asynchronous vibration facilitates a backward crawling gait (fig. S52 and movie S7), reaching a maximum speed of 40 mm s^{-1} with a phase difference of $T/2$ (T represents period of the excitation voltage) and a frequency of 450 Hz (movie S8). Leveraging its inherent softness and superior performance, the soft crawling robot can maneuver through curved tubes and navigate within a rugged stomach model (Fig. 4F and movies S9 and S10), showcasing its bioinspired adaptability to complex terrains and environments.

The low-driving electric field required for SBE-based artificial muscles paves the way for untethered applications. We developed an untethered soft crawling robot (Fig. 4G and figs. S53 and S54) integrating with a boost module, a microcontroller unit, an infrared wireless receiver, a calibration unit, and a battery. Although the total weight of the untethered robot reaches 29.43 g, it is powered by only six artificial muscles (weight of 6 × 0.18 g). This design enables both crawling and turning (Fig. 4H and movie S11). The design and integration of an untethered robotic system, traditionally a challenge in the deployment of dielectric elastomer actuators (*41*), are addressed by utilizing our SBE-based artificial muscles, which show superior output performance under a low-driving electric field.

Conclusions

This work presents a class of SBE with high electromechanical sensitivity through the hetero-cross-linking–induced phase separation strategy. After characterizing the mechanical and electrical properties of SBE under varying feeding ratios with commercially available silicone elastomers, we developed an efficient fabrication process to fabricate SBE-based artificial muscles that can synchronously exhibit high actuation performance in energy density, power density, response speed, electromechanical efficiency, and life span. We demonstrate a robotic arm and multimodal soft crawling robots that show high energy density and untethered capability. These advancements hold promise for the next generation of electrically driven soft robots that require enhanced output performance, ultralong life span, and excellent integrity.

REFERENCES AND NOTES

1. Y. Chen *et al.*, *Nature* **575**, 324–329 (2019).
2. G. Li *et al.*, *Nature* **591**, 66–71 (2021).
3. C. Tang *et al.*, *Sci. Robot.* **7**, eabm8597 (2022).
4. X. Ji *et al.*, *Sci. Robot.* **4**, eaaz6451 (2019).
5. G. Gu, J. Zou, R. Zhao, X. Zhao, X. Zhu, *Sci. Robot.* **3**, eaat2874 (2018).
6. G. Grasso, S. Rosset, H. Shea, *Adv. Funct. Mater.* **33**, 2213821 (2023).
7. E. Leroy, R. Hinchet, H. Shea, *Adv. Mater.* **32**, e2002564 (2020).
8. X. Ji *et al.*, *Adv. Funct. Mater.* **31**, 2006639 (2021).
9. M. Duduta, E. Hajiesmaili, H. Zhao, R. J. Wood, D. R. Clarke, *Proc. Natl. Acad. Sci. U.S.A.* **116**, 2476–2481 (2019).
10. J. Ham *et al.*, *Adv. Mater. Technol.* **8**, 2200903 (2023).
11. R. Pelrine, R. Kornbluh, Q. Pei, J. Joseph, *Science* **287**, 836–839 (2000).
12. C. Keplinger *et al.*, *Science* **341**, 984–987 (2013).
13. E. Acome *et al.*, *Science* **359**, 61–65 (2018).
14. X. Dong *et al.*, *Sci. Robot.* **6**, eabe3950 (2021).
15. Y. Shi *et al.*, *Science* **377**, 228–232 (2022).
16. L. An, F. Wang, S. Cheng, T. Lu, T. J. Wang, *Smart Mater. Struct.* **24**, 035006 (2015).
17. T. Lu, C. Ma, T. Wang, *Extreme Mech. Lett.* **38**, 100752 (2020).
18. Z. Suo, *Acta Mech. Solida Sin.* **23**, 549–578 (2010).
19. Y. Jiang *et al.*, *Adv. Mater.* **35**, e2300246 (2023).
20. W. Feng *et al.*, *Nat. Commun.* **15**, 4222 (2024).
21. L. J. Yin *et al.*, *Nat. Commun.* **12**, 4517 (2021).
22. L. J. Romasanta, M. A. Lopez-Manchado, R. Verdejo, *Prog. Polym. Sci.* **51**, 188–211 (2015).
23. J. Y. Sun *et al.*, *Nature* **489**, 133–136 (2012).
24. J. P. Gong, Y. Katsuyama, T. Kurokawa, Y. Osada, *Adv. Mater.* **15**, 1155–1158 (2003).
25. M. Yang *et al.*, *Nat. Nanotechnol.* **19**, 588–603 (2024).
26. G. Gu, U. Gupta, J. Zhu, L. Zhu, X. Zhu, *IEEE Trans. Robot.* **33**, 1263–1271 (2017).
27. W. Yuan *et al.*, *Adv. Mater.* **20**, 621–625 (2008).
28. H. Zhao *et al.*, *Adv. Funct. Mater.* **28**, 1804328 (2018).
29. S. Kim *et al.*, *Sci. Robot.* **8**, eadf4278 (2023).
30. S. Xu, Y. Chen, N. P. Hyun, K. P. Becker, R. J. Wood, *Proc. Natl. Acad. Sci. U.S.A.* **118**, e2103198118 (2021).
31. P. Huang, H. Fu, M. W. M. Tan, Y. Jiang, P. S. Lee, *Adv. Mater. Technol.* **9**, 2301642 (2023).
32. D. Yang *et al.*, *J. Mater. Chem. A Mater. Energy Sustain.* **3**, 9468–9479 (2015).
33. D. Yang *et al.*, *Compos. Sci. Technol.* **155**, 160–168 (2018).
34. X. Zhao, *Soft Matter* **10**, 672–687 (2014).
35. Y. Zhou *et al.*, *J. Mech. Phys. Solids* **153**, 104483 (2021).
36. Z. Peng, Y. Shi, N. Chen, Y. Li, Q. Pei, *Adv. Funct. Mater.* **31**, 2008321 (2021).
37. S. Jiang, C. Tang, X. J. Liu, H. Zhao, *Adv. Eng. Mater.* **24**, 2101017 (2022).
38. F. B. Albuquerque, H. Shea, *Smart Mater. Struct.* **30**, 125022 (2021).
39. P. Caspari, S. J. Dünki, F. A. Nüesch, D. M. Opris, *J. Mater. Chem. C Mater. Opt. Electron. Devices* **6**, 2043–2053 (2018).
40. Z. Ren *et al.*, *Adv. Mater.* **34**, e2106757 (2022).
41. S. I. Rich, R. J. Wood, C. Majidi, *Nat. Electron.* **1**, 102–112 (2018).

ACKNOWLEDGMENTS

We thank the following individuals for their valuable contributions and assistance throughout this research: W. Wang and J. Cao for chemical analysis; L. Wang for fatigue tests and analysis; L. Zhang for XCT imaging; Z. Qin and J. Feng for the assistance in thin film preparation; and X. Chen for the discussion of the dynamic model. We also thank the support of the Xplorer Prize. **Funding:** This work was supported by the National Key R&D Program of China (grant no. 2024YFB4707504); the National Natural Science Foundation of China (grant nos. 52025057, 91948302, and 52275024); and the State Key Laboratory of Mechanical System and Vibration (grant MSVZD202401). **Author contributions:** Conceptualization: X.S., J.Z., B.L., G.G., X.Z.; Funding acquisition: G.G., X.Z.; Investigation: X.S., P.Y., R.W.; Methodology: X.S., J.Z., B.L.; Project administration: J.Z., B.L., G.G., X.Z.; Supervision: G.G., X.Z.; Visualization: X.S.; Writing – original draft: X.S. Writing – review & editing: X.S., J.Z., B.L., G.G., X.Z. **Competing interests:** The authors declare that they have no competing interests. **Data and materials availability:** All data are available in the main text or the supplementary materials. Sources, synthesis and characterization of all materials are described in the methods section.

License information: Copyright © 2025 the authors, some rights reserved; exclusive licensee American Association for the Advancement of Science. No claim to original US government works. https://www.science.org/about/science-licenses-journal-article-reuse

SUPPLEMENTARY MATERIALS

science.org/doi/10.1126/science.adr3521
Materials and Methods; Figs. S1 to S54; Tables S1 to S3; References (*42*–*45*); Movies S1 to S11

Submitted 27 June 2024; accepted 31 October 2025

10.1126/science.adr3521

BIOCATALYSIS

Biocatalytic, asymmetric radical hydrogenation of unactivated alkenes

Jaicy Vallapurackal†, Rajib Mandal†, Justin Bossenbroek, Aris V. Rubio, Ethan Poladian, James D. Collings, Cesar Torres, Matthew Hendrickson, Julian Morales, Max B. Lyons, Kyle Schultz, Hannah S. Shafaat, K. N. Houk, Soumitra V. Athavale*

Alkene hydrogenation is a cornerstone of chemical synthesis, yet enzymatic strategies remain limited to electron-deficient substrates by means of hydride transfer. Using heme enzymes, we unlock a hydrogenation pathway for the asymmetric reduction of unactivated olefins. A silane-promoted heme-cysteine redox cycle in the active site catalyzes sequential hydrogen atom transfer to challenging scaffolds, including 1,1-disubstituted as well as tri- and tetrasubstituted alkenes. The evolved enzymes are promiscuous and oxygen tolerant, use Earth-abundant iron, and can operate on the gram scale under ambient conditions. Orthogonal hydrogen atom sources enable site-divergent asymmetric isotope labeling. Mechanistic and computational studies support a stepwise radical process. Our work introduces a biochemical approach for stereoselective olefin reduction and provides a platform for next-generation biocatalytic hydrogenation.

Hydrogenation of carbon-carbon double bonds is a foundational reaction in organic chemistry, widely used in small-molecule synthesis, industrial processes, and biochemistry. Notably, the strategies developed by synthetic chemists to catalyze olefin reductions could not be more different from that used by nature (Fig. 1, A and B). In synthetic chemistry, transition metal–catalyzed hydrogenation using gaseous H_2 (e.g., with Pd, Pt, Rh, and Ir) remains the dominant approach—refined over a century into a textbook transformation (*1*–*4*). This pathway has not been used by biology. Instead, biological olefin reductions proceed through the delivery of so-called hydride equivalents from organic cofactors, such as reduced flavin mononucleotide ($FMNH_2$) and/or reduced flavin adenine dinucleotide ($FADH_2$) or reduced nicotinamide adenine dinucleotide phosphate [NAD(P)H] (Fig. 1A) (*5*, *6*). This ancient, evolutionarily conserved biochemical logic—central to oxidoreductase catalysis—relies on anionic hydride addition and is inherently limited to polarized, electron-deficient alkenes, such as α,β-unsaturated carbonyl compounds (e.g., by means of ene-reductases). Enzymes that reduce isolated, unactivated olefins are exceedingly rare, highly substrate specific, and still dependent on the same hydride-based mechanism, which highlights the universality—and the limitations—of natural enzymatic olefin reduction (*7*–*9*).

Although chemical methods offer superb versatility, enzymatic olefin reduction has nonetheless inspired catalytic approaches that enable highly enantioselective hydrogenations (*10*). Achieving precise spatial control over the delivery of hydrogen atoms—the smallest reactive groups in chemistry—is inherently challenging, and asymmetric hydrogenation has an illustrious history in synthetic and organometallic chemistry (*11*). This precision has traditionally been realized for substrates that promote highly organized transition states, typically through chelation, including electron-deficient olefins (*12*, *13*). Chiral iridium catalysts mark a high point in the field, with seminal advances extending the scope to unfunctionalized, noncoordinating alkenes (*14*, *15*). However, most successful systems remain focused on styrenyl compounds, and the asymmetric reduction of other classes of unbiased, unactivated olefins continues to be a challenge (*16*, *17*). Moreover, the nearly universal syn-addition mechanism of transition metal–catalyzed hydrogenation precludes asymmetric anti-reduction, limiting stereochemical diversity. State-of-the-art systems for unactivated olefins also rely on rare, expensive metals (e.g., Ir); elaborate chiral ligands; and pressurized, anaerobic hydrogen atmospheres—factors that detract from practicality and sustainability.

Enzymes offer compelling opportunities. Ene-reductases stand as a biocatalytic success story, often outperforming transition metal catalysts at the process scale, but with activity limited to electron-deficient olefins (*18*, *19*). Developing a biocatalytic platform capable of reducing unactivated olefins would be transformative but requires fundamentally new active-site mechanisms. In this work, we describe such a mechanism: a radical hydrogenation paradigm that can be engineered into heme proteins to establish a biochemical logic for the asymmetric reduction of unactivated olefins.

Our mechanistic framework, which we call biocatalytic cooperative metal hydrogen atom transfer (BioHAT), draws inspiration from Kattamuri and West's cooperative hydrogen atom transfer (cHAT) chemistry (Fig. 1C) and broader studies in metal hydrogen atom transfer (MHAT) (*20*–*25*). In this envisioned pathway (Fig. 1D), (i) the enzyme's resting state (a ferric heme protein) reacts with a hydride donor (e.g., phenylsilane) to generate an active-site metal-hydride intermediate; (ii) this intermediate engages in MHAT to reduce the olefin, generating a carbon-centered radical and a reduced metal center; (iii) the resulting radical undergoes enantiodetermining hydrogen atom abstraction (HAA) from a strategically positioned cysteine side chain, forming the product and a thiyl radical; and (iv) the thiyl radical is subsequently reduced by electron transfer (ET) from the metal center, regenerating the resting-state ferric enzyme. In this system, one hydrogen atom originates from the silane-derived hydride (via the metal center), and the other from the cysteine thiol (through solvent exchange). This orthogonal hydrogen atom origin—a hallmark of cHAT chemistry (*20*)—is in stark contrast to classical metal-catalyzed hydrogenation, where both hydrogens are delivered in a syn fashion from metal-coordinated dihydrogen. BioHAT, by contrast, imposes no such restriction, allowing syn- or anti-addition and enabling independent stereocontrol during each hydrogen delivery step. In principle, this framework could allow unprecedented control over regio-, diastereo-, and enantioselectivity in olefin hydrogenation, features that have long eluded small-molecule catalysts and are likely inaccessible by means of conventional transition metal chemistry.

Metalloenzyme-catalyzed hydride transfer has precedent in abiotic chemistry. Hartwig and colleagues' seminal study demonstrated silane-derived Zn–H intermediates in carbonic anhydrase-catalyzing enantioselective ketone reductions (*26*, *27*). Contemporaneously with the development of our work, silane-driven enantioselective reduction of ketones and highly electron-poor olefins have been reported with engineered hemoglobins and nonheme iron dioxygenases, respectively (*28*, *29*). However, all of these systems operate through anionic hydride transfer. Radical-based hydrogenation of unactivated olefins—such as envisioned in BioHAT—remains inaccessible to existing enzymatic platforms (*30*, *31*).

Discovery and development of BioHAT

A two-stage strategy was designed to engineer an active site with the requisite features for BioHAT. In stage 1 (Fig. 2A), we screened metalloenzymes for asymmetric, intramolecular olefin-olefin coupling of substrate **1**. This probe reaction, representative of MHAT reactivity, was inspired from the analogous 5-exo-trig cyclization with $Fe(acac)_3$ (*32*). This mechanistically simpler transformation shares key steps with the proposed BioHAT pathway but does not require an active-site

Department of Chemistry and Biochemistry, University of California Los Angeles, Los Angeles, CA, USA. *Corresponding author. Email: athavale@chem.ucla.edu †These authors contributed equally to this work.

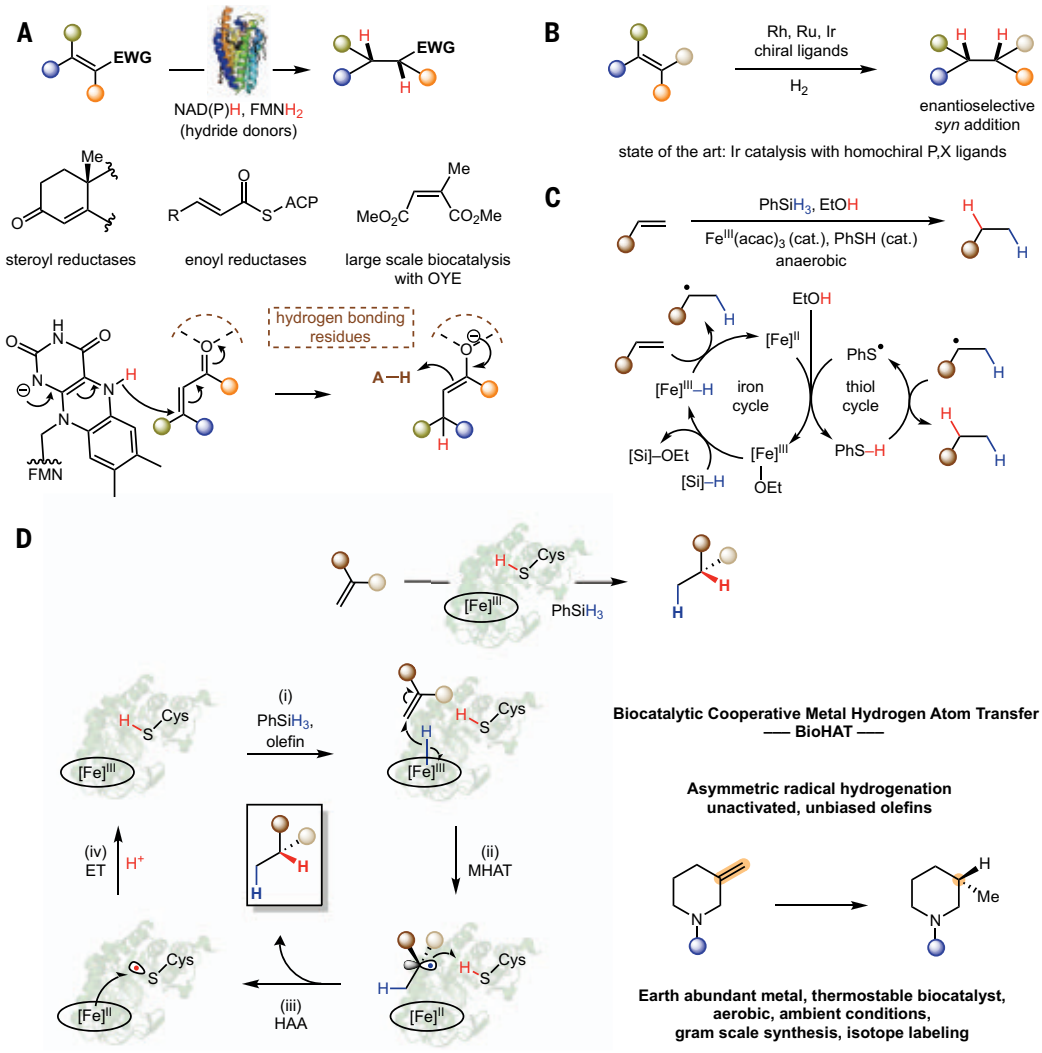


Fig. 1. BioHAT: A biochemical logic for asymmetric hydrogenation of unactivated olefins. (**A**) Natural enzymes mediate olefin hydrogenation through hydride reductions with organic cofactors. Substrates are largely restricted to electron-deficient olefins. Active-site hydrogen bonding activates the substrate for hydride attack, which is followed by protonation with an acidic residue (HA). Biocatalysts such as old yellow enzyme (OYE) and other ene reductases are of high preparative importance. EWG, electron withdrawing group. (**B**) Asymmetric hydrogenation with transition metals is highly versatile and can reduce electron neutral olefins but is inaccessible to biology. Its mechanism results in a syn delivery of hydrogen atoms. (**C**) Inspiration: cHAT with silanes as reductants, catalytic iron, and thiophenol as cocatalyst. Asymmetric versions of this transformation have remained elusive. (**D**) This work: Importing a radical hydrogenation paradigm (BioHAT) to enzymology.

cysteine. Therefore, existing metalloprotein libraries could be leveraged to identify enzymes capable of supporting an MHAT catalytic cycle. In stage 2 (Fig. 2B), the MHAT-competent enzymes identified in stage 1 were further engineered by introducing targeted active-site Cys mutations to support a full BioHAT hydrogenation cycle.

In stage 1, a diverse library of metalloenzymes, including Fe, Cu, Mn, Co, and Ni proteins, were screened for the probe reaction in whole-cell and lysate preparations. Nonracemic product formation was detected with several heme proteins, indicating an active-site MHAT process (see supplementary materials). For further development, we selected a protoglobin mutant from *Aeropyrum pernix* ($ApePgb_{GLVRQL}$) (*33*), which we designate as **HAT**$_{OC}$ (hydrogen atom transfer olefin cyclase). Protoglobins are small (~200 amino acids), thermostable archaeal hemoproteins, highly expressed and easily purified in *Escherichia coli*, and pioneering work from the Arnold group has established their effectiveness as new-to-nature biocatalysts (*33*–*36*). Concurrently with our studies, the cyclization was recently reported with P450 enzymes by the Ward group (*37*).

With asymmetric MHAT reactivity confirmed in protoglobins, we advanced to stage 2, testing the BioHAT hydrogenation hypothesis by constructing active-site Cys mutants. Ten Cys mutants of **HAT**$_{OC}$ were tested for BioHAT hydrogenation of *N*-tosyl-2-methylallylamine (**3**), a substructure of **1**. Five mutants—at positions 59, 60, 93, 145, and 149—produced the reduced product **4** (supplementary materials). None of the olefin cyclase hits in stage 1 nor did any members in our broader metalloenzyme collection exhibit this reduction activity, which supports the hypothesis that a strategically placed Cys residue is mechanistically essential for turning on olefin reduction through BioHAT. When tested with prochiral olefin **5**, these mutants delivered enantioenriched product **6**, establishing initial activity for asymmetric hydrogenation (Fig. 2B). The stereochemical outcome was dependent on the position of the cysteine, further supporting its direct role in the enantiodetermining HAA step (supplementary materials). For instance, **HAT**$_{OC}$**-V60C** and **HAT**$_{OC}$**-Q145C** produced opposite enantiomers of the product. Among these, the V60C mutant delivered the highest enantioselectivity. We designate this pioneering mutant as **HAT**$_{R}$**-1** (hydrogen atom transfer reductase, generation 1).

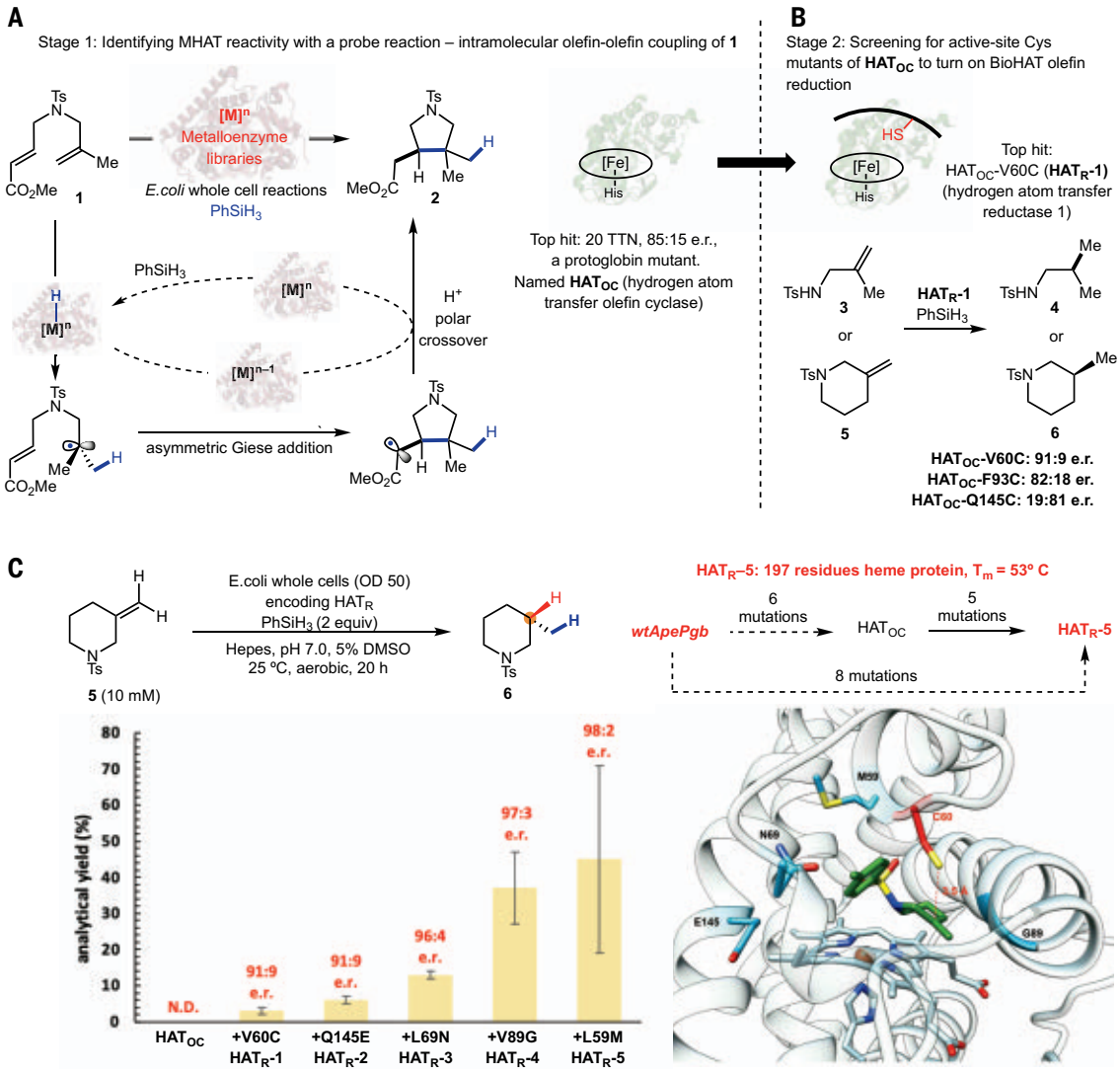


Fig. 2. Strategy for discovering BioHAT activity and directed evolution of HAT_R enzymes. (**A**) Stage 1: The intramolecular olefin cyclization of **1** as a probe reaction for MHAT activity. This radical coupling is expected to proceed through a pathway that does not necessitate a Cys residue for termination, allowing the screening of existing metalloenzyme libraries. A protoglobin mutant, now called HAT_{OC} (hydrogen atom transfer olefin cyclase) was identified to catalyze this reaction with initial activity. (**B**) Stage 2: Incorporation of an active site Cys into HAT_{OC} turns on BioHAT activity. The V60C mutant (HAT_R-1, hydrogen atom transferase 1) showed initial activity with substrates **3** and **5**. The position of Cys incorporation changes enantioselectivity. (**C**) Directed evolution of BioHAT activity. Analytical yields represent means of six experiments (technical triplicates for two biological duplicates) with error bars signifying means ± standard deviations. Cumulatively, the final variant HAT_R-5 is eight mutations distant from its natural ancestor wtApePgb (wild-type *Aeropyrum pernix* protoglobin). HAT_R-5 was modeled with a reference MicroED structure (PDB: 8EUM) and homology protein modeling using Modeller for loop refinement (*51*,*52*). The alkyl radical was docked using AutoDock Vina (*53*) to identify key binding poses approximating the HAA step, where the 60C residue, in red, is in proximity to the radical (see supplementary materials for further details). Single-letter abbreviations for the amino acid residues are as follows: A, Ala; C, Cys; D, Asp; E, Glu; F, Phe; G, Gly; H, His; I, Ile; K, Lys; L, Leu; M, Met; N, Asn; P, Pro; Q, Gln; R, Arg; S, Ser; T, Thr; V, Val; W, Trp; and Y, Tyr.

HAT_R-1 catalyzed the reduction of **5** with phenylsilane under aerobic whole-cell catalysis to yield product **6** in ~3% yield [~15 total turnover number (TTN)] and promising stereoselectivity [91:9 enantiomeric ratio (e.r.) *S*-enantiomer]. Subsequent directed evolution resulted in improvements in activity and selectivity (Fig. 2C; see supplementary materials for details). Evolution involved iterative rounds of site-saturation mutagenesis (SSM) of active-site residues followed by whole-cell reaction screening in a 96-well plate format for identifying improved activity mutants. In each round, improved activity mutants were then evaluated for enantioselectivity. Thus, four rounds of directed evolution gave variant **HAT_R-5** [HAT_{OC}-V60C, Gln^{145}→Glu (Q145E), L69N, V89G, L59M] that catalyzed the reaction under screening conditions in ~45% analytical yield (~400 TTNs) and 98:2 e.r. The 197-residue hemeprotein **HAT_R-5** has traversed eight mutations from its wild-type ancestor (wtApePgb). Although the starting enzyme **HAT_{OC}** exhibits a melting temperature (T_m) of 65°C, each round of evolution resulted in a modest loss in thermostability, with **HAT_R-5** showing a T_m of 53°C (supplementary materials). Whole-cell reactions of **5** with the final variants—particularly with **HAT_R-5**—gave poor reproducibility, as indicated by the large error bars in Fig. 2C. The variability is attributed to the low aqueous solubility of **5**, which resulted in stochastic precipitation during the reaction. This problem is solved by using purified **HAT_R-5** in the presence of the nonionic micellar surfactant TPGS-750-M (*38*), which results in homogeneous reactions and marked improvement in yield and reproducibility. Thus, reactions of **5** with purified enzyme in the presence of 6% w/v of TPGS-750-M gave reproducibly

high yields (>90%) (see supplementary materials for discussion and optimization details).

Substrate scope and preparative reactions

Among unactivated olefins, exocyclic alkenes and 1,1-disubstituted, nonstyrenyl olefins, with minimal stereoelectronic difference between their substituents—such as the model compound **5**—represent some of the most formidable challenges in asymmetric hydrogenation, even with state-of-the-art iridium catalysts (*39*, *40*). The products contain methyl-substituted stereocenters, which are especially valuable in medicinal chemistry owing to the well-documented "magic methyl" effect (*41*). Such olefins thus provide an ideal testing ground for the potential of BioHAT.

Purified **HAT$_R$-5** shows activity across a range of 3-methylene-piperidine substrates (Fig. 3A). All reactions are performed at ambient conditions without any precautions to exclude oxygen. Diverse substitutions on the sulfonyl group are tolerated. Yields vary with the nature of the nitrogen protecting group, but enantioselectivity is generally excellent (>95:5 e.r.). Remaining mass balance (checked for **5** and **21**) is the unreacted substrate (e.g., see tables S9 and S34). Under these conditions, no background reaction is observed in the absence of protein (i.e., with hemin and a thiol alone; see supplementary materials). Reductively sensitive substituents (**9** to **13**), including an iodo, nitro, cyano, and ketone groups—possible liabilities under traditional hydrogenation conditions—are tolerated. With the aldehyde **13**, substantial competing reduction to the carbinol is also seen (supplementary materials). Evolving HAT$_R$ variants with improved chemoselectivity for olefin reduction in the presence of aldehydes remains a future goal. Substrates bearing heterocycles, including pyridines (**14** and **15**) and a thiophene (**16**) retain moderate to good yields and enantioselectivity. Amides and carbamates (**17** to **19**) are excellent substrates. The free amine **20** demonstrated low activity.

Analogous pyrrolidine substrates (**21** to **25**) are accepted but show diminished yields and enantioselectivity compared with their piperidine counterparts. The 3-vinyl azepine analog **26** is reduced with moderate yields, whereas the 4-vinyl azepine **27**—with the more distant desymmetrizing N-tosyl group—gives lower yield but high enantioselectivity. Linear scaffolds (**28** to **30**), whose geometries diverge from the model cyclic substrate **5**, fare poorly.

Styrenyl substrates, such as **31** and **32**, are typically unreactive under cHAT conditions because HAA from a thiol to a stabilized, tertiary benzylic radical is endergonic (*20*). The bond dissociation energy (BDE) of the Cys S–H (~86 kcal mol^{-1}) is well matched for favorable HAA by a tertiary alkyl radical (3° C–H, BDE ~ 95 kcal mol^{-1}) with an expected rate constant of ~10^6 M^{-1} s^{-1} (*42*–*44*). By contrast, HAA by a tertiary benzylic radical—such as that formed from **31** or **32**—is thermodynamically and kinetically disfavored [3° benzylic C–H, BDE ≤ 86 kcal mol^{-1}, equilibrium constant (K_{eq}) ~ 10^{-3}] (*42*, *43*). Consistently, the HAT$_R$ lineage shows no detectable product formation with **31** or **32**. However, a distinct protein variant, **HAT$_R$-Ma**—a mutant derived from *Methanosarcina acetivorans* protoglobin (wtMaPgb Y61D, W63L, V64Q, R92C) and constructed during our Cys mutant screens—exhibits initial reactivity with moderate enantioselectivity. This result suggests that tuning the active-site environment, particularly the positioning and local polarity surrounding the Cys residue, may lower the effective S–H BDE and enable reactivity with electronically stabilized radical intermediates.

Trisubstituted (**33**) and even tetrasubstituted (**34**) olefins are competent. With **33**, complementary enantioselectivity is achieved with **HAT$_R$-5** and **HAT$_R$-Ma**. For the more challenging tetrasubstituted olefin **34**, the evolved

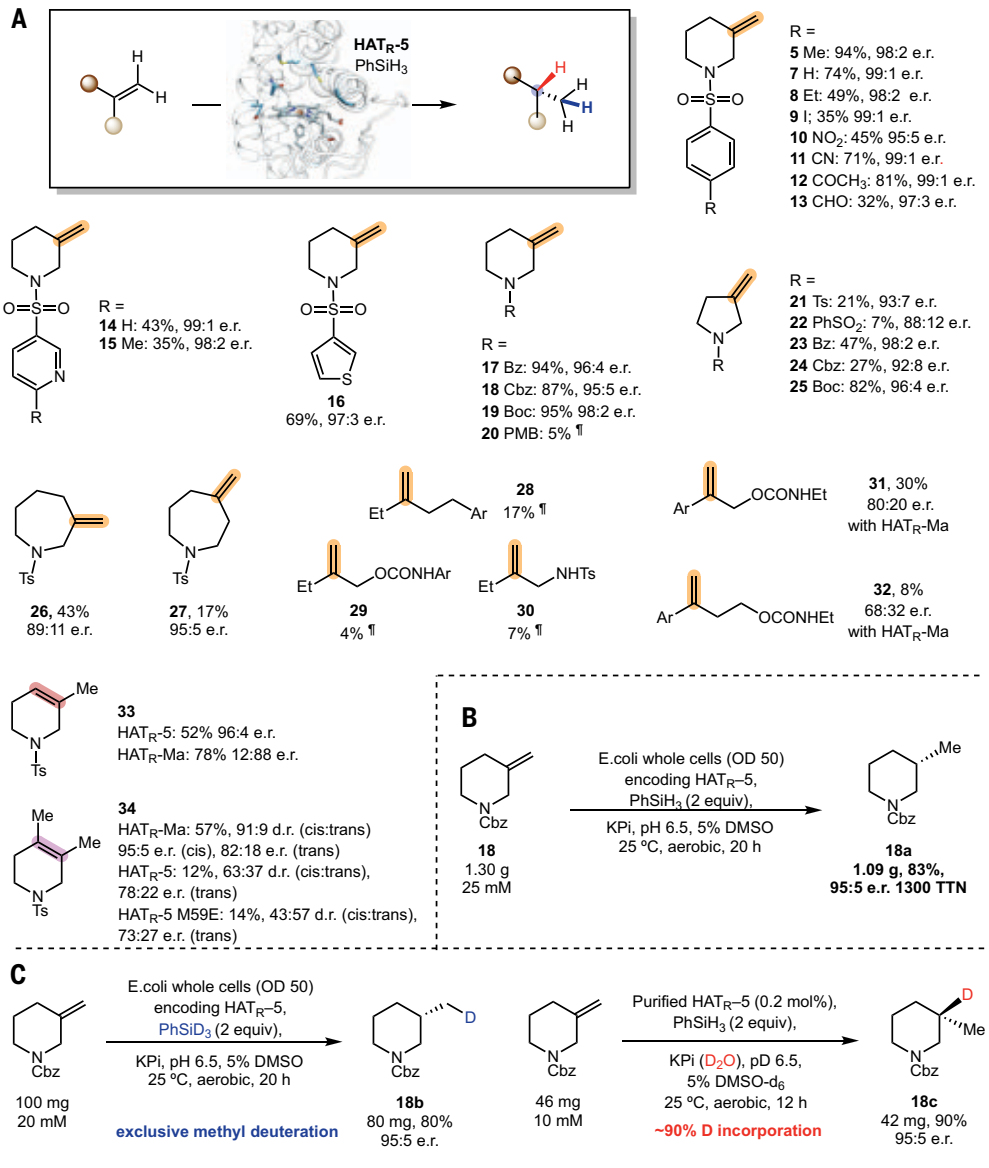


Fig. 3. Substrate scope of BioHAT and preparative scale reactions. (**A**) Conditions: 0.2 mol% enzyme, potassium phosphate buffer (KPi, 50 mM, pH 6.5), dimethyl sulfoxide (DMSO) (5% v/v), TPGS-750-M (6% w/v), olefin (1 equiv, 5 mM), phenylsilane (4 equiv), 25°C, 4 hours. Analytical yields are reported as average of triplicate experiments. Bz, benzoyl; Cbz, carboxybenzyl; Boc, butyloxycarbonyl; PMB, p-methoxybenzyl; Ts, tosyl; Ar, p-methoxyphenyl. ¶e.r. was not determined because chiral resolution conditions could not be found. (**B**) Gram-scale hydrogenation of **18**. (**C**) Preparative, site-divergent asymmetric deuteration.

lineage enzymes (HAT_R-*5*, HAT_R-*5* M59E) show modest activity, whereas 57% analytical yield is observed with **HAT_R-Ma**. Diastereoselectivity and enantioselectivity varies with the catalyst. **HAT_R-Ma** is highly selective for the cis reduced product [91:9 diastereomeric ratio (d.r.), 95:5 e.r.], whereas the other two enzymes give low but distinct diastereoselectivity. A marginal preference for the trans product is seen with **HAT_R-*5* M59E**, which indicates that subtle changes in the active site can reverse stereochemical outcome. The development of diastereodivergent enzymes, especially for asymmetric anti-hydrogenation of unactivated tetrasubstituted olefins, may be within reach with future directed evolution.

The choice of model compound ***5*** during the directed evolution campaign results in a preference for the piperidine scaffold. However, the observed activity across other substrate classes, including styrenyl, linear, trisubstituted, and tetrasubstituted olefins, highlights the potential of BioHAT as a broadly applicable platform for asymmetric olefin reduction.

The preparative utility of BioHAT enzymes is exemplified by a gram-scale synthesis of **18a** using whole-cell catalysis (Fig. 3B). Starting from a 2-liter *E. coli* culture expressing **HAT_R-*5***, a reaction of 1.30 g of **18** with two equivalents of phenylsilane produced the product in 83% isolated yield (1.09 g), excellent enantioselectivity (95:5 e.r.), and TTN of ~1300. The transformation is performed under ambient, aerobic conditions without special precautions; does not require any precious metal or chiral ligand preparation; and is readily scalable, demonstrating its practicality for asymmetric hydrogenations.

BioHAT enables precise, site-selective isotopic labeling by independently delivering the two hydrogen atoms from orthogonal sources: the hydride from phenylsilane (via the active-site Fe–H) and the proton from water (via the active-site Cys thiol). As a result, isotopic composition at each carbon of the reduced product can be controlled by simply choosing isotopically labeled silane or water (Fig. 3C). In line with this expectation, preparative-scale, site-selective asymmetric deuteration was achieved. Exclusive deuteration at the terminal (methyl) position is obtained by using $PhSiD_3$ in a whole-cell reaction. The complementary isotopomer—with deuteration at the methine position—was accessed with purified enzyme in D_2O with $PhSiH_3$. In both cases, high enantioselectivity (95:5) was maintained. This capability can be valuable for diverse applications, including the study of bioactive molecule metabolism (e.g., using deuterium for pharmacokinetic profiling) and radioligand binding assays (e.g., through tritium labeling) (*45*–*47*).

Mechanistic studies

Mechanistic investigations support a stepwise radical pathway for BioHAT (Fig. 4), rather than a concerted HAT-HAA event: (i) When the radical trap TEMPO is added, TEMPO adducts are observed by high-resolution mass spectrometry (HRMS), confirming interception of discrete radical intermediates (supplementary materials). (ii) Similar enantioselectivity is obtained for ***5*** and the trisubstituted olefin ***33***, as both are expected to proceed through a common tertiary radical intermediate **5b** before the enantiodetermining HAA step. (iii) Subjecting substrate **1** to hydrogenation with **HAT_R-*3*** or **HAT_R-*5*** leads primarily to cyclized product **2**, with only trace amounts of reduced product **1b**. In this case, **1** functions as a radical clock probe, with rapid 5-exo-trig cyclization [expected cyclization rate constant (k_{cyc}) > 10^7 M^{-1} s^{-1}] (*48*) from a discrete intermediate radical **1a** outcompeting intermolecular HAA from the 60C thiol. Alternative cationic or anionic pathways are further ruled out by isotope labeling results, mutagenesis studies, and substrate reactivity patterns (see section 8.6 in supplementary materials).

The Fe(III)- or Fe(II)-thiol catalytic cycle is further supported by observations 4 to 6 (Fig. 4B). Enzymatic activity is inhibited by dithionite (table S16), consistent with the ferrous resting state being unable to form the active-site hydride or with Fe(II)–H species being incapable of initiating MHAT with the olefin. The enzymatic reaction behaves comparably under anaerobic conditions (table S16), consistent with the intermediate thiyl radical (and not oxygen) acting as a transient oxidant for ferrous reoxidation to the active ferric state. The experimental redox potential for **HAT_R-*5*** Fe(II) to Fe(III) oxidation was determined to be +0.22 V (fig. S15), which is well within the oxidative capability of a cysteine thiyl radical (thiyl to thiolate E° ~ +0.75 V) (*49*, *50*). Finally, we have observed that other silanes can also act as reductants with **HAT_R-*5*** and enantioselectivity for the model substrate ***5*** remains the same (table S17), which suggests that the silane's role is limited to active-site Fe(III)–H formation upstream of the radical transfer steps. In enzymatic reactions with $PhMe_2SiH$, the anticipated by-product, $PhMe_2SiOH$, was detected (fig. S16).

The feasibility of the stepwise radical process was benchmarked by density functional theory (DFT) calculations with a model iron-porphyrin system and methanethiol as a cysteine side chain mimic (Fig. 4C; see supplementary materials for details). For the Fe(III)-porphyrin-hydride **Int-1**, the doublet had the lowest Gibbs free energy compared with the quartet and sextet spin states. Upon introduction of the olefin, **Int-1** undergoes an MHAT through **TS-HAT** with a barrier of 12.6 kcal mol^{-1} (doublet), furnishing an alkyl radical and a triplet Fe(II) species [**Int-2**, change in Gibbs free energy (ΔG) = –16.5 kcal mol^{-1}] after a spin-crossover from the open-shell singlet Fe(II) surface. The alternative state of this intermediate—an Fe(III)-alkyl species—was found to be highly disfavored (e.g., for the doublet, ΔG = +9.6 kcal mol^{-1}; see supplementary materials). The alkyl radical is subsequently quenched by means of HAA from methanethiol. This step proceeds through the **TS-HAA** transition state with an activation barrier of 10.6 kcal mol^{-1}, resulting in the formation of the hydrogenated product and a thiyl radical (**Int-*3***, ΔG = −25.0 kcal mol^{-1}) with triplet Fe(II). The subsequent direct, outer-sphere ET between the ferrous-porphyrin and the thiyl radical was calculated to be prohibitive by Marcus theory (supplementary materials). Instead, the redox step was computed to be feasible through a proton-coupled electron transfer (PCET) mediated by a bridging water molecule. The lowest-energy PCET transition state (**TS-PCET**) was found on the sextet surface and proceeds with an activation barrier of 6.1 kcal mol^{-1}. This step results in the formation of a thiol and sextet porphyrin-Fe(III)-OH (**Int-4**), marking a second spin-crossover event. These computations provide a theoretical framework for understanding the radical hydrogen atom transfer and redox events occurring in the active site.

BioHAT overcomes key limitations of small-molecule cHAT (*29*). It delivers high TTNs (>1000; Fig. 3B) with broad reactivity, whereas the only reported asymmetric small-molecule system, despite using highly engineered substrates, is restricted to <10 TTNs and falters in providing useful enantioselectivity (*21*). The superior enzymatic performance is speculated to arise from several distinctive features. First, we assume that BioHAT promotes accelerated active-site Fe–H formation with virtually no background reactivity outside the enzyme. The mechanism of heme Fe–H formation from silanes remains unclear but likely differs from the "concerted interchange" pathway of nonheme iron complexes (*23*, *25*) owing to the restricted coordination environment of the heme. Second, a deactivation pathway proposed with small molecule cHAT is minimized because the engineered Cys thiol group is too distant (>8 Å) for Fe-Cys adduct formation, and its buried position precludes disulfide side products (*21*). Third, improved enantioselectivity is achieved through direct HAA from a Cys thiol rather than an Fe-bound species, with the tertiary protein scaffold providing a more effective chiral environment for asymmetric induction than the interactions accessible with small molecules. Finally, the active site promotes precise spatial organization of the Fe center, thiol, and substrate, enabling atom transfer and ET processes with a level of control that is difficult to achieve with small-molecule catalysts. Rationally engineering these interdependent processes (with small molecules) is extremely challenging, but directed evolution allows an agnostic exploration of structural (sequence) space to discover biocatalysts that can orchestrate these steps efficiently. Future investigations will focus

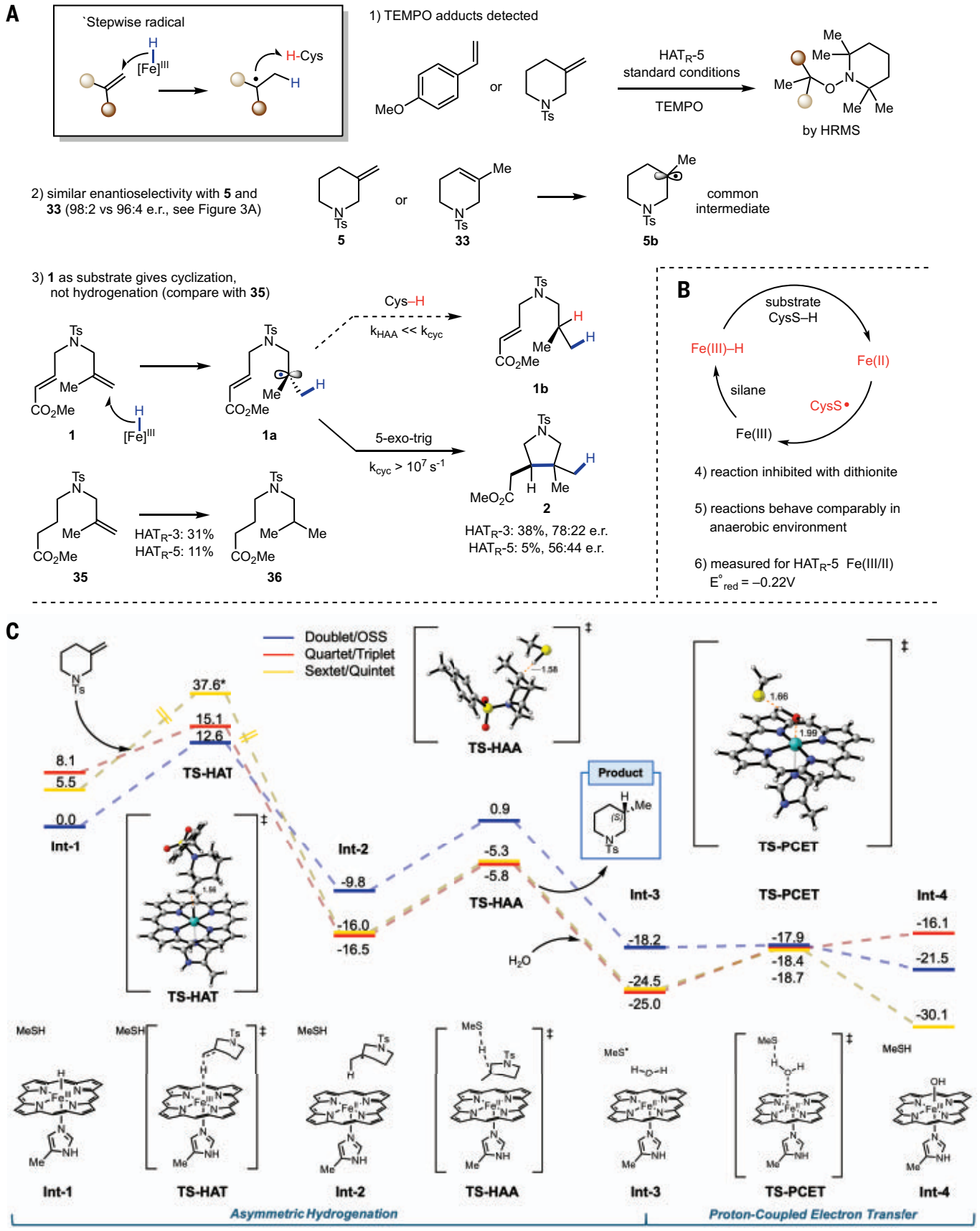


Fig. 4. Mechanistic investigations supporting stepwise radical transfer. (**A**) Observations 1 to 3 are consistent with a discrete radical intermediate. (**B**) Observations 4 to 6 are consistent with the Fe(III)- or Fe(II)-thiol redox cycle. (**C**) DFT modeling of the hydrogen atom transfer and ET steps. Values refer to Gibbs free energies in kilocalories per mole. *Frequency and single-point energies were calculated using optimized geometries for the quartet. See the supplementary materials for details.

on comprehensive computational, kinetic, mutagenesis, and spectroscopic studies to unravel the mechanistic basis of this orchestration.

BioHAT imports a radical hydrogenation paradigm to biochemistry and allows for the asymmetric reduction of challenging, unactivated olefins with Earth-abundant, iron-containing genetically encoded catalysts. The radical mechanism offers a pathway for orthogonal stereocontrol during both hydrogen atom deliveries, including for selective isotope labeling. These enzymes are thermostable, oxygen tolerant, amenable to gram-scale synthesis, and readily evolvable. Given the vast natural diversity of heme proteins, the simplicity of activating BioHAT by means of cysteine introduction, and the power of directed evolution, we anticipate the future cultivation of stereoselective hydrogenation biocatalysts for virtually any type of olefin.

REFERENCES AND NOTES

1. S. Nishimura, *Handbook of Heterogeneous Catalytic Hydrogenation for Organic Synthesis* (Wiley, 2001).
2. J. G. de Vries, C. J. Elsevier, Eds., *The Handbook of Homogeneous Hydrogenation* (Wiley, ed. 1, 2006).
3. A. J. Birch, D. H. Williamson, in *Organic Reactions*, S. E. Denmark, Ed. (Wiley, ed. 1, 2011), pp. 1–186.
4. P. G. Andersson, I. J. Munslow, Eds., *Modern Reduction Methods* (Wiley, ed. 1, 2008).
5. H. S. Toogood, J. M. Gardiner, N. S. Scrutton, *ChemCatChem* **2**, 892–914 (2010).
6. S. Roth, R. Niese, M. Müller, M. Hall, *Angew. Chem. Int. Ed.* **63**, e202314740 (2024).
7. Q. Xu *et al.*, *J. Mol. Biol.* **404**, 403–417 (2010).
8. M. Huang *et al.*, *Drug Metab. Rev.* **46**, 362–378 (2014).
9. R. Cervinka *et al.*, *Chembiochem* **22**, 2693–2696 (2021).
10. S. G. Ouellet, A. M. Walji, D. W. C. MacMillan, *Acc. Chem. Res.* **40**, 1327–1339 (2007).
11. J. M. Brown, in *Asymmetric Hydrogenation and Transfer Hydrogenation*, V. Ratovelomanana-Vidal, P. Phansavath, Eds. (Wiley, ed. 1, 2021), pp. 1–24.
12. W. S. Knowles, *Angew. Chem. Int. Ed.* **41**, 1998–2007 (2002).
13. R. Noyori, M. Kitamura, T. Ohkuma, *Proc. Natl. Acad. Sci. U.S.A.* **101**, 5356–5362 (2004).
14. C. Margarita, P. G. Andersson, *J. Am. Chem. Soc.* **139**, 1346–1356 (2017).
15. R. Bigler *et al.*, *Angew. Chem. Int. Ed.* **59**, 2844–2849 (2020).
16. S. Kraft, K. Ryan, R. B. Kargbo, *J. Am. Chem. Soc.* **139**, 11630–11641 (2017).
17. C. S. G. Seo, R. H. Morris, *Organometallics* **38**, 47–65 (2019).
18. H. S. Toogood, N. S. Scrutton, *ACS Catal.* **8**, 3532–3549 (2019).
19. A. Papadopoulou, C. Peters, S. Borchert, K. Steiner, R. Buller, *Org. Process Res. Dev.* **26**, 2102–2110 (2022).
20. P. V. Kattamuri, J. G. West, *J. Am. Chem. Soc.* **142**, 19316–19326 (2020).
21. S. R. Buzsaki *et al.*, *J. Am. Chem. Soc.* **146**, 17296–17310 (2024).
22. K. Iwasaki, K. K. Wan, A. Oppedisano, S. W. M. Crossley, R. A. Shenvi, *J. Am. Chem. Soc.* **136**, 1300–1303 (2014).
23. D. Kim, S. M. W. Rahaman, B. Q. Mercado, R. Poli, P. L. Holland, *J. Am. Chem. Soc.* **141**, 7473–7485 (2019).
24. S. W. M. Crossley, C. Obradors, R. M. Martinez, R. A. Shenvi, *Chem. Rev.* **116**, 8912–9000 (2016).
25. S. L. Shevick *et al.*, *Chem. Sci.* **11**, 12401–12422 (2020).
26. P. Ji, J. Park, Y. Gu, D. S. Clark, J. F. Hartwig, *Nat. Chem.* **13**, 312–318 (2021).
27. R. Chen, C. S. Kayrouz, E. McAmis, D. S. Clark, J. F. Hartwig, *Angew. Chem. Int. Ed.* **63**, e202407111 (2024).
28. X. Zhang *et al.*, *Chem* **10**, 2577–2589 (2024).
29. Z. Wan *et al.*, *Nat. Synth.* **4**, 976–986 (2025).
30. Y. Nakano, K. F. Biegasiewicz, T. K. Hyster, *Curr. Opin. Chem. Biol.* **49**, 16–24 (2019).
31. B. Wang *et al.*, *Angew. Chem. Int. Ed.* **62**, e202311099 (2023).
32. J. C. Lo, Y. Yabe, P. S. Baran, *J. Am. Chem. Soc.* **136**, 1304–1307 (2014).
33. N. J. Porter, E. Danelius, T. Gonen, F. H. Arnold, *J. Am. Chem. Soc.* **144**, 8892–8896 (2022).
34. L. Schaus *et al.*, *Angew. Chem. Int. Ed.* **62**, e202208936 (2023).
35. S. Gao *et al.*, *J. Am. Chem. Soc.* **145**, 20196–20201 (2023).
36. A. Pesce, M. Bolognesi, M. Nardini, in *Microbial Globins - Status and Opportunities*, R. K. Poole, Ed., vol. 63 of *Advances in Microbial Physiology* (Academic Press, 2013), pp. 79–96.
37. X. Zhang, D. Chen, M. Álvarez, T. R. Ward, *Nature* **644**, 381–390 (2025).
38. M. Cortes-Clerget *et al.*, *Nat. Commun.* **10**, 2169 (2019).
39. Z. Zhang, N. A. Butt, W. Zhang, *Chem. Rev.* **116**, 14769–14827 (2016).
40. S. Singh, J. M. Hernández-Lobato, *J. Org. Chem.* **89**, 12467–12478 (2024).
41. D. Aynetdinova *et al.*, *Chem. Soc. Rev.* **50**, 5517–5563 (2021).
42. Y.-R. Luo, *Comprehensive Handbook of Chemical Bond Energies* (CRC Press, 2007).
43. F. Dénès, M. Pichowicz, G. Povie, P. Renaud, *Chem. Rev.* **114**, 2587–2693 (2014).
44. C. Tronche *et al.*, *Tetrahedron Lett.* **37**, 5845–5848 (1996).
45. K. Gevaert *et al.*, *Proteomics* **8**, 4873–4885 (2008).
46. C. S. Elmore, R. A. Bragg, *Bioorg. Med. Chem. Lett.* **25**, 167–171 (2015).
47. J. Atzrodt, V. Derdau, W. J. Kerr, M. Reid, *Angew. Chem. Int. Ed.* **57**, 1758–1784 (2018).
48. P. Tauh, A. G. Fallis, *J. Org. Chem.* **64**, 6960–6968 (1999).
49. P. S. Surdhar, D. A. Armstrong, *J. Phys. Chem.* **91**, 6532–6537 (1987).
50. P. Huston, J. H. Espenson, A. Bakac, *J. Am. Chem. Soc.* **114**, 9510–9516 (1992).
51. E. Danelius, N. J. Porter, J. Unge, F. H. Arnold, T. Gonen, *J. Am. Chem. Soc.* **145**, 7159–7165 (2023).
52. N. Eswar *et al.*, *Nucleic Acids Res.* **31**, 3375–3380 (2003).
53. O. Trott, A. J. Olson, *J. Comput. Chem.* **31**, 455–461 (2010).

ACKNOWLEDGMENTS

We thank B. Jolly and the UCLA Master of Applied Chemical Sciences (MACS) instrumentation facility for analytical support and O. Gutierrez for assistance with chiral separations. The *E. coli* Nissle(T7) strain was kindly provided by A. Wilks. S.V.A. acknowledges F. H. Arnold for her generosity in sharing metalloenzyme libraries. K. E. Rivera Cruz is acknowledged for his assistance with protein electrochemistry. **Funding:** This work was supported by UCLA Department of Chemistry and Biochemistry startup funds to S.V.A. H.S.S. and J.D.C. acknowledge support from National Institutes of Health grant GM128852. K.N.H. acknowledges support from National Science Foundation grant CHE-2153972. **Author contributions:** Project conceptualization, planning, direction, and writing: S.V.A. Molecular biology and library preparations: J.V., K.S. Initial activity discovery: J.V. Directed evolution: J.V., J.B. Substrate scope experiments: J.V., R.M. Synthesis: R.M., M.H., J.M., M.B.L. Preparative scale reactions: R.M., M.H. Deuterium labeling studies: R.M. Computational studies under the mentorship of K.N.H.: A.V.R., E.P. Protein expression, purification, and preliminary spectroscopy: J.D.C. and C.T. with mentorship from H.S.S. All authors contributed to assembling the final draft of the manuscript. **Competing interests:** S.V.A. is an inventor on a provisional patent application prepared through UCLA based on the results presented in this work. The authors declare no other competing interests. **Data and materials availability:** All data needed to evaluate the conclusions in this study are present in the main text or the supplementary materials. Synthetic procedures are provided for the generation of chemical reagents, and biological materials are available by reasonable request to the corresponding author. **License information:** Copyright © 2025 the authors, some rights reserved; exclusive licensee American Association for the Advancement of Science. No claim to original US government works. https://www.science.org/about/science-licenses-journal-article-reuse

SUPPLEMENTARY MATERIALS

science.org/doi/10.1126/science.aea4737
Materials and Methods; Supplementary Text; Figs. S1 to S199; Tables S1 to S52; References (*54*–*125*); MDAR Reproducibility Checklist

Submitted 11 July 2025; accepted 7 October 2025; published online 16 October 2025
10.1126/science.aea4737

MATERIALS DESIGN

A stoichiometrically conserved homologous series with infinite structural diversity

Hengdi Zhao[1], Xiuquan Zhou[1,2], Ziliang Wang[3], Patricia E. Meza[3], Yihao Wang[1], Denis T. Keane[4], Steven J. Weigand[4], Saul H. Lapidus[5], Duck-Young Chung[1], Christopher Wolverton[3], Vinayak P. Dravid[3], Stephan Rosenkranz[1], Mercouri G. Kanatzidis[1,6]*

We describe a compositionally guided structural evolution within a stoichiometrically conserved framework, $BaSbQ_3$ ($Q = Te_{1-x}S_x$), where each value of x gives rise to a distinct phase. The fundamental building blocks, A_1 ($BaSbSTe_2$) and B_n ($Ba_nSb_nS_{n-1}Te_{2n+1}$), were composed of modular double rocksalt slabs stacked with functional polytelluride zigzag chains, with each phase differing only in the size and assembly of these blocks. Ten compounds were synthesized that maintained a coherent chemical identity that arose from this isovalent, isoelectronic substitution of Te and S. We envision that the phase formation at a molecular level unfolds in stages of extension, termination, and assembly and propose a design concept of "anionic disparity," where phase homologies and polytelluride hierarchical networks can be controlled by leveraging differences in anion electron affinity and sizes.

A central ambition in materials science is the predictive synthesis of compounds with targeted structures and functions. Molecular systems have seen notable design control, but achieving similar precision in extended inorganic frameworks remains elusive, as small compositional changes can trigger abrupt structural shifts. This difficulty arises not from lack of synthetic skill, but from incomplete understanding of the structure-directing principles that govern crystallization. Homologous series offer an underutilized opportunity to uncover principles linking composition and structure for achieving structural predictability and compositional control.

Phase homologies in inorganic chemistry trace back to the foundational work of Magnéli and collaborators, who, in the 1950s, reported a systematic series of nonstoichiometric titanium oxides (Ti_nO_{2n-1}) formed through crystallographic shear mechanisms, where each member has a different stoichiometry (*1*). These Magnéli phases revealed that complex solids could be organized into homologous families with predictable structural motifs and stoichiometries (*1*, *2*). This concept was further extended to oxides (*3*–*5*), intermetallics (*6*–*10*), chalcogenides (*11*–*14*), and halides (*15*, *16*) in subsequent decades, offering a pathway toward rationalizing and discovering new compounds.

Although considerable progress has recently been claimed in using machine learning (ML) and artificial intelligence (AI) (*17*–*19*) to predict vast numbers of hypothetical materials, their effectiveness has been criticized recently (*20*, *21*). Constrained primarily by substituting elements within known structures, their predictive power is largely limited to materials with established structure types, leaving those with truly new structures or metastable phases beyond reach. Therefore, predicting chemically sound and experimentally synthesizable phases with new structures remains a challenge for extended solids.

By contrast, the search for new compounds with AI and ML has been notably more successful in fields where more extensive sets of chemical principles have been established, such as organic (*22*–*26*) and molecular (*27*, *28*) chemistry. To bridge this design-rules gap in solid-state chemistry, it is essential to develop powerful chemically intuitive frameworks, such as phase homologies, that provide both predictive structure-composition relationships and practical guidance for synthesis. Our group has emphasized the predictive power of phase homologies as "compound-generating machines," using them not only to classify known solids but also to guide the deterministic design and synthesis of entirely new materials with defined structural architectures (*11*, *12*).

Here, we introduce a design concept, termed "anionic disparity," to create and control structural homologies through targeted anion mixing. This principle leverages the differential electron affinities of anionic species to both direct their site occupancy, forming new ordered multianion structures, and concurrently manipulate the electron distribution within anionic substructures. Specifically, we applied this concept to the starting compound $BaSbTe_3$, which features alternating double rocksalt slabs and polytelluride zigzag chains, to address the challenge of controlling tellurium-based structure motifs.

We present the chemical rules that generate the homologous members and how these rules can be used to design new members. We initially hypothesized that starting from $BaSbTe_3$, the isoelectronic substitution of sulfur for isovalent tellurium could lead to one of three outcomes: (i) a solid solution with random S and Te (S/Te) substitution; (ii) an ordered multianion arrangement of S and Te within the $BaSbTe_3$ structure (*29*); or (iii) a frustrated scenario in which the disparity in bonding drives a complete destabilization of the original structure, giving rise to a new framework. However, the outcome was not any of the expected scenarios. Instead, we observed the emergence of a previously unknown class of structurally related compounds, a polymorphic homologous series, where all members shared the same nominal composition $BaSbQ_3$ ($Q = Te_{1-x}S_x$) yet exhibited distinct and systematically evolving structures. We outline design rules and then describe each member of this series in detail and sequence, starting with the Te-rich end member and proceeding through phases with progressively higher sulfur content.

Design principles

We hypothesized that by introducing a more electronegative but isovalent element from the same group of the periodic table, such as sulfur, into a chemical system containing different types of telluride anions, such as Te^{2-} and polytelluride $[Te_n]^{2-}$ anions, we could avoid formation of solid solutions by taking advantage of the large difference in size and electronegativity and instead induce a preferential ordering between the two types of chalcogenide ions. We further hypothesized that the constant sum of cationic contributions from Ba and Sb would disproportionately amplify the anionic disparity between sulfur and tellurium.

Sulfur, with its higher electron affinity, selectively occupies the more electron-rich Te^{2-} sites, forming a new ordered multianion structure. This selective substitution of Te^{2-} with S^{2-} also effectively modifies electron distributions within the tellurium network, transforming more remaining tellurium from electron-rich telluride Te^{2-} to the more electron-poor polytelluride state of $[Te_n]^{2-}$. These reactions would drive the structural evolution of different polytelluride hierarchical networks from single zigzag chains to extended square nets. This hypothesis is consistent with the observations that S substitutions systematically promote an enriched polytelluride fraction (Table 1). This strategy was deemed possible because single polytelluride zigzag chains and extended polytelluride square nets have been observed in $BaSbTe_3$ (*30*) and $BaSbSTe_2$ (*31*), respectively.

[1]Materials Science Division, Argonne National Laboratory, Lemont, IL, USA. [2]Department of Chemistry, Georgetown University, Washington, DC, USA. [3]Department of Materials Science and Engineering, Northwestern University, Evanston, IL, USA. [4]DuPont-Northwestern-Dow Collaborative Access Team (DND-CAT) Synchrotron Research Center, Northwestern University, Lemont, IL, USA. [5]X-ray Science Division, Advanced Photon Source, Argonne National Laboratory, Argonne, IL, USA. [6]Department of Chemistry, Northwestern University, Evanston, IL, USA. *Corresponding author. Email: m-kanatzidis@northwestern.edu

Table 1. Summary of crystal structures of synthesized homologous phases from single-crystal x-ray diffraction at 293 K. Note that all chemical formulas are normalized to $Z = 2$ for comparison, where Z is the number of formula units per unit cell. [Te_n] represents polytelluride, and Te refers to all tellurium contents. Detailed coordination and bond-distance analyses can be found in the supplementary materials.

Phase	Homologous value	Formula	Space group	Structure type	Ribbon [Te_n]	S/Te ratio	[Te_n]/Te ratio
I	$(B_2)_2$	$Ba_4Sb_4Te_{12}$	$P2_12_12_1$	$BaBiSe_3$	$[Te_2]^{2-}$	0	0.17
II	$(B_4)_2$	$Ba_8Sb_8S_6Te_{18}$	$P2_12_12_1$	$SrBiSe_3$	$[Te_3]^{2-}$	0.33	0.33
III	A_1B_4	$Ba_5Sb_5S_4Te_{11}$	$P2_1/m$	New	$[Te_3]^{1-}$	0.36	0.27
IV	A_1B_5	$Ba_6Sb_6S_5Te_{13}$	$P2_1/m$	New	$[Te_4]^{2-}$	0.38	0.31
V	A_1B_6	$Ba_7Sb_7S_6Te_{15}$	$P2_1/m$	New	$[Te_5]^{3-}$	0.4	0.33
VI	A_1B_7	$Ba_8Sb_8S_7Te_{17}$	$P2_1/m$	New	$[Te_6]^{4-}$	0.41	0.35
VII	B_4B_5	$Ba_9Sb_9S_7Te_{20}$	$P2_1/m$	New	$[Te_7]^{5-}$	0.35	0.35
VIII	$A_1B_4(B_5)_2$	$Ba_{15}Sb_{15}S_{12}Te_{33}$	$P2_1/m$	New	$[Te_{11}]^{7-}$	0.36	0.33
IX	$(A_1)_2(B_5)_4$	$Ba_{22}Sb_{22}S_{18}Te_{48}$	$Pnma$	New	$[Te_{16}]^{10-}$	0.38	0.33
X	B_∞	$BaSbSTe_2$	$Pmm2(0\beta0)000$	$SrBiTe_3$	$[Te]^{1-}$	0.5	0.5

Guided by this design principle, we synthesized 10 representative members of a new homologous series of $BaSbQ_3$ (Q = $Te_{1-x}S_x$) (Table 1). Each compound exhibits a distinct crystal structure type, yet all members share the same nominal composition of Ba:Sb:Q equal to 1:1:3, and the progression in structure from one member to the next was predictable. All structures in this homology comprise two types of fundamental building blocks. One is a two-octahedra-wide rocksalt slab, noted as A_1 = $BaSbSTe_2$, and the other is a modular rocksalt slab stacked with adjustable polytelluride chains, formulated as $B_n = Ba_nSb_nS_{n-1}Te_{2n+1}$ or $B_n = Ba_nSb_nS_{n-1}Te_{n+2}[Te_{n-1}]$, with [$Te_n$] representing the polytelluride component. The polytelluride component scaled with the S/Te-substitution levels (Table 1), reaffirming the anion-driven structural evolutions.

The difference from one member to the next was primarily the length of the modular blocks and the connectivity of all blocks, which is governed by the S/Te ratio. In this homologous family of $BaSbQ_3$, the anion disparity between Te and S offered an effective method to control the size of the polytelluride networks. The increasing S fraction in the formula $BaSbQ_3$ systematically reconfigured the polytelluride fragments in the structure and led to a continuous evolution from a single zigzag polytelluride chain to infinitely extended two-dimensional polytelluride square nets.

Homologous phase evolution of A_mB_n = $(BaSbSTe_2)_m(Ba_nSb_nS_{n-1}Te_{2n+1})$

Phase I (Fig. 1A; $BaSbTe_3$, or $Ba_4Sb_4Te_{10}[Te_2]$, where [Te] specifies the polytelluride) represents the Te-only, first member of the homologous series without sulfur incorporation. It crystallized in the $BaBiSe_3$-type structure (*30*, *32*) in the orthorhombic space group $P2_12_12_1$ (space group no. 19) with $a = 4.6240(9)$ Å, $b = 16.915(3)$ Å, and $c = 18.058(4)$ Å (numbers in parentheses are errors in the last digit). A two-block-wide distorted double rocksalt slab of (Sb_4Te_{10}) alternates with one polytelluride zigzag chain of [Te_2] along the b axis, with Ba cations sandwiched in between (Fig. 1A). Each ($Ba_4Sb_4Te_{10}$)[Te_2] block is mirror reflected along the b axis and connects between the ($Ba_4Sb_4Te_{10}$) double rocksalt slab and the [Te_2] zigzag Te chain of its adjacent neighbor along the c axis, forming a larger orthorhombic cell with the space group of $P2_12_12_1$. Both the double rocksalt slabs and the zigzag chains extend infinitely along the a axis, forming the infinite slabs and chains (fig. S1B).

With the substitutional incorporation of a small amount of sulfur, we observed **Phase II** (Fig. 1C; $Ba_8Sb_8S_6Te_{18}$ or $Ba_8Sb_8S_6Te_{12}[Te_6]$), isostructural with $SrBiSe_3$ (*33*), also crystallized in the orthorhombic space group $P2_12_12_1$ (no. 19) with $a = 4.4476(4)$ Å, $b = 16.5502(14)$ Å, and $c = 35.400(3)$ Å. Similar to **Phase I**, it also featured alternating double rocksalt slabs and polytelluride zigzag chains separated by Ba cations. However, both double rocksalt slabs and polytelluride chains were widened to be a four-block-wide double rocksalt slab of ($Ba_8Sb_8S_6Te_{12}$) stacked with three polytelluride zigzag chains of [Te_6]. The fact that this small level of S substitution results in an entire phase homology rather than a simple solid solution of **Phase I** (scenario 1) or an ordered substitution within the parent lattice (scenario 2) suggests a far more intricate formation mechanism.

By incorporating more sulfur into our synthesis, we obtained **Phase III** (Fig. 1J; $Ba_5Sb_5S_4Te_{11}$, or $Ba_5Sb_5S_4Te_8[Te_3]$), which crystallized in a new structure type in the monoclinic space group $P2_1/m$ (no. 11) with $a = 16.630(3)$ Å, $b = 4.4864(9)$ Å, $c = 22.494(5)$ Å, and $\beta = 99.63(3)°$. Similar to **Phase II**, it also hosted the four-block-wide double rocksalt slabs of ($Sb_8S_6Te_{12}$) alternating with three-polytelluride zigzag chains of [Te_6] along the a axis, with Ba cations interspersed. Differently, each ($Ba_8Sb_8S_6Te_{12}$)[Te_6] block in **Phase III** is parallel to its neighbor and bridged by another isolated one-block-wide double rocksalt slab of ($Sb_2S_2Te_4$) surrounded by Ba^{2+} cations. This bridging unit (highlighted in light blue in Fig. 1J) is a key feature distinguishing **Phase III** from **Phase II**.

As noted above, these phases can be described in terms of the A_1 block (light blue fragment in Fig. 1P) and the B_n ($n \geq 2$) blocks (darker blue; a representative B_4 fragment is shown in Fig. 1P). Each B_n fragment consists of two capping, or "*C*" fragments (gray-shaded blocks), with (n−2) extendable "*E*" fragments (navy blue–shaded blocks) inserted in between (in general, each B_n can be expressed as $E_{n-2}C_2$). Note that the *E* and *C* fragments differ both structurally and compositionally in anions. Using this notation, **Phases I**, **II**, and **III** can be expressed as $(B_2)_2$, $(B_4)_2$, and A_1B_4, respectively. Intriguingly, the B_n block can be further extended, which leads to the formation of **Phase IV** (Fig. 1K; $Ba_6Sb_6S_5Te_{13}$, A_1B_5), **Phase V** (Fig. 1L; $Ba_7Sb_7S_6Te_{15}$, A_1B_6), **Phase VI** (Fig. 1M; $Ba_7Sb_8S_7Te_{17}$, A_1B_7), and, lastly, **Phase X** [Fig. 1O; $BaSbSTe_2$, B_∞ (*31*)], with incremental length of B_n fragments between each phase. These phases demonstrate that A_1 and B_n fragments can act as robust modular fundamental building blocks for rational structural assembly. Leveraging the predictive framework of phase homologies, we propose that additional hypothetical structures, indicated by dashed, semi-transparent boxes in Fig. 1, fill the gaps between the known phases.

The above seven phases shown in Fig. 1 are homologs and can be generalized with the chemical formula of $A_mB_n = (BaSbSTe_2)_m(Ba_nSb_nS_{n-1}Te_{2n+1})$, or $A_mB_n = (BaSbSTe_2)_m(Ba_nSb_nS_{n-1}Te_{n+2}[Te_{n-1}])$, where $m = [0, 1]$ and $n \geq 2$. This notation describes a series of specific phases starting from **Phase I**, with two modular blocks featuring rocksalt slabs and polytellurides, A_m and B_n (Fig. 1). The n values signify the length of the B_n blocks. When $m = 0$, the phases lack the A_m block, as shown in the left column of Fig. 1. The right column displays members that contain both A_m and B_n blocks. The B_n backbone extends by the

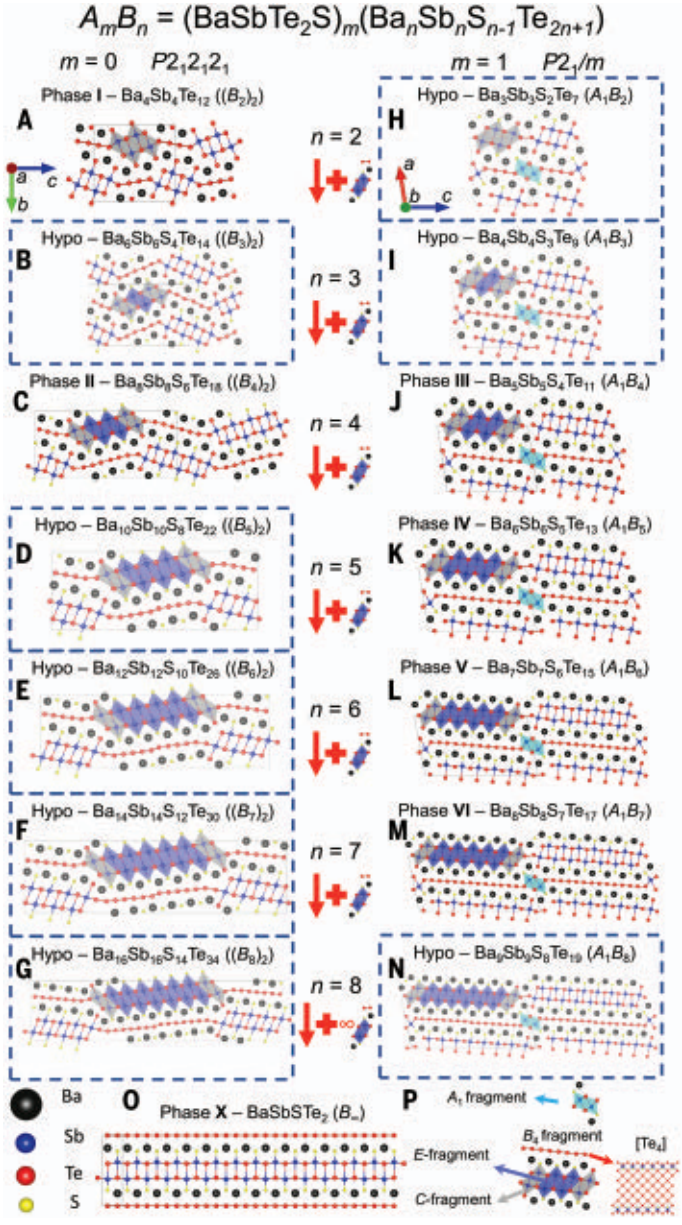


Fig. 1. Crystal structures. Both known and hypothetical structures are shown for the $m = 0$ and $m = 1$ series. The hypothetical structures (hypo) are faded and marked by a dashed box, with adjusted transparency. (**A** to **G**) $(B_n)_2$, and (**H** to **N**) A_1B_n phases, with $n = [2, 8]$, and (**O**) the B_∞ phase. The evolution of the modular B_n building block that essentially differentiated each adjacent phase is shown in the middle column. (**P**) The individual A_1 fragment (marked by light blue color) and a representative B_4 fragment with highlighted extendable *E* rocksalt part (navy blue color), capping rocksalt part *C* (gray color), and the polytelluride of $[Te_4]$.

addition of (E_1, or BaSbSTe[Te]) units, which increases the length of both the rocksalt slabs and the associated polytelluride ribbons. Furthermore, by collectively depicting both S and Te as chalcogen (Q), the general chemical formula can be rewritten as $A_mB_n = [BaSbQ_3]_{m+n}$.

Energetic proximity and hierarchical assembly of homologous phases

First-principles calculations of these homologous series revealed both metastability and proximity in the formation energies among all 10 experimentally discovered phases (table S1). Typical density functional theory (DFT) formation energies can have inherent uncertainties, even with corrections, that may span tens of milli–electron volts per atom (*34*). However, our calculated energy differences among these phases, excluding the end members (**Phases I** and **X**), fall well within such margins (~10 meV; table S1). The energetic proximity among these essentially degenerate polymorphs suggests that their selective formation was not driven by simple thermodynamic stabilization. Furthermore, the stepwise addition of B_n that formed multiple polymorphs, analogous to the addition of CH_2 in alkenes, suggests an unconventional phase-formation mechanism. The structural evolution unfolds in three conceptual stages: extension, termination, and assembly.

Extension

The reaction starts with many extendable fragments of $Sb_2S_2Te_2$ (E_1 fragments, marked in Fig. 2B) dissolved inside the reaction container (Fig. 2A). When two E_1 fragments bond between Sb and Te, a two-block-wide E_2 fragment is formed (Fig. 2C). Subsequently, the two-block-wide E_2 fragments can add another E_1, forming a three-block-wide E_3 fragment (Fig. 2D). This chain addition process systematically expands the rocksalt-like backbone.

Termination

The extension process terminates when a C_1 fragment adds to each side of E_n and forms an E_nC_2 fragment (Fig. 2E). Termination occurs because the C_1 fragment exhibits a different degree of distortion than the E_1 fragment (see detailed discussion in the supplementary materials and figs. S11 to S14). As the length of the E_n fragment increases, accumulated distortions lead to steric frustration in packing S and Te atoms efficiently, making the addition of another E_1 fragment energetically or sterically unfavorable. The C_1 fragment effectively satisfies the reactive edge of the growing E_n fragment in a manner that another E_1 unit cannot, thereby halting the one-dimensional extension of the rocksalt slab. This step is analogous to chain-termination reactions in polymerization processes.

Assembly

Both the $E_{n-2}C_2$ and $[Te_n]$ polytelluride chains are negatively charged and stabilized with Ba^{2+} cations as the bridge, assembling as B_n (Fig. 2F). Similarly, the A_1 fragment is assembled from E_1 and one polytelluride chain (Fig. 2G). Finally, with a sufficiently high concentration of the required molecular fragments, they assemble into extended solids. For instance, with B_4 fragments as the only dominating fragments, **Phase II** $[(B_4)_2]$ consists of alternating B_4 fragment forms (Fig. 2H). Conversely, with coexisting B_4 and A_1 fragments, the phase would shift to **Phase III** (A_1B_4), which is made of B_4 fragments bridged by A_1 blocks (Fig. 2I). After assembly, each A_1 and B_n block contributes as $A_1 = BaSbSTe_2$ and $B_n = Ba_nSb_nS_{n-1}Te_{n+2}[Te]_{n-1}$, respectively, with $[Te_n]$ representing the polytelluride fragments.

In addition, the conceptual stages discussed above also suggest that the reaction vessel could host many different B_n fragments simultaneously (Fig. 2A), which is implied by the observation of additional phases such as **Phase VII** (Fig. 3, A and B; $Ba_9Sb_9S_7Te_{20}$, B_4B_5), **Phase VIII** [Fig. 3, C, D, and G; $Ba_{15}Sb_{15}S_{12}Te_{33}$, $A_1B_4(B_5)_2$], and **Phase IX** [Fig. 3, E and F; $Ba_{22}Sb_{22}S_{18}Te_{48}$, $(A_1)_2(B_5)_4$], where various B_n fragments coprecipitate into long-range ordered crystal structures. To be more specific, **Phase VII** (Fig. 3B; B_4B_5) consists of one B_4 block alternating with another B_5 block along the *c* axis (Fig. 3A), whereas **Phase VIII** [Fig. 3D; $A_1B_4(B_5)_2$] is built from one B_4 block, one B_5 block, and another B_5 block that couples with an A_1 block (Fig. 3, C and G). The alternating A_1-B_5-B_4-B_5 building blocks repeating along the *c* axis is also corroborated by the high-angle annular dark field image (Fig. 3G and figs. S28 and S29). Interestingly, this structure can also be viewed as the ordered intergrowth of one **Phase VII** (Fig. 3B; B_4B_5) connecting another **Phase IV** (Fig. 1K; A_1B_5) along the *c* axis. Finally, **Phase IX** [Fig. 3F; $(A_1)_2(B_5)_4$] is composed of two A_1 blocks

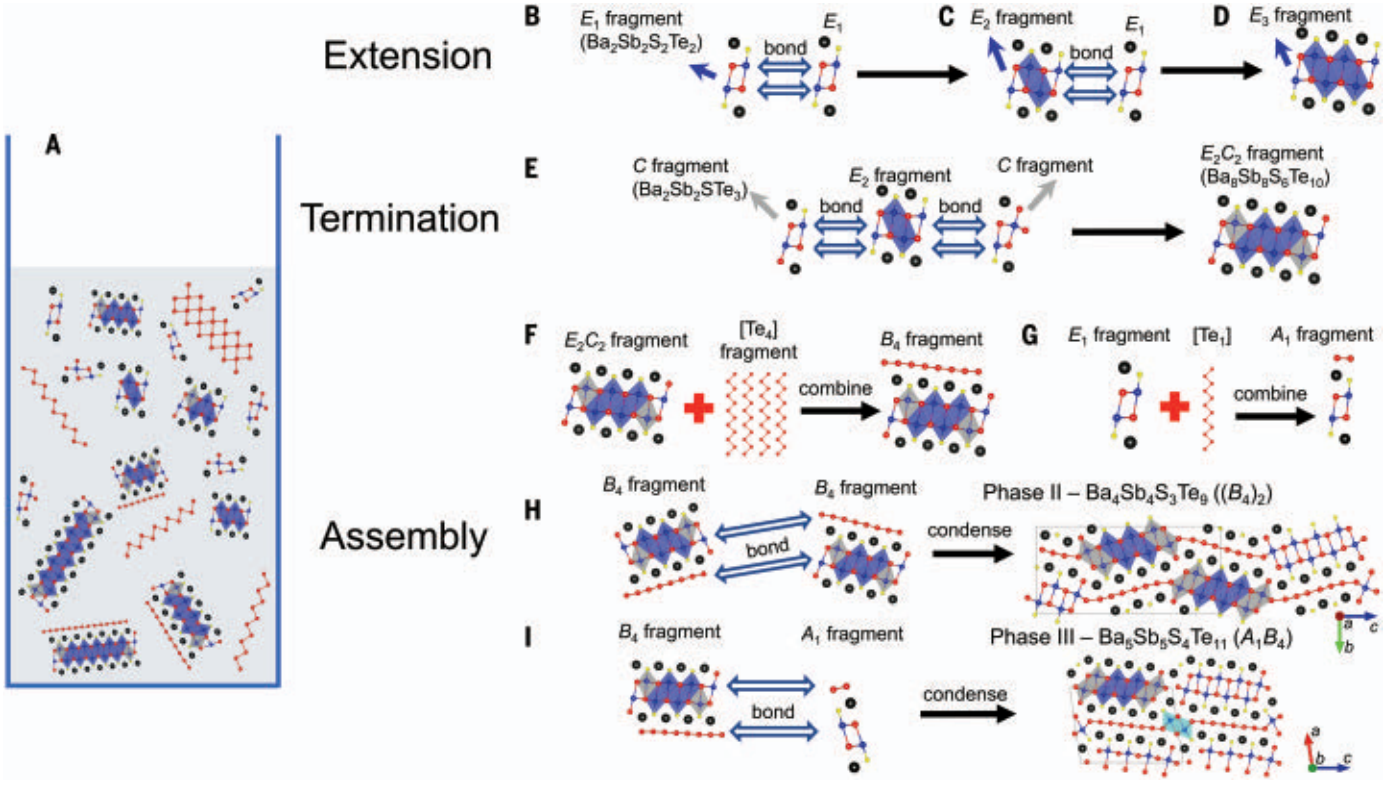


Fig. 2. A hypothetical phase-formation concept. (**A**) A schematic of the reaction vessel with different molecular fragments; the extension process from (**B**) E_1 to (**C**) E_2 and subsequently to (**D**) E_3, where E represents the extendable part of B_n fragments. (**E**) A representative termination process where a E_2 fragment is capped on each aside by the capping, C, assembling to an E_2C_2 molecular fragment. The representative assembly process of (**F**) an E_2C_2 fragment stacked with the polytelluride fragment, forming a B_4 fragment; (**G**) an E_1 fragment stacked with the polytelluride fragment, forming an A_1 fragment; (**H**) two B_4 fragments forming the $(B_4)_2$ phase; and (**I**) one A_1 fragment and another B_4 fragment forming the A_1B_4 phase.

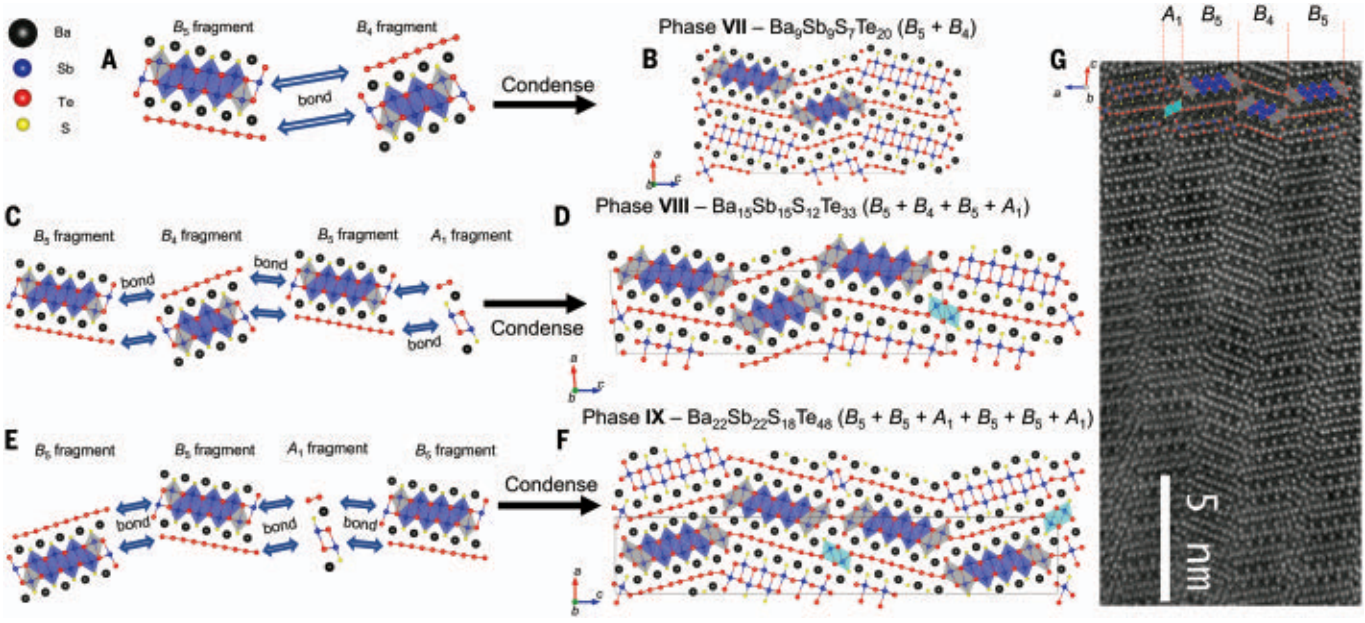


Fig. 3. Fragment assembly. The molecular fragments assembly process and crystal structure of (**A** and **B**) **Phase VII**, $Ba_9Sb_9S_7Te_{20}$, B_4B_5; (**C** and **D**) **Phase VIII**, $Ba_{15}Sb_{15}S_{12}Te_{33}$, $A_1B_4(B_5)_2$; and (**E** and **F**) **Phase IX**, $Ba_{22}Sb_{22}S_{18}Te_{48}$, $(A_1)_2(B_5)_4$. (**G**) The high-angle annular dark field image of **Phase VIII**, $Ba_{15}Sb_{15}S_{12}Te_{33}$, $A_1B_4(B_5)_2$, overlapped with the solved crystal structure model. Note that these phases incorporate multiple types of B_n fragments, highlighting the potential for modular assembly of diverse structures through flexible combinations of A_1 and B_n blocks.

and four B_5 blocks, whose structure can be viewed as sequentially connected B_5-B_5-A_1-B_5-B_5-A_1 fragments (Fig. 3E).

The potential of a nearly free combination of any number and length of different A_1 and B_n fragments, as demonstrated by **Phases VII** to **IX**, serves as further evidence for the existence of A_1 and B_n as fundamental building blocks, which form in situ first and assemble into extended solids. Another notable feature of this homologous family is the emergence of isomerism. The chemical formula of **Phase VIII** [Fig. 3D; $A_1B_4(B_5)_2$] can be reduced from $Ba_{15}Sb_{15}S_{12}Te_{33}$ to $(Ba_5Sb_5S_4Te_{11})_3$, which is identical to that of **Phase III** (Fig. 1J; $Ba_5Sb_5S_4Te_{11}$, A_1B_4). Thus, **Phases VIII** and **III** represent nearly energetically degenerate polymorphs, or constitutional isomers, based on the different connectivity and arrangement of A_1 and B_n building blocks, yielding the same overall stoichiometry but distinct crystal structures. The existence of such isomers points to a rich structural landscape that is accessible through the combinatorial assembly of the fundamental A_1 and B_n fragments.

Prediction of new homologous members

To accommodate any arbitrary combinations of different A_1 and B_n blocks, $\Sigma_{m,n}A_mB_n$, three indices are sufficient to describe the entire homologous series: the M index, which is the total number of A_1 blocks; the N index, which is the sum of n for all B_n blocks; and the L index, which is the number of B_n blocks involved. Structurally, the N and L indices separate the extendable (E_1) and the capping (C_1) parts of the B_n fragment, as they differ both structurally and compositionally.

Excluding **Phase I** as the only Te-only phase, any phase with the index of (M, N, L) can be described by the general formula of $Ba_{M+N}Sb_{M+N}S_{M+N-L}Te_{2M+2N+L}$ (or $Ba_{M+N}Sb_{M+N}S_{M+N-L}Te_{2M+N+2L}[Te_{N-L}]$), with ($N$−$L$) indicating the number of polytellurides. Note that the general formula can also be written as $(BaSbQ_3)_{M+N}$, forming the homologous series that all can be reduced to simply $BaSbQ_3$ (Q = S or Te). A detailed explanation regarding this general formula can be found in the supplementary materials.

The modular structure leads to predictable unit-cell parameters. Accordingly, all structures have unit-cell parameters with one short axis ~4.5 Å (b axis), another axis ~16.5 Å (a axis), and a third modular axis scaling with the index of (M, N, L). Ignoring the β angle differences, each A_1 block and E and C fragments in Fig. 1P scale roughly as 4.75, 4.338, and 4.52 Å, respectively. The comparison between the calculated and measured c axis is summarized in table S2. This simple model essentially captures the incremental features of the c axis well but, undesirably, overlooks the β angle information, which arises from the spatial orientations of building blocks.

To incorporate this missing piece of information, we adopted a more sophisticated calculation model that considers both the length and orientations of each building block. As evident from **Phases I** and **II** under the orthorhombic cell, each B_n fragment extends along the c axis and tilts along the a axis (Fig. 1, A and C), which can be described by a modular unit-cell matrix (see details in the supplementary materials). In addition, building blocks assemble into extended solids with staggered arrangements, that is, the first one tilts toward the ($+a$) direction, whereas the next one tilts toward the ($-a$) direction (fig. S20). Consequently, all $(B_n)_2$ phases crystallized with an orthorhombic cell as the tilting angle cancel out because of the staggered arrangements.

However, the mismatched sizes of the A_1 and B_n fragments lead to the monoclinic cells observed for each A_1B_n phase (Fig. 1, J to M), with β angles determined by the residual tilting angles due to incomplete cancellation. Furthermore, this prediction rule is not limited to $(B_n)_2$ and A_1B_n phases but extends to all homologous members, including those that involve more than one type of B_n block. For example, the slight β angle offset in **Phase VII** (Fig. 3B; B_4B_5) is a result of an incomplete cancellation of tilting angles caused by the different modular lengths of B_4 and B_5 fragments (Fig. 3A). By contrast, the orthorhombic structure of **Phase IX** [Fig. 3F; $(A_1)_2(B_5)_4$], whose structure features sequentially connected B_5-B_5-A_1-B_5-B_5-A_1 fragments (Fig. 3E), represents a case of completely compensated tilting angles.

A comparison of calculated and experimentally measured β angles and c axes that shows the promising predictive power of the unit-cell matrix method is summarized in table S3. The above calculation method also suggests that different arrangements from the same collection of molecular fragments would lead to slightly different unit-cell parameters, providing a method to distinguish such isomers. For instance, **Phase VIII** (B_5-B_4-B_5-A_1 connectivity) could have a hypothetical isomer with the B_5-B_5-B_4-A_1 connectivity under slightly different unit-cell parameters. A detailed discussion regarding how to use this calculation model to predict the unit-cell parameters can be found in the supplementary materials.

With the chemical composition and unit-cell parameters, the next essential information is the detailed atomic arrangements, which concern the connectivity between each molecular fragment and the space group symmetry. Based on all the synthesized structures, the involvement of the A_1 fragment or mismatched B_n fragments prefers centrosymmetric symmetry, with $Pnma$ and $P2_1/m$ for orthorhombic and monoclinic systems, respectively, whereas all phases with matched B_n fragments, such as $(B_n)_2$ phases, crystallize under the chiral $P2_12_12_1$ space group.

All structures can be viewed as sequentially connected fragments in a staggered way along the modular c axis. A mirror reflection along the ~16.5-Å crystal axis is performed on every other fragment, and all fragments assemble into extended solids, with the bond between the Sb from the SbQ_2 slab and the polytelluride [Te_n]. The above connectivity rule would likely limit the structure to containing only an even number of fragments, which is consistent with all 10 members that we observed (Table 1). Considering the simplest case of combining two types of fragments, connectivity with the same B_n results in $(B_n)_2$ phases (Fig. 1, A and C; **Phases I** and **II**), whereas the involvement of A_1 fragments leads to the formation of A_1B_n phases (Fig. 1, J to M; **Phases III** to **VI**).

Following these chemical principles, we successfully predicted multiple new homologous members belonging to $(B_n)_2$ and A_1B_n phases. Selected hypothetical structures are showcased in Fig. 1 to fill in the gaps between **Phases I** to **VI**, that is, Fig. 1, B and D to G, for $(B_n)_2$ phases and Fig. 1, H, I, and N, for A_1B_n phases. Encouragingly, although the $(B_3)_2$ phase in $BaSbQ_3$ is yet to be synthesized, its structure type has been observed (*35*, *36*), reaffirming the predictive power of the homologous method. Moreover, the summarized design rules can be naturally extended to accommodate any arbitrary number and length of A_1 and B_n fragments.

Polytelluride hierarchical networks controlled by electron affinity

The structural feature shared by the entire homologous family is the modular polytelluride fragments that continuously evolve from quasi–one-dimensional single zigzag chains, $(B_2)_2$, to quasi–two-dimensional square nets, B_∞. Telluride anions, $[Te_n]^{2-}$, compared with $[S_n]^{2-}$ and $[Se_n]^{2-}$, tend to have more versatile chain bondings (*37*). Because of its higher electron affinity and isovalent nature, S^{2-} preferentially substitutes the more electron-rich terminal Te^{2-} sites, which are on the outer side of each double rocksalt slab, leading to a rigid B_n fragment geometry shared by all homologous members. In these S/Te substitutions, the more electronegative S^{2-} ions selectively occupy rocksalt sites, whereas the polytelluride fragments remain composed exclusively of Te as $[Te_n]^{2-}$ units. In addition, the substitution of S also dedicates the systematic evolution of polytelluride hierarchical networks.

Such correlations are evident from the observations that the number of terminal sulfur sites scales with the number of polytelluride sites from the general formula of $B_n = Ba_nSb_nS_{n-1}Te_{n+2}[Te_{n-1}]$ (also in Fig. 4 and Table 1 with a correlated S/Te and $[Te_n]$/Te ratio). The valence state of polytelluride modulates with the length of B_n (Table 1), with

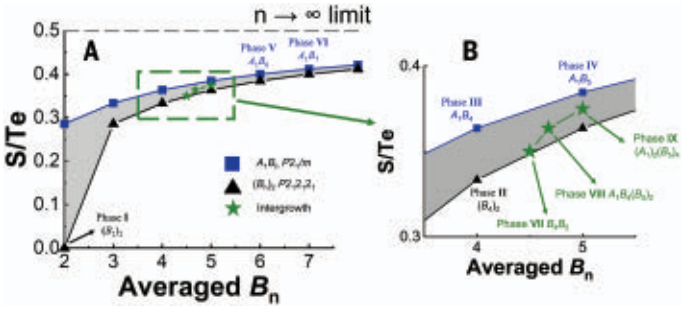


Fig. 4. Phase information. (**A**) Compositional phase diagram of the $BaSbQ_3$ (Q = S or Te) homologous series, organized by the S/Te ratio and the averaged B_n block length, with (**B**) an expanded view where interphase structures occur. Blue squares represent A_1B_n phases ($P2_1/m$), black triangles represent $(B_n)_2$ phases ($P2_12_12_1$), and green stars represent intergrowth phases composed of multiple building blocks, which can also be viewed as a linear combination of A_1B_n and $(B_n)_2$ phases. The gray-shaded region outlines the compositional range accessible to this homologous series. The smooth progression along this curve illustrates the systematic structural expansion enabled by anionic disparity and modular assembly.

the evolutions from $[Te_2]^{2-}$ dimers in **Phase I**, $(B_2)_2$, to $[Te_3]^{2-}$ trimers in **Phase II**, $(B_4)_2$, and eventually to square nets of Te with an incommensurately modulated charge density wave (CDW) in **Phase X**, B_∞ (*31*).

In addition, the inclusion of the A_1 block can fine-tune the electron distributions among polytelluride fragments, as each A_1 block carries a net –1 charge, expressed as $[BaSbSTe_2]^-$. Accordingly, the presence of A_1 fragments drives the polytelluride fragments to further buckle and maximize the Te···Te contacts in order to balance the charge, leading to an even more electron-poor configuration of polytelluride. As a result, the valence state of polytelluride for all A_1B_n phases scales as $[Te_n]^{(n-2)-}$ (Table 1). For instance, polytelluride networks forming nearly undistorted ribbons with Te···Te contact distances between 3.115 and 3.239 Å are observed in all A_1B_n phases (**Phases III** to **VI**; figs. S3 to S6), as compared to the dimers and trimers ($d_{Te\cdots Te}$ ~2.775 to 3.714 Å) in $(B_n)_2$ phases (**Phases I** and **II**; figs. S1 and S2).

As the polychalcogenide functional fragments are known to dictate physical properties, first-principles calculations reveal adjustable band gaps from 0.57 eV [fig. S24A; $(B_2)_2$] to 0.35 eV [fig. S24C; $(B_4)_2$] and eventually below the sensitivity of DFT calculations (fig. S24H; B_∞). The tunable electronic properties are also reflected in electrical transport measurements on selected homologous phases. As polytelluride networks continued to extend longer, diminishing electrical resistivity and activation gaps were observed (fig. S27). Note that the artificial metallicity of **Phase X** (fig. S24H; B_∞) with a strong Fermi surface-nesting effect is highly electronically unstable and can lead to emerging phenomena such as an incommensurate CDW order and pressure-induced superconductivity (*31*).

Figure 4 shows a compositional phase diagram of the discovered and predicted members according to their S/Te ratio and the average length of B_n building blocks. The structural boundaries between different homologous members and intergrowth phases highlight how structural complexity evolves with increasing sulfur content and B_n length. The smooth progression of phases along the plotted trend—marked by blue squares for A_1B_n compounds, black triangles for $(B_n)_2$ members, and green stars for intergrowth phases—illustrates how the systematic incorporation of sulfur leads to the modular expansion of structural motifs. The gray-shaded region delineates the compositional domain accessible within this homologous family and suggests where new members could be targeted. Figure 4 also highlights symmetry trends, with different structural types associated with distinct crystallographic space groups (e.g., $P2_1/m$ versus $P2_12_12_1$) and underscores the role of anionic disparity in driving the formation of increasingly complex architectures. Notably, the intergrowth phases demonstrate that the same overall composition can yield structurally distinct polymorphs through different arrangements of modular fragments, pointing to a form of unlimited structural isomerism, which is rare in inorganic solids.

Summary and outlook

We have unveiled a new homologous heterostructural series comprising at least 10 members with ordered multianion crystal structures with the same composition of $BaSbQ_3$ ($Q = Te_{1-x}S_x$), characterized by modular rocksalt slabs with adjustable functional polytelluride fragments. It is a family of stoichiomorphs, compounds of fixed stoichiometry but distinct structural identities driven by isovalent chalcogen mixing. The structural diversity is directly driven by systematic variation in composition, specifically the S/Te ratio. The formation and structural evolution of this series are driven by the difference in electron affinity between sulfur and tellurium under a constant cationic environment.

This chemical principle not only directs site-selective anion substitution but also dictates the fragmentation and condensation of polytelluride networks. The formation principle is based on extension, termination, and modular assembly at the molecular level. The structural coherence of these modular A_1 and B_n blocks is strongly supported by the discovery of ordered intergrowth phases (**Phases VII** to **IX**), where distinct motifs combine in a predictable and reproducible manner. Building on this insight, we have identified the underlying chemical rules that govern block compatibility and connectivity. These rules allow us to deterministically predict and design all yet-undiscovered A_1B_n and $(B_n)_2$ phases within this homologous family, establishing a framework that is readily adaptable to AI- and ML-guided materials discovery based on modular composition.

Despite the focus on anionic disparity in this work, the cation sites also present opportunities for further tuning and discovery. For instance, we have realized that previously reported seemingly unrelated compounds actually belong to this particular series. For example, $KThSb_2Se_6$ (*38*) and $BaLaBi_2Se_6$ (*38*) crystallize in the $(B_2)_2$ structure, and $KLa_2Sb_3S_9$ (*35*) and $TlLa_2Sb_3Se_9$ (*36*) in the $(B_3)_2$ structure, which suggests that further structural diversity with tunability is possible by focusing on the cation sites. All these materials are poised for exploration across a range of physical phenomena, including electronic, optical, and thermal transport behaviors.

REFERENCES AND NOTES

1. S. Andersson *et al.*, *Acta Chem. Scand.* **11**, 1641–1652 (1957).
2. A. Magnéli, *Acta Crystallogr.* **6**, 495–500 (1953).
3. S. Yudintsev, S. Stefanovskii, *Dokl. Earth Sci.* **401**, 319–325 (2005).
4. W. Gong *et al.*, *J. Am. Ceram. Soc.* **107**, 6574–6582 (2024).
5. B. Beznosikov, K. Aleksandrov, *Crystallogr. Rep.* **45**, 792–798 (2000).
6. J.-Y. Pivan, R. Guérin, M. Sergent, *J. Solid State Chem.* **68**, 11–21 (1987).
7. Y. M. Prots, W. Jeitschko, *Inorg. Chem.* **37**, 5431–5438 (1998).
8. L. Siggelkow, V. Hlukhyy, B. Wahl, T. F. Fässler, *Eur. J. Inorg. Chem.* **2011**, 4012–4024 (2011).
9. A. Weiland, J. B. Felder, G. T. McCandless, J. Y. Chan, *Chem. Mater.* **32**, 1575–1580 (2020).
10. A. Tursina, E. Khamitcaeva, A. Gribanov, D. Gnida, D. Kaczorowski, *Inorg. Chem.* **54**, 3439–3445 (2015).
11. A. Mrotzek, M. G. Kanatzidis, *Acc. Chem. Res.* **36**, 111–119 (2003).
12. M. G. Kanatzidis, *Acc. Chem. Res.* **38**, 359–368 (2005).
13. M. A. Viti, Z. Li, C. C. Laing, C. Wolverton, M. G. Kanatzidis, *J. Am. Chem. Soc.* **147**, 25350–25360 (2025).
14. M. A. Viti, Z. Li, C. Wolverton, M. G. Kanatzidis, *J. Am. Chem. Soc.* **147**, 29994–30008 (2025).
15. I. W. Gilley, T. E. Wiggins, E. H. Sargent, M. G. Kanatzidis, *Acc. Chem. Res.* **58**, 2243–2254 (2025).
16. E. S. Vasileiadou *et al.*, *J. Am. Chem. Soc.* **143**, 2523–2536 (2021).
17. A. Merchant *et al.*, *Nature* **624**, 80–85 (2023).
18. N. J. Szymanski *et al.*, *Nature* **624**, 86–91 (2023).
19. C. Zeni *et al.*, *Nature* **639**, 624–632 (2025).
20. J. Leeman *et al.*, *PRX Energy* **3**, 011002 (2024).

21. A. K. Cheetham, R. Seshadri, *Chem. Mater.* **36**, 3490–3495 (2024).
22. T. Dai *et al.*, *Nature* **635**, 890–897 (2024).
23. C. W. Coley *et al.*, *Science* **365**, eaax1566 (2019).
24. J. M. Granda, L. Donina, V. Dragone, D.-L. Long, L. Cronin, *Nature* **559**, 377–381 (2018).
25. A. F. de Almeida, R. Moreira, T. Rodrigues, *Nat. Rev. Chem.* **3**, 589–604 (2019).
26. M. H. S. Segler, M. Preuss, M. P. Waller, *Nature* **555**, 604–610 (2018).
27. K. T. Butler, D. W. Davies, H. Cartwright, O. Isayev, A. Walsh, *Nature* **559**, 547–555 (2018).
28. B. Sanchez-Lengeling, A. Aspuru-Guzik, *Science* **361**, 360–365 (2018).
29. A. Tassanov, H. Lee, Y. Xia, J. M. Hodges, *J. Am. Chem. Soc.* **146**, 32627–32639 (2024).
30. K. Volk, G. Cordier, R. Cook, H. Schäfer, *Z. Naturforsch. B. J. Chem. Sci.* **35**, 136–140 (1980).
31. Z.-Z. Luo *et al.*, *J. Am. Chem. Soc.* **147**, 6753–6762 (2025).
32. D.-Y. Chung *et al.*, *J. Am. Chem. Soc.* **119**, 2505–2515 (1997).
33. R. Cook, H. Schäfer, *Rev. chimie Minerale* **19**, 19–27 (1982).
34. J.-H. Pöhls, M. Heyberger, A. Mar, *J. Solid State Chem.* **290**, 121557 (2020).
35. S.-J. Kim, S.-J. Park, S.-A. Yim, *Bull. Korean Chem. Soc.* **25**, 485–490 (2004).
36. L. T. Menezes, Z. W. Richter-Bisson, A. Assoud, B. A. Kuropatwa, H. Kleinke, *Z. Anorg. Allg. Chem.* **647**, 81–85 (2021).
37. D. M. Smith, J. A. Ibers, *Coord. Chem. Rev.* **200–202**, 187–205 (2000).
38. K.-S. Choi, L. Iordanidis, K. Chondroudis, M. G. Kanatzidis, *Inorg. Chem.* **36**, 3804–3805 (1997).

ACKNOWLEDGMENTS

Funding: This work was primarily supported by the US Department of Energy (DOE), Office of Science, Basic Energy Sciences, Materials Sciences and Engineering Division. This material is based upon work supported by Laboratory Directed Research and Development (LDRD) funding from Argonne National Laboratory, provided by the Director, Office of Science, of the DOE under contract no. DE-AC02-06CH11357. EDX and SEM work was performed at the Center for Nanoscale Materials and Advanced Photon Source, both DOE Office of Science User Facilities, was supported by the DOE, Office of Basic Energy Sciences, under contract no. DE-AC02-06CH11357. Work at the Advanced Photon Source (APS) at Argonne National Laboratory was supported by the DOE, Office of Science, Office of Basic Energy Sciences under contract no. DE-AC02-06CH11357. Small-angle X-ray scattering works were performed at the DuPont-Northwestern-Dow Collaborative Access Team (DND-CAT) located at Sector 5 of the Advanced Photon Source (APS). DND-CAT is supported by Northwestern University, The Dow Chemical Company, and DuPont de Nemours, Inc. Z.W. acknowledges support from the Ford Motor Company, and C.W. acknowledges support from the DOE, Office of Science, Basic Energy Sciences under grant DE-SC0014520. Microscopy was conducted in the EPIC facility (RRID: SCR_026361) of Northwestern University's NUANCE Center, which has received support from the SHyNE Resource (NSF ECCS-2025633), the International Institute for Nanotechnology (IIN), and Northwestern's MRSEC program (NSF DMR-2308691). This work is based on research conducted at the Center for High-Energy X-ray Sciences (CHEXS), which is supported by the National Science Foundation (BIO, ENG, and MPS Directorates) under award DMR-2342336. **Author contributions:** The work was conceived by H.Z., X.Z., D.-Y.C., and M.G.K. with input from all authors. H.Z. carried out the synthesis, laboratory and synchrotron x-ray diffraction, electrical transport measurements, data analysis, and writing. X.Z. carried out data analysis and writing. Z.W. and C.W. performed first-principles electronic band structure calculations and data analysis. P.E.M. and V.P.D. carried out high-resolution transmission electron microscopy measurements and data analysis. Y.W. performed electrical transport measurements. D.T.K. and S.J.W. performed synchrotron small-angle x-ray scattering. S.H.L. carried out synchrotron powder x-ray diffraction. H.Z. and S.R. performed single-crystal synchrotron x-ray diffraction measurements. S.R., D.-Y.C., and M.G.K. supervised the project. **Competing interests:** The authors declare no competing financial interests. **Data and materials availability:** All data, including structural and physical property characterizations, and detailed structure descriptions are available in the manuscript or in the supplementary materials. Additional crystallographic information files (CIFs) are CSD nos. 2402260, 2402470, and 2473033 to 2473041. **License information:** Copyright © 2025 the authors, some rights reserved; exclusive licensee American Association for the Advancement of Science. No claim to original US government works. https://www.science.org/about/science-licenses-journal-article-reuse

SUPPLEMENTARY MATERIALS

science.org/doi/10.1126/science.aea8088
Materials and Methods; Supplementary Text; Figs. S1 to S31; Tables S1 to S3; References (*39*–*51*); Data S1

Submitted 21 July 2025; accepted 2 October 2025

10.1126/science.aea8088

PLANT SCIENCE

Cell wall patterning regulates plant stem cell dynamics

Xianmiao Zhu[1,2,3]†, Xing Chen[1,2,3]†, Yangxuan Liu[1,2], Yimin Zhu[1,2,3], Geshuang Gao[1,2,3], Miao Lan[1,2], Yihao Fu[1,2,3], Yimin Gu[1,2], Han Han[4], Wenjuan Cai[1,5], Raymond Wightman[6], Mingjun Gao[7], Yiliang Ding[8], Weibing Yang[1,2,9]*

The plant cell wall regulates development through spatiotemporal modulation of its chemical and mechanical properties. Pectin methylesterification is recognized as a rheological switch controlling wall stiffness. Here, we reveal a bimodal methylesterification pattern in the shoot meristem: Mature walls exhibit high methylesterification, whereas demethylesterified pectins are deposited at new cross walls. This spatial heterogeneity is established through nuclear sequestration of *PECTIN METHYLESTERASE5* (*PME5*) mRNA. MYB3R4-driven transcription, combined with RZ-1B/1C-mediated retention, creates a mitotically associated *PME5* mRNA reservoir in the nucleus. Nuclear envelope disassembly synchronizes *PME5* messenger RNA (mRNA) release with cell plate formation, enabling precise demethylesterification at division planes. Perturbation of this spatial control compromises stem cell maintenance or breaks division patterning. Our study uncovers an mRNA compartmentalization mechanism that couples stem cell dynamics with pectin modification.

The cell wall, primarily composed of cellulose microfibrils, hemicellulose, pectin, and structural proteins, provides mechanical resistance against turgor pressure while simultaneously permitting controlled cell expansion through viscoelastic remodeling (*1*). New cell walls are assembled at the end of cell division, and undergo constant reconstruction as cells grow and differentiate (*2*–*4*). Changes in wall properties induce microtubule reorganization, leading to altered tissue mechanics that further instruct cell wall remodeling (*5*–*7*). In the shoot apical meristem (SAM), polar auxin transport forms self-organizing concentration gradients that specify organ initiation sites (*8*–*11*), and cytokinin signaling creates complementary inhibitory domains that stabilize phyllotactic patterns (*12*). Manipulation of wall properties through exogenous expansin application or expression of pectin-modifying enzymes can override these biochemical signals to induce ectopic primordium formation (*13*, *14*), highlighting the integration of biochemical and mechanical signaling in plant development (*15*, *16*).

Pectin, the most complex class of cell wall polysaccharides, forms a hydrophilic gel-like matrix embedding cellulose and hemicellulose (*17*, *18*). Demethylesterification of pectin, catalyzed by pectin methylesterases (PMEs) (*19*, *20*), enables Ca^{2+} cross-linking or polygalacturonase-mediated degradation, creating mechanical microdomains, which fine-tune wall flexibility (*20*–*23*). This postsynthetic modification system, regulated by pH gradients and PME inhibitors (PMEIs), acts as a biochemical rheostat for cell expansion (*24*–*26*). Emerging evidence suggests that pectin methylesterification influences developmental processes such as organ primordium growth, apical hook formation, stomatal dynamics, and lateral root development (*14*, *27*–*30*). A reticulated network formed by de-esterified homogalacturonans and RALF-LRX also regulate wall integrity and growth (*31*, *32*).

Contrasting pectin methylesterification patterns in new and mature walls

To investigate pectin modification in proliferating meristematic tissues, we conducted immunocytochemical labeling in the SAM of *Arabidopsis*. Monoclonal antibodies, including JIM5, JIM7, LM19, and LM20, were used to detect various pectin configurations (table S1) (*20*, *33*–*37*). JIM5 and JIM7 recognize homogalacturonans (HGs) with varying degrees of methylesterification, with JIM5 preferentially binding lowly esterified epitopes. We observed broad binding of JIM7 to cell walls throughout the SAM, whereas JIM5 labeling was restricted to the pith of the stem but absent in the SAM cells (fig. S1), consistent with the low stability of the JIM5 epitopes (*34*). LM20, targeting highly methylesterified galacturonic acid (GalA) residues, also exhibited broad labeling across the shoot apex, with stronger signals at the cell-to-cell contact regions (three-way junctions) (Fig. 1A). By contrast, LM19, which specifically binds to de-esterified HGs, displayed a patchy pattern reminiscent of the newly formed cross walls (cell plates) (Fig. 1B). We confirmed this by 4′,6-diamidino-2-phenylindole (DAPI) staining, showing that LM19 immunofluorescence signals appeared shortly after nuclear separation and persisted at the cell plates until the completion of cytokinesis (fig. S2). Propidium iodide (PI) has been used as a cell wall probe for its high affinity to weakly esterified pectins as demonstrated in root hairs, pollen tubes, and leaf pavement cells (*38*, *39*). However, in shoot meristem cells, PI staining is relatively uniform, suggesting that the pectin configuration recognized by LM19 in the new cross walls of dividing cells may differ from that by PI (fig. S3, A and B).

Using immunolabeling combined with structured illumination microscopy (DeepSIM), we resolved pectin organization at ~ 100-nm lateral resolution. In the anticlinal walls of the SAM, LM20-labeled epitopes were widely distributed along the mature cell walls (Fig. 1C and fig. S3C), with an average interparticle distance of ~1.39 ± 0.65 μm (range: 0.26 to 3.92 μm). In comparison, LM19-labeled particles were more densely packed, with an average distance of ~0.46 ± 0.25 μm (range: 0.11 to 1.25 μm), approximately one-third the distance between LM20-labeled particles (Fig. 1C). Thus, two distinct patterns of pectin methylesterification are present in the shoot meristem cells: (i) condensed de-esterified pectin networks at cell division sites, and (ii) extended methylesterified pectin matrices in mature walls.

Demethylesterified pectins influence cell division plane orientation

Pectins are synthesized in highly methylesterified forms, which undergo subsequent modification through de-esterification catalyzed by pectin methylesterases (PMEs) (*40*, *41*). To investigate the functional role of pectin demethylesterification in new cross walls, we suppressed endogenous PME activity by its inhibitor, PMEI5 (*27*). Using a mitosis-specific *CSLD5* promoter (*42*, *43*), we overexpressed *PMEI5* specifically in dividing cells (Fig. 1D). Methanol release and PECTOPLATE radial diffusion assays confirmed decreased PME activity in the shoot apex of *pCSLD5::PMEI5* plants (fig. S4, A and B). Immunofluorescence showed enhanced LM20 labeling (fig. S4C) and near-absence of LM19 signals in developing cell plates (Fig. 1E), indicating compromised pectin demethylesterification upon *PMEI5* overexpression.

[1]CAS Centre for Excellence in Molecular Plant Sciences, Institute of Plant Physiology and Ecology, Chinese Academy of Sciences, Shanghai, China. [2]Key Laboratory of Plant Carbon Capture, CAS Centre for Excellence in Molecular Plant Sciences, Institute of Plant Physiology and Ecology, Chinese Academy of Sciences, Shanghai, China. [3]University of Chinese Academy of Sciences, Beijing, China. [4]Co-Innovation Center for Sustainable Forestry in Southern China, College of Life Sciences, Nanjing Forestry University, Nanjing, China. [5]Core Facility Center, CAS Centre for Excellence in Molecular Plant Sciences, Chinese Academy of Sciences, Shanghai, China. [6]Microscopy Core Facility, Sainsbury Laboratory, University of Cambridge, Cambridge, UK. [7]Ministry of Education Key Laboratory for Biodiversity Science and Ecological Engineering, National Observations and Research Station for Wetland Ecosystems of the Yangtze Estuary, Institute of Biodiversity Science and Institute of Eco-Chongming, School of Life Sciences, Fudan University, Shanghai, China. [8]John Innes Centre, Norwich Research Park, Norwich, UK. [9]CAS-JIC Center of Excellence for Plant and Microbial Sciences (CEPAMS), Institute of Plant Physiology and Ecology, Chinese Academy of Sciences, Shanghai, China. ***Corresponding author. Email: wbyang@cemps.ac.cn** †These authors contributed equally to this work.

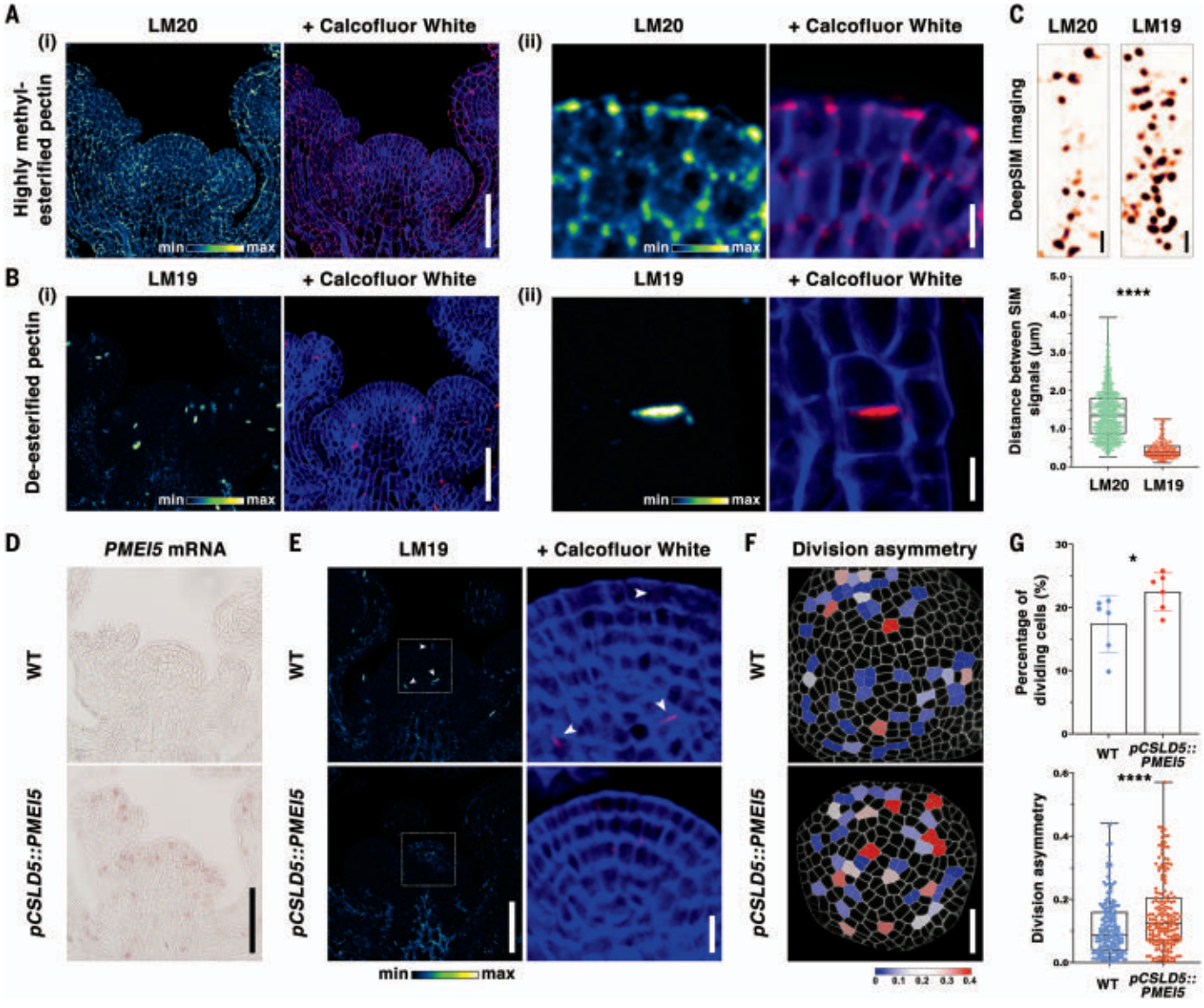


Fig. 1. Distinct pectin methylesterification patterns in new and mature cell walls of *Arabidopsis* shoot meristem. (**A** and **B**) Immunostaining of highly methylesterified pectins with LM20 (A) and demethylesterified pectins with LM19 (B) in *Arabidopsis* shoot apical meristem (SAM). (i) Overview of the SAM. (ii) Higher-magnification view. Immunofluorescence signals are displayed using the "Green Fire Blue" lookup table when shown alone and in red when merged with the Calcofluor White signals (shown in blue), which label cellulose and chitin. Scale bars, 50 µm (i) and 5 µm (ii). (**C**) DeepSIM super-resolution imaging of LM20 and LM19 immunofluorescence signals in anticlinal walls of the SAM. The DeepSIM signals are displayed using the "gem" lookup table. Bottom panel shows the quantification of the shortest distance between SIM signals. Scale bar, 2 µm. (**D**) In situ hybridization for *PMEI5* mRNA in wild-type (WT) and *pCSLD5::PMEI5* SAMs. Scale bar, 50 µm. (**E**) Comparison of LM19 immunofluorescence signals in WT and *pCSLD5::PMEI5* SAMs. Right panels show higher magnification of the regions outlined in the left panels, with arrowheads indicating new cross walls. Scale bars, 50 µm (left panel) and 10 µm (right panel). (**F**) Analysis of daughter cell asymmetry in the epidermis (L1) of wild-type and *pCSLD5::PMEI5* SAMs. Asymmetry was estimated by the standard deviation of daughter cell area over mean daughter cell area and displayed as heatmaps using MorphoGraphX (*69*). Scale bar, 20 µm. (**G**) Quantification of cell division over 16 hours ($n = 6$ SAMs for WT and 6 SAMs for *pCSLD5::PMEI5*) and daughter cell asymmetry ($n = 210$ cells for WT and 177 cells for *pCSLD5::PMEI5*). *$P = 0.0489$ in top panel of (G) and ****$P < 0.0001$ in bottom panels of (C) and (G) (two-tailed *t* test).

Time-lapse imaging showed that mitotic overexpression of *PMEI5* slightly promoted new cell wall formation rather than impairing it (fig. S5A). Furthermore, the morphology of these new walls remained intact (fig. S5B). Key factors, including KNOLLE (essential for vesicle fusion) (*44*) and CSLD5 (required for early cell plate assembly) (*42*, *43*), were both properly localized to the new cross walls (fig. S5, C to F). Thus, pectin demethylesterification is not required for cell plate assembly.

By contrast, cell division patterning was disrupted in *pCSLD5::PMEI5*, as evidenced by increased asymmetry of daughter cells at the SAM (Fig. 1, F and G), disorganized cell files on the stem (fig. S5G), and slanted walls in the root (fig. S5H). These phenotypes essentially resembled those observed in the constitutive *PMEI5* overexpression plants (*27*, *45*). Although *PMEI5* overexpression was confined to dividing cells in *pCSLD5::PMEI5*, it exerts long-term influences on postmeristematic plant architecture (fig. S5, I and J), reinforcing the notion that misorientation of the early division plane propagates structural disorganization during tissue differentiation (*46*). On the basis of these results and previous studies (*27*, *45*), we propose that pectin demethylesterification modulates division-plane orientation through a noncanonical pathway that is distinct from preprophase band–mediated guidance.

PME5 promotes pectin demethylesterification in dividing cells

To elucidate the molecular basis of pectin demethylesterification during cell division, we systematically analyzed the expression of *PME* genes. Among the 66 *PME*s in *Arabidopsis* (*19*), RNA sequencing data identified 12 genes with detectable expression at the shoot apex (fig. S6, A and B, and data S1) (*47*). mRNA in situ hybridization revealed generally low transcript abundance for most of these genes, except *PME5* and *PME44*, which displayed patchy and epidermal distribution, respectively (fig. S6C). The expression patterns of *PME5* and *PME44* were further verified by confocal live imaging in the transcriptional reporters (fig. S7, A and B, and movies S1 and S2). For the other 10 *PME*s, although in situ hybridization did not yield clear signals, their promoter activities were detected either in a few cells on the abaxial side of flower primordia (fig. S7C) or within deeper regions of the stem (fig. S7D and table S2).

The nonuniform distribution of *PME5* mRNA suggests cell cycle–regulated expression, which was confirmed by fluorescence in situ hybridization (FISH), showing that *PME5* mRNAs were exclusively detected in mitotic cells (Fig. 2A). Analysis of the *PME5* promoter sequence identified four mitosis-specific activator (MSA) elements (CCGTT or AACGG), which are recognized by the MYB3R transcription factors MYB3R1 and MYB3R4 in *Arabidopsis* (*48*, *49*) (fig. S8A). Electrophoretic mobility shift (EMSA) and dual luciferase assays indicate that MYB3R1 and MYB3R4 directly bind to the wild-type but not the MSA-mutated *PME5* promoter and activate its expression (fig. S8, B to D). Consequently, the mRNA levels of *PME5* were substantially reduced in the SAMs of the *myb3r1 myb3r4* double mutant (fig. S8E). These results collectively demonstrate that MYB3R1 and MYB3R4 promote *PME5* expression in dividing cells. In a *pPME5::mNeonGreen-PME5* translational reporter, fluorescence signals were not observed until later stages of the cell cycle. Once expressed, the mNeonGreen-PME5 fusion proteins localized predominantly to developing cell plates (Fig. 2B). Down-regulation of *PME5* expression using a dexamethasone (DEX)–inducible RNA silencing system (*50*) led to misoriented walls in the root stem cells (fig. S9, A and B). The SAMs of the *PME5*-silenced plants exhibited reduced levels of demethylesterified pectin and slightly increased daughter cell asymmetry (fig. S9, C to E). These phenotypes were similar to, but weaker than, those observed in the *PMEI5* overexpression plants, suggesting a degree of redundancy among PMEs. The expression levels of *WUSCHEL* (*WUS*) were comparable between wild-type, *PME5*-silenced, and *PMEI5* overexpression plants, indicating that demethylesterification of new cross-wall pectin does not affect stem cell maintenance (fig. S9F). These data support the role of PME5 in mediating pectin demethylesterification during new cross-wall formation for proper cell division patterning.

Nuclear sequestration of *PME5* mRNA

Protein-coding mRNAs normally undergo rapid cytoplasmic export after transcription. *PME5* mRNA was found to be strictly retained within the nucleus (Fig. 2C and fig. S10A). Only after nuclear envelope breakdown was *PME5* mRNA detected in the cytoplasm (Fig. 2D and fig. S10A). Although mRNA nuclear sequestration is rare across eukaryotes, *CDC20* mRNA encoding a core cell cycle regulator can be nuclear localized (*51*). Double RNA FISH demonstrated that *PME5* mRNA colocalized with *CDC20* mRNA in the nucleus (fig. S10B) but was spatially separated from the cytoplasmic *CYCB1;2* mRNA (fig. S10C). These results suggest a model in which nuclear sequestration of *PME5* mRNA ensures that its protein is produced when needed, specifically during cell plate formation. This dual regulatory function maintains the highly methylesterified state in mature cell walls while facilitating localized demethylesterification in the newly formed cross walls.

When expressed under the control of the constitutive *UBQ10* promoter, *GFP-PME5* chimeric RNA localized to the nucleus in all examined cell types (fig. S11A, top panels), indicating that *PME5* mRNA nuclear sequestration is independent of cellular differentiation status or cell cycle stage. Furthermore, *PME5* mRNA transcribed from its full-length cDNA displayed similar nuclear localization (fig. S11A, bottom panels), ruling out the involvement of post-transcriptional processing. Because RNA subcellular targeting can be controlled by the RNA's own sequences (*52*, *53*), we next characterized the cis-acting elements responsible for *PME5* mRNA nuclear localization. A series of 201–base pair (bp) deletions, spanning the entire *PME5* coding sequence with ~100-bp overlap, were fused to *GFP* (green fluorescent protein) and expressed in wild-type plants (fig. S11B). Using RNA FISH assays, we systematically

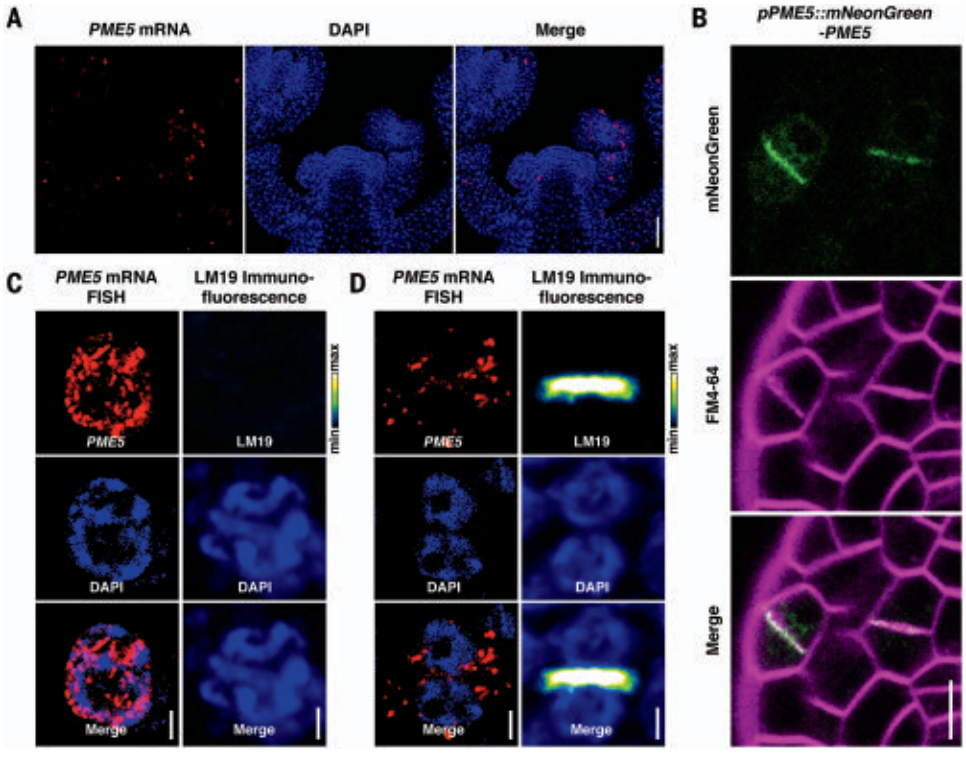


Fig. 2. Nuclear sequestration of *PME5* mRNA mediates spatial variability in pectin modification. (**A**) Nonhomogeneous expression of *PME5* mRNA in the shoot apex, as detected by RNA fluorescence in situ hybridization (FISH). RNA FISH signals are displayed in red. The nucleus was labeled by 4′,6-diamidino-2-phenylindole (DAPI) staining and is shown in blue. Scale bar, 50 μm. (**B**) Subcellular distribution of PME5 proteins, showing predominant accumulation at the cell plates. PME5 was fused with an acid-tolerant fluorescent protein, mNeonGreen, and expressed under the control of its own promoter. Cell membranes were stained with FM4-64 shown in magenta. Scale bar, 5 μm. (**C** and **D**) Correlation between *PME5* mRNA nuclear releasing and pectin demethylesterification in the new cross walls. *PME5* mRNA FISH and LM19 immunostaining (demethylesterified pectins) in cells at the prophase (C) and cytokinesis (D) stages. *PME5* mRNA displayed exclusive nuclear localization in prophase cells, which relocalized to the cytoplasm after nuclear envelope breakdown. Mitotic stages were determined by the morphology of the DAPI-stained nucleus (in blue). Immunofluorescence signals are shown using the "Green Fire Blue" lookup table. Scale bar, 2 μm.

analyzed the localization of the 13 truncated *GFP-PME5* fusion RNAs. Most chimeric RNAs localized to the nucleus, except for the Δ1–201 deletion, which was distributed in both the nucleus and the cytoplasm (fig. S11C). Because the Δ103–303 mRNA remained nuclear localized, we inferred that the nuclear localization signal is likely located within the 1–102 bp region. Indeed, deletion of this 102 bp abolished *PME5* nuclear localization (Fig. 3A and fig. S11D). However, a chimeric mRNA containing *PME5* 1–102 bp fused with the *GFP* coding sequence displayed cytoplasmic localization (fig. S11E), indicating that this region functions as a necessary but not sufficient nuclear targeting signal. These results imply that *PME5* mRNA nuclear localization requires cooperative interactions between multiple sequence elements or depends on its secondary structure established by the full-length transcript.

PME5 mRNA nuclear sequestration preserves mature wall methylesterification for stem cell maintenance

Although nuclear sequestration of *PME5* mRNA explains localized demethylesterification of new cell walls, it also raises the question of why such modification is inhibited in mature walls. To investigate this, we engineered a truncated variant (*PME5*$^{\Delta 1–102}$) by removing nucleotides

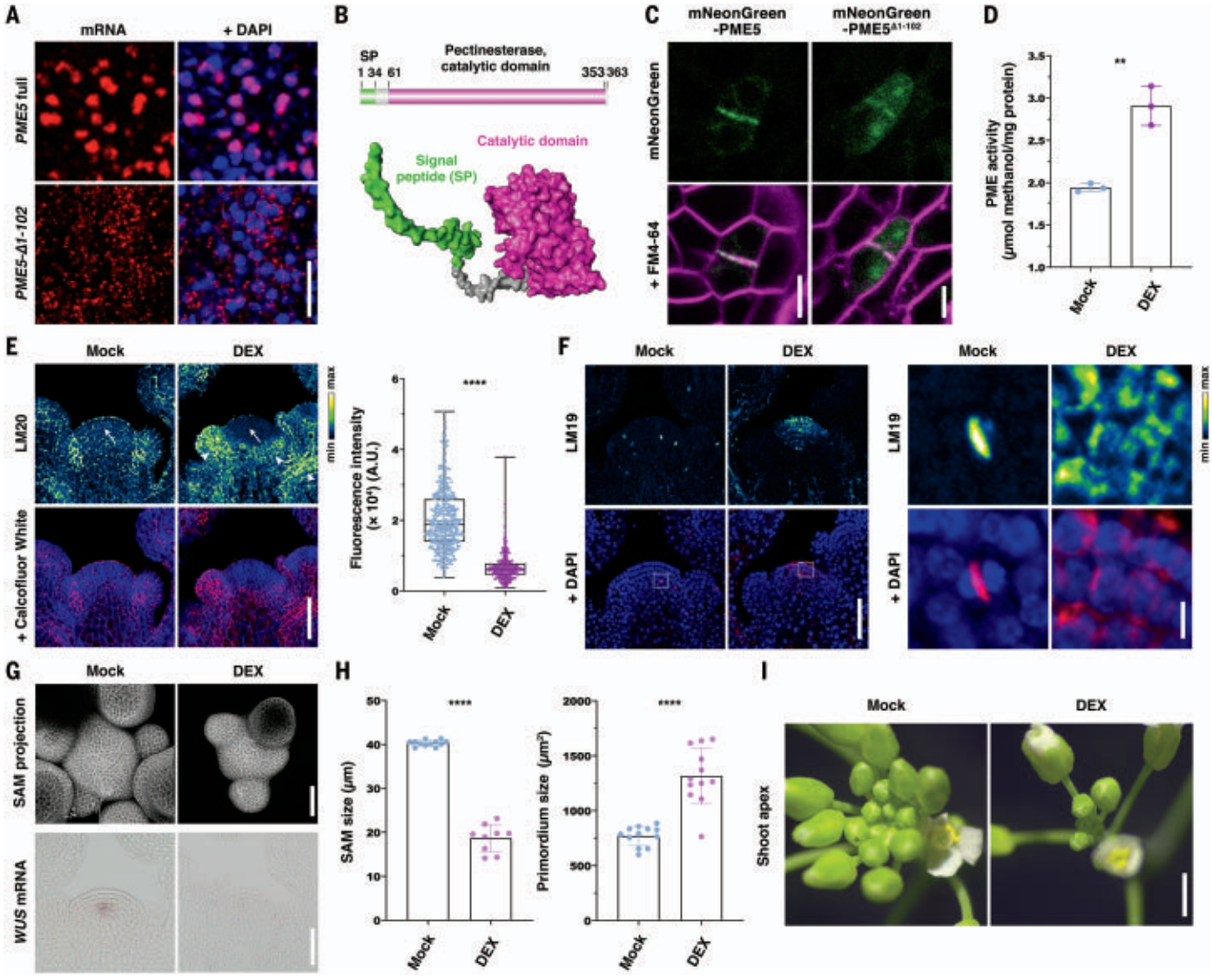


Fig. 3. High methylesterification in mature cell walls is essential for stem cell maintenance. (**A**) Subcellular localization of full-length and truncated *PME5* mRNAs. Scale bar, 20 μm. (**B**) Prediction of PME5 protein domains (top panel) and structure (bottom panel). SP, signal peptide. The structure was computed using AlphaFold2 and illustrated by the PyMol Molecular Graphics System (version 2.0; Schrödinger). (**C**) Subcellular distribution of PME5 and PME5$^{\Delta 1–102}$ proteins. Scale bars, 5 μm. (**D**) Measurement of pectin methylesterase (PME) activity by methanol release assay. Inducible overexpression of *PME5*$^{\Delta 1–102}$ enhanced PME activity. (**E**) Immunofluorescence labeling of LM20 shows reduced pectin methylesterification in the SAM region (indicated by arrows) upon *PME5*$^{\Delta 1–102}$ overexpression. Arrowheads in the right panel highlight increased LM20 signals in the cells surrounding the SAM and in the vasculature, suggesting a feedback response to enhanced demethylesterification. Scale bar, 50 μm. (**F**) LM19 staining reveals accumulation of demethylesterified pectin in *PME5*$^{\Delta 1–102}$ overexpression cells. Right panels show higher magnification of the regions outlined in the left panels. Scale bars, 50 μm (left panels) and 5 μm (right panels). (**G**) SAM morphology and *WUS* expression in *pUBQ10::GVG:PME5*$^{\Delta 1–102}$*-GFP* plants after mock or DEX treatments. *WUS* mRNA was detected by in situ hybridization. Scale bars, 40 μm (top panel) and 30 μm (bottom panel). (**H**) Quantification of SAM and primordium size. *PME5*$^{\Delta 1–102}$ overexpression reduced SAM size while promoting flower primordium growth. (**I**) Morphology of *pUBQ10::GVG:PME5*$^{\Delta 1–102}$*-GFP* shoot apices after mock or DEX treatments, showing premature shoot meristem termination upon *PME5*$^{\Delta 1–102}$ overexpression. Scale bar, 2 mm. $^{**}P = 0.0021$ (D) and $^{****}P < 0.0001$ (E and H) (two-tailed *t* test).

1 to 102 (which encode only the signal peptide), thereby decoupling the catalytic activity of PME5 from its mRNA localization (Fig. 3B). Compared to the full-length PME5 protein, $PME5^{\Delta 1-102}$ was distributed in both the cell wall and the cytosol (Fig. 3C). We expressed $PME5^{\Delta 1-102}$ under the control of the DEX-inducible promoter. In the *pUBQ10::GVG:*$PME5^{\Delta 1-102}$*-GFP* plants, DEX application at the shoot apex resulted in enhanced pectin methylesterase activity (Fig. 3D and fig. S12A), leading to a reduction in the levels of mature wall pectin methylesterification (Fig. 3E) and accumulation of demethylesterified pectin distributed in the cell wall and the cytosol of the SAM cells (Fig. 3F). Additionally, we observed increased LM20 immunofluorescence signals in the cells surrounding the SAM and in the vasculature (Fig. 3E, marked by arrowheads), likely reflecting an overcompensation response to maintain pectin homeostasis in these postmeristematic tissues. These results suggest that loss of mRNA nuclear sequestration causes precocious PME5 protein translation and premature pectin demethylesterification.

The $PME5^{\Delta 1-102}$ overexpression plants exhibited smaller SAMs with reduced cell division activity, which terminated prematurely after producing clustered siliques (Fig. 3, G to I, and fig. S12, B and C). RNA sequencing of the induced shoot meristems revealed down-regulation of developmental genes and up-regulation of defense-related genes upon $PME5^{\Delta 1-102}$ overexpression (fig. S13, A to D), suggesting that disruption of pectin homeostasis triggers cell wall integrity responses and immune activation (*54*, *55*). We also detected elevated expression of genes encoding pectin methylesterase inhibitors (*PMEIs*) (fig. S13E), suggesting transcriptional feedback that may contribute to the increased LM20 labeling associated with $PME5^{\Delta 1-102}$ overexpression. The growth defects of the *pUBQ10::GVG:*$PME5^{\Delta 1-102}$*-GFP* plants, along with down-regulation of *WUS* expression (Fig. 3G, bottom panels), indicate that excessive pectin demethylesterification in mature walls compromises shoot meristem activity. This impairment in stem cell maintenance was consistent with the smaller SAMs observed in the *gosamt1 gosamt2* mutant where polysaccharide methylation is greatly reduced (*56*). Therefore, preserving appropriate levels of pectin methylesterification is essential for sustaining functional stem cell niches.

RZ-1B and RZ-1C mediate *PME5* mRNA nuclear sequestration

Our findings thus far established *PME5* mRNA nuclear sequestration as a mechanism underlying pectin methylesterification and stem cell activity. We attempted to identify the protein(s) that mediate *PME5* mRNA nuclear localization. In a semi–in vivo approach (*57*), biotin-labeled *PME5* mRNAs were incubated with nuclear extracts isolated from wild-type plants, and the captured proteins were subjected to affinity purification and mass spectrometry analysis (fig. S14A). Applying thresholds of fold change > 2 and $P < 0.1$, we identified 171 high-confidence interactors, including three putative RNA-binding proteins: AT1G22330, RZ-1B (AT1G60650), and ATKH25 (AT5G15270) (fig. S14B). Subcellular localization assays in tobacco (*Nicotiana tabacum*) leaf cells revealed that among these three proteins, RZ-1B and ATKH25 were localized to the nucleus (fig. S14C). Given our focus on nuclear mRNA localization factors, these two genes were prioritized for functional characterization.

ATKH25 encodes a K homology (KH) domain RNA binding protein, and RZ-1B is a glycine-rich RNA binding protein with a zinc finger domain. Initial characterization of *atkh25* and *rz-1b* single mutants showed no defects in *PME5* mRNA nuclear retention (fig. S14D). In *Arabidopsis*, RZ-1C, a homolog of RZ-1B, localizes to the nucleus and functions redundantly with RZ-1B to regulate shoot meristem development and plant growth (*58*). Therefore, we analyzed the *rz-1b rz-1c* double mutant. Compared to the wild-type plants, *PME5* mRNA nuclear sequestration was largely abolished when *RZ-1B* and *RZ-1C* were simultaneously disrupted, resulting in precocious export into the cytoplasm (Fig. 4A and fig. S14, D and E). These findings demonstrate that RZ-1B and RZ-1C cooperatively contribute to *PME5* mRNA nuclear localization.

RZ-1B and RZ-1C regulate pectin methylesterification and shoot meristem morphogenesis

In vitro RNA pull-down assays confirmed that both RZ-1B and RZ-1C recombinant proteins could bind biotin-labeled *PME5* mRNA, and this interaction was dependent on their RNA recognition motifs (Fig. 4B). Immunoprecipitation of GFP-tagged RZ-1B and RZ-1C proteins with an antibody against GFP revealed specific enrichment of *PME5* mRNA in the shoot meristem cells of *pUBQ10::GFP-RZ-1B* and *pUBQ10::GFP-RZ-1C* transgenic plants (Fig. 4C), demonstrating direct binding and nuclear retention of *PME5* transcripts in vivo.

RZ-1B and RZ-1C are expressed uniformly at the shoot apex (fig. S15A and movies S3 and S4), and both proteins formed discrete nuclear speckles (fig. S15B). In the *rz-1b rz-1c* mutant, there was a ~54% reduction in LM20 labeling signals (Fig. 4D). By contrast, LM19 staining revealed broader signals in both the walls and the cytosol (Fig. 4E), suggesting enhanced pectin demethylesterification. Compared to wild-type, the *rz-1b rz-1c* mutant plants exhibited smaller SAMs with much larger cells, impaired cell division activity, and suppressed *WUS* expression (Fig. 4, F to H, and fig. S15, C to H), indicative of defective meristem maintenance. The cellular defects and altered pectin modification patterns in the *rz-1b rz-1c* double mutant, both of which were rescued by the GFP-RZ-1C fusion protein (fig. S16), recapitulated the phenotypes observed in the $PME5^{\Delta 1-102}$ inducible overexpression lines. Collectively, our data suggest that RZ-1B and RZ-1C act as key regulators linking mRNA nuclear sequestration to pectin dynamics and shoot meristem homeostasis.

Nuclear sequestration of other *PME* family mRNAs

To determine whether mRNA nuclear sequestration represents a general phenomenon within the *PME* family, we analyzed the subcellular localization of additional *PME* transcripts. Owing to the low abundance of most endogenous *PME* transcripts in *Arabidopsis*, we overexpressed *GFP* fusions of 11 *PME* genes (*pUBQ10::GFP-PMEs*) and conducted RNA FISH on the shoot tissues of the transgenic plants. Our results showed that among the *PME* genes examined, five displayed diffuse cytoplasmic localization with low signals, a pattern indicative of rapid transcript turnover. Notably, in addition to *PME5*, six *PMEs* (*PME1*, *PME18*, *PME25*, *PME31*, *PME51*, and *PME53*) predominantly accumulated in the nucleus (fig. S17 and table S2). Therefore, mRNA nuclear retention is a common feature among a subset of *PME* genes.

Evolutionary conservation of spatiotemporal pectin methylesterification patterns across plant species

We further explored pectin methylesterification patterns in the shoot meristems of three phylogenetically divergent plant species: soybean (*Glycine max*), tomato (*Solanum lycopersicum*), and maize (*Zea mays*). Comparative immunofluorescence analysis revealed accumulation of LM20 signals at cell-cell junctions, indicating conservation of methylesterified pectin distribution across these species (fig. S18A). Similarly to that in *Arabidopsis*, LM19 exhibited intense labeling in the newly formed cross walls of dividing cells in these species (fig. S18B). Additional LM19 immunofluorescence signals were detected in the L1 cells of soybean and tomato shoot meristems, suggesting interspecies variation in epidermal pectin patterning. This contrast between conserved cytokinetic pectin modification and distinct epidermal remodeling highlights both universal biomechanical constraints and species-level adaptive specialization. Demethylesterification of new cell wall pectin, consistently detected in various species, supports an evolutionarily conserved spatiotemporal regulation of pectin modification.

Discussion

As critical structural determinants of plant cell wall dynamics, pectins play dual roles in maintaining tissue integrity and enabling developmental plasticity (*18*–*24*, *59*, *60*). Our study uncovers spatial heterogeneity in pectin methylesterification across new and old walls in the

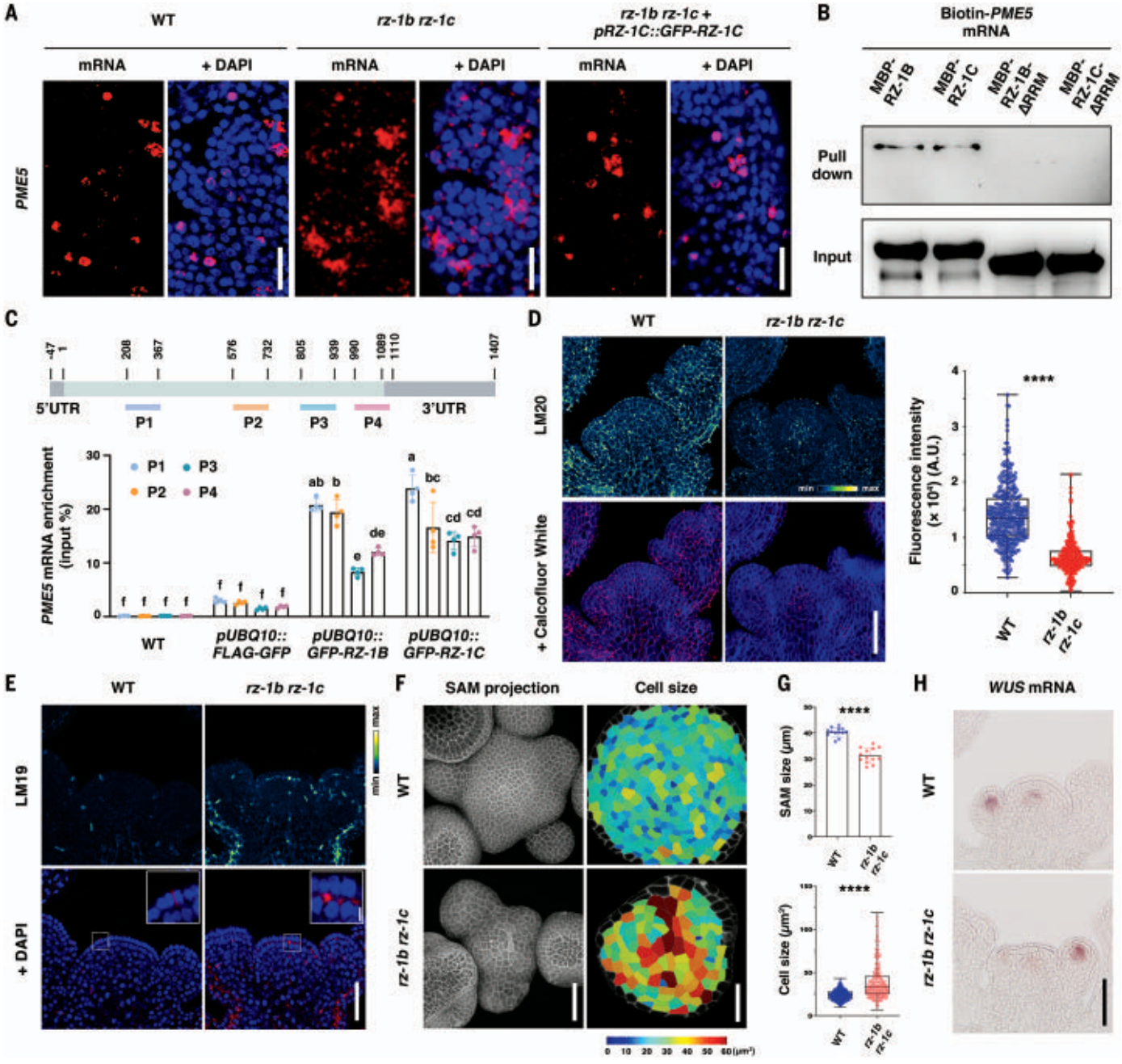


Fig. 4. RZ-1B and RZ-1C contribute to *PME5* mRNA nuclear sequestration and stem cell maintenance. (**A**) Subcellular localization of *PME5* mRNA. Simultaneous mutation in *RZ-1B* and *RZ-1C* led to *PME5* mRNA redistribution into both the nucleus and the cytoplasm, which was rescued by *GFP-RZ-1C*. Scale bars, 20 μm. (**B**) Direct interaction between RZ-1B/1C proteins and *PME5* mRNA revealed by in vitro RNA pull-down assays. Biotin-labeled *PME5* RNA specifically bound to full-length RZ-1B and RZ-1C, whereas truncated variants lacking the RNA recognition motif (ΔRRM) failed to interact. (**C**) RNA immunoprecipitation of the RZ-1B/1C proteins and *PME5* mRNA in vivo. Enrichments of *PME5* RNA fragments were found in *pUBQ10::GFP-RZ-1B* and *pUBQ10::GFP-RZ-1C* compared to WT (Col-0) or *pUBQ10::FLAG-GFP* plants. RNA enrichment was quantified by quantitative reverse transcription polymerase chain reaction. UTR, untranslated region. (**D**) LM20 immunofluorescence of the SAMs, showing reduced methylesterification levels in *rz-1b rz-1c*. Scale bar, 50 μm. (**E**) LM19 immunostaining reveals enhanced pectin demethylesterification in *rz-1b rz-1c*. Insets in the bottom panels show higher magnification of the outlined regions. Scale bars, 50 μm (SAM overview) and 5 μm (inset images). (**F**) Comparison of SAM morphology and cell size of WT and *rz-1b rz-1c*. The L1 cells were segmented in MorphoGraphX and shown as heatmaps. Scale bars, 40 μm (left panel) and 20 μm (right panel). (**G**) Quantification of SAM size ($n = 13$ SAMs for WT and 13 SAMs for *rz-1b rz-1c*) and cell size ($n = 859$ cells for WT and 527 cells for *rz-1b rz-1c*). (**H**) Comparison of *WUS* expression in WT and *rz-1b rz-1c* SAMs by RNA in situ hybridization. Reduced *WUS* mRNA levels in *rz-1b rz-1c* suggests compromised stem cell maintenance. Scale bar, 40 μm. Letters in (C) indicate statistically significant differences between the genotypes, as calculated by two-way analysis of variance with Tukey's multiple comparisons test ($P < 0.05$). ****$P < 0.0001$ (two-tailed *t* test) (D and G).

shoot meristem (fig. S19). Highly methylesterified pectins dominate mature wall regions, consistent with their proposed role in establishing mechanical gradients that preserve stem cell identity (*61*–*63*). By contrast, transient demethylesterification at the cell plates affects division plane orientation (*45*). Cell plate formation is orchestrated by the phragmoplast through gradual scaffolding of new cell wall components (*2*–*4*, *64*). Transient pectin demethylesterification during this process may establish an adaptive microenvironment, enabling stabilization of the forming cell plates in response to mechanical and geometric constraints (*65*, *66*). These findings support that precise control over the establishment and orientation of cell division planes is essential for proper patterning and morphogenesis (*66*).

Nuclear sequestration of *PME5* mRNA represents an unconventional regulatory strategy, which extends beyond previous observations for *Drosophila* nonpolyadenylated *histone* and *Arabidopsis CDC20* mRNAs (*51*, *67*). The nonlinear and sequence-independent interaction of RZ-1B and RZ-1C with *PME5* mRNA suggests that the RNA's secondary or tertiary structure, potentially nucleated by the 1–102 bp region, may play a predominant role in governing its nuclear localization. Our characterization of nuclear *PME5* and additional six *PME* mRNAs implies that this mechanism may be more widespread than previously thought (*51*). The inverse correlation between *PME5* mRNA nuclear retention and cytoplasmic translation efficiency provides insights into how meristematic cells maintain distinct pectin profiles in neighboring wall domains. Such compartmentalized regulation likely contributes to stiffness transitions during cell division (*68*), while ensuring structural continuity in mature wall regions. The spatiotemporal variability in pectin methylesterification, along with its influence on cell division patterns and stem cell maintenance, highlights the importance of precise wall remodeling in plant morphogenesis.

REFERENCES AND NOTES

1. D. J. Cosgrove, *Nat. Rev. Mol. Cell Biol.* **6**, 850–861 (2005).
2. M. R. Facette, C. G. Rasmussen, J. M. Van Norman, *Curr. Opin. Plant Biol.* **47**, 47–55 (2019).
3. Y. Gu, C. G. Rasmussen, *Plant Cell* **34**, 103–128 (2022).
4. D. Delmer, R. A. Dixon, K. Keegstra, D. Mohnen, *Plant Cell* **36**, 1257–1311 (2024).
5. O. Hamant *et al.*, *Science* **322**, 1650–1655 (2008).
6. B. Landrein, G. Ingram, *J. Exp. Bot.* **70**, 3507–3519 (2019).
7. F. Zhao *et al.*, *Plant Physiol.* **181**, 1191–1206 (2019).
8. D. Reinhardt *et al.*, *Nature* **426**, 255–260 (2003).
9. M. G. Heisler *et al.*, *Curr. Biol.* **15**, 1899–1911 (2005).
10. R. S. Smith *et al.*, *Proc. Natl. Acad. Sci. U.S.A.* **103**, 1301–1306 (2006).
11. H. Jönsson, M. G. Heisler, B. E. Shapiro, E. M. Meyerowitz, E. Mjolsness, *Proc. Natl. Acad. Sci. U.S.A.* **103**, 1633–1638 (2006).
12. F. Besnard *et al.*, *Nature* **505**, 417–421 (2014).
13. A. J. Fleming, S. McQueen-Mason, T. Mandel, C. Kuhlemeier, *Science* **276**, 1415–1418 (1997).
14. A. Peaucelle *et al.*, *Curr. Biol.* **21**, 1720–1726 (2011).
15. V. Mirabet, P. Das, A. Boudaoud, O. Hamant, *Annu. Rev. Plant Biol.* **62**, 365–385 (2011).
16. E. Coen, D. J. Cosgrove, *Science* **379**, eade8055 (2023).
17. D. Mohnen, *Curr. Opin. Plant Biol.* **11**, 266–277 (2008).
18. C. T. Anderson, J. Pelloux, *Annu. Rev. Plant Biol.* **76**, 85–113 (2025).
19. F. Micheli, *Trends Plant Sci.* **6**, 414–419 (2001).
20. W. G. Willats *et al.*, *J. Biol. Chem.* **276**, 19404–19413 (2001).
21. P. Fayant *et al.*, *Plant Cell* **22**, 2579–2593 (2010).
22. Y. Chebli, M. Kaneda, R. Zerzour, A. Geitmann, *Plant Physiol.* **160**, 1940–1955 (2012).
23. C. Xiao, C. Somerville, C. T. Anderson, *Plant Cell* **26**, 1018–1035 (2014).
24. S. Wolf, G. Mouille, J. Pelloux, *Mol. Plant* **2**, 851–860 (2009).
25. J. Safran *et al.*, *Plant Cell* **35**, 3073–3091 (2023).
26. K. T. Haas, R. Wightman, E. M. Meyerowitz, A. Peaucelle, *Science* **367**, 1003–1007 (2020).
27. S. Wolf *et al.*, *Proc. Natl. Acad. Sci. U.S.A.* **111**, 15261–15266 (2014).
28. S. Amsbury *et al.*, *Curr. Biol.* **26**, 2899–2906 (2016).
29. K. Jonsson *et al.*, *Curr. Biol.* **31**, 1154–1164.e3 (2021).
30. G. Wachsman, J. Zhang, M. A. Moreno-Risueno, C. T. Anderson, P. N. Benfey, *Science* **370**, 819–823 (2020).
31. S. Moussu *et al.*, *Science* **382**, 719–725 (2023).
32. S. Schoenaers *et al.*, *Nat. Plants* **10**, 494–511 (2024).
33. J. P. Knox, P. J. Linstead, J. King, C. Cooper, K. Roberts, *Planta* **181**, 512–521 (1990).
34. W. G. Willats *et al.*, *Carbohydr. Res.* **327**, 309–320 (2000).
35. M. H. Clausen, W. G. Willats, J. P. Knox, *Carbohydr. Res.* **338**, 1797–1800 (2003).
36. Y. Verhertbruggen, S. E. Marcus, A. Haeger, J. J. Ordaz-Ortiz, J. P. Knox, *Carbohydr. Res.* **344**, 1858–1862 (2009).
37. K. Thorne, B. R. Urbanowicz, M. G. Hahn, in *Plant Cell Walls: Research Milestones and Conceptual Insights*, A. Geitmann, Ed. (CRC Press, 2024), pp. 206–236.
38. C. M. Rounds, E. Lubeck, P. K. Hepler, L. J. Winship, *Plant Physiol.* **157**, 175–187 (2011).
39. A. J. Bidhendi, B. Altartouri, F. P. Gosselin, A. Geitmann, *Cell Rep.* **28**, 1237–1250.e6 (2019).
40. J. Pelloux, C. Rustérucci, E. J. Mellerowicz, *Trends Plant Sci.* **12**, 267–277 (2007).
41. M. A. Atmodjo, Z. Hao, D. Mohnen, *Annu. Rev. Plant Biol.* **64**, 747–779 (2013).
42. W. Yang *et al.*, *Curr. Biol.* **26**, 1404–1415 (2016).
43. F. Gu *et al.*, *Plant Cell* **28**, 1722–1737 (2016).
44. W. Lukowitz, U. Mayer, G. Jürgens, *Cell* **84**, 61–71 (1996).
45. Z. Li *et al.*, *Development* **148**, dev199504 (2021).
46. A. M. Mills, C. G. Rasmussen, *J. Cell Sci.* **135**, jcs260127 (2022).
47. C. Schuster *et al.*, bioRxiv 2024.07.08.602577 (2024).
48. M. Ito *et al.*, *Plant Cell* **10**, 331–341 (1998).
49. W. Yang *et al.*, *Science* **371**, 1350–1355 (2021).
50. R. Schwab, S. Ossowski, M. Riester, N. Warthmann, D. Weigel, *Plant Cell* **18**, 1121–1133 (2006).
51. W. Yang, R. Wightman, E. M. Meyerowitz, *Mol. Cell* **68**, 1108–1119.e3 (2017).
52. H. Washida *et al.*, *Plant Cell Physiol.* **50**, 1710–1714 (2009).
53. R. Sorenson, J. Bailey-Serres, *Proc. Natl. Acad. Sci. U.S.A.* **111**, 2373–2378 (2014).
54. L. Vaahtera, J. Schulz, T. Hamann, *Nat. Plants* **5**, 924–932 (2019).
55. S. Wolf, *Annu. Rev. Plant Biol.* **73**, 323–353 (2022).
56. H. Temple *et al.*, *Nat. Plants* **8**, 656–669 (2022).
57. Y. F. Zhou *et al.*, *Nat. Commun.* **12**, 6525 (2021).
58. Z. Wu *et al.*, *Plant Cell* **28**, 55–73 (2016).
59. K. T. Haas, R. Wightman, A. Peaucelle, H. Höfte, *Cell Surf.* **7**, 100054 (2021).
60. J. Du, C. T. Anderson, C. Xiao, *Nat. Plants* **8**, 332–340 (2022).
61. P. Milani *et al.*, *Plant J.* **67**, 1116–1123 (2011).
62. D. Kierzkowski *et al.*, *Science* **335**, 1096–1099 (2012).
63. S. Robinson *et al.*, *J. Exp. Bot.* **64**, 4729–4744 (2013).
64. F. Miart *et al.*, *Plant J.* **77**, 71–84 (2014).
65. A. L. Cleary, L. G. Smith, *Plant Cell* **10**, 1875–1888 (1998).
66. E. Schaefer *et al.*, *Science* **356**, 186–189 (2017).
67. C. Iampietro *et al.*, *Dev. Cell* **29**, 468–481 (2014).
68. A. Bonfanti *et al.*, *Proc. Natl. Acad. Sci. U.S.A.* **120**, e2302985120 (2023).
69. P. Barbier de Reuille *et al.*, *eLife* **4**, 05864 (2015).

ACKNOWLEDGMENTS

We thank A. Peaucelle for insightful discussions during project development. We are grateful to O. Hamant, C. Dean, J.-W. Wang, Z. Wu, and A. Gurzadyan for discussions and comments. We thank R. Smith for suggestions on MorphoGraphX analysis, G. Jürgens for the *KNOLLE-GFP* reporter, Z. Wu for the *rz-1b rz-1c* mutant and *pRZ-1C::GFP-RZ-1C* complementation seeds, and S. Wang for mass spectrometry analysis. **Funding:** This work was supported by CAS Strategic Priority Research Program (Type-B; XDB0630200 and XDB27030107), the CAS Project for Young Scientists in Basic Research (YSBR-108), National Key Research and Development Program of China (2022YFF1001803), and the National Natural Science Foundation of China (NSFC) (32170325). R.W. acknowledges support from the Leverhulme Trust (grant RPG-2015-285). **Author contributions:** Conceptualization: W.Y. Methodology: X.Z., X.C., Y.L., Y.Z., G.G., M.L., Y.F., H.H., W.C., R.W., M.G., Y.D., and W.Y. Investigation: X.Z., X.C., Y.L., Y.Z., G.G., M.L., Y.F., Y.G., H.H., R.W., M.G., Y.D., and W.Y. Visualization: X.Z., X.C., W.Y., Y.Z., M.L., H.H., W.C., and R.W. Validation: X.Z., X.C., Y.L., Y.Z., and W.Y. Funding acquisition: W.Y. Project administration: X.Z., and W.Y. Supervision: W.Y. Writing – original draft: X.Z., H.H., and W.Y. Writing – review & editing: X.Z., H.H., R.W., and W.Y. **Competing interests:** The authors declare no competing interests. **Data and materials availability:** RNA sequencing data are available at the NCBI Gene Expression Omnibus (GEO; https://www.ncbi.nlm.nih.gov/geo/) under accession number GSE303053. All data are available in the main text or the supplementary materials, and all materials are available upon request. **License information:** Copyright © 2025 the authors, some rights reserved; exclusive licensee American Association for the Advancement of Science. No claim to original US government works. https://www.science.org/about/science-licenses-journal-article-reuse

SUPPLEMENTARY MATERIALS

science.org/doi/10.1126/science.ady4102
Materials and Methods; Figs. S1 to S19; Tables S1 to S3; References (*70*, *71*); Reproducibility Checklist; Data S1 and S2; Movies S1 to S4

Submitted 23 April 2025; accepted 9 October 2025

10.1126/science.ady4102



z- dbDNA™ Technology

Touchlight, a leader in synthetic DNA manufacturing, announced today the use of its proprietary z- dbDNA™ technology as a critical starting material in the manufacture of a cutting-edge gene therapy in a U.S.-based clinical study.

This development underscores the transformative potential of dbDNA in driving the development of safe, effective, and scalable therapies. It follows Touchlight's receipt in 2025 of a GMP certificate for the production of dbDNA at its state-of-the-art facility in Hampton, UK. dbDNA's unique design, a linear, closed-end DNA construct free of bacterial sequences, ensures high purity and stability, making it an ideal platform for gene therapy applications. Unlike conventional plasmid DNA, dbDNA is manufactured using a cell-free process that is faster and more scalable, whilst eliminating the risk of antibiotic resistance or other unwanted contaminants. These characteristics of dbDNA align with regulatory guidelines and the growing need for safer, more efficient biomanufacturing processes. Touchlight remains committed to empowering researchers and biopharmaceutical companies with the tools they need to push the boundaries of genetic medicine. The company's ongoing collaborations and innovations continue to support the development of life-changing therapies for patients worldwide.

Touchlight
For info: +44 20 8481 9200
info@touchlight.com

Quick Differentiation Kits for iPSC derived neurons

Amsbio announces an innovative range of induced pluripotent stem cell (iPSC) kits for researchers requiring a rapid, reproducible, and scalable means of generating specific neural cell types without sacrificing cell purity. Streamlined protocols allow researchers to efficiently differentiate iPSCs into target neural cells within just 1-2 weeks. Scientists can now produce neurons as needed, ensuring greater flexibility and control in design of disease modelling, regenerative medicine, and drug screening experiments. Avoiding use of animal-derived components, these kits support human-relevant research without reliance on animal models. These easy-to-use kits produce differentiated cells with no genetic footprint left behind, via a proprietary non-integrating transcription factor-based approach. Users can choose from Sendai virus or synthetic mRNA formats. Alternatively, diseased and control cell lines that have already been differentiated are available for all the below-mentioned neural cell types. Created using human iPS cells made under license from The California Institute for Regenerative Medicine (CIRM), the Quick-Neuron™ Excitatory differentiation kit sets a new benchmark for producing highly pure populations of excitatory/glutamatergic neurons. Furthermore, patch clamp experiments showed these neurons generate spontaneous action potentials. The Quick-Neuron™ Dopaminergic Differentiation kit uses synthetic mRNA to enable rapid, reproducible differentiation of iPSCs into highly pure dopaminergic neuron populations. Similarly, the new Quick-Neuron™ GABAergic Differentiation Kit enables easy and efficient differentiation of your iPS cell line into GABAergic neurons in just 10 days using synthetic mRNA. Amsbio also offers a range of high-quality human iPSC-derived GABAergic neurons. This exciting new range also includes Quick-Neuron™ Cholinergic Differentiation Kits for rapid, easy, and efficient differentiation of iPS cells into cholinergic neurons. All cells produced by our kits have been validated for expression of neuronal markers and display typical neurite outgrowth.

AMS Biotechnology
For info: +44-1235-828200
www.amsbio.com

High-quality synthetic DNA solutions

4basebio PLC (AIM: 4BB) ("4basebio"), a specialist in synthetic DNA manufacturing and nucleic acids for next-generation therapeutics, announces refreshed branding and the launch of its new website, reflecting the company's continued growth and success in this rapidly advancing field. Since completing its £40 million investment in November 2024, 4basebio has achieved several major milestones in its mission to deliver scalable, high-quality synthetic DNA solutions to the global market. Notably, in April this year, the company received MHRA GMP certification for the manufacture and supply of synthetic DNA for clinical use. The company's redesigned website provides a more intuitive access point for partners and customers, providing detailed information and support for 4basebio's expanding capabilities across synthetic DNA, mRNA, gene editing, and plasmid-free manufacturing. With a newly curated content hub, users can also access a range of specialist resources, including data, whitepapers, articles, case studies, and more. The rebrand aligns with 4basebio's broader commercial strategy, which includes an increased presence at industry events, expanded customer engagement efforts, and a continued focus on delivering high-quality synthetic DNA starting materials for next-generation genetic medicines.

4basebio PLC
For info: +44 (0) 1223 967943
info@4basebio.com

IVD Mimix

Revvity, Inc. announced the launch of three Mimix™ reference standards for IVD use, designed for monitoring of next-generation sequencing (NGS) or droplet digital polymerase chain reacting (ddPCR) assays designed to detect somatic mutations in genomic DNA (gDNA) from human samples. These cell line-derived reference standards have undergone appropriate design controls to meet U.S. Food and Drug Administration (FDA) regulatory requirements, which helps laboratories integrate them into existing workflows to support monitoring test performance, assay variation, and to help identify increases in random or systemic errors. Offering the Mimix reference standards for IVD indicates the products have been developed and manufactured in accordance with applicable quality system requirements, allowing for improved reliability and precision of these reference standards. The three Mimix reference standards cover key cancer testing applications. Leveraging 14 years of experience in developing oncology reference standards, Revvity's Mimix controls are derived from human cell lines rather than synthetic sources, which helps maintain genomic complexity and more closely mimic patient samples.

Revvity
For info: 781-462-5126
chet.murray@revvity.com

Electronically submit your new product description or product literature information! Go to www.science.org/about/new-products-section for more information.

Newly offered instrumentation, apparatus, and laboratory materials of interest to researchers in all disciplines in academic, industrial, and governmental organizations are featured in this space. Emphasis is given to purpose, chief characteristics, and availability of products and materials. Endorsement by *Science* or AAAS of any products or materials mentioned is not implied. Additional information may be obtained from the manufacturer or supplier.

ScienceCareers.org
ScienceCareers

What's Your Next Career Move?

From networking to mentoring to evaluating your skills, find answers to your career questions on *Science* Careers

To view the complete collection, visit **ScienceCareers.org/booklets**



ScienceCareers
FROM THE JOURNAL SCIENCE AAAS

ScienceCareers.org
ScienceCareers
OPPORTUNITIES IN CHINA

郑州大学
ZHENGZHOU UNIVERSITY

Zhengzhou University

welcomes outstanding scholars worldwide



I.Introduction to Zhengzhou University

Zhengzhou University (ZZU), located in Zhengzhou, Henan Province, China, is a prestigious higher education institution with a rich historical heritage and beautiful natural surroundings. As a "Double First-Class" Initiative university supported by the Chinese government, Zhengzhou University is one of China's key "211 Project" universities and a Ministry-Province Co-Constructed University. It also holds the distinction of being the largest higher education institution in Asia.

Zhengzhou University (ZZU) now has 13 major discipline categories, including Philosophy, Economics, Law, Education, Literature, History, Science, Engineering, Agriculture, Medicine, Management, Art and Interdisciplinary Studies, also has excellent research capabilities, ranking 203rd globally in the 2025-2026 U.S. News World University Rankings. It has 5 ESI top 1‰ disciplines: Chemistry, Materials Science, Clinical Medicine, Engineering, and Pharmacology & Toxicology; In addition, Clinical Medicine, Chemistry, Materials Science, Engineering, Pharmacology & Toxicology, Biology & Biochemistry, Molecular Biology & Genetics, Neuroscience & Behavior, Immunology, Environment & Ecology, Physics, Social Sciences, General Computer Science, Agricultural Sciences, Microbiology, Plant & Animal Science, Mathematics, Psychiatry & Psychology, and Geosciences have entered the ESI top 1% globally.

II. Recruitment

Global Top Scholars/Talents

ZZU is seeking talents who have achieved systematic and innovative accomplishments in their field, made significant contributions, and possess extensive international academic influence, including recipients of prestigious international academic awards or leading scholars of equivalent caliber worldwide.

Leading Academics/Scholars

ZZU is seeking candidates with profound academic expertise and visionary scholarly perspectives, who have achieved internationally recognized significant academic accomplishments in their research field and are capable of leading their discipline to surpass or set international advanced standards as a disciplinary leader. Prior experience holding the position of an associate professor (or an equivalent or higher position) at renowned overseas universities or research institutions is required; however, exceptionally outstanding candidates may be considered with relaxed qualifications under special circumstances.

Outstanding Young Scholars

ZZU is seeking candidates who hold a doctoral degree from a prestigious domestic or international university, with academic qualifications comparable to those of an assistant professor at a world-class university, and demonstrating the potential to become a leading talent.

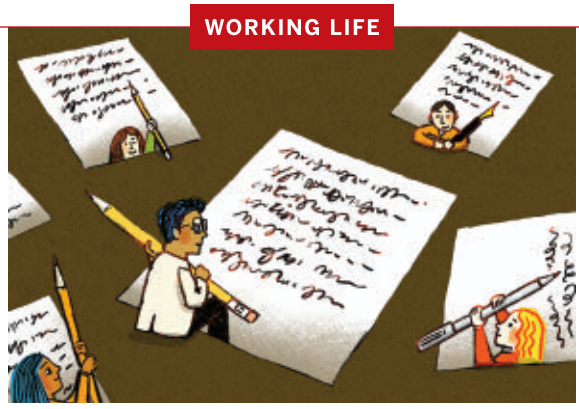
In addition to the above, the Excellent Youth Science Fund Project (Overseas) of the National Natural Science Foundation of China (NSFC) is a scientific fund project launched by the NSFC in 2021, which mainly targets the fields of natural sciences and engineering technology. Successful applicants will receive joint research support funds from the NSFC, Henan Province, and Zhengzhou University with a maximum total of 9 million RMB, and will enjoy globally competitive job compensation simultaneously. Zhengzhou University cordially invites outstanding young talents to join us and submit applications for the Excellent Youth Science Fund Project (Overseas) through us.

III. How to Apply

Please send the CV along with a cover letter stating the research discipline and the recruitment position applied for to:

rcb@zzu.edu.cn. (Global Top Scholars/Talents, Leading Academics/Scholars, Applicants for the NSFC Fund Project)

rczp@zzu.edu.cn. (Outstanding Young Scholars)



A writing pact

Arjav Shah

It was 10 p.m. on a winter night in Boston and I was sitting in my department's common lounge, staring at a blank Word document. My thesis proposal deadline loomed. I hadn't written a word, despite weeks of thinking. Earlier that evening, when I met another Ph.D. student, Sachin, for our regular monthly dinner, he was equally stuck—buried under the weight of a fellowship application. So, we made a pact: After dinner, we would sit together, laptops open, phones away, no excuses. It was the spark I needed to finally start writing.

It often takes me weeks or even months to begin writing something, no matter what it is—a research proposal, a manuscript, even this essay. I tend to put it off, reasoning that at some point I will land in that perfect moment where my mind, body, and external environment are all in sync for thoughts to flow. But that moment doesn't always arrive, and I end up putting together a hastily written piece only when the deadline becomes dangerously close.

Sachin and I both grew up in India, where competition is fierce and striving for excellence is prized, and we carried a perfectionist mindset into graduate school. There we faced new pressures: adjusting to a new academic system while navigating the limited fellowships and opportunities available to international students. Half-hearted proposals wouldn't do. We didn't want our first drafts to be "good enough"; we wanted them to be flawless. But the result was paralysis.

We set out to make a change on that cold winter night. Having someone beside me changed everything. It was a means to ensure accountability. Seeing Sachin write forced me to put down my phone in embarrassment when I was tempted to scroll, and focus on work myself.

Our informal pact soon became a habit. We scheduled weekly 90-minute sessions, which gave us a distraction-free space to write something, however imperfect. The length was intentional: long enough to get into the zone, but short enough to fit it into our schedules.

We began each session by naming a small goal—write a paragraph, put together a figure caption, tackle a tricky transition, or complete some other well-defined task. That 5-minute planning ritual made the rest of the session surprisingly productive. Instead of worrying about writing an entire proposal, we only had to finish a tiny piece of it.

Those small wins built momentum and confidence. A few sentences grew into paragraphs, then into complete proposals—with enough time before the deadline to get feedback from mentors and colleagues. Writing never got easy, as I'd hoped, but it became less isolating and more productive.

Sachin and I had both seen our peers face similar challenges and wanted to bring this experience to a broader group. So, 2 years after we began our weekly meetups, we launched peer co-working sessions for second-year Ph.D. students in our department who were preparing their thesis proposals. Each week, a group gathered in a quiet seminar room with laptops, coffee, and pastries. We started with 5 minutes of goal setting, followed by 75 minutes of silent, focused writing, and ended with a short reflection period.

The room often felt tense and serious at first. But as people opened up during the reflection period, a sense of relief spread: None of us was alone. One student told us the sessions "took away the fear of the blank page." Another mentioned they used the time to tackle the hardest tasks because they knew the peer support would keep them honest.

Over 2 years, dozens of students have now attended. What began as two overwhelmed students staring at blank screens has grown into a small community that makes writing less lonely. Our experience showed us that accountability, camaraderie, and a shared sense of purpose can lower the barriers that make writing so intimidating.

Graduate programs often focus on teaching students how to do research, but they rarely offer formal support for communicating it. Organizing and promoting peer writing groups like ours could change that. Because no one should have to write alone. □

Arjav Shah is a recent Ph.D. graduate of the Massachusetts Institute of Technology and founder and CEO of Drosera Biotechnologies Inc.
Send your career story to SciCareerEditor@aaas.org.

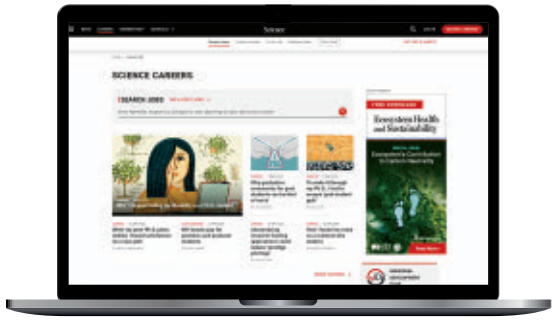
ILLUSTRATION: ROBERT NEUBECKER



Let *Science* Careers help advance your career.

- Register for a free online account on **ScienceCareers.org**.
- Search hundreds of job postings.
- Sign up to receive job alerts that match your criteria.
- Upload your resume into our database to connect with employers.
- Watch one of our many webinars on different career topics such as job searching, networking, and more.
- Download our career booklets, including Career Basics, Careers Beyond the Bench, and Developing Your Skills.
- Complete a personalized career plan at "my IDP."
- Read relevant career advice articles from our library of thousands.

Visit **ScienceCareers.org** today — all resources are free



SCIENCECAREERS.ORG

ScienceCareers
FROM THE JOURNAL SCIENCE AAAS

TRILLIONS OF MICROBES ONE ESSAY

The NOSTER *Science* Microbiome Prize is an international prize that rewards innovative research by investigators who have completed their terminal degree in the last 10 years and are working on the functional attributes of microbiota. The research can include any organism with the potential to contribute to our understanding of human or veterinary health and disease, or to guide therapeutic interventions. The winner and finalists will be chosen by a committee of independent scientists chaired by a senior editor of *Science*. The top prize includes complimentary membership to AAAS, an online subscription to *Science*, and USD 25,000. Submit your research essay today.



Djenet Bousbaine, Ph.D.
2025 Winner

NOSTER | Science
MICROBIOME
PRIZE

Apply by 14 February 2026 at www.science.org/noster

Sponsored by Noster Inc.